Holography and extreme phases of matter

Edwan Préau

Université Paris Cité

École doctorale des Sciences de la Terre et de l'Environnement et Physique de l'Univers - ED560

Laboratoire AstroParticules et Cosmologie (APC) - Groupe Théorie

Holography and extreme phases of matter

Par Edwan Préau

Thèse de doctorat de Physique de l'Univers

Dirigée par Elias Kiritsis

Présentée et soutenue publiquement le 23 Juin 2023

Devant un jury composé de :

Marika Taylor	Professeure (University of Southampton)	Rapporteure
David Mateos	Professeur (Universitat de Barcelona)	Rapporteur
Daniele Steer	Professeure (Université Paris Cité)	Examinatrice
Giuseppe Policastro	Directeur de Recherche (École Normale Supérieure)	Examinateur
Constantin Bachas	Directeur de recherche (École Normale Supérieure)	Examinateur
Francesco Bigazzi	Professeur (University of Florence)	Examinateur
Elias Kiritsis	Directeur de recherche (Université Paris Cité)	Directeur de thèse
Francesco Nitti	Professeur (Université Paris Cité)	Membre invité

Acknowledgements

There are several people that I would like to thank for the role they played during the writing of this thesis.

First of all, I warmly thank my Phd supervisors Elias Kiritsis and Francesco Nitti, for suggesting this stimulating research topic and for all the useful advice and knowledge that they provided me. I also thank Matti Järvinen for our continuous collaboration during these three years, and for greeting me at APCTP in Pohang.

I am grateful to Micaela Oertel for sharing her knowledge of neutrino transport in neutron stars and answering my numerous questions, and to Niko Jokela and Aleksi Vuorinen, for interesting discussions and for hosting me at the University of Helsinki during the time when this thesis was being written.

I would like to express my gratitude to David Mateos and Marika Taylor for accepting to give of their time to review my thesis, and to Daniele Steer, Giuseppe Policastro, Constantin Bachas and Francesco Bigazzi for taking part in the jury for my defense.

I thank Julien Serreau and Costas Bachas for taking part in my Phd monitoring committee, as well as the members of the doctoral school, especially Alessandra Tonazzo, Alissa Marteau and Irena Nikolic. In addition, I am grateful to Sabine Tesson for her kindness and her help with administrative tasks.

It is a pleasure to thank my fellow Phd students at APC for the good time spent together, and especially the students in the theory group for our lively discussions. I thank Pierre Auclair, Hugo Roussille, Jani Kastikainen, Valentin Nourry, Konstantin Leyde, Pilar Ivanez-Ballesteros, Thomas Colas and Théo Boyer, with special thanks to Hugo for his help with Mathematica.

My final thanks go to my parents for encouraging me in the path that I have chosen, and to Sujin, for bringing joy into my life.

Abstract

In this thesis, we address two topics related to the physics of dense baryonic matter in the V-QCD holographic model for QCD. In a first part, the single V-QCD baryon solution is analyzed. An important part of this analysis is the construction of the five-dimensional Tachyon-Chern-Simons action. The most general form of the Tachyon-Chern-Simons 5-form, compatible with symmetries and flavor anomalies, is determined. It is the sum of a non-trivial gauge-invariant 5-dimensional form and a non-invariant closed 5-form that reproduces the flavor anomalies. The single baryon solution is then considered, and identified as a bulk axial instanton. The baryon ansatz and the field equations are derived and the boundary conditions are determined, which ensure that the solution has finite boundary energy and unit baryon charge. The boundary baryon number, which is computed from the universal (closed) part of the Tachyon-Chern-Simons action, is shown to coincide with the bulk axial instanton number. Finally, we present a numerical computation for the baryon solution. The spectrum of spin and isospin modes is also computed by quantizing the light fluctuations around the baryon. It is shown that there is a partial restoration of chiral symmetry at the baryon center. In a second part, we initiate the study of neutrino transport in holography, with the eventual project of extending the analysis to V-QCD. As a first step, a (toy) model for cold and luke-warm strongly-coupled nuclear matter at finite baryon density is used to study neutrino transport. The complete charged current two-point correlators are computed in the strongly-coupled medium and their impact on neutrino transport is analyzed. The full result is compared with various approximations for the current correlators and the distributions, including the degenerate approximation, the hydrodynamic approximation as well as the diffusive approximation and we comment on their successes. Further improvements are discussed.

Keywords— Holography, dense matter, QCD, flavor anomalies, instantons, baryons, neutrino transport

Résumé court

Dans cette thèse, nous abordons deux sujets liés à la physique de la matière baryonique dense dans le modèle de QCD holographique V-QCD. Dans une première partie, la solution de baryon unique est analysée dans le modèle V-QCD. Une partie importante de cette analyse est la construction de l'action de Chern-Simons tachyonique en cinq dimensions. La forme la plus générale de la 5-forme de Chern-Simons tachyonique, compatible avec les symétries et les anomalies de saveur, est déterminée. C'est la somme d'une forme à 5 dimensions invariante de jauge non triviale et d'une forme à 5 dimensions fermée non invariante, qui reproduit les anomalies de saveur. La solution de baryon unique est ensuite considérée et identifiée comme un instanton axial dans le bulk. L'ansatz pour le baryon et les équations du mouvement sont établies et les conditions aux limites sont déterminées, ce qui garantit que la solution a une énergie de bord finie et un nombre baryonique égal à 1. Le nombre baryonique du bord, qui est calculé à partir de la partie universelle (fermée) de l'action de Chern-Simons tachyonique, coïncide avec le nombre instantonique axial du bulk. Enfin, nous présentons un calcul numérique pour la solution baryonique. Le spectre des modes de spin et isospin est également calculé en quantifiant les fluctuations de basse énergie autour du baryon. Nous mettons en évidence une restauration partielle de la symétrie chirale au centre du baryon. Dans une deuxième partie, nous initions l'étude du transport des neutrinos en holographie, avec le projet à termes d'étendre l'analyse à la V-QCD. Dans un premier temps, un modèle(-jouet) pour la matière nucléaire fortement couplée, froide ou tiède, à densité baryonique finie, est utilisé pour étudier le transport des neutrinos. Les corrélateurs à deux points complets du courant chargé sont calculés dans le milieu fortement couplé et leur impact sur le transport des neutrinos est analysé. Le résultat est comparé à diverses approximations pour les corrélateurs des courants et les distributions statistiques, y compris l'approximation dégénérée, l'approximation hydrodynamique ainsi que l'approximation diffusive et nous commentons leurs succès. Des pistes d'amélioration sont discutées.

Mots-clés — Holographie, matière dense, QCD, anomalies de saveur, instantons, baryons, transport de neutrinos

Résumé de la thèse

La matière qui compose le monde phénoménologique peut exister dans diverses phases, qui sont caractérisées par des propriétés physiques différentes. Lorsque que les conditions de pression ou de température sont modifiées, la matière peut être amenée à changer de phase, dans un processus que l'on appelle une transition de phase. L'exemple le plus célèbre de transition de phase est bien sûr l'ébullition de l'eau, par laquelle l'eau passe de l'état liquide à l'état gaseux.

La transition liquide-gaz de l'eau est une conséquence de la brisure des liaisons hydrogène entre les molécules d'eau, du fait de l'injection d'énergie thermique. De manière plus générale, les transitions de phase se produisent typiquement lorsque la température, ou la pression, est de l'ordre de l'échelle des interactions qui contrôlent la dynamique microscopique du système. L'interaction la plus forte que nous connaissions est *l'interaction forte*, qui lie entre eux les nucléons dans les noyaux atomiques, et les quarks et gluons élémentaires au sein des nucléons. L'échelle de l'interaction forte est de l'ordre de 100 MeV, ce qui correspond à des températures extrêmes d'environ 10^{12} K, et des densités massiques de l'ordre de la densité de saturation nucléaire $\rho_0 \simeq 2.5 \times 10^{17}\,\mathrm{kg.m^{-3}}$. À titre de comparaison, cela correspond à des températures cent mille fois plus élevées qu'au cœur du soleil, et des densités 10^{12} fois plus grandes.

À ce jour, notre connaissance des phases que prend la matière dans des conditions si extrêmes de température et de densité reste incomplète, aussi bien du point de vue théorique qu'expérimental. Ce problème est intrinsèquement lié à l'objectif plus général de déterminer les propriétés de l'interaction forte, décrite par la théorie de la chromodynamique quantique (QCD). Par ailleurs, cette question est plus qu'une simple curiosité théorique. En effet, on sait qu'il existe des systèmes macroscopiques observables où ces conditions sont réalisées. D'une part, de telles températures ont dû exister à un moment dans l'histoire de l'univers primordial. D'autre part, ces immenses densitées sont a priori atteintes au cœur des étoiles à neutron.

Malgré la simplicité conceptuelle de la QCD, le caractère fortement couplé de la théorie à des énergies bien en-dessous d'une centaine de MeV rendent les prédictions théoriques difficiles dans ce régime. Il existe cependant des méthodes rigoureuses qui fournissent une description précise de la matière de QCD dans certaines régions de son diagramme de phase. Pour des énergies bien au-dessus de 100 MeV, la matière de QCD est bien comprise dans le cadre de la QCD perturbative, tandis que sa description à basse énergie (bien en dessous de 100 MeV) est contrôlée par la théorie effective chirale. En plus de ces deux approches, l'avancée la plus récente dans notre compréhension du diagramme de phase de la QCD est venue de la méthode numérique de la QCD sur réseau, qui est adaptée pour décrire le régime de basse densité.

La région qu'aucune des méthodes susmentionnées n'est capable de décrire correspond au régime de la QCD dense et froide, à des densités entre environ 2 et 40 fois la densité nucléaire ρ_0, et grande devant l'échelle de la température. Cette région du diagramme de

phase est d'autant plus intéressante qu'elle correspond au régime atteint dans les étoiles à neutron. Les observations d'étoiles à neutron offrent donc une opportunité sans précédent d'obtenir des données expérimentales sur les propriétés de la matière dense, et ont déjà commencé à contraindre ces propriétés.

Bien que les données issues des étoiles à neutron soient amenées à jouer un rôle majeur pour améliorer notre compréhension de la matière dense, il est d'égale importance de développer des outils théoriques pour décrire la physique dans ce régime. Du fait du couplage fort, une méthode non-perturbative est nécessaire. Dans ce travail, l'approche que nous avons suivie est celle de la correspondance holographique.

La correspondance holographique fournit un outil pour étudier les problèmes de couplage fort en théorie quantique des champs. Les principes fondamentaux de la correspondance et de son application à la QCD sont résumés brièvement dans le chapitre 2 de cette thèse. La méthode holographique associe à une certaine théorie quantique en quatre dimensions, une théorie duale semi-classique en cinq dimensions, qui inclut le champ gravitationnel. La dimension supplémentaire du dual gravitationnel est interprétée comme l'échelle d'énergie dans la théorie quantique. Ce qui rend la méthode non-perturbative est que le dual d'une théorie fortement couplée est faiblement courbé, de telle manière que la théorie gravitationnelle peut être simplement décrite par la relativité générale. Ainsi, des observables quantiques non-perturbatives peuvent être déterminées en procédant à la place à un calcul de relativité générale.

La capacité de l'holographie à adresser des problèmes fortement couplés a rapidement fait de la QCD l'un de ses objets principaux, avec pour résulat l'élaboration des premiers modèles de QCD holographique. Bien que l'exemple originel de correspondence ait été formulé pour une théorie supersymétrique et conforme, des méthodes ont été pensées pour briser à la fois supersymétrie et invariance conforme. De plus, l'étude des boucles de Wilson en holographie a permis de déterminer les conditions nécessaires à la réalisation d'une phase confinée. Tous ces éléments entrent dans la construction du modèle de Sakai et Sugimoto (WSS), que nous présentons dans la deuxième section du chapitre 2.

Le modèle WSS est probablement le plus abouti des modèles top-down de QCD holographique. Il contient à la fois les secteurs de couleur et de saveur, avec des spectres de mésons et boules de glu globalement proches des donnés expérimentales ou des résulats de la QCD sur réseau. Il inclut également des états baryoniques, dont la construction est prsentée dans le chapitre 2. Le modèle a cependant plusieurs limitations, parmi lesquelles la trivialité du groupe de renormalisation pour la constante de couplage de Yang-Mills, et l'absence de réaction du secteur de saveur sur la couleur. Pour dépasser ces limitations, la meilleure stratégie à ce stade est de considérer des modèles holographiques bottom-up.

Nous présentons dans la dernière section du chapitre 2 le modèle de QCD holographique qui est considéré dans cette thèse: le modèle de Veneziano-QCD (V-QCD). La V-QCD est le plus sophistiqué des modèles bottom-up pour la QCD holographique. Il inclut en particulier la réaction du secteur de saveur sur le secteur de couleur, qui est cruciale pour étudier la matière de QCD à grande densité baryonique. Le modèle de V-QCD a déjà été étudié dans

plusieurs régimes: dans le vide, à température finie et à température et densité finies, dans le régime où les quarks sont déconfinés. Dans tous ces régimes, plusieurs observables de QCD (spectres de mésons et de boules de glu, thermodynamique, susceptibilités) ont été calculées et comparées avec succès avec les données expérimentales et la QCD sur réseau.

Une composante importante qui doit toujours être étudiée en V-QCD, est le régime où la matière est composée de baryons. Puisque l'on sait que la matière de QCD froide reste dans la phase baryonique au moins jusqu'à des densités deux fois supérieures à la densité nucléaire, inclure les baryons est crucial pour construire une description appropriée de la matière dense.

Dans ce travail, nous avons étudié deux probèmes liés à la physique de la matière baryonique dense en V-QCD, discutés respectivement dans les chapitres 3 et 4. Dans le chapitre 3, nous décrivons ce qui est la première étape pour la construction de matière baryonique en V-QCD, à savoir le calcul de la solution correspondant à un baryon unique. Nous avons à la fois établi le formalisme approprié pour le baryon de V-QCD (section 5.1), et calculé une solution numérique explicite (section 5.2). Un élément important de cette analyse a été l'étude du terme topologique de Chern-Simons, que l'on sait être nécessaire pour stabiliser la taille des solutions baryoniques en holographie. Jusqu'à maintenant, ce terme n'avait pas été étudié en détail en V-QCD, car il ne jouait aucun rôle dans les régimes étudiés. Dans une approche bottom-up, ce terme a été construit ici comme la 5-forme la plus générale compatible avec les symétries et les anomalies de saveur de la QCD. En incluant ce terme de Chern-Simons nouvellement construit dans l'action de V-QCD, nous avons ensuite déterminé les équations du mouvement et les conditions aux limites que la solution de baryon doit vérifier.

Dans la section 5.2, nous présentons une solution numérique explicite à ce problème différentiel, qui correspond à un soliton statique pour les champs de saveur dans le dual gravitationnel. Cette solution est calculée pour un modèle spécifique dans la classe V-QCD, qui est obtenu en fittant la thermodynamique à basse densité et le spectre de mésons dans le vide aux données expérimentales et de la QCD sur réseau. Le baryon décrit par cette solution solitonique est caractérisé dans la théorie du bord par un nombre skyrmionique égal à 1, et le profil du champ de pions est proche du skyrmion du modèle de Skyrme. Néanmoins, le baryon de V-QCD est plus réaliste que le skyrmion, puisqu'il est couplé à tous les mésons plus massifs. Par ailleurs, son influence sur le condensat chiral peut aussi être étudiée, ce qui montre le comportement attendu d'une restauration partielle de la symétrie chirale au centre du baryon. Le spectre de baryons est obtenu en quantifiant les modes d'excitations autour de la solution statique. Nous avons calculé le sous-secteur du spectre de spin-isospin, à partir de la solution pour un soliton en rotation lente. La comparaison avec les données expérimentales pour les masses des nucléons et de l'isobar Δ montre une erreur de l'ordre de 20%, ce qui est cohérent avec les corrections d'ordre $\mathcal{O}(1/N_c)$ attendues dans la limite d'un grand nombre de couleurs N_c.

Dans le chapitre 4, nous nous intéressons au problème de calculer les coefficients radiatifs des neutrinos dans la matière des étoiles à neutron. Le transport de neutrinos joue un

rôle important dans les premiers instants de la formation d'une étoile à neutron. Quand une étoile à neutron se forme dans une supernova à effondrement de cœur, l'émission de neutrinos énergiques depuis le cœur chaud et dense est probablement le méchanisme principal qui mène au départ du choc de la supernova. Par ailleurs, après le départ du choc, la proto-étoile à neutron qui reste comme résidu se refroidit principalement par l'émission de neutrinos.

Cependant, les coefficients radiatifs pour le transport de neutrinos dans la matière de QCD dense restent mal connus. Le manque de données expérimentales ne peut être compensée par des calculs théoriques du fait du couplage fort. De nombreuses approximations ont été considérées dans la littérature, mais leurs résultats dépendent fortement des modèles. L'holographie a le potentiel d'apporter une contribution décisive dans ce problème, puisqu'elle permet d'effectuer des calculs en couplage fort.

Dans ce travail, nous avons initié l'étude du transport de neutrinos en holographie, en considérant comme première étape un simple modèle-jouet. Il s'agit du modèle bottom-up le plus simple pour décrire une matière baryonique à température et densité finies. La matière décrite par ce modèle est composée de quarks supersymétriques et déconfinés, tandis que le groupe de renormalisation du couplage de Yang-Mills est trivial. Malgré les différences essentielles entre ce modèle et la matière réelle dans les étoiles à neutron, son étude permet d'établir certains comportements qualitatifs attendus des modèles holographiques en général.

En particulier, nous avons étudié un ensemble d'approximations pour les coefficients radiatifs, dont la plus importante est l'approximation hydrodynamique. Cette dernière décrit le régime où les énergies leptoniques impliquées dans le transport de neutrinos (énergie des neutrinos, potentiels chimiques des électrons et des neutrinos) sont faibles devant l'échelle d'énergie microscopique, donnée à haute densité par le potentiel chimique baryonique. Pour étudier l'applicabilité de cette approximation, nous avons procédé, dans le modèle holographique considéré, à une analyse des coefficients radiatifs dans l'espace des paramètres en densité baryonique et en énergie des neutrinos. Cette analyse révèle que l'approximation hydrodynamique est assez bonne à haute densité (avec une erreur de l'ordre de 20 à 50%), alors qu'elle devient inutilisable à basse densité.

Nous concluons le chapitre 4 par une comparaison des résultats obtenus avec des calculs précédents dans la littérature. Cette analyse révèle que les opacités calculées avec le modèle holographique sont supérieures par un ordre de grandeur aux résultats obtenus par diverses approximations dans la matière baryonique, et beaucoup plus faibles (par deux ordres de grandeur) que ce que prédit un calcul perturbatif dans la matière de quarks. Cela suggère que les effets non-perturbatifs ont tendance à réduire l'oppacité des neutrinos.

Les pistes de continuation sont multiples pour chaque sujet, et plusieurs sont mentionnées à la fin de chacun des chapitres 3 et 4. D'un point de vue plus large, l'objectif général qui suit ce travail est d'obtenir une description de la matière baryonique dense en V-QCD. L'idée sera d'étendre la solution pour un baryon unique afin de déterminer le dual holographique d'un état contenant une densité finie de baryons. Par ailleurs, une fois cette

construction effectuée, le projet devra converger avec l'étude du transport des neutrinos, afin d'étudier les propriétés de transport de la matière baryonique en V-QCD.

À termes, le programme global de cette approche utilisant le modèle de V-QCD, est d'établir un modèle holographique standard pour la QCD (à grand N_c). Un tel modèle sera construit par un fit commun des données de QCD dans tous les régimes où elles sont disponibles, et permettra de faire des prédictions solides dans le régime de matière dense et froide. Étant donné qu'un fit de cette ampleur est un défi d'un point de vue numérique, les méthodes modernes d'intelligence artificielle seront probablement les mieux adaptées pour accomplir cette tâche.

Contents

Introduction

The matter that the phenomenological world is made of can exist in various phases, that are characterized by qualitatively different physical properties. Under varying conditions of pressure and temperature, the phase of matter can be modified, as it undergoes a process called a phase transition. The most famous example of a phase transition is of course the boiling of water, by which water goes from the liquid phase to the gaseous phase.

The liquid-gas transition in water is a result of the breaking of the hydrogen bounds between the water molecules, due to the injected thermal energy. More generally, phase transitons typically occur when the temperature, or pressure, is of the order of the scale of the interactions that control the microscopic dynamics of the system. The strongest interaction that we know of is the *strong interaction*, that binds together the nucleons in atomic nuclei, and the elementary quarks and gluons within the nucleons. The scale of the strong interaction is of the order of 100 MeV, corresponding to extreme temperatures of about 10^{12} K, and mass densities of the order of the nuclear saturation density $\rho_0 \simeq 2.5 \times 10^{17}\,\mathrm{kg.m^{-3}}$. For comparison, these correspond to temperatures a hundred thousand times higher than in the core of the sun, and densities 10^{12} times larger.

The problem of understanding the phases of matter in such extreme conditions is more than a theoretical curiosity. Indeed, macroscopic systems are known where these conditions should be realized. On the one hand, such high temperatures must have existed at some point in the history of the early universe. On the other hand, these enormous densities are expected to be reached in the core of neutron stars.

Under such extreme conditions of temperature and density, the phase of matter is controlled by the strong interaction. In our modern understanding, the strong interaction is described by the theory of Quantum Chromodynamics (QCD) [1]. Despite the conceptual simplicity of the theory, the strongly-coupled nature of QCD at energies below a few hundred MeV makes it very hard to make theoretical predictions in this regime.

There are however well-controlled methods that give an accurate description of QCD matter in some regions of its phase diagram. At energies well above 100 MeV, QCD matter is well understood in terms of perturbative QCD [2, 3, 4], whereas its low energy description (well below 100 MeV) is controlled by the chiral effective field theory [17, 18, 19]. In addition to those two approaches, the most recent breakthrough in our understanding of the QCD phase diagram came from the numerical lattice QCD method, which is appropriate to

describe the regime of low density.

The remaining part that none of the above methods is able to capture corresponds to the regime of dense and cold QCD, at densities between about 2 and 40 times the nuclear density ρ_0, and large compared with the temperature scale. Interestingly, this region of the phase diagram is the regime that is probed by neutron star matter. Neutron star observations therefore offer a unique opportunity to obtain experimental data on the properties of dense QCD matter, and have already started putting constraints on these properties [66, 68, 79, 8].

Although neutron star data will play a major role in improving our understanding of dense QCD matter, it is equally important to develop theoretical frameworks to address the physics in this regime. Because of the strong coupling, a non-perturbative method is necessary. In this work, we considered the non-perturbative approach given by the holographic correspondence.

The holographic correspondence, [91, 92, 93, 87], has provided a new tool as well as a new paradigm for strong coupling effects in Quantum Field Theory. In its application to QCD, holography has provided very interesting and intuitive ways to address confinement, [107, 135], the calculation of Wilson loops, [110, 109], the spectra of glueballs and mesons, [107, 116], the origin of flavor anomalies and their relation to supergravity Chern-Simons terms, [93], as well as the related chiral symmetry breaking, [136, 121, 124, 137, 138], along the large-N ideas of Coleman and Witten, [14].

The strong coupling phenomena in QCD-like theories have been investigated via holography using a variety of models. A first class contains top-down string-theoretic models that have been developed to describe both Yang-Mills (YM), [93] as well as QCD, [121, 124]. Bottom-up models, more or less faithful to string theory dicta, have also been developed both for YM, [144, 145, 146, 147, 149] and QCD, [143, 111, 150]. The holographic models usually attempt to describe a specific regime of interest, for example the finite temperature thermodynamics or the finite density dynamics. Others, like [145] and [150], attempt to provide a complete description of the dynamics in several different regimes.

The different models have various advantages, that range from simplicity (but being crude in the quantitative part) to complexity (but being closer to real data). The most complete bottom-up model for YM is Improved Holographic QCD, [145, 147] which has been shown to describe quantitatively rather well both $T = 0$ physics for pure YM as well as finite temperature physics, [148]. Its extension to include flavor results in the so-called Veneziano-QCD (V-QCD) model [150, 151].

V-QCD is the most sophisticated bottom-up model for holographic QCD. It includes in particular the back-reaction of the flavor sector on the color sector, which is crucial to address QCD matter at high baryonic density. The V-QCD model has already been studied in several regimes: in vacuum [150, 161], at non-zero temperature [163], and at non-zero temperature and density, in the regime where the quarks are deconfined [164]. In all these regimes, several QCD observables (meson and glueball spectra, thermodynamics, susceptibilities) were computed and successfully compared with lattice and experimental

data.

An important component that still needs to be studied in V-QCD, is the regime where matter is composed of actual baryons. Since it is known that cold QCD matter remains in the baryonic phase at least up to two times the nuclear density [26], including baryons is crucial for giving a proper description of dense matter. In [174], baryonic matter was introduced in V-QCD via a simple homogeneous approximation. This approximation turned out to produce sensible results for the QCD phase diagram and the equation of state of neutron star matter [165]. We would like however to have better control over the construction of baryonic matter in V-QCD, beyond this approximation.

In this work, we addressed two problems related to the physics of dense baryonic matter in V-QCD. In the first part (chapter 3), we made the first step towards constructing baryonic matter in V-QCD, by computing the single baryon solution. We both determined the appropriate formalism to describe the V-QCD baryon [5], and found an explicit numerical solution [6]. In the second part (chapter 4), we focused on the transport properties of the dense QCD matter. This problem is related to the transport of neutrinos in neutron stars, which plays a crucial role in the mechanism of supernova explosions [62] and the subsequent cooling of neutron stars [85, 84]. Here, we inititated the study of neutrino transport in holography, by considering first a simple toy model. Eventually, the project is to extend the analysis to V-QCD, which would provide a holographic model for neutrino transport in neutron stars.

The organization of this thesis is as follows. The first chapter gives a brief review of our current knowledge of the QCD phase diagram, from the three well-controlled methods that are perturbative QCD, chiral effective field theory and lattice QCD. We also discuss the current status of the experimental constraints from neutron star observations. In the second chapter, a brief introduction to the holographic correspondence and its application to QCD is provided. We then introduce the bottom-up V-QCD model that was used in this work.

The original work in itself is presented in chapters 3 and 4. Chapter 3 discusses the construction of the V-QCD baryon, first the formalism [5] and then the numerical solution [6], whereas the holographic analysis of neutrino transport is presented in chapter 4. Several technical details are left to the appendix.

Chapter 1

Phases of QCD

In this first chapter, we discuss the current status of our understanding of the properties of QCD matter in various phases. We give a brief review of what is known about the phase diagram of QCD from perturbative QCD, effective field theory and lattice QCD. We then point out the region of cold and dense QCD matter as the one which is still out of reach of current methods, and explain how neutron star observations provide experimental data on the properties of QCD in this regime.

1.1 Asymptotic freedom

Quantum Chromodynamics (QCD) is the quantum field theory that describes the strong interaction between quarks mediated by gluons. The gluons are the excitations of a gauge field $\mathcal{A}_\mu^{ab}$ in the adjoint representation of an SU(3) group, whereas the quarks arise from a spinor field ψ_i^a in the fundamental representation of SU(3). The fields are labeled by color indices a and b, that run over the three colors $1 \leq a, b \leq 3$. There are $N_f = 6$ different flavors of quarks, associated with the flavor index $1 \leq i \leq 6$, that are characterized by (generically) different masses. The Lagrangian of QCD is given by the minimal gauge-invariant Lagrangian coupling the gluon gauge-field to the quarks

$$\mathcal{L}_{\text{QCD}} = -\frac{1}{2g_{YM}^2}\text{Tr}\Big(G_{\mu\nu}G^{\mu\nu}\Big) + \sum_{i=1}^{N_f}\bar{\psi}_i\Big(i\gamma^\mu(\partial_\mu - i\mathcal{A}_\mu) - m_i\Big)\psi_i\,, \tag{1.1.1}$$

where g_{YM} is the strong coupling constant and $G_{\mu\nu}$ the field strength for the gluon gauge field. The color indices are implicit and the index i runs over the flavors of quarks, with masses m_i. The theory is renormalizable, and at small coupling the renormalization group (RG) flow equation for the Yang-Mills coupling is given by [2, 3]

$$\frac{\partial g_{YM}}{\partial \log \mu} = -\frac{1}{48\pi^2}(11N_c - 2N_f)g_{YM}^3 + \mathcal{O}(g_{YM}^4)\,, \tag{1.1.2}$$

where μ is the energy scale, and N_c the number of colors, equal to 3 in QCD. The all important minus sign in front of the beta function implies that, as long as N_c is superior to $\frac{2}{11}N_f$, the Yang-Mills coupling decreases with the energy scale. This property is famously known as the *asymptotic freedom* of non-abelian gauge theories [2, 3]. In particular, QCD, as we know it today, has $N_c = 3$ colors and $N_f = 6$ flavors, so that it is weakly coupled in the ultraviolet (UV). On the contrary, asymptotic freedom also implies that the Yang-Mills coupling grows at low energy, meaning that QCD is *strongly coupled* in the infrared (IR). The transition between the strongly coupled and the weakly coupled regime is characterized by an energy scale proper to QCD.

There are several ways of defining the QCD scale, either as an integration constant for the perturbative RG flow (1.1.2) (in that case it is usually denoted Λ_{QCD}), or directly from the masses of hadrons observed experimentally. The various definitions all give values typically between 200 MeV and 300 MeV.

The non-perturbative nature of QCD in the IR is the main reason why so much theoretical effort is still spent in controlling low-energy QCD. For this, most of the discussion in the following will address the strongly-coupled regime of QCD. For now however, we will focus on the perturbative regime of QCD.

As far as the phase of QCD matter is concerned, asymptotic freedom implies that the quarks and gluons interact weakly at high temperature and/or density (compared with the QCD scale). In this regime, the propagating degrees of freedom correspond to long-lived quark and gluon quasiparticles, which form a weakly-coupled *quark-gluon plasma*. Because of the perturbative nature of the strong interaction in this plasma, several of its properties can be computed analytically. These include thermodynamics but also out-of-equilibrium observables, such as transport coefficients or thermal radiation [4].

Another important result of the perturbative QCD calculations is in the quantitative estimate of the precise scale at which weakly-coupled results become accurate. At low density, it was found that the perturbative results are already quite precise for $T \gtrsim 600 - 800\,\text{MeV}$ [4, 7], whereas the corresponding baryon chemical potential for the state-of-the-art calculation at small temperature is around $\mu_B \simeq 2.6\,\text{GeV}$ [8]. It is believed that this last result can still be improved by pushing the perturbative calculation to higher order, which is currently the subject of active work [9, 10].

At small temperature and high baryon density, the asymptotic freedom of QCD has also made it possible to exhibit the likely existence of a *color supercoducting phase* [11, 12], where the quark and gluon degrees of freedom develop a gap, and the low energy excitations are instead given by bound pairs of quarks. At asymptotically large chemical potential, the transition temperature T_c^Δ below which the quark-gluon plasma enters the color-superconducting phase was found to be proportional to the superconducting gap at zero temperature Δ. The density dependence of the gap can also be computed, resulting

in [12]

$$T_c^{\Delta}(\mu_B) \propto \Delta(\mu_B) \propto \left(\log\left(\frac{\mu_B}{\Lambda_{\rm QCD}}\right)\right)^{\frac{5}{2}} \mu_B\,, \tag{1.1.3}$$

where the coefficients of proportionality are constants.

In figure 1.1, we summarize the contents of this section according to the QCD phase diagram. We show the typical region where QCD matter is well described by the weakly-coupled quark-gluon plasma, and a sketch of the expected location of the color-superconducting phase. The other features present in the figure are related to the regimes discussed in the rest of this chapter.

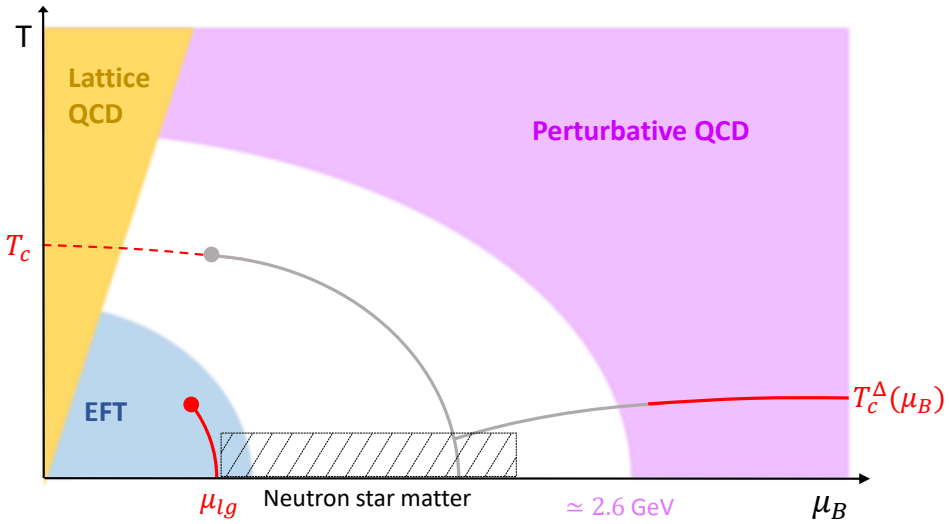

Figure 1.1: Schematic representation of the QCD phase diagram, in the plane of baryon number chemical potential and temperature. The colored areas indicate the regions where QCD matter can be described by well-controlled methods. Full lines indicate first-order phase transitions and the dashed line is the smooth deconfining crossover at low density. The dots symbolize critical points. The red features are well established results, whereas the gray ones are speculative. The hatched region indicates the regime probed by neutron star matter.

1.2 QCD at low energy

We will now discuss the opposite limit in energy scales, that is the low energy limit of QCD. The asymptotically free RG flow of the Yang-Mills coupling (1.1.2) implies that QCD is strongly-coupled in the IR. An important consequence of the increase of the coupling at low energy is that QCD exhibits the property of confinement in the IR [13]. That is, the quarks and gluons cannot be directly observed, and are enclosed together within color-singlet bound states: the hadrons.

Although the low energy hadronic states are color singlets, they still interact via a residual strong force, known as the *nuclear force*. The latter can be understood as arising from the exchange of virtual mesons. The coupling from this residual interaction is weak at energies well below the QCD scale, such that QCD can effectively be described by a theory of weakly-coupled hadrons in the IR limit. The appropriate language to formalize this theory is that of Effective Field Theory (EFT).

The EFT approach [17, 18, 19] exploits the fact that, in the limit of vanishing quark masses $m_i \to 0$, the QCD Lagrangian (1.1.1) exhbitis a global chiral symmetry group $U(N_f)_L \times U(N_f)_R$, that rotates the left and right-handed quark fields in flavor space

$$\psi_i^L \to \left(U_L\right)_i^j \psi_j^L \quad , \quad \psi_i^R \to \left(U_R\right)_i^j \psi_j^R \, . \tag{1.2.1}$$

Guided by phenomenology[1] (more precisely, the fact that the mass of the pions is much smaller than the other hadrons), it is assumed that the chiral symmetry is spontaneously broken at low energies, to the diagonal subgroup $U(N_f)_V \equiv U(N_f)_{L+R}$. In these conditions, the pion fields $\pi^a(x)$ are understood as the massless Goldstone bosons that arise in the low-energy spectrum of the theory. The pions are collected in the so-called pion matrix

$$U(x) = \exp\left(\frac{i}{f_\pi}\pi^a(x)\tau^a\right) , \tag{1.2.2}$$

where they parametrize the Lie algebra of the broken axial part of the symmetry group, the τ^a's being the generators of the Lie algebra. By convention, the pion fields are normalized by the pion decay constant f_π.

The low-energy effective Lagrangian for QCD is then written as a functional of the matrix U, and it is called the *Chiral Lagrangian*. The latter is constructed as a perturbative series

$$\mathcal{L}(U) = \mathcal{L}^{(2)}(U) + \mathcal{L}^{(4)}(U) + \dots \, , \tag{1.2.3}$$

where the parameter of the expansion is given by $(p/\Lambda_\chi)^2$, p being the typical momentum scale and $\Lambda_\chi \simeq 1\,\text{GeV}$ the hadronic scale (roughly the mass of the lightest massive hadron

[1] Upon a few reasonable assumptions, it can actually be proven that the chiral group is spontaneously broken to the diagonal subgroup in the large N_c limit of QCD [14]. At $N_c = 3$, this can also be checked from first principles via numerical lattice calculations [15, 16].

for massless quarks). Specifically, the $\mathcal{L}^{(2n)}$ terms in (1.2.3) are of order $(p/\Lambda_\chi)^{2n}$, and the dots indicate terms of order $(p/\Lambda_\chi)^6$ and higher. The terms of the series are constructed as the most general functionals of U that are compatible with the symmetries of QCD, including chiral symmetry. The general terms determined by the symmetries depend on unknown parameters, called the *low-energy constants*. In particular, the quadratic part of the chiral Lagrangian is given by the non-linear sigma model

$$\mathcal{L}^{(2)}(U) = \frac{1}{4} f_\pi^2 \mathrm{Tr}\big(\partial_\mu U \partial^\mu U^\dagger\big)\,, \tag{1.2.4}$$

which contains a single low energy constant f_π.

There is no way to compute the low energy constants within the EFT, so that they need to be measured experimentally for phenomenological applications. Those constants can in principle be determined from the QCD Lagrangian, but this requires non-perturbative approaches such as the numerical lattice QCD method discussed in the next section. Lattice QCD has been able to compute some low energy constants (see e.g. [20]), but in practice experimental measurements still give the most precise values.

The Lagrangian (1.2.3) gives an accurate description of the pion physics in the case of massless quarks. However, the quarks are known to have finite masses in real QCD, meaning that the chiral symmetry is explicitly broken and the observed pions are not massless. The mass of the pions m_π is much smaller than the other hadrons though, so that the explicit breaking of the chiral symmetry can be treated perturbatively[2]. The chiral symmetry is said to be an approximate symmetry of QCD, with the pions as pseudo-Goldstone bosons. The chiral Lagrangian (1.2.3) is modified to include new terms proportional to m_π^2, with m_π^2 of order $\mathcal{O}(p^2)$ in the low-energy expansion. In particular, the quadratic part (1.2.4) contains the mass term for the pions[3]

$$\mathcal{L}^{(2)}(U) = \frac{1}{4} f_\pi^2 \mathrm{Tr}\Big(\partial_\mu U \partial^\mu U^\dagger + m_\pi^2 \big(U + U^\dagger\big)\Big)\,. \tag{1.2.5}$$

[2]We implicitely assumed here that only the two lightest flavors are included in the EFT, such that the Goldstone bosons acually correspond to the pions observed experimentally. The strange quark (and the associated bosons, the kaons and eta meson) with a mass of the order of 100 MeV can also be treated with the chiral Lagrangian to some extent [19], but it results in larger errors in the predictions of the EFT. The charm, bottom and top quarks have masses larger than 1 GeV, so they cannot be described by the chiral Lagrangian

[3]This form where the mass term for the pions appears explicitly is often used in chiral EFT calculations. It assumes that the QCD θ angle is equal to zero, such that the charged and neutral pions have the same mass. The θ angle is constrained experimentally to be smaller than 10^{-10}. The general expression including the theta angle is better expressed in terms of the quark mass matrix M, as $\mathcal{L}^{(2)}(U) = (1/4) f_\pi^2 \mathrm{Tr}\Big(\partial_\mu U \partial^\mu U^\dagger + a f_\pi \big(MU + U^\dagger M^\dagger\big)\Big)$, with a a low energy constant, whose value is fixed by the Gell-Mann-Oakes-Renner relation. This is also the appropriate form for a number of flavors larger than 2.

Another important ingredient that misses from the pion Lagrangian (1.2.3) is baryons. Despite their mass being of the order of the hadronic scale Λ_χ, it is indeed a daily observation that low energy QCD matter contains nucleons, which are stable baryonic states. In a phenomenological approach, the nucleons are added as external particles, and the chiral Lagrangian (1.2.3) is completed with terms that couple the pions to the nucleons. This can be done in a way that is consistent with chiral symmetry [21], and maintaining the structure of the chiral Lagrangian as a low energy expansion. For example, the leading order πN Lagrangian takes the form

$$\mathcal{L}^{(1)}_{\pi N} = \bar{\Psi}\left(i\gamma^\mu D_\mu - M_N + \frac{g^A}{2}\gamma^\mu\gamma^5 u_\mu\right)\Psi\,, \tag{1.2.6}$$

$$D_\mu \equiv \partial_\mu + \frac{1}{2}\left[\xi^\dagger, \partial_\mu \xi\right] \quad , \quad u_\mu \equiv i\left\{\xi^\dagger, \partial_\mu \xi\right\} \quad , \quad \xi \equiv \sqrt{U}\,,$$

with Ψ the nucleon spinor field. Those new terms come with additional low energy constants, such as the axial coupling g^A in (1.2.6). In addition to the pion-nucleon couplings, the complete description of the nucleon-nucleon interactions in this formalism requires the introduction of nucleon-nucleon contact terms. The latter model the short-range interactions due to the exchange of heavier mesons (notably the ω meson), that are integrated out in the chiral Lagrangian.

The chiral Lagrangian gives a good description of QCD matter at low temperature and density. In particular, the two and three-nucleon interactions that are computed from the EFT are rather successful in describing the structure and interactions of light and medium-mass nuclei [22, 23, 24, 25]. The phase of QCD in this region of the phase diagram is understood as follows. In the limit of vanishing temperature and density, QCD matter takes the form of a pion gas. As the baryon chemical potential μ_B is increased, the fluid undergoes a first order "liquid-gas" phase transition to the nuclear matter [27, 28, 29, 30, 31, 32, 33, 34]. At zero temperature, this transition is characterized by the baryon density jumping from zero to a finite value, which happens when the chemical potential is equal to the energy per nucleon in an iron nucleus

$$\mu_{lg} = M_N - E_{\text{b,iron}}\,, \tag{1.2.7}$$

with M_N the nucleon mass and $E_{\text{b,iron}} \simeq 8\,\text{MeV}$ the nucleon binding energy for iron. At $\mu_B > \mu_{lg}$, the nuclear matter phase is well described by the chiral Lagrangian, up to an upper bound where the effective theory starts losing accuracy. The state-of-the-art upper bound in densities is about two times the nuclear saturation density $n_0 \simeq 0.16\,\text{fm}^{-3}$[26]. The corresponding upper bound on the chemical potential has large uncertainties, but it can be estimated from the results[4] of [26] that $\mu_B - M_N$ is between 30 and 100 MeV, i.e.

[4]The value of μ_B is not computed in [26], but at zero temperature μ_B is related to the pressure P and the energy per particle (excluding the mass) E/A via $\mu_B = M_N + E/A + P/n_B$.

roughly $\mu_B \simeq 1\,\mathrm{GeV}$. Beyond $2n_0$, the many-body nucleon interactions become large, and the lack of precise experimental data already for three-body interactions make the effective theory unusable.

When the temperature is increased, the liquid-gas transition at zero temperature extends to a line in the phase diagram, that ends at a critical point. This point is located at a value of the temperature close to the binding energy per nucleon in cold nuclear matter $T_{lg} \simeq 10\,\mathrm{MeV}$ [31, 33]. At temperatures $T > T_{lg}$ and much smaller than 100 MeV, QCD matter is described by a gas of pions and nucleons. When the temperature is of the order of 100 MeV, the gas also contains higher excited hadronic states. The hadron gas at these temperatures is modeled by the so-called Hadron Resonance Gas (HRG) model, whose free energy is that of an ideal gas containing all the infinitely many hadronic species

$$F(T,\mu_B,V) = \sum_{\mathrm{i}\in\mathrm{mesons}} F^B_{m_i}(T,V) + \sum_{\mathrm{i}\in\mathrm{baryons}} F^F_{m_i}(T,\mu_B,V)\,, \tag{1.2.8}$$

where V is the volume, and $F^B_{m_i}$ and $F^F_{m_i}$ are respectively the single particle partition functions for bosons and fermions, with mass m_i. The HRG model was found to reproduce well the numerical lattice QCD[5] thermodynamics at small density [36, 37], as well as the observed yields of hadronic species produced in heavy-ion collisions [38]. Note that, as the particle densities increase, the interactions between the hadrons in the gas should become larger and invalidate the ideal gas picture used in the HRG. This should happen both at large T and μ_B. At low μ_B, it turns out that the main correction which makes a difference to describe the experimental results from heavy-ion collisions, comes from the hard-core short-range repulsion [38]. The latter is introduced via excluded volume corrections, implemented as a shift of the chemical potentials

$$\mu \to \mu - v_{\mathrm{eigen}}\, p(T,\mu)\,, \tag{1.2.9}$$

where p is the pressure, and the eigenvolume of the particles v_{eigen} is a dimensionful parameter.

The HRG description does not apply anymore when the deconfinement temperature T_c is reached. The best tool to describe the transition and the properties of the stongly-coupled quark-gluon plasma that exists at $T > T_c$, is the numerical lattice QCD method.

1.3 Lattice QCD at low baryon density

In this section, we review briefly the principles of lattice QCD, together with some of its main successes and limitations. Lattice QCD is a numerical method, which aims at computing QCD observables on a discrete lattice, directly from the QCD Lagrangian (1.1.1).

[5] See below for a brief review of the lattice QCD methods.

As such, it takes full account of the strongly-coupled nature of QCD at low-energy, leaving it to a computer to perform the non-perturbative calculations that cannot be done analytically.

As we shall discuss below, lattice QCD for now is best suited for the calculation of observables in a static system at equilibrium, at temperature T and zero baryon chemical potential. The expectation value of an operator O in such a system can be written as a Euclidean path integral over field configurations $\{\mathcal{A}_\mu, \psi_i, \bar{\psi}_i\}$,

$$\langle O \rangle = \frac{1}{Z} \int \prod_\mu D\mathcal{A}_\mu \prod_i D\psi_i D\bar{\psi}_i \; O \, \mathrm{e}^{-S^E_{\mathrm{QCD}}} \,, \tag{1.3.1}$$

where the probability weight of a given configuration is controlled by the QCD Euclidean action

$$S^E_{\mathrm{QCD}} = \int_0^{1/T} \mathrm{d}\tau \int \mathrm{d}^3x \left[\frac{1}{2g^2_{YM}} \mathrm{Tr}\Big(G_{\mu\nu} G^{\mu\nu} \Big) + \sum_{i=1}^{N_f} \bar{\psi}_i \Big(i\gamma^\mu_E (\partial_\mu + i\mathcal{A}_\mu) + m_i \Big) \psi_i \right], \tag{1.3.2}$$

the γ^μ_E being the Euclidean gamma matrices. Z is the QCD partition function

$$Z = \int \prod_\mu D\mathcal{A}_\mu \prod_i D\psi_i D\bar{\psi}_i \, \mathrm{e}^{-S^E_{\mathrm{QCD}}} \,. \tag{1.3.3}$$

Upon discretizing space-time, the path integral is replaced by an integral over the field values at each lattice point x

$$\int \prod_\mu D\mathcal{A}_\mu \prod_i D\psi_i D\bar{\psi}_i \to \prod_x \int \prod_\mu \mathrm{d}\mathcal{A}_{\mu,x} \prod_i \mathrm{d}\psi_{i,x} \mathrm{d}\bar{\psi}_{i,x} \,. \tag{1.3.4}$$

Actually, instead of the gauge fields themselves, the gauge-invariant discretization of the QCD action [13] is written in terms of the link variables

$$U_{\mu,x} \equiv \exp\left(ia\mathcal{A}_{\mu,x} \right), \tag{1.3.5}$$

where a is lattice spacing. (1.3.5) is the discrete version of the Wilson line. Another obstruction to the naive discretization (1.3.4), is that Grassmanian integrals cannot be defined numerically. This problem is avoided by noting that the fermionic action in (1.3.2) is quadratic, so that the Grassmanian integrals can be performed analytically. In particular, the discretized version of the expectation value of a pure glue operator $O(U_\mu)$ takes the form

$$\langle O \rangle = \frac{1}{Z} \int \prod_{x,\mu} \mathrm{d}U_{\mu,x} \; O(U_{\mu,x}) \prod_i \det\left(i\gamma^\mu_E (\partial_\mu + i\mathcal{A}_\mu) + m_i \right) \mathrm{e}^{-S^E_{\mathrm{YM,dis}}(U_{\mu,x})} \,, \tag{1.3.6}$$

where $S^E_{\text{YM,disc}}$ is the discretized version of the Euclidean Yang-Mills action. Despite the factor of i, the determinant of the Dirac operator in (1.3.6) is a real and positive quantity, such that the factor that multiplies O in the integrand can be interpreted as the probability of a given configuration of the gauge fields on the lattice $\{U_{\mu,x}\}$. The integral can therefore be evaluated with a Monte-Carlo algorithm. In this method, a large number N_U of configurations of the gauge fields are generated randomly according to the appropriate probability weight. For each configuration i, the value of the operator O_i is evaluated, and the expectation value is computed by averaging over the configurations

$$\langle O \rangle = \frac{1}{N_U} \sum_{i=1}^{N_U} O_i \,. \tag{1.3.7}$$

(1.3.7) is guaranteed to converge towards the exact result (1.3.6) in the limit $N_U \to \infty$ by the law of large numbers.

Lattice QCD has been able to improve our understanding of QCD at finite temperature and low density in an unprecedented manner. The QCD thermodyanmics has been computed [39, 40, 41], including the equation of state, as well as several screening masses [42, 43]. We refer to [44, 45, 46] for reviews. One of its most important results is the determination of the nature of the phase transition between the hadronic gas and the quark-gluon plasma. The latter was found to correspond to a smooth crossover, which happens gradually for temperatures between $T \simeq 145\,\text{MeV}$ and $165\,\text{MeV}$ [47, 48, 49, 50].

Unfortunately, the methods of lattice QCD face a major obstacle at finite baryon number chemical potential μ_B, which is known as the *sign problem*. When a finite μ_B is introduced, the Dirac operator in the QCD Lagrangian (1.3.2) is effectively replaced by

$$M_D \equiv i\gamma^\mu_E(\partial_\mu + i\mathcal{A}_\mu) + m_i \to \tilde{M}_D(\mu_B) \equiv i\gamma^\mu_E(\partial_\mu + i\mathcal{A}_\mu) + m_i + \mu_q \gamma^0_E \,, \tag{1.3.8}$$

where $\mu_q \equiv \mu_B/N_c$ is the quark number chemical potential. The expectation value of an operator at finite μ_B will therefore be evaluated by replacing the determinant of M_D by that of $\tilde{M}_D$ in (1.3.6). However, unlike that of the zero-density Dirac operator, the determinant of $\tilde{M}_D$ is not real anymore. This means that what could be interpreted as a probability in (1.3.6) is now a complex number, so that the Monte-Carlo method cannot be used anymore to compute the expectation values. Note that, even if the operator O is real, such that the expectation value can be computed with the real part of the determinant, the sign of the real part will not be positive for all configurations (hence the "sign" problem). In absence of alternative numerical methods to compute such highly-dimensional integral[6] as (1.3.6), lattice QCD is unable to compute the properties of QCD at finite baryonic density. Note that a similar problem is encountered when one tries to compute real-time observables on

[6]More precisely, the average can still be formulated in terms of positive probabilities, by absorbing the sign of the real part in the operator. However, computing the resulting integral with the Monte-Carlo method can be shown to be a NP-hard problem [51].

the lattice[7], even at $\mu_B = 0$, since in Lorentzian signature $-S^E_{\rm QCD}$ should be replaced by $iS_{\rm QCD}$ in (1.3.1).

The situation is actually not so grim as it seems, and lattice physicists have found ways to go around the sign problem, at least to some extent. Several methods exist [54, 55, 56, 57], among which the simplest conceptually is the Taylor expansion around $\mu_B = 0$ [58, 59]. The idea is to expand the pressure $p(T, \mu_B)$ for chemical potential μ_B smaller than the temperature

$$p(T,\mu_B)T^{-4} = p(T,0)T^{-4} + \sum_{n=1}^{\infty} \chi_{2n} \left(\frac{\mu_B}{T}\right)^{2n} , \tag{1.3.9}$$

where the χ_{2n} are the baryon number susceptibilities

$$\chi_{2n} \equiv \frac{1}{(2n)!} \frac{\mathrm{d}^{2n}\big(p/T^4\big)}{\mathrm{d}\big(\mu_B/T\big)^{2n}}\bigg|_{\mu_B=0} . \tag{1.3.10}$$

The latter can be computed on the lattice as zero-density expectation values. As is clear from (1.3.9), this method is adequate only for chemical potentials up to the scale of the temperature. This is also true for the other methods that have been developped.

To summarize, the successes of the numerical lattice QCD method give us a good understanding of many properties of QCD at small density. This includes the important region around the deconfining crossover, which is not accessible to both the hadronic models and perturbative QCD. Lattice QCD typically applies for $\mu_B \lesssim T$, as indicated on figure 1.1. However, the sign problem prevents it from exploring phases at $\mu_B \gg T$.

The region which remains blank in figure 1.1, at chemical potentials $1\,\mathrm{GeV} \lesssim \mu_B \lesssim 2.6\,\mathrm{GeV}$ larger than the temperature, cannot be described by either of the well controlled methods that are perturbative QCD, chiral effective field theory and lattice QCD. As such, it is still largely an uncharted region of the phase diagram.

Many models have been elaborated to try and address the physics of QCD in this region (see the reviews [60, 61] and references therein). However, beyond suggesting a very rich phase structure, those models are unable to produce solid results in the dense regime of QCD. This region is all the more interesting that the corresponding conditions are realized in macroscopic systems observed in nature, i.e. in the core of neutron stars. In the next section, we discuss how neutron star observations put experimental constraints on the properties of dense QCD matter.

1.4 Dense QCD and neutron stars

Neutron stars are the most compact stars observed in the universe, that are formed as the remnant of the supernova explosion of a giant star [62]. With masses between 1 and 2

[7] Although there are techniques to estimate spectral functions and transport coefficients from equilibrium correlators [52, 53].

solar masses, and radii of 10 to 20 kilometers, the density at the center of these objects can reach several times the nuclear saturation density $n_0 \simeq 0.16\,\mathrm{fm}^{-3}$. These are baryon densities much higher than what can be currently reached in experiments on Earth, so that the observation of neutron stars offers a unique window to probe the properties of QCD matter at very high density.

Neutron stars are self-gravitating objects whose strucure is determined by the Einstein equations, together with the dynamics of strongly-interacting matter. To a good approximation[8] they are spherically symmetric, sourcing a metric of the form

$$\mathrm{ds}^2 = -\mathrm{e}^{\Phi(r)}\mathrm{dt}^2 + \left(1 - \frac{2Gm(r)}{r}\right)^{-1} dr^2 + r^2 \mathrm{d}\Omega_2^2\,, \tag{1.4.1}$$

where r is a radial coordinate, equal to 0 at the center of the star. It can be shown that $m(r)$ is the gravitational mass enclosed within radius r. The matter that consitutes the neutron star is modeled by a static perfect fluid, with stress-energy tensor

$$T_{\mu\nu} = \mathrm{diag}(p(r) + \varepsilon(r), p(r), p(r), p(r))\,, \tag{1.4.2}$$

$p(r)$ being the pressure and $\varepsilon(r)$ the energy density. For the ansatz (1.4.1)-(1.4.2), the Einstein equations reduce to the so-called Tolman-Oppenheimer-Volkov (TOV) equations

$$\frac{\mathrm{d}p}{\mathrm{d}r} = -\frac{G}{r^2}\left(p(r) + \varepsilon(r)\right)\left(m(r) + 4\pi r^3 p(r)\right)\left(1 - \frac{2Gm(r)}{r}\right)^{-1}\,, \tag{1.4.3}$$

$$\frac{\mathrm{d}m}{\mathrm{d}r} = 4\pi r^2 \varepsilon(r) \quad , \quad \frac{\mathrm{d}\Phi}{\mathrm{d}r} = -\frac{p'(r))}{p(r) + \varepsilon(r)}\,, \tag{1.4.4}$$

with G the gravitational constant. For the system (1.4.3)-(1.4.4) to be closed, an additional relation between the pressure and the energy density is necessary. The relation $p = p(\varepsilon)$ is a microscopic property of neutron star matter, known as the equation of state. For a given value of the central density ε_c, the structure of a neutron star is fully determined by its equation of state. In particular, knowing the equation of state makes it possible to determine the mass M and radius R of the star as a function of ε_c. Conversely, knowing the functions $(R(\varepsilon_c), M(\varepsilon_c))$, or equivalently $M(R)$, allows to infer the equation of state of neutron-star matter. This means that observing the masses and radii of many neutron stars to construct the function $M(R)$ (the so-called M-R diagram) puts constraints on the equation of state of dense QCD matter.

The available data from neutron star observations already puts significant constraints on the equation of state [64]. To date, the masses of more than 60 neutron stars have been

[8] The shape of a typical neutron star is slightly different from a sphere due to its rotation. Even for the fastest rotation velocities (milisecond pulsars), the deviation remains small and can be treated perturbatively [63].

measured [65], some of which with accuracies of less than 1% at the 1-σ confidence level. The most accurate measurements are for pulsars in a binary system, whose masses can be determined via the Shapiro delay of the periodic signal when the pulsar passes behind its companion. Most of the recorded masses are between 1.2 and 1.6 solar masses, but some very massive neutron stars were also observed. The most significant measurements include the pulsars J1614-2230 ($M = (1.908 \pm 0.016)M_\odot$) [66, 67], J0348+0432 ($M = (2.01 \pm 0.04)M_\odot$) [68] and J0740+6620 ($M = (2.08 \pm 0.07)M_\odot$) [69, 70], with $M_\odot$ the solar mass. These observations imply that the equation of state of neutron stars should be sufficiently stiff to support such high masses. That is, the speed of sound $c_s^2 = \partial p/\partial \varepsilon$ in neutron star matter cannot be too low. In practice, this 2-solar mass condition is already sufficient to discard many equations of state proposed in the literature [66].

Measuring the radius of a neutron star is more difficult than the mass. The main methods are based on the analysis of the thermal emission from the surface, each method focusing on different properties of the emission. These include spectroscopic measurements [71, 72] (the standard method for other types of stars) and pulse profile modeling [73]. Both methods have much larger uncertainties than the mass measurements, due to the fact that they involve the complex physics of the neutron star atmosphere. Most recent results are due to the pulse profile modeling method, which is the one used by the ongoing NICER experiment. This method infers the radius of the star from the observation of the periodic component of the thermal X-ray emission. The latter is understood as arising from the existence of hot spots at the surface of the star, that enhance the thermal signal when the star rotation brings them on the line of sight. Given a model for the properties of the spots, the mass and radius of the star can then be inferred from the gravitational lensing of the signal. Using this technique, NICER has been able to determine the radii of pulsars J0030+0451 and J0740+6620 within 10% of accuracy at the 1-σ confidence level (up to systematics) [74, 75], which gives interesting constraints on the neutron star equation of state [76, 77]. Several other pulsars have been observed, and their investigation is ongoing [78].

Another type of observation that brings information about the properties of neutron star matter is that of a neutron star merger. Such an event can be detected via the emitted gravitational wave signal, which may be observed with the LIGO/Virgo interferometers. To date, LIGO/Virgo has confirmed one such observation, GW170817 [79], and another likely event GW190425 [80]. Apart from the mass of the binary, the observed gravitational wave signal depends on the tidal deformation of the stars during the inspiral, such that a larger deformation enhances the gravitational wave emission. Such an effect is quantified by a quantity Λ called the tidal deformability, which is correlated with the equation of state. The analysis of GW170817 made it possible to bound the tidal deformability of the two neutron stars that merged, which is often presented in terms of the inferred deformability of a $1.4M_\odot$ neutron star $\Lambda_{1.4} = 190^{+390}_{-120}$, at the 90% confidence level [81]. The most interesting part of this result is the upper bound on Λ, which favors compact stars, and therefore soft equations of state, giving a complementary constraint to the 2-solar mass

condition.

It is expected that the continued observational effort to measure neutron star masses, radii and tidal deformabilities should eventually provide us with sharp constraints on the equation of state. Including the condition of matching with the effective field theory result at low energy, and perturbatibe QCD at high energy, it was shown in [8] that the current observational constraints already reduces a lot the space of possible equations of state.

Although it plays a major role in neutron star physics, the equation of state is only a single observable from the dense QCD matter, which is far from determining all of its properties. In particular, it is not very sensitive to the nature of the degrees of freedom that QCD matter is effectively made of. On the contrary, transport phenomena are typically much more sensitive to those phase properties [82]. Neutron stars have also the potential to give us information about the transport properties of QCD matter, if they are observed during the cooling stage. This period after the formation of the star in a supernova lasts for about 10^5 years, during which the star cools mainly via neutrino emission [83, 84]. The neutrinos that are trapped in the core radiate towards the surface, by scattering inside neutron star matter (see Chapter 4 below for a detailed review of the formalism used to describe neutrino transport). If this neutrino flux can be observed, this will provide us with information on the transport of weak charge in dense QCD matter. The main prospect for obtaining this kind of data would be the observation of a galactic supernova, for which the late time signal is expected to depend on the properties of dense QCD matter [85]. Observing the thermal flux from a cooling neutron star also provides us in principle with information about transport, but there is some degeneracy with the dependence on the characteristics of the outer layers of the star [86, 85].

The contents of this chapter are summarized by figure 1.1. The colored areas indicate the region of the phase diagram where our understanding of the properties of QCD matter is good:

- At high temperature and density, where the perturbative picture applies,
- At low temperature and density, where effective field theory can be used,
- At finite temperature and low density, where the numerical lattice QCD method is effective .

Beyond those regions, that is for cold and dense QCD matter, our knowledge is very limited. In particular, the properties of matter in the core of neutron stars (hatched area) cannot be predicted by a solid theoretical model. However, the experimental data from neutron star observation is providing us with constraints which should help constructing an efficient phenomenological model.

The work presented in this thesis is part of a more general program, which aims at investigating the properties of dense QCD matter via the holographic approach. This

approach has the significant advantage that holographic models are defined over the whole phase diagram, as long as QCD remains strongly-coupled. This implies that the models can be compared with real QCD data at temperature and densities where such data exist, and make predictions for dense QCD matter. Apart from this phenomenological prospect, another important asset of holography is that it provides an intuitive (gravitational) picture of the strongly coupled matter, which may help our understanding of its dynamics. Finally, dynamical real time phenomena and dissipation, which are difficult to describe in other approaches (including lattice QCD), are naturally described in holographic theories.

The next chapter discusses the holographic approach to QCD. We start by introducing the fundamental concepts, and then describe in more details the V-QCD framework, which is the most complete framework for holographic QCD, and the one that is used in this work.

Chapter 2

Holographic QCD

This chapter presents a brief introduction to the main ingredients for the construction of holographic models of QCD. We start from the basics of the holographic correspondence, before discussing how confinement is implemented in holography. As an illustration, we then describe the top-down Witten-Sakai-Sugimoto model, whose construction is representative of the ingredients that holographic QCD models should contain. It is in particular an inspiration for the bottom-up V-QCD model that we used in this work. The latter is introduced in the last part of this chapter.

2.1 Basics of the gauge/gravity duality

We provide in this section a brief introduction to the basic principles underlying the holographic (or AdS/CFT) correspondence. The discussion will remain at the descriptive level, and we refer the reader to the available reviews [87, 88, 89, 90] for more details about the duality and its tests.

The holographic correspondence [91, 92, 93] is a well-motivated and amply tested conjecture that states the duality between a large N quantum field theory (QFT), and a semi-classical gravitational theory defined on a higher-dimensional space, which henceforth will be called the *bulk*. It is a strong-coupling/weak-coupling duality in the sense that, if the quantum theory is strongly coupled, then the holographic dual is weakly curved and vice versa. Via this duality, quantum observables whose evaluation would require a non-perturbative calculation, can instead be derived from classical computations in general relativity.

In order to present some generic features of the holographic correspondence, we shall first focus on the case of a conformal field theory (CFT). Assuming the CFT to admit a holographic dual (in this case, it is called a *holographic CFT*[1]), the dual geometry cor-

[1]Not all CFT's admit holographic duals, as the existence of the dual gravitational description

responds to the negatively-curved anti-de Sitter space. In particular, the original correspondence [91] was formulated for an explicit 4-dimensional conformal field theory (CFT): $\mathcal{N} = 4$ SU(N) super-Yang-Mills (SYM). The latter was postulated to be dual to type IIB string theory on $AdS_5 \times S^5$, which at large N and large 't Hooft coupling reduces to type IIB supergravity on $AdS_5 \times S^5$. In the following the S^5 factor does not play an important role so we will focus on the AdS part of the geometry.

The geometric properties of AdS space can be interpreted from the point of view of the holographic duality. In the so-called Poincaré coordinates[2], the AdS_5 metric can be written as

$$ds^2 = \frac{\ell^2}{r^2}\left(dr^2 + \eta_{\mu\nu} dx^\mu dx^\nu\right), \tag{2.1.1}$$

where ℓ is the AdS length and $\eta_{\mu\nu}$ the 4-dimensional Minkowski metric. A notable property of the AdS space, is that it possesses a conformal boundary. In the Poincaré coordinates, this boundary is located at $r = 0$, and has the geometry of Minkowski space, which is precisely the space-time on which the dual CFT is defined. That is, the CFT_4 dual to AdS_5 may be thought of as living at the boundary of AdS.

Another interesting property of the AdS metric (2.1.1) is related to its isometries. First of all, it is clear that (2.1.1) is invariant under Poincaré transformations of the boundary coordinates x^μ. Also, it is easy to check that a rescaling of the coordinates

$$x^\mu \to \lambda x^\mu \quad , \quad r \to \lambda r \,, \tag{2.1.2}$$

also leaves the AdS metric invariant. These symmetries are strongly reminiscent of the conformal symmetry of the dual CFT. In fact, the full isometry group of AdS is precisely isomorphic to the 4-dimensional conformal group SO(2,4). Therefore, the conformal symmetry of the boundary theory is seen to be realized as the isometries of the gravitational dual.

In addition to the boundary coordinates x^μ, the emergence of the fifth "holographic" coordinate r can also be understood in terms of the boundary theory. Due to the warp factor ℓ/r in (2.1.1), the proper distance $L(r)$ measured by a local observer at a given position r, is rescaled compared with the distance as measured along the flat directions of the boundary L_b

$$L(r) = \frac{\ell}{r} L_b \,. \tag{2.1.3}$$

Conversely, for a fixed value L of the proper distance measured by the local observers, the corresponding boundary distance changes with r as

$$L_b(r) = \frac{r}{\ell} L \,. \tag{2.1.4}$$

imposes constraints on the structure of the dual CFT [91, 94, 95, 96].

[2]Note that the Poincaré coordinates cover only a finite patch of AdS, called the Poincaré patch. The CFT defined on flat space is actually dual to the Poincaré patch, rather than the full AdS space.

This means that larger and larger distances are probed in the boundary theory as r increases. The holographic coordinate is therefore interpreted as the (inverse) energy scale in the quantum theory, with the AdS boundary ($r = 0$) identified as the UV limit, and the interior ($r \to \infty$) as the IR limit.

When discussing holographic QCD, the QCD-like theories that one wants to describe are typically not conformal, and become conformal only in the UV limit. In these conditions, the geometry of the bulk is only asymptotically AdS near the boundary, but deviates from it in the interior. In spite of this, it is still expected that the general properties of the correspondence as stated for the conformal case should hold: the QFT lives at the boundary of the bulk, and the holographic coordinate is interpreted as the running energy scale. The deviation from AdS in the interior of the bulk is then understood as the non-trivial RG flow of the boundary theory[3].

2.1.1 Holographic dictionary

We now discuss the correspondence at the level of the boundary quantum operators, where it translates into the so-called holographic dictionary [93]. The latter associates to every gauge-invariant boundary operator a dual field in the bulk with the same quantum numbers under the global symmetries of the theory. In particular, a scalar operator $\mathcal{O}(x)$ has a dual scalar field in the bulk $\phi(x, r)$. The boundary value of the dual field is identified as a source $\phi_0(x)$ for the operator $\mathcal{O}$ in the boundary theory

$$\phi_0(x) = \lim_{r\to 0} \phi(x, r)\,. \tag{2.1.5}$$

Equation (2.1.5) is actually correct only for massless fields, and for massive scalar fields ϕ it should be generalized to

$$\phi_0(x) = \lim_{r\to 0} \Big(r^{-\Delta_-} \phi(x, r) \Big) \quad , \quad \Delta_- \equiv \frac{1}{2}\Big(d - \sqrt{d^2 + 4m^2\ell^2} \Big)\,, \tag{2.1.6}$$

where d is the dimension of the boundary and m the mass of the (bulk) scalar field. With this identification, a quantitative formulation of the correspondence may be written as

$$\Big\langle \exp\Big(\int \mathrm{d}^d x\, \phi_0(x) \mathcal{O}(x) \Big) \Big\rangle_{\mathrm{QFT_d}} = \exp\Big(- S^{d+1}_{\text{on-shell}} \Big) \Big|_{\phi \underset{r\to 0}{\sim} r^{\Delta_-}\phi_0}\,, \tag{2.1.7}$$

where the left-hand side is the (off-shell) generating functional of the boundary QFT, and the right-hand side the on-shell partition function for the bulk gravitational theory. Note

[3]Such an identification results in the notion of *holographic RG flow*. The properties of such flows and their relation with the RG flow of the boundary theory is the topic of a vast literature; see e.g. [97, 98, 100, 101, 102, 103, 104].

that equation (2.1.7) is written in Euclidean signature. There is a similar formula for Lorentzian signature but it involves a more subtle construction [105].

We wrote (2.1.7) for the example of a specific scalar operator, but it should be understood that the equality generalizes to all types of (single-trace[4]) operators, where the source ϕ_0 should be replaced by the boundary value of the appropriate bulk field. In particular, an important component of the holographic dictionary is that about the holographic duals of conserved currents. If the boundary theory possesses a global symmetry, associated with a conserved current J^μ, then the bulk theory contains a dual vector field A_μ. Moreover, it can be shown that the conservation of the current implies that the bulk theory is invariant under gauge transformations of the vector field A_μ, which is therefore a gauge field. The corresponding gauge group is the continuous version of the global symmetry group in d+1 dimensions.

A crucial example is given by the current associated with translation invariance, that is the stress-energy tensor $\mathcal{T}^{\mu\nu}$. Applying the holographic dictionary to $\mathcal{T}^{\mu\nu}$ as above, implies that the dual bulk field is a spin-2 gauge field, whose gauge transformations are given by diffeomorphisms. That is, the stress-energy tensor is dual to the bulk metric. We therefore reach the important conclusion that the holographic dual of a translation-invariant theory includes dynamical gravity.

2.1.2 Holography at finite temperature

We shall now discuss how a finite temperature in the boundary theory is realized in the gravitational dual. An equilibrium thermal state in the boundary theory is described by its partition fonction. The latter may be obtained from the Lorentzian path integral by performing a Wick rotation of the time coordinate

$$t \to -it_E \,, \tag{2.1.8}$$

to go to Euclidean signature, and compactifying the time direction such that

$$t_E \sim t_E + \frac{1}{T} \,, \tag{2.1.9}$$

where T is the temperature. In Euclidean signature, the holographic dual of a thermal state will therefore contain a compact time direction, whose periodicity should correspond to the temperature of the boundary state.

At a given temperature, and for fixed sources (i.e. for a given theory), there are generically several competing solutions to the bulk equations of motion, corresponding to different states in the boundary theory. Among those, the boundary equilibrium state corresponds

[4]Multi-trace operators can also be included, but the identification of the source from the boundary behavior of the dual field should be modified [106].

to the solution with lowest free energy. Which solution dominates may depend on the temperature, which signals a phase transition in the boundary theory. In particular, deconfined phases are typically dual to black holes in the bulk, where the Hawking temperature of the black hole is equal to the boundary temperature.

The simplest example is again given by $\mathcal{N} = 4$ SYM, which at finite temperature is dual to an AdS black hole [107], with metric

$$\mathrm{d}s^2 = \frac{\ell^2}{r^2}\left(f(r)^{-1}\mathrm{d}r^2 - f(r)\mathrm{d}t^2 + \mathrm{d}\vec{x}^2\right) \quad , \quad f(r) = 1 - \frac{r^4}{r_H^4}\,, \tag{2.1.10}$$

in Poincaré coordinates. In equation (2.1.10), r_H corresponds to the horizon radius, which is related to the Hawking temperature T_H via

$$r_H = \frac{1}{\pi T_H}\,. \tag{2.1.11}$$

The Euclidean continuation of the black hole metric is obtained by the transformation $t \to -it_E$

$$\mathrm{d}s_E^2 = \frac{\ell^2}{r^2}\left(f(r)^{-1}\mathrm{d}r^2 + f(r)\mathrm{d}t_E^2 + \mathrm{d}\vec{x}^2\right)\,. \tag{2.1.12}$$

Requiring that (2.1.12) does not have a conical singularity at the horizon [108] implies that the Euclidean time direction should be periodic, with period $1/T_H$. From the identification with (2.1.9), this means that the Hawking temperature of the black hole is the temperature of the boundary theory.

2.1.3 Confinement in holography

As discussed in the previous chapter, the confinement of color charge plays a major role in the low energy dynamics of QCD. It is therefore one of the basic properties that holographic models of QCD should exhibit. It is the purpose of this subsection to explain what is the criterium for confinement from the point of view of the gravitational dual.

The observable which is used to indentify the confining behavior of a gauge theory is the expectation value of the so-called Wilson loop [13] operator

$$W_C \equiv \mathrm{Tr}\left\{\mathcal{P}\exp\left(\oint_C \mathcal{A}_\mu \mathrm{d}x^\mu\right)\right\}\,, \tag{2.1.13}$$

where $\mathcal{A}$ is the gauge-field operator, C is a closed contour in space-time and $\mathcal{P}$ is the path ordering operator. A confining theory is characterized by an area law for the Wilson loop

$$\langle W_C\rangle = \exp\Big(icS(C)\Big)\,, \tag{2.1.14}$$

where c is a constant and $S(C)$ refers to the area enclosed by the path C.

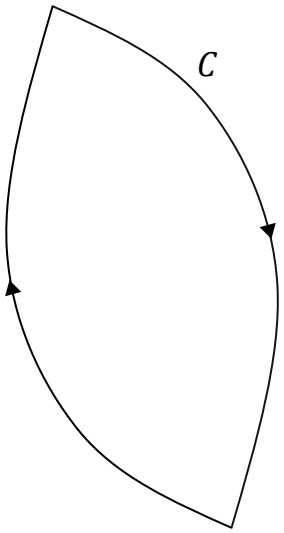

Figure 2.1: The Wilson loop

In QCD, $\mathcal{A}_\mu$ corresponds to the gluon field, and the expectation value of the Wilson loop W_C evaluates the probability of observing a quark-antiquark pair forming at some point on the contour C, and annihilating at some other point, as shown in figure 2.1. The area suppression of W_C (2.1.14) implies that, for contours of given large diameter D, it is much more probable to observe a narrow loop with $S(C) \sim D$ than a broad loop having $S(C) \sim D^2$. In particular, resolving the individual quarks in a macroscopic detector of size L would correspond to observing a broad loop with $S(C) \sim L^2$, which is heavily suppressed. Instead, what is observed is a line-like contour describing the path of a free particle, the latter being a bound state of the quark and anti-quark (a meson).

The holographic correspondence provides a simple method to compute the expectation value of Wilson loops from the gravitational description [109, 110]. The idea is to consider the bulk classical string worldsheet Σ, whose boundary coincides with the path C defining the Wilson loop at the AdS boundary (see figure 2.2). The expectation value of the Wilson loop is then identified with the on-shell partition function of the dual string worldsheet Σ

$$\langle W_C \rangle = \exp\left(i S^{\text{NB}}_{\text{on-shell}}(C) \right). \tag{2.1.15}$$

The on-shell action is evaluated on the surface Σ that extremizes the Nambu-Goto action S^{NB}.

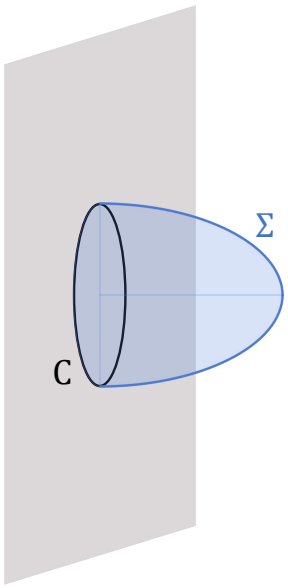

Figure 2.2: The string wolrdsheet dual to the Wilson loop. The AdS boundary is represented by the gray surface, and the boundary of the worldsheet Σ coincides with the loop C.

With the prescription (2.1.15) for evaluating Wilson loops, it is possible to investigate the confining behavior of given bulk geometries. The typical criterium for confinement to occur is for the geometry to end at a finite value r_0 of the holographic coordinate[5], where r_0 gives the confining scale of the boundary theory. A simple heuristic way of understanding how this works is as follows. Let us consider a rectangular Wilson loop of finite extent T in the time direction t, and $L \ll T$ in the spatial direction x, as shown in the left of figure 2.3. Then the dual worldsheet in the bulk is essentially invariant under time-translation, and takes the form shown in the right of figure 2.3 in the (r, x) plane. As one increases the size of the loop L, the worldsheet extends deeper and deeper in the bulk, until it is forced to stick to the end of space at $r = r_0$. For $L \gg r_0$, the action of the worldsheet therefore goes as

$$S^{\text{NB}}_{\text{on-shell}}(C) \sim LT\,, \tag{2.1.16}$$

which is precisely the area of the Wilson loop. For $r_0 \to \infty$, there is no obstacle to the

[5]In some cases, including the bottom-up soft wall backgrounds [111, 112, 113], the "end of space" should be understood in an effective sense. That is the space does not end at r_0, but the dilaton becomes so large at $r > r_0$ that the minimizing worldsheet cannot go much beyond r_0.

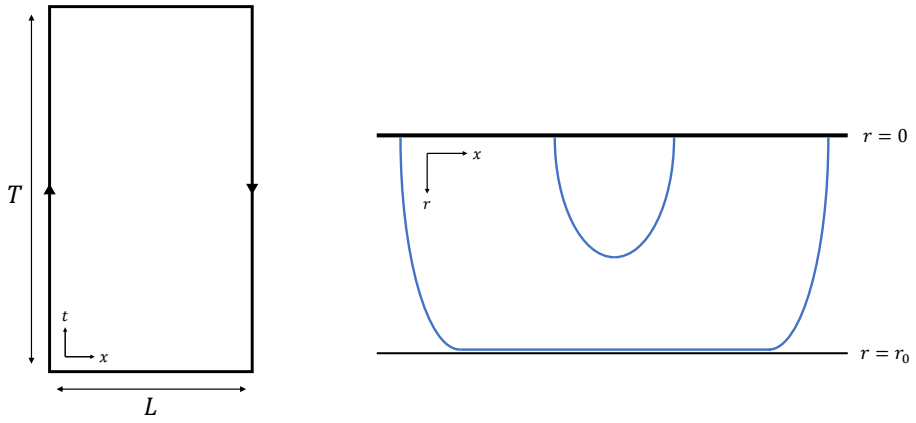

Figure 2.3: **Left:** A rectangular Wilson loop, with length T in the time direction, and L in a spatial direction denoted x. **Right:** Schematic view of the worldsheet dual to the rectangular loop, shown in the the (x, r) plane. r is the holographic coordinate, such that the boundary is located at $r = 0$. The confining background is such that the geometry ends at a finite value $r = r_0$. We show two examples of loop, with $L \ll r_0$ and $L \gg r_0$.

worldsheet extending ever deeper in the bulk, so that the area law (2.1.16) is not obtained and the background is deconfined.

One way of constructing confining backgrounds is to compactify one of the spatial directions of the boundary [107]. The simplest example is given by the AdS soliton geometry [114], which can be obtained from the Euclidean AdS black-hole (2.1.12) by Wick rotating one of the spatial coordinates into a new Lorentzian time $x_1 \to it$

$$\mathrm{d}s^2 = \frac{\ell^2}{r^2}\left(f(r)^{-1}\mathrm{d}r^2 + f(r)\mathrm{d}t_E^2 - \mathrm{d}t^2 + \mathrm{d}x_2^2 + \mathrm{d}x_3^2\right) . \tag{2.1.17}$$

The geometry described by (2.1.17) ends smoothly at $r = r_H$, which implies that the dual QFT is confining. r_H is not interpreted in terms of a temperature anymore, but rather as the confining scale of the boundary theory.

The boundary theory dual to the AdS soliton geometry shows an interesting behavior in the IR. To see this, remember that the Euclidean black hole (2.1.12) is dual to the SYM theory, defined on a Euclidean space with one compact coordinate of size proportional to r_H. In the low energy limit, at distances much larger than r_H, this theory becomes effectively 3-dimensional. Furthermore, if the boundary conditions for the fermion fields of the SYM theory are chosen to be anti-periodic along the compact direction, then the

spin 1/2 fields acquire a mass proportional to r_H^{-1}. The scalar fields can also be shown to acquire a mass due to quantum effects, whereas only the SU(N) gauge fields remain massless. As a result, the low energy limit of the theory dual to the Euclidean black hole corresponds to the Yang-Mills theory in three Euclidean dimensions. By performing the analytic continuation $x_1 \to it$, we see that, at low energy, the dual of the AdS soliton (2.1.17) reduces to (large N) Yang-Mills in (2+1) dimensions. This observation is the basis for the construction of the top-down holographic QCD model that is discussed in the next section.

2.2 The Witten-Sakai-Sugimoto model

We introduce in this section an explicit top-down construction of a holographic QCD model, known as the Witten-Sakai-Sugimoto (WSS) model. This model can reproduce a large amount of known properties of QCD with very few parameters. In addition to reviewing the successes of the holographic approach to QCD, the presentation of this model will also help understanding some aspects of the V-QCD framework that was used in this work. The latter is discussed in the next section.

The glue sector of the WSS model is designed to behave as the four-dimensional Yang-Mills theory at low energy. In analogy with the AdS soliton (2.1.17), this can be obtained by compactifying one of the spatial directions of the five-dimensional SYM theory [107], with supersymmetry-breaking boundary conditions around the circle. The gravitational dual to this construction can be computed in string theory, along the same lines as for the four-dimensional SYM [115]. The resulting ten-dimensional metric may be written as

$$\mathrm{d}s^2 = \left(\frac{U}{R}\right)^{\frac{3}{2}} \left(\eta_{\mu\nu}\mathrm{d}x^\mu \mathrm{d}x^\nu + f(U)\mathrm{d}\tau^2\right) + \left(\frac{R}{U}\right)^{\frac{3}{2}} \left(f(U)^{-1}\mathrm{d}U^2 + U^2\mathrm{d}\Omega_4^2\right) ,$$

$$f(U) \equiv 1 - \frac{U_{\rm KK}^3}{U^3} , \tag{2.2.1}$$

where the holographic coordinate U extends from the boundary at $U = \infty$, to a finite value $U_{\rm KK}$ where the geometry smoothly ends. The geometry depends on two dimensionful parameters: $U_{\rm KK}$ and the radius of curvature R, which determine the periodicity of the compact coordinate τ

$$\tau \sim \tau + \frac{2\pi}{M_{\rm KK}} \quad , \quad M_{\rm KK} \equiv \frac{3}{2}\frac{U_{\rm KK}^{1/2}}{R^{3/2}} . \tag{2.2.2}$$

As expected from the field theoretic picture, the boundary theory dual to (2.2.1) has a phenomenology close to that of Yang-Mills. In particular, the fact that the geometry ends at a finite value of U implies confinement and a discrete spectrum of normalizable modes, which is identified as the glueball spectrum. The masses of the glueballs were even found to be in rather good agreement with the results of lattice QCD [116, 117]. However, since the

boundary theory possesses a single scale $M_{\rm KK}$, the glueball masses are of the order of $M_{\rm KK}$, which is also the scale at which the Yang-Mills picture breaks down. As a consequence, the low energy spectrum contains, in addition to the glueballs, all the Kaluza-Klein modes that arise from excitations along the compact dimension [118]. Another important difference with the actual Yang-Mills theory, is that the model does not exhibit any sort of asymptotic freedom, since the four-dimensional Yang-Mills coupling is simply a constant.

2.2.1 Adding flavor

Despite the limitations that we mentioned, the phenomenological successes of the holographic Yang-Mills model described above gave an incentive to develop it further, so as to get closer to QCD. In particular, QCD possesses, in addition to the glue part, a flavor sector with matter in the fundamental representation of the gauge group (the quarks). For massless quarks, the theory exhibits a global chiral symmetry group $U(N_f)_L \times U(N_f)_R$, where N_f is the number of flavors. Then, according to the holographic dictionary (see section 2.1), the gravitational dual of a theory containing a massless flavor sector should include a $U(N_f)_L \times U(N_f)_R$ gauge theory. The flavor sector is therefore implemented by adding (flavor) D-branes in the bulk [119, 120], whose low energy dynamics are well known in string theory to be described by $U(N)$ gauge theories.

In the WSS model [121], the specific set of D-branes that realizes the flavor sector is given by an ensemble of N_f coincident D8-branes, paired with N_f anti-D8-branes ($\overline{\rm D8}$-branes). Those branes are nine-dimensional objects that are taken to be localized in the compact dimension, where the branes and anti-branes are separated by a finite distance L (see figure 2.4). The D8 generate the left-handed group $U(N_f)_L$, and the $\overline{\rm D8}$ the right-handed one $U(N_f)_R$.

The vacuum of the boundary theory with the quarks will then be dual to the solution of the bulk equations of motion including the D-branes. The general bulk solution where the branes back-react on the geometry is not known, but the problem simplifies in the quenched limit

$$N_f \ll N_c \,. \tag{2.2.3}$$

In this limit, the branes can be treated as probes on the glue geometry (2.2.1), and their dynamics solved on this fixed background.

The general solution for the brane configuration depends on the separation L between the branes and anti-branes at $U \to \infty$. The solution turns out to be trivial in the antipodal case $L = \pi M_{\rm KK}^{-1}$, meaning that the separation between the branes along the compact coordinate τ does not depend on U [121]. Even so, the shrinking of the compact dimension in the interior implies that the proper distance between the branes decreases, until they merge at $U = U_{\rm KK}$ (see figure 2.4). The consequence of this merging is that, instead of $U(N_f)_L \times U(N_f)_R$, the chiral group reduces in the IR to the diagonal subgroup $U(N_f)_V$. Therefore, the WSS model realizes geometrically the spontaneous breaking of the chiral

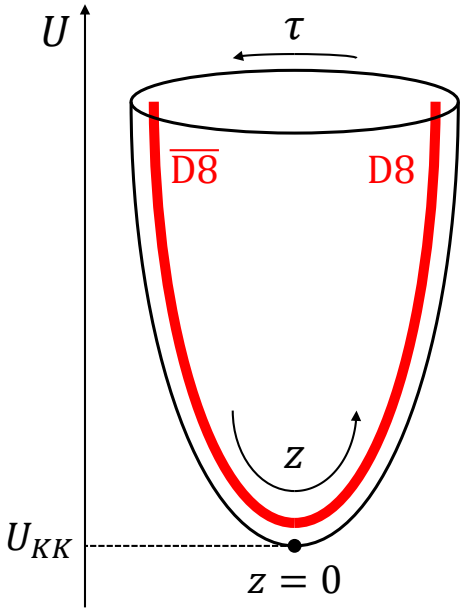

Figure 2.4: A sketch of the flavor branes' configuration in the confining geometry of the WSS model, in the (τ, U) subspace. We show the case of antipodal branes, which merge at the point where the geometry ends $U = U_{\rm KK}$.

symmetry in the QCD vacuum. Note that the picture is analogous for general L, except that the branes merge earlier, at $U_0 > U_{\rm KK}$.

Apart from the spontaneous chiral symmetry breaking, the WSS model is succesful in reproducing several aspects of the mesonic properties of QCD. These include the structure of the chiral Lagrangian, the QCD chiral anomalies, and the meson spectrum, which was found to be in reasonable quantitative agreement with experimental data [121]. As part of the successes regarding the spectrum, the model reproduces the Witten-Veneziano formula [122, 123] for the mass of the η' meson in the large N limit. The meson interactions that are computed from the WSS model were also shown to compare well with data [124]. In particular, the model exhibits vector meson dominance in various sectors, including for the electromagnetic form factor of the pion. Note that this last property is common to all proper holographic models.

To give a credible account of the IR physics of QCD, the spectrum of the model should include all the types of hadrons. That is, in addition to the glueballs and mesons, baryon

states should also appear. In the next section, we discuss how baryons are realized in the WSS model. Studying this concrete example gives a good idea of the basic properties that are expected of baryon solutions in holography. We will also identify clearly what are the specificities of the WSS baryon.

2.2.2 Holographic baryons

Baryon states are realized in holography as solitonic configurations of the bulk theory [125, 126], which realizes the intuition from large N_c QCD [127]. In the WSS model, the baryonic soliton corresponds to an instanton for the chiral $U(N_f)$ gauge fields A_M, which are the holographic dual of the (boundary) QCD chiral currents. Note that there is a single remaining (unbroken) gauge group $U(N_f)$ since the two stacks of branes merge into a single object in the IR, as shown on figure 2.4. The action that describes the dynamics of the gauge field in the bulk is given by the low energy effective action of the flavor D-branes. The latter contains a quadratic Yang-Mills part and a topological Chern-Simons (CS) term, which may be written as

$$S = S_{\mathrm{YM}} + S_{\mathrm{CS}}\,, \tag{2.2.4}$$

$$S_{\mathrm{YM}} = -\frac{\lambda N_c}{216\pi^3 U_{\mathrm{KK}}}\int \mathrm{d}^4x\mathrm{d}z\mathrm{Tr}\left(\frac{1}{2}h(z)F_{\mu\nu}^2 + \frac{9U_{\mathrm{KK}}^3}{4R^3}k(z)F_{\mu z}^2\right)\,, \tag{2.2.5}$$

$$h(z) \equiv \left(1+\frac{z^2}{U_{\mathrm{KK}}^2}\right)^{-\frac{1}{3}} \quad , \quad k(z) \equiv 1+\frac{z^2}{U_{\mathrm{KK}}^2}\,, \tag{2.2.6}$$

$$S_{\mathrm{CS}} = \frac{N_c}{24\pi^2}\int \mathrm{Tr}\left(A\wedge F^2 - \frac{i}{2}A^3\wedge F - \frac{1}{10}A^5\right)\,, \tag{2.2.7}$$

where F is the chiral field strength and $\lambda = g_{YM}^2 N_c$ the 't Hooft coupling. The integral is over the four coordinates x^μ of the flat boundary, and a new holographic coordinate z, related to U via

$$z \equiv U_{\mathrm{KK}}\sqrt{\frac{U^3}{U_{\mathrm{KK}}^3}-1}\ \sin(\tau M_{\mathrm{KK}})\,. \tag{2.2.8}$$

We consider the anti-podal case shown in figure 2.4, where the anti-branes are taken to sit at $\tau = -(\pi/2M_{\mathrm{KK}})$ and the branes at $\tau = (\pi/2M_{\mathrm{KK}})$. This implies that z goes from $-\infty$ on the $\overline{\mathrm{D8}}$, to $+\infty$ on the D8, being equal to 0 at the point where the space ends.

The instanton dual of the baryon state is a solution of the bulk equations of motion for the action (2.2.4), with unit instanton number

$$\frac{1}{8\pi^2}\int \mathrm{d}^3x\mathrm{d}z\,\mathrm{Tr}\Big(F\wedge F\Big) = 1\,. \tag{2.2.9}$$

The integral in (2.2.9) is over the four-dimensional Euclidean space spanned by the holographic coordinate z and the three spatial directions of the boundary x^i. To discuss the properties of the instanton solution, it is useful to first consider the case of a flat geometry, corresponding to $h(z) = k(z) = 1$ in (2.2.5). In that case, the non-abelian structure of the instanton solution would be given by the standard BPST instanton, in an SU(2) subgroup of the full U(N_f) chiral group

$$A_M(\vec{x}, z) = -i\frac{\xi^2}{\xi^2 + \rho^2} g\partial_M g^{-1}\,, \tag{2.2.10}$$

where ρ is the instanton size, and ξ the distance to the center of the solution

$$\xi \equiv \sqrt{(\vec{x} - \vec{X})^2 + (z - Z)^2}\,, \tag{2.2.11}$$

$(\vec{X}, Z)$ being the position of the instanton in the four-dimensional Euclidean space. g is an SU(2) matrix given by

$$g(\vec{x}, z) = \frac{1}{\xi}\big((z - Z) - i(\vec{x} - \vec{X}).\sigma\big)\,, \tag{2.2.12}$$

where $\vec{\sigma} = (\sigma_1, \sigma_2, \sigma_3)$ contains the Pauli matrices.

If the instanton does indeed describe a baryon, it should also source the abelian part of the gauge field $\hat{A}_M$, which is dual to the baryon number current. This is realized via the CS part of the action (2.2.7), which includes a Coulomb interaction between the abelian gauge field and the instanton density

$$S_{\rm CS} \supset \frac{N_c}{64\pi^2}\epsilon^{MNPQ}\int \mathrm{d}^4x\mathrm{d}z\, \hat{A}_0 \mathrm{Tr}\big(F_{MN}F_{PQ}\big)\,. \tag{2.2.13}$$

With this coupling, the solution for the abelian gauge field sourced by the instanton can also be computed exactly in the flat limit

$$\hat{A}_0(\vec{x}, z) = \frac{96\pi^3}{\lambda}\frac{R^3}{U_{\rm KK}^2}\frac{1}{\xi^2}\left[1 - \frac{\rho^4}{(\rho^2 + \xi^2)^2}\right]\,. \tag{2.2.14}$$

Apart from the position of the center, the size of the instanton ρ is the only parameter of the solution (2.2.10) and (2.2.14). In absence of the coupling to the electric field $\hat{A}_0$, it is well known that the scale invariance of the classical Yang-Mills theory implies that all the sizes give a possible solution. However, the coupling to $\hat{A}_0$ breaks the scale invariance of the action, so that solutions of different sizes have different energies. In flat space, the energy of a solution of size ρ goes as

$$E_{\rm flat}(\rho) = M_0 + \frac{\hat{E}}{\rho^2}\,, \tag{2.2.15}$$

with M_0 and $\hat{E}$ two positive constants. So the true solution that minimizes the energy is such that $\rho \to \infty$, meaning that the coupling to the electric field destroys the instanton solution.

The geometry (2.2.1) on which the WSS instanton is defined is not flat, which implies that the solution is different from the BPST instanton. Qualitatively, the instanton tends to shrink due to the space-time curvature. This gives a competing effect with the Coulomb repulsion (2.2.15), resulting in an instanton of definite finite size. The solution on the curved background cannot be derived exactly, but it turns out that the size of the instanton ρ is much smaller than the bulk radius of curvature R at large 't Hooft coupling

$$\frac{\rho}{R} \sim \lambda^{-\frac{1}{2}} \ll 1\,. \tag{2.2.16}$$

In these conditions, the instanton is well approximated by the BPST instanton (2.2.10) and (2.2.14), as long as we consider distances to the center much smaller than $\lambda^{1/2}\rho$. Then, the energy of the solution can be computed exactly up to order $\mathcal{O}(\lambda^0)$, which results in an expression of the form

$$E(\rho, Z) = M_0 \left[1 + \frac{1}{\lambda}\left(E_g \lambda \rho^2 + \frac{\hat{E}}{\lambda\rho^2} + E_{g,Z} Z^2\right) + \mathcal{O}(\lambda^{-2})\right]\,. \tag{2.2.17}$$

The first term $M_0 \sim \lambda N_c$ is the mass of the BPST instanton, which gives the leading order contribution to the classical part of the baryon mass at $\lambda \gg 1$. The terms at order $\mathcal{O}(\lambda^0)$ give the dependence of the energy on the parameters of the solution. The gravitational contribution which favors small instantons is given by the term proportional to ρ^2, whereas the term that goes as ρ^{-2} comes from the Coulomb repulsion. From the point of view of the boundary theory, the gravitational term is interpreted as the effect of the confining strong force (recall that the glue sector of the theory is dual to the geometry (2.2.1)). As for the Coulomb repulsion, it simply implements the fact that higher baryon densities result in higher energies.

Note that the background curvature has another effect, that corresponds to the Z^2 term in (2.2.17). The latter implies that the baryon solution should sit at $z = 0$, that is at the point where the geometry caps off. The four-dimensional translational invariance of the BPST instanton is thus broken in the holographic direction, but remains intact along the boundary directions.

Most of the properties of the WSS baryon solution are expected to be common to other holographic models of QCD:

- The boundary baryon state is dual to an instanton configuration of the chiral gauge fields in the bulk;
- The gravitational attraction makes the instanton shrink, whereas the Coulomb repulsion from the topological Chern-Simons term makes it inflate. The competition of the two effects results in a finite size for the baryon;

- The baryon tends to fall towards the IR region (the interior of the geometry) due to the background curvature.

However, the fact that the baryon size is parametrically small at large 't Hooft coupling λ is a specificity of the WSS model. On the one hand, this property is very handy for computing the baryonic properties, since at leading order in λ^{-1}, the solution is equivalent to the flat space BPST instanton. On the other hand, it implies that the baryon size is much smaller than the confining scale $M_{\rm KK}^{-1}$, which clashes with the expectation from QCD.

Despite this issue with the baryon size, the WSS model was shown to be quite succesful in reproducing QCD data in the baryonic sector as well. These include the mass splittings in the baryon spectrum [128], but also static properties [129], including some nucleon flavor form factors and baryon-meson vertices. Those observables turn out to be independent of λ: apart from the zero-point energy, the spectrum is determined by the order $\mathcal{O}(\lambda^0)$ term in (2.2.17), and the relevant size in the flavor form factors is controlled by the mass of the rho meson rather than the instanton size.

However, the main limitation of the WSS model for baryons is that some baryonic observables do depend on λ. These include mainly the zero-point energy $M_0 \sim \lambda M_{\rm KK}$, which is parametrically larger than the confining scale, and the gravitational form factors (the matrix elements of the stress-energy tensor). This shortcoming of the WSS model is a consequence of the fact that the 't Hooft coupling λ appears as a parameter of the low energy theory. That is, the dimensional transmutation from λ to $M_{\rm KK}$ is not realized, and some hadronic scales end-up depending on λ in addition to $M_{\rm KK}$.

In summary, the WSS model gives an elegant top-down construction of a holographic theory which contains many properties in common with QCD. The glue sector is dual to the bulk geometry, and the flavor sector to probe D-branes. Apart from the number of colors N_c, the model contains only two parameters: the 't Hooft coupling λ and the mass scale $M_{\rm KK}$[6]. The theory exhibits confinement, spontaneous breaking of the chiral symmetry, and its spectrum contains all the types of hadrons, with properties that are mostly in quite good agreement with experimental or lattice data (with two parameters!). However, the model also has several limitations. Apart from the fact that the results are valid only at leading order in the large N_c limit (which is common to all holographic models), these include:

- The absence of separation between the UV cut-off of the four-dimensional description and the confining scale, both of which are given by M_{KK}. As a consequence, the glue sector does not exactly correspond to the Yang-Mills theory in four-dimensions;

[6]Above, we focused on the case of anti-podal branes, but the brane separation L can be considered as an additional parameter of the model.

- The trivial RG flow of the four-dimensional 't Hooft coupling λ, and the fact that it appears as a parameter of the low energy theory;
- The fact that the embedding of the flavor branes can only be computed in the quenched approximation $N_f \ll N_c$, where the back-reaction on the geometry is negligible;
- A point that was not mentioned above: the bifundamental "tachyon" field dual to the quark bilinear operator $\bar{\psi}\psi$ is non-local [132]. As a consequence, it is hard to implement a finite quark mass in the model[7]. In the WSS model, the tachyon field arises as the low energy excitations of open strings that connect the branes to the anti-branes. Because the branes are separated along the compact direction τ, those strings are stretched to a macroscopic size $L \sim M_{\rm KK}^{-1}$.

In the next section, we present the holographic model that was used in this work. This so-called Veneziano-QCD (V-QCD) model is the most complete framework for holographic QCD, which is able to overcome all the limitations of the WSS model mentioned above. In particular, it makes it possible to implement the back-reaction of the flavor sector on the glue sector, which is crucial for our present purpose of investigating the properties of dense QCD matter.

2.3 The bottom-up V-QCD framework

In this section, we will introduce the (semi-)bottom-up V-QCD framework that was used in this work. Until now, the holographic models that we have been considering were top-down models. That is, models where the holographic dual of the strongly coupled QFT is given by an explicit construction in string theory. However, the bulk theory that we ended up dealing with in the large N and strong coupling limit, reduced to a classical theory of gravity and other fields (such as the WSS gauge field), defined on a specific five-dimensional geometry. From this observation, the philosophy of the bottom-up approach is to start directly from a five-dimensional classical theory, whose field content is determined from the holographic dictionary. The action that determines the dynamics of the bulk fields may then be written in terms of low energy parameters, in the spirit of effective field theory. As we will see, the V-QCD action builds up on the successes of the top-down models, in particular the WSS model, by using an ansatz qualitatively similar to the low energy actions that arise in string theory. In that sense, V-QCD should be considered as a semi-bottom-up model, as it satisfies all the qualitative properties implied by string theory (unlike many other bottom-up models).

[7]There are ways of improving the model to include quark masses [130, 131, 132, 129, 133], but explicit calculations can only be done perturbatively in the quark mass.

The cost of considering a bottom-up approach is that the UV completion of the bulk theory is not known (although we have some intuition of the underlying string theory [134]), and the low energy theory that is built typically contains more parameters than the top-down models. Also, the exact form of the boundary QFT is not known. However, it is the best approach to tailor a theory as close as possible to QCD[8]. Indeed, starting from the holographic dictionary ensures that the boundary operator algebra contains the main operators that are important for the low energy dynamics of QCD. In particular, the tachyon field dual to the quark bilinear $\bar{\psi}\psi$, which is difficult to include in top-down models, is naturally part of the bottom-up bulk theory. Also, imposing the number of flavors N_f to be of the same order as the number of colors N_c, does not require to solve complicated brane dynamics, but simply the back-reaction of the flavor fields on the metric.

The physics of the V-QCD model has been analyzed in various phases, showing good agreement with QCD data where it is available. The structure of the confining and chirally broken vacuum has been derived, both at zero quark mass [150] and finite quark mass [160], and at finite θ-angle [166]. The spectra of the mesonic excitations at zero temperature was shown to be discrete and gapped (modulo the pions) [161], with linear trajectories for the radial excitations $m_n^2 \sim n$. Moreover, it has been shown that the V-QCD potentials can be fitted efficiently to experimental data for meson spectra, with accuracies better than 10% for most of the states [162].

V-QCD has also been studied at finite temperature T [163] and quark number chemical potential μ_q, when ignoring the baryonic states [164]. The structure of the phase diagram in the (T, μ_q) plane was shown to exhibit chiral and deconfining[9] phase transitions, where the critical temperature $T_c(\mu_q)$ decreases with the chemical potential, and vanishes at some critical value μ_c. The thermodynamics at $\mu_q = 0$ was also computed, and shown to compare well with lattice results [165].

Having exposed the motivation for its construction, as well as its successes thus far, we will now proceed to reviewing the V-QCD model. As mentioned above, V-QCD is a bottom-up, five-dimensional holographic model for QCD with N_c colors and N_f flavors, which captures both glue and flavor dynamics, i.e. the flavor sector is fully backreacting. The holographic description in terms of a 5-dimensional theory is assumed to be valid in the Veneziano large-N limit,

$$N_c, N_f \to \infty, \quad x \equiv \frac{N_f}{N_c} \quad \text{and} \quad \lambda_t \equiv g_{\rm YM}^2 N_c \ \text{finite}\,, \tag{2.3.1}$$

[8] As we will explain below, the convenient approach in practice is to first tailor the glue sector of the theory to the properties of Yang-Mills, and then tailor the full theory with flavors to QCD. This is also described in more detail in section 3.2.2.

[9] It is well known that there is no order parameter for confinement in QCD, when quarks are taken into account. However, in the large N limit, the confined and deconfined phases can be distinguished by the scaling of the free energy in the number of colors. The free energy is of order $\mathcal{O}(1)$ in the confined phase, whereas it is of order $\mathcal{O}(N_c^2)$ in the deconfined phase.

where $g_{\rm YM}$ is the Yang-Mills coupling.

The holographic model consists of a five-dimensional bulk theory whose dynamical fields are in one-to-one correspondence with the lowest-dimensional gauge-invariant operators in QCD. These are:

1. The five-dimensional metric g_{ab}, dual to the stress-tensor;

2. A scalar field λ (the *dilaton*) dual to the operator $\mathrm{Tr}F_{\mu\nu}F^{\mu\nu}$ (where $F_{\mu\nu}$ is the Yang-Mills field strength) and encoding the running 't Hooft coupling;

3. A set of $U(N_f)_L \times U(N_f)_R$ non-Abelian gauge fields, denoted $\mathbf{L}_M$, $\mathbf{R}_M$, dual to the chiral flavor currents $\mathbf{J}^{(L)}_\mu$, $\mathbf{J}^{(R)}_\mu$, whose matrix elements are:

$$\left(\mathbf{J}^{(L)}_\mu\right)^i_j = \bar{q}^i_L \gamma_\mu q_{L\,j}, \qquad \left(\mathbf{J}^{(R)}_\mu\right)^i_j = \bar{q}^i_R \gamma_\mu q_{R\,j} \qquad i,j = 1\ldots N_f\,, \tag{2.3.2}$$

   where $q_{L/R\,i}$ are the left-handed and right-handed quarks in the fundamental representation of $U(N_f)_{L,R}$;

4. An $N_f \times N_f$ complex scalar field matrix T^i_j (the *tachyon*) in the bi-fundamental representation of $U(N_f)_L \times U(N_f)_R$, dual to the quark bilinear $\bar{q}^i_R q_{L\,j}$.

All the above operators have dimension 4 or smaller. To those, one can add the Yang-Mills instanton density $\mathrm{Tr}(F\wedge F)$, which describes the CP-odd sector of QCD, related to the θ angle. The CP-odd sector has been analyzed in V-QCD [166], but for the present purpose we can as well consider that the θ angle is experimentally constrained to be less than 10^{-10}, and set it to zero.

The bottom-up nature of the model then resides in truncating the spectrum to the low-dimension operators listed above[10], and writing a phenomenological action describing the dynamics of the corresponding bulk fields. The general structure of the action is obtained from string theory. It involves a few a priori unknown functions of the scalars T and λ, whose relevant features are fixed by a mixture of theoretical and phenomenological motivations.

The five-dimensional action for the bulk fields takes the following form:

$$S_{V-QCD} = S_g + S_{DBI} + S_{CS}\,. \tag{2.3.3}$$

The first term S_g depends on the color sector alone, while the second and third terms describe the coupled flavor-color degrees of freedom. S_{DBI} is a Dirac-Born-Infeld-type

[10]The criterium for the truncation is actually not only given by the dimension of the operators. There are other operators of dimension less than 4 that are not taken into account, such as $\bar{\psi}[\gamma^\mu,\gamma^\nu]\psi$ or the traceless part of $\mathrm{Tr}(F_{\mu\nu}F_{\rho\sigma})$. Those operators are ignored because they are expected to be dual to massive higher excitations of strings, due to their higher tensor structure.

action which contains the kinetic terms of the tachyon and gauge fields, whereas S_{CS} is a generalized Tachyon-Chern-Simons action whose role is crucial to correctly recover chiral anomalies. If we think of this model as originating from a (non-critical) string theory, then the color action describes the low-energy effective theory of closed string fields, while the DBI and Tachyon-Chern-Simons actions describe the open string sector living on the world-volume of N_f pairs of space-filling D4-branes and anti D4-branes. Below we shall describe in more detail the first two terms in the action. The construction of the TCS term is part of the results from the work carried out in this thesis, so it will be discussed later, in section 3.1.3.

The action S_g in (2.3.3) gives a holographic description of the pure glue sector in terms of the Einstein-dilaton theory of the fields λ and g_{MN}. It has the form:

$$S_g[g,\lambda] = M^3 N_c^2 \int d^5x\sqrt{-g}\left[R - \frac{4}{3\lambda^2}g^{MN}\partial_M\lambda\partial_N\lambda + V_g(\lambda)\right] \quad , \quad 0 < \lambda < +\infty. \quad (2.3.4)$$

This is the action for the five-dimensional Improved Holographic QCD (IHQCD) holographic model for pure Yang-Mills theory [145]. The UV regime of the theory corresponds to the small-λ region, and the IR is reached as $\lambda \to +\infty$. The dilaton potential $V_g(\lambda)$ is chosen in such a way that it allows for a logarithmically running coupling constant in the UV, leads to color confinement (i.e. a Wilson loop area law) and has a qualitatively correct glueball spectrum. These requirements fix the large-λ and small-λ behavior of $V_g(\lambda)$ as follows [145].

For small λ, one requires an analytic behavior of the glue potential:

$$V_g(\lambda) = \frac{12}{\ell_g^2}\left[1 + V_{g,1}\lambda + O(\lambda^2)\right] \quad , \quad \lambda \to 0\,. \quad (2.3.5)$$

The leading term in the expansion ensures that the model admits an asymptotically AdS_5 solution with AdS length ℓ_g and with $\lambda \to 0$ as one approaches the boundary. The second term ensures that λ (identified with the running 't Hooft coupling in the UV) has the correct perturbative running, and the coefficient $V_{g,1}$ is fixed by matching the first β-function coefficient of four-dimensional Yang-Mills. Similarly, higher-order terms in the expansion (2.3.5) can be fixed by matching higher-order β-function coefficients.

For large λ, matching the expected qualitative behavior of Yang-Mills at low-energy requires [145]:

$$V_g(\lambda) \sim \lambda^{4/3}(\log\lambda)^{1/2} \quad , \quad \lambda \to +\infty\,. \quad (2.3.6)$$

With this asymptotics, the Wilson loop follows an area law. Moreover, the model has a discrete spectrum of glueball excitations, with masses m_n obeying Regge-like asymptotics $m_n^2 \propto n$, both in the scalar and in the tensor sectors.

We now come to the DBI part of the action, the second term in (2.3.3). In most of the previous works in the context of V-QCD [150, 151, 156, 157, 160, 161, 163, 164, 166], only the Abelian vector part of the gauge fields was relevant, and moreover the tachyon matrix

was restricted to be the identity matrix times a real function τ. These assumptions apply when considering homogeneous solutions (the vacuum, or a thermal equilibrium state) and neglecting quark mass differences. In this case the DBI action reduces to an action for a single Abelian gauge field and a real scalar τ. For illustrative purposes, we first present this simplified version of the DBI action, because it already contains the phenomenological potentials which characterize the model. The full DBI action including the non-Abelian structure will be presented in section 3.1.2.

The simplified DBI action was taken to be of the form, [138, 150]:

$$S_{DBI,simpl}[g_{ab},\lambda,\tau,v_M] = -M^3 N_c N_f \times \\ \times \int d^5x V_f(\lambda,\tau)\sqrt{-\det\left(g_{MN}+\kappa(\lambda)\partial_M\tau\partial_N\tau + w(\lambda)F_{MN}\right)}\,, \tag{2.3.7}$$

where the field τ is defined by the tachyon ansatz

$$T^i_j = \tau\delta^i_j \quad , \quad \tau\in\mathbb{R}\,, \tag{2.3.8}$$

and F_{MN} is the field strength of the vector $U(1)$ gauge field v_M, defined such that:

$$(\mathbf{L}_M)^i_j = (\mathbf{R}_M)^i_j = v_M\delta^i_j \quad , \quad i,j=1\ldots N_f\,. \tag{2.3.9}$$

The form of the action (2.3.7) is modeled after the Abelian form of Sen's DBI action for unstable D-branes [159], which governs top-down holographic models of flavor that incorporate chiral symmetry breaking (such as the WSS model discussed in the previous section). Lacking a top-down description, the phenomenological character of the DBI action (2.3.7) is encoded in three functions of the scalars $V_f(\lambda,\tau),\kappa(\lambda),w(\lambda)$, which affect both the flavor dynamics and its interaction with color. These functions are constrained by consistency and phenomenological requirements, which are discussed in detail in [161] and that we summarize below[11].

- $V_f(\lambda,\tau)$ controls the overall effect of flavor over the color background, and it is crucial (for example) for the correct description of chiral symmetry breaking. More specifically, we assume that, at large values of τ, it behaves asymptotically as:

  $$V_f(\lambda,\tau)\sim e^{-a(\lambda)\tau^2} \quad , \quad \tau\to+\infty\,, \tag{2.3.10}$$

  with $a(\lambda)>0$. The behavior (2.3.10) is modeled after Sen's action for unstable D-branes, and it implies that as $\tau\to\infty$ the space-filling flavor branes disappear [159, 138].

[11] The functions κ and w can in principle also depend on the tachyon field. We shall not consider such a dependence in this work.

- The effective scalar potential including the DBI contribution is

$$V_{eff}(\lambda,\tau) = V_g(\lambda) - \frac{N_f}{N_c} V_f(\lambda,\tau)\,. \tag{2.3.11}$$

As $\tau \to \infty$, chiral symmetry is broken, the flavor sector decouples due to (2.3.10) and $V_{eff}(\lambda)$ reduces to $V_g(\lambda)$. On the other hand, for $\tau = 0$ (which corresponds to the UV), the effective dilaton potential contains a flavor contribution:

$$V_{eff}(\lambda,\tau=0) = V_g(\lambda) - \frac{N_f}{N_c} V_{f,0}(\lambda) \quad , \quad V_{f,0}(\lambda) \equiv V_f(\lambda,0)\,. \tag{2.3.12}$$

At small tachyon, the flavor potential V_f follows an expansion of the form:

$$V_f(\lambda,\tau) = V_{f,0}(\lambda)\left[1 - \hat{a}(\lambda)\tau^2 + \mathcal{O}\left(\tau^4\right)\right]\,. \tag{2.3.13}$$

- For the correct UV behavior, all functions of λ have a regular power-law expansion in λ around $\lambda = 0$, similar to the one of V_g in (2.3.5):

$$\begin{aligned}
&V_{eff}(\lambda,\tau=0) = V_0\left[1 + V_1\lambda + O(\lambda^2)\right]\,,\\
&V_{f,0}(\lambda) = W_0\left[1 + W_1\lambda + O(\lambda^2)\right],\\
&\kappa(\lambda) = \kappa_0\left[1 + \kappa_1\lambda + O(\lambda^2)\right], \qquad\qquad \lambda \to 0\,,\\
&w(\lambda) = w_0\left[1 + w_1\lambda + O(\lambda^2)\right],\\
&\hat{a}(\lambda) = 1 + a_1\lambda + \mathcal{O}(\lambda^2)\,,
\end{aligned} \tag{2.3.14}$$

where W_0, κ_0 etc. are constants. The UV AdS length is now given by the effective potential (2.3.11) evaluated at $\lambda = 0, \tau = 0$:

$$\frac{12}{\ell^2} = \frac{12}{\ell_g^2} - xW_0, \tag{2.3.15}$$

where ℓ_g^2 was defined in (2.3.5) and x in (2.3.1). The other expansion coefficients are fixed by matching the UV behavior of the QCD operators (dimensions, two-point function normalization, etc.).

- In the IR regime, thermodynamics and the qualitative features of the meson trajectories constrain the large-λ behavior of the functions $V_{f,0}(\lambda)$, $\kappa(\lambda)$ and $w(\lambda)$. In particular, qualitatively consistent results are obtained if we assume that, to leading order as $\lambda \to +\infty$:

$$V_{f,0} \sim W_{IR}\lambda^{v_p}, \quad \kappa \sim \kappa_{IR}\lambda^{-4/3}(\log\lambda)^{1/2}, \quad w \sim w_{IR}\lambda^{-4/3}(\log\lambda), \quad a \sim a_{IR}, \tag{2.3.16}$$

where W_{IR}, κ_{IR}, w_{IR}, a_{IR} and v_p are constants, and $4/3 < v_p < 10/3$.

2.3.1 Vacuum solution

The Poincaré-invariant vacuum of the dual field theory is described by a bulk solution to the classical field equations in which all the gauge fields are set to zero. Assuming that the quark mass matrix is proportional to the identity[12], the solution is characterized by the three functions $A(r), \lambda(r)$ and $\tau(r)$:

$$ds^2 = e^{2A(r)}\left(dr^2 + \eta_{\mu\nu}dx^\mu dx^\nu\right), \quad \lambda = \lambda(r), \quad \tau = \tau(r)\,. \tag{2.3.17}$$

Here, r is the holographic radial coordinate, and x^μ , $\mu = 0\ldots 3$ are identified with the coordinates of 4d Minkowski space-time, on which the dual field theory is defined.

With the gauge fields identically zero, the TCS action does not contribute to the field equations, and the Poincaré-invariant solution (2.3.17) is completely determined by the first two terms in (2.3.3).

While in general the equations of motion have to be solved numerically, the asymptotic behavior of the solution in the UV and IR can be obtained analytically and it is fixed by the asymptotic behavior of the potentials discussed in the previous section. Below, we give a review of the asymptotics of the V-QCD vacuum solution. These results are necessary to understand the boundary conditions satisfied by the baryon solution that is analyzed in the next chapter.

UV asymptotics. The region of the geometry corresponding to the UV of the dual field theory is the region where $e^A \to +\infty$ and $\lambda \to 0$ [145]. If the radial coordinate is chosen as in (2.3.17), this region corresponds to the limit $r \to 0$, and one finds (see e.g. [145, 161]):

$$A(r) = -\log\left(\frac{r}{\ell}\right) + \frac{4}{9\log(r\Lambda)} + \mathcal{O}\left(\frac{1}{\log(r\Lambda)^2}\right), \tag{2.3.18}$$

$$\lambda(r) = -\frac{1}{V_1}\frac{8}{9\log(r\Lambda)} + \mathcal{O}\left(\frac{1}{\log(r\Lambda)^2}\right), \tag{2.3.19}$$

$$\begin{aligned}\frac{1}{\ell}\tau(r) = {} & mr(-\log(r\Lambda))^c\left(1 + \mathcal{O}\left(\frac{1}{\log(r\Lambda)}\right)\right) \\ & + \Sigma\, r^3(-\log(r\Lambda))^{-c}\left(1 + \mathcal{O}\left(\frac{1}{\log(r\Lambda)}\right)\right).\end{aligned} \tag{2.3.20}$$

In the equations above, ℓ is the AdS length, V_1 is the first subleading coefficient in the effective potential (see equation (2.3.14)), and Λ, m and Σ are integration constants of the field equations. In terms of the dual field theory, Λ is a scale which measures the breaking of conformal invariance in the UV (it is the holographic manifestation of the QCD scale); m is

[12] This implies that the quark masses are all the same.

the quark mass[13] and Σ is the quark condensate. The independent leading and subleading terms in the tachyon expansion correspond to a field theory operator of dimension $\Delta = 3$, with the extra logarithm reproducing the QCD mass anomalous dimension. The exponent c is determined by the $O(\lambda)$ terms in the expansions of the potentials (2.3.14), see [161]:

$$c = \frac{4}{3}\left(1 + \frac{\kappa_1 - a_1}{V_1}\right). \tag{2.3.21}$$

IR asymptotics The IR region of the geometry corresponds to $e^A \to 0$ and $\lambda \to +\infty$, [145]. In the chiral symmetry breaking solution (for which $\tau \neq 0$) the tachyon also diverges in this limit [150]. With the glue potential behaving as in (2.3.6), the IR is found in the limit $r \to +\infty$, and we have [145, 150]:

$$\lambda(r) = \mathrm{e}^{\frac{3r^2}{2R^2}+\lambda_c}\left(1 + \mathcal{O}\left(r^{-2}\right)\right), \tag{2.3.22}$$

$$\mathrm{e}^{A(r)} = \sqrt{\frac{r}{R}}\mathrm{e}^{-\frac{r^2}{R^2}+A_c}\left(1 + \mathcal{O}\left(r^{-2}\right)\right), \tag{2.3.23}$$

$$\tau(r) = \tau_0\left(\frac{r}{R}\right)^{C_\tau}\left(1 + \mathcal{O}\left(r^{-2}\right)\right). \tag{2.3.24}$$

Here, C_τ, A_c, and λ_c are constants determined by the asymptotics of the various potentials (2.3.14) and (2.3.15), and the first of these constant must obey $C_\tau > 1$; R and τ_0 are integration constants which are (implicit) functions of the integration constants appearing in the UV. In particular, R plays the role of the non-perturbative IR scale of the theory.

[13] Recall that we are assuming a quark mass matrix proportional to the identity.

Chapter 3

The V-QCD baryon

Baryon bound states are difficult to describe quantitatively in terms of quarks and gluons. In the large-N limit however, [127], they have a nice description as solitons of the effective chiral theory, [139, 140]. This theory, beyond the ad-hoc higher derivative term introduced by Skyrme to stabilize the solitons, contains a topological term that is crucial for making the solitons fermions in the case of N_c odd, [140]. Once the quarks are coupled to external sources that are flavor gauge fields, this topological part of the action becomes gauged and reproduces the well-known flavor anomalies, [140, 141, 142].

The issue of flavor anomalies and the associated topological terms, is an important ingredient of the low-energy dynamics of QCD. In the effective chiral Lagrangian, such terms emanate from Witten's five-form topological term, [140], whose quantized coefficient is given by the number of colors, N_c. Such a term is written as a five dimensional (topological) integral over a five-manifold with a single boundary which is identified with the four-dimensional spacetime on which QCD is defined. Once the theory is coupled to vector sources L_μ, R_μ for the flavor currents, the Noether procedure has given eventually the gauged WZW term, [140, 141, 142], that controls the anomalous variations of the effective action under flavor transformations. This action must be both P and C invariant as is expected from QCD without a θ angle[1]. Higher topological terms that are gauge invariant start at six-derivatives, [167, 168] and have been analyzed up to eight derivatives [169]. However, in this context the chiral condensate and its size fluctuations are absent from the low energy dynamics of the chiral Lagrangian.

The issue of the relevant parity-odd terms in holographic models is also diverse[2]. In

[1]The relevant P and C transformations are defined in appendix A.

[2]In this theory the combined parity transformation P is the product of two transformations P_1 and P_2 that are defined in appendix A. P_2 acts in the usual way on the boundary space coordinates. P_1 acts on the fields. In most cases in holography, parity-odd refers to P_2-odd in our notation, and it always involves the Levi-Civita tensor. From now on we will be careful in specifying the type of parity transformation we refer to, P_1, P_2 or $P = P_1P_2$.

the simplest bottom-up model, the hard wall model [143], the relevant terms are five-dimensional Chern-Simons terms involving the flavor gauge fields L_μ, R_μ. They do not include, in particular, contributions from the quark condensate field, T, which is dual to the quark-mass operator and controls chiral symmetry breaking. Moreover, in this simple model, chiral symmetry breaking occurs by fiat rather than dynamically.

In the more realistic top-down model of Sakai and Sugimoto [121, 124], the topological terms arise again from a five-dimensional Chern-Simons term that involves the (now unique) flavor gauge field A_μ. As explained in section 2.2, the reason that the gauge field is unique is that in the chirally broken case, the branes and antibranes fuse to a single brane and A_μ is the left-over gauge field after the fusion. However, as it was anticipated later [170], this Chern-Simons term is not enough to describe the physics of baryons and an extra contribution, localized at some IR boundary on the flavor brane was added by hand [170]. Again, here the tachyon field is absent as it is a fluctuation of a non-local string.

The V-QCD theory has in general a P_2-odd five dimensional Tachyon-Chern-Simons term that is not only a functional of the flavor gauge fields, $A_\mu^{L,R}$ but also of the (matrix-valued) tachyon field, [138]. As already shown in [138], an analysis of a general tachyon-dependent CS term is notoriously difficult, and this is why, in that reference, it was determined based on string theory calculations for a tachyon field that is proportional to the identity matrix. In this work we shall go a step further and we shall assume that

$$T = \tau U \tag{3.0.1}$$

where U is a unitary matrix and τ a single real field [3]. Both τ and the unitary matrix U are five-dimensional fields. With this assumption, we shall perform a comprehensive search for the most general tachyon-dependent CS term that is compatible with all symmetry expectations, and which reproduces the flavor anomalies of QCD. From now on we shall call these terms the Tachyon-Chern-Simons terms or TCS for short.

The TCS term beyond anomalies is also relevant for dynamical questions. Because of its structure, and the fact that it is proportional to the five-dimensional ϵ-tensor, it does not contribute in several relatively-uniform bulk solutions. Solutions, with full Poincaré ISO(3,1) invariance, or $\mathbb{R}\times$SO(3) invariance relevant at finite temperature and density are not affected by the TCS term. In the presence of a (weak) electromagnetic field the TCS term contributes to the two-point functions of currents, [185, 186].

In a similar spirit, it is known that the (T)CS term can mediate mixing and translational invariance instabilities in finite density contexts, [187, 188, 189, 190], leading to spatially modulated phases. Finally, being cubic to leading order in the flavor gauge fields, it is important in the determination of the three point function of the flavor currents.

[3] A chiral rotation can transform U to the identity. It cannot however change the value of τ. This means that flavor symmetry is broken to the diagonal vector $U(N_f)$ but not further, as in the chiral limit of QCD. The most general form of the tachyon matrix would be instead $T = \mathcal{T}U$, where $\mathcal{T}$ is a Hermitian matrix. If the latter is non-trivial, the tachyon matrix cannot (in general) be brought to be proportional to the identity matrix by a L-R gauge transformation.

Probably, the most important role of the (T)CS term so far, beyond anomalies, is in the determination of the baryon soliton solution in the holographic context. The baryon ansatz is sufficiently complicated so that it contributes non-trivially, in several ways. In particular, the soliton would have the tendency to shrink to a point, but the CS term is crucial in its stabilisation. As reviewed in section 2.2 in the context of the WSS model, the soliton is essentially an instanton of the flavor symmetry group, and because of the CS term it acquires a $U(1)_B$ charge. This has a dual effect. First it makes the soliton a baryon. Second the $U(1)_B$ charge repulsion in the bulk stabilizes the soliton that would like otherwise to collapse as it happens in simpler cases, [128, 171].

This chapter discusses the construction of the single baryon solution in V-QCD. It is divided in two parts. In the first part, we introduce the formalism for the baryon solution, including the construction of the TCS term, and the derivation of the appropriate baryon ansatz. In the second part, we compute numerically the baryon solution for a specific model in the V-QCD class. We then analyze the quantization of the collective modes of the solution, which results in the calculation of the baryon spin-isospin spectrum. The chapter ends with a discussion of limitations, advantages and further directions.

3.1 Tachyon-dependent Chern-Simons term and formalism for the baryon solution

This section is based on my original work [5].

The goal in this section is two-fold:

1. To analyze the general structure of the TCS term and to understand the relevance of different parts in dynamics and anomalies.

2. To write the appropriate ansatz of the baryon solution, to derive the equations of motion, and to understand the boundary conditions relevant for the solution as well as the conditions for obtaining the correct baryon number.

In this work, we fully answer these questions provided we are in the exact chiral limit. This implies in particular that the tachyon field will be taken to have the form (3.0.1), where τ is a real scalar function and U is a (spacetime-dependent) unitary matrix. In the chiral limit, we are able, on the one hand, to write down the most general combination of tachyon-dependent Chern-Simons-like terms compatible with symmetries and anomalies of the boundary theory, and with (bulk) gauge-invariance. On the other hand, we work out the appropriate ansatz for a cylindrically-symmetric bulk instanton which is regular, horizonless, has finite mass and unit baryon charge with respect to the boundary theory, and is therefore the candidate for a single-baryon state in V-QCD.

3.1.1 Summary

In order to make our main results more directly accessible, we start the discussion by giving a brief summary of the contents of this section.

CS terms

We call the TCS part of the bulk action anything which is written as a bulk integral of a five-form,

$$S_{CS} = \frac{iN_c^2}{4\pi^2}\int_{bulk}\Omega_5 \tag{3.1.1}$$

where the normalization is chosen for convenience. We assume[4] that Ω_5 may depend only on the flavor sector fields (the tachyon modulus τ, the unitary matrix U and the flavor gauge fields), but *not* on the glue sector fields (the metric and dilaton). Under this assumption, we write the most general form Ω_5 which is compatible with the discrete symmetries and such that, under a bulk gauge transformation, the variation of (3.1.1) reduces to a UV-boundary term which reproduces the flavor anomalies of QCD. These restrictions largely (but not completely) fix the form Ω_5. It must be the sum of three terms:

$$\Omega_5 = \Omega_5^0 + \Omega_5^c + dG_4, \tag{3.1.2}$$

which have the following properties:

1. The first term Ω_5^0 is gauge-invariant (under bulk gauge-transformations) but not closed; it is the sum of four terms:

$$\Omega_5^0 = \sum_{i=1}^{4} f_i(\tau)F_5^i(U, F^L, F^R), \tag{3.1.3}$$

   where the $f_i(\tau)$ are arbitrary functions of the tachyon modulus, and $F_5^i(U, F^L, F^R)$ are specific gauge-invariant five-forms which depend on U, its gauge-covariant derivative DU, and the field-strengths F^L and F^R of the left and right flavor gauge fields, and are given explicitly in section 3.1.3.1. The functions $f_i(\tau)$ can be constrained to some degree if one makes further assumptions. In particular, their value at $\tau = 0$ can be fixed by asking that in the chirally unbroken phase with trivial tachyon field $\tau = 0$, (3.1.1) matches the standard gauge Chern-Simons action in 5d for the left and right gauge fields.

2. The second term in (3.1.2) is closed but not exact and it is completely fixed by the flavor anomaly (including the overall coefficient):

$$\Omega_5^c = -\frac{1}{60}Tr[(U^\dagger dU)^5] \tag{3.1.4}$$

[4]This assumption is dictated by string theory.

3. The third term in (3.1.2) is written in terms of a 4-form G_4, which is fixed, up to a few arbitrary functions $h_i(\tau)$. However as it only enters the action via a boundary term, only the values at $\tau = 0$ of $h_i(\tau)$ matter, and these values are completely fixed by the QCD flavor anomaly.

To summarize, the TCS action is parametrized by two sets of functions $f_i(\tau)$ and $h_i(\tau)$. The $f_i(\tau)$'s have no effect on anomaly matching, but enter the field equations in the presence of non-trivial gauge-field configurations; the $h_i(\tau)$'s on the other hand are irrelevant for the dynamics, and their boundary value is fixed by anomaly matching (therefore this description has a certain redundancy).

In order to match the flavor anomaly, we have to make a further assumption of *IR regularity* on the matrix U as it usually happens in holography. This can be translated into the requirement that the matrix U should go to constant fast enough in the IR, so that there is no IR contributions to the on-shell action or to the anomalous variation of the action under gauge symmetry[5]. The same argument (no IR contributions to the on-shell action and anomaly) requires the functions $f_i(\tau)$ and $h_i(\tau)$ to vanish fast enough in the IR (which corresponds to the limit $\tau \to +\infty$ in the chirally broken phase).

The V-QCD baryon

As we mentioned earlier, the TCS action is crucial for correctly describing baryons in holographic theories. The second part of this work is devoted to lay out the general grounds for constructing the baryon as an asymptotically-AdS soliton solution of the bulk theory with the following properties:

- It is time-independent and spherically symmetric with respect to the boundary spatial directions;
- It is a finite-energy excited state over the QCD vacuum. This requires in particular that all bulk fields which are turned on must have vev-like asymptotics near the AdS boundary and must reduce to the vacuum fast enough at spatial infinity $|\vec{x}| \to +\infty$;
- It has baryon-number equal to one with respect to the boundary abelian vector flavor symmetry $U(1)_B$;
- It is horizonless: the baryon number is not *fractionalized*, i.e. it is not provided by deconfined degrees of freedom like in a quark-gluon plasma state.

Here, we construct a bulk $SU(2)$ instanton configuration of the $U(N_f)$ flavor axial gauge fields, depending on the four directions $(r, \vec{x})$ together with a nontrivial function

[5]This can often be rephrased more rigorously in terms of normalizable vs. non-normalizable solutions of the field equations near the IR: one then assumes that only normalizable configurations are physical.

$U(\tau, |\vec{x}|)$ describing the non-abelian part of the tachyon, which satisfies all above requirements. We argue later that we can neglect the backreaction of the baryon fields on the background fields (the metric, dilaton and tachyon modulus), that we take to be fixed on the homogeneous vacuum solution[6]. Indeed the baryon contributes to order N_c, which is negligible compared to N_c^2 and $N_c N_f$ in the Veneziano limit. Specifically, the construction involves the following steps:

1. We derive the full equations of motion for the instanton;

2. We identify the boundary conditions such that the finite-energy condition is satisfied. The boundaries here are 1) the near-AdS region UV boundary $r \to 0$, where the solution should satisfy vev-like boundary conditions for all the fields; 2) the boundary at spatial infinity $|\vec{x}| \to \infty$, where the fields have to vanish fast enough so that one can meaningfully describe the solution as a localized lump of finite energy in the boundary field theory;

3. We identify suitable "regularity" conditions in the IR region of the geometry (using both a gauge-invariant formulation, and in a Lorenz-like gauge);

4. We show that, under these conditions, the boundary baryon charge coincides with the bulk instanton number of the solution.

The last item on this list is particularly important because it shows that baryon configurations are topologically stable in the bulk.

We find that, remarkably, the derivation of the baryon number does not depend in any manner on the non-closed part of the TCS action Ω_5^0 and the corresponding TCS potentials $f_i(\tau)$ in equation (3.1.3). Rather, the generation of the baryon number and the contribution of the CS terms to the equations of motion (responsible for the stabilization of the baryon size) are ensured by two distinct parts of the TCS action (closed and non-closed, respectively). Although slightly counter-intuitive, it is not a contradiction. The reason is that the result for the baryon number simply tells us what should be the boundary behavior of the tachyon field for N_B to be non-zero (it should have a Skyrmion winding from (D.38)). It does not guarantee that a solution with such boundary conditions exists though. In particular, it is expected that no finite size solution should exist when Ω_5^0 vanishes ($f_i(\tau) = 0$).

The rest of this section is organised as follows. The first two subsections discuss the structure of the non-abelian V-QCD flavor action. Section 3.1.2 introduces the full DBI action, and the expansion that we consider, whereas the form of V-QCD Tachyon-Chern-Simons terms is determined in section 3.1.3. In section 3.1.4 we give the ansatz of the baryon state as an $SU(2)$ instanton of the bulk flavor sector. Then, in section 3.1.5, we

[6]The last requirement in the list above is trivial in this probe regime, since a horizon can only arise if the backreaction on the metric is non-negligible.

write the expression for the baryon energy, which generates the equations of motion for the ansatz fields. Finally, in section 3.1.6 we discuss the boundary conditions at the UV boundary and spatial infinity, as well as the conditions at the IR end of the bulk spacetime, which have to be satisfied in order for the baryon to have finite energy and unit charge. In that section we also compute the baryon charge of the solution and discuss its relation to the bulk instanton number. Several technical details are left to the Appendix.

3.1.2 Full DBI action

The first step to investigate the V-QCD baryon solution is to determine the appropriate form of the V-QCD flavor action used to describe its dynamics. We start here by discussing how the DBI part of the action is treated, whereas the TCS part will be discussed in the next subsection.

The V-QCD action was introduced in the previous chapter, section 2.3. The simplified DBI action (2.3.7) presented there is adapted to describe the dynamics of abelian gauge fields. However, the baryon solution has a non-trivial non-abelian stucture in the chiral group. To analyze baryons, it is therefore necessary to work with the full DBI action, including the non-abelian part. The full DBI action is the non-abelian generalization of (2.3.7), in which the full matrix nature of the tachyon and of the left and right gauge fields is explicit. It is again based on Sen's action, deformed by the same three phenomenological functions of the dilaton and tachyon $V_f(\lambda,T),\kappa(\lambda),w(\lambda)$ [150]:

$$S_{\rm DBI}=-\frac{1}{2}M^3N_c\,{\rm STr}\int {\rm d}^5x\,V_f(\lambda,T^\dagger T)\left(\sqrt{-\det\mathbf{A}^{(L)}}+\sqrt{-\det\mathbf{A}^{(R)}}\right)\,, \tag{3.1.5}$$

where the symmetrized trace over the flavor indices STr is defined as

$${\rm STr}(M_1M_2\dots M_n)=\frac{1}{n!}\sum_{\sigma\in S_n}{\rm Tr}(M_{\sigma(1)}M_{\sigma(2)}\dots M_{\sigma(n)})\,, \tag{3.1.6}$$

for every integer n and matrices $M_1,M_2,\dots,M_n$, with S_n the symmetric group. The convention for the normalization of the $SU(N_f)$ generators is

$${\rm Tr}\left(t_a^{(L)}t_b^{(L)}\right)=\frac{1}{2}\delta^{ab}\quad,\quad {\rm Tr}\left(t_a^{(R)}t_b^{(R)}\right)=\frac{1}{2}\delta^{ab}\,. \tag{3.1.7}$$

The fields appearing in (3.1.5) are

$$\mathbf{A}^{(L)}_{MN}\equiv g_{MN}+w(\lambda)\mathbf{F}^{(L)}_{MN}+\frac{\kappa(\lambda)}{2}\left[(D_MT)^\dagger D_NT+(D_NT)^\dagger D_MT\right]\,, \tag{3.1.8}$$

$$\mathbf{A}^{(R)}_{MN}\equiv g_{MN}+w(\lambda)\mathbf{F}^{(R)}_{MN}+\frac{\kappa(\lambda)}{2}\left[D_MT(D_NT)^\dagger+D_NT(D_MT)^\dagger\right]\,, \tag{3.1.9}$$

where $\mathbf{F}_{MN}$ is the field strength for the gauge fields and the covariant derivative is such that

$$D_M T = \partial_M T + iT\mathbf{L}_M - i\mathbf{R}_M T\,. \tag{3.1.10}$$

The bold font indicates that the $U(1)$ part is included in the gauge fields.

There is no simple way to express $\sqrt{-\det \mathbf{A}^{(L/R)}}$ though, even with the help of the permutativity of the symmetrized trace and within the SU(2) ansatz[7]. In order to make the problem tractable, in the following we consider the same kind of expansion that was considered in [174]. That is, the DBI action is expanded up to quadratic order in the non-abelian field strengths, where the non-abelian part of the tachyon covariant derivatives is considered to be of the same order as the field strength. In the quadratic approximation, the symmetrized trace can be replaced by a simple trace in the DBI action without ambiguity.

We shall work in the chiral limit, with all quark masses set to zero. In this case, in the chirally broken phase, the flavor group is broken in the large-N limit to the diagonal $U(N_f)$ subgroup [14]. This is realized in the bulk theory by considering tachyon field configurations of the form:

$$T = \tau\, U\,, \tag{3.1.11}$$

where τ is a real scalar and U is a unitary matrix[8]

The quantities $\mathbf{A}^{(L/R)}$ defined in (3.1.8)-(3.1.9) can be written as

$$\mathbf{A}^{(L)}_{MN} = \tilde{g}^{(L)}_{MN} + w(\lambda)F^{(L)}_{MN} + \kappa(\lambda)\tau^2 D_{(M}U^\dagger D_{N)}U\,, \tag{3.1.12}$$

$$\mathbf{A}^{(R)}_{MN} = \tilde{g}^{(R)}_{MN} + w(\lambda)F^{(R)}_{MN} + \kappa(\lambda)\tau^2 D_{(M}U D_{N)}U^\dagger\,, \tag{3.1.13}$$

where the abelian part $\hat{F}^{(L/R)}_{MN}$ of the field strength and the tachyon derivatives were collected in an effective metric:

$$\tilde{g}^{(L/R)}_{MN} \equiv g_{MN} + w(\lambda)\hat{F}^{(L/R)}_{MN} + \kappa(\lambda)\partial_M\tau\partial_N\tau\,. \tag{3.1.14}$$

As in [174], we made the simplifying assumption that the potentials w and κ depend on the dilaton only. 2-tensor indices can be raised and lowered using the effective metric (3.1.14) according to the following convention

$$M^A{}_B = \left((\tilde{g}^{(L/R)})^{-1}\right)^{AC} M_{CB} \quad , \quad M_A{}^B = M_{AC}\left((\tilde{g}^{(L/R)})^{-1}\right)^{CB}\,, \tag{3.1.15}$$

where which of L or R should be used will depend on which component (L or R) of the DBI action we are considering.

[7]Note however that, with the SU(2) ansatz, the computation can be done in principle at any finite order in the non-abelian gauge fields.

[8]The chirally broken vacuum corresponds to a bulk solution with a non-zero profile for τ and $U = \mathbb{I}$ (up to chiral transformations). This solution indeed breaks the flavor symmetry to the diagonal $U(N_f)$.

The expansion of the DBI Lagrangian up to quadratic order in the non-abelian field strengths is then obtained from

$$\begin{aligned}\sqrt{-\det \mathbf{A}^{(L)}} = \sqrt{-\det \tilde{g}^{(L)}}\times \\ \times \Bigg(1 + \frac{1}{2} w \,\mathrm{tr}\left((\tilde{g}^{(L)})^{-1} F^{(L)}\right) + \frac{1}{2}\kappa\tau^2 \mathrm{tr}\left((\tilde{g}^{(L)})^{-1} D_{(M}U^\dagger D_{N)} U\right) \\ - \frac{1}{4}\mathrm{tr}\Bigg(\left((\tilde{g}^{(L)})^{-1}\left(wF^{(L)} + \kappa\tau^2 D_{(M}U^\dagger D_{N)}U\right)\right)^2\Bigg) \\ + \frac{1}{8}\Bigg(\mathrm{tr}\Big((\tilde{g}^{(L)})^{-1}\left(wF^{(L)} + \kappa\tau^2 D_{(M}U^\dagger D_{N)}U\right)\Big)\Bigg)^2 \\ + \mathcal{O}\left(\left((\tilde{g}^{(L)})^{-1}\left(wF^{(L)} + \kappa\tau^2 D_{(M}U^\dagger D_{N)}U\right)\right)^3\right)\Bigg),\end{aligned} \tag{3.1.16}$$

$$\begin{aligned}\sqrt{-\det \mathbf{A}^{(R)}} = \sqrt{-\det \tilde{g}^{(R)}}\times \\ \times \Bigg(1 + \frac{1}{2} w \mathrm{tr}\left((\tilde{g}^{(R)})^{-1} F^{(R)}\right) + \frac{1}{2}\kappa\tau^2 \mathrm{tr}\left((\tilde{g}^{(R)})^{-1} D_{(M}U D_{N)} U^\dagger\right) \\ - \frac{1}{4}\mathrm{tr}\left(\left((\tilde{g}^{(R)})^{-1}\left(wF^{(R)} + \kappa\tau^2 D_{(M}U D_{N)}U^\dagger\right)\right)^2\right) \\ + \frac{1}{8}\left(\mathrm{tr}\left((\tilde{g}^{(R)})^{-1}\left(wF^{(R)} + \kappa\tau^2 D_{(M}U D_{N)}U^\dagger\right)\right)\right)^2 \\ + \mathcal{O}\left(\left((\tilde{g}^{(R)})^{-1}\left(wF^{(R)} + \kappa\tau^2 D_{(M}U D_{N)}U^\dagger\right)\right)^3\right)\Bigg),\end{aligned} \tag{3.1.17}$$

where the trace over the space-time indices is denoted by tr. The term linear in F in the first line will vanish upon taking the (flavor) trace of the full expression. Also, as mentioned before, the U covariant derivatives should be considered as of the same order as the field strength. The final expression for the expansion of the DBI action (3.1.5) up to quadratic order in the non-abelian field strength is therefore

$$\begin{aligned}S_{\mathrm{DBI}} = -M^3 N_c \int \mathrm{d}^5x\, V_f(\lambda,\tau^2)\sqrt{-\det \tilde{g}^{(L)}}\times \\ \times \Bigg[\frac{1}{2} + \frac{1}{4}\kappa\tau^2\left((\tilde{g}^{(L)})^{-1}\right)^{(MN)} S_{MN} \\ - \frac{1}{8}w^2\left((\tilde{g}^{(L)})^{-1}\right)^{MN}\left((\tilde{g}^{(L)})^{-1}\right)^{PQ}\mathrm{Tr}\, F^{(L)}_{NP}F^{(L)}_{QM} \\ + \frac{1}{16}w^2\mathrm{Tr}\left(\left((\tilde{g}^{(L)})^{-1}\right)^{[MN]} F^{(L)}_{NM}\right)^2 + \mathcal{O}\left((F^{(L)})^3\right)\Bigg]\end{aligned} \tag{3.1.18}$$

$$+ (L \leftrightarrow R)\,,$$

where we defined the symmetric 2-tensor

$$S_{MN} \equiv \mathrm{Tr} D_{(M} U^\dagger D_{N)} U = \mathrm{Tr} D_{(M} U D_{N)} U^\dagger\,. \tag{3.1.19}$$

3.1.3 Tachyon-Chern-Simons terms

We now discuss the TCS term in the brane action, i.e., S_{CS} in (2.3.3). The Tachyon-Chern-Simons term arises as a part of the Wess-Zumino sector, which has been considered in [137, 138] and adjusted in connection to V-QCD in [150, 161, 166].

The Wess-Zumino term can be derived in flat-space boundary string field theory, [182, 183, 184]. We sketch here the main points of the construction, see [138] for details. The expression of the full WZ term is

$$S_{\rm WZ} = T_4 \int C \wedge \mathrm{str}\ e^{i\mathcal{F}}, \tag{3.1.20}$$

where T_4 is the tension of the flavor D4 branes, C is a formal sum of the RR potentials $C = \sum_n (-1)^{\frac{5-n}{2}} C_n$, str denotes the supertrace as defined in [138], and $\mathcal{F} = d\mathcal{A} - i\mathcal{A}\wedge\mathcal{A}$ is the curvature of the superconnection

$$i\mathcal{A} = \begin{pmatrix} i\mathbf{L} & T^\dagger \\ T & i\mathbf{R} \end{pmatrix} \tag{3.1.21}$$

in terms of the gauge fields $\mathbf{L}$, $\mathbf{R}$, and the tachyon T defined above. Expanding the exponential in (3.1.20) we find four different terms

$$S_{\rm WZ} = T_4 \int C_5 \wedge Z_0 + C_3 \wedge Z_2 + C_1 \wedge Z_4 + C_{-1} \wedge Z_6 \tag{3.1.22}$$

where the Z_{2n}'s are the coefficients arising from the expansion of the exponential. The terms in (3.1.22) play different roles in QCD, [138, 134]. As the theory lives in five dimensions, the first term contains the five-form flux under which the flavor branes are charged. The second term is important for the correct holographic implementation of the $\mathrm{U}(1)_A$ anomaly, [138]. The third term controls the CP-odd interactions associated with magnetic strings. Here, we shall only discuss further the last term, which is the one important for constructing the baryon solution.

The last term in (3.1.22) may be written as

$$S_{\rm CS} = \frac{iN_c}{4\pi^2} \int \Omega_5 \tag{3.1.23}$$

where $d\Omega_5 = Z_6$ and we inserted an explicit expression for the constant $F_0 = dC_{-1}$. F_0 is the flux that is proportional to N_c and supports the bulk geometry associated with the glue. It is the analogue of the RR five-form in the ten-dimensional $AdS_5 \times S^5$ solution. In string theory Z_6 can be computed straightforwardly, but it is somewhat nontrivial to carry out the integration to find explicitly the five form Ω_5. This task was done in [138] for the case where the tachyon is proportional to the unit matrix, $T = \tau\mathbb{I}$.

In the rest of this section we derive a generalized expression for the TCS action, which is the generalization of the results above to V-QCD and to the more general tachyon configuration with a nontrivial U matrix in equation (3.1.11).

First, as we are following a bottom-up approach, there is no reason a priori to resort to the flat space expression of the Wess-Zumino term given in (3.1.20). Therefore, we consider a general TCS action which satisfy known constraints from the bulk gauge symmetry as well as the anomaly structure of QCD. Second, instead of taking the tachyon proportional to the unit matrix, we consider a more general Ansatz (already written down in section 3.1.2)

$$T = \tau U \tag{3.1.24}$$

where τ is scalar and U is a generic SU(N_f) matrix. While this Ansatz is not the most general one, it will be sufficient for our purposes. Notice that the presence of the U matrix allows one to write down expressions which are covariant in the full left and right handed flavor transformations, rather than only the vectorial transformations. Moreover, the fluctuations of the U field are the pions, so that U maps to the exponential $\exp(i\lambda_a\pi_a/f_\pi)$ at the boundary as the notation suggests, which makes it possible to explicitly compare to chiral effective theory.

3.1.3.1 Constructing the Tachyon-Chern-Simons term

We proceed to the construction of the TCS action. We require that it satisfies the following constraints (to be discussed in more detail below):

- The TCS action has the expected behavior under discrete symmetries, i.e., it is even under both parity (P) and charge conjugation (C) whose actions are defined in appendix A.4.
- Its variation under infinitesimal (bulk) gauge transformations is closed, $d\delta\Omega_5 = 0$, and therefore integrates to a boundary term.
- The gauge transformation of the boundary term matches with the expression for the flavor anomaly in QCD.
- When chiral symmetry is preserved, $\tau = 0$, the result agrees with the standard CS action for D-branes.

- All IR contributions to observables vanish[9].

In what follows, we construct the most general action satisfying these properties. Details are given in Appendix D and here we only sketch the main points.

The CS action is even under P if for the simple parity operation acting on the forms (P_1 in Appendix A), Ω_5 is odd. The extra minus sign then comes from reversing the space-time coordinates (P_2 in Appendix A). Under the action of C on the forms, Ω_5 is required to be even. We therefore start by writing down the most general five-form which is P_1 odd and C even, where the transformation properties of the various fields are given in Appendix A.

The ansatz is given as a linear combination of all possible single-trace 5-forms composed out of U, the gauge fields, their covariant derivatives, and the one-form $d\tau$, with the coefficients being functions of the only available scalar τ:

$$\Omega_5 = \sum_{i=1}^{45} \bar{f}_i(\tau) F_5^{(i)}[U, \mathbf{L}, \mathbf{R}] + d\tau \wedge \sum_{i=1}^{11} g_i(\tau) F_4^{(i)}[U, \mathbf{L}, \mathbf{R}] \tag{3.1.25}$$

The forms $F_4^{(i)}$ and $F_5^{(i)}$ are listed explicitly in Appendix D. Notice that we do not expect dependence on the closed string sector (i.e. on the metric or dilaton) to appear in these terms, as it happens in standard string theory.

The most drastic constraint is then the requirement that $d\delta\Omega_5 = 0$. After imposing this constraint, the general solution can be written as

$$\Omega_5 = \Omega_5^0 + \Omega_5^c + dG_4 \tag{3.1.26}$$

where Ω_5^0 is invariant under gauge transformations and Ω_5^c is closed, so that indeed (trivially) $d\delta\Omega_5 = 0$.

The nontrivial part of the derivation is to show that (3.1.26) is the only solution. This is discussed in appendix D. In (3.1.26), Ω_5^0 is the most general gauge covariant 5-form with the expected eigenvalues under P and C:

$$\begin{aligned}
\Omega_5^0 = {} & f_1(\tau)\big[\mathrm{Tr}(DU \wedge \mathbf{F}^{(L)} \wedge \mathbf{F}^{(L)} U^\dagger) + \mathrm{Tr}(DUU^\dagger \wedge \mathbf{F}^{(R)} \wedge \mathbf{F}^{(R)})\big] \\
& + f_2(\tau)\big[\mathrm{Tr}(DU \wedge \mathbf{F}^{(L)} U^\dagger \wedge DUU^\dagger \wedge DUU^\dagger) \\
& \qquad + \mathrm{Tr}(DUU^\dagger \wedge \mathbf{F}^{(R)} \wedge DUU^\dagger \wedge DUU^\dagger)\big] \\
& + f_3(\tau)\big[\mathrm{Tr}(DU \wedge \mathbf{F}^{(L)} U^\dagger \wedge \mathbf{F}^{(R)}) + \mathrm{Tr}(DUU^\dagger \wedge \mathbf{F}^{(R)} U \wedge \mathbf{F}^{(L)} U^\dagger)\big] \\
& + f_4(\tau)\mathrm{Tr}(DUU^\dagger \wedge DUU^\dagger \wedge DUU^\dagger \wedge DUU^\dagger \wedge DUU^\dagger)\,.
\end{aligned} \tag{3.1.27}$$

and depends on four arbitrary functions of τ.

[9] This requirement becomes non-trivial as the type of bulk geometries that are relevant are mildly singular (but are compatible with the Gubser bound).

The closed term Ω_5^c is completely fixed (up to exact forms which we include in G_4 in (3.1.26)) to be

$$\Omega_5^c = g_0 \mathrm{Tr}((U^\dagger \mathrm{d}U)^5) \tag{3.1.28}$$

where g_0 is a constant. Lastly, G_4 is a generic 4-form, i.e., a linear combination of all the possible P_1 odd and C even 4-forms:

$$G_4 = \sum_{i=1}^{11} h_i(\tau) F_4^{(i)}[U, \mathbf{L}, \mathbf{R}] \ . \tag{3.1.29}$$

Explicit expressions for the forms $F_4^{(i)}$ can be found in Appendix D. Recall that Ω_5 depends only on the boundary value of G_4 and therefore only on $h_i(\tau = 0)$, so that the functional form of $h_i(\tau)$ is irrelevant for the final result, except that the functions should vanish for $\tau \to \infty$ in order to avoid undesired IR boundary terms.

The next step is to require agreement of the gauge transformation of the boundary term with the flavor anomalies of QCD. That is, we write $\delta\Omega_5^c = d\delta G_4^c$ and set

$$\delta G_4^c + \delta G_4\Big|_{\mathrm{bdry}} = -\frac{1}{6}\mathrm{Tr}\left[\Lambda_L\left((\mathrm{d}\mathbf{L})^2 - \frac{i}{2}\mathrm{d}(\mathbf{L}^3)\right) - (L \leftrightarrow R)\right] + d(\cdots) \ . \tag{3.1.30}$$

where Λ_L is the generator of the left-handed gauge transformation and the right hand side encodes the flavor anomalies, see e.g. [140, 141, 138]. Notice that the contribution to the action from the last two terms of (3.1.26) is localized on the UV boundary, because consistency requires that IR contributions vanish. As we detail in Appendix D, the condition (3.1.30) completely fixes these terms near the boundary, and therefore also the action from these terms is fully determined. The result for this part of the action may be written as

$$\frac{iN_c}{4\pi^2}\int \Omega_5^c + dG_4 = -\frac{1}{60}\frac{iN_c}{4\pi^2}\int \mathrm{Tr}((U^\dagger \mathrm{d}U)^5) + \frac{iN_c}{4\pi^2}\int G_4\Big|_{\mathrm{bdry}} \tag{3.1.31}$$

where

$$\begin{aligned}
24\, G_4\Big|_{\mathrm{bdry}} = \Big\{ & 2\Big[\mathrm{Tr}(\mathbf{L}\wedge\mathbf{F}^{(L)}\,U^\dagger\wedge DU) + \mathrm{Tr}(\mathbf{L}\,U^\dagger\wedge DU\wedge\mathbf{F}^{(L)})\Big] + \\
& + \Big[\mathrm{Tr}(\mathbf{L}\,U^\dagger\wedge DU\,U^\dagger\wedge\mathbf{F}^{(R)}\,U) + \mathrm{Tr}(\mathbf{L}\,U^\dagger\wedge\mathbf{F}^{(R)}\wedge DU)\Big] + \\
& + i\Big[\mathrm{Tr}(\mathbf{L}\wedge\mathbf{L}\,U^\dagger\wedge\mathbf{R}\wedge DU) - \mathrm{Tr}(\mathbf{L}\wedge\mathbf{L}\,U^\dagger\wedge DU\,U^\dagger\wedge\mathbf{R}\,U)\Big] + \\
& + i\Big[\mathrm{Tr}(\mathbf{L}\wedge\mathbf{F}^{(L)}\,U^\dagger\wedge\mathbf{R}\,U) + \mathrm{Tr}(\mathbf{L}\,U^\dagger\wedge\mathbf{R}\,U\wedge\mathbf{F}^{(L)})\Big] + \\
& + 2i\mathrm{Tr}(\mathbf{L}\wedge\mathbf{L}\wedge\mathbf{L}\,U^\dagger\wedge DU) - 2\mathrm{Tr}(\mathbf{L}\wedge\mathbf{L}\wedge\mathbf{L}\,U^\dagger\wedge\mathbf{R}\,U) + \\
& + 2\mathrm{Tr}(\mathbf{L}\,U^\dagger\wedge DU\,U^\dagger\wedge DU\,U^\dagger\wedge\mathbf{R}\,U) - \mathrm{Tr}(\mathbf{L}\,U^\dagger\wedge DU\wedge\mathbf{L}\,U^\dagger\wedge DU) + \\
& - 2i\mathrm{Tr}(\mathbf{L}\,U^\dagger\wedge\mathbf{R}\,U\wedge\mathbf{L}\,U^\dagger\wedge DU) - 2i\mathrm{Tr}(\mathbf{L}\,U^\dagger\wedge DU\,U^\dagger\wedge DU\,U^\dagger\wedge DU)\Big\} +
\end{aligned} \tag{3.1.32}$$

$$+\left\{L\leftrightarrow R\right\}+\mathrm{Tr}(\mathbf{L}\,U^\dagger\wedge\mathbf{R}\,U\wedge\mathbf{L}\,U^\dagger\wedge\mathbf{R}\,U)\ .$$

In particular, $g_0=-1/60$. The explicitly $L\leftrightarrow R$ symmetrized expression is given in Appendix D. Notice that the last term in (3.1.32) is already symmetric. As one can check, this expressions matches (up to a four dimensional total derivative) the Wess-Zumino terms of chiral Lagrangians given in the literature [140, 141], see appendix D.

There is however a subtlety in the above derivation. Namely, we assumed that the IR contributions from integrating the closed terms vanish. For the contribution from dG_4 in (3.1.26) this can be easily obtained by adjusting the τ dependence of the coefficient functions as $\tau\to\infty$. But in the Ω^{ϵ}_5 term, the coefficient g_0 is required to be a constant, which cannot be set to zero in the IR. Therefore an IR contribution seems unavoidable. We solve this by requiring that the solution for U is such that the IR boundary term vanishes. In Appendix D we argue that this is satisfied given relatively mild assumptions on the asymptotic IR behavior of U. Such an asymptotic regularity condition for U may be expected due to the following reason: the geometry in the confined phase ends in an IR singularity at $r\to\infty$, where all components of the metric vanish so that the space-time shrinks to a single point [145, 150]. In our choice of coordinates, this single point is seemingly described by a 4-dimensional manifold at the boundary $r\to\infty$. At this IR boundary, regularity conditions may be needed in analogy to spherical or cylindrical coordinates in flat space, where the single point at the origin $r=0$ is mapped to a higher dimensional space (sphere), and regularity conditions for the angular dependence at $r=0$ is required to ensure the regularity of the full solution.

More generally, even if the space-time is singular at $r\to\infty$, the holographic consistency of models like the present one relies on considering as physical only field configurations which vanish (or more precisely, are normalizable in a precise sense given by the radial Hamiltonian) at the IR endpoint of space-time. Often this condition can be imposed without having to specify extra input at the singularity (in which case we say that the singularity is *repulsive* and the holographic model is *calculable* [145, 181]). In short, our IR boundary conditions for holographically acceptable configurations must be such that the term (3.1.28) does not contribute in the IR. This is satisfied in particular by the baryon solutions we discuss in later sections.

After the boundary term has been fixed, the only free functions in our results are the f_i's in (3.1.27). They are however not fully arbitrary: due to the requirement of vanishing IR contributions to the action, these functions should vanish fast enough in the IR, i.e., as $\tau\to\infty$. Moreover, the analysis of [174] suggests that the Tachyon-Chern-Simons action should vanish faster than the DBI action in the IR.

There are also conditions at the UV boundary. For the chirally-symmetric vacuum, for which $\tau=0$ and $U=\mathbb{I}$, we expect that the Tachyon-Chern-Simons action should reduce to the standard expression

$$S_{\rm CS}(\tau=0)=\frac{N_c}{24\pi^2}\int\mathrm{Tr}\Big(\mathbf{L}\wedge\mathbf{F}^{(L)}\wedge\mathbf{F}^{(L)}+\frac{i}{2}\mathbf{L}\wedge\mathbf{L}\wedge\mathbf{L}\wedge\mathbf{F}^{(L)}\tag{3.1.33}$$

$$- \frac{1}{10}\mathbf{L}\wedge\mathbf{L}\wedge\mathbf{L}\wedge\mathbf{L}\wedge\mathbf{L} - (L\leftrightarrow R)\Big)$$

up to boundary terms. This is the case if

$$f_1(0) = -\frac{1}{6}\,, \quad f_2(0) = \frac{i}{12}\,, \quad f_3(0) = -\frac{1}{12}\,, \quad f_4(0) = \frac{1}{60}\,. \tag{3.1.34}$$

Finally, setting $U = \mathbb{I}$, the TCS action reduces to that of [138] if

$$\begin{aligned} f_1(\tau) &= -\frac{1}{6}e^{-\tau^2}\,, & f_2(\tau) &= \frac{i}{12}(1+\tau^2)e^{-\tau^2}\,, \\ f_3(\tau) &= -\frac{1}{12}e^{-\tau^2}\,, & f_4(\tau) &= \frac{1}{120}(2+2\tau^2+\tau^4)e^{-\tau^2}\,. \end{aligned} \tag{3.1.35}$$

That is, our result generalizes the expressions of [138] to $U \neq \mathbb{I}$ for these choices of the functions. We remark that the action with this choice satisfies all the requirements discussed above. A simple generalization of these functions, which we use below, is to allow the normalizations of the tachyon field between the DBI and TCS terms to be different. We choose

$$\begin{aligned} f_1(\tau) &= -\frac{1}{6}e^{-b\tau^2}\,, & f_2(\tau) &= \frac{i}{12}(1+b\tau^2)e^{-b\tau^2}\,, \\ f_3(\tau) &= -\frac{1}{12}e^{-b\tau^2}\,, & f_4(\tau) &= \frac{1}{120}(2+2b\tau^2+b^2\tau^4)e^{-b\tau^2}\,, \end{aligned} \tag{3.1.36}$$

where b is a positive constant. It was argued in [174], within an approximation scheme for the baryon, that regularity of the solution requires $b > 1$. We shall observe the same for the baryon solutions considered in this work.

The precise functions $f_i(\tau)$ here were chosen by modifying slightly the string theory result, based on the superconnection formalism, [138]. The modification is the parameter b inserted in the exponent. However, nothing guarantees that this is the correct choice for QCD. More constraints on these functions should be derived in order to fix their form.

The TCS terms we have constructed, are written in terms of τ and U separately. This is general enough, if the tachyon can be split according to equation (3.1.24). However, as discussed in more detail in section 3.1.4.4, in the general case with non-zero quark masses, one has to use the more general tachyon ansatz

$$T = HU \tag{3.1.37}$$

where now H is a Hermitian matrix, and the TCS terms must be generalized.

3.1.4 Cylindrically symmetric ansatz for a single baryon

As we discussed in the introduction, the presence of the TCS terms is crucial when searching for baryon solutions. Indeed, the TCS action is responsible for stabilising the baryon size and position.

If we think of this model as originating from a five-dimensional non-critical string theory, a baryon is described by a D_0 brane, [134]. The analogue of the C_4 flux sourcing the D_3 branes, in this case is a zero-form field strength $F_0 \sim N_c$. Its Chern-Simons coupling on the one-dimensional world-volume of the D_0 brane is

$$\int d\tau A_\tau F_0 \sim N_c \int d\tau A_\tau \tag{3.1.38}$$

where A_τ is the world-line gauge field. This is the analogue of the $F_5 \wedge A$ Chern-Simons coupling on the D_5 baryon brane in N=4 sYM. As usual, fundamental string end-points are charged under A_τ and N_c of them are needed to screen the induced charge on the D_0 (baryon) brane, as in the $N = 4$ sYM case. Moreover, on the D_4+$\overline{D}_4$ flavor branes there is a C_1 coupling to the flavor instanton number. C_1 is the RR gauge field under which D_0 branes are minimally charged. Therefore D_0 number transmutes to flavor instanton number as in the SS model, [128, 171].

Therefore, in the gravity approximation that we shall be using, a single static baryon D_0 brane, is realised in the bulk as a Euclidean instanton of the non-abelian bulk gauge fields extended in the three spatial directions plus the holographic direction. In this section we describe the ansatz that is used to compute the instanton solution in the bulk. On general grounds, it is expected that an appropriate ansatz can be determined by requiring that the solution is maximally symmetric, that is symmetric under all the symmetries of the bulk action (2.3.3) compatible with the boundary conditions. In the case of the baryon solution, this means all the symmetries of the action compatible with the baryon number being non-zero [10].

3.1.4.1 Ansatz for the glue sector

As explained in the next subsection, we shall consider a baryon whose flavor quantum numbers are a U(2) subgroup of the $U(N_f)$ flavor group. This implies that the flavor action (composed of the DBI (3.1.18) and TCS (3.1.23) actions) for the baryon ansatz does not depend on N_f[11] and is of order N_c. On the other hand, the glue action (2.3.4) is of order N_c^2. So, at leading order in N_c, the glue sector composed of the metric and dilaton is not affected by the presence of the baryon and is identical to the vacuum solution. The latter depends only on the holographic coordinate r

$$\mathrm{d}s^2 = \mathrm{e}^{2A(r)}(-\mathrm{d}t^2 + \mathrm{d}\mathbf{x}^2 + \mathrm{d}r^2)\,, \tag{3.1.39}$$

$$\lambda = \lambda(r)\,. \tag{3.1.40}$$

[10] A non-zero baryon number breaks in particular Lorentz invariance. It also breaks charge conjugation, which should send a baryon solution to a distinct anti-baryon solution.

[11] When considering that the on-shell action for the baryon solution should correspond to the classical contribution to the baryon mass, this is the expected scaling at large N_c. This scaling was equally reproduced in the context of the WSS model [128].

Let us comment some more on this result that the baryon is a probe on the color background. In fact, it is well-known that SU(N_f) instantons are constructed from a single embedded SU(2) instanton that is then conjugated to cover the full SU(N_f) group. This gives rise to many charged moduli associated to the one-instanton solution. However, here such parameters are fixed and are not moduli. Therefore, in this case the effective (active) number of flavors is two, and a non-backreaction approximation for a single baryon is valid. Note, that if flavor were to be gauged, this approximation would be invalidated.

3.1.4.2 Gauge fields ansatz

The left and right handed gauge fields are denoted

$$\mathbf{L} = L + \hat{L}\mathbb{I}_{N_f} \quad , \quad \mathbf{R} = R + \hat{R}\mathbb{I}_{N_f} \,, \tag{3.1.41}$$

where L and R correspond to the $SU(N_f)$ part of the gauge fields, and $\hat{L}$ and $\hat{R}$ to the $U(1)$ part. From these we define the vector and axial vector gauge fields as

$$\mathbf{V} = \frac{\mathbf{L}+\mathbf{R}}{\sqrt{2}} \quad , \quad \mathbf{A} = \frac{\mathbf{L}-\mathbf{R}}{\sqrt{2}} \,. \tag{3.1.42}$$

We look for a static instanton configuration for the $U(N_f)$ gauge fields. This configuration belongs to a non-trivial class of the homotopy group of $U(N_f)$ on the 3-sphere at infinity of the 4-dimensional Euclidean space spanned by $(\vec{x}, r)$. Because for any $N_f > 1$, the homotopy groups of $U(N_f)$ and $SU(2)$ are equal

$$\pi_3\left(U(N_f)\right) = \pi_3\left(SU(2)\right) = \mathbb{Z} \,, \tag{3.1.43}$$

a $U(N_f)$ instanton can be constructed by embedding an $SU(2)$ instanton in $U(N_f)$ (acting with global $U(N_f)$ on an instanton for an $SU(2)$ subgroup of $U(N_f)$).

Because the TCS action (3.1.23) contains cubic couplings for the gauge fields, a consistent ansatz should contain all the matrices in the Lie Algebra of U(N_f) that can be written as a product of two SU(2) generators

$$\sigma^a \sigma^b = \delta^{ab}\mathbb{I}_2 + i\epsilon^{abc}\sigma^c \,, \tag{3.1.44}$$

where the σ^a's are the Pauli matrices and $\mathbb{I}_2$ is the 2 by 2 identity matrix in the same subsector of the chiral group as the SU(2) subgroup. This implies that the SU(2) instanton couples via the TCS term to the gauge field in the direction of $\mathbb{I}_2$. The full flavor structure of the baryon ansatz is therefore that of a U(2) subgroup

$$\mathbf{L} = L^a \frac{\sigma_L^a}{2} + L^{\mathrm{T}}\mathbb{I}_{2,L} \quad , \quad \mathbf{R} = R^a \frac{\sigma_R^a}{2} + R^{\mathrm{T}}\mathbb{I}_{2,R} \,, \tag{3.1.45}$$

where the superscript T stands for trace, as the corresponding part contains the abelian part of the gauge field. Note however that, although $\mathbb{I}_2$ generates a U(1) subgroup of the

chiral group, in general[12] it is not a subgroup of the abelian part of $\mathrm{U}(\mathrm{N}_f)$. In other words, $\mathbb{I}_2$ is a combination of $\mathbb{I}_{N_f}$ and an $\mathrm{SU}(\mathrm{N}_f)$ generator

$$\mathbb{I}_2 = \frac{2}{N_f}\mathbb{I}_{N_f} + \left(\mathbb{I}_2 - \frac{2}{N_f}\mathbb{I}_{N_f}\right) . \tag{3.1.46}$$

The traceless matrix that appears in (3.1.46) is not any matrix, as it is equal to minus the traceless part of the strong hypercharge

$$Y \equiv \frac{1}{N_c}\mathbb{I}_{N_f} + \begin{pmatrix} 0 & & & & \\ & 0 & & & \\ & & 1 & & \\ & & & \ddots & \\ & & & & 1 \end{pmatrix} = \left(\frac{1}{N_c} + \frac{N_f - 2}{N_f}\right)\mathbb{I}_{N_f} - \left(\mathbb{I}_2 - \frac{2}{N_f}\mathbb{I}_{N_f}\right) , \tag{3.1.47}$$

where by convention the 2 flavors of the SU(2) subgroup are assumed to correspond to the down and up (note that at zero quark mass, this choice is arbitrary). The fact that the gauge field ansatz (3.1.45) contains a part in the direction of $\mathbb{I}_2$ is therefore a sign that the baryon is charged under baryon number and hypercharge. Because a single combination of the two charges appears, the baryon number and hypercharge will not be independent for the classical soliton solution. Specifically, we find that for this ansatz

$$Y = N_B \, , \tag{3.1.48}$$

which is the expected result for a baryon composed of the first two flavors[13].

To find a relevant U(2) instanton ansatz we follow [173] and look for a configuration that is invariant under a maximal set of symmetries of the action (2.3.3), compatible with a finite baryon number. In particular, we look for a U(2) instanton solution that is invariant under cylindrical transformations. These correspond to rotations in the 3-dimensional space spanned by $\mathbf{x}$, up to a global SU(2) rotation.

As we look for a static solution, we impose in addition invariance under time-reversal[14]

$$t \to -t \quad , \quad L^{\mathrm{T}} \to -L^{\mathrm{T}} \quad , \quad R^{\mathrm{T}} \to -R^{\mathrm{T}} \, . \tag{3.1.49}$$

Note that the definition of time-reversal reduces to that of [173] for $N_f = 2$ flavors. For $N_f > 2$, the time component of the non-abelian gauge field will be non-zero, but proportional to the abelian part. The same was observed in the context of the WSS model in [128].

[12] With the exception of $N_f = 2$.

[13] This does not mean that the baryon spectrum does not contain higher hypercharge states, with $Y > N_B$. The baryon spectrum is calculated by quantizing the collective modes of the soliton, including in particular the rotations in isospin space. Such rotations move the baryon around in the full chiral group, so they will imply the existence of higher hypercharge baryon states.

[14] The action on the time component of the gauge fields is necessary for the TCS action to be invariant under time reversal.

Then, the static, cylindrically symmetric ansatz takes the form:

$$L_i^a = -\frac{1+\phi_2^L(\xi,r)}{\xi^2}\epsilon_{iak}x_k + \frac{\phi_1^L(\xi,r)}{\xi^3}(\xi^2\delta_{ia} - x_i x_a) + \frac{A_1^L(\xi,r)}{\xi^2}x_i x_a\,, \tag{3.1.50}$$

$$L_r^a = \frac{A_2^L(\xi,r)}{\xi}x_a\,, \tag{3.1.51}$$

$$L_0^{\mathrm{T}} = \Phi^L(r,\xi)\,, \tag{3.1.52}$$

where $i,k=1,2,3$ refer to spatial indices, $\xi \equiv \sqrt{x_1^2+x_2^2+x_3^2}$ is the 3-dimensional spatial radius and $a=1,2,3$ is the index for the components in the $SU(2)_L$ basis (the Pauli matrices σ_a divided by 2). A similar ansatz can be written for the right-handed gauge field with corresponding fields $\phi_1^R, \phi_2^R, A_1^R, A_2^R, \Phi^R$. These are a priori independent from the left-handed degrees of freedom, as is the embedding of the corresponding $SU(2)_R$ in $SU(N_f)_R$.

The choice of the ansatz partially fixes the gauge but there is still a residual $U(1)_L \times U(1)_R$ invariance that preserves the cylindrical symmetry, corresponding to the $SU(2)$ transformation

$$g_{(L/R)} = \exp\left(i\alpha_{(L/R)}(\xi,r)\frac{x\cdot\sigma}{2\xi}\right)\,, \tag{3.1.53}$$

where

$$x\cdot\sigma \equiv x^a\sigma^a\,. \tag{3.1.54}$$

Under this gauge transformation, $\left(A_1^{(L/R)}, A_2^{(L/R)}\right)$ is the gauge field, $\phi_1^{(L/R)} + i\phi_2^{(L/R)}$ has charge $+1$ and $\Phi^{(L/R)}$ is neutral.

The V-QCD action possesses another discrete parity symmetry

$$P\ :\ \mathbf{x}\to-\mathbf{x}\quad,\quad L\leftrightarrow R\,. \tag{3.1.55}$$

A general instanton solution is a linear combination of a P-even instanton and a P-odd instanton. As discussed in Appendix B, only the P-even part can generate a finite energy solution. So we also impose the parity symmetry (3.1.55) on the ansatz (3.1.50)-(3.1.52) for the instanton solution. This relates right and left-handed quantities in the following manner:

$$A_1 \equiv A_1^L = -A_1^R\quad,\quad A_2 \equiv A_2^L = -A_2^R\,, \tag{3.1.56}$$

$$\phi_1 \equiv \phi_1^L = -\phi_1^R\quad,\quad \phi_2 \equiv \phi_2^L = \phi_2^R\,, \tag{3.1.57}$$

$$\Phi \equiv \Phi^L = \Phi^R\,. \tag{3.1.58}$$

Also, the right and left-handed gauge fields should belong to the same $SU(2)$ subgroup of $U(N_f)$[15]. Our ansatz is now fully specified by 5 real functions

$$A_{\bar{\mu}} \equiv (A_1, A_2) \quad , \quad \phi \equiv \phi_1 + i\phi_2 \quad \text{and} \quad \Phi \,, \tag{3.1.59}$$

depending on the two variables $x^{\bar{\mu}} \equiv (\xi, r)$, that we will use as coordinates on a 2D space. The constraints (3.1.56)-(3.1.58) fix the vector part of the remaining $U(1)_L \times U(1)_R$ gauge invariance, leaving only a residual (axial) $U(1)$ invariance, corresponding to the $SU(2)_A$ transformation

$$g_L = g_R^\dagger = \exp\left(i\alpha(\xi, r)\frac{x\cdot\sigma}{2\xi}\right) . \tag{3.1.60}$$

Under the transformation (3.1.60), $A_{\bar{\mu}}$ is the gauge field, ϕ has charge $+1$ and Φ is neutral, with gauge transformations

$$A_{\bar{\mu}} \to A_{\bar{\mu}} + \partial_{\bar{\mu}}\alpha \quad , \quad \phi \to \mathrm{e}^{i\alpha}\phi \quad , \quad \Phi \to \Phi \,. \tag{3.1.61}$$

3.1.4.3 Tachyon ansatz

The most general cylindrically symmetric[16] ansatz for the tachyon field is

$$T^{ij} = \rho(r,\xi)\delta^{ij} + \varphi(r,\xi)\frac{(x\cdot\sigma)^{ij}}{\xi} \,, \tag{3.1.62}$$

where ρ and φ are two complex scalar fields and i and j are the indices in the fundamental representation of the right and left handed $SU(2)$ subgroup, respectively. The parity transformation acts on the tachyon field as $T(x) \to T^\dagger(-x)$ [138]. Imposing the parity symmetry implies that i and j in (3.1.62) describe the same space and constrains ρ and φ to obey

$$\rho \in \mathbb{R} \quad , \quad \varphi \in i\mathbb{R} \,. \tag{3.1.63}$$

The tachyon matrix restricted to the $SU(2)$ subgroup $T^{SU(2)}$ can therefore be cast in the shape of a scalar times an $SU(2)$ matrix

$$\begin{aligned} T^{SU(2)} = \rho\mathbb{I}_2 + \varphi\frac{x\cdot\sigma}{\xi} &= \tau(r,\xi)\left(\cos\theta(r,\xi)\,\mathbb{I}_2 + i\sin\theta(r,\xi)\frac{x\cdot\sigma}{\xi}\right) \\ &= \tau(r,\xi)\exp\left(i\theta(r,\xi)\frac{x\cdot\sigma}{\xi}\right) , \end{aligned} \tag{3.1.64}$$

[15] This implies in particular that the manifest $SU(2)_V$ invariance of the $SU(2)$ ansatz simply maps to invariance under the conserved diagonal subgroup $SU(N_f)_V$ of the chiral symmetry when lifted to $SU(N_f)$.

[16] Up to a global $SU(2)$ transformation.

where τ and θ are respectively the modulus and phase of the complex number $\rho+\varphi$, where ρ and φ are defined in (3.1.64),

$$\tau \equiv \sqrt{|\rho|^2+|\varphi|^2} \quad , \quad \theta \equiv \arctan\left(-\frac{i\varphi}{\rho}\right). \tag{3.1.65}$$

Equation (3.1.64) reproduces the Skyrmion ansatz (equation (16) in [172]) for the unitary part of the tachyon. The $SU(N_f)$ tachyon ansatz is then obtained by embedding $T^{SU(2)}$ in $SU(N_f)$

$$T = \tau(r,\xi)U(r,\xi)\,, \tag{3.1.66}$$

where $U(r,\xi)$ is the $SU(N_f)$ matrix resulting from the embedding of $\exp\left(i\theta(r,\xi)\frac{x\cdot\sigma}{\xi}\right)$.

Note that under the residual $U(1)_A$ gauge freedom (3.1.60), the tachyon in equation (3.1.64) transforms as

$$\theta \to \theta - \alpha\,. \tag{3.1.67}$$

Source and vev Depending on whether we set the quark mass m to 0 or not, the vev term should be identified differently from the tachyon near-boundary expansion. In this work, we will consider the case in which all quarks are massless. The situation with non-zero quark mass will be treated elsewhere.

In the massless quark case, the chiral condensate is simply the coefficient of the leading term of the tachyon, in the near-boundary expansion as $r \to 0$

$$T^{SU(2)}(r,\xi) = \ell\Sigma(\xi)\exp\left(i\theta(0,\xi)\frac{x\cdot\sigma}{\xi}\right) r^3(-\log(r\Lambda))^{-c}\,(1+\cdots)\,. \tag{3.1.68}$$

We used the fact that the near-boundary behavior of the tachyon modulus is still given by (2.3.20), except that the amplitude of the chiral condensate Σ generically depends on ξ due to the presence of the baryon. From (3.1.68), the pion matrix is identified to be

$$U_P(\xi)^\dagger \equiv \exp\left(i\theta(0,\xi)\frac{x\cdot\sigma}{\xi}\right). \tag{3.1.69}$$

The associated near-boundary expansion of the flavor gauge fields can be found in Appendix G.1.

To summarize the content of this section, the ansatz for the instanton solution (3.1.50)-(3.1.52), (3.1.56)-(3.1.58) and (3.1.64) contains 7 dynamical fields

$$\Phi(r,\xi) \quad , \quad \phi(r,\xi) \equiv \phi_1(r,\xi) + i\phi_2(r,\xi) \quad , \quad A_{\bar\mu}(r,\xi) \equiv (A_\xi(r,\xi), A_r(r,\xi))\,, \tag{3.1.70}$$
$$\tau(r,\xi) \quad , \quad \theta(r,\xi)\,,$$

with a $U(1)$ gauge redundancy under which the fields transform as

$$\phi \to \mathrm{e}^{i\alpha}\phi \quad , \quad A_{\bar\mu} \to A_{\bar\mu} + \partial_{\bar\mu}\alpha \quad , \quad \theta \to \theta - \alpha\,. \tag{3.1.71}$$

3.1.4.4 Comments on non-zero quark masses

In the presence of a non-trivial quark mass matrix M_{ij}, the near-boundary asymptotics (3.1.68) must be modified, and the leading asymptotics is now:

$$T_{ij} \simeq M_{ij}\, r(-\log r\Lambda)^c + \dots \tag{3.1.72}$$

Since the nontrivial matrix nature of T starts at leading order, we cannot assume the decomposition (3.1.66) but the most general form:

$$T = H(r,\xi)U(r,\xi) \tag{3.1.73}$$

where the scalar field $\tau(r,\xi)$ is replaced by the Hermitian matrix field $H(r,\xi)$. Near the boundary $r \to 0$, equation (3.1.72) requires to leading order:

$$H(r,\xi) = H_0 r(-\log r\Lambda)^c + O(r^3), \quad U(r,\xi) = U_0 + O(r^2) \qquad r \to 0 \tag{3.1.74}$$

where H_0 is a constant Hermitian matrix and U_0 is a constant unitary matrix such that $(H_0U_0)_{ij} = M_{ij}$.

Notice that now the matrix U contributes to the source term in the near-boundary asymptotics. As a consequence, in this case we cannot interpret $U(r=0)$ as the pion matrix as in equation (3.1.69) in the massless case.

Furthermore, due to equation (3.1.74), U is constrained to go to a constant matrix as a function of $\vec{x}$, at leading order in r. This is very different from the massless quark case, in which the leading asymptotics of $U(r,\xi)$ is unconstrained, and in particular it is allowed to be a non-trivial function of the space-time coordinates to leading order in r. This changes drastically the on-shell asymptotics of our TCS terms[17].

As a consequence, the baryon ansatz has to be modified in the massive quark case, and we will not discuss this case further in the present work.

3.1.5 Constructing the baryon solution

We discuss in this section the construction of the baryon solution. As mentioned in the previous section, a baryon state is realized in the bulk as an instanton solution on the 4D Euclidean space parametrized by $(r,\vec{x})$. The instanton is a configuration of the ansatz of equations (3.1.50)-(3.1.52) and (3.1.64) that obeys the bulk equations of motion. Constructing the baryon solution therefore requires deriving the equations of motion obeyed by the 7 fields of the ansatz in (3.1.70). These field equations are obtained by substituting the ansatz into the general field equations (C.1),(C.6) and (C.8). We present here the general procedure for the computation of the equations of motion and give more details in Appendix F.

[17] even assuming that the quark mass matrix is proportional to the identity, in which case the decomposition (3.1.66) still holds.

As discussed in the previous section, the baryon can be treated as a flavor probe on the glue background. Note that the modulus of the tachyon field τ is also non-zero in vacuum (2.3.17). In the Veneziano limit where N_c and N_f are both large and of the same order, the tachyon modulus couples to the glue sector at leading order in N_c. Because of that, the back-reaction of the baryon on the tachyon background is also of order $\mathcal{O}(1/N_c)$. The leading order baryon solution is therefore a probe on the vacuum background, and the back-reaction on the background can be computed order by order in $1/N_c$. In the following, we first discuss the leading order probe baryon solution and then consider the back-reaction. We do not expect the color back-reaction to be qualitatively important for the flavor structure of the baryon, which is its most important dynamical property. This motivates the approximation that we consider later, where we compute the back-reaction on the tachyon modulus alone, assuming the color background to remain unchanged.

We start the discussion of the baryon construction by a few general results. First note that, for this particular ansatz, the effective metric $\tilde{g}_{MN}$ in equation (3.1.14) is the same in the L and R sectors. We will simply denote it $\tilde{g}_{MN}$ and it is given by the matrix:

$$\begin{pmatrix} -\mathrm{e}^{2A} & -\partial_r\Phi & -\frac{x_1}{\xi}\partial_\xi\Phi & -\frac{x_2}{\xi}\partial_\xi\Phi & -\frac{x_3}{\xi}\partial_\xi\Phi \\ \partial_r\Phi & \mathrm{e}^{2A}+\kappa(\partial_r\tau)^2 & \kappa\frac{x_1}{\xi}\partial_r\tau\partial_\xi\tau & \kappa\frac{x_2}{\xi}\partial_r\tau\partial_\xi\tau & \kappa\frac{x_3}{\xi}\partial_r\tau\partial_\xi\tau \\ \frac{x_1}{\xi}\partial_\xi\Phi & \kappa\frac{x_1}{\xi}\partial_r\tau\partial_\xi\tau & \mathrm{e}^{2A}+\kappa\left(\frac{x_1}{\xi}\right)^2(\partial_\xi\tau)^2 & \kappa\frac{x_1}{\xi}\frac{x_2}{\xi}(\partial_\xi\tau)^2 & \kappa\frac{x_1}{\xi}\frac{x_3}{\xi}(\partial_\xi\tau)^2 \\ \frac{x_2}{\xi}\partial_\xi\Phi & \kappa\frac{x_2}{\xi}\partial_r\tau\partial_\xi\tau & \kappa\frac{x_1}{\xi}\frac{x_2}{\xi}(\partial_\xi\tau)^2 & \mathrm{e}^{2A}+\kappa\left(\frac{x_2}{\xi}\right)^2(\partial_\xi\tau)^2 & \kappa\frac{x_2}{\xi}\frac{x_3}{\xi}(\partial_\xi\tau)^2 \\ \frac{x_3}{\xi}\partial_\xi\Phi & \kappa\frac{x_3}{\xi}\partial_r\tau\partial_\xi\tau & \kappa\frac{x_1}{\xi}\frac{x_3}{\xi}(\partial_\xi\tau)^2 & \kappa\frac{x_2}{\xi}\frac{x_3}{\xi}(\partial_\xi\tau)^2 & \mathrm{e}^{2A}+\kappa\left(\frac{x_3}{\xi}\right)^2(\partial_\xi\tau)^2 \end{pmatrix}, \tag{3.1.75}$$

where the order of the columns (and lines) is $(0|r|1|2|3)$. Its determinant is:

$$\begin{aligned} -\det\tilde{g} = \mathrm{e}^{10A} - \mathrm{e}^{6A}w^2\left((\partial_r\Phi)^2+(\partial_\xi\Phi)^2\right) + \mathrm{e}^{8A}\kappa\left((\partial_r\tau)^2+(\partial_\xi\tau)^2\right) - \\ - \mathrm{e}^{4A}\kappa w^2\left(\partial_r\Phi\partial_\xi\tau-\partial_\xi\Phi\partial_r\tau\right)^2 . \end{aligned} \tag{3.1.76}$$

Another useful observation is that, because the equations of motion are covariant under the residual gauge transformations (3.1.71), the phase θ in the tachyon ansatz (3.1.64) can be absorbed into the gauge field. By doing so, the dynamical field content (3.1.70) can be reduced to a set of 6 fields invariant under the residual gauge freedom. In practice, if we define

$$g(\theta) \equiv \exp\left(i\theta\frac{x\cdot\sigma}{2\xi}\right), \tag{3.1.77}$$

then we consider the following redefinition of the gauge fields

$$\mathbf{L}_M \to \tilde{\mathbf{L}}_M \equiv g(\theta)\mathbf{L}_M g(\theta)^\dagger + ig(\theta)\partial_M g(\theta)^\dagger , \tag{3.1.78}$$

$$\mathbf{R}_M \to \tilde{\mathbf{R}}_M \equiv g(\theta)^\dagger\mathbf{R}_M g(\theta) + ig(\theta)^\dagger\partial_M g(\theta) , \tag{3.1.79}$$

which for the ansatz (3.1.50)-(3.1.52) is equivalent to

$$A_{\bar{\mu}} \to \tilde{A}_{\bar{\mu}} \equiv A_{\bar{\mu}} + \partial_{\bar{\mu}}\theta \quad , \quad \phi \to \tilde{\phi} \equiv \mathrm{e}^{i\theta}\phi \quad , \quad \Phi \to \Phi \, . \tag{3.1.80}$$

From (3.1.71), it is clear that the gauge field thus redefined is invariant under the residual gauge transformation (3.1.60).

We shall use these gauge-invariant fields in some of our future calculations in this chapter. When we do that, we will always write the tildes so that it is clear that we are using the gauge-invariant fields. Working with the gauge-invariant fields is identical to working in the unitary gauge.

3.1.5.1 Probe instanton

At leading order in N_c, one can consider the probe regime where the geometry of the bulk, the dilaton and the modulus of the tachyon field are fixed to their background value (describing the V-QCD vacuum solution) and search for an instanton solution for the gauge fields, plus an associated non-trivial solution for the unitary part of the tachyon field. In our case, there is no abelian field strength in the background (no baryon number density in the vacuum). Because of this, it is consistent to expand the DBI action at quadratic order in the abelian field strength also

$$\begin{aligned} S_{\rm DBI} = -M^3 N_c \int \mathrm{d}^5 x \, V_f(\lambda,\tau^2)\sqrt{-\det \tilde{g}} \times \\ \times \left(\left[\frac{1}{2} + \frac{1}{4}\kappa\tau^2 \left(\tilde{g}^{-1}\right)^{MN} S_{MN} - \frac{1}{8} w^2 \left(\tilde{g}^{-1}\right)^{MN} \left(\tilde{g}^{-1}\right)^{PQ} \mathrm{Tr}\, \mathbf{F}^{(L)}_{NP} \mathbf{F}^{(L)}_{QM} + \right.\right. \\ \left.\left. + \mathcal{O}\left((\mathbf{F}^{(L)})^3 \right) \right] + (L \leftrightarrow R) \right) \, , \end{aligned} \tag{3.1.81}$$

where S_{MN} was defined in (3.1.19) and $\tilde{g}$ is now the effective background metric

$$\tilde{g}_{MN} \equiv g_{MN} + \kappa(\lambda)\partial_M\tau\partial_N\tau = g_{MN} + \kappa(\lambda(r)) \left(\tau'(r)\right)^2 \delta^r_M \delta^r_N \, , \tag{3.1.82}$$

which takes a diagonal form

$$\tilde{g} = \begin{pmatrix} -\mathrm{e}^{2A} & 0 & 0 & 0 & 0 \\ 0 & \mathrm{e}^{2A} + \kappa(\partial_r\tau)^2 & 0 & 0 & 0 \\ 0 & 0 & \mathrm{e}^{2A} & 0 & 0 \\ 0 & 0 & 0 & \mathrm{e}^{2A} & 0 \\ 0 & 0 & 0 & 0 & \mathrm{e}^{2A} \end{pmatrix} . \tag{3.1.83}$$

Its determinant is given by

$$-\det \tilde{g} = \mathrm{e}^{10A}(1 + \mathrm{e}^{-2A}\kappa(\partial_r\tau)^2) \, . \tag{3.1.84}$$

SU(2) ansatz Substituting the ansatz (3.1.50)-(3.1.52), (3.1.56)-(3.1.58) and (3.1.64) into the bulk action (3.1.81) and (3.1.23) yields the expression for the instanton energy[18] in terms of the fields of (3.1.70)

$$E = E_{\rm DBI} + E_{\rm CS}\,, \tag{3.1.85}$$

$$\begin{aligned} E_{\rm DBI} = 4\pi M^3 N_c \int {\rm d}r{\rm d}\xi\, V_f(\lambda,\tau){\rm e}^A\sqrt{1+{\rm e}^{-2A}\kappa(\partial_r\tau)^2}\,\times \\ \times\left({\rm e}^{2A}\xi^2\kappa(\lambda)\tau^2\left(\frac{1}{1+{\rm e}^{-2A}\kappa(\partial_r\tau)^2}\tilde{A}_r^2+\tilde{A}_\xi^2+\frac{(\tilde{\phi}+\tilde{\phi}^*)^2}{2\xi^2}\right)+\right. \\ +w(\lambda)^2\left(\frac{1}{8}\frac{1}{1+{\rm e}^{-2A}\kappa(\partial_r\tau)^2}\xi^2(F_{\bar{\mu}\bar{\nu}})^2+\frac{1}{2}\left(|{\rm D}_\xi\phi|^2+\frac{1}{1+{\rm e}^{-2A}\kappa(\partial_r\tau)^2}\,|{\rm D}_r\phi|^2\right)+\right. \\ \left.\left.+\frac{\left(1-|\phi|^2\right)^2}{4\xi^2}-\xi^2\left(\frac{1}{1+{\rm e}^{-2A}\kappa(\partial_r\tau)^2}(\partial_r\Phi)^2+(\partial_\xi\Phi)^2\right)\right)\right)\,, \end{aligned} \tag{3.1.86}$$

$$\begin{aligned} E_{\rm CS} = \frac{4N_c}{\pi}\int {\rm d}r{\rm d}\xi\,\epsilon^{\bar{\mu}\bar{\nu}}\partial_{\bar{\mu}}\Phi\times \\ \times\left[(f_1(\tau)+f_3(\tau))\left(\tilde{A}_{\bar{\nu}}+\frac{1}{2}(-i\phi^*D_{\bar{\nu}}\phi+h.c.)+\frac{1}{4i}\partial_{\bar{\nu}}(\tilde{\phi}^2-(\tilde{\phi}^*)^2)\right)+\right. \\ \left.+\frac{1}{2}(3if_2(\tau)-f_1(\tau)-f_3(\tau))(\tilde{\phi}+\tilde{\phi}^*)^2A_{\bar{\nu}}\right]\,. \end{aligned} \tag{3.1.87}$$

The differential equations obeyed by the fields of the ansatz are then obtained by extremizing the energy (3.1.85) with respect to variations of the fields[19]. The expressions for these equations (F.38)-(F.43) are presented in appendix F. It is also checked that substituting the ansatz directly into the general equations of motion (F.26)-(F.28) yields the same equations as extremizing the energy (3.1.85).

[18]Strictly speaking, this is the bulk action, which as we shall evaluate it on the solutions of our equations of motion will also be the on-shell action. As all fields considered are time-independent, the boundary energy differs from this action by a trivial $-\int dt$ factor and this is why we shall call it the "energy" from now on.

[19]It is well-known that substituting an ansatz into the action and then varying the action to derive the equations of motion leads to wrong results. However, symmetry sometimes can protect this procedure. In our case, the SU(2) instanton ansatz (3.1.50)-(3.1.52), (3.1.56)-(3.1.58) and (3.1.64) fixes most of the gauge invariance, and therefore one could worry that deriving the equations of motion for the fields of the ansatz in this manner may not reproduce all the constraints obeyed by these fields. However we can show that the constraints that one misses in this procedure are trivially satisfied by our ansatz as it has cylindrical symmetry.

3.1.5.2 Inhomogeneous tachyon

To go beyond the probe limit, we now consider the back-reaction on the tachyon modulus τ. We will assume that the color sector remains fixed to its vacuum value, and write the equations of motion for the tachyon modulus coupled to the baryon fields. At leading order in the Veneziano limit, the baryon fields are given by the probe baryon solution, and the correction to the tachyon background starts at order $\mathcal{O}(1/N_f)$. Note that considering such a back-reaction will imply that τ will depend on the 3-dimensional radius ξ. Its EoM is (C.4).

In this case the expression (3.1.81) for the expanded DBI action can still be used but the effective metric, although symmetric, is not diagonal anymore:

$$\begin{pmatrix} -\mathrm{e}^{2A} & 0 & 0 & 0 & 0 \\ 0 & \mathrm{e}^{2A}+\kappa(\partial_r\tau)^2 & \kappa\frac{x_1}{\xi}\partial_r\tau\partial_\xi\tau & \kappa\frac{x_2}{\xi}\partial_r\tau\partial_\xi\tau & \kappa\frac{x_3}{\xi}\partial_r\tau\partial_\xi\tau \\ 0 & \kappa\frac{x_1}{\xi}\partial_r\tau\partial_\xi\tau & \mathrm{e}^{2A}+\kappa\left(\frac{x_1}{\xi}\right)^2(\partial_\xi\tau)^2 & \kappa\frac{x_1}{\xi}\frac{x_2}{\xi}(\partial_\xi\tau)^2 & \kappa\frac{x_1}{\xi}\frac{x_3}{\xi}(\partial_\xi\tau)^2 \\ 0 & \kappa\frac{x_2}{\xi}\partial_r\tau\partial_\xi\tau & \kappa\frac{x_1}{\xi}\frac{x_2}{\xi}(\partial_\xi\tau)^2 & \mathrm{e}^{2A}+\kappa\left(\frac{x_2}{\xi}\right)^2(\partial_\xi\tau)^2 & \kappa\frac{x_2}{\xi}\frac{x_3}{\xi}(\partial_\xi\tau)^2 \\ 0 & \kappa\frac{x_3}{\xi}\partial_r\tau\partial_\xi\tau & \kappa\frac{x_1}{\xi}\frac{x_3}{\xi}(\partial_\xi\tau)^2 & \kappa\frac{x_2}{\xi}\frac{x_3}{\xi}(\partial_\xi\tau)^2 & \mathrm{e}^{2A}+\kappa\left(\frac{x_3}{\xi}\right)^2(\partial_\xi\tau)^2 \end{pmatrix}. \tag{3.1.88}$$

Its determinant is given by:

$$-\det\tilde{g} = \mathrm{e}^{10A}\left(1+\mathrm{e}^{-2A}\kappa\left((\partial_r\tau)^2+(\partial_\xi\tau)^2\right)\right). \tag{3.1.89}$$

Soliton energy With the new metric (3.1.88), substituting the ansatz of equations (3.1.50)-(3.1.52), (3.1.56)-(3.1.58) and (3.1.64) into the DBI action (3.1.81) and the TCS action (3.1.23) yields the following result for the soliton energy

$$E = E_{\mathrm{DBI}} + E_{\mathrm{CS}}\,, \tag{3.1.90}$$

$$\begin{aligned} E_{\mathrm{DBI}} = 4\pi M^3 N_c N_f \int \mathrm{d}r\mathrm{d}\xi\,\xi^2 \sqrt{1+\mathrm{e}^{-2A}\kappa\left((\partial_r\tau)^2+(\partial_\xi\tau)^2\right)}\,V_f(\lambda,\tau)\,\mathrm{e}^{5A} - E_{\mathrm{DBI,vac}} + \\ + 4\pi M^3 N_c \int \mathrm{d}r\mathrm{d}\xi \sqrt{1+\mathrm{e}^{-2A}\kappa\left((\partial_r\tau)^2+(\partial_\xi\tau)^2\right)}\,V_f(\lambda,\tau)\,\mathrm{e}^{A}\times \\ \times\left(\mathrm{e}^{2A}\xi^2\kappa(\lambda)\tau^2\left(\mathrm{e}^{2A}\Delta_{rr}\tilde{A}_r^2+\left(1-\mathrm{e}^{2A}\Delta_{\xi\xi}\right)\tilde{A}_\xi^2+\frac{(\tilde{\phi}+\tilde{\phi}^*)^2}{2\xi^2}-\right.\right. \\ \left.\left.-2\mathrm{e}^{2A}\Delta_{\xi r}\tilde{A}_r\tilde{A}_\xi\right)+\right. \\ \left.+\,w(\lambda)^2\left(\frac{1}{8}\mathrm{e}^{2A}\left[\Delta_{rr}\left(1-\mathrm{e}^{2A}\Delta_{\xi\xi}\right)-\mathrm{e}^{2A}\Delta_{\xi r}^2\right]\xi^2(F_{\bar{\mu}\bar{\nu}})^2+\right.\right. \end{aligned}$$

$$+\frac{1}{2}\left(\left(1-\mathrm{e}^{2A}\Delta_{\xi\xi}\right)|\mathrm{D}_\xi\phi|^2+\mathrm{e}^{2A}\Delta_{rr}\,|\mathrm{D}_r\phi|^2\right)+$$
$$+\frac{\left(1-|\phi|^2\right)^2}{4\xi^2}-\frac{1}{2}\mathrm{e}^{2A}\Delta_{\xi r}(D_r\phi^*D_\xi\phi+h.c.)-$$
$$-\xi^2\Big(\mathrm{e}^{2A}\Delta_{rr}(\partial_r\Phi)^2+\left(1-\mathrm{e}^{2A}\Delta_{\xi\xi}\right)(\partial_\xi\Phi)^2-$$
$$-2\mathrm{e}^{2A}\Delta_{\xi r}\partial_\xi\Phi\partial_r\Phi\Big)\Big)\Big)\,, \tag{3.1.91}$$

$$E_{\rm CS}=\frac{4N_c}{\pi}\int \mathrm{d}r\mathrm{d}\xi\,\epsilon^{\bar\mu\bar\nu}\partial_{\bar\mu}\Phi\times$$
$$\times\left[(f_1(\tau)+f_3(\tau))\left(\tilde A_{\bar\nu}+\frac{1}{2}(-i\phi^*D_{\bar\nu}\phi+h.c.)+\frac{1}{4i}\partial_{\bar\nu}(\tilde\phi^2-(\tilde\phi^*)^2)\right)+\right.$$
$$\left.+\frac{1}{2}(3if_2(\tau)-f_1(\tau)-f_3(\tau))(\tilde\phi+\tilde\phi^*)^2\tilde A_{\bar\nu}\right]\,, \tag{3.1.92}$$

where in the DBI part, $E_{\rm DBI,vac}$ refers to the DBI contribution to the vacuum energy and the symbol Δ is defined in (F.53)-(F.55). The equations of motion are obtained by extremizing the energy (3.1.90) with respect to small deformations of the ansatz fields (3.1.70). They are presented in Appendix F.2.

3.1.6 Boundary conditions

The field equations presented in the previous section must be subject to appropriate boundary conditions both at spatial infinity $\xi\to+\infty$ and at the UV boundary $r\to 0$. Moreover, certain (generalized) regularity conditions must be imposed at the center of the instanton $\xi=0$ and in the bulk interior. In this section we present the conditions that are imposed on the fields of the ansatz (3.1.70) for the bulk instanton solution to be the dual of a single baryon at the boundary.

The discussion assumes that the dynamics for the tachyon modulus τ is also solved and the equations of motion given by (F.56)-(F.62) (this corresponds to what was referred to as the *inhomogeneous tachyon* case in the previous section). The conditions that are presented will also apply in the probe approximation, where τ is assumed to be a background field and the equations of motion are given by (F.38)-(F.43).

3.1.6.1 Baryon charge and mass

We start by deriving the expression for the baryon charge and mass in the boundary theory, in terms of the fields of the ansatz (3.1.70). We will then use these results to determine

the boundary conditions required for the charge to be equal to unity and the mass to be finite.

We first discuss the calculation of the baryon charge, whose details can be found in appendix D.1. The baryon current at the boundary is given by (D.37)

$$\begin{aligned} N_c J_B^\mu \,\omega_4 = -\frac{iN_c}{48\pi^2}\,\mathrm{d}x^\mu \wedge \Big[&-4i\mathrm{Tr}(L\wedge F^{(L)}) + \mathrm{Tr}(L\wedge L\wedge L) + 4i\mathrm{Tr}(R\wedge F^{(R)}) - \\ &- \mathrm{Tr}(R\wedge R\wedge R) + 6\mathrm{Tr}(DU\wedge F^{(L)}U^\dagger) + 6\mathrm{Tr}(DUU^\dagger\wedge F^{(R)}) - \\ &- 2i\mathrm{Tr}(DUU^\dagger\wedge DUU^\dagger\wedge DUU^\dagger)\Big]\Big|_{UV}\,, \end{aligned} \tag{3.1.93}$$

where we denoted by ω_4 the Minkowski volume 4-form

$$\omega_4 \equiv \mathrm{d}t\wedge\mathrm{d}x^1\wedge\mathrm{d}x^2\wedge\mathrm{d}x^3\,. \tag{3.1.94}$$

Remarkably, as shown in the appendix, the baryon number current only arises from the closed, G_4 term (3.1.32) in the TCS action and does not depend on the non-closed part of the CS action Ω_5^0 in (3.1.26), (3.1.27). That is, it is also independent of the functions $f_i(\tau)$ which are the only degrees of freedom in the CS action that were not fixed by general arguments in section 3.1.3.

Because no external gauge fields are present in the UV boundary theory, the non-abelian gauge field at $r=0$ should vanish. The baryon number current is therefore simply

$$J_B^\mu\,\omega_4 = -\frac{1}{24\pi^2}\,\mathrm{d}x^\mu\wedge\mathrm{Tr}(\mathrm{d}UU^\dagger\wedge\mathrm{d}UU^\dagger\wedge\mathrm{d}UU^\dagger)\Big|_{UV}\,. \tag{3.1.95}$$

Then the baryon number is[20]

$$N_B = \frac{1}{24\pi^2}\int\Big[\mathrm{Tr}(\mathrm{d}UU^\dagger\wedge\mathrm{d}UU^\dagger\wedge\mathrm{d}UU^\dagger)\Big]\Big|_{UV}\,, \tag{3.1.96}$$

which is nothing but the Skyrmion number for a matrix that is identified as the pion field at the boundary[21],

$$U_P(\xi) = U(r=0,\xi)^\dagger\,. \tag{3.1.97}$$

Substituting the tachyon ansatz (3.1.64) into (3.1.96), we finally obtain the expression of the baryon number in terms of the phase θ at the boundary

$$N_B = \frac{1}{\pi}\big(\theta(\xi=\infty)-\theta(0)\big)\,. \tag{3.1.98}$$

[20]Remember that the baryon density is $\rho_B = J^0$ and the raising of indices for the Levi-Civita tensor is such that $\epsilon_{0123} = -\epsilon^{0123} = 1$.

[21] As discussed in section 3.1.4.4, this identification only makes sense for vanishing quark masses. Moreover, if we take the expression (3.1.96) at face value, for non-zero quark masses the matrix $U(r,\xi)$ has to asymptote to a constant at $r=0$, and the resulting baryon number vanishes identically. This suggests that for non-zero quark mass both the baryon ansatz (as well as the form of the TCS action) must be generalized.

The expression for the baryon number in (3.1.96) is a boundary topological number but is not manifestly topologically stable in the bulk. On the other hand, a state with baryon number equal to 1 is expected to be dual to a solution of the bulk equations of motion with instanton number equal to 1 [126]. We would therefore like to relate the baryon number (3.1.96) to the bulk instanton number

$$\begin{aligned} N_{\text{instanton}} &= \frac{1}{8\pi^2}\int_{\text{bulk}} \text{Tr}\left(\mathbf{F}^{(L)}\wedge\mathbf{F}^{(L)} - \mathbf{F}^{(R)}\wedge\mathbf{F}^{(R)}\right) \\ &= \frac{1}{2\pi}\int \text{drd}\xi\, \epsilon^{\bar{\mu}\bar{\nu}}\left(F_{\bar{\mu}\bar{\nu}} + \partial_{\bar{\mu}}\left(-i\phi^* D_{\bar{\nu}}\phi + h.c.\right)\right)\,, \end{aligned} \tag{3.1.99}$$

where in the second line we substituted the instanton ansatz. The detailed calculation is presented in Appendix D.2.1. There it is found that, in terms of the baryon ansatz (3.1.50)-(3.1.52) and (3.1.64), the condition for the baryon number to equal the instanton number can be written as the vanishing of an IR integral

$$\int \text{d}\xi\, \left(\tilde{A}_\xi(|\tilde{\phi}|^2-1) + \partial_\xi\tilde{\phi}_1 + \partial_\xi\tilde{\phi}_1\tilde{\phi}_2 - \partial_\xi\tilde{\phi}_2\tilde{\phi}_1\right)\Big|_{IR} = 0\,. \tag{3.1.100}$$

This condition on the instanton solution follows from the regular IR asymptotics presented in Table 3.1 that will be discussed in detail in the next section.

Another global property of the baryon solution that can be used to identify the right boundary conditions is the mass of the nucleon. The mass of the nucleon is the sum of a classical contribution, equal to the classical instanton energy (3.1.85) evaluated on the solution, and quantum corrections:

$$M_{\text{nucleon}} = E + \delta M_Q\,. \tag{3.1.101}$$

Requiring the classical contribution to the mass to be finite sets the boundary conditions for the ansatz fields at $\xi\to\infty$, as in Table 3.1. The derivation of Table 3.1 is the topic of the next subsection.

In terms of the expansion in N_c, the classical mass is of order $\mathcal{O}(N_c)$, whereas the quantum corrections start at order $\mathcal{O}(1)$. Computing the quantum corrections requires to take the sum of the ground state energies for the infinite set of bulk excitations on the instanton background, and subtract the vacuum energy. It is not known how to do this calculation, so we can only assume that the classical mass gives the dominant contribution. Note that it is correct at least in the large N_c limit.

The experimental spectrum of baryons contains the nucleons but also many excited states, such as the isobar Δ. Here we focus for concreteness on the nucleon mass, but the mass of the excited states can be derived by an appropriate quantization of the perturbation modes of the instanton solution. This will be discussed in the next section.

$\xi \to 0$	$\xi \to \infty$	UV	IR
$\frac{\tilde{\phi}_1}{\xi} \to \mathfrak{f}_1(r)$	$\xi^{1/2}\tilde{\phi}_1 \to 0$	$\tilde{\phi}_1^2 + \tilde{\phi}_2^2 \to 1$	$\tilde{\phi}_1 \to 0$
$\frac{1+\tilde{\phi}_2}{\xi} \to 0$	$\xi^{1/2}(-1+\tilde{\phi}_2) \to 0$	$\partial_\xi \tilde{\phi}_1 + \tilde{A}_\xi \tilde{\phi}_2 \to 0$	$\partial_r \tilde{\phi}_2 \to 0$
$\tilde{A}_\xi - \frac{\tilde{\phi}_1}{\xi} \to 0$	$\xi^{3/2}\tilde{A}_\xi \to 0$	$\partial_r \tilde{A}_\xi \to 0$	$\tilde{A}_\xi \to 0$
$\tilde{A}_r \to 0$	$\xi^{3/2}\tilde{A}_r \to 0$	$\tilde{A}_r \to 0$	$\tilde{A}_r \to 0$
$\partial_\xi \Phi \to 0$	$\xi^{3/2}\partial_{\bar{\mu}}\Phi \to 0$	$\Phi \to 0$	$\partial_r \Phi \to 0$
$\partial_\xi \tau \to 0$	$\tau \to \tau_b(r)$	$r^{-2}\,\tau \to 0$	$\tau \to \tau_b(r_{\rm IR})$

Table 3.1: Gauge invariant boundary conditions for the fields of the baryon solution (3.1.70).

3.1.6.2 Boundary conditions for the gauge invariant fields

We are now ready to derive the boundary conditions relevant to the baryon solution. We present here the general conditions for the gauge-invariant fields (3.1.80) and discuss separately the 4 boundaries of the (ξ, r) space.

$\underline{\xi = 0}$: The boundary conditions in the limit where the 3D radius ξ goes to 0 are chosen as in the first column of Table 3.1, where $\mathfrak{f}_1(r)$ is some function of the holographic coordinate. The first 4 conditions come from requiring that $\tilde{\mathbf{L}}$ (3.1.78) and $\tilde{\mathbf{R}}$ (3.1.79) are well defined 5D vectors at $\xi = 0$. The last two conditions respectively come from requiring that the abelian field strength $\hat{F}$ (F.16) and the tachyon covariant derivative $D_M T$ are well defined at $\xi = 0$. The detailed asymptotics of the fields in this limit are presented in Appendix G.4.

$\underline{\text{UV :}}$ The boundary conditions in the UV limit $r \to 0$, are chosen as in the third column of Table 3.1. The first three conditions in the column originate from requiring that there are no sources for the gauge fields at the boundary. The fourth condition for $\tilde{A}_r$ is a consequence of (G.7), which originates from the near-boundary analysis of the constraint (F.38). Finally, the condition for Φ corresponds to setting the baryon chemical potential μ to 0, and that for τ is due to our choice to work with massless quarks, as mentioned before.

The UV asymptotics of the fields are discussed in more details in Appendix G.1.

$\underline{\xi \to \infty}$: The boundary conditions in the limit $\xi \to \infty$ are chosen as in the second column of Table 3.1 and come from requiring that the instanton energy in (3.1.85) is finite. In particular, the condition for the tachyon modulus τ is that it goes to its value in vacuum

$\tau_b(r)$. For Φ we set the additional condition that the baryon chemical potential μ is equal to 0. Finally, for $\tilde{\phi}_2$, the finite energy condition is

$$\partial_r \tilde{\phi}_2(r,\xi) \underset{\xi\to\infty}{\to} 0\,, \tag{3.1.102}$$

or equivalently

$$\tilde{\phi}_2(r,\xi) \underset{\xi\to\infty}{\to} \tilde{\phi}_2(0,\infty)\,. \tag{3.1.103}$$

The value of $\tilde{\phi}_2$ on the UV boundary at $\xi \to \infty$ is determined by the requirement that the baryon number (3.1.98) is equal to 1. This condition is for the tachyon phase at the boundary $\theta(r=0,\xi)$ to be such that

$$\theta(r=0,\infty) - \theta(r=0,0) = \pi\,. \tag{3.1.104}$$

Because the sources for the gauge fields at the boundary are required to vanish, $\tilde{\phi}_2(r=0,\xi) = -\cos\theta(r=0,\xi)$. Then, from the condition that $\tilde{\phi}_2 = -1$ at $\xi = 0$, we deduce that $\theta(r=0,0) = 0$. (3.1.104) therefore implies that

$$\tilde{\phi}_2(r,\xi) \underset{\xi\to\infty}{\to} -\cos\pi = 1\,. \tag{3.1.105}$$

The detailed asymptotics of the fields in the limit $\xi \to \infty$ are presented in Appendix G.2.

IR : The regularity conditions in the IR limit $r \to \infty$ are chosen as in the last column of Table 3.1. The ansatz fields obey second order differential equations, whose general solutions are a linear combination of two independent solutions. These independent solutions can be chosen such that one is finite in the IR while the other is singular. The regularity conditions correspond to the choice of the IR finite solutions. In that case, the precise IR asymptotics of the solution are presented in Appendix G.3. Note that the resulting conditions match those imposed in [172] for chiral symmetry to be broken on the IR wall:

$$(\mathbf{L}-\mathbf{R})|_{r_{\rm IR}} = 0 \quad , \quad \left(\mathbf{F}^{(L)}_{\mu r} + \mathbf{F}^{(R)}_{\mu r}\right)\Big|_{r_{\rm IR}} = 0\,. \tag{3.1.106}$$

As far as the tachyon modulus τ is concerned, it should match the vacuum solution far from the baryon center, so in particular in the IR at $r \to \infty$. The IR behavior of τ will therefore be given by (2.3.24).

3.1.6.3 Boundary conditions in Lorenz gauge

The non-linear second-order differential system of equations of motion (F.38)-(F.43) is not elliptic. This is due to the presence of constraint equations. While this is not problematic per se, it can lead to trouble when one tries to solve the problem numerically (which we will eventually do in an upcoming work). This is because the gauge invariance indicates

$\xi \to 0$	$\xi \to \infty$	$r \to 0$	$r \to r_{\rm IR} \to \infty$
$\partial_\xi \tilde{\phi}_1 - (A_\xi + \partial_\xi \theta) \to 0$	$\xi^{1/2} \tilde{\phi}_1 \to 0$	$\tilde{\phi}_1 \to \sin\theta$	$\tilde{\phi}_1 \to 0$
$\frac{1+\tilde{\phi}_2}{\xi} \to 0$	$\xi^{1/2}\left(\tilde{\phi}_2 - 1\right) \to 0$	$\tilde{\phi}_2 \to -\cos\theta$	$\partial_r \tilde{\phi}_2 \to 0$
$\partial_\xi A_\xi \to 0$	$\partial_\xi A_\xi \to 0$	$A_\xi \to 0$	$A_\xi \to 0$
$A_r \to 0$	$\xi^{3/2}\left(A_r - \frac{\pi}{r_{\rm IR}}\right) \to 0$	$\partial_r A_r \to 0$	$\partial_r A_r \to 0$
$\partial_\xi \Phi \to 0$	$\Phi \to 0$	$\Phi \to 0$	$\partial_r \Phi \to 0$
$\theta \to 0$	$\theta \to \pi\left(1 - \frac{r}{r_{\rm IR}}\right)$	$\partial_r \theta + A_r \to 0$	$\theta \to 0$
$\partial_\xi \tau \to 0$	$\tau \to \tau_b(r)$	$\tau \to 0$	$\tau \to \tau_b(r_{\rm IR})$

Table 3.2: Boundary conditions in Lorenz gauge.

that given boundary conditions, the solution is not unique. This can be avoided, if one works with an elliptic system instead.

Equations (F.38)-(F.43) can be recast in elliptic form if we write them in terms of the gauge variant fields (3.1.50)-(3.1.51), and then fix the gauge with the Lorenz condition

$$\partial_r A_r + \partial_\xi A_\xi = 0\,. \tag{3.1.107}$$

Note that this condition leaves a residual gauge freedom of the form

$$A_{\bar{\mu}} \to A_{\bar{\mu}} + \partial_{\bar{\mu}} \mathfrak{f} \quad , \quad \partial_r^2 \mathfrak{f} + \partial_\xi^2 \mathfrak{f} = 0 \quad , \quad \mathfrak{f}(0,\xi) = 0\,. \tag{3.1.108}$$

The convenient choice that we present below for the fixing of the residual gauge freedom (3.1.108) requires to introduce an IR cut-off $r_{\rm IR}$.

The equations of motion in Lorenz gauge are listed in appendix F.1.3 and the relevant boundary conditions written in Table 3.2. Because of the gauge fixing these conditions contain additional information compared with Table 3.1 that we discuss again separately for each boundary of the (r, ξ) space.

UV : In the UV limit $r \to 0$, the only difference with the gauge invariant conditions Table 3.1 is the additional condition for A_r, which comes from imposing the Lorenz gauge (3.1.107) near the boundary.

$\xi \to \infty$: For compatibility with the condition (3.1.104) $\partial_\xi \theta$ should go to 0 as $\xi \to \infty$, so A_ξ should also tend to 0 according to the gauge-invariant condition in Table 3.1. Then the Lorenz gauge condition in the limit where $\xi \to \infty$ reads

$$\partial_r A_r = 0 = -\partial_r^2 \theta\,, \tag{3.1.109}$$

so that θ at $\xi = \infty$ should be of the form

$$\theta \to \pi + \text{constant} \times r\,. \tag{3.1.110}$$

Then, for a solution with $N_B = 1$, we proved in section 3.1.6.1 that the instanton number (3.1.99) should also be equal to 1. The latter can be written as a boundary integral

$$N_{\text{instanton}} = \frac{1}{\pi}\int_0^{r_{\text{IR}}} \mathrm{d}r \left[A_r + \tilde{\phi}_1 \partial_r \tilde{\phi}_2 - \tilde{\phi}_2 \partial_r \tilde{\phi}_1\right]_{\xi=0}^{\xi=\infty} = \frac{1}{\pi}\int_0^{r_{\text{IR}}} \mathrm{d}r \left[A_r\right]_{\xi=0}^{\xi=\infty}\,, \tag{3.1.111}$$

where, to obtain the first integral above we used the boundary conditions in Table 3.2, and to obtain the second integral above we used the boundary conditions in Table 3.1. We find it convenient to choose a residual gauge (3.1.108) such that the instanton winding occurs at $\xi = \infty$[22]. In this case the condition that $\tilde{A}_r = 0$ at $\xi = \infty$ implies that θ has to go to

$$\theta \to \pi\left(1 - \frac{r}{r_{\text{IR}}}\right)\,, \quad \xi \to +\infty \tag{3.1.112}$$

$\xi = 0$ and IR : Once (3.1.112) is imposed, what remains of the residual gauge freedom (3.1.108) corresponds to the freedom of choosing the profile of θ on the 1-dimensional space composed of the lines at $\xi = 0$ and $r = r_{\text{IR}}$, with the condition that θ goes to 0 at the two endpoints of this line. The simplest choice is to set

$$\theta(r, 0) = \theta(r_{\text{IR}}, \xi) = 0\,, \tag{3.1.113}$$

for which the tachyon field is well defined at $\xi = 0$ and the stronger IR gauge condition proposed in (D.24) is obeyed. Then, the boundary conditions at $\xi = 0$ and $r = r_{\text{IR}}$ come from the gauge-invariant ones Table 3.1, with the additional derivative constraints on A_ξ and A_r due to the gauge choice.

To summarize, these boundary conditions ensure that a topological instanton in the bulk has finite bulk energy (therefore finite boundary mass) and unit baryon charge. The question of solving the field equation and finding such smooth solutions must be tackled numerically, and will be addressed in the next section.

3.1.6.4 Further comments

In the WSS model, the size of the instanton becomes small at large 't Hooft coupling λ. The flat space BPST instanton therefore gives a good approximation to the WSS instanton solution near its center. By contrast, there is no possibility in V-QCD which would make the size of the instanton parametrically small. Instead, the size is set by the

[22] Another possible choice would be to place it at $\xi = 0$ as in [175]. That choice has the advantage that U is regular at $\xi \to \infty$ in the limit $r_{\text{IR}} \to \infty$, but instead it is not well defined at $\xi = 0$.

mass scale of the boundary theory which roughly corresponds to $\Lambda_{\rm QCD}$. The curvature of the background space-time should therefore be taken into account in the calculation of the V-QCD instanton, for which there is no simple BPST approximation.

Moreover, the size of the baryon of the construct is clearly N_c-independent. The reason is that it is a solution to the gravitational equations to leading order in N_c and the solutions are N_c independent.

3.2 Numerical baryon solution and baryon spectrum

This section is based on my original work [6].

In the previous section, we have established the baryon instanton-like ansatz and its field equations, as well as the boundary conditions it should satisfy in order for the corresponding state in the boundary theory to have finite mass and unit baryon charge. Whether or not a full solution exists satisfying these field equations is a question which can only be addressed numerically. The corresponding equations are a set of non-linear partial differential equations in a two-dimensional space, whose numerical resolution is non-trivial.

The purpose of the work presented in this section is to compute and analyze the numerical baryon solution in a specific model in the V-QCD class. We first obtain numerically the static instanton solution (which corresponds to the baryon ground state), and then analyse the instanton collective modes and their quantization (which correspond to baryon excited states).

As important ingredient of this work, we present a specific model in the V-QCD class which offers a good quantitative match to low-energy QCD parameters, including some parameters in the flavor sector (like the pion decay constant) which were not correctly reproduced in previous models.

3.2.1 Summary

We start by giving a summary of the results presented in this section.

Fit to QCD data

We carry out an extensive comparison of the model predictions to experimental and lattice QCD data in order to pin down the parameters of the V-QCD action in section 3.2.2. The comparison consists of two main steps:

1. Qualitative comparison to QCD physics. The action both in the limit of weak and infinitely strong coupling, up to a few remaining parameters, can be determined by

requiring that the model respects known properties of QCD such as confinement and asymptotic freedom. This work has been done in earlier literature [145, 150, 161, 160, 174], and we simply review the results here.

2. Quantitative comparison to QCD data. The details of the action at intermediate coupling, as well as the few remaining weak and strong coupling parameters, can be tuned so that the predictions of the model match with QCD data. In this step, the dependence of the predictions on the exact values of the model parameters is typically weak. In spite of this, the model has been able to describe various observables to a high precision [147, 165, 162].

As for the second step, the work in this section extends the earlier work where the full V-QCD model was separately compared to data for thermodynamics [165] and to meson spectra [162]:

- We fit the model parameters to data for thermodynamics and spectra simultaneously.
- Unlike in [162] (where the model was fitted to a large number of excited meson states), we stress the lowest lying meson states.
- Importantly, we require a good match of the model with the experimental value of the pion decay constant $f_\pi \approx 92$ MeV, which was poorly reproduced in both previous fits.

We now discuss the fit in more detail. The V-QCD model contains two sectors, corresponding to gluons (improved holographic QCD [145]) and quarks (tachyon Dirac-Born-Infeld actions for space filling branes [137, 138]). The former sector can be separately compared to data from lattice analysis of pure Yang-Mills theory [147]. In this work, we use the fit of [162] for the gluon sector, and check explicitly that it reproduces both the lattice data for the thermodynamics of Yang-Mills at $N_c = \infty$ (see figure 3.1) and for the glueball spectrum (see table 3.4) to a good precision.

Most of the freedom in the full V-QCD model is however in the quark sector. In order to determine the model parameters in this sector, we compare the predictions to

- Lattice data for the thermodynamics of full QCD with $N_f = 2+1$. We use both the data for the equation of state at vanishing chemical potential (see figure 3.2) and for the first nontrivial cumulant of the pressure at nonzero chemical potential (see figure 3.3).
- Experimental data for lowest lying meson masses and the pion decay constant. See table 3.6.

The final values of the model parameters are given in table 3.5. Apart from a few exceptions, the model depends on these parameters through four different functions of the coupling, which are shown in figure 3.4 for the final fit.

The fit in figures 3.2, 3.3 and table 3.6 has rather good quality. However, the agreement when fitting the thermodynamics [165] and the spectra [162] separately was significantly better. This is the case because the combined fit is challenging: there is some clear tension between the fit to the properties of the finite temperature state and the zero temperature vacuum state. It is likely that this tension can be reduced by carrying out a simultaneous numerical fit of all parameters to all data. We do not attempt to do this technically demanding task here, but are planning to return to it in future work. In particular, we expect that the methods of machine learning should be of particular relevance to address this problem. Notice also that, at least to our knowledge, an overall fit to QCD data of the similar extent as presented in this work has not been attempted in any other model in earlier literature.

Static baryon solution

Starting from the formalism introduced in the previous section, we compute in section 3.2.3 the numerical bulk solution for a single static baryon, with the V-QCD potentials presented in Section 3.2.2.[23] In the Veneziano limit $N_c \to \infty,\ N_f \to \infty$, the baryon contribution to the bulk action is of order N_c, which is negligible compared to N_c^2 and $N_c N_f$. This implies that the leading order baryon solution can be treated as a "probe" on the background dual to the vacuum of the boundary theory.

The numerical baryon solution is computed both at leading order and including the first corrections to the background, which are of order $\mathcal{O}(1/N_c, 1/N_f)$. The leading order baryon solution is reliably calculated, by ignoring both the tachyon and glue backreactions. The backreaction of the baryon solution to the tachyon is computed by neglecting the glue backreaction for simplicity. It is expected that the back-reaction on the color sector, does not affect the qualitative results for the tachyon backreaction.

For the leading order probe solution, the following results are obtained:

- The instanton number and bulk Lagrangian densities (figure 3.5) are confined to a region of finite extent in the bulk, which confirms the solitonic nature of the baryon solution. The integrals of these densities give respectively the baryon number, which is confirmed to be equal to 1 numerically, and the classical contribution to the nucleon mass. The latter is found to be relatively close to the experimental nucleon mass for $N_c = 3$ colors

$$M_0 \simeq \frac{N_c}{3} \times 1150\,\mathrm{MeV}\,. \tag{3.2.1}$$

  We recall however, that the full result for the V-QCD baryon mass should also include quantum corrections: these should be computed from the perturbations around the baryon, together with an appropriate subtraction of the similar fluctuations around the vacuum state. Computing these corrections goes beyond the scope of this work.

[23] In addition, the solutions with a different choice of potentials are discussed in Appendix I.

Although these corrections are subleading at large N_c, starting at order $\mathcal{O}\left(N_c^0\right)$, they may give a sizeable contribution when N_c is set to 3. Note that this state of affairs regarding quantum corrections is not particular to our model, and is true also for both the Skyrme model and other holographic models.

- In the previous section, it was found that, for the baryon solution, the pion matrix at the boundary follows the Skyrmion hedgehog ansatz

$$U_P(\xi) = \exp\left(i\theta(\xi)\frac{x\cdot\sigma}{\xi}\right), \tag{3.2.2}$$

with ξ the 3-dimensional radius. Also, the baryon number was shown to be equal to the skyrmion number for the pion matrix. This indicates that the baryon solution in V-QCD is qualitatively similar to the Skyrme model skyrmion solution[24]. To measure the difference with the Skyrme model skyrmion, the pion phase $\theta(\xi)$ is compared with the Skyrme result in figure 3.6. This indicates that the two solutions are quantitatively close.

At the next order in the large N expansion, the back-reacted solution provides the following information:

- The modulus of the chiral condensate $\left|\left\langle\bar{\psi}\psi\right\rangle\right|$ is observed to decrease towards the baryon center, as shown in figure 3.7. This signals the expected partial restoration of the chiral symmetry inside the baryon.

- The correction to the baryon Lagrangian density from the back-reaction is calculated numerically and presented in figure 3.8. The observed behavior is well understood in terms of the chiral restoration, which has two effects. First, the negative contribution in the UV is mainly understood as a direct consequence of the decrease of the contribution from the chiral condensate to the Lagrangian density. Second, a positive correction is observed in the IR, which corresponds to a shift of the baryon towards the IR. This shift also contributes to the negative region in Figure 3.8, and is understood as a consequence of the weakening of the IR-repelling bulk force felt by the baryon in the chirally broken background. The results also indicate that the correction to the classical soliton mass is negative, and relatively small in absolute value.

Rotating baryon solution and spin-isospin spectrum

The second part of this section is devoted to the quantization of the isospin collective coordinates of the bulk soliton dual to a baryon. In the large N_c limit, the moment of

[24]This should not come as a surprise, as we already know that the dual boundary theory can be understood in the confined phase as a chiral effective theory coupled to a tower of massive mesons.

inertia λ of the baryon is of order $\mathcal{O}(N_c)$ and the quantization is that of a solid rotor. The result of this procedure is the derivation of the spin-isospin baryon spectrum for the V-QCD model considered in this work.

The starting point for the quantization of the collective coordinates is the classical bulk solution obtained by a time-dependent isospin rotation of the static soliton, parametrized by

$$V(t) \equiv \exp\left(it\,\omega^a \lambda^a\right) \in SU(N_f)_{L+R}$$

with ω^a the rotation velocity. In this work we restrict to the following regime:

- Only an SU(2) subgroup (the same where the static soliton sits) of the full isospin subgroup is quantized. This means that we impose that $V(t) \in SU(2)_{L+R}$. By doing so, we compute only a subset of the full spin-isospin spectrum, corresponding to baryons composed of quarks with 2 flavors (or equivalently, the states with strong hypercharge $Y = 1$).

- The rotation is assumed to be stationary and slow. In terms of the rotation velocity ω^a, this means that ω^a is assumed to be a constant and obey $\omega^2 \ll M_0/\lambda$. This regime describes well the baryon states with spins

$$s \ll N_c \ .$$

The quantization therefore requires the calculation of the bulk solution corresponding to a slowly rotating baryon. This calculation is done at linear order in ω. Already at this order, it turns out that a simple rotation of the static soliton fields with $V(t) \in SU(2)_{L+R}$ is not a solution of the bulk equations of motion. Instead, as soon as the soliton is made to rotate, some new flavor fields are turned on in the bulk, at linear order in ω [177]. These are the flavor equivalents of the magnetic field sourced by a rotating charge.

The appropriate ansatz for the rotating fields is constructed in section 3.2.5, by imposing the same symmetries as for the static solution, apart from time-reversal. These include 3-dimensional rotations and parity. Once this ansatz is determined, the construction of the rotating soliton solution follows the same steps as in the static case:

- We derive the expression of the moment of inertia of the soliton in terms of the ansatz fields.

- We derive the full equations of motion for the fields of the rotating ansatz.

- We identify the boundary conditions such that the moment of inertia is finite. The boundaries here are 1) the near-AdS region UV boundary $r \to 0$, where the solution should satisfy vev-like boundary conditions for all the fields; 2) the boundary at spatial infinity $|\vec{x}| \to \infty$, where the fields have to vanish fast enough for the moment of inertia to be finite.

- We identify suitable regularity conditions in the IR region of the geometry.

The last part of this section presents the results of the numerical calculation for the solution to the equations of motion obeyed by the rotating ansatz fields. The spin-isospin baryon spectrum resulting from this solution is shown in table 3.3. We emphasize that

Spin	V-QCD mass	Experimental mass
$s = \frac{1}{2}$	$M_N \simeq 1170\,\mathrm{MeV}$	$M_N = 940\,\mathrm{MeV}$
$s = \frac{3}{2}$	$M_\Delta \simeq 1260\,\mathrm{MeV}$	$M_\Delta = 1234\,\mathrm{MeV}$

Table 3.3: Baryon spin-isospin spectrum in the V-QCD model with the potentials of section 3.2.2, compared with experimental data.

these numbers were obtained by substituting $N_c = 3$ in the leading order large N_c and N_f result. In principle, at small values of N_c and N_f, this result is not expected to be quantitatively accurate.

3.2.2 The V-QCD model: comparison to data

This section describes the procedure for constructing the specific model in the V-QCD class that was used to compute the numerical baryon solution. The parameters of the model are determined by comparing to QCD data. This is done in two stages: In the first stage, we choose the asymptotics of the functions so that the model has the potential to resemble QCD. In the second stage, we fit the remaining parameters to QCD data. In earlier work, this second step has been done for pure Yang-Mills [147] (see also [197, 198]), as well as for full QCD by fitting the thermodynamics [165] and meson spectrum [162] separately. Here we carry out a simultaneous fit to the thermodynamic and spectrum data for full QCD, with a slightly higher weight on the spectrum fit because it probes directly the vacuum phase which is relevant for the current study. Apart from just combining the earlier thermodynamics and spectra fits, we also choose a different set of observables for the latter fit as compared to [162]. In this reference, the stress was on fitting a high number of meson masses including relatively heavy states, in order to obtain a good description of Regge trajectories. Here we focus on the mesons with lowest masses and also fit the pion decay constant.

The V-QCD action was introduced in section 2.3, but we will reproduce the expressions here, so that it is clear what are the parameters that take part in the fit. The five-dimensional action

$$S_{V-QCD} = S_g + S_{DBI} + S_{CS} \tag{3.2.3}$$

is the sum of three terms[25]. The action for the glue sector is

$$S_g = M^3 N_c^2 \int d^5x \sqrt{-g} \left[R - \frac{4}{3\lambda^2} g^{MN} \partial_M \lambda \partial_N \lambda + V_g(\lambda) \right] , \tag{3.2.4}$$

and the flavor action contains a DBI and a CS term. The simplified abelian form of the DBI action introduced in section 2.3 is given by

$$\begin{aligned} S_{DBI,simpl} = & - M^3 N_c N_f \times \\ & \times \int d^5x \; V_f(\lambda,\tau) \sqrt{-\det\left(g_{MN} + \kappa(\lambda) \partial_M \tau \partial_N \tau + w(\lambda) F_{MN}\right)} . \end{aligned} \tag{3.2.5}$$

This simplified form is sufficient to discuss the fit to QCD data, which is based on properties of the vacuum and equilibrium thermal states. The CS term was presented in section 3.1.3. We will not reproduce its expression here since it is not needed for the background analysis. We emphasize however that this term is included in the action for the V-QCD model, which is necessary for stabilizing the size of the baryon solutions that we construct below.

3.2.2.1 Comparing V-QCD to data: asymptotics

We now discuss how the potentials $V_g(\lambda)$, $V_f(\lambda,\tau)$, $\kappa(\lambda)$ and $w(\lambda)$ are determined. We start by considering the asymptotic constraints as $\lambda \to 0$ (UV) or $\lambda \to \infty$ (IR), which arise from comparison to QCD. The constraints on the asymptotics were already briefly sketched in section 2.3. Here we provide a more detailed discussion.

In the UV, the field theory becomes weakly coupled and it is far from obvious that gauge/gravity duality can provide useful predictions. In this region we follow the usual practice for bottom-up models and adjust the model by hand so that it mimics closely the behavior of QCD in the perturbative regime. Such choices are expected to give good boundary conditions for the more interesting, strongly coupled IR physics.

In order to write down the asymptotics as $\lambda \to 0$, we write down the effective potential

$$V_{eff}(\lambda,\tau) = V_g(\lambda) - \frac{N_f}{N_c} V_f(\lambda,\tau) , \tag{3.2.6}$$

as well as the expansion of the flavor potential at small tachyon:

$$V_f(\lambda,\tau) = V_{f,0}(\lambda) \left[1 - \hat{a}(\lambda)\tau^2 + \mathcal{O}\left(\tau^4\right) \right] . \tag{3.2.7}$$

The UV behavior is in general chosen such that the geometry is asymptotically AdS_5 and the asymptotics of the bulk fields match with the expected (free field) UV dimensions

[25]The action generically contains an additional CP-odd term that couples the flavor fields to the holographic axion, dual to the $\mathrm{Tr}(G \wedge G)$ operator. This term was derived in [161, 166] based on the ideas of [138]. We do not write this term here because, as explained in Section 3.2.5.1, the coupling to the axion is ignored in the following.

of the dual operators. Moreover, one can require that the logarithmic running of the dilaton agrees with the two-loop perturbative running of the QCD coupling. This maps the subleading terms in the potential V_g and the effective potential V_{eff} to the two-loop β functions of the YM theory and full QCD, respectively. We implement this constraint here for the gluon potential V_g only, and choose to fit the other higher order coefficients to low energy data instead. The explicit definitions of the UV expansions take the form

$$\begin{aligned}
&V_g(\lambda) = V_{g,0}\left[1 + V_{g,1}\lambda + O(\lambda^2)\right] \\
&V_{eff}(\lambda, \tau = 0) = V_0\left[1 + V_1\lambda + O(\lambda^2)\right] \\
&V_{f,0}(\lambda) = W_0\left[1 + W_1\lambda + O(\lambda^2)\right], \\
&\kappa(\lambda) = \kappa_0\left[1 + \kappa_1\lambda + O(\lambda^2)\right], \qquad\qquad \lambda \to 0, \\
&w(\lambda) = w_0\left[1 + w_1\lambda + O(\lambda^2)\right], \\
&\hat{a}(\lambda) = 1 + a_1\lambda + \mathcal{O}(\lambda^2)\,.
\end{aligned} \tag{3.2.8}$$

Here the coefficients $V_{g,0}$ and V_0 are linked to the radii of the UV AdS_5 geometry in the absence of flavors, and for the full background, respectively:

$$V_{g,0} = \frac{12}{\ell_g^2}\,, \qquad V_0 = V_{g,0} - xW_0 = \frac{12}{\ell^2}\,. \tag{3.2.9}$$

We fixed the normalization of the tachyon field such that $\hat{a}(\lambda = 0) = 1$[26].

The requirement that the asymptotic dimension of the $\bar{q}q$ operator equals 3 sets

$$\kappa_0 = \frac{2\ell^2}{3}\,. \tag{3.2.10}$$

The subleading coefficients $V_{g,1}$ and $V_{g,2}$ are determined by comparing to the YM β function, which sets

$$V_{g,1} = \frac{11}{27\pi^2}\,, \qquad V_{g,2} = \frac{4619}{46656\pi^4}\,. \tag{3.2.11}$$

The rest of the parameters are left free at this point.

The IR ($\lambda \to \infty$) asymptotics of the various functions is chosen such that the model agrees with various qualitative features. First, the asymptotics of $V_g(\lambda)$ is adjusted such that the model has a discrete glueball spectrum with Regge-like linear radial trajectories (i.e. that the masses behave as $m_n^2 \sim n$ as a function of the radial excitation number n). This requirement automatically implies also color confinement and magnetic screening, [145].

The geometry ends in a "good" IR singularity according to the classification by Gubser [200]. Second, several requirements constrain the asymptotics of the functions in the DBI action:

[26]This is without loss of generality, as we have left the normalization of the tachyon kinetic term free for the moment.

- The IR singularity should remain fully repulsive, so that the boundary conditions for the background and fluctuations are properly determined [150].
- The meson mass spectrum needs to be discrete, admit linear Regge-like radial trajectories, and all meson trajectories should have the same universal slope [161][27]. The mass gap of, say, vector mesons should grow linearly with quark mass at large values of the mass [160].
- The flavor action should vanish in the IR for chirally broken backgrounds, corresponding to the annihilation of the flavor branes in the IR, [159]. Moreover, the phase diagram as a function of x, T, μ and the θ-angle, should have the qualitatively correct structure.

These requirements can be met if we choose the flavor action which behaves as

$$V_f(\lambda,\tau) \sim e^{-a(\lambda)\tau^2}, \qquad \tau \to +\infty \tag{3.2.12}$$

with $a(\lambda) > 0$, and require that as $\lambda \to \infty$

$$\begin{aligned} &V_g \sim V_{IR}\lambda^{4/3}(\log\lambda)^{1/2}, \quad V_{f,0} \sim W_{IR}\lambda^{v_p}, \\ &\kappa \sim \kappa_{IR}\lambda^{-4/3}(\log\lambda)^{1/2}, \quad a \sim a_{IR}, \quad w \sim w_{IR}\lambda^{-4/3}(\log\lambda)^{w_l}, \end{aligned} \tag{3.2.13}$$

with $4/3 < v_p < 10/3$ and $w_l > 1/2$ (see [161] for details).

3.2.2.2 Comparing V-QCD to data: fit of parameters

After the asymptotics of the potentials have been fixed, the remaining task is to determine the leftover freedom by doing a more precise comparison to QCD data. We shall be using lattice data for the thermodynamics of the YM theory and QCD as well as glueball masses, and experimental data for meson masses and decay constants.

The complete ansatz is given by

$$V_g(\lambda) = 12\left[1 + V_{g,1}\lambda + \frac{V_{g,2}\lambda^2}{1+c_\lambda\lambda/\lambda_0} + V_{\rm IR}e^{-\lambda_0/(c_\lambda\lambda)}\left(\frac{c_\lambda\lambda}{\lambda_0}\right)^{4/3}\sqrt{\log(1+c_\lambda\lambda/\lambda_0)}\right] \tag{3.2.14}$$

$$V_f(\lambda,\tau) = V_{f,0}(\lambda)\left(1+\tau^4\right)^{\tau_p}\exp\left(-a(\lambda)\tau^2\right) \tag{3.2.15}$$

$$V_{f,0}(\lambda) = W_0 + W_1\lambda + \frac{W_2\lambda^2}{1+c_f\lambda/\lambda_0} + W_{\rm IR}\left(1+\frac{\bar{W}_1\lambda_0}{c_f\lambda}\right)e^{-\lambda_0/(c_f\lambda)}(c_f\lambda/\lambda_0)^2 \tag{3.2.16}$$

[27] There is a certain freedom in this direction. Tachyon condensation induces a mass term for the axial gauge field in the bulk, and depending on bulk IR asymptotics, it may change the slope of the radial trajectories for the axial and vector mesons, [156, 157]. It is not yet clear whether this is true in QCD, [201].

$$a(\lambda) = 1 + \frac{1}{2} a_{\rm st} \left[1 + \tanh\left(-a_{\rm sh} + \log(\lambda/\lambda_0)\right)\right] \tag{3.2.17}$$

$$\kappa(\lambda) = \kappa_0 \left[1 + \bar{\kappa}_0 \left(1 + \frac{\bar{\kappa}_1 \lambda_0}{c_\kappa \lambda}\right) e^{-\lambda_0/(c_\kappa \lambda)} \frac{(c_\kappa \lambda/\lambda_0)^{4/3}}{\sqrt{\log(1 + c_\kappa \lambda/\lambda_0)}}\right]^{-1} \tag{3.2.18}$$

$$\begin{aligned} w(\lambda) = w_0 \Bigg\{ & 1 + \frac{w_1 c_w \lambda/\lambda_0}{1 + c_w \lambda/\lambda_0} + \\ & + \ \bar{w}_0 e^{-\hat{\lambda}_0/(c_w \lambda)} \frac{(c_w \lambda/\lambda_0)^{4/3}}{\log(1 + c_w \lambda/\lambda_0)} \left[1 + w_{\rm as} \left(\log\left(1 + c_w \lambda/\lambda_0\right)\right)^4\right] \Bigg\}^{-1} \end{aligned} \tag{3.2.19}$$

where $\lambda_0 = 8\pi^2$. We have also chosen $v_p = 2$ in the IR, and set $\ell_g = 1$, so that the AdS radius is given by

$$\ell = \frac{1}{\sqrt{1 - x W_0/12}} \tag{3.2.20}$$

and consequently, from (3.2.10)

$$\kappa_0 = \frac{2}{3\left(1 - x W_0/12\right)} \ . \tag{3.2.21}$$

Requiring agreement with the two-loop β-function of Yang-Mills fixes the subleading coefficients of V_g in the UV to the values given in (3.2.11).

We now set $x = 2/3$, roughly corresponding to QCD with $N_f = 2$ light quarks and $N_c = 3$. The rest of the parameters are fitted to data. In addition to the parameters of the potentials, we also fit the 5D Planck mass M and the characteristic scale Λ of the background solutions, which is roughly dual to the scale Λ_{QCD} in field theory, see section 2.3.1.

The fit is carried out in steps. We fit the various functions sequentially to appropriately chosen observables as we explain below. Although the best strategy would be a global fit of all the parameters to all appropriate data, this is numerically very demanding and we are not yet able to do it.

The function V_g is chosen to be the same as in the fit of [162] where it was determined through a global fit to the QCD spectrum. Even if it was not directly fitted to the data from Yang-Mills theory, it does produce a good description of the lattice data for Yang-Mills thermodynamics [148] and the glueball spectra [202, 203, 204], see figure 3.1[28] and table 3.4.

The next function to be fitted is $V_f(\lambda, \tau)$ at zero tachyon, i.e., $V_{f,0}(\lambda)$. For this function, we mostly use the lattice data for QCD thermodynamics at high temperatures and zero density in the chirally symmetric phase. As we are working at zero quark mass in the

[28] In this figure, the Planck mass M and the scale parameter Λ were fitted independently of the later fits to full QCD data. This reflects the dependence on x of these parameters: the values for Yang-Mills are those with $x = 0$, whereas for full QCD we take $x = 2/3$.

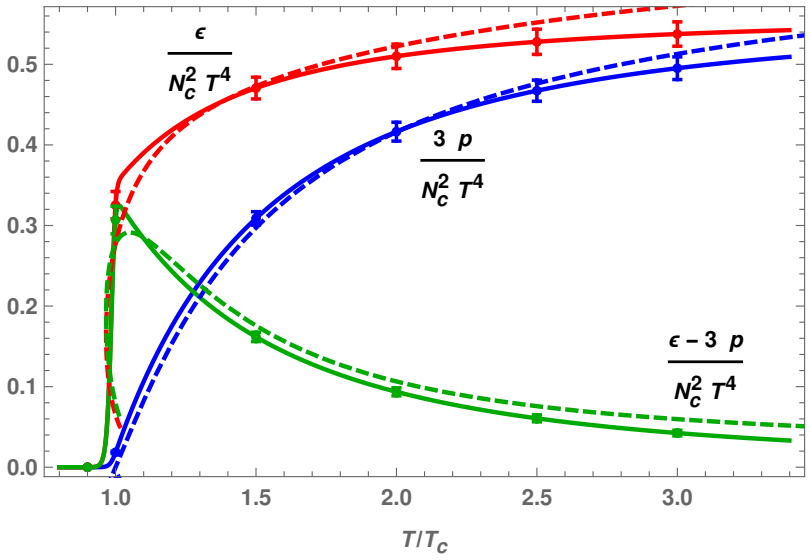

Figure 3.1: Our result for the thermodynamics of pure Yang-Mills theory (dashed curves) compared to lattice data interpolated to $N_c \to \infty$ [148] (solid curves and error bars). The red, blue, and green curves show the normalized energy density, pressure, and interaction measure, respectively.

holographic model, chiral symmetry is fully restored in this phase, meaning that the tachyon is identically zero. This means that the thermodynamics only depends on $V_{f,0}$ through the effective potential

$$V_{eff}(\lambda, \tau = 0) = V_g(\lambda) - xV_{f,0}(\lambda)\,. \tag{3.2.22}$$

In order to present our results, we introduce a reference value $M_{\rm UV}$ for the Planck mass, defined by

$$M_{\rm UV}^3 \equiv \frac{1}{45\pi^2\ell^3}\left(1+\frac{7x}{4}\right) \quad , \quad x \equiv \frac{N_f}{N_c}\,, \tag{3.2.23}$$

where $x = 2/3$. This expression gives the value of the Planck mass for which there is agreement of the pressure with the perturbative QCD result in the limit $T \to \infty$. We fitted the effective potential (3.2.22) to latice data for various fixed values of the Planck mass M, while the other scale parameter Λ, which only affects the temperature scale in the plots, was allowed to vary freely. Figure 3.2 shows fits with $M^3/M_{\rm UV}^3 = 1.5$ (dashed thin black curves) and $M^3/M_{\rm UV}^3 = 4$ (solid thin black curves).[29] Note that, although the fit results are determined mostly by $V_{eff}(\lambda, \tau = 0)$, M and Λ, they also depend on other

[29] In the right hand plot disentangling the two curves is difficult because they almost overlap.

Ratio	Model	Lattice ($N_c = 3$)	Lattice ($N_c = \infty$)
$m_{0^{*++}}/m_{0^{++}}$	1.52	1.603 ± 0.042 [202] 1.719 ± 0.016 [204]	1.835 ± 0.032 [202] 1.903 ± 0.018 [204]
$m_{2^{++}}/m_{0^{++}}$	1.29	1.346 ± 0.037 [202] 1.437 ± 0.011 [204]	1.451 ± 0.048 [202] 1.497 ± 0.008 [204]
$T_c/m_{0^{++}}$	0.162	0.182 ± 0.004 [202, 203]	0.181 ± 0.003 [202, 203]

Table 3.4: Our results for glueball mass ratios and the ratio of the mass to the critical temperature compared to lattice results.

parameters of the theory via the critical temperature of the phase transition between the chirally-unbroken and the chirally-broken vacuum.

When fitting, we therefore took the critical temperature as an additional fit parameter. In the next step of the fitting procedure, which is discussed below, the tachyon dependent functions were adjusted such that the critical temperature is indeed close to the fitted value. The two values will however be slightly different, and therefore the results for the thermodynamics with the final fit parameters differ from the direct fits of the effective potential. The discrepancy is clearly visible in figure 3.2.

The best fits to thermodynamics were obtained at low $M^3/M_{\rm UV}^3 \lesssim 2$. However, in the analysis that follows we chose a high value $M^3/M_{\rm UV}^3 \simeq 4$. The reason is that such high values lead to a better description of the spectrum and in particular of the pion decay constant, which, as we remarked above, are stressed in the fit. We also note that there is a simple flat direction in this fit as the thermodynamics is unchanged under uniform rescalings of the coupling $\lambda \mapsto c\lambda$ in the effective potential. This happens because the kinetic term in (3.2.4) is invariant under such rescalings, so that a constant in V_{eff} multiplying λ can be eliminated through a field redefinition. We use this freedom to ensure that the constructed effective potential is consistent with the choice of V_g, meaning, in particular, that $V_{f,0}$ is set to be positive and monotonic.

The most complicated step in the fit is the next step, where we choose the form of $V_f(\lambda, \tau)$ at nonzero tachyon, including the function $a(\lambda)$ in the exponential factor, and the tachyon kinetic term $\kappa(\lambda)$. These functions are probed by the chirally broken vacuum, which has nonzero bulk tachyon condensate. The main observables are the pion decay constant, the mass of the ρ meson, and the mass of the lightest scalar flavor nonsinglet (i.e., isotriplet for $N_f = 2$) state. When doing the fit, it is important to keep an eye on the ratio of the meson masses to the critical temperature.

As it turns out, fitting the thermodynamics and meson spectra simultaneously leads to

tensions in the choices of potentials. The basic issue is that it is difficult to find a choice of function that would, at the same time, give high enough pion decay constant, heavy enough scalar states, and the experimentally observed meson mass to critical temperature ratio. In order to alleviate this tension we introduced an ansatz for the tachyon dependence of V_f in (3.2.15) and (3.2.17), which is somewhat more detailed than those used in previous studies. This ansatz has the following properties

- It includes a new parameter τ_p in (3.2.15), controlling a term which depends on the tachyon only. We find that increasing τ_p leads to better fits, so we choose the value $\tau_p = 1$ which is close to the maximal possible value. This maximum arises because $V_f(\lambda, \tau)$ needs to be monotonic in τ at small λ, otherwise no appropriate background solutions exist.

- The exponent in the tachyon exponential a in (3.2.15), is taken to be a function of the dilaton $a(\lambda)$. $a(\lambda)$ needs to be constant at both large and small λ, but may have a step in the middle. The fit result is that the IR value of $a(\lambda)$ should be significantly higher than the UV value (that was normalized to one).

In addition, the function $\kappa(\lambda)$ has three free parameters (notice that κ_0 in the ansatz (3.2.18) is given in (3.2.21)). One of these (in practice $\bar{\kappa}_1$) is fitted such that the final critical temperature is close to that obtained from the fit of V_{eff} discussed above. Due to tension with the fit to thermodynamics, we however choose a value that is a bit higher than obtained in the fit. The other two parameters $\bar{\kappa}_0$ and c_κ, are used to adjust the function such that the pion decay constant and the scalar masses are optimal. This means, in practice, taking $\bar{\kappa}_0$ to be close to the critical value beyond which the model stops to be confining for mesons (see [161]), and adjusting c_κ according to the fit of the masses and the decay constant.

The remaining task is to fit the function $w(\lambda)$, parametrized in (3.2.19). The spectra, in particular the vector and axial meson masses, do depend on this parameter. But as it turns out, the dependence is rather weak. Therefore, we fit this function to lattice data on the baryon number susceptibility

$$\chi_B(T) = \frac{1}{N_c^2} \frac{\partial^2 p(T,\mu)}{\partial \mu^2}\Big|_{\mu=0} \tag{3.2.24}$$

following [165]. Here μ is the quark chemical potential. For the parameter $w_{\rm as}$ in (3.2.19), we choose a small value[30]

$$w_{\rm as} = 2 \times 10^{-5} \tag{3.2.25}$$

so that this fit is essentially independent of the IR modification (i.e., the factor in the square brackets in (3.2.19)). Due to the weak dependence of the spectrum on $w(\lambda)$ the last two steps of the fitting procedure need to be done in part in parallel: in practice we

[30]This value can also be chosen to be zero without affecting the quality of the fits.

Parameter	Value
$M^3/M^3_{\rm UV}$	4.929 (3.8)
Λ	4107 MeV (3350 MeV)
$M^3/M^3_{\rm UV}\|_{x=0}$	1.4
$V_{\rm IR}$	1.804
c_λ	2.833
W_0	2.376
W_1	0.04603
W_2	0.02546
$W_{\rm IR}$	1.783
$\bar{W}_1$	4.357
c_f	1.463

Parameter	Value
τ_p	1
$a_{\rm st}$	2.5
$a_{\rm sh}$	1.5
$\bar{\kappa}_0$	2.429
$\bar{\kappa}_1$	0.32
c_κ	2.0
w_0	1.17
w_1	52.5
$\bar{w}_0$	200
c_w	0.18
$w_{\rm as}$	2×10^{-5}

Table 3.5: Choices of model parameters, split in groups. For the first two parameters, the Planck mass M and the scale Λ, the first set of values are determined by the ρ mass and f_π, whereas the values in parentheses are the values preferred by the fit to thermodynamics. We also set $x = 2/3$ and $b = 10$ for the additional parameter appearing in the CS action.

determine first $V_f(\lambda, \tau)$ and $\kappa(\lambda)$ using a choice of $w(\lambda)$ that produces a rough fit to the lattice data for the susceptibility. When $V_f(\lambda, \tau)$ and $\kappa(\lambda)$ are known, we then tune $w(\lambda)$ to obtain a good fit as the last step.

The final parameter values are collected in table 3.5. The fits for the QCD thermodynamics are shown in figures 3.2 and 3.3. The results for the most important meson masses and the f_π are given in table 3.6.

Before discussing the details of the fit results, we give a summary of the observables that the various parameters were fitted to. Notice that the parameters in table 3.5 were grouped in six groups. In the first group (top left), we show the final values fixed to f_π and m_ρ for the mass scales M and Λ, as well as the values preferred by the fit to the lattice results for thermodynamics (values in parentheses). The value of M at $x = 0$ is the one used in Figure 3.1 for the thermodynamics of pure Yang-Mills.

The parameters of V_g (middle left group) were not fitted here but we used the values

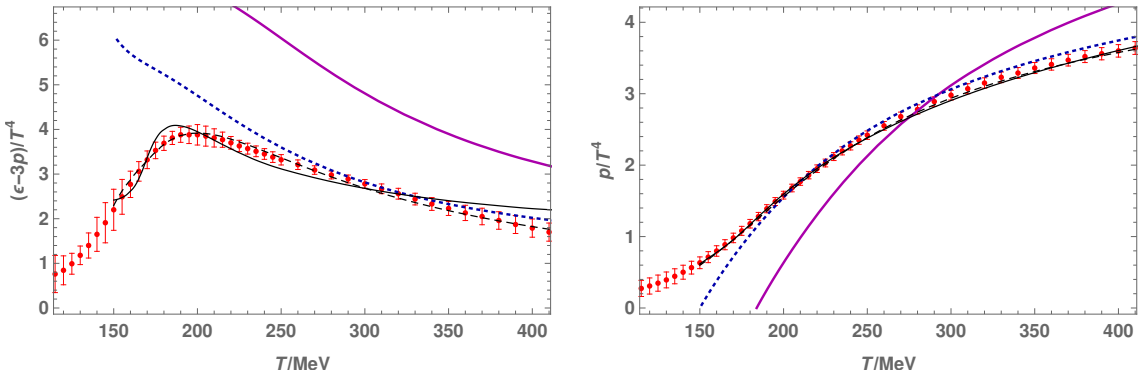

Figure 3.2: Fits to the thermodynamics lattice data [40] of QCD with 2+1 flavors. The thin black solid ($M^3/M_{\rm UV}^3 = 1.5$) and dashed curves ($M^3/M_{\rm UV}^3 = 4$) are direct fits of the effective potential (3.2.22). The dotted blue and solid magenta curves are final fits, with scale parameters M and Λ optimized for thermodynamics and spectrum data, respectively. The fit parameters are given in table 3.5. These two fits have different transition temperature compared with the direct fits of the effective potential; see the text for details.

from [162]. The thermodynamics and glueball masses from this choice were however seen to agree well with lattice data (figure 3.1 and table 3.4).

The parameters of the $V_{f,0}$ potential (the bottom left group) are fitted to the thermodynamic data of figure 3.2 and the parameters of the w potential (the bottom right group) are fitted to the susceptibility in figure 3.3. The remaining parameters of the tachyon potential V_f (top right group) were adjusted to obtain a spectrum that mimics that of QCD, as shown in table 3.6. The parameters of the κ potential (middle right group) were fitted in part to the thermodynamics and in part to the spectrum.

Apart from the parameters fitted to data here, there is a single parameter arising from the CS sector, which was discussed in section 3.1.3. The most general CS term contains four functions $f_i(\tau)$ which are only known at $\tau = 0$ and at $\tau = \infty$. We will use here the functions derived in [138] arising from flat space string theory, up to the parameter b which corresponds to a rescaling of the tachyon field in the CS term. The corresponding expressions for the $f_i(\tau)$ are given in (3.1.36). Our results here turn out to have little dependence on different finite values of this additional parameter; we set $b = 10$ following [174].

We now discuss some additional details of the fit. Figures 3.2 and 3.3, show the final fit to the thermodynamic data, with the values of M and Λ given in the parentheses in table 3.5.

The dotted blue curves in figure 3.2, show the results for the thermodynamic fit to the

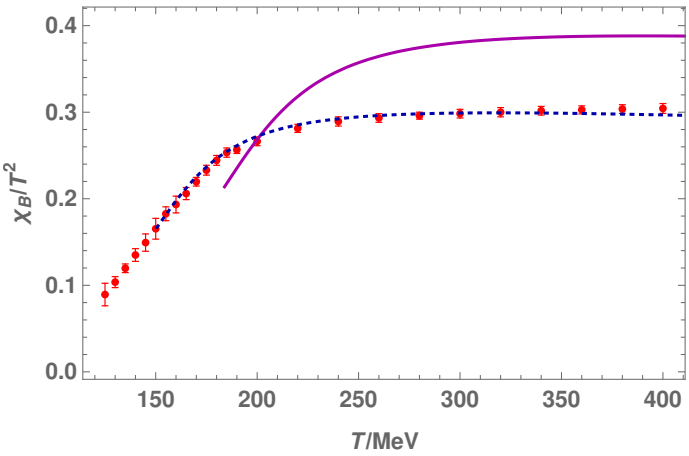

Figure 3.3: Fits to the lattice data (with 2+1 flavors) [205] for the light quark susceptibility of QCD. The dotted blue and solid magenta curves are final fits with scale parameters optimized for thermodynamics and spectrum data, respectively.

equation of state. They differ from the direct fit of V_{eff}, the solid black curve, because the transition temperature was adjusted differently in the final fit, in order to obtain a better agreement with the experimental meson spectrum. As we pointed out above, the final transition temperature is determined, apart from the effective potential, by the values of $\bar{\kappa}_0$, $\bar{\kappa}_1$ and c_κ in table 3.5.

Finally, the solid magenta curves show the fit for the values of M and Λ that reproduce the values of f_π and the ρ mass, i.e., the values in table 3.5 which are not in parentheses. Their difference to the dashed blue curves therefore demonstrates the remaining tension between the fits to thermodynamic and spectrum data. Because we are interested in baryons in the zero temperature vacuum state in this work, we chose to use this latter fit in the analysis of the properties of the baryon solution in the rest of this section.

Notice that we only fit the lattice data above the QCD crossover, and in the deconfined phase of the holographic model, where the phases are separated by a first order phase transition. The phase transition in the model, is at the same time a deconfining transition as well as a chiral restoration transition. Since we are in the massless quark case this is in agreement with universality arguments, [163]. It is possible to obtain higher order phase transitions by tuning the potentials [207], but such tuning would contradict the other constraints we have set, in particular the requirement of linear radial glueball trajectories. However, it is expected that stringy loop corrections, which map to the pressure of pions and other light hadrons on the QCD side, can make the transition continuous also in the current setup for the holographic model [163]. Such corrections are neglected in the holographic model, but may be added as in the second reference in [163]. After the holographic

Quantity	Model	Experiment [206]
f_π	92 MeV*	92 MeV
m_ρ	775 MeV*	775 MeV
m_{ρ^*}	886 MeV	1465 ± 25 MeV
m_{a_1}	1240 MeV	1230 ± 40 MeV
m_{π^*}	1260 MeV	1300 ± 100 MeV
m_{a_0}	639 MeV	–

Table 3.6: Fitted low lying (flavor nonsinglet) meson masses and the pion decay constant. The values of the scale parameters M and Λ were chosen such that the values of f_π and m_ρ, marked with asterisks, match exactly the experimental values.

model has been fitted to lattice data, even simple hadron resonance gas models for the confined phase equation of state match almost continuously with the model in the deconfined phase [208].

Regarding the meson spectrum, we compare in table 3.6 the masses of the flavor nonsinglet mesons (i.e. the fluctuation modes with vanishing trace in flavor space) to the experimental values of isospin $I = 1$ mesons from the particle data group tables [206]. We also include the pion decay constant, and its value is used together with the ρ meson mass to determine the final values of M and Λ, as mentioned above.

Of the remaining mesons, the mass of the lowest axial vector and the mass of the first pion excitation agree very well with the experimental values. The mass of the excitation of the ρ meson is however too low. As it turns out, requiring the scalar mass to be high with respect to the ρ mass leads to a situation where excited states in all sectors are rather close to the ground states. One should however also notice that the state in QCD that we are comparing is suspected not to be a clean radial excitation of the ρ but to contain a significant hybrid component [206]. This may in part explain the difference in the numbers.

As we remarked above, the mass of the lowest scalar m_{a_0} is low: it is slightly less than m_ρ. We do not attempt to compare this mass directly to the experimental data as the scalar sector in QCD has a rather involved structure with several states that resemble pion and kaon molecules. Nevertheless our result is too low to be identified with any known state in the spectrum. This is perhaps not surprising since similar issues often appear in simple potential quark models. We do note, however, that the model of [156, 157], which is closely related to V-QCD, does produce a significantly heavier flavor non-singlet scalar state. We also remark that we did not try to fit the pion mass as we carried out the fit at zero quark mass. It would be simple to fit the pion mass accurately by turning on a

nonzero quark mass.

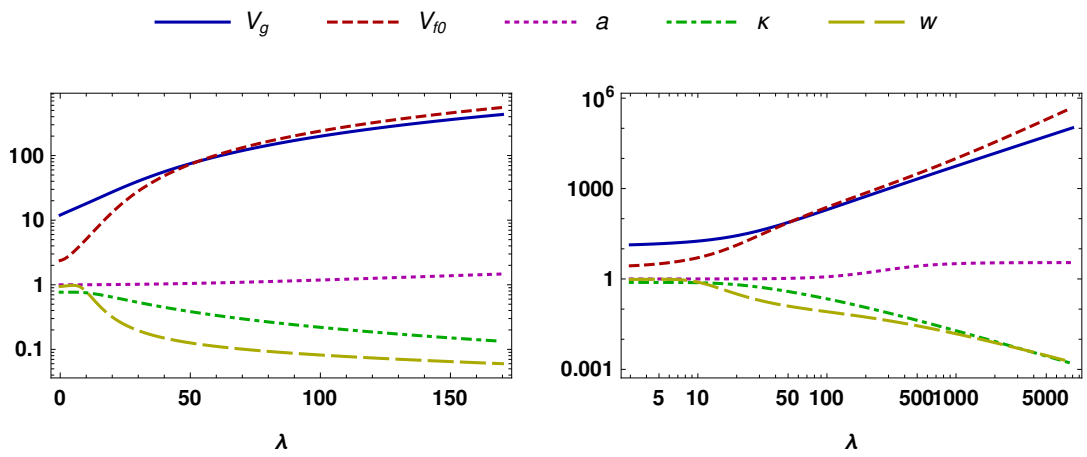

Figure 3.4: Potentials for the choice of parameters given in Table 3.5. Notice that the left (right) plot uses linear (logarithmic) scale for the dilaton λ.

Finally we show the potentials after the fit in figure 3.4. We remark that all the functions are simple, i.e. monotonic functions with no rapid changes in behavior. Notice also that even though we list a high number of parameters in table 3.5, almost all of these parameters only appear through the functional form of the functions shown in these plots. As the asymptotic form of the functions is fixed by comparison of QCD properties independently of the values of the parameters, they only affect the details of the functions in the middle, i.e., for $\lambda/\lambda_0 = \mathcal{O}(1)$. That is, despite the high number of parameters, the details of the model and therefore predictions for the observables are tightly constrained from the beginning, and the fit basically amounts to small tuning of the final results.

3.2.3 The static soliton

Based on the formalism described in the previous section, we discuss here the numerical solution for the bulk instanton dual to a static baryon state at the boundary.

The ansatz that is relevant for the instanton solution was presented in section 3.1.4. We fix the residual U(1) gauge freedom by the Lorenz condition (3.1.107), for which the equations of motion obeyed by the ansatz fields take an elliptic form (see appendix F.1.3). The most general form of the equations of motion including the back-reaction on the tachyon field are listed in appendix F.2. Those are the non-linear differential equations that were solved numerically, with the boundary conditions listed in table 3.2.

3.2.3.1 Probe and back-reacting solutions

As explained in the previous section, we shall consider a baryon whose flavor quantum numbers are a $U(2)$ subgroup of the $U(N_f)$ flavor group. This implies that the flavor action (composed of the DBI and CS actions in (3.2.3)) for the baryon ansatz does not depend on N_f and is of order N_c. On the other hand, the glue action is of order N_c^2. Likewise, the tachyon modulus background contributes a factor N_f more than the baryon fields to the bulk action, which can be seen explicitly from (3.2.27) below. So, at leading order in the Veneziano limit, both the glue sector (metric and dilaton) and the tachyon modulus τ are not affected by the presence of the baryon, and remain identical to the vacuum solution.

We start by computing the numerical baryon solution in this leading order probe regime. In this case, the equations of motion reduce to the form given in appendix F.1.3.

In the Veneziano limit, the back-reaction on the background starts at order $\mathcal{O}(1/N_c)$. At this order, the correction to the glue sector (metric and dilaton) and tachyon modulus τ can be computed by solving the linearized Einstein-dilaton equations sourced by the probe baryon solution, together with the linearized equations for τ. Qualitatively, we do not expect a dramatic effect on the glue sector from the presence of the baryon. Correspondingly, the back-reaction on the glue sector is not expected to affect much the flavor structure of the baryon, which is its most important dynamical property. This motivates the approximation that we consider in the following, where the baryon is assumed to back-react only on the tachyon background. The full equations of motion including the back-reaction on the tachyon are given in appendix F.2.

In summary, we consider two different regimes for the baryon solution, with different treatments of the tachyon modulus:

- The *probe baryon* solution, where the tachyon modulus τ is fixed to its vacuum value. This corresponds to the solution at leading order in the Veneziano expansion. At this order, the chiral condensate profile around the baryon is trivial, but the other flavor properties of the baryon are expected to be qualitatively correct.

- The *back-reacted tachyon* regime, where the equations of motion for τ are solved, with the gauge fields and tachyon phase θ fixed to the probe baryon solution. In the Veneziano limit, this will reproduce the leading order $\mathcal{O}(1/N_f)$ correction to the tachyon background, assuming no back-reaction on the glue sector. In this case, the solution obtained for the tachyon modulus should give a good idea of the qualitative behavior of the chiral condensate in presence of the baryon.

3.2.3.2 Baryon mass

Once the soliton solution is found, several static properties of baryons can be computed [173, 129]. The most elementary of these properties is the nucleon mass. This mass is the

sum of a classical contribution and quantum corrections

$$M_{\rm nucleon} = M_0 + \delta M_Q \,. \tag{3.2.26}$$

The classical contribution is computed from the bulk on-shell action evaluated on the soliton solution. It corresponds to the energy of the soliton, whose expression was presented in section 3.1.5. Here, we reproduce this expression for the purpose of introducing some definitions. In the approximation where the back-reaction on the glue sector is neglected, the soliton mass is given by

$$M_0 = N_c\Big(N_f S_\tau + S_B\Big) - E_{DBI,vac}\,, \tag{3.2.27}$$

where $E_{\rm DBI,vac}$ is the DBI contribution to the vacuum energy

$$E_{DBI,vac} = \int {\rm d}r{\rm d}\xi\, 4\pi\xi^2 \rho_{DBI,vac} \quad , \quad \rho_{DBI,vac} \equiv M^3\sqrt{1+{\rm e}^{-2A}\kappa(\partial_r\tau_0)^2}\, V_f(\lambda,\tau_0){\rm e}^{5A}, \tag{3.2.28}$$

with $\tau_0(r)$ the vacuum profile of the tachyon field. The baryon contribution to the bulk action is split into two pieces

$$S_\tau = \int {\rm d}r{\rm d}\xi\, 4\pi\xi^2\rho_\tau \quad , \quad S_B = \int {\rm d}r{\rm d}\xi\, 4\pi\xi^2\rho_B\,, \tag{3.2.29}$$

$$\rho_\tau \equiv M^3\sqrt{1+{\rm e}^{-2A}\kappa\left((\partial_r\tau)^2+(\partial_\xi\tau)^2\right)}\, V_f(\lambda,\tau){\rm e}^{5A}\,, \tag{3.2.30}$$

$$\begin{aligned}
\rho_B \equiv M^3\sqrt{1+{\rm e}^{-2A}\kappa\left((\partial_r\tau)^2+(\partial_\xi\tau)^2\right)}\, V_f(\lambda,\tau)\,{\rm e}^{A}\times \\
\times\Bigg(\kappa(\lambda)\tau^2\Bigg({\rm e}^{2A}\Delta_{rr}\tilde{A}_r^2+\left(1-{\rm e}^{2A}\Delta_{\xi\xi}\right)\tilde{A}_\xi^2+\frac{(\tilde{\phi}+\tilde{\phi}^*)^2}{2\xi^2}- \\
-2{\rm e}^{2A}\Delta_{\xi r}\tilde{A}_r\tilde{A}_\xi\Bigg)+ \\
+w(\lambda)^2\Bigg(\frac{1}{8}{\rm e}^{2A}\left[\Delta_{rr}\left(1-{\rm e}^{2A}\Delta_{\xi\xi}\right)-{\rm e}^{2A}\Delta_{\xi r}^2\right](F_{\bar{\mu}\bar{\nu}})^2+ \\
+\frac{1}{2\xi^2}\left(\left(1-{\rm e}^{2A}\Delta_{\xi\xi}\right)|{\rm D}_\xi\phi|^2+{\rm e}^{2A}\Delta_{rr}\,|{\rm D}_r\phi|^2\right)+ \\
+\frac{\left(1-|\phi|^2\right)^2}{4\xi^4}-\frac{1}{2\xi^2}{\rm e}^{2A}\Delta_{\xi r}(D_r\phi^*D_\xi\phi+h.c.)- \\
-\Big({\rm e}^{2A}\Delta_{rr}(\partial_r\Phi)^2+\left(1-{\rm e}^{2A}\Delta_{\xi\xi}\right)(\partial_\xi\Phi)^2- \\
-2{\rm e}^{2A}\Delta_{\xi r}\partial_\xi\Phi\partial_r\Phi\Big)\Bigg)\Bigg)+
\end{aligned}$$

$$+\frac{1}{\pi^2\xi^2}\epsilon^{\bar{\mu}\bar{\nu}}\partial_{\bar{\mu}}\Phi\times$$
$$\times\left[(f_1(\tau)+f_3(\tau))\left(\tilde{A}_{\bar{\nu}}+\frac{1}{2}(-i\phi^*D_{\bar{\nu}}\phi+h.c.)+\frac{1}{4i}\partial_{\bar{\nu}}(\tilde{\phi}^2-(\tilde{\phi}^*)^2)\right)+\right.$$
$$\left.+\frac{1}{2}(3if_2(\tau)-f_1(\tau)-f_3(\tau))(\tilde{\phi}+\tilde{\phi}^*)^2\tilde{A}_{\bar{\nu}}\right]. \tag{3.2.31}$$

The covariant quantities $F_{\bar{\mu}\bar{\nu}}$ and $D_{\bar{\mu}}\phi$ are defined in Appendix A.5 and the symbol $\Delta_{\bar{\mu}\bar{\nu}}$ in (F.53)-(F.55). The $f_i(\tau)$ are the Chern-Simons potentials, whose expressions are given in (3.1.36). Note that, as far as flavor fields are concerned, S_τ depends only on the tachyon modulus τ, whereas S_B contains the dependence on the baryon fields. In particular, in the leading order probe baryon regime, only S_B contributes to M_0. The total bulk Lagrangian density will be denoted by ρ_M

$$\rho_M \equiv N_c(N_f\rho_\tau+\rho_B)-\rho_{DBI,vac}\,. \tag{3.2.32}$$

As discussed in section 3.1.6, computing the quantum corrections δM_Q is a difficult problem that goes beyond the scope of this work. Another comment is that we considered here the mass of the nucleon, but the experimental spectrum of baryons also contains many excited states, such as the isobar Δ. The calculation of the spin dependence of the baryon mass spectrum is the subject of section 3.2.4.

3.2.3.3 Numerical results

We present in this subsection the numerical solution for the static baryon configuration. The equations of motion written in appendix F are solved with the gradient descent method[31], imposing the boundary conditions of table 3.2. The same kind of method was used in [195, 178] to compute baryon solutions in other holographic models. We focus here on the results and give more details about the numerical method in appendix H. We start by presenting the leading order probe baryon solution and then discuss the back-reaction. We recall that the back-reacting solution is computed assuming no back-reaction on the color sector (metric and dilaton).

Probe baryon solution

We start with the numerical results obtained for the probe baryon solution. In this case the modulus of the tachyon field τ is fixed to its background value, and the equations of motion take the form presented in appendix F.1.3.

The instanton number and bulk Lagrangian density in the (ξ, r)-plane are presented in figure 3.5, where all dimensionful quantities are expressed in units of the classical soliton

[31]The name heat diffusion method also appears in the literature.

mass (3.2.27). The bulk Lagrangian density is given by (3.2.32) , whereas the expression for the instanton number density can be obtained by dividing equation (3.1.99) by $4\pi\xi^2$

$$\rho_{N_i} \equiv \frac{1}{8\pi^2\xi^2}\epsilon^{\bar{\mu}\bar{\nu}}\Big[F_{\bar{\mu}\bar{\nu}} + \partial_{\bar{\mu}}\big(-i\phi^* D_{\bar{\nu}}\phi + h.c.\big)\Big]\,. \tag{3.2.33}$$

Figure 3.5 shows the expected behavior for a solitonic configuration, that is the densities are confined to a region of finite extent in the bulk. The size of this lump in the ξ direction gives an estimate of the baryon size, which is of the order of M_0^{-1}. The numerical value for the classical soliton mass M_0 is obtained by integrating the Lagrangian density in Figure 3.5

$$M_0 \simeq \frac{N_c}{3} \times 1150\,\mathrm{MeV}\,. \tag{3.2.34}$$

This number is expected to give the leading contribution to the nucleon mass in the V-QCD model with the parameters of Table 3.5. As discussed above, the full result for the nucleon mass also receives quantum corrections (3.1.101) whose evaluation is an unsolved problem.

In Figure 3.6, we also plot the profile at the boundary ($r = 0$) for the non-abelian phase θ of the tachyon field (3.1.64). As stated above, the pion matrix in the boundary theory (3.1.69) reproduces[32] the skyrmion hedgehog ansatz, and the associated skyrmion number is equal to the baryon number. Figure 3.6 should therefore be compared with the corresponding plot of the pion field in the Skyrme model skyrmion solution in the chiral limit [176]. This plot is reproduced[33] in Figure 3.6. It makes it clear that the shape of the boundary skyrmion is close to that of the Skyrme model. Note, in particular, that the asymptotic behavior is the same:

$$\theta(0,\xi) \underset{\xi\to 0}{\sim} \xi \quad , \quad \theta(0,\xi) - \pi \underset{\xi\to\infty}{\sim} \frac{1}{\xi}\,. \tag{3.2.35}$$

This can be seen from the asymptotic analysis in appendix G.

Back-reacted tachyon

We now discuss the numerical results obtained when taking into account the back-reaction on the tachyon field. In this case, the gauge fields and tachyon phase θ are fixed to the probe baryon solution, and the equation of motion for the tachyon modulus τ is solved on this background. The corresponding equation of motion for τ is written in appendix F.2.

[32] This comparison is well defined even though the phase θ transforms under the residual $U(1)$ gauge freedom: the boundary gauge transformations of U_P match exactly those of the pion matrix in the Skyrme model, and the gauge is fixed in both cases by requiring the absence of sources for the gauge fields.

[33] Notice that θ goes from 0 to π, instead of π to 0 for the skyrmion, because the boundary value of the tachyon field is the conjugate of the pion matrix (3.1.69). So it is actually $\pi - F_{\mathrm{skyrmion}}$ that is plotted in Figure 3.6.

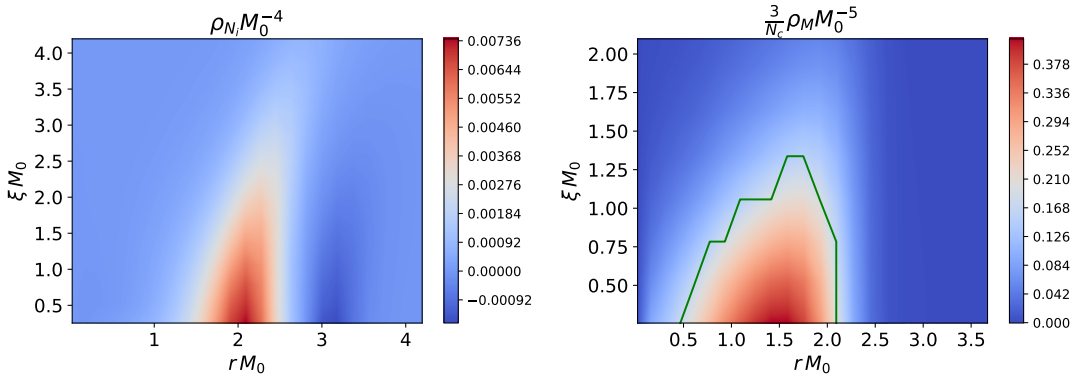

Figure 3.5: Instanton number (3.2.33) (left) and bulk Lagrangian (3.2.32) (right) density for the static soliton solution in the probe baryon regime. All quantities are expressed in units of the classical mass of the soliton (3.2.27). The center of the soliton is located at $\xi = 0$ where the density diverges as ξ^{-1}. The UV boundary is located at $r = 0$. The green line in the right plot indicates the boundary of the region over which the mean value is computed to define the relative difference in Figure 3.8.

For a back-reacted tachyon, the chiral condensate profile around the baryon can be computed from the near-boundary behavior of the tachyon modulus

$$\tau(r,\xi) \underset{r\to 0}{\sim} \Sigma(\xi)\, r^3\,, \tag{3.2.36}$$

where Σ is proportional to the modulus of the chiral condensate $\left|\langle\bar{\psi}\psi\rangle\right|$. The relative difference of $\Sigma(\xi)$ with the vacuum value $\Sigma(\infty)$ is plotted in Figure 3.7. This shows the expected behavior, where the chiral symmetry tends to be restored inside the baryon. Note that the result that is shown is valid in the limit of large N_c and large N_f. There is a priori no guarantee for it to be a quantitatively accurate approximation when a small number of flavors (for example $N_f = 2$ or 3) is substituted in the leading large N_f result. So, at small N_f and N_c, Figure 3.7 should not be considered as more than an indication of the qualitative behavior of the chiral condensate in presence of the baryon.

Another interesting information that can be extracted from this back-reacted tachyon solution, is the effect of the back-reaction on the soliton mass (3.2.27). The leading order correction to the on-shell Lagrangian density due to the back-reaction on τ can be expressed as

$$N_c^{-1}\delta\rho_M = \frac{1}{2}N_f\delta\tau^2\frac{\delta^2 S_\tau}{\delta\tau^2}\bigg|_{\text{probe}} + \delta\tau\frac{\delta S_B}{\delta\tau}\bigg|_{\text{probe}} + \mathcal{O}\big(N_f^{-2}\big)\,, \tag{3.2.37}$$

where $\delta\tau$ refers to the order $\mathcal{O}\big(N_f^{-1}\big)$ correction to τ, and S_τ and S_B are defined in (3.2.29).

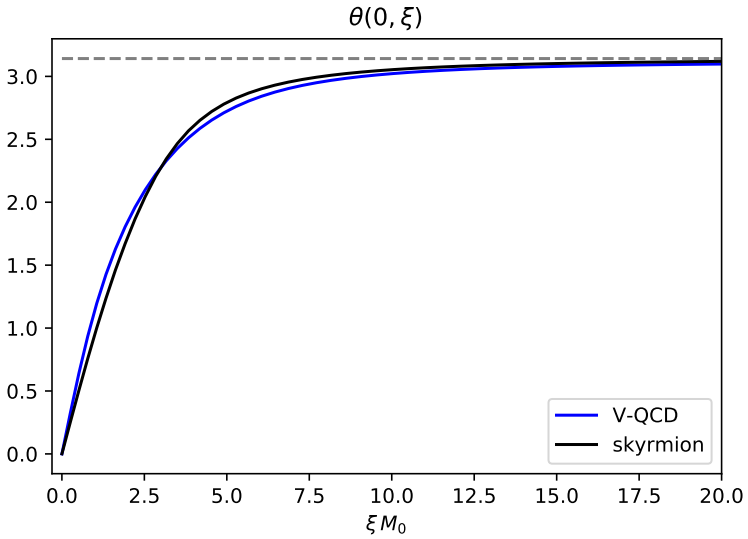

Figure 3.6: Radial profile of the non-abelian phase of the tachyon field (3.1.64) at the UV boundary (blue line). The dashed gray line indicates the asymptotic value π. For comparison, we also plotted in black the profile for the pion fields in the skyrmion solution of the Skyrme model. The parameters of the Skyrme model were chosen such that f_π and the soliton mass are equal to those of the V-QCD model, with the parameters of Table 3.5.

Note that we dropped the terms that vanish on-shell

$$\left.\frac{\delta S_\tau}{\delta\tau}\right|_{\text{probe}} = \left.\frac{\delta S_B}{\delta\varphi_B}\right|_{\text{probe}} = 0 \quad , \quad \varphi_B \in \{\Phi, \phi, A_{\bar{\mu}}, \theta\}\,. \tag{3.2.38}$$

Equation (3.2.37) can be simplified by using the back-reacted equations of motion for the tachyon modulus

$$\left.\frac{\delta(N_f S_\tau + S_B)}{\delta\tau}\right|_{\text{back-react}} = 0\,, \tag{3.2.39}$$

which, at leading order in N_f, implies that

$$\left.\frac{\delta S_B}{\delta\tau}\right|_{\text{probe}} + N_f\delta\tau\left.\frac{\delta^2 S_\tau}{\delta\tau^2}\right|_{\text{probe}} = \mathcal{O}\big(N_f^{-1}\big)\,, \tag{3.2.40}$$

and finally

$$N_c^{-1}\delta\rho_M = -\frac{1}{2}N_f\delta\tau^2\left.\frac{\delta^2 S_\tau}{\delta\tau^2}\right|_{\text{probe}} + \mathcal{O}\big(N_f^{-2}\big)\,. \tag{3.2.41}$$

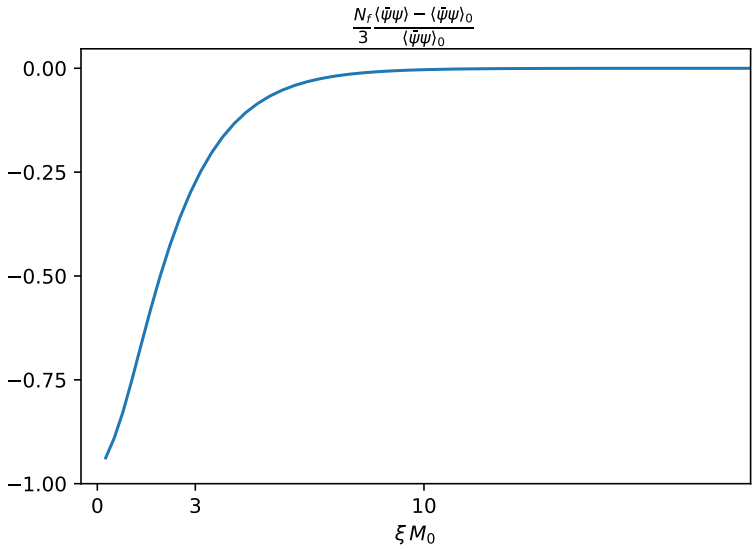

Figure 3.7: Chiral condensate profile around the static soliton solution in the back-reacted tachyon regime, where the baryon center is at $\xi = 0$. The plotted quantity is the relative difference between the modulus of the chiral condensate and the chiral condensate in vacuum. In the Veneziano limit $N_c, N_f \to \infty$, the difference is of order $\mathcal{O}(1/N_f)$, so that it has to be multiplied by N_f in order to obtain a finite result. We also divide by 3, which means that what the figure shows is the large N_f result, where the value $N_f = 3$ is substituted for the number of flavors. As discussed in the text, there is no reason for this result to be quantitatively accurate for $N_f = 3$, but it gives an indication of the qualitative behavior.

Although the correction to the mass (3.2.41) is suppressed by a factor $\mathcal{O}(1/N_f)$ in the Veneziano limit, it can be sizeable when a realistic value is substituted for N_f. Figure 3.8 shows the relative difference between the bulk Lagrangian density for the back-reacted solution and the probe baryon solution, when setting $N_f = 3$ in the leading large N result. As for the chiral condensate, there is no reason for the result to be quantitatively accurate at $N_f = 3$, but it gives an indication of the qualitative behavior.

We should also emphasize that the definition of the relative difference which is shown in Figure 3.8 is not the standard one, where the difference of the two quantities that are compared is divided by the quantity of reference (as in (3.2.45) for instance). The usual definition of the relative difference is not appropriate to compare the densities over the (ξ, r) plane, since the place where the densities go to zero is not exactly the same for the probe and back-reacted solutions. Instead, we define the relative difference by dividing the

difference of the two densities by a reference value $\bar{\rho}_M$

$$\Delta_{\rm rel}\rho_M \equiv \frac{\rho_{M,\text{back-reacted}} - \rho_{M,\text{probe}}}{\bar{\rho}_M} \,. \tag{3.2.42}$$

$\bar{\rho}_M$ is defined as the mean value of the probe density over the region of the bulk where most of the density is contained. To be more precise, the criterion that we used to define the relevant region is given by

$$\frac{3}{N_c}\rho_M \geq 0.7 M_0^4 \,, \tag{3.2.43}$$

whose boundary is shown by the green line in the right of Figure 3.5. In practice, the mean value is then computed numerically by averaging over the cells contained in the given region, denoted $\mathcal{A}$ here

$$\bar{\rho}_M = \frac{1}{N_{\rm cells}} \sum_{i\in\mathcal{A}} \rho_M(i) \,, \tag{3.2.44}$$

where $N_{\rm cells}$ is the number of grid cells contained in $\mathcal{A}$.

Figure 3.8 indicates that there is a region near the UV boundary where the back-reacted Lagrangian density decreases with respect to the probe solution. This is understood easily as coming from the decrease of the tachyon modulus in presence of the baryon, which is dual to the decrease of the chiral condensate observed in Figure 3.7. Another noticeable feature of Figure 3.8 is the shift of the baryon Lagrangian density towards the IR. This can be understood as another consequence of the partial chiral restoration at the baryon center. Indeed, the interaction of the baryon with the tachyon modulus results in a repulsive force from the IR. So a decrease of the tachyon modulus weakens this force, and implies the observed shift towards the IR.

Even at small values of N_f, the relative difference between the probe and back-reacted solutions is observed to be relatively small numerically, of the order of a few 10%. This is also the case at the level of the soliton masses

$$\frac{N_f}{3}\frac{M_{0,\text{back-reacted}} - M_{0,\text{probe}}}{M_{0,\text{probe}}} \simeq -10\% \,. \tag{3.2.45}$$

Here again, the number in (3.2.45) is the leading large N_f result, that cannot precisely be trusted for small N_f and should be considered as indicative.

3.2.4 Quantization of the isospin collective modes

The baryon states of equal half-integer spin and isospin are found by quantizing the soliton collective coordinates (or zero modes) around the static solution [176]. These modes are

- The spatial position of the soliton $\vec{X} = (X^1, X^2, X^3)$.

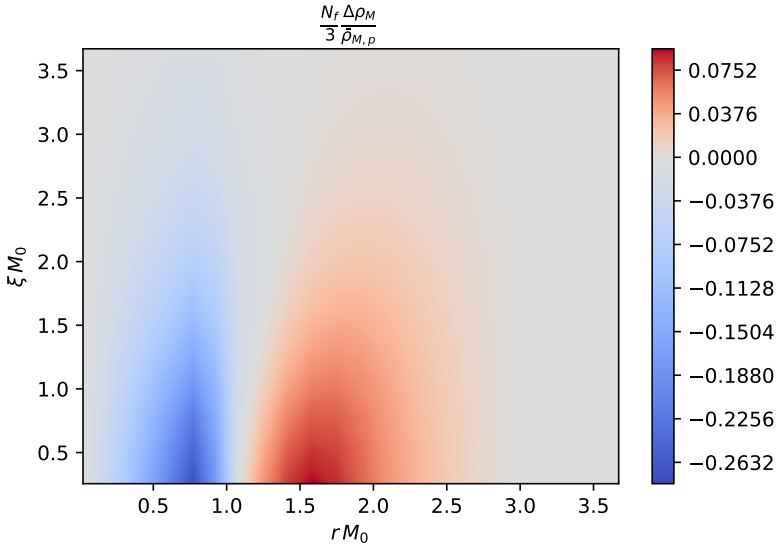

Figure 3.8: Relative difference of bulk Lagrangian density for the static soliton solution in the probe baryon and the back-reacted tachyon regime. The relative difference is defined as the difference of the two densities divided by the mean value of the probe density (3.2.44). The mean value is taken over the area delimited by the green line in the right of Figure 3.5, which is the region where the density is substantially different from zero. The ratio is multiplied by N_f in order to obtain something finite in the Veneziano limit. The UV boundary is located at $r = 0$ and the baryon center at $\xi = 0$.

- The isospin orientation of the soliton, encoded in an $SU(N_f)_V$ matrix[34] V.

The baryon solution can be deformed in many ways in addition to these modes, such as changing the position of the soliton in the holographic direction, or the size of the soliton [128]. Quantizing such modes leads to a tower of excited baryon states in each spin sector. In the following, we focus on the lowest states of these towers and consider only the quantization of the zero modes.

There is no guarantee in principle that the rotation modes can be studied as those of a rigid rotor, independently from the dilation mode of the soliton. In [128], it was actually found that the geometry of the collective modes manifold for dilation and isospin rotation

[34]The relevant collective coordinates are actually only a subgroup of the isospin group $SU(N_f)_V$. For instance, for $N_f = 2$ they are the elements of $SU(2)_V/\mathbb{Z}_2$ and for $N_f = 3$, the elements of $SU(3)_V/U(1)_Y$, where $U(1)_Y$ refers to the strong hypercharge subgroup.

had to be such that the modes are rather quantized as a 4D harmonic oscillator, with energy levels given by equation (5.24) in this reference. The rigid rotor is a good approximation to the harmonic oscillator only when its fundamental frequency is very large compared with its inverse moment of inertia. In QCD, this condition is fulfilled in the large N_c limit. This property is reproduced in the holographic QCD model of [128], as is manifest from the large N_c limit of the energy levels, equation (5.31) in [128]. Their equation (5.24) also indicates that the rigid rotor (large N_c) approximation is better for lower spins. In the following, we assume that the rotation modes can be treated as those of a rigid rotor. According to the previous discussion, once we set the number of colors to its physical value $N_c = 3$, this should not induce too large errors for the low spin modes that exist in real QCD ($s = 1/2$ and $3/2$). Note that the same rigid rotor approximation was considered in the context of the hard wall model [177] .

The spatial position of the baryon is actually irrelevant to the study of baryon states, so it will be kept fixed at $\vec{X} = 0$. We are therefore left with the problem of quantizing the isospin rotation mode of the soliton. To do so, we consider a configuration where the soliton isospin orientation $V(t)$ evolves with time, but sufficiently slowly to be approximated by the ansatz

$$\mathbf{L}(t) = V(t)\mathbf{L}^{(\mathrm{sol})}(r,\xi)\,V(t)^\dagger - i\mathrm{d}V(t)V(t)^\dagger\,, \tag{3.2.46}$$

$$\mathbf{R}(t) = V(t)\mathbf{R}^{(\mathrm{sol})}(r,\xi)\,V(t)^\dagger - i\mathrm{d}V(t)V(t)^\dagger\,, \tag{3.2.47}$$

$$T(t) = V(t)T^{(\mathrm{sol})}(r,\xi)\,V(t)^\dagger\,, \tag{3.2.48}$$

where the superscript (sol) refers to the field evaluated in the static soliton solution. $V(t)$ is parametrized as

$$V(t) \equiv \exp\left(it\,\omega^a\lambda^a\right), \tag{3.2.49}$$

the λ^a's being the generators of $SU(N_f)$, and the angular velocity is identified to be

$$\omega^a\lambda^a = -iV(t)^\dagger\frac{\mathrm{d}V(t)}{\mathrm{d}t}\,. \tag{3.2.50}$$

We assume that the rotation is stationary

$$\frac{\mathrm{d}\omega^a}{\mathrm{d}t} = 0\,, \tag{3.2.51}$$

and slow, so that ω can be treated as a perturbation on top of the static soliton background. Also, *from now on we restrict to the case of* $N_f = 2$. This means that we shall quantize only a subset of the full isospin rotations. Specifically, we restrict to $V(t) \in SU(2)_V$, in the same subgroup as the baryon solution.

The starting point for the quantization of the isospin rotation modes is the classical Lagrangian that controls their dynamics. The latter is obtained in the next section by

substituting the slowly rotating ansatz (3.2.46)-(3.2.48) into the bulk action (3.2.3) and evaluating it on-shell for the slowly rotating soliton solution

$$L_{\rm rot} = -M_0 + \frac{1}{2}\lambda\vec{\omega}^2\,, \tag{3.2.52}$$

where M_0 is the mass of the static soliton and λ its moment of inertia. The classical Hamiltonian is then computed, and quantized in the canonical way described in Appendix K. As a result, the eigenstates of the Hamiltonian are shown to have same spin and isospin and its eigenvalues are given by

$$E_s = M_0 + \frac{1}{2\lambda}s(s+1)\,, \tag{3.2.53}$$

where s refers to the spin. In particular, the nucleon states correspond to $s = 1/2$ and the isobar Δ to $s = 3/2$.

3.2.5 The rotating soliton

This section is dedicated to the calculation of the rotating soliton solution, from which can be computed the moment of inertia λ that controls the splitting of the baryon energy levels (3.2.53). We start by determining the ansatz relevant to the solution, before deriving the equations of motion for the fields of the ansatz as well as the boundary conditions they should obey. We finally describe the numerical solution for the rotating solution. We work with a slowly rotating soliton, at first order in the rotation velocity ω. Also, we recall that we only consider the quantization of the subsector of the chiral group that contains the 2 flavors of the soliton solution.

3.2.5.1 Ansatz for the rotating instanton

Substituting the naive ansatz (3.2.46)-(3.2.48) with $V(t) \in SU(2)$ into the equations of motion, reveals that this ansatz in itself cannot solve the time-dependent equations of motion. The reason is that the components $(L/R)^a_0$ and $(L^{\rm T}/R^{\rm T})_{r,i}$ in (3.1.45) are turned on at linear order in ω [177], as is the abelian phase of the tachyon ($\det T - 1$). Accordingly, the ansatz (3.2.46) for the gauge fields should be supplemented by

$$L_0(t) = V(t)L_0^{(\rm rot)}(r,\xi;\vec{\omega})\,V(t)^\dagger - i\partial_0 V(t)V(t)^\dagger\,, \tag{3.2.54}$$

$$L^{\rm T}_{r,i}(t) = L^{{\rm T},({\rm rot})}_{r,i}(r,\xi;\vec{\omega})\,, \tag{3.2.55}$$

and likewise for the right-handed fields. Also, the ansatz for the tachyon field (3.2.48) should be modified to

$$T(t) = V(t)T^{(\rm rot)}(r,\xi;\vec{\omega})V(t)^\dagger\,, \tag{3.2.56}$$

where $\mathbf{L}^{(\rm rot)}$ and $(\det T^{(\rm rot)} - 1)$ start at linear order in ω.

To determine relevant ansätze for $\mathbf{L}^{(\mathrm{rot})}$ and $T^{(\mathrm{rot})}$, we proceed as in the case of the static soliton and impose the maximal number of symmetries of the bulk action. In the rotating case, this includes the cylindrical symmetry and parity. For $N_f = 2$ flavors, the cylindrical symmetry of the static soliton solution (3.1.50)-(3.1.52) implies that a constant isospin rotation of the soliton is equivalent to a constant spatial rotation. So the soliton rotating in isospin space can be seen as rotating instead in physical space, with angular momentum $\vec{\omega}$. In particular, $\vec{\omega}$ transforms as a pseudo-vector in 3-dimensional space[35]. At linear order in $\vec{\omega}$, the cylindrically symmetric ansatz for the gauge fields of the rotating soliton is then [175, 177]

$$(L/R)_i = V(t)(L/R)_i^{(\mathrm{sol})}V(t)^\dagger \quad , \quad (L/R)_r = V(t)(L/R)_r^{(\mathrm{sol})}V(t)^\dagger \,, \tag{3.2.57}$$
$$(L/R)_0^{\mathrm{T}} = (L/R)_0^{\mathrm{T},(\mathrm{sol})} \,,$$

$$(L/R)_0 = V(t)\Bigg(\omega_b\left[\chi_1^{(L/R)}(r,\xi)\epsilon^{abc}\frac{x^c}{\xi} + \chi_2^{(L/R)}(r,\xi)\left(\frac{x^a x^b}{\xi^2} - \delta^{ab}\right)\right] + \tag{3.2.58}$$
$$+ \frac{v^{(L/R)}(r,\xi)}{\xi^2}(\vec{\omega}.\vec{x})x^a \ + \omega^a\Bigg)\frac{\sigma^a}{2}V(t)^\dagger \,,$$

$$(L/R)_i^{\mathrm{T}} = \frac{\rho^{(L/R)}(r,\xi)}{\xi}\left(\omega_i - (\vec{\omega}\cdot\vec{x})\frac{x_i}{\xi^2}\right) + B_\xi^{(L/R)}(r,\xi)(\vec{\omega}\cdot\vec{x})\frac{x_i}{\xi^2} + Q^{(L/R)}(r,\xi)\epsilon_{ibc}\omega^b\frac{x^c}{\xi}, \tag{3.2.59}$$

$$(L/R)_r^{\mathrm{T}} = B_r^{(L/R)}(r,\xi)\frac{\vec{\omega}\cdot\vec{x}}{\xi} \,, \tag{3.2.60}$$

where the superscript (sol) refers to the field in the static soliton configuration[36], and we introduced the new 2-dimensional fields

$$\chi_{1,2}^{(L/R)} \quad , \quad v^{(L/R)} \quad , \quad \rho^{(L/R)} \quad , \quad B_{\bar{\mu}}^{(L/R)} \quad , \quad Q^{(L/R)} \,. \tag{3.2.61}$$

Imposing symmetry under the parity transformation (the full transformation $P = P_1 \cdot P_2$ in terms of the definitions in Appendix A)

$$P: \quad \vec{x} \to -\vec{x} \quad , \quad L \leftrightarrow R \quad , \quad \vec{\omega} \to \vec{\omega} \,, \tag{3.2.62}$$

[35]Strictly speaking, $\vec{\omega}$ is a definite 3-dimensional vector, and the rotation breaks the cylindrical symmetry. However, as is standard for broken symmetries, the appropriate ansatz can be derived by assuming that $\vec{\omega}$ transforms as a pseudo-vector (in that case, $\vec{\omega}$ is regarded as a field, called a spurion).

[36]At order $\mathcal{O}(\omega^2)$, the static fields will receive corrections from the rotation. These could in principle contribute to the moment of inertia in (3.2.74). It is not the case because the static fields sit at a saddle point of the static action. The leading contribution to the Lagrangian (3.2.74) from the $\mathcal{O}(\omega^2)$ correction to the static fields therefore starts at order $\mathcal{O}(\omega^4)$, corresponding to an $\mathcal{O}(\omega^2)$ correction to the moment of inertia.

relates the right-handed and left-handed fields as

$$\begin{aligned}
\chi_1 \equiv \chi_1^L = -\chi_1^R \quad , \quad \chi_2 \equiv \chi_2^L = \chi_2^R \,, \\
v \equiv v^L = v^R \,, \\
\rho \equiv \rho^L = -\rho^R \,, \\
B_{\bar{\mu}} \equiv B_{\bar{\mu}}^L = -B_{\bar{\mu}}^R \,, \\
Q \equiv Q^L = Q^R \,.
\end{aligned} \tag{3.2.63}$$

For the tachyon field, the ansatz that has the right transformation properties under 3-dimensional rotations and parity takes the form

$$T = V(t) \exp\left(i\zeta(r,\xi) \frac{\vec{\omega}\cdot\vec{x}}{\xi} \right) T^{(sol)} V(t)^\dagger \quad , \quad \zeta(r,\xi) \in \mathbb{R} \,. \tag{3.2.64}$$

The ansatz thus defined is invariant under a $U(1)_s \times U(1)_r$ residual gauge freedom, where the first factor was already present in the static case (3.1.60), as denoted by the subscript "s", and the second factor appears in the rotating solution, as denoted by the subscript "r". This new factor is an axial $U(1)$ gauge freedom that is a subgroup of the chiral $U(1)_A$

$$\hat{g}_L = \hat{g}_R^\dagger = \exp\left(i\beta(r,\xi) \frac{\vec{\omega}\cdot\vec{x}}{\xi} \right) , \tag{3.2.65}$$

under which only $B_{\bar{\mu}}$, ρ and ζ transform, with transformation rules

$$B_{\bar{\mu}} \to B_{\bar{\mu}} + \partial_{\bar{\mu}}\beta \quad , \quad \rho \to \rho + \beta \quad , \quad \zeta \to \zeta - 2\beta \,. \tag{3.2.66}$$

Also, the complex scalar field

$$\chi \equiv \chi_1 + i\chi_2 \,, \tag{3.2.67}$$

transforms as a charge 1 complex scalar field under $U(1)_s$ in (3.1.60).

In the case of a rotating soliton, one should in principle consider the coupling to the holographic axion $\mathfrak{A}$, dual to the boundary Yang-Mills instanton density operator $\mathrm{Tr}\,(G \wedge G)$ [145, 161, 166]. This coupling appears because of the additional residual $U(1)_A$ gauge freedom (3.2.65), which turns on the abelian phase of the tachyon ζ and the axial part of the abelian gauge field $B_{\bar{\mu}}$ and ρ. However, as for the other color fields, the action of the baryon on the axion is suppressed by a factor $\mathcal{O}\big(N_c^{-1}\big)$ in the large N_c limit. The rotating baryon solution will therefore decouple from the axion field at leading order in N_c. At next-to-leading order, the axion will contribute to the order $\mathcal{O}\big(N_c^{-1}\big)$ correction to the moment of inertia[37]. In the following, we consider the same approximation as in the static

[37] The g_{0i} component of the metric will also be turned on by rotation, and contribute at order $\mathcal{O}\big(N_c^{-1}\big)$

case and ignore the action on the color sector. This implies in particular that we set the axion to 0.

As in the case of the static soliton, there exists a redefinition of the ansatz fields such that the tachyon phases θ and ζ are absorbed into the gauge fields

$$\tilde{\chi} \equiv \mathrm{e}^{i\theta}\chi \quad , \quad \tilde{B}_{\bar{\mu}} \equiv B_{\bar{\mu}} + \frac{1}{2}\partial_{\bar{\mu}}\zeta \quad , \quad \tilde{\rho} \equiv \rho + \frac{1}{2}\zeta \,. \tag{3.2.68}$$

The resulting fields are invariant under the residual gauge freedom (3.1.60) and (3.2.65). In addition to this field redefinition, for later use it is also convenient to define the field strength for the $B_{\bar{\mu}}$ gauge field

$$B_{\bar{\mu}\bar{\nu}} \equiv \partial_{\bar{\mu}} B_{\bar{\nu}} - \partial_{\bar{\nu}} B_{\bar{\mu}} \,, \tag{3.2.69}$$

and the covariant derivative for the ρ and χ field

$$D_{\bar{\mu}}\rho = \partial_{\bar{\mu}}\rho - B_{\bar{\mu}} \quad , \quad D_{\bar{\mu}}\chi = (\partial_{\bar{\mu}} - iA_{\bar{\mu}})\chi \,. \tag{3.2.70}$$

Lorenz gauge

Because we obtain the static soliton solution by fixing the residual gauge freedom (3.1.60) to the Lorenz gauge

$$\partial_r A_r + \partial_\xi A_\xi = 0 \,, \tag{3.2.71}$$

we work in the same gauge for the rotating soliton. Also, we fix the additional gauge freedom (3.2.65) by imposing a similar Lorenz condition for $B_{\bar{\mu}}$

$$\partial_r B_r + \partial_\xi B_\xi = 0 \,. \tag{3.2.72}$$

For this choice, the equations of motion for $B_{\bar{\mu}}$ (J.8) and (J.9) are elliptic and can be solved numerically by a heat diffusion method upon setting the right boundary conditions.

Note that the Lorenz condition (3.2.72) leaves a residual gauge freedom of the form

$$B_{\bar{\mu}} \to B_{\bar{\mu}} + \partial_{\bar{\mu}}\mathfrak{f} \quad , \quad \partial_r^2\mathfrak{f} + \partial_\xi^2\mathfrak{f} = 0 \quad , \quad \mathfrak{f}(0,\xi) = 0 \,. \tag{3.2.73}$$

Part of the choice of boundary conditions will correspond to the choice of residual gauge freedom (3.2.73). The explicit choice that we make is discussed below, in Section 3.2.5.3.

3.2.5.2 Moment of inertia and equations of motion

The Lagrangian for the rotational collective modes of the soliton is obtained by substituting the ansatz (3.2.57)-(3.2.60) and (3.2.64) into the bulk action (3.2.3). This yields the Lagrangian of a rigid rotor

$$L_{rot} = -M_0 + \frac{1}{2}\lambda\vec{\omega}^2 \,, \tag{3.2.74}$$

where M_0 is the mass of the static soliton (3.2.27), and we defined the moment of inertia

$$\lambda \equiv \lambda_{DBI} + \lambda_{CS}\,, \tag{3.2.75}$$

$$\lambda_{DBI} = \int \mathrm{d}r\mathrm{d}\xi\, 4\pi\xi^2 \rho_{\lambda,DBI} \quad , \quad \lambda_{CS} = \int \mathrm{d}r\mathrm{d}\xi\, 4\pi\xi^2 \rho_{\lambda,CS}\,, \tag{3.2.76}$$

$$\begin{aligned}
\rho_{\lambda,DBI} \equiv -\frac{2}{3}M^3 N_c V_f(\lambda,\tau)\mathrm{e}^A\sqrt{1+\mathrm{e}^{-2A}\kappa\left((\partial_r\tau)^2+(\partial_\xi\tau)^2\right)}\times \\
\times\Bigg(\mathrm{e}^{2A}\kappa(\lambda)\tau^2\Bigg(4\mathrm{e}^{2A}\Delta_{rr}\tilde{B}_r^2+4(1-\mathrm{e}^{2A}\Delta_{\xi\xi})\left[\tilde{B}_\xi^2+\frac{2}{\xi^2}\tilde{\rho}^2\right]- \\
-8\mathrm{e}^{2A}\Delta_{\xi r}\tilde{B}_\xi\tilde{B}_r-2\tilde{\chi}_1^2\Bigg)- \\
-w(\lambda)^2\Bigg(\frac{1}{2}(1-\mathrm{e}^{2A}\Delta_{\xi\xi})|D_\xi\chi|^2+\frac{1}{2}\mathrm{e}^{2A}\Delta_{rr}|D_r\chi|^2- \\
-\frac{1}{2}\mathrm{e}^{2A}\Delta_{\xi r}\left(D_\xi\chi^* D_r\chi+h.c.\right)+\frac{1}{4}(1-\mathrm{e}^{2A}\Delta_{\xi\xi})(\partial_\xi v)^2+ \\
+\frac{1}{4}\mathrm{e}^{2A}\Delta_{rr}(\partial_r v)^2-\frac{1}{2}\mathrm{e}^{2A}\Delta_{\xi r}\partial_r v\partial_\xi v+ \\
+\frac{1}{2\xi^2}(v^2+|\chi|^2)(1+|\phi|^2)-v(\chi\phi^*+h.c.)- \\
-2\mathrm{e}^{2A}\Delta_{rr}\xi^{-2}(D_r\rho)^2-2(1-\mathrm{e}^{2A}\Delta_{\xi\xi})\xi^{-2}(D_\xi\rho)^2+ \\
+4\mathrm{e}^{2A}\Delta_{\xi r}\xi^{-2}D_r\rho D_\xi\rho-2\mathrm{e}^{2A}\Delta_{rr}(\partial_r Q)^2- \\
-2(1-\mathrm{e}^{2A}\Delta_{\xi\xi})(\partial_\xi Q)^2+4\mathrm{e}^{2A}\Delta_{\xi r}\partial_r Q\partial_\xi Q- \\
-2\xi^{-2}Q^2\Big[2-\mathrm{e}^{2A}\xi\left(\partial_\xi\Delta_{\xi\xi}+\mathrm{e}^{2A}\partial_r(\mathrm{e}^{-2A}\Delta_{\xi r})\right)\Big]- \\
-\frac{1}{2}\Big[\mathrm{e}^{2A}\Delta_{rr}(1-\mathrm{e}^{2A}\Delta_{\xi\xi})-\mathrm{e}^{4A}\Delta_{\xi r}^2\Big](B_{\bar{\mu}\bar{\nu}})^2\Bigg)\Bigg)\,,
\end{aligned} \tag{3.2.77}$$

where the Δ symbol is defined in Appendix J,

$$\begin{aligned}
\rho_{\lambda,CS} \equiv \frac{2N_c}{3\pi^2\xi^2}\epsilon^{\bar{\mu}\bar{\nu}}\Bigg(D_{\bar{\mu}}\rho\Big(\left(f_1(\tau)+f_3(\tau)\right)(D_{\bar{\nu}}\phi\,\chi^*+h.c.)- \\
-2(2f_3(\tau)-f_1(\tau))\left(D_{\bar{\nu}}\tilde{\phi}+h.c.\right)\tilde{\chi}_1- \\
-4(f_1(\tau)-f_3(\tau)-if_2(\tau))\tilde{A}_{\bar{\nu}}\tilde{\phi}_1\tilde{\chi}_2\Big)+ \\
+\tilde{\rho}\Big(2(f_3(\tau)-if_2(\tau))\big(-F_{\bar{\mu}\bar{\nu}}\,\tilde{\phi}_1\tilde{\chi}_2+\tilde{A}_{\bar{\mu}}(i\partial_{\bar{\nu}}\phi\chi^*+h.c.)\big)- \\
-\partial_{\bar{\nu}}\tau f_1'(\tau)(D_{\bar{\mu}}\phi\chi^*+h.c.)+\partial_{\bar{\nu}}\tau f_3'(\tau)(D_{\bar{\mu}}\tilde{\phi}\tilde{\chi}+h.c.)- \\
-2i\partial_{\bar{\nu}}\tau f_2'(\tau)\tilde{A}_{\bar{\mu}}\tilde{\phi}_1\tilde{\chi}_2\Big)+
\end{aligned}$$

$$
\begin{aligned}
&+ 2\partial_{\bar\nu}\tau(f_1'(\tau) - f_3'(\tau))D_{\bar\mu}\rho\,\tilde\chi_1\tilde\phi_1 + \\
&+ \partial_{\bar\mu}(\xi Q)\Big((f_1(\tau)+f_3(\tau))\,(i\chi^* D_{\bar\nu}\phi + h.c.) + \\
&\qquad + 4(f_1(\tau)+f_3(\tau)-3if_2(\tau))\tilde A_{\bar\nu}\,\tilde\phi_1\tilde\chi_1\Big) + \\
&+ 2\partial_{\bar\nu}\tau(f_1'(\tau)+f_3'(\tau))\partial_{\bar\mu}(\xi Q)\tilde\phi_1\tilde\chi_2 - \\
&- 8(f_1(\tau)+f_3(\tau))\xi Q\, D_{\bar\mu}\rho\partial_{\bar\nu}\Phi + 8\partial_{\bar\nu}\tau(f_1'(\tau)+f_3'(\tau))\xi Q\tilde\rho\partial_{\bar\mu}\Phi + \\
&+ v\Big(B_{\bar\mu\bar\nu}\Big[\frac{1}{2}(f_1(\tau)+f_3(\tau))\,(|\phi|^2-1) + (f_1(\tau)-f_3(\tau)-if_2(\tau))\tilde\phi_1^2\Big] + \\
&\quad + (f_1(\tau)+f_3(\tau))\xi Q F_{\bar\mu\bar\nu} - 2(f_3(\tau)-if_2(\tau))\tilde B_{\bar\mu}(D_{\bar\nu}\tilde\phi + h.c.)\tilde\phi_1\Big) + \\
&+ v\partial_{\bar\nu}\tau\Big((f_1'(\tau)+f_3'(\tau))\big(\tilde B_{\bar\mu}(1-|\phi|^2) - 2\xi Q\tilde A_{\bar\mu}\big) + 2if_2'(\tau)\tilde B_{\bar\mu}\tilde\phi_1^2\Big)\Big). \qquad (3.2.78)
\end{aligned}
$$

We recall that the tildes on the static fields refer to the redefined fields that contain the non-abelian tachyon phase θ (3.1.80). The total bulk Lagrangian density for the rotating fields is denoted by ρ_λ

$$\rho_\lambda \equiv \rho_{\lambda,DBI} + \rho_{\lambda,CS}\,. \qquad (3.2.79)$$

The equations of motion for the fields of the rotating soliton ansatz are obtained by extremizing the moment of inertia (3.2.75) with respect to small deformations of the fields. They are presented in Appendix J.

3.2.5.3 Boundary conditions

We present in Table 3.7 the boundary conditions that are imposed on the fields of the rotating soliton ansatz (3.2.57)-(3.2.60) and (3.2.64), which obey the equations of motion (J.5)-(J.12). We discuss separately the 4 boundaries of the (ξ, r) space

- **UV :** In the UV limit $r \to 0$, the condition that $v, \tilde\chi, B_\xi, \rho$ and Q should vanish comes from requiring that there is no source for the gauge fields at the boundary. Moreover, the condition for B_r comes from imposing the Lorenz gauge.

  The condition for ζ is somewhat more subtle than the other fields. The reason is that, because the quark mass is set to 0, there is no source term for the tachyon field. The abelian phase ζ is therefore not associated with any source. At the level of the near-boundary behavior, it translates into the fact that the boundary value of ζ appears in front of the vev term for the tachyon field

  $$T(r,\xi) \underset{r\to 0}{=} \ell\Sigma(\xi)\exp\left(i\zeta(0,\xi)\frac{\vec\omega\cdot\vec x}{\xi} + i\theta(0,\xi)\frac{x\cdot\sigma}{\xi}\right) r^3(-\log(r\Lambda))^{-c}\,(1+\cdots)\,, \qquad (3.2.80)$$

  where the dots refer to terms that go to 0 near the boundary; $\Sigma(\xi)$ is proportional to the modulus of the chiral condensate in the boundary theory $\left|\langle\bar\psi\psi\rangle\right|$. The UV

$\xi \to 0$	$\xi \to L \to \infty$	$r \to 0$	$r \to r_{\rm IR} \to \infty$
$v + \tilde{\chi}_2 \to 0$	$v \to -1$	$v \to -1$	$\partial_r v \to 0$
$\tilde{\chi}_1 \to 0$	$\tilde{\chi}_1 \to 0$	$\tilde{\chi}_1 \to -\sin\theta$	$\tilde{\chi}_1 \to 0$
$\partial_\xi \tilde{\chi}_2 \to 0$	$\tilde{\chi}_2 \to -1$	$\tilde{\chi}_2 \to \cos\theta$	$\partial_r \tilde{\chi}_2 \to 0$
$\partial_\xi B_\xi \to 0$	$\partial_\xi B_\xi \to 0$	$B_\xi \to 0$	$B_\xi \to 0$
$B_r \to 0$	$B_r \to 0$	$\partial_r B_r \to 0$	$\partial_r B_r \to 0$
$\partial_\xi \rho - B_\xi \to 0$	$\rho \to 0$	$\rho \to 0$	$\rho \to 0$
$Q \to 0$	$Q \to 0$	$Q \to 0$	$\partial_r Q \to 0$
$\zeta \to 0$	$\zeta \to 0$	$r\zeta \to 0$	$\zeta \to 0$

Table 3.7: Boundary conditions for the rotating soliton solution in Lorenz gauge.

condition for ζ will therefore not come from a choice of source at the boundary, but rather from the requirement that the solution be regular. The equation of motion for ζ (J.12) has two linearly independent solutions, one of which behaves as r^{-2} near the boundary and the other as r^0. Requiring that

$$r\zeta \underset{r\to 0}{\to} 0\,, \tag{3.2.81}$$

will therefore select the regular behavior.

- $\underline{\xi \to L\,(L \to \infty)}$: Requiring that the moment of inertia (3.2.75) should be finite imposes that, as $\xi \to \infty$

$$\xi^{3/2}\tilde{\chi}_1 \to 0 \quad , \quad \xi^{3/2}\partial_{\bar{\mu}}\tilde{\chi}_2 \to 0 \quad , \quad \xi^{3/2}\partial_{\bar{\mu}} v \to 0\,, \tag{3.2.82}$$

$$\xi^{3/2}\left(B_{\bar{\mu}} + \frac{1}{2}\partial_{\bar{\mu}}\zeta\right) \to 0 \quad , \quad \xi^{1/2}\left(\rho + \frac{1}{2}\zeta\right) \to 0 \quad , \quad \xi^{3/2}\partial_{\bar{\mu}} Q \to 0\,. \tag{3.2.83}$$

For regularity $\partial_\xi \zeta$ should go to 0 as $\xi \to \infty$ so B_ξ should also tend to 0 from (3.2.83). Then the Lorenz gauge condition in the limit where $\xi \to \infty$ reads

$$\partial_r B_r = 0 = -\frac{1}{2}\partial_r^2 \zeta\,, \tag{3.2.84}$$

so at $\xi \to \infty$, ζ should take the form

$$\zeta \underset{\xi\to\infty}{\to} \zeta^{(0)} + r\zeta^{(1)}\,. \tag{3.2.85}$$

In the UV, from (3.2.83)

$$\lim_{\xi\to\infty}\zeta(\xi,0) = -2\lim_{\xi\to\infty}\rho(\xi,0) = 0\,, \tag{3.2.86}$$

because the source for ρ is set to 0. We shall further fix the residual gauge freedom (3.2.73) such that $\zeta = 0$ in the IR. With this choice, the linear part also vanishes in (3.2.85) and

$$\zeta \underset{\xi\to\infty}{\to} 0\,. \tag{3.2.87}$$

The final condition for B_ξ, $\partial_\xi B_\xi \to 0$ rather than $B_\xi \to 0$, is chosen to impose Lorenz gauge even at finite L in the numerical solution.

- **IR :** As for the static soliton, the conditions in the IR limit $r \to r_{\rm IR}$ are regularity conditions. In section 3.1, it was found that the resulting conditions for the gauge fields were equivalent to the conditions imposed in the hard-wall model for chiral symmetry to be broken on the IR wall

$$(\mathbf{L}-\mathbf{R})|_{r_{\rm IR}} = 0 \quad , \quad \left(\mathbf{F}^{(L)}_{\mu r} + \mathbf{F}^{(R)}_{\mu r}\right)\Big|_{r_{\rm IR}} = 0\,. \tag{3.2.88}$$

In the following, our strategy is to assume that the IR regularity conditions for the gauge field are still equivalent to (3.2.88) in the case of the rotating soliton. This assumption will be confirmed numerically if a solution can be found with this behavior in the IR. It can also be checked analytically by studying the IR asymptotics of the equations of motion. With the ansatz (3.2.57)-(3.2.60), (3.2.88) translates to

$$\chi_1|_{\rm IR} = 0 \quad , \quad B_\xi|_{\rm IR} = 0 \quad , \quad \rho|_{\rm IR} = 0\,, \tag{3.2.89}$$

$$\partial_r\chi_2|_{\rm IR} = 0 \quad , \quad \partial_r Q|_{\rm IR} = 0\,. \tag{3.2.90}$$

Finally, the condition for B_r comes from the Lorenz gauge (3.2.72) and, as stated in the previous point, the residual gauge freedom (3.2.73) is chosen such that $\zeta = 0$ in the IR.

- $\xi = 0$: The boundary conditions in the limit where ξ goes to 0 come from requiring that $\tilde{\mathbf{L}}$ and $\tilde{\mathbf{R}}$ are well defined vectors at $\xi = 0$ and that the field strength (J.1)-(J.4) is a well defined 2-tensor. The additional constraint on B_ξ is imposed by the choice of Lorenz gauge. The final condition $\zeta \underset{\xi\to 0}{\to} 0$ fixes what remained of the residual gauge freedom (3.2.73) after setting ζ to 0 in the IR. Note that for this choice the tachyon matrix (3.2.64) is well defined at $\xi = 0$.

3.2.5.4 Numerical results : the spin-isospin spectrum

We present in this subsection the numerical solution for the slowly rotating soliton configuration. The equations of motion written in appendix J are solved with the gradient descent method, imposing the boundary conditions of Table 3.7.

At linear order in ω, the rotating solution is a probe on the static background. At leading order in N_f, the static background will correspond to the probe baryon solution presented in Section 3.2.3.3. Order $\mathcal{O}\big(N_f^{-1}\big)$ corrections to the rotating solution will come from including the back-reaction on the tachyon in the static background, as discussed in Section 3.2.3.3. We start by presenting the leading order probe baryon solution and then discuss the back-reaction. We recall that the back-reacting solution is computed assuming no back-reaction on the color sector (metric and dilaton).

Probe baryon background

We start with the numerical results obtained for the probe baryon background. In this case the modulus of the tachyon field τ is fixed to its vacuum value, and the equations of motion take the form presented in appendix J.3.

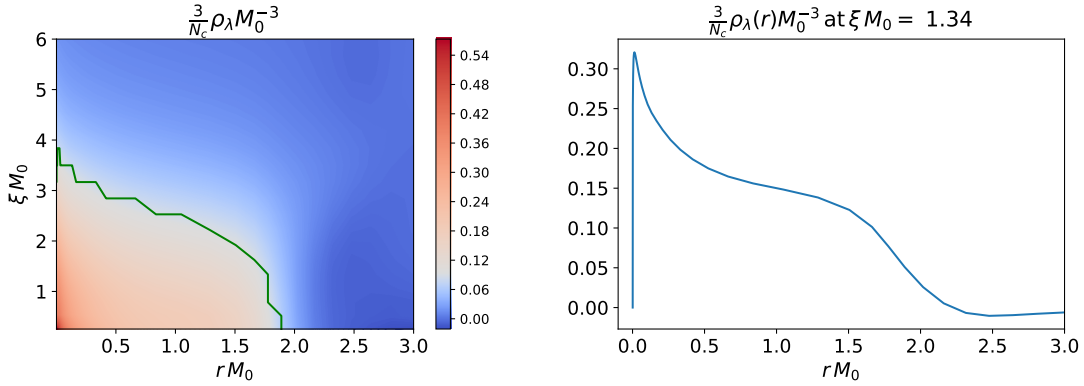

Figure 3.9: **Left:** bulk Lagrangian density for the rotating fields (3.2.79) in the probe baryon approximation. All quantities are expressed in units of the classical mass of the static soliton M_0 (3.2.27). The center of the soliton is located at $\xi = 0$ where the density diverges as ξ^{-1}. The UV boundary is at $r = 0$, and the green line indicates the boundary of the region over which the mean value is computed to define the relative difference in figure 3.10. **Right:** Same as the left figure, but at some given value of the 3-dimensional radius ξ. This figure makes it clear that the Lagrangian density eventually reaches 0 as $r \to 0$, as it should in absence of sources.

The bulk Lagrangian density for the rotating fields (3.2.79) in the (ξ, r)-plane is presented in Figure 3.9, where all dimensionful quantities are expressed in units of the classical soliton mass M_0 (3.2.27). As for the static fields, Figure 3.9 shows the expected behavior for a solitonic configuration, that is the densities are confined to a region of finite extent in the bulk. The size of the lump is again of the order of M_0^{-1}.

Note that the density is observed to have a maximum very close to the UV boundary. This is associated with the flavor gauge fields of the rotating solution having the same kind of sharp behavior near the boundary. However, it is possible to check that the smooth vev-like behavior is recovered asymptotically as one goes closer to $r = 0$

$$\mathbf{A}_\mu \sim r^2 \times \text{vev}\,.$$

To check this, one needs to go very close to the boundary $r = 0$, so log coordinates $u = \log(r)$ are more appropriate. We have explicitly checked that the vev behavior is recovered very near the boundary. We believe that this feature is a peculiarity of the UV behavior of our choice of V-QCD potentials, and that it can be avoided with a better choice. In particular, this behavior is not observed for the potentials of [165], for which the solution is analyzed in Appendix I.

The numerical value for the classical moment of inertia density λ in (3.2.75) is obtained by integrating the Lagrangian density in Figure 3.9

$$\frac{1}{\lambda} \simeq \frac{3}{N_c} \times 60\,\text{MeV}\,. \tag{3.2.91}$$

From this result, the spin-isospin spectrum of the baryons (3.2.53) can be computed and compared with experimental QCD data, as shown in Table 3.8. We set $N_c = 3$ in the large N result to make this comparison. We recall that the estimation (3.2.34) for the soliton mass gives only the classical contribution, which can receive sizeable $\mathcal{O}\big(N_c^0\big)$ quantum corrections at finite N_c. Likewise, (3.2.91) is the leading order contribution to the moment of inertia in the Veneziano limit. Also, the V-QCD potentials presented in Section 3.2.2 were not fitted to baryonic properties, but rather to QCD thermodynamics and mesonic properties. In light of these remarks, the precise numerical value for the baryon spectrum presented in Table 3.8 should not be taken too seriously, but rather as an indicative result. In particular, we shall not mention the numerical accuracy of the result as it is much better than the theoretical uncertainty.

Back-reacted tachyon background

We now discuss the slowly rotating soliton solution computed on the static background that takes into account the back-reaction on the tachyon field. The corresponding equations of motion for the rotating fields are written in Appendix J.2.

Spin	V-QCD mass	Experimental mass
$s = \frac{1}{2}$	$M_N \simeq 1170\,\text{MeV}$	$M_N = 940\,\text{MeV}$
$s = \frac{3}{2}$	$M_\Delta \simeq 1260\,\text{MeV}$	$M_\Delta = 1234\,\text{MeV}$

Table 3.8: Baryon spin-isospin spectrum in the V-QCD model with the potentials of Section 3.2.2, compared with experimental data.

We are interested in the effect of the back-reaction on the soliton moment of inertia (3.2.75). In the large N_f limit, the correction is of order $\mathcal{O}\big(N_f^{-1}\big)$

$$\delta\lambda = \delta\tau \frac{\delta\lambda}{\delta\tau}\bigg|_{\text{probe}} + \mathcal{O}\big(N_f^{-2}\big)\,, \tag{3.2.92}$$

where $\delta\tau$ refers to the order $\mathcal{O}\big(N_f^{-1}\big)$ correction to τ. Figure 3.10 shows the relative difference between the bulk Lagrangian density for the back-reacted and probe backgrounds, when setting $N_f = 3$ in the large N result. The definition of the relative difference is analogous to the static case (3.2.42)

$$\Delta_{\text{rel}}\rho_\lambda \equiv \frac{\rho_{\lambda,\text{back-reacted}} - \rho_{\lambda,\text{probe}}}{\bar{\rho}_\lambda}\,, \tag{3.2.93}$$

where the criterion defining the region over which the mean value $\bar{\rho}_\lambda$ is computed is now given by

$$\frac{3}{N_c}\rho_\lambda \geq M_0^2\,. \tag{3.2.94}$$

This region is delimited by the green line in figure 3.9.

The dominant effect of the tachyon back-reaction observed in Figure 3.10 is the same as in the static case shown in Figure 3.8: the density decreases in the UV and is shifted towards the IR. Even more strikingly than for the soliton mass in the static case, even at small values of N_f, the relative difference between the probe and back-reacted solutions is observed to be small numerically, of the order of a few percent. At the level of the soliton moment of inertia we obtain

$$\frac{N_f}{3}\frac{\frac{1}{\lambda_{\text{back-reacted}}} - \frac{1}{\lambda_{\text{probe}}}}{\frac{1}{\lambda_{\text{probe}}}} \simeq 0.37\%\,. \tag{3.2.95}$$

As for the static mass, we would like to emphasize here again that precise quantitative results such as (3.2.95) cannot be trusted when substituting a small number of flavors in the large N result. The result in (3.2.95) should be considered as an indication, that the moment of inertia does not seem to be affected much by the back-reaction of the baryon on the background.

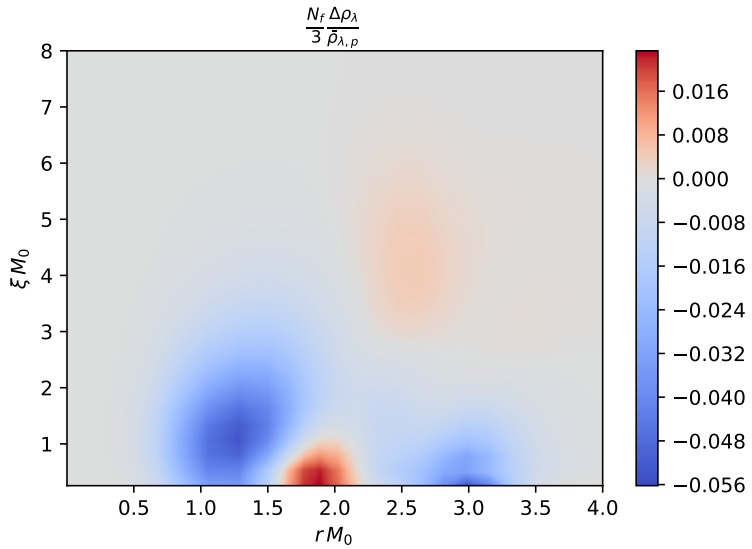

Figure 3.10: Relative difference of bulk Lagrangian density for the slowly rotating soliton computed on the probe baryon and the back-reacted tachyon backgrounds. The relative difference is defined as the difference of the two densities divided by the mean value of the probe density. The mean value is taken over the area delimited by the green line in the left of Figure 3.9, which is the region where the density is substantially different from zero. The ratio is multiplied by N_f in order to obtain something finite in the Veneziano limit. The UV boundary is located at $r = 0$ and the baryon center at $\xi = 0$.

3.3 Discussion and outlook

In the first part of this chapter, we have determined the form of the Tachyon-Chern-Simons action in V-QCD in the chiral limit and set up the formalism for obtaining single-baryon configurations. Several questions remain open.

The most important drawback of the TCS action that was obtained is that it is limited to the exact chiral limit. We have assumed an ansatz for (3.1.2) which, based on the factorization of the tachyon (3.0.1), is made up of terms of the form:

$$\Omega_5 \supset f(\tau) \times 5\text{-form}(U, \text{gauge fields}) \tag{3.3.1}$$

However this cannot be the full story when quark masses are non-zero: if this is the case, instead of (3.0.1), the scalar function τ must be replaced by a Hermitian matrix (see footnote 5). Therefore, one cannot write the simple ansatz (3.3.1) for the TCS terms,

which instead must have a more complicated dependence on the matrix T, such that it effectively reduces to the form (3.3.1) for zero quark masses.

A possible way to proceed is to return to the superconnection formalism of Quillen, (see [138] for a description) which has been used and shown to be relevant in string theory calculations of the Tachyon-Chern-Simons terms, [138]. In a recent paper [191], it was shown that it is an appropriate formalism for anomalies. If this formalism is used in our analysis here, it will reduce the four unknown tachyon dependent functions that can appear to only one. It is possible that within the superconnection formalism, the problem of writing the general TCS term may be tractable. The difficult part is in writing the anomaly related tachyon-dependent six form as the exterior derivative of a five-form.

The other result from this chapter is the construction of the V-QCD baryon configuration, for which we found a concrete numerical solution. The solution presented here has several advantages with respect to similar constructions in the literature, as well as some limitations. In order to discuss them, we shall compare the results of this work with the two main models of holographic QCD in which single-baryon solutions were analyzed. These are the top-down Witten-Sakai-Sugimoto model (WSS) [121, 124, 128] and the bottom-up Hard-Wall model (HW) [143, 178].

The main improvement with respect to both models mentioned above is that the V-QCD background solution on which the baryon solution is constructed is a more accurate description of the QCD vacuum. The V-QCD vacuum possesses a rich structure, including the running of the Yang-Mills coupling and the spontaneous breaking of the chiral symmetry in the chiral limit. Moreover, it incorporates the back-reaction of the flavor sector onto the color sector, due to the Veneziano limit. The model can have several parameters that can be adjusted to experimental data if one wants to produce a precise phenomenological model for strongly-coupled QCD [161, 163] although generically, the dependence on these parameters is weak.

We now focus on the comparison with the HW model. In the HW model, a baryon state was constructed as a bulk axial instanton for the chiral gauge fields, using the same kind of ansatz that is considered in this work [173]. However, the main difference is that the bulk geometry was arbitrarily fixed to AdS_5, where a hard wall was placed in the IR for the boundary theory to be confining. Because of the gravitational potential, the bulk soliton was found to fall on the IR wall. This indicates that the hard wall model is too crude to stabilize the baryon solution dynamically. Moreover, since its position is at the very end of space, the properties of the soliton will strongly depend on the IR boundary conditions.

On the contrary, the baryon solution that is constructed in the present work is well localized in the holographic direction. It stands at a value of the holographic coordinate of the order of the inverse of the soliton mass. This is due to the fact that, beyond the metric, the V-QCD vacuum contains another field under which the baryon is charged: the tachyon

field[38] dual to the quark bilinear operator. The combined effect of the baryon boundary conditions and the interaction of the gauge fields with the tachyon field, result in a force that balances the gravitational attraction towards the IR.

We now discuss the WSS model. As discussed in section 2.2, the main drawback of the baryon solution that was constructed in [128] is that the baryon size was found to be parametrically small at large 't Hooft coupling. Instead, the size of the baryon solution that we derived in V-QCD is set by the mass scale of the boundary theory, which roughly corresponds to $\Lambda_{\rm QCD}$. Note that this was not an obstacle to the calculation of meaningful baryon form factors in the WSS model, as the latter were found to be related to the scale set by the rho meson mass rather than the soliton mass [129]. Nevertheless, the infinitesimal size of the soliton will be an issue for classical fields in the bulk, such as the chiral condensate, as well as the gravitational form factors.

Another aspect where our construction is an improvement, compared with previous settings, lies in the tachyon dependence of the bulk action. First, the DBI form of the kinetic action for the flavor fields contains an infinite sum of corrections compared with the quadratic action considered in the HW model. In vacuum, such a square-root behavior was found to play an important role to reproduce linear trajectories for the meson spectrum [161]. Although in the WSS model the same kind of action was introduced in [130], the present work is the first one in which a baryon solution is computed by keeping the full DBI action for the tachyon[39]. Second, and most importantly, we consider for the fist time the tachyon dependence of the topological Chern-Simons (CS) term. In our bottom-up approach, this term was constructed as the most general topological action compatible with QCD symmetries and chiral anomalies.

The approach we followed here presents also some limitations. Apart from the usual drawbacks which are intrinsic in a bottom-up model (a certain amount of indeterminacy in the action, no known embedding as a low energy approximation of string theory), the most important limitation is that the solution presented here is only valid in the exact chiral limit. This is related to the CS term mentioned above: as was explained in the first section, our construction only applies in the limit of zero quark masses, as turning on non-zero quark masses requires modifying both the CS term and the instanton ansatz.

Finally we should mention that, in this work, we focused on a small subsector of the baryon spectrum. This is due to the specific ansatz considered for the quantization of the soliton excitations:

[38]The baryon solution including a non-trivial tachyon in the context of the HW model was considered in [196, 178]. In that work it was also found, as in our model, that considering a non-trivial tachyon resulted in a repulsive force on the baryon from the IR, although the mechanism for this to happen is different (in our case the baryon is a probe on the tachyon background). At large chiral condensate, this could eventually make the baryon detach from the IR wall, but only a finite distance from it.

[39]Note that the calculation is done here by expanding the DBI action at quadratic order in the non-abelian fields, but keeping the abelian part of the tachyon fully non-linear.

- We considered only the zero-modes, which resulted in the spin-isospin spectrum of the baryons. However, the experimentally observed baryon spectrum contains higher excited states for each isospin eigenvalue. These states are understood in the holographic picture as non-zero modes of the soliton, that is modes that are associated with a non-trivial potential, for which the soliton solution sits at the minimum. These include for instance the dilation and oscillating modes considered in the WSS model [128].

- Within the isospin zero-modes, we focused on a subgroup containing $N_f = 2$ flavors. For phenomenology, it is interesting to quantize higher subgroups, in particular $N_f = 3$. When introducing asymmetric masses for the quarks, this will make it possible to discuss the properties of holographic hyperons.

- We restricted to the case of a slowly rotating soliton, which is enough to compute the spin-isospin spectrum at $s \ll N_c$. In particular, at linear order in the rotation velocity ω, there is no deformation of the static fields, such that the cylindrical symmetry is preserved. The consequence on the spectrum is that only states with equal spin and isospin $s = I$ are reproduced. States that do not obey $s = I$ are observed experimentally, such as N(1520) or $\Delta(1950)$. Reproducing such states will require a rotating ansatz that deviates from cylindrical symmetry. This can be obtained, for example, by computing the solution at next order in ω.

- The assumption of slow rotation also means that the linear Regge trajectories that are observed experimentally cannot be reproduced. Namely, the spin-isospin spectrum that we compute is that of the rigid rotor, for which the masses go as $M \sim s^2$ at large spin, instead of $M \sim s^{1/2}$ for a linear trajectory. It is expected that reaching the linear regime, if it can be reached in this framework, will require to consider states with $s \gtrsim N_c$. For such high spins, the relevant ansatz for the rotating soliton should be fully non-cylindrical. In particular, it will reproduce the linear Regge behavior if it turns out that the solution resembles a string at high rotation velocity [192].

All the points above can be the subject of future improvements.

Chapter 4

Holographic neutrino transport

The work presented in this chapter will be the subject of an upcoming paper.

Neutrino transport plays a pivotal role in various astrophysical processes involving dense QCD matter. The most studied class of such processes are the core collapse supernovae which occur in the last stages of the lifetime of massive stars. Neutrino-driven heating and turbulence are crucial ingredients in the complex dynamics that leads to the explosion of the star (see the reviews [210, 211]). Strong explosions, similar to what is observed in nature, are only obtained in simulations that properly take into account these ingredients.

Neutrino interactions are also important in the physics of neutron stars. Right after a neutron star is formed in a supernova explosion, its temperature is comparable to the QCD scale, and subsequently cools down due to neutrinos emitted by various processes [83, 212]. Neutrino cooling is the main mechanism for the first $\sim 10^5$ years (after which photon cooling dominates).

Apart from a supernova remnant, a hot neutron star can also be formed as a product of a binary neutron star collision. The observation of gravitational waves from the merger event GW170817 by the LIGO and Virgo collaborations together with the analysis of the electromagnetic signal from the kilonova has boosted the interest in neutron stars recently [79, 213]. State-of-the-art neutron star binary merger simulations are now developing towards a stage where the effects of neutrino transport are included [214, 215]. While it can be estimated that this effect is relatively small in the actual merger phase, neutrino emission affects significantly the evolution of the hypermassive neutron star after the merger within timescales accessible in simulations [216]. This is expected to hold even for a class of events where a black hole is formed: analysis of the electromagnetic signal from GW170817 suggests that a collapse to a black hole took place about one second after the merger in this event [217], which is easily long enough for neutrino effects to matter. Moreover, neutrinos affect drastically the composition of the ejecta, the evolution of the

torus, and the jet formation after the merger [218].

The importance of neutrino transport has sparked a wide literature studying the neutrino emission rates and opacities in dense matter. Most theoretical studies of neutrino transport focus on the nuclear matter phase, which is natural as most of the matter in neutron stars and in the collapsing core in the supernova process is known to be in this phase, and various effective theory tools are available for nuclear matter. There is a vast literature on this topic, see [219, 220, 221, 222].

Computing the emissivities and opacities at high densities boils down to computing the correlators of the currents of the weak interactions in the strongly interacting QCD matter. Standard methods for estimating these correlators include the use of mean-field theory [223] and the addition of correlation effects through ring resummation, i.e., the random phase approximation [224, 225] and its improvements (see, e.g., [226, 227]). Results in various limits and approximation schemes, such as the degenerate limit and the "elastic" approximation where the recoil of the nucleon is neglected [228], have been worked out.

However, for the highest densities reached in core collapse supernovae or in the cores of massive neutron stars, other phases than regular nuclear matter may appear. Phase transitions may play an important role in neutrino transport: while the equation of state typically changes modestly at phase boundaries (e.g. densities may jump by an $\mathcal{O}(1)$ factor at a first order transition), observables related to transport can easily change by orders of magnitude. Perhaps the most natural transition to consider is the transition from nuclear matter to quark matter, where neutrino emissivities are expected to be larger than in regular nuclear matter by orders of magnitude. This is indicated by analyses both in the ungapped regime [229, 230, 231, 232, 233], and in color-superconducting phases [241, 242, 243, 12]. But estimates for neutrino transport are also available in phases with pion [234, 235, 236] or kaon condensates [237, 238] and nuclear matter with superfluidity [239, 240].

At high densities in QCD, i.e., densities well above the nuclear saturation density $n_s \approx 0.16$ fm^{-3}, all these results include however sizable or uncontrolled uncertainties. This happens because first-principles methods are not reliable in this region of the phase diagram. For the equation of state, loop expansions in chiral perturbation theory for pure neutron matter converge below $n \approx 2n_s$ [244], while perturbation theory requires densities above $n \approx 40n_s$ to be reliable [245], which is clearly higher than the densities reached in neutron star cores. The uncertainty of the equation of state [8, 246, 247] readily affects the estimates of neutrino opacities and emissivities, and approximations used in the computation of the current-current correlators bring in additional uncertainty. The importance of the uncertainties in the densest regions is enhanced because the neutrino interactions with QCD matter become significantly stronger with increasing density. In the absence of reliable first-principle methods, it is therefore useful to analyze neutrino transport in this region by alternative and complementary approaches, such as the gauge/gravity duality.

The holographic correspondence has proved to be useful to study the properties of QCD, in particular the properties of hot QCD plasma produced in heavy ion collisions. Examples include the description of the far-from-equilibrium dynamics right after the collision [248,

249], and the famous estimate for the shear viscosity in strongly coupled plasma [250, 251]. Naturally, transport in hot quark gluon plasma at low densities has been studied also in holographic models that mimic properties of QCD more closely, see for example [145] and [252]-[257].

There has also been a considerable interest in studying dense matter by using the gauge/gravity correspondence (see recent reviews [151, 258]). The equation of state of QCD matter at high density has been analyzed both in the nuclear matter [174, 259, 260, 208, 261] and quark matter [262, 165, 263, 264] phases as well as in more exotic phases [265, 266, 267, 268, 269], aiming at applications in neutron star physics. Also transport coefficients in quark matter, i.e., viscosities and conductivities, have been estimated [270, 271].

In this work, we initiate the holographic study of neutrino transport. We consider a simple holographic model, based on an Einstein-Yang-Mills action. In this model, charged black hole geometries (Reissner-Nordström black holes) are interpreted as the dual of dense unpaired quark matter in QCD. We analyze charged current interactions in holographic matter, leading to estimates for the emission and absorption of neutrinos. Neutral current interactions (neutrino scattering) will be discussed in future work.

The structure of this chapter is as follows. We start by giving a brief summary of the results in section 1. In section 2, we review the formalism used to describe neutrino transport. The holographic model that is used to compute the charged current 2-point functions is introduced in section 3, with the calculation of the correlators described in section 4. Section 5 is devoted to the analysis of the results obtained for the neutrino radiative coefficients.

4.1 Summary of results

The transport of neutrinos is described by the Boltzmann equation[1] for the neutrino distribution f_ν

$$(K_\nu \cdot \partial) f_\nu = j(E_\nu)(1 - f_\nu) - \frac{1}{\lambda(E_\nu)} f_\nu \,,$$

with K_ν the on-shell neutrino 4-momentum and E_ν the neutrino energy. The radiative coefficients j and λ are properties of the medium: j is the neutrino emissivity and λ the mean free path. As reviewed in section 4.2, the calculation of the neutrino radiative coefficients in a neutron star requires the knowledge of the chiral current two-point function in dense QCD matter. Computing this correlator is a strongly-coupled issue, which remains unsolved. As mentioned in the introduction, several approximations have been considered in the literature but these remain highly model-dependent.

In this work, the approach that we follow is to compute the chiral current two-point function holographically, using the simplest holographic model where this calculation can

[1] Written in flat space here, for simplicity.

be done. We focus here on the charged current contribution, leaving the analysis of the neutral current for future work. The model contains many of the properties that are expected from a quark-gluon plasma at finite density but also has simplifications that are unphysical. It has an underlying scaling symmetry in the absence of baryon density, and the mechanism of chiral symmetry breaking is not (yet) implemented. Therefore our calculation should be considered as a first step towards performing this calculation in a successful theory, like holographic V-QCD, [150].

An important property of holographic strongly coupled theories at finite density is the following: although scaling symmetries are broken by the finite density, there is an emergent one-dimensional scaling symmetry at zero temperature which is also accompanied by a large density of states at very low energies, [272] and can even be responsible for glassy behaviour, [273]. This symmetry is associated to an AdS_2 factor[2] in the geometry of the relevant black hole. Such a regime exists in our theory and it is the one that controls most of the calculation. It has been also seen in the phenomenologically successful and more complete model of V-QCD, in [164]. It is an interesting question, that we do not address in this paper, to investigate what are the signals of this behavior, in both neutrino transport as well as the dynamics of neutron star mergers.

The holographic toy model that we consider is a bottom-up model where, in addition to the metric, the 5-dimensional bulk contains gauge fields belonging to the $U(N_f)_L \times U(N_f)_R$ flavor group dual to the field theory chiral current operators. The bulk holographic action which controls the dynamics of these fields, is the Einstein-Yang-Mills action

$$S = S_c + S_f \,.$$

$$S_{\rm c} = M^3 N_c^2 \int {\rm d}^5x\sqrt{-g}\,\left(R + \frac{12}{\ell^2}\right)\,,$$

$$S_f = -\frac{1}{8\ell}(M\ell)^3 w_0^2 N_c \int {\rm d}^5x\sqrt{-g}\left({\rm Tr}\,\mathbf{F}^{(L)}_{MN}\mathbf{F}^{MN,(L)} + {\rm Tr}\,\mathbf{F}^{(R)}_{MN}\mathbf{F}^{MN,(R)}\right)\,,$$

where $\mathbf{F}^{(L/R)}$ is the field strength for the chiral gauge fields, N_c the number of colors and ℓ the AdS length. The model has two dimensionless parameters, $M\ell$ and w_0 and these enter in the physics of the dual, strongly-coupled quantum field theory. As detailed in Appendix O, the parameters are fixed to match the lattice result for the QCD thermodynamics in the deconfined phase at low baryon density.

The background solution is the gravitational dual of a medium composed of quark matter at equilibrium, at finite temperature T and quark number chemical potential μ. We consider isospin symmetric matter, with isospin chemical potential

$$\mu_3 = 0\,.$$

[2] AdS_d stands for the anti-de Sitter geometry in d space-time dimensions. AdS_d is a constant negative curvature manifold with infinite volume and maximal O(2,d-1) symmetry.

Neutron star matter is known to be far from isospin symmetry, as it contains many more neutrons than protons. This isospin asymmetry may have a significant influence on the transport of neutrinos, as can be seen for example in the condition for β-equilibrium below. In this work, we restrict to the isospin symmetric case for the sake of simplicity[3] , leaving the study of isospin imbalance for future work. The corresponding gravitational dual corresponds to a charged AdS black-hole with a charge proportional to μ.

To this strongly-coupled medium, we add neutrinos and electrons so that we have full charge neutrality. The neutrinos that scatter in this medium are assumed to be sufficiently close to equilibrium for the chemical potential μ_ν to be well defined, and at $\beta-$equilibrium with the quarks and electrons

$$\mu_\nu = \mu_e + \mu_3 = \mu_e \,.$$

However, the distribution of neutrinos is generically different from the equilibrium distribution. In particular, it is expected that there is generically no Fermi surface with chemical potential μ_ν associated to it.

Following the usual holographic procedure, the charged current two-point function is then evaluated from the solution to the equations of motion for gauge field perturbations on the black-hole background. The correlators are computed numerically for energies ω and momenta k between 0 and a few times r_H^{-1}, r_H being the horizon radius.

From the numerical solution for the chiral current correlator, the neutrino charged current radiative coefficients can be computed as a function of the neutrino energy. This calculation is the main result of this work. When completed with the neutral current coefficients, it can be used to simulate numerically the transport of neutrinos, in the kind of quark matter described by our holographic model. The numerical results are discussed in detail in Section 4.5. Here, we give a summary of this analysis.

Approximations

We considered in this work several approximations, in which the radiative coefficients have simpler expressions. Apart from academic interest, these approximations are useful to obtain a better qualitative understanding of the exact numerical results. We list them below

- *The degenerate approximation*, where the expressions in the limit of $\mu \gg T$ are used for the Bose-Einstein and Fermi-Dirac equilibrium distributions n_b and n_f. In this limit, the weak processes which contribute to neutrino transport are clearly identified. This is summarized in table 4.1.

- *The hydrodynamic approximation*, where the radiative coefficients are computed by expanding the charged current 2-point function $G_c^R(\omega, k)$ at leading order in the

[3] As we discuss later in this introduction, a non-zero μ_3 may change non-trivially the background solution and phase, and makes the computation of current correlators more involved.

hydrodynamic expansion, that is at leading order in $r_H\omega$ and $r_H k$. Note that, at $\mu \gg T$, the parameters of the expansion are ω/μ and k/μ, rather than ω/T and k/T. As reviewed in Section 4.4, this emergence of a hydrodynamic behavior at low temperature is a consequence of the AdS_2 geometry of an extremal horizon.

In relation to this, a cautionary note is relevant here. Typically, as $T \to 0$, like in the case studied here, hydrodynamics is known to break down as the non-hydrodynamic poles of the energy-momentum tensor correlators are moving towards zero energy and momentum and eventually collide with the hydrodynamic poles. However, in an AdS_2 regime, like the one encountered here, there are indications that there is a kind of hydrodynamics that survives, [299]. The relevant poles of the correlators were studied in a toy model in [300]. An infinite lattice of equidistant poles were found that seemed to collide once in a while with the hydrodynamic pole. However, we have found that the presence of such an infinite lattice of poles do not seem to affect our two-point correlator of currents and its leading hydrodynamic behaviour. We suspect that this is because the residues of these poles are very small in this regime. A calculation of these residues, in a large d limit, using the framework of [301] seems to corroborate this expectation. It is however a topic that may be important more generally, and more is needed to understand it fully.

The leading order hydrodynamic expression for the retarded correlator of the charged currents, is given by

$$G^R_{c,\lambda\sigma}(\omega,k) = -i\sigma\left(P^{\perp}_{\lambda\sigma}(\omega,k)\omega + P^{\parallel}_{\lambda\sigma}(\omega,k)\frac{\omega^2-k^2}{\omega+iDk^2}\right) ,$$

where $P^{\perp}$ and $P^{\parallel}$ are respectively the projectors transverse and longitudinal to the 3-momentum k. In this approximation, the only strongly-coupled calculation required to determine the charged current correlator, is that of the two transport coefficients: the conductivity σ and the diffusivity D. In the simple holographic model considered in this work, analytic expressions can be derived for the transport coefficients

$$\sigma = \frac{|M_{ud}|^2}{8r_H}N_c(M\ell)^3 w_0^3 \quad , \quad D = \frac{1}{2}r_H ,$$

where M_{ud} is the ud component of the Cabibbo-Kobayashi-Maskawa (CKM) matrix, $M\ell$, w_0 and N_c are the parameters of the theory and r_H is the horizon radius of the dual black hole, which is an explicit function of the baryon density and temperature.

The hydrodynamic approximation approaches the exact result in the limit where all the leptonic energies μ_e, μ_ν, E_ν are much smaller than r_H^{-1}. At $\mu \gg T$, $r_H\mu_e$ (and $r_H\mu_\nu$) is found to asymptote to a constant close to 1, (4.3.26). For $r_H E_\nu$ also smaller than one, the leptonic energies are therefore at the limit of the regime of validity of the hydrodynamic approximation. As we summarize in more details below,

this approximation typically gives a good qualitative description of the radiative coefficients, but its accuracy is around a few tens percent.

- *The diffusive approximation*, where the hydrodynamic approximation is used, and it is further assumed that the dominant contribution to the radiative coefficients comes from the time-time component of the retarded 2-point function. We show in Appendix Q that this approximation is valid in the degenerate and hydrodynamic regime

$$T \ll \mu_e, \mu_\nu, E_\nu \ll \mu \,.$$

We use the diffusive and degenerate approximation to derive approximate expressions for the opacities

$$\kappa(E_\nu) \equiv j(E_\nu) + \frac{1}{\lambda(E_\nu)} \,.$$

The results are shown in (4.5.22) for neutrinos, and in (4.5.25)-(4.5.26) for anti-neutrinos. When it comes to describing the actual numerical results, these approximate expressions were found to be inaccurate. However, the expression at $E_\nu = 0$ (4.5.27)

$$\kappa_{e,0} = \frac{G_F^2 \sigma}{\pi^2} \mu_\nu^4 \,,$$

which originates fully in the transverse part of the correlator, was found to be in good agreement with the exact result for baryon densities $n_B \gtrsim 10^{-2}\,\mathrm{fm}^{-3}$. (4.5.27) is therefore a good estimate of the typical scale of the opacities as a function of the baryon density.

Properties of the radiative coefficients

We now summarize the main properties of the numerical solution for the neutrino radiative coefficients, that are presented in Section 4.5. The radiative coefficients depend on several parameters: the neutrino energy E_ν, but also the parameters of the theory $M\ell$ and w_0, as well as the environmental parameters μ and T. As detailed in Appendix O, $M\ell$ and w_0 are fixed by matching the zero-density thermodynamics of the model to the free quark-gluon plasma result. As for the environmental parameters, the temperature is fixed to values typical of young neutron stars[4] [274]

$$T = 10\,\mathrm{MeV} \,,$$

and we investigate the remaining 2-dimensional parameter space, of neutrino energy E_ν and baryon density n_B. We consider regimes of energy and density that are typical of transport

[4]Of course, the temperature is not constant as a function of the distance to the center of the star. However, the typical relative variation is of order 1.

in a neutron star, i.e. energies below ten times the temperature [274] and densities much larger than the thermal scale

$$E_\nu \lesssim 10\,T \quad , \quad n_B \gg T^3\,.$$

We first discuss the charged current polarization functions, which are the direct outcome of the holographic calculations. The polarization functions at $n_B = 1\,\mathrm{fm}^{-3}$ are shown in figure 4.13. The comparison with the leading order hydrodynamic prediction reveals that the polarization functions look qualitatively similar to the hydrodynamic expressions. We also evaluate quantitatively the difference between the two, focusing on the region of the energy-momentum space which is relevant to the calculation of the neutrino opacities. As a result, we find that the error from the hydrodynamic approximation to the transverse polarization function is comprised between 0 and about 50%, whereas for the longitudinal part it ranges from 0 to about 100%.

The next step of the analysis in section 4.5 is the discussion of the neutrino opacities themselves. The latter were computed numerically for a whole range of baryon densities n_B and neutrino energy E_ν, for values typical of transport in a neutron star

$$10^{-3}\,\mathrm{fm}^{-3} \leq n_B \leq 1\,\mathrm{fm}^{-3} \quad , \quad 0 \leq E_\nu \leq 100\,\mathrm{MeV}\,.$$

The solutions at the two extreme values of the density, $n_B = 10^{-3}\,\mathrm{fm}^{-3}$ and $n_B = 1\,\mathrm{fm}^{-3}$, are shown as a function of the neutrino energy in figure 4.16. The general qualitative behavior depends mainly on the statistical factors, so that it agrees with other calculations discussed in the literature: the opacities increase with both the density and the neutrino energy. When the baryon chemical potential is much larger than the temperature, a dip is observed in the neutrino opacity for energies close to the neutrino chemical potential μ_ν.

The accuracy of the various approximations introduced before is then analyzed in detail, over the full parameter space of density and neutrino energy. The corresponding 2-dimensional plots of the relative differences are shown in figures 4.18 to 4.23. The main conclusion from this analysis is that the accuracy of the approximations are typically better at high baryonic density. In particular, for $n_B \gtrsim 10^{-1}\,\mathrm{fm}^{-3}\big(T/(10\,\mathrm{MeV})\big)^3$, the hydrodynamic approximation is within 0 to 50% from the exact neutrino opacity, whereas the error is less than 30% for anti-neutrinos (see figure 4.1). That is, extracting only the leading order transport coefficients σ and D from the holographic calculation is a sufficient input to obtain a good estimate of the opacities at those densities.

At densities $n_B \lesssim 10^{-2}\,\mathrm{fm}^{-3}\big(T/(10\,\mathrm{MeV})\big)^3$, the hydrodynamic approximation is much cruder, with errors exceeding 100% at high neutrino energy. This means that higher order transport coefficients are required to produce a reasonable approximation. For even smaller densities, as μ/T becomes of order 1, $r_H E_\nu$ becomes larger than 1 for $E_\nu \gtrsim T$. In this case, the hydrodynamic expansion breaks down, and the full holographic 2-point function is needed to compute the opacities. The reason for this breakdown is that the hydrodynamic expansion (4.4.44) and (4.4.53) is an expansion in $(r_H\omega, r_H k)$, where ω and k depend on

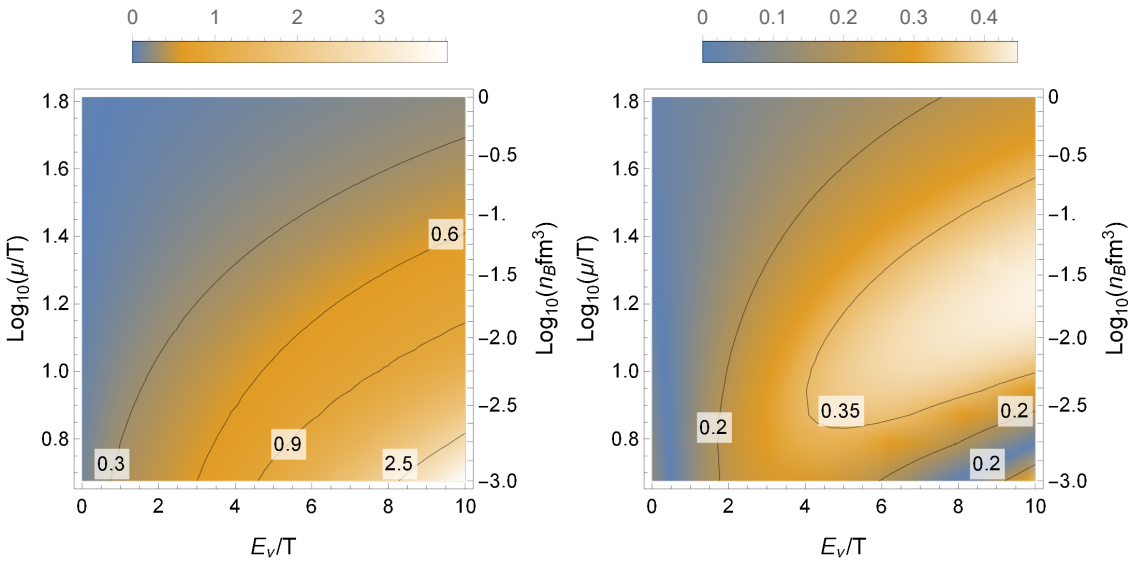

Figure 4.1: Relative difference between the hydrodynamic approximation and the exact opacities, for neutrinos (**Left**) and anti-neutrinos (**Right**).

the leptonic energies in the radiative integrals. In particular, large values of $r_H\omega$ and $r_H k$ are explored for large $r_H E_\nu$. This is discussed in detail in section 4.5.2.

Comparison with the literature

In the last section of this work, our results are compared with other calculations of the neutrino radiative coefficients from the literature. We focus on the recent results in non-relativistic nuclear matter from [274], and the calculations in weakly-coupled quark matter from [231]. The opacities computed from the holographic model

$$\kappa_{e^-}(0) \simeq 6.2\times 10^2\,\mathrm{km}^{-1}\left(\frac{n_B}{0.1\,\mathrm{fm}^{-3}}\right)^{\frac{5}{3}}\left(\frac{(M\ell)^3}{(M\ell)^3_{\mathrm{free}}}\right)^{-\frac{1}{2}}\left(\frac{w_0^2(M\ell)^3}{(w_0^2(M\ell)^3)_{\mathrm{free}}}\right)^{\frac{5}{6}},$$

are found to be about an order of magnitude larger than the results from approximate calculations in nuclear matter, which is about two orders of magnitude smaller than the perturbative result in quark matter (see figure 4.2). This indicates that, although the holographic matter is deconfined, the strong coupling implies that the neutrino opacity is highly suppressed compared with the perturbative estimate. We caution however that the model we used is not very close to the real theory and more effort is needed to corroborate the results.

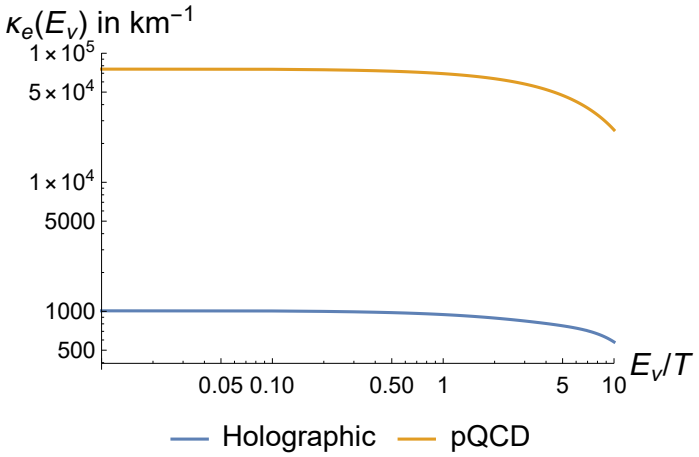

Figure 4.2: Neutrino opacity from our holographic result (blue) compared with the perturbative QCD result [231] (orange), at $n_B = 0.11\,\mathrm{fm}^{-3}$ and $T = 10\,\mathrm{MeV}$. The opacity is expressed in km^{-1}.

4.2 Formalism for the transport of neutrinos

In this section, we give a complete review of the elements of formalism that are used to describe the transport of neutrinos. The idea is to make clear the connection between neutrino transport and the retarded chiral-current two-point function, which is the quantity that we compute in this work using holographic methods. We start from the basic definitions of the real-time correlators in the closed-time-path formalism, before deriving the Boltzmann equation, obeyed by the neutrino distribution function. The collision term in the Boltzmann equation depends on the neutrino self-energy in the medium of propagation. The charged current contribution to the self-energy is then computed explicitly at quadratic order in the Fermi weak coupling constant G_F, in terms of the chiral current two-point function. The final form of the neutrino Boltzmann equation is presented at the end of this section.

4.2.1 Definitions in the closed-time-path formalism

The mathematical objects which contain the information about the transport of neutrinos in a given medium, are the (exact) real-time propagators of the neutrinos

$$iG_{\alpha\beta}(x_1, x_2) \equiv \left\langle \mathcal{T}\psi_\alpha(x_1)\bar{\psi}_\beta(x_2)\right\rangle \,, \tag{4.2.1}$$

where ψ the neutrino spinor field. $\mathcal{T}$ is a time-ordering operator, for which the possible choices are made explicit below (see (4.2.4)-(4.2.7)). The brackets refer to the expectation

value in the medium at finite temperature. The convenient formalism to compute out-of-equilibrium real-time quantities such as (4.2.1) is the so-called Schwinger-Keldysh, or closed-time-path (CTP) formalism. The latter relies on the fact that all real-time correlation functions can be written as correlation functions on a specific path in the complex time plane: the CTP, shown in figure 4.3.

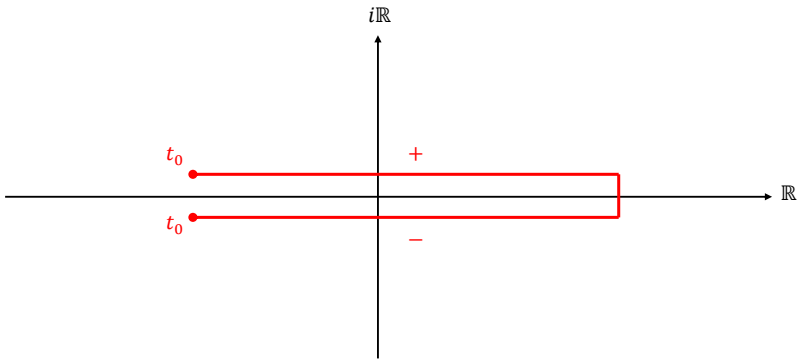

Figure 4.3: The closed-time-path. The turning point of the contour on the right of the figure should thought of as being pushed to infinity.

In particular, the propagators can be expressed in terms of the two-point correlation function on the CTP, which is defined as

$$iG_{\alpha\beta}(x_1, x_2) \equiv \left\langle T_C \psi_\alpha(x_1) \bar{\psi}_\beta(x_2) \right\rangle \equiv \mathrm{Tr}\Big\{ \rho(t_0) T_C \psi_\alpha(x_1) \bar{\psi}_\beta(x_2) \Big\}\,, \tag{4.2.2}$$

where $\rho(t_0)$ is the density matrix at the initial time on the CTP, C denotes the CTP and T_C is the time-ordering operator on the CTP. The CTP two-point function can be split into several pieces depending on the location of the points x_1 and x_2 on the path, which is written in matrix form as

$$G(x_1, x_2) = \Big(G^{\epsilon\epsilon'}(x_1, x_2) \Big)_{\epsilon,\epsilon'=\pm} = \begin{bmatrix} G^{++}(x_1, x_2) & G^{+-}(x_1, x_2) \\ G^{-+}(x_1, x_2) & G^{--}(x_1, x_2) \end{bmatrix}\,, \tag{4.2.3}$$

where the indices + and − refer to the upper and lower branches of the path as indicated in figure 4.3 so that ϵ (ϵ') gives to the location of the point x_1 (x_2). The correlation functions $G^{\epsilon\epsilon'}$ can be defined in terms of regular propagators as

$$iG^{++}_{\alpha\beta}(x_1,x_2) \equiv iG^{F}_{\alpha\beta}(x_1,x_2) \equiv \left\langle T\psi_\alpha(x_1)\bar{\psi}_\beta(x_2)\right\rangle , \tag{4.2.4}$$

$$iG^{--}_{\alpha\beta}(x_1,x_2) \equiv iG^{\bar{F}}_{\alpha\beta}(x_1,x_2) \equiv \left\langle T_A\psi_\alpha(x_1)\bar{\psi}_\beta(x_2)\right\rangle , \tag{4.2.5}$$

$$iG^{+-}_{\alpha\beta}(x_1,x_2) \equiv iG^{<}_{\alpha\beta}(x_1,x_2) \equiv -\left\langle \bar{\psi}_\beta(x_2)\psi_\alpha(x_1)\right\rangle , \tag{4.2.6}$$

$$iG^{-+}_{\alpha\beta}(x_1,x_2) \equiv iG^{>}_{\alpha\beta}(x_1,x_2) \equiv \left\langle \psi_\alpha(x_1)\bar{\psi}_\beta(x_2)\right\rangle . \tag{4.2.7}$$

In the above expressions, T and T_A are respectively the real time-ordering and reverse time-ordering operators.

The retarded and advanced propagators are combinations of (4.2.4)-(4.2.7)

$$G^{R}_{\alpha\beta}(x_1,x_2) \equiv G^{F}_{\alpha\beta}(x_1,x_2) - G^{<}_{\alpha\beta}(x_1,x_2) = -i\theta\big(x_1^0-x_2^0\big)\left\langle\{\psi_\alpha(x_1),\bar{\psi}_\beta(x_2)\}\right\rangle , \tag{4.2.8}$$

$$G^{A}_{\alpha\beta}(x_1,x_2) \equiv G^{F}_{\alpha\beta}(x_1,x_2) - G^{>}_{\alpha\beta}(x_1,x_2) = i\theta\big(x_2^0-x_1^0\big)\left\langle\{\psi_\alpha(x_1),\bar{\psi}_\beta(x_2)\}\right\rangle . \tag{4.2.9}$$

Note that the four propagators in (4.2.4)-(4.2.7) are not independent. In particular, the anti-commutation relations for the fermion field operators imply that

$$G^{<} + G^{>} = G^{F} + G^{\bar{F}} . \tag{4.2.10}$$

Also, from the definition of the time ordering

$$G^{F}(x_1,x_2) = \theta\big(x_1^0-x_2^0\big)G^{>}(x_1,x_2) + \theta\big(x_2^0-x_1^0\big)G^{<}(x_1,x_2) . \tag{4.2.11}$$

Therefore, all correlators in (4.2.4)-(4.2.9) can be expressed in terms of $G^<$ and $G^>$.

Relations at equilibrium for bosonic two-point functions

Although only fermions were considered above, the CTP formalism is perfectly well adapted to describe bosonic real-time correlators as well. As we shall see in the next section, the transport of neutrinos is controlled by the chiral current real-time two-point functions in the medium. The latter is a bosonic correlator, which can be expressed in terms of the two-point function on the CTP

$$iG_{\mu\nu}(x_1,x_2) \equiv \langle T_C J_\mu(x_1)J_\nu(x_2)\rangle , \tag{4.2.12}$$

where J refers to the chiral current and we omitted the flavor indices. When the medium is at equilibrium, the 2-point function (4.2.12) obeys further constraints that we present here. Only the results are given, but the derivations are standard and simple. They are reviewed in Appendix L.1.

The first useful property obeyed by the 2-point function at equilibrium is related to the time-translation invariance of the system. If we focus on the time dependence of the propagators, it implies that

$$G_{\mu\nu}(t_1, t_2) = G_{\mu\nu}(\Delta t, 0) \equiv G_{\mu\nu}(\Delta t) \quad , \quad \Delta t \equiv t_1 - t_2 \,. \tag{4.2.13}$$

In particular, the retarded and advanced propagators are

$$iG^R_{\mu\nu}(\Delta t) = \theta(\Delta t) \left\langle [J_\mu(\Delta t), J_\nu(0)] \right\rangle \quad , \quad iG^A_{\mu\nu}(\Delta t) = -\theta(-\Delta t) \left\langle [J_\mu(0), J_\nu(-\Delta t)] \right\rangle \,. \tag{4.2.14}$$

In momentum space, the expressions (4.2.14) imply that the behavior of the retarded 2-point function under a change of sign of p^0 is fixed

$$\mathrm{Im}\, G^R_{\mu\nu}(-p^0) = -\mathrm{Im}\, G^R_{\mu\nu}(p^0) \quad , \quad \mathrm{Re}\, G^R_{\mu\nu}(-p^0) = \mathrm{Re}\, G^R_{\mu\nu}(p^0) \,. \tag{4.2.15}$$

The other equilibrium result that we use is a consequence of the so-called Kubo-Martin-Schwinger (KMS) symmetry. The latter gives a relation between the forward and backward propagators

$$G^<_B(p) = \mathrm{e}^{-\beta p^0} G^>_B(p) \,. \tag{4.2.16}$$

Using this result, $G^<_{\mu\nu}$ and $G^>_{\mu\nu}$ can be expressed in terms of the imaginary part of $G^R_{\mu\nu}$ only

$$G^<_{\mu\nu}(p) = 2i n_b(p^0) \mathrm{Im}\, G^R_{\mu\nu}(p) \,, \tag{4.2.17}$$

$$G^>_{\mu\nu}(p) = 2i\big(n_b(p^0) + 1\big) \mathrm{Im}\, G^R_{\mu\nu}(p) \,, \tag{4.2.18}$$

where n_b is the Bose-Einstein distribution

$$n_b(E) \equiv \frac{1}{\mathrm{e}^{\beta E} - 1} \,. \tag{4.2.19}$$

4.2.2 Boltzmann equation for neutrinos

We introduce in this subsection the equation which controls the dynamics of neutrino transport. The fundamental equation obeyed by the neutrino propagator is an exact QFT result, called the Kadanoff-Baym equation [296]. Upon certain semi-classical limits, this equation results in the Boltzmann equation for the neutrino distribution function, which is what neutrino transport simulations aim at solving. We first review the derivation of the Kadanoff-Baym equation from the Schwinger-Dyson equation, and then explain how the Boltzmann equation arises.

Note that the curvature of the space-time has an influence on the transport of neutrinos inside a neutron star. The equations obeyed by the neutrino propagators should therefore be written in a generally covariant form. To keep the presentation of the formalism as simple as possible, we consider the case of flat space-time. The covariant form can be inferred from the final form of the equations.

4.2.2.1 Kadanoff-Baym equation

To derive the Kadanoff-Baym equation, the starting point is the Schwinger-Dyson equation on the CTP contour. The latter relates the exact neutrino propagator G to the free propagator G^0 and the neutrino self-energy Σ

$$G(x_1, x_2) = G^0(x_1, x_2) + \int_C \mathrm{d}^4u\mathrm{d}^4v\, G^0(x_1, u)\Sigma(u, v)G(v, x_2)\,, \tag{4.2.20}$$

which is written diagrammatically in figure 4.4. The area of integration C contains inte-

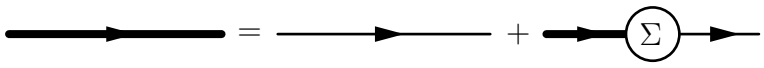

Figure 4.4: Diagrammatic representation of the Schwinger-Dyson equation (4.2.20). Thick lines correspond to exact fermion propagators and thin lines to free propagators.

grations over spatial coordinates and over the CTP contour. The self-energy is equal to the interacting part of the 1PI 2-point function

$$-i\Sigma \equiv \left\langle \psi\bar{\psi}\right\rangle_{\text{1PI}} - \left\langle \psi\bar{\psi}\right\rangle_{\text{1PI, free}}\,. \tag{4.2.21}$$

(4.2.20) is valid for any x_1, x_2 on the CTP and can be understood as a matrix equation, if we write the self-energy Σ in matrix form as in (4.2.3)

$$\Sigma(x_1, x_2) = \left(\Sigma^{\epsilon\epsilon'}(x_1, x_2)\right)_{\epsilon,\epsilon'=\pm} = \begin{bmatrix} \Sigma^{++}(x_1, x_2) & \Sigma^{+-}(x_1, x_2) \\ \Sigma^{-+}(x_1, x_2) & \Sigma^{--}(x_1, x_2) \end{bmatrix}\,. \tag{4.2.22}$$

In particular, the $+-$ component of (4.2.20) reads

$$\begin{aligned} G^<(x_1, x_2) \equiv G^{+-}(x_1, x_2) = G^{0,+-}(x_1, x_2) + \\ + \int_{t_0}^{\infty} \mathrm{d}^3u\mathrm{d}^3v\mathrm{d}u_{0,+}\mathrm{d}v_{0,+} G^{0,++}(x_1, u)\Sigma^{++}(u, v)G^{+-}(v, x_2) - \\ - \int_{t_0}^{\infty} \mathrm{d}^3u\mathrm{d}^3v\mathrm{d}u_{0,+}\mathrm{d}v_{0,-} G^{0,++}(x_1, u)\Sigma^{+-}(u, v)G^{--}(v, x_2) - \\ - \int_{t_0}^{\infty} \mathrm{d}^3u\mathrm{d}^3v\mathrm{d}u_{0,-}\mathrm{d}v_{0,+} G^{0,+-}(x_1, u)\Sigma^{-+}(u, v)G^{+-}(v, x_2) + \end{aligned}$$

$$+\int_{t_0}^{\infty} \mathrm{d}^3u\mathrm{d}^3v\mathrm{d}u_{0,-}\mathrm{d}v_{0,-}G^{0,+-}(x_1,u)\Sigma^{--}(u,v)G^{--}(v,x_2)\,, \tag{4.2.23}$$

where the subscripts + and − on the real times u_0 and v_0 indicate on which branch of the CTP the integral is performed. We then use the fact that the free propagator G^0 is the inverse of the Dirac operator $i\partial\!\!\!/ - m$, which implies in particular that

$$(i\partial\!\!\!/_x - m)G^{0,+-}(x,y) = 0 \quad , \quad (i\partial\!\!\!/_x - m)G^{0,++}(x,y) = \delta(x-y)\,. \tag{4.2.24}$$

Applying the Dirac operator to (4.2.23) therefore results in the following equation for $G^<$

$$(i\partial\!\!\!/_{x_1} - m)G^<(x_1,x_2) = \int \mathrm{d}^4v\left[\Sigma^{++}(x_1,v)G^<(v,x_2) - \Sigma^<(x_1,v)G^{--}(v,x_2)\right]\,. \tag{4.2.25}$$

(4.2.25) is called the Kadanoff-Baym equation for the propagator $G^<(x_1,x_2)$. In analogy to the neutrino propagator, we define $\Sigma^< = \Sigma^{+-}$ and $\Sigma^> = \Sigma^{-+}$.

The first step towards the Boltzmann equation, is to go from (4.2.25) to an equation for $G^<$ in momentum space. The appropriate way of doing so for correlators which generically are not translation-invariant, is via a *Wigner transform*, that is a Fourier transform with respect to the separation between the two points

$$F(X,k) \equiv \int \mathrm{d}^4y\, \mathrm{e}^{ik\cdot y} F\left(X+\frac{y}{2}, X-\frac{y}{2}\right)\,. \tag{4.2.26}$$

Note that the Wigner transform of a convolution is not the product of the Wigner transforms. We shall however consider the semiclassical *gradient approximation*

$$k \gg \partial_X\,, \tag{4.2.27}$$

which corresponds to requiring that the system is sufficiently dilute for the mean free path of a neutrino to be much larger than its de Broglie wavelength. In this approximation, the Wigner transform of a convolution is simply the product of the Wigner transforms. Then, assuming (4.2.27) and Wigner transforming (4.2.25) gives

$$(K\!\!\!/ - m)G^<(X,k) = \Sigma^{++}(X,k)G^<(X,k) - \Sigma^<(X,k)G^{--}(X,k)\,, \tag{4.2.28}$$

where we defined

$$K^\mu \equiv -k^\mu + \frac{i}{2}\partial_X^\mu\,. \tag{4.2.29}$$

There is another way of writing the Schwinger-Dyson equation, which is shown in figure 4.5. Starting from this alternative writing, the adjoint Kadanoff-Baym equation can be shown to be

$$G^<(X,k)\left(\overleftarrow{K\!\!\!/^*} - m\right) = G^{++}(X,k)\Sigma^<(X,k) - G^<(X,k)\Sigma^{--}(X,k)\,. \tag{4.2.30}$$

Figure 4.5: Alternative writing of the Schwinger-Dyson equation. The difference with figure 4.4 is whether the exact propagator comes before or after the self energy in the right-hand side.

Taking the trace of the difference of (4.2.28) and (4.2.30) results in an equation that depends only on the $+-$ and $-+$ correlators

$$i\partial_\mu^X \mathrm{Tr}\left\{\gamma^\mu G^<(X,k)\right\} = -\mathrm{Tr}\left\{G^>(X,k)\Sigma^<(X,k) - \Sigma^>(X,k)G^<(X,k)\right\}\,, \tag{4.2.31}$$

where we used the fact that for every two-point function F

$$F^{++} + F^{--} = F^< + F^>\,. \tag{4.2.32}$$

4.2.2.2 The Boltzmann equation

We now explain how the Boltzmann equation for the neutrino distribution function is derived from (4.2.31). This requires considering the so-called quasi-particle approximation.

The quasi-particle approximation consists in assuming that the propagator for the system out of equilibrium can be written in the same form as the free propagator at equilibrium[5]

$$\begin{aligned} iG^{0,<}(k) = -(\not{k} + m + \mu\gamma_0)\frac{\pi}{E_p}\Big[&n_f(E_p-\mu)\delta(E_p - k^0 - \mu) - \\ &- (1-n_f(E_p+\mu))\delta(E_p + k^0 + \mu)\Big]\,, \end{aligned} \tag{4.2.33}$$

$$\begin{aligned} iG^{0,>}(k) = (\not{k} + m + \mu\gamma_0)\frac{\pi}{E_p}\Big[&(1-n_f(E_p-\mu))\delta(E_p - k^0 - \mu) - \\ &- n_f(E_p+\mu)\delta(E_p + k^0 + \mu)\Big]\,, \end{aligned} \tag{4.2.34}$$

[5]See appendix L.2 for a review of the derivation of (4.2.33)-(4.2.34), and appendix L.3 for a more detailed discussion of the quasi-particle approximation.

but replacing the Fermi-Dirac distribution by space-time dependent particle and anti-particle distributions, $f_\nu(X;\vec{k})$ and $f_{\bar{\nu}}(X;\vec{k})$

$$iG^<_\nu(X;k_\nu) = -(\not{k}_\nu + \mu_\nu\gamma_0)\frac{1-\gamma^5}{2}\frac{\pi}{E_\nu}\Big[f_\nu(X;\vec{k}_\nu)\delta(E_\nu - k^0_\nu - \mu_\nu) - \\ - (1 - f_{\bar{\nu}}(X;-\vec{k}_\nu))\delta(E_\nu + k^0_\nu + \mu_\nu)\Big]\,, \tag{4.2.35}$$

$$iG^>_\nu(X;k_\nu) = \frac{1-\gamma^5}{2}(\not{k}_\nu + \mu_\nu\gamma_0)\frac{\pi}{E_\nu}\Big[(1 - f_\nu(X;\vec{k}_\nu))\delta(E_\nu - k^0_\nu - \mu_\nu) - \\ - f_{\bar{\nu}}(X;-\vec{k}_\nu)\delta(E_\nu + k^0_\nu + \mu_\nu)\Big]\,. \tag{4.2.36}$$

In the above expressions, we neglected the neutrino mass, E_ν is the on-shell neutrino energy

$$E_\nu = \sqrt{\vec{k}^2_\nu}\,, \tag{4.2.37}$$

and μ_ν is the chemical potential of neutrinos at $\beta-$equilibrium with the medium, which is related to the electron (μ_e) and isospin (μ_3) chemical potentials via

$$\mu_\nu = \mu_e + \mu_3\,. \tag{4.2.38}$$

Note also the presence of the left-handed projectors $(1-\gamma^5)/2$, which account for the left-handed nature of the neutrinos in the Standard Model.

The Boltzmann equations for neutrinos and anti-neutrinos are then obtained by substituting (4.2.35)-(4.2.36) into the Kadanoff-Baym equation (4.2.31)

$$(K_\nu\cdot\partial)f_\nu(X;\vec{k}_\nu) = -\frac{i}{4}\mathrm{Tr}\Big[\not{K}_\nu\Sigma^<(K_\nu)(1-f_\nu) + \Sigma^>(K_\nu)\not{K}_\nu f_\nu\Big]\,, \tag{4.2.39}$$

$$(K_\nu\cdot\partial)f_{\bar{\nu}}(X;\vec{k}_\nu) = \frac{i}{4}\mathrm{Tr}\Big[\not{K}_\nu\Sigma^<(-K_\nu)f_{\bar{\nu}} + \Sigma^>(-K_\nu)\not{K}_\nu(1-f_{\bar{\nu}})\Big]\,, \tag{4.2.40}$$

where K_ν is the on-shell neutrino momentum

$$K^\lambda_\nu \equiv \big(E_\nu,\vec{k}_\nu\big)\,. \tag{4.2.41}$$

The quasi-particle approximation is exact in the limit of free particles at equilibrium (both thermodynamic and $\beta-$equilibrium). It is therefore justified when the neutrino mean free path is large compared to the typical neutrino wavelength, and the neutrinos are close to equilibrium. In a neutron star, the neutrinos are at equilibrium for layers of the star such that the optical depth to the surface is much larger than one for all neutrino energies. This is typically the case in the core of the star, but not near the neutrinosphere. The quasiparticle approximation is expected to be valid near the core, but it is not clear to what

extent it is justified up to the neutrinosphere. In absence of alternative methods to the Boltzmann equation (solving directly the Kadanoff-Baym equation is too complicated), it is always assumed in astrophysical simulations that the quasiparticle approximation applies for neutrinos. We will therefore follow the same assumptions here.

As we shall see in the next subsection, the real time propagators for the electrons also appear in the neutrino Boltzmann equations, via the self-energies. The electrons are assumed to be at equilibrium with chemical potential μ_e, and in a regime where the quasiparticle approximation can be used. Within those assumptions, the electron propagators are given by

$$iG_e^<(t;p_e) = -(\not{p}_e + m_e + \mu_\epsilon\gamma_0)\frac{\pi}{E_e}\Big[f_e(t;\vec{p}_e)\delta(E_e - p_e^0 - \mu_e) - \\ - (1 - f_{\bar{e}}(t;-\vec{p}_e))\delta(E_e + p_e^0 + \mu_e)\Big]\,, \tag{4.2.42}$$

$$iG_e^>(t;p_e) = (\not{p}_e + m_e + \mu_e\gamma_0)\frac{\pi}{E_e}\Big[(1 - f_e(t;\vec{p}_e))\delta(E_e - p_e^0 - \mu_e) - \\ - f_{\bar{e}}(t;-\vec{p}_e)\delta(E_e + p_e^0 + \mu_e)\Big]\,, \tag{4.2.43}$$

where f_e and $f_{\bar{e}}$ are the electron and positron distribution functions, and $E_e \equiv \sqrt{\vec{k}_e^2 + m_e^2}$ is the on-shell electron energy.

4.2.3 Charged current self-energy

As we have explained in the previous section, the Boltzmann equation is determined by the neutrino self-energy. In this section, we derive the neutrino self-energy (4.2.21) at leading order in the weak coupling Fermi constant G_F. We restrict our analysis in this work to the contribution from the charged current interaction of electronic neutrinos with the baryonic matter

$$u + e^- \rightleftharpoons d + \nu_e\,. \tag{4.2.44}$$

This means that several other components are not considered here:

- The neutrino self-energy receives a contribution from the *neutral current* interactions

$$\nu + q \rightleftharpoons \nu + q \quad , \quad \bar{\nu} + q \rightleftharpoons \bar{\nu} + q\,, \tag{4.2.45}$$

$$q + q' \rightleftharpoons \nu + \bar{\nu} + q + q'\,, \tag{4.2.46}$$

  where q and q' are quarks. Those interactions are not negligible a priori and should be taken into account when addressing neutrino transport. The calculation of neutral current neutrino self-energies in holography will be the subject of a future work.

- In general, the other charged leptons contribute if they are present in the medium. In particular, there may be a significant *muon* component in the core of neutron stars [283, 284]. We assume in this work that the only charged leptons present in the medium are electrons. In presence of muons, the muonic neutrinos also couple to the medium, and their transport is described by a separate Boltzmann equation.

- The propagating neutrinos do not interact only with the baryonic matter, but also with the leptons contained in the medium. Assuming the leptonic component to be composed of electrons, the corresponding charged current processes are given by

$$\nu_e + e^- \rightleftharpoons \nu_e + e^- \quad , \quad \bar{\nu} + e^+ \rightleftharpoons \bar{\nu} + e^+ \,. \tag{4.2.47}$$

$$e^+ + e^- \rightleftharpoons \nu_e + \bar{\nu}_e \,. \tag{4.2.48}$$

  The contribution to the neutrino self-energy from these leptonic processes can be derived from a weakly-coupled calculation, which can be added independently from the strongly coupled component considered here. The expressions can be found in [285].

The Feynman diagram for the $+-$ neutrino self-energy from the reaction (4.2.44) at order $\mathcal{O}(G_F^2)$ is represented in figure 4.6. Applying the Feynman rules in the limit where

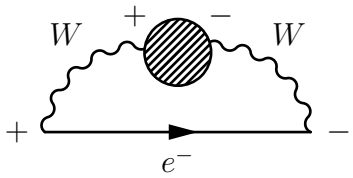

Figure 4.6: Diagram for the calculation of the charged current $+-$ neutrino self-energy at leading order in the electroweak interactions. Lines correspond to free propagators, whereas the hatched blob denotes the W current-current correlator in the dense medium $\left\langle J_\mu^- J_\nu^+ \right\rangle$. This two-point function is the exact non-perturbative quantity, that is computed holographically in this work. For illustration, the one-loop contributions to this correlator are shown in figure 4.7, where only the quark component is considered here. The $+$ and $-$ are the Schwinger-Keldysh indices referring to the location of the operators on the CTP contour in figure 4.3.

the neutrino momentum is much smaller than the W-boson mass[6] yields the following

[6] In which case the free W diagonal propagators reduce to $-iG^{0;\pm\pm}_{W,\mu\nu} = \frac{\delta_{\mu\nu}}{M_W^2}$. See appendix M for a review of the weak vertices involved in neutrino interactions.

result for the self-energy

$$\Sigma_c^<(X;k_\nu) = -2iG_F^2 \int \frac{\mathrm{d}^4 k_e}{(2\pi)^4} \gamma^\lambda (1-\gamma^5)\big(iG_e^<(k_e)\big)\gamma^\sigma(1-\gamma^5)\big(iG^>_{c,\sigma\lambda}(k_e-k_\nu)\big)\,. \quad (4.2.49)$$

where we defined the W boson 2-point function

$$iG_{c,\sigma\lambda} \equiv \left\langle J^-_\sigma J^+_\lambda \right\rangle\,, \quad (4.2.50)$$

$J^\pm_\lambda$ being the W boson current. The expression for the backward self-energy $\Sigma_c^>$ is obtained from (4.2.49) by exchanging the $<$ and $>$.

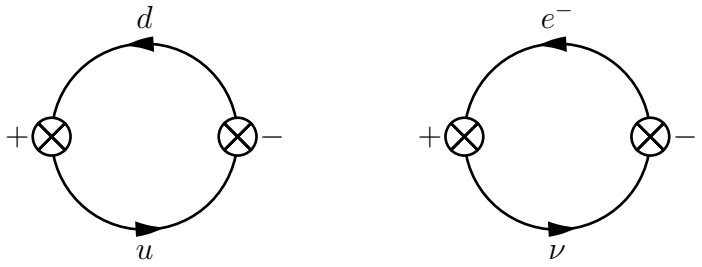

Figure 4.7: 1-loop diagram for the W $-+$ current-current correlator, from the quark (left) and lepton (right) contributions. Only the quark component is included in this work.

We now proceed to write the quark contribution to the W current J^+_λ in terms of the chiral currents $J^{(L/R)}_\lambda$. As we shall see in the next section, the latter are the duals of the bulk gauge fields in the holographic set-up. We assume here for simplicity that N_f is even and the quarks are divided into an equal number of up and down type quarks. Later we will set $N_f = 2$. The quark W current is

$$J^{+,\lambda} = -M^{\mathrm{CKM}}_{ij}\bar{u}^i\gamma^\lambda\frac{1-\gamma^5}{2}d^j\,, \quad (4.2.51)$$

where u is a vector that gathers the $N_f/2$ up flavors of quarks (of weak isospin $I^3 = 1/2$) and d gathers the $N_f/2$ down flavors of quarks (of weak isospin $I^3 = -1/2$), N_f being the number of flavors. M^{CKM}_{ij} is the CKM matrix that determines the mixing between mass and weak eigenstates of the quarks. As for the chiral currents, they are expressed as

$$J^{(L/R),\lambda}_{ij} = \bar{q}^i\gamma^\lambda\frac{1\mp\gamma^5}{2}q^j\,, \quad (4.2.52)$$

where the minus sign is for the left-handed current. The vector q contains all the N_f flavors of quarks

$$q = \begin{pmatrix} u \\ d \end{pmatrix} . \tag{4.2.53}$$

In order to write the W current (4.2.51) in terms of the chiral currents (4.2.52), we introduce the enlarged CKM matrix

$$\tilde{M}^{\mathrm{CKM}} \equiv \left(\begin{array}{c|c} \mathbf{0} & M^{\mathrm{CKM}} \\ \hline \mathbf{0} & \mathbf{0} \end{array}\right) , \tag{4.2.54}$$

of size $N_f \times N_f$. (4.2.51) can then be written as

$$J^{+,\lambda} = -\tilde{M}^{\mathrm{CKM}}_{ij} J^{(L),\lambda}_{ij} . \tag{4.2.55}$$

4.2.4 Emissivity and absorption

In this subsection, the results from Sections 4.2.2 and 4.2.3 are combined to obtain the final form of the kinetic equation obeyed by the neutrino distributions. From there, the radiative coefficients that control the neutrino transport are identified, and classified according to the radiative process they correspond to.

Substituting the expression for the charged current self-energy (4.2.49) into the Boltzmann equations (4.2.39) and (4.2.40) results in the following kinetic equations for the neutrino and anti-neutrino distribution functions

$$\begin{aligned} \frac{K_\nu \cdot \partial}{E_\nu} f_\nu = \frac{iG_F^2}{4} \int \frac{\mathrm{d}^3 k_e}{(2\pi)^3} \frac{1}{E_e E_\nu} \times \\ \times \Big[L_e^{\lambda\sigma} \Big((1-f_\nu) f_e G^{>}_{c,\sigma\lambda}(q_{e\nu}) - f_\nu (1-f_e) G^{<}_{c,\sigma\lambda}(q_{e\nu}) \Big) + \\ + L_{\bar{e}}^{\lambda\sigma} \Big((1-f_\nu)(1-f_{\bar{e}}) G^{>}_{c,\sigma\lambda}(q_{\bar{e}\nu}) - f_\nu f_{\bar{e}} G^{<}_{c,\sigma\lambda}(q_{\bar{e}\nu}) \Big) \Big], \end{aligned} \tag{4.2.56}$$

$$\frac{K_\nu \cdot \partial}{E_\nu} f_{\bar{\nu}} = -\frac{iG_F^2}{4} \int \frac{\mathrm{d}^3 k_e}{(2\pi)^3} \frac{1}{E_e E_\nu} \times$$

$$\times \Big[L_e^{\lambda\sigma} \Big(f_{\bar\nu} f_e G^{>}_{c,\sigma\lambda}(q_{e\bar\nu}) - (1-f_{\bar\nu})(1-f_e) G^{<}_{c,\sigma\lambda}(q_{e\bar\nu}) \Big) + \\ + L_{\bar e}^{\lambda\sigma} \Big(f_{\bar\nu}(1-f_{\bar e}) G^{>}_{c,\sigma\lambda}(q_{\bar e\bar\nu}) - (1-f_{\bar\nu}) f_{\bar e} G^{<}_{c,\sigma\lambda}(q_{\bar e\bar\nu}) \Big) \Big], \tag{4.2.57}$$

where f_ν and $f_{\bar\nu}$ both have argument $(X, \vec{k}_\nu)$, and f_e and $f_{\bar e}$ argument $(X, \vec{k}_e)$. We defined several condensed notations for the momenta $k_e - k_\nu$ in the different leptonic sectors

$$q_{e\nu} \equiv (E_e - E_\nu - \mu_e + \mu_\nu, \vec{k}_e - \vec{k}_\nu) \quad , \quad q_{e\bar\nu} \equiv (E_e + E_\nu - \mu_e + \mu_\nu, \vec{k}_e + \vec{k}_\nu)\,, \tag{4.2.58}$$

$$q_{\bar e\nu} \equiv (-E_e - E_\nu - \mu_e + \mu_\nu, -\vec{k}_e - \vec{k}_\nu) \quad , \quad q_{\bar e\bar\nu} \equiv (-E_e + E_\nu - \mu_e + \mu_\nu, -\vec{k}_e + \vec{k}_\nu)\,, \tag{4.2.59}$$

and the lepton tensors

$$L^{\lambda\sigma}_{(e/\bar e)} \equiv \mathrm{Tr}\left[(\not{K}_e \pm m_e)\gamma^\sigma(1-\gamma_5)\not{K}_\nu\gamma^\lambda(1-\gamma^5) \right]. \tag{4.2.60}$$

In (4.2.60) the $+$ is for e and the $-$ for $\bar e$, and the K's refer to the on-shell momenta

$$K_e \equiv (E_e, \vec{k}_e) \quad , \quad K_\nu \equiv (E_\nu, \vec{k}_\nu)\,. \tag{4.2.61}$$

Computing explicitly the trace in (4.2.60) gives

$$L^{\lambda\sigma}_{\bar e} = L^{\lambda\sigma}_e = 8\left(K_e^\lambda K_\nu^\sigma + K_e^\sigma K_\nu^\lambda - (K_e.K_\nu)\eta^{\lambda\sigma} + i\epsilon^{\lambda\sigma\alpha\beta} K_{e,\alpha} K_{\nu,\beta} \right). \tag{4.2.62}$$

Note that the antisymmetric part will vanish in the contraction with the current-current correlator if the medium is assumed to be isotropic and the interactions preserve parity.

The transport equation for neutrinos can be further simplified by assuming that the medium in which they scatter is at equilibrium. This implies that the electrons follow the Fermi-Dirac distribution

$$f_e(\vec{k}_e) = n_f(E_e - \mu_e) \equiv n_e \quad , \quad f_{\bar e}(\vec{k}_e) = n_f(E_e + \mu_e) \equiv n_{\bar e}\,, \tag{4.2.63}$$

and the chiral current 2-point functions can be expressed in terms of the retarded correlators according to (4.2.17) and (4.2.18). Then, (4.2.56) and (4.2.57) become

$$\frac{K_\nu\cdot\partial}{E_\nu} f_\nu = -\frac{G_F^2}{2}\int \frac{\mathrm{d}^3k_e}{(2\pi)^3}\frac{1}{E_e E_\nu} L_e^{\lambda\sigma} \times \\ \times \Big[\mathrm{Im}\, G^R_{c,\sigma\lambda}(q_{e\nu}) \big((1-f_\nu) n_e (1+n_b(q^0_{e\nu})) - f_\nu (1-n_e) n_b(q^0_{e\nu}) \big) + \\ + \mathrm{Im}\, G^R_{c,\sigma\lambda}(q_{\bar e\nu}) \big((1-f_\nu)(1-n_{\bar e})(1+n_b(q^0_{\bar e\nu})) - f_\nu n_{\bar e} n_b(q^0_{\bar e\nu}) \big) \Big], \tag{4.2.64}$$

$$\frac{K_\nu\cdot\partial}{E_\nu} f_{\bar\nu} = \frac{G_F^2}{2}\int \frac{\mathrm{d}^3k_e}{(2\pi)^3}\frac{1}{E_e E_\nu} L_e^{\lambda\sigma} \times$$

$$\times \Big[\mathrm{Im}\, G^R_{c,\sigma\lambda}(q_{e\bar\nu}) \left(f_{\bar\nu} n_e (1 + n_b(q^0_{e\bar\nu})) - (1 - f_{\bar\nu})(1 - n_e) n_b(q^0_{e\bar\nu}) \right) + \\ + \mathrm{Im}\, G^R_{c,\sigma\lambda}(q_{\bar e\bar\nu}) \left(f_{\bar\nu} (1 - n_{\bar e})(1 + n_b(q^0_{\bar e\bar\nu})) - (1 - f_{\bar\nu}) n_{\bar e} n_b(q^0_{\bar e\bar\nu}) \right) \Big] . \tag{4.2.65}$$

The emissivities $j(E_\nu), \bar j(E_\nu)$ and mean free paths $\lambda(E_\nu), \bar\lambda(E_\nu)$ are defined such that

$$\frac{K_\nu \cdot \partial}{E_\nu} f_\nu \equiv j(E_\nu)(1 - f_\nu) - \frac{1}{\lambda(E_\nu)} f_\nu \,, \tag{4.2.66}$$

$$\frac{K_\nu \cdot \partial}{E_\nu} f_{\bar\nu} \equiv \bar j(E_\nu)(1 - f_{\bar\nu}) - \frac{1}{\bar\lambda(E_\nu)} f_{\bar\nu} \,. \tag{4.2.67}$$

The two radiative coefficients are themselves the sum of two terms, corresponding to the contributions from electrons and positrons

$$j(E_\nu) = j_{e^-}(E_\nu) + j_{e^+}(E_\nu) \quad , \quad \bar j(E_\nu) = \bar j_{e^-}(E_\nu) + \bar j_{e^+}(E_\nu) \,, \tag{4.2.68}$$

$$\frac{1}{\lambda(E_\nu)} = \frac{1}{\lambda_{e^-}(E_\nu)} + \frac{1}{\lambda_{e^+}(E_\nu)} \quad , \quad \frac{1}{\bar\lambda(E_\nu)} = \frac{1}{\bar\lambda_{e^-}(E_\nu)} + \frac{1}{\bar\lambda_{e^+}(E_\nu)} \,. \tag{4.2.69}$$

In the quasi-particle picture, each of these coefficients can be associated with a given weak interaction process between the neutrinos and the baryonic matter

$$e^- + u \rightleftharpoons \nu + d \,: \quad \left(j_{e^-} \,, \lambda_{e^-} \right) \quad , \quad d + e^+ \rightleftharpoons \bar\nu + d \,: \quad \left(\bar j_{e^+} \,, \bar\lambda_{e^+} \right) , \tag{4.2.70}$$

$$u \rightleftharpoons \nu + d + e^+ \,: \quad \left(j_{e^+} \,, \lambda_{e^+} \right) \quad , \quad d \rightleftharpoons \bar\nu + u + e^- \,: \quad \left(\bar j_{e^-} \,, \bar\lambda_{e^-} \right) . \tag{4.2.71}$$

These are identified as the various versions of the β reaction (4.2.44). Note that, as mentioned before, the purely leptonic processes are not included. Also, as far as the baryonic component of the medium is concerned, the quasi-particle picture is not expected to give a good description of the interaction of the leptons with the strongly-coupled QCD matter. Writing the weak reactions as in (4.2.70)-(4.2.71) corresponds to approximating the chiral current two-point functions with the 1-loop contribution, which comes from the diagrams in figure 4.7. However, at strong coupling, the exact 2-point functions receive contributions from all numbers of loops, which means that the weak processes that occur typically involve many quarks and gluons. It is still useful to make the identification as in (4.2.70)-(4.2.71) because it summarizes the exchange of flavor charges that occurs in each reaction. It also makes it clear what is the relation between the various coefficients that we defined and the weak processes that are usually considered in the literature, from a weakly-coupled perspective.

From (4.2.64) and (4.2.65), the expressions for the various contributions to the emissivity and absorption can be identified to be

$$j_{e^-}(E_\nu) = -\frac{G_F^2}{2} \int \frac{\mathrm{d}^3 k_e}{(2\pi)^3} \frac{1}{E_e E_\nu} L_e^{\lambda\sigma} \mathrm{Im}\, G^R_{c,\sigma\lambda}(q_{e\nu}) n_e \big(1 + n_b(q^0_{e\nu})\big) \,,$$

$$j_{e^+}(E_\nu) = -\frac{G_F^2}{2}\int \frac{\mathrm{d}^3k_e}{(2\pi)^3}\frac{1}{E_eE_\nu}L_e^{\lambda\sigma}\mathrm{Im}\,G^R_{c,\sigma\lambda}(q_{\bar{e}\nu})(1-n_{\bar{e}})\big(1+n_b(q^0_{\bar{e}\nu})\big)\,, \tag{4.2.72}$$

$$\frac{1}{\lambda_{e^-}(E_\nu)} = -\frac{G_F^2}{2}\int \frac{\mathrm{d}^3k_e}{(2\pi)^3}\frac{1}{E_eE_\nu}L_e^{\lambda\sigma}\mathrm{Im}\,G^R_{c,\sigma\lambda}(q_{e\nu})(1-n_e)n_b(q^0_{e\nu})\,,$$

$$\frac{1}{\lambda_{e^+}(E_\nu)} = -\frac{G_F^2}{2}\int \frac{\mathrm{d}^3k_e}{(2\pi)^3}\frac{1}{E_eE_\nu}L_e^{\lambda\sigma}\mathrm{Im}\,G^R_{c,\sigma\lambda}(q_{\bar{e}\nu})n_{\bar{e}}n_b(q^0_{\bar{e}\nu})\,, \tag{4.2.73}$$

$$\bar{j}_{e^-}(E_\nu) = -\frac{G_F^2}{2}\int \frac{\mathrm{d}^3k_e}{(2\pi)^3}\frac{1}{E_eE_\nu}L_e^{\lambda\sigma}\mathrm{Im}\,G^R_{c,\sigma\lambda}(q_{e\bar{\nu}})(1-n_e)n_b(q^0_{e\bar{\nu}})\,,$$

$$\bar{j}_{e^+} = -\frac{G_F^2}{2}\int \frac{\mathrm{d}^3k_e}{(2\pi)^3}\frac{1}{E_eE_\nu}L_e^{\lambda\sigma}\mathrm{Im}\,G^R_{c,\sigma\lambda}(q_{\bar{e}\bar{\nu}})n_{\bar{e}}n_b(q^0_{\bar{e}\bar{\nu}})\,, \tag{4.2.74}$$

$$\frac{1}{\bar{\lambda}_{e^-}(E_\nu)} = -\frac{G_F^2}{2}\int \frac{\mathrm{d}^3k_e}{(2\pi)^3}\frac{1}{E_eE_\nu}L_e^{\lambda\sigma}\mathrm{Im}\,G^R_{c,\sigma\lambda}(q_{e\bar{\nu}})n_e\big(1+n_b(q^0_{e\bar{\nu}})\big)\,,$$

$$\frac{1}{\bar{\lambda}_{e^+}(E_\nu)} = -\frac{G_F^2}{2}\int \frac{\mathrm{d}^3k_e}{(2\pi)^3}\frac{1}{E_eE_\nu}L_e^{\lambda\sigma}\mathrm{Im}\,G^R_{c,\sigma\lambda}(q_{\bar{e}\bar{\nu}})(1-n_{\bar{e}})\big(1+n_b(q^0_{\bar{e}\bar{\nu}})\big)\,. \tag{4.2.75}$$

Detailed balance Because the medium in which the neutrinos scatter is assumed to be at equilibrium, the charged current emissivities and mean free paths (4.2.72)-(4.2.75) are actually related by a detailed balance condition. In terms of the fermionic and bosonic equilibrium distribution functions, detailed balance refers to the equalities

$$n_e\big(1+n_b(q^0_{e\nu})\big) = (1-n_e)n_b(q^0_{e\nu})\mathrm{e}^{-\beta(E_\nu-\mu_\nu)}\,, \tag{4.2.76}$$

$$(1-n_{\bar{e}})\big(1+n_b(q^0_{\bar{e}\nu})\big) = n_{\bar{e}}n_b(q^0_{\bar{e}\nu})\mathrm{e}^{-\beta(E_\nu-\mu_\nu)}\,, \tag{4.2.77}$$

$$n_e\big(1+n_b(q^0_{e\bar{\nu}})\big) = (1-n_e)n_b(q^0_{e\bar{\nu}})\mathrm{e}^{-\beta(-E_\nu-\mu_\nu)}\,, \tag{4.2.78}$$

$$(1-n_{\bar{e}})\big(1+n_b(q^0_{\bar{e}\bar{\nu}})\big) = n_{\bar{e}}n_b(q^0_{\bar{e}\bar{\nu}})\mathrm{e}^{-\beta(-E_\nu-\mu_\nu)}\,, \tag{4.2.79}$$

which imply that

$$j_{e^-,e^+}(E_\nu) = \frac{\mathrm{e}^{-\beta(E_\nu-\mu_\nu)}}{\lambda_{e^-,e^+}(E_\nu)}\,, \tag{4.2.80}$$

$$\bar{j}_{e^-,e^+}(E_\nu) = \frac{\mathrm{e}^{-\beta(E_\nu+\mu_\nu)}}{\bar{\lambda}_{e^-,e^+}(E_\nu)}\,. \tag{4.2.81}$$

Due to the detailed balance relations, the emissivity and absorption are not independent quantities. It is therefore sufficient to study one of the two quantities, or a linear

combination. The usual quantity that is considered is the opacity corrected for stimulated absorption [274],

$$\kappa(E_\nu) \equiv j(E_\nu) + \frac{1}{\lambda(E_\nu)}\,, \tag{4.2.82}$$

which determines the (E_ν-dependent) location of the neutrinosphere.

We conclude this section by commenting on the expressions obtained for the neutrino radiative coefficients (4.2.72)-(4.2.75). Up to kinematic and statistical factors that are straightforwardly determined from the quasi-particle approximation (4.2.42)-(4.2.43), all the contributions are expressed in terms of only one function : *the imaginary part of the retarded 2-point function for the charged chiral currents*. All the processes in (4.2.70)-(4.2.71) are captured by this single correlator. Computing this correlator in neutron-star matter is a strongly-coupled problem, which is why the transport of neutrinos in neutron stars remains an unsettled issue. In this work, we consider a simple holographic model where the strongly-coupled computation of the chiral current 2-point function can be done exactly. The holographic model and the computation of the retarded correlator are described in the next sections.

4.3 The holographic model

We introduce in this section the holographic model that is used to compute the charged current retarded correlator. It is the simplest bottom-up model describing the dynamics of chiral current operators. We assume therefore the strongly interacting medium is described by a strongly interacting quantum theory with N_f quarks and $U(N_f)_L \times U(N_f)_R$ chiral symmetry. According to holographic duality, this theory is dual to a five dimensional gravitational theory that lives on five dimensional Anti-de Sitter space AdS_5, which is a constant negative curvature space with a four-dimensional boundary. It is this form of the theory that we solve using gravitational methods in order to compute the two-point current-current correlator.

The background solution of this model at finite temperature and density will be then reviewed, and the expressions of the particle densities will be determined as a function of the chemical potentials.

4.3.1 Action

We consider a five-dimensional asymptotically AdS bulk theory, whose field content is dictated by the types of operators that we want the dual (boundary) quantum field theory to include. In the present case, the operators of interest are the chiral currents $J_\mu^{(L/R)}$, which are dual to chiral gauge fields in the five dimensional bulk $\mathbf{L}_M$ and $\mathbf{R}_M$. The latter, are elements of the Lie algebra of the chiral group $\mathrm{U}(N_f)_L\times\ \mathrm{U}(N_f)_R$. The bulk gravitational

action is constructed as the sum of a color and a flavor part

$$S = S_c + S_f \,. \tag{4.3.1}$$

The action for the color sector is the 5-dimensional Einstein-Hilbert action

$$S_{\rm c} = M^3 N_c^2 \int {\rm d}^5x\sqrt{-g}\,\left(R + \frac{12}{\ell^2}\right)\,, \tag{4.3.2}$$

where R is the 5D Ricci scalar, M the 5D Planck mass, ℓ the AdS radius and N_c the number of colors. For the flavor sector, we make the simplest choice of a quadratic Yang-Mills action for the chiral gauge fields

$$S_f = -\frac{1}{8\ell}(M\ell)^3 w_0^2 N_c \int {\rm d}^5x\sqrt{-g}\left({\rm Tr}\,\mathbf{F}^{(L)}_{MN}\mathbf{F}^{MN,(L)} + {\rm Tr}\,\mathbf{F}^{(R)}_{MN}\mathbf{F}^{MN,(R)}\right)\,, \tag{4.3.3}$$

where w_0 is the flavor Yang-Mills coupling, and $\mathbf{F}^{(L/R)}$ are the field strengths of the gauge fields $\mathbf{L}$ and $\mathbf{R}$

$$\mathbf{F}^{(L)} \equiv {\rm d}\mathbf{L} - i\mathbf{L}\wedge\mathbf{L} \quad , \quad \mathbf{F}^{(R)} \equiv {\rm d}\mathbf{R} - i\mathbf{R}\wedge\mathbf{R}\,. \tag{4.3.4}$$

As usual in holographic theories, the number of colors N_c is assumed to be large in order for the semi-classical treatment of the bulk theory to be valid. Since we are interested in describing dense baryonic matter, the back-reaction of the flavor sector on the glue sector will play an important role. In order for this back-reaction to be finite, we consider the so-called Veneziano large N limit

$$N_c \to \infty \quad , \quad N_f \to \infty \quad , \quad \frac{N_f}{N_c} \text{ fixed}\,. \tag{4.3.5}$$

Although N_c and N_f are assumed to be large, finite values of N_c and N_f will eventually be substituted in the large N result for phenomenological applications. Specifically, N_c will be set to 3, and from now on we fix the flavor sector to be composed of $N_f = 2$ massless flavors. When the chiral group is ${\rm U}(2)_L\times{\rm U}(2)_R$, the chiral currents and their dual gauge fields can be decomposed in the Pauli basis $\{\sigma_a\}$

$$J^{(L)}_\mu = \frac{1}{2}\hat{J}^{(L)}_\mu\mathbb{I}_2 + \frac{1}{2}\sum_{a=1}^3 J^{a,(L)}_\mu\sigma_a \quad , \quad \mathbf{L}_M = \frac{1}{2}\hat{L}_M\mathbb{I}_2 + \frac{1}{2}\sum_{a=1}^3 L^a_M\sigma_a\,,$$

$$J^{(R)}_\mu = \frac{1}{2}\hat{J}^{(R)}_\mu\mathbb{I}_2 + \frac{1}{2}\sum_{a=1}^3 J^{a,(R)}_\mu\sigma_a \quad , \quad \mathbf{R}_M = \frac{1}{2}\hat{R}_M\mathbb{I}_2 + \frac{1}{2}\sum_{a=1}^3 R^a_M\sigma_a\,, \tag{4.3.6}$$

and the CKM matrix (4.2.54) takes the form

$$\tilde{M}^{\rm CKM} = \begin{pmatrix} 0 & M_{ud} \\ 0 & 0 \end{pmatrix}\,. \tag{4.3.7}$$

Then, substituting the decomposition (4.3.6) into the definition of the charged current (4.2.55) gives

$$J^{+,\lambda} = -\frac{1}{2} M_{ud} \Big(J_1^{(L),\lambda} - i J_2^{(L),\lambda} \Big) \,. \tag{4.3.8}$$

Among the bulk gauge fields, the charged currents will therefore be dual to L_1 and L_2, that is the non-abelian left-handed gauge fields orthogonal to the isospin direction.

4.3.2 Background solution

We now present the background solution for the bulk action (4.3.2), at finite temperature and density. The dual state of matter that it describes in the dual boundary theory corresponds to a plasma of deconfined (generalized) quarks and gluons. Introducing a finite density of deconfined baryonic matter is equivalent to sourcing the bulk baryon number gauge field with a chemical potential

$$\hat{V}_0 \Big|_{\text{boundary}} = 2\mu \,, \tag{4.3.9}$$

where we defined the vector gauge field

$$\mathbf{V}_M \equiv \mathbf{L}_M + \mathbf{R}_M = \frac{1}{2} \hat{V}_M \mathbb{I}_2 + \frac{1}{2} \sum_{a=1}^{3} V_M^a \sigma_a \,. \tag{4.3.10}$$

μ is the quark number chemical potential, related to the baryon number chemical potential by $\mu_B = N_c \mu$. Then, the background solution is given by the solution of the Einstein-Maxwell equations obeying the boundary condition (4.3.9), together with appropriate regularity conditions in the IR. The derivation of the solution is reviewed in appendix N. It corresponds to an asymptotically AdS_5 Reissner-Nordström (RN) black-hole[7], with metric

$$\mathrm{ds}^2 = \mathrm{e}^{2A(r)} \left(-f(r) \mathrm{dt}^2 + f(r)^{-1} \mathrm{dr}^2 + \vec{\mathrm{dx}}^2 \right) \,, \tag{4.3.11}$$

where

$$\mathrm{e}^{A(r)} = \frac{\ell}{r} \quad , \quad f(r) = 1 - \left(\frac{r}{r_H} \right)^4 \left(1 + 2 \left(1 - \pi T r_H \right) \right) + 2 \left(1 - \pi T r_H \right) \left(\frac{r}{r_H} \right)^6 \,, \tag{4.3.12}$$

$$r_H = \frac{2}{\pi T} \left(1 + \sqrt{1 + \frac{w_0^2}{3 N_c} \frac{\mu^2}{\pi^2 T^2}} \right)^{-1} \,. \tag{4.3.13}$$

[7] The phase diagram and the associated thermodynamics of RN black holes has been studied in holography in [279, 280].

The background solution for the gauge field is given by

$$\hat{V}_0 = 2\mu \left(1 - \left(\frac{r}{r_H}\right)^2\right) . \tag{4.3.14}$$

In (4.3.11), the coordinate r is the holographic coordinate, defined such that the AdS boundary is located at $r = 0$ and the horizon at $r = r_H$. Note that the background that we consider is such that all non-abelian gauge fields vanish. In particular, the field dual to the isospin current is not sourced, meaning that the dual thermal state is isospin symmetric, with isospin chemical potential

$$\mu_3 = 0 . \tag{4.3.15}$$

In the following, we consider conditions relevant for neutron stars, where the baryon chemical potential is much higher than the temperature, i.e. $\mu \gg T$. In this limit, the charged black-hole is nearly extremal and the horizon radius is essentially controlled by the chemical potential

$$r_H = \sqrt{\frac{3N_c}{w_0^2}} \frac{2}{\mu} \left(1 + \mathcal{O}\left(\frac{T}{\mu}\right)\right) . \tag{4.3.16}$$

4.3.3 Particle densities

In (4.3.14), the background gauge field is expressed in terms of the baryon number chemical potential $\mu_B = N_c\mu$. Instead of the chemical potential, the relevant physical observable is given by the dual thermodynamic state variable, that is the baryon density. In this subsection, we explain how the chemical potential μ is traded for the baryon density n_B. We also compute the chemical potentials for the leptons at equilibrium with the baryonic matter.

The baryon density is defined to be the vev of the 0 component of the baryon current

$$n_B \equiv \frac{1}{N_c} \left\langle \hat{J}_L^0 + \hat{J}_R^0 \right\rangle , \tag{4.3.17}$$

and the current vev is obtained by differentiating the grand-canonical potential Ω with respect to μ_B. The holographic correspondence states that Ω is equal to minus the Euclidean on-shell bulk action, [279, 280]

$$\Omega = -S^E_{\text{on-shell}} = -(M\ell)^3 \left(N_c^2 r_H^{-4} + N_c \frac{w_0^2}{6} \mu^2 r_H^{-2}\right) V_3 , \tag{4.3.18}$$

where V_3 is the volume of the boundary 3-dimensional Euclidean space. This gives the following expression for the equilibrium density

$$n_B(\mu, T) = -\frac{1}{V_3} \frac{\partial \Omega}{\partial \mu_B} = (M\ell)^3 w_0^2 (r_H T)^{-2} T^2 \mu , \tag{4.3.19}$$

where the dimensionless quantity $r_H T$ is a function of the ratio μ/T that we reproduce here for convenience

$$r_H T = \frac{2}{\pi}\left(1+\sqrt{1+\frac{w_0^2}{3N_c}\frac{\mu^2}{\pi^2 T^2}}\right)^{-1} . \tag{4.3.20}$$

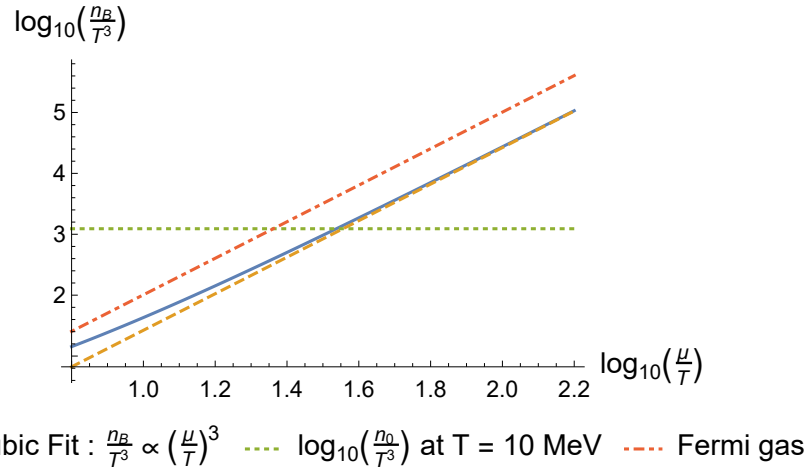

Figure 4.8: The dependence of the baryon number density n_B on the baryonic chemical potential μ. The precise quantity that is shown is the density in units of the temperature, n_B/T^3. The latter does not depend independently on T and μ, but only on μ/T. The dashed orange line corresponds to the cubic fit at high density $\mu \gg T$, (4.3.21). For comparison with the typical scales in a neutron star, the dotted green line indicates the value of the nuclear saturation density $n_0 \simeq 0.16\,\mathrm{fm}^{-3}$, in units of the temperature at $T = 10\,\mathrm{MeV}$. We also compare our result with the degenerate Fermi gas at $\beta-$equilibrium, which is shown as the red dot-dashed line.

At high density $\mu \gg T$, the expression (4.3.19) simplifies and n_B is found to behave as μ^3

$$n_B(\mu) = \frac{(M\ell)^3 w_0^4}{12N_c}\mu^3\left(1+\mathcal{O}\left(\frac{T}{\mu}\right)\right) . \tag{4.3.21}$$

The profile for n_B/T^3 as a function of μ/T is shown in figure 4.8, where the parameters are those of Appendix O. For comparison, figure 4.8 also shows the relation between n_B and μ in the case where all fermionic species are described by a degenerate Fermi gas. The quark matter described by our model is seen to have a harder equation of state than the degenerate Fermi gas, but the two are relatively close.

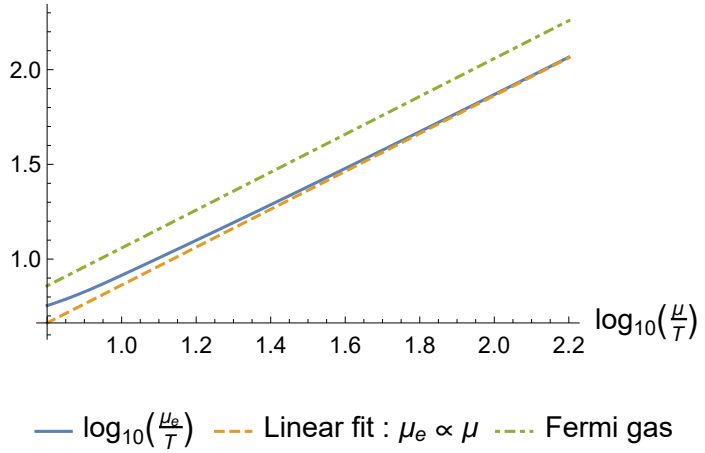

Figure 4.9: The dependence of the electron chemical potential on the baryonic chemical potential μ. The precise quantity that is shown is the chemical potential in units of the temperature, μ_e/T. The latter does not depend independently on T and μ, but only on μ/T. The dashed orange line corresponds to the linear fit at high density $\mu \gg T$, (4.3.26). We compare our result with the degenerate Fermi gas at $\beta-$equilibrium, which is shown as the green dot-dashed lines.

In addition to the particle densities, the calculations for the transport of neutrinos close to equilibrium also require the knowledge of the leptonic chemical potentials μ_e and μ_ν for given μ and T. μ_ν is related to the isospin chemical potential μ_3 and the electron chemical potential μ_e via the condition of $\beta-$equilibrium (4.2.38). Since μ_3 is set to 0, μ_ν and μ_e are equal in the medium that we consider.

The electrons are described by a relativistic Fermi liquid at equilibrium, so the relation between the electron density n_{e^-} and the electron chemical potential μ_e is known explicitly

$$\frac{n_{e^-}}{T^3} = \frac{1}{\pi^2}\int_{\frac{m_e}{T}}^{\infty} \mathrm{d}x \frac{x\sqrt{x^2-\left(\frac{m_e}{T}\right)^2}}{1+\mathrm{e}^{x-\frac{\mu_e}{T}}}\,. \tag{4.3.22}$$

Likewise, the positron density is given by

$$\frac{n_{e^+}}{T^3} = \frac{1}{\pi^2}\int_{\frac{m_e}{T}}^{\infty} \mathrm{d}x \frac{x\sqrt{x^2-\left(\frac{m_e}{T}\right)^2}}{1+\mathrm{e}^{x+\frac{\mu_e}{T}}}\,. \tag{4.3.23}$$

Moreover, the electron fraction

$$Y_e \equiv \frac{n_{e^-}-n_{e^+}}{n_B}\,, \tag{4.3.24}$$

is fixed by the condition of charge neutrality in the medium

$$Y_e = \frac{N_c}{6}\,. \tag{4.3.25}$$

Combining (4.3.22)-(4.3.25) and (4.3.19) then gives a relation that fixes μ_e as a function of μ and T.

At high density $\mu \gg T$, the leptonic chemical potentials behave linearly in μ

$$\mu_\nu = \mu_e = M\ell\, w_0^{\frac{4}{3}} \left(\frac{\pi^2}{24}\right)^{\frac{1}{3}} \mu \left(1 + \mathcal{O}\left(\frac{T}{\mu}\right)\right)\,. \tag{4.3.26}$$

In figure 4.9 we show the dependence of μ_e on μ/T, for the parameters of Appendix O. Figure 4.9 also shows the comparison with the chemical potentials in a degenerate Fermi gas at $\beta-$equilibrium. μ_e is observed to be of the same order as in the Fermi gas.

4.4 Holographic calculation of the chiral current 2-point functions

This section discusses the calculation of the retarded 2-point function for the charged current (4.2.55), in the holographic model presented above. To do so, we follow the now standard prescription of [297], and study the linearized field equations for small perturbations $\delta L^{1,2}$ of the bulk gauge fields dual to the chiral currents $J^{1,2}_{(L)}$

$$\partial_M \left(\sqrt{-g}\, \left(\partial^M \delta L^{N,a} - \partial^N \delta L^{M,a}\right)\right) = 0\,. \tag{4.4.1}$$

We choose the axial gauge

$$\mathbf{L}_r^{1,2} = 0\,, \tag{4.4.2}$$

and define the 4-dimensional Fourier transform of the perturbation as

$$\delta L^a_\mu(r;t,\vec{x}) = \int \frac{\mathrm{d}k^4}{(2\pi)^4} \mathrm{e}^{-i(\omega t - \vec{k}.\vec{x})} \mathcal{L}^a_{\mu,k}(r)\,. \tag{4.4.3}$$

To avoid clutter, the k dependence of $\mathcal{L}^a_\mu$ will not be written explicitly in the following. We also omit the flavor index in most places, since the action is invariant under exchange of $\mathcal{L}^1$ and $\mathcal{L}^2$. We first present the general expression for the 2-point functions. We then study its behavior in the hydrodynamic limit.

4.4.1 General expression

The general tensor structure of the chiral current 2-point function can be inferred from the symmetries of the background. The finite temperature plasma is invariant under SO(3) spatial rotations, as well as chiral transformations[8]. This implies that the 2-point function can be decomposed into a longitudinal and transverse part to the 3-momentum $\vec{k}$, according to

$$\left\langle J_\lambda^{(L),a} J_\sigma^{(L),b} \right\rangle^R (\omega, \vec{k}) = \delta^{ab} \left(P^\perp_{\lambda\sigma}(\omega, \vec{k}) i\Pi^\perp_{(L)}(\omega, \vec{k}) + P^\parallel_{\lambda\sigma}(\omega, \vec{k}) i\Pi^\parallel_{(L)}(\omega, \vec{k}) \right) , \tag{4.4.4}$$

where $a, b \in \{1, 2\}$ and the non-zero components of $P^\perp$ and $P^\parallel$ are

$$P^\perp_{ij}(\omega, \vec{k}) = \delta_{ij} - \frac{k_i k_j}{\vec{k}^2} , \tag{4.4.5}$$

$$P^\parallel_{00} = \frac{\vec{k}^2}{\omega^2 - \vec{k}^2} \ , \ P^\parallel_{0i} = P^\parallel_{i0} = -\frac{\omega k_i}{\omega^2 - \vec{k}^2} \ , \ P^\parallel_{ij} = \frac{k_i k_j}{\vec{k}^2} \frac{\omega^2}{\omega^2 - \vec{k}^2} . \tag{4.4.6}$$

The sum of the two projectors is the flat 4-dimensional projector transverse to k^μ

$$P^\perp_{\mu\nu} + P^\parallel_{\mu\nu} = \eta_{\mu\nu} - \frac{k_\mu k_\nu}{k^2} \equiv P_{\mu\nu} \quad , \quad k_\mu = \left(-\omega, \vec{k} \right) . \tag{4.4.7}$$

Note that we did not include any term involving the Levi-Civita tensor in (4.4.4) because the bulk action is symmetric under parity ($\vec{x} \leftrightarrow -\vec{x}$). Also, the polarization functions have the following properties :

- At $\vec{k} = 0$, the transverse and longitudinal directions cannot be distinguished anymore, so that the 2-point function should be written as

$$\left\langle J_\lambda^{(L),a} J_\sigma^{(L),b} \right\rangle^R (\omega, 0) = \delta^{ab} P_{\lambda\sigma} \, i\Pi_{(L)}(\omega) , \tag{4.4.8}$$

  which implies that

$$\Pi^\parallel_{(L)}(\omega, 0) = \Pi^\perp_{(L)}(\omega, 0) . \tag{4.4.9}$$

- Due to the shape of the longitudinal projector (4.4.6), and since the retarded 2-point function should be regular at $\omega = k$, $\Pi^\parallel$ vanishes for light-like momenta as

$$\Pi^\parallel(\omega, \vec{k})\Big|_{\omega^2 \to \vec{k}^2} \sim \omega^2 - \vec{k}^2 . \tag{4.4.10}$$

[8]Remember that this model does not account for neither explicit or spontaneous breaking of the chiral symmetry. Chiral symmetry imposes that the correlator should obey the Ward identity $\langle J_\lambda J_\sigma \rangle \, k^\sigma = 0$.

The 3-dimensional part of the gauge field perturbation can also be decomposed into transverse and longitudinal parts

$$\mathcal{L}_i^{\perp} = \mathcal{L}_i - \frac{k_i}{\vec{k}^2}\left(k_j \mathcal{L}_j\right) , \tag{4.4.11}$$

$$\mathcal{L}_i^{\parallel} = \frac{k_i}{\vec{k}^2}\left(k_j \mathcal{L}_j\right) . \tag{4.4.12}$$

We now write the equations of motion (4.4.1) component by component. In the axial gauge (4.4.2), the $N = r$ component implies a constraint

$$\partial_r \mathcal{L}_0 + \frac{f(r)}{\omega}\partial_r\left(k_i \mathcal{L}_i\right) = 0 , \tag{4.4.13}$$

and the other equations of motion are

$$\partial_r\left(\frac{1}{r}\partial_r \mathcal{L}_0\right) - \frac{\sqrt{\vec{k}^2}}{r f(r)} E^{\parallel} = 0 , \tag{4.4.14}$$

$$\partial_r\left(\frac{f(r)}{r}\partial_r \mathcal{L}_i^{\parallel}\right) + \frac{1}{r f(r)}\frac{\omega k_i}{\sqrt{\vec{k}^2}} E^{\parallel} = 0 , \tag{4.4.15}$$

$$\partial_r\left(\frac{f(r)}{r}\partial_r \mathcal{L}_i^{\perp}\right) + \frac{1}{r f(r)}\left(\omega^2 - f(r)\vec{k}^2\right)\mathcal{L}_i^{\perp} = 0 . \tag{4.4.16}$$

We defined the longitudinal electric field

$$E^{\parallel} \equiv \sqrt{\vec{k}^2}\,\mathcal{L}_0 + \frac{\omega}{\sqrt{\vec{k}^2}}\left(k_j \mathcal{L}_j\right) . \tag{4.4.17}$$

Because of the constraint (4.4.13), (4.4.14) and (4.4.15) are actually the same equation, which can be written as a differential equation for $E^{\parallel}$

$$\partial_r\left(\frac{f(r)}{r}\frac{\partial_r E^{\parallel}}{\omega^2 - f(r)\vec{k}^2}\right) + \frac{1}{r f(r)} E^{\parallel} = 0 . \tag{4.4.18}$$

The charged current retarded 2-point function is then extracted from the solution to the equations of motion (4.4.16) and (4.4.18), with infalling boundary conditions at the horizon [297]. The on-shell action for the infalling solution reads

$$S_{\text{on-shell}} = \frac{1}{8\ell}(M\ell)^3 w_0^2 N_c \int \frac{\mathrm{d}^4 k}{(2\pi)^4}\left[\frac{\ell}{r} f(r)\left(\mathcal{L}_i^{\perp,a}(-k)\partial_r \mathcal{L}_i^{\perp,a}(k) - \right.\right. \\ \left.\left. - E^{\parallel,a}(-k)\frac{\partial_r E^{\parallel,a}(k)}{\omega^2 - f(r)k^2}\right)\right]_{r=r_H}^{r=\epsilon} , \tag{4.4.19}$$

with ϵ a UV cut-off. The AdS boundary contribution to (4.4.19) can be rewritten as

$$S_{\text{on-shell}} = \frac{1}{8\ell}(M\ell)^3 w_0^2 N_c \int_{r=\epsilon} \frac{\mathrm{d}^4k}{(2\pi)^4}\left[\frac{\ell}{r}\mathcal{L}_a^\lambda(-k)\delta^{ab}\left(P^\perp_{\lambda\sigma}(k)\frac{\partial_r\mathcal{L}_i^\perp(k)}{\mathcal{L}_i(k)}+\right.\right.$$
$$\left.\left.+\,P^\parallel_{\lambda\sigma}(k)\frac{\partial_r E^\parallel(k)}{E^\parallel(k)}\right)\mathcal{L}_b^\sigma(k)\right]^{r=\epsilon}. \tag{4.4.20}$$

According to the prescription of [297], this implies that the polarization functions for the left-handed chiral currents are given by

$$\Pi^\perp_{(L)}(\omega,\vec{k}) = -\frac{1}{4}(M\ell)^3 w_0^2 N_c \frac{1}{\epsilon}\left.\frac{\partial_r\mathcal{L}_i^\perp}{\mathcal{L}_i^\perp}\right|_{r=\epsilon}, \tag{4.4.21}$$

$$\Pi^\parallel_{(L)}(\omega,\vec{k}) = -\frac{1}{4}(M\ell)^3 w_0^2 N_c \frac{1}{\epsilon}\left.\frac{\partial_r E^\parallel}{E^\parallel}\right|_{r=\epsilon}. \tag{4.4.22}$$

To obtain the polarization functions for the charged current $\Pi_c^{\perp,\parallel}$, (4.3.8) implies that (4.4.21)-(4.4.22) should be multiplied by a factor $\frac{1}{2}|M_{ud}|^2$

$$\Pi^\perp_{c}(\omega,\vec{k}) = -\frac{1}{8}(M\ell)^3 w_0^2 N_c |M_{ud}|^2 \frac{1}{\epsilon}\left.\frac{\partial_r\mathcal{L}_i^\perp}{\mathcal{L}_i^\perp}\right|_{r=\epsilon}, \tag{4.4.23}$$

$$\Pi^\parallel_{c}(\omega,\vec{k}) = -\frac{1}{8}(M\ell)^3 w_0^2 N_c |M_{ud}|^2 \frac{1}{\epsilon}\left.\frac{\partial_r E^\parallel}{E^\parallel}\right|_{r=\epsilon}. \tag{4.4.24}$$

Whether the expressions (4.4.23) and (4.4.24) give finite results or need to be regularized depends on the near-boundary behavior of the solutions. The latter is obtained by solving (4.4.16) and (4.4.18) at $r \to 0$

$$\mathcal{L}^\perp = \mathcal{L}_0^\perp + r^2\left(\mathcal{L}_2^\perp - \frac{1}{2}(\omega^2-\vec{k}^2)\mathcal{L}_0^\perp \log r\right)\left(1+\mathcal{O}(r^2)\right), \tag{4.4.25}$$

$$E^\parallel = E_0^\parallel + r^2\left(E_2^\parallel - \frac{1}{2}(\omega^2-\vec{k}^2)E_0^\parallel \log r\right)\left(1+\mathcal{O}(r^2)\right), \tag{4.4.26}$$

with the two independent integration constants given by the source $\mathcal{L}_0^\perp, E_0^\parallel$ and vev terms $\mathcal{L}_2^\perp, E_2^\parallel$. This behavior implies that the polarization functions are subject to a logarithmic UV divergence, which behaves as $(\omega^2-k^2)\log\epsilon$. The log term contributes only to the real part of the polarization functions, whereas the imaginary part does not need to be regularized. Since only the imaginary part enters in the expression for the neutrino radiative coefficients, no regularization is required for our purpose.

4.4.2 Hydrodynamic limit

We study in this section the hydrodynamic limit for the retarded 2-point function of the charged current, whose dual field is not sourced by a chemical potential. The expression for the correlators is given by (4.4.23) and (4.4.24). The hydrodynamic limit corresponds to the limit of ω and $\vec{k}$ small compared with the temperature. In this regime, the correlators can be expressed in a systematic expansion in ω and k, whose coefficients correspond to the transport coefficients of the corresponding currents [298]. At leading order in the hydrodynamic expansion, the 00 component of the retarded 2-point function exhibits an imaginary diffusive pole of diffusivity D

$$\langle J_0 J_0 \rangle^R = \frac{\sigma \vec{k}^2}{\omega + iD\vec{k}^2} \left(1 + O\big(\omega, \vec{k}^2\big)\right) , \tag{4.4.27}$$

where the transport coefficient σ which controls the residue is the DC conductivity. The notation O refers to a term that is at most of the indicated order, but can be much smaller depending on the relative values[9] of ω and $\vec{k}^2$. In particular, since the imaginary part of the retarded Green's function is odd in ω (see (4.2.15)), the first correction to the numerator in (4.4.27) should be of order $\mathcal{O}(\omega^2)$ when $\vec{k} = 0$. From (4.4.4), (4.4.27) then implies that the leading order hydrodynamic approximation to the longitudinal polarization function is given by

$$\Pi^{\parallel}(\omega, k) = \frac{-i\sigma(\omega^2 - \vec{k}^2)}{\omega + iD\vec{k}^2} \left(1 + O\big(\omega, \vec{k}^2\big)\right) . \tag{4.4.28}$$

As for the transverse part of the correlator, it is not associated with any hydrodynamic mode, so that it is analytic in the hydrodynamic limit

$$\Pi^{\perp}(\omega, k) = ic_0\omega \left(1 + \mathcal{O}\big(\omega^2, \vec{k}^2\big)\right) + \mathcal{O}\big(\omega, \vec{k}^2\big) , \tag{4.4.29}$$

where c_0 is a real constant, and we made explicit the decomposition into real and imaginary parts. Note that the corrections to the imaginary part start at order $\mathcal{O}\big(\omega^3, \omega\vec{k}^2\big)$, since $\operatorname{Im}\Pi^{\perp}$ is odd in ω according to (4.2.15). Using the fact that, when $\vec{k} = 0$, the transverse and longitudinal polarization functions are equal, the coefficient at linear order in ω in (4.4.29) is shown to correspond to the conductivity

$$\Pi^{\perp}(\omega, k) = -i\sigma\omega \left(1 + \mathcal{O}\big(\omega^2, \vec{k}^2\big)\right) + \mathcal{O}\big(\omega^2, \vec{k}^2\big). \tag{4.4.30}$$

The shape of the correlators (4.4.28) and (4.4.30) is determined by hydrodynamics, but the transport coefficients D and σ are computed from the microscopic theory. In the present

[9] The terms that appear in the expansion in the parentheses of (4.4.27) do not correspond to a simple double Taylor expansion in ω and $\vec{k}^2$. Instead, corrections to the denominator will yield terms of the form $\frac{a\omega^2 + b\vec{k}^4}{\omega + iD\vec{k}^2}$. These are always small corrections for ω and $\vec{k}^2$ small and real, but they are not of a definite order in ω or $\vec{k}^2$.

case, the holographic calculation makes it possible to extract analytic expressions for the leading order transport coefficients.

In this work, we are interested in conditions typical of neutron star matter, where the baryon chemical potential μ is much larger than the temperature T. In this regime and for the bulk action (4.3.3), it can be shown that the hydrodynamic approximation to the 2-point function (4.4.28)-(4.4.30) is valid not only at $\omega, k \ll T$, but extends to $T \ll \omega, k \ll \mu$ [299]. In the following, we summarize the procedure for computing the hydrodynamic approximation to the 2-point function at $\mu \gg T$ from the equations of motion (4.4.16) and (4.4.18), and give the expression for the transport coefficients D and σ. We refer to [299] for more details [10].

4.4.2.1 Transverse correlator

We start by analyzing the transverse polarization function (4.4.23), whose expression at leading order in the hydrodynamic expansion is given by (4.4.30). To compute $\Pi^{\perp}$ in the hydrodynamic regime, we solve the equations of motion for the transverse fluctuations (4.4.16) at $\omega, k, T \ll \mu$. To do this, a small parameter $\epsilon \ll 1$ is introduced, and we consider the following scaling of the energy, momentum and temperature

$$r_H\omega \to \epsilon\, r_H\omega \quad , \quad r_H k \to \epsilon^a r_H k \quad , \quad r_H T \to \epsilon^b r_H T \quad , \quad a, b > 0\,. \tag{4.4.31}$$

Since we are interested in the linear terms in the hydrodynamic expansion, we consider $(r_H k)^2 \ll r_H\omega$, that is $a > 1/2$. As far as the temperature exponent is concerned, $b < 1$ corresponds to the usual hydrodynamic limit $\omega \ll T$, whereas $b \geq 1$ corresponds to the regime where $\omega > T$ but the hydrodynamic approximation remains valid as long as $\omega \ll \mu$. The bulk is then divided into two regions where different approximations to the equation of motion (4.4.16) are valid

- *The outer region*, where the holographic coordinate r is sufficiently far from the horizon for
$$\frac{\omega^2}{f^2}\mathcal{L}^{\perp} \ll \partial_r^2\mathcal{L}^{\perp} \quad , \quad \frac{k^2}{f}\mathcal{L}^{\perp} \ll \partial_r^2\mathcal{L}^{\perp}\,, \tag{4.4.32}$$
to be obeyed. For $a > 1/2$, this region includes the boundary at $r = 0$, and inside it the equation of motion (4.4.16) reduces to
$$\partial_r\left(\frac{f(r)}{r}\partial_r\mathcal{L}^{\perp}\right) = 0\,. \tag{4.4.33}$$

[10] The problem considered in [299] is not exactly the same, as they consider perturbations of the gauge field in the group under which the black hole is charged (in our case, such a gauge field is dual to a current that enters the neutral current, but does not contribute to the charged current). In that case, the gauge field perturbation couples to the metric perturbation, and the linearized Maxwell equations have to be solved together with the linearized Einstein equations. The general method that they use still applies to the present case though, which is even simpler.

The solution to (4.4.33) is given by

$$\mathcal{L}^{\perp}_{\text{out}} = A + B \int_0^r \mathrm{d}r' \frac{r'}{f(r')}\,, \tag{4.4.34}$$

with A and B two integration constants.

- *The inner region*, where the holographic coordinate r is sufficiently close to the horizon for

$$\omega^2 \gg f(r)k^2\,, \tag{4.4.35}$$

to be obeyed[11]. For $b < 1$, the outer region extends down to the horizon, and the solution in the inner region reduces to an infalling boundary condition for the outer solution at the horizon

$$B = i r_H \omega A\,. \tag{4.4.36}$$

For $b \geq 1$, the solution in the inner region is better analyzed by zooming on the near-horizon geometry, which is done by defining

$$u \equiv \epsilon\, \zeta\,, \tag{4.4.37}$$

where $u = 1 - r/r_H$. ζ is the radial coordinate that describes the AdS_2-Schwarzschild factor of the near-horizon geometry (which has an additional $\mathbb{R}^3$ factor). For $b = 1$, the equation of motion (4.4.16) reduces in the inner region to the equation for a massless scalar field in AdS_2-Schwarzschild

$$\partial_\zeta \left((4\pi r_H T \zeta + 12\zeta^2)\partial_\zeta \mathcal{L}^{\perp} \right) + \frac{(r_H\omega)^2}{4\pi r_H T\zeta + 12\zeta^2}\mathcal{L}^{\perp} = 0\,. \tag{4.4.38}$$

The infalling solution in the inner region is then given by

$$\mathcal{L}^{\perp}_{\text{in}} = C \left(\frac{3\zeta}{3\zeta + \pi r_H T} \right)^{-\frac{i\omega}{4\pi T}}\,, \tag{4.4.39}$$

with C an integration constant.

For $b > 1$, $\omega \gg T$ implies that the near-horizon region of the AdS_2-Schwarzschild space-time is not probed by the perturbation, and the equation of motion (4.4.16) reduces in the inner region to the equation for a massless scalar field in AdS_2

$$\partial_\zeta \left(12\zeta^2 \partial_\zeta \mathcal{L}^{\perp} \right) + \frac{(r_H\omega)^2}{12\zeta^2}\mathcal{L}^{\perp} = 0\,. \tag{4.4.40}$$

[11] In general, the inner region is simply defined as a region where $r_H - r \ll r_H$. When considering $(r_H\vec{k})^2 \ll 1$, the additional condition (4.4.35) can be added. This results in $\vec{k}^2$ disappearing from the inner equation of motion.

The infalling solution in the inner region is then given by

$$\mathcal{L}^{\perp}_{\text{in}} = C \exp\left(\frac{i r_H \omega}{12\zeta}\right), \tag{4.4.41}$$

with C an integration constant.

The full solution at leading order in ϵ is finally obtained by imposing that the outer and inner solutions (4.4.34) and (4.4.41) (or (4.4.39)) are equal in the region where they match. It can be shown that there exists such a matching region, where the outer and inner regions overlap. This region is reached by setting u to be of order $\mathcal{O}(\epsilon^c)$, with $1-a<c<1$. In practice, this amounts to defining

$$u \equiv \epsilon^c v \iff \zeta = \epsilon^{c-1} v\,, \tag{4.4.42}$$

and equating $\mathcal{L}^{\perp}_{\text{out}}(v)$ and $\mathcal{L}^{\perp}_{\text{in}}(v)$ for v of order 1. Proceeding as such, the solution to (4.4.16) in the outer region is obtained as

$$\mathcal{L}^{\perp}_{\text{out}}(r) = A\left(1 + i r_H \omega \int_0^{\frac{r}{r_H}} \mathrm{d}x \frac{x}{f(x)} + \mathcal{O}\big(\epsilon^2, \epsilon^{1+b}, \epsilon^{2a}\big)\right). \tag{4.4.43}$$

Then, from (4.4.23), the transverse polarization function is found to follow the hydrodynamic behavior (4.4.30)

$$\Pi^{\perp}_c(\omega,\vec{k}) = -\frac{|M_{ud}|^2}{8} r_H^{-2} (M\ell)^3 w_0^2 N_c \Big(- i r_H \omega \left(1 + \mathcal{O}\big((r_H\omega)^2, (r_H\vec{k})^2, r_H T\big)\right) + \\ + \mathcal{O}\big((r_H\omega)^2, (r_H\vec{k})^2, r_H^2 \omega T\big)\Big). \tag{4.4.44}$$

The DC conductivity is identified to be

$$\sigma = \frac{|M_{ud}|^2}{8 r_H} N_c (M\ell)^3 w_0^2\,, \tag{4.4.45}$$

with r_H the black-hole horizon radius, whose expression is given by (4.3.13). This result agrees with the universal result derived in [302]. For $\mu \gg T$, the expression simplifies to

$$\sigma = \frac{1}{16} |M_{ud}|^2 \sqrt{\frac{N_c}{3}} \left(M\ell\, w_0\right)^3 \mu \left(1 + \mathcal{O}\left(\frac{T}{\mu}\right)\right). \tag{4.4.46}$$

4.4.2.2 Longitudinal correlator

We now turn to the longitudinal polarization function (4.4.24), whose expression at leading order in the hydrodynamic expansion is given by (4.4.28). In this case, the equation of

motion that has to be solved at $\omega, k, T \ll \mu$ is (4.4.18). A small parameter $\epsilon \ll 1$ is again introduced, and the same kind of scaling of the energy, momentum and temperature as in (4.4.31) is considered. To describe the diffusive pole of the longitudinal correlator, we want to include in the calculation terms of order $(r_H\vec{k})^2$. Therefore, unlike the transverse case, we now consider general positive values for the momentum exponent a.

The bulk is still divided into outer and inner regions, which are defined as in the previous section. The longitudinal equation of motion (4.4.18) is solved separately in each region as follows

- In the outer region, (4.4.18) reduces to

$$\partial_r \left(\frac{f(r)}{r} \frac{\partial_r E^{\parallel}}{\omega^2 - f(r)k^2} \right) = 0 \,, \tag{4.4.47}$$

  with solution

$$E^{\parallel}_{\text{out}} = A + B \int_0^r \mathrm{d}r' r' \frac{\omega^2 - f(r')\vec{k}^2}{f(r')} \,, \tag{4.4.48}$$

  with A and B two integration constants.

- In the inner region, the shape of the equation of motion depends on the relative size of the energy ω and the temperature T. For $b < 1$, the outer region extends down to the horizon, and the solution in the inner region reduces to an infalling boundary condition for the outer solution at the horizon

$$B = \frac{iA}{(r_H\omega)^2 + \frac{1}{2}i(r_H\vec{k})^2} \,. \tag{4.4.49}$$

  For $b = 1$, the equation of motion (4.4.18) in the inner region takes the same form (4.4.38) as in the transverse case (with $\mathcal{L}^{\perp}$ replaced by $\hat{E}^{\parallel}$), and the infalling solution is

$$E^{\parallel}_{\text{in}} = C \left(\frac{3\zeta}{3\zeta + \pi r_H T} \right)^{-\frac{i\omega}{4\pi T}} \,, \tag{4.4.50}$$

  with C an integration constant.

  For $b > 1$ ($\omega \gg T$), (4.4.18) has the form (4.4.40) in the inner region and the infalling solution is given by

$$E^{\parallel}_{\text{in}} = C \exp\left(\frac{i r_H \omega}{12\zeta} \right) , \tag{4.4.51}$$

  with C an integration constant.

By matching the two solutions, the solution to (4.4.18) in the outer region is obtained as

$$E^{\parallel}_{\text{out}}(r) = A \Bigg(1 + \frac{i}{(r_H\omega)^2 + \frac{1}{2}i(r_H\vec{k})^2} \int_0^{\frac{r}{r_H}} \mathrm{d}x\, x \frac{(r_H\omega)^2 - f(x)(r_H\vec{k})^2}{f(x)} \times$$

$$\times \left(1+\mathcal{O}\big(\epsilon,\epsilon^{b},\epsilon^{2a}\big)\right)\Big)\,. \tag{4.4.52}$$

Then, from (4.4.24), the longitudinal polarization function is found to follow the hydrodynamic behavior (4.4.28)

$$\Pi_c^{\parallel}(\omega,\vec{k}) = r_H^{-2}\frac{-ir_H\sigma\big((\omega r_H)^2-(\vec{k}r_H)^2\big)}{\omega r_H+\frac{1}{2}i(\vec{k}r_H)^2}\Big(1+\mathcal{O}\big(\omega r_H,(\vec{k}r_H)^2,r_H T\big)\Big)\,. \tag{4.4.53}$$

The diffusivity is identified to be

$$D=\frac{1}{2}r_H\,, \tag{4.4.54}$$

which, for $\mu \gg T$, simplifies to

$$D=\frac{\sqrt{3N_c}}{w_0}\mu^{-1}\left(1+\mathcal{O}\left(\frac{T}{\mu}\right)\right)\,. \tag{4.4.55}$$

4.5 Analysis of the radiative coefficients

This section is dedicated to the analysis of the neutrino charged current radiative coefficients computed from the holographic model, which are the final target of this work. The coefficients are computed by performing the integrals over the loop electron momentum (4.2.72)-(4.2.75), where the charged current retarded 2-point function is computed holographically following Section 4.4. We first draw the consequences of the presence of the statistical factor to determine which coefficients dominate and which are suppressed.

We then introduce a set of approximations that help understand the behavior of the computed coefficients. These include the hydrodynamic approximation discussed in the previous section for the correlators. Finally, we present the numerical results for the radiative coefficients, and estimate the accuracy of the various approximations. We end the section by comparing the results of this work with some examples of radiative coefficients that are currently used to describe neutrino transport in simulations.

4.5.1 Statistics at large baryonic density

We assume in this subsection that the conditions in the medium where the neutrinos scatter are typical of neutron stars, so that the baryonic and electron densities are very high, $\mu/T, \mu_e/T \gg 1$. In these conditions, the medium at equilibrium is highly degenerate. We investigate here the consequences of having such a highly degenerate medium for the neutrino radiative coefficients (4.2.72)-(4.2.75).

As far as the neutrino chemical potential μ_ν is concerned, we recall that $\beta-$equilibrium (4.2.38) with $\mu_3 = 0$ implies that it is equal to the electron chemical potential, μ_e.

The effect of a high density will appear via the statistical factors in (4.2.72)-(4.2.75), which contain the electron Fermi-Dirac distribution, and the Bose-Einstein distribution from the chiral currents correlator at equilibrium. Below, we review the degenerate limit of the statistical factors, which is valid at high density. These approximations depend on the fact that the distributions are evaluated against the imaginary part of the retarded 2-point functions for the chiral currents. By dimensional analysis, at $\mu \gg T$, the 2-point functions obey

$$\mathrm{Im}\, G_c^R(\omega, k) = \mu^2 F\left(\frac{\omega}{\mu}, \frac{k}{\mu}\right)\left(1 + \mathcal{O}\left(\frac{T}{\mu}\right)\right), \tag{4.5.1}$$

where F is some dimensionless function which vanishes linearly at $\omega = 0$. Given these properties, within the integrand of the radiative coefficients (4.2.72)-(4.2.75), the Bose-Einstein factors can be approximated by

$$n_b(\omega) = -\theta(-\omega) - \frac{\pi^2}{6}\left(\frac{T}{\mu}\right)^2 \delta'\left(\frac{\omega}{\mu}\right) + \mathcal{O}\left(\frac{T}{\mu}\right)^3, \tag{4.5.2}$$

where θ is the Heaviside distribution and δ the Dirac distribution. When the integration path is such that $\omega \geq \omega_0 \gg T$, the Bose-Einstein distribution is exponentially suppressed

$$n_b(\omega) = \mathrm{e}^{-\beta\omega_0}\left(\frac{T}{\mu}\delta\left(\frac{\omega - \omega_0}{\mu}\right) + \mathcal{O}\left(\frac{T}{\mu}\right)^2\right) + \mathcal{O}\left(\mathrm{e}^{-2\beta\omega_0}\right). \tag{4.5.3}$$

At high electronic chemical potential $\mu_e \gg T$, the distributions for the electrons and positrons at equilibrium (4.2.63) are approximated by

$$n_e = \theta(\mu_e - E_e) - \frac{\pi^2}{6}\left(\frac{T}{\mu}\right)^2 \delta'\left(\frac{E_e - \mu_e}{\mu}\right) + \mathcal{O}\left(\frac{T}{\mu}\right)^3 + \mathcal{O}(\mathrm{e}^{-\beta\mu_e}), \tag{4.5.4}$$

$$n_{\bar{e}} = \mathrm{e}^{-\beta(\mu_e + E_e)} + \mathcal{O}(\mathrm{e}^{-2\beta\mu_e}). \tag{4.5.5}$$

In particular, (4.5.5) implies that the following processes involving positrons

$$\nu + d + e^+ \to u \qquad \text{and} \qquad d + e^+ \to \bar{\nu} + u \tag{4.5.6}$$

are exponentially suppressed

$$\frac{1}{\lambda_{e^+}} \ : \ n_{\bar{e}} n_b(q^0_{\bar{e}\nu}) = \mathcal{O}(\mathrm{e}^{-\beta(E_e + \mu_e)}),$$
$$\bar{j}_{e^+} \ : \ n_{\bar{e}} n_b(q^0_{\bar{e}\bar{\nu}}) = \mathcal{O}(\mathrm{e}^{-\beta(E_e + \mu_e)}), \tag{4.5.7}$$

where the momenta $q_{\ell\ell'}$ were defined in (4.2.59); their time components are

$$q^0_{e\nu} \equiv E_e - E_\nu - \mu_e + \mu_\nu = E_e - E_\nu \quad , \quad q^0_{e\bar{\nu}} \equiv E_e + E_\nu - \mu_e + \mu_\nu = E_e + E_\nu, \tag{4.5.8}$$

$$q^0_{\bar{e}\nu} \equiv -E_e - E_\nu - \mu_e + \mu_\nu = -E_e - E_\nu \quad , \quad q^0_{\bar{e}\bar{\nu}} \equiv -E_e + E_\nu - \mu_e + \mu_\nu = -E_e + E_\nu \,. \tag{4.5.9}$$

Moreover, (4.5.2) implies that the emission of a neutrino by the decay of an up quark is also suppressed

$$j_{e^+} \;:\; (1-n_{\bar{e}})\big(1+n_b(q^0_{\bar{e}\nu})\big) = 1 - \theta(E_e+E_\nu) + \mathcal{O}\left(\frac{T}{\mu}\right)^2 = \mathcal{O}\left(\frac{T}{\mu}\right)^2 .$$

The only positronic process that may play a significant role in the transport of neutrinos at high density, is the absorption of an anti-neutrino by the medium, resulting in the emission of a positron

$$\bar{\nu} + u \to d + e^+ \tag{4.5.10}$$

The statistical factor for this process is approximated by

$$\frac{1}{\bar{\lambda}_{e^+}} \;:\; (1-n_{\bar{e}})\big(1+n_b(q^0_{\bar{e}\bar{\nu}})\big) = \theta(q^0_{\bar{e}\bar{\nu}}) + \mathcal{O}\left(\frac{T}{\mu}\right)^2 , \tag{4.5.11}$$

which is of order 1 at electron energies $E_e \leq E_\nu$.

The charged current sector also accounts for weak processes involving electrons

$$e^- + u \rightleftharpoons \nu + d \qquad \text{and} \qquad d \rightleftharpoons \bar{\nu} + u + e^- \tag{4.5.12}$$

For the processes involving neutrinos, the degenerate approximations are given by

$$j_{e^-} \;:\; n_e\big(1+n_b(q^0_{e\nu})\big) = \theta(\mu_e - E_e)\theta(q^0_{e\nu}) + \mathcal{O}\left(\frac{T}{\mu}\right)^2 , \tag{4.5.13}$$

$$\frac{1}{\lambda_{e^-}} \;:\; (1-n_e)n_b(q^0_{e\nu}) = -\theta(E_e-\mu_e)\theta(-q^0_{e\nu}) + \mathcal{O}\left(\frac{T}{\mu}\right)^2 . \tag{4.5.14}$$

This shows that the emission of neutrinos dominates for $E_\nu < \mu_\nu$, whereas the absorption dominates for $E_\nu > \mu_\nu$. From the detailed balance condition (4.2.80), the ratio of the subleading coefficient to the leading one is given by a Boltzmann factor $\mathrm{e}^{-\beta|E_\nu-\mu_\nu|}$. When $|E_\nu - \mu_\nu| \lesssim T^2/\mu$, both terms are of the same order $\mathcal{O}(T/\mu)^2$.

For the processes involving anti-neutrinos, the statistical factors are approximated by

$$\bar{j}_{e^-} \;:\; (1-n_e)n_b(q^0_{e\bar{\nu}}) = -\theta(E_e-\mu_e)\theta(-q^0_{e\bar{\nu}}) + \mathcal{O}\left(\frac{T}{\mu}\right)^2 , \tag{4.5.15}$$

$$\frac{1}{\bar{\lambda}_{e^-}} \;:\; n_e\big(1+n_b(q^0_{e\bar{\nu}})\big) = \theta(\mu_e - E_e)\theta(q^0_{e\bar{\nu}}) + \mathcal{O}\left(\frac{T}{\mu}\right)^2 . \tag{4.5.16}$$

(4.5.15) implies that the emission of anti-neutrinos is suppressed for $\mu_\nu > 0$. From the detailed balance condition (4.2.81), the suppression of the emissivity with respect to the absorption is given by a Boltzmann factor $\mathrm{e}^{-\beta(E_\nu+\mu_\nu)}$.

To summarize the contents of this section, we show in Table 4.1 the radiative processes that contribute to the transport of neutrinos for a given neutrino energy, as well as the associated radiative coefficients.

E_ν	$E_\nu < \mu_\nu$	$\mu_\nu < E_\nu$
ν processes	$e^- + u \to \nu + d$	$\nu + d \to e^- + u$
$\bar{\nu}$ processes	$\bar{\nu} + u + e^- \to d$ $\bar{\nu} + u \to d + e^+$	$\bar{\nu} + u + e^- \to d$ $\bar{\nu} + u \to d + e^+$
coefficients	$j_{e^-}, \bar{\lambda}_{e^-}, \bar{\lambda}_{e^+}$	$\lambda_{e^-}, \bar{\lambda}_{e^-}, \bar{\lambda}_{e^+}$

Table 4.1: Radiative processes that contribute to the transport of neutrinos as a function of the neutrino energy E_ν, in the degenerate limit.

4.5.2 Approximations to the neutrino radiative coefficients

In this subsection, we present and analyze a set of approximations that result in simpler expressions for the radiative coefficients. Although not required for the calculation of the coefficients which can be done numerically, the approximations presented below provide some qualitative understanding of the numerical results. Here, we define and investigate the regime of validity of the approximations, leaving the numerical analysis of their accuracy for the next subsection. They are defined as follows:

The degenerate approximation, which corresponds to replacing the equilibrium statistical distributions n_b and n_f by their expression in the limit of $\mu \gg T$, (4.5.2) and (4.5.4). This approximation is of course well known and purely related to the statistical factors whose general expression is analytically known. It is therefore not of much use for numerical calculations. However, it simplifies a lot the expression of the opacities, which helps a better conceptual understanding of the neutrino transport. The degenerate approximation is exact in the limit of $\mu/T \to \infty$.

The hydrodynamic approximation, where the charged current 2-point function is replaced by the leading order hydrodynamic expressions (4.4.28) and (4.4.30), with the transport coefficients given by (4.4.45) and (4.4.54). From Section 4.4.2, this approximation is expected to be exact when all energies μ_e, μ_ν, E_ν are much smaller than the baryonic chemical potential μ, because in this case we will have $r_H\omega, r_H k \ll 1$. Below we discuss its validity in more detail.

At the level of the two-point functions, the criterion for the validity of the hydrodynamic approximation was shown in Section 4.4.2 to correspond to $r_H\omega, r_H k \ll 1$. The radiative coefficients (4.2.72)-(4.2.75) are defined as integrals over the loop electron momentum containing the retarded charged current 2-point function, which is a function of two arguments ω and k. For the radiative coefficients, we therefore need to determine the

region in the (ω, k) plane which contributes to the calculation of the integral.

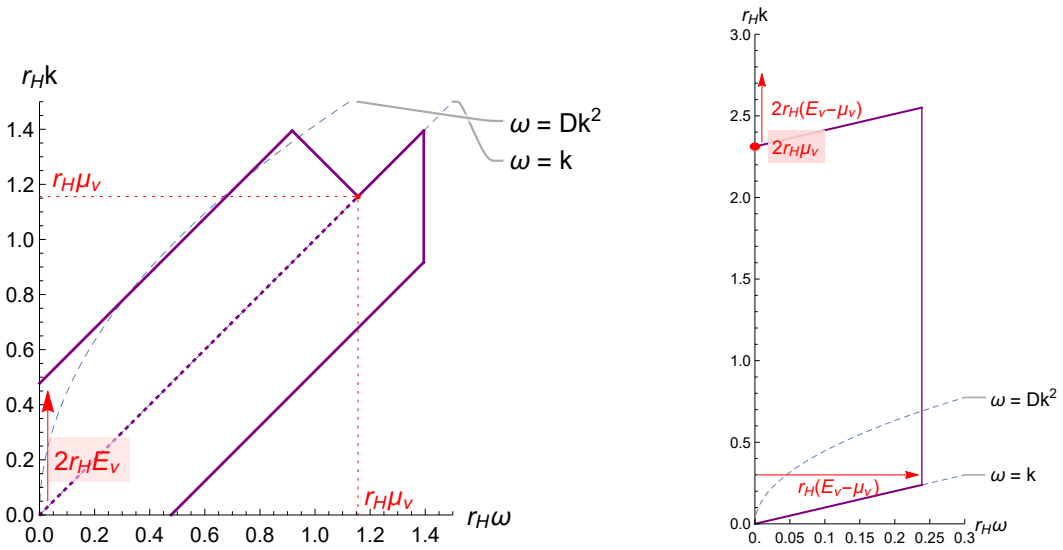

Figure 4.10: Region of the (ω, k) plane which contributes to the calculation of the radiative coefficients, for $n_B = 1\,\mathrm{fm}^{-3}$ and $T = 10\,\mathrm{MeV}$. We consider neutrino energies between 0 and 100 MeV. The left plot shows the region for neutrino energies $E_\nu < \mu_\nu$, where the dotted line corresponds to $E_\nu = 0$. It should be combined with the right plot when $E_\nu > \mu_\nu$.

The corresponding region is shown in figure 4.10, where the baryon density n_B is taken to be much larger than T^3, and the neutrino energy E_ν to go from 0 to a few times T. For concreteness, the figure is constructed by setting $n_B = 1\,\mathrm{fm}^{-3}$, and $E_\nu = 0 - 10T$, which is the range of energies investigated in the numerical analysis of the next subsection. We use the anti-symmetry of the imaginary part of the retarded two-point function (4.2.15) to restrict to the half space $\omega > 0$. Then, the boundaries of the integration area are determined from the Fermi-Dirac and Bose-Einstein distributions, which behave as step functions at high density, as well as the range of neutrino energies.

All possible values of the angle θ between the electron and neutrino momentum are taken into account. In the left figure, the dotted line in the middle corresponds to $E_\nu = 0$, and it separates the region relevant to the calculation of $1/\bar{\lambda}_{e^-}$ (below) from that relevant to j_{e^-} (above). The output of this analysis is that the scales that control the size of the region are shown to be controlled by the leptonic energies[12]. This confirms that we enter the hydrodynamic regime when μ_e, μ_ν and E_ν are much smaller than μ.

[12]For the situation considered here where $n_B = 1\,\mathrm{fm}^{-3}$ and $E_\nu < 100\,\mathrm{MeV}$, E_ν is always smaller than the chemical potential μ_ν. When E_ν becomes significantly larger than μ_ν, the shape of the

Notice that, for $\mu \gg T$, μ_e (and μ_ν) are actually proportional to μ, according to (4.3.26). Whether or not the hydrodynamic approximation is relevant to the calculation of the radiative coefficients therefore depends on the parameters of the bulk action, w_0 and $M\ell$. For the values of the parameters derived from matching the ideal plasma thermodynamics (O.3) and (O.6), the following number is found for the leptonic chemical potentials in units of the horizon radius

$$r_H\mu_\nu = r_H\mu_e \simeq 1.17 \left(\frac{(M\ell)^3}{(M\ell)^3_{\text{free}}}\right)^{\frac{1}{2}} \left(\frac{w_0^2(M\ell)^3}{\left(w_0^2(M\ell)^3\right)_{\text{free}}}\right)^{\frac{1}{6}} \left(1+\mathcal{O}\left(\frac{T}{\mu}\right)\right), \tag{4.5.17}$$

where we also set the number of colors to $N_c = 3$. This number is of order 1, which explains why the hydrodynamic approximation can produce sensible results. Notice that the dependence on the parameters of the bulk action is weak.

The diffusive approximation, where the leading hydrodynamic expression of the retarded 2-point function is used, and it is assumed that the time-time component of the retarded 2-point function dominates completely the integral in the calculation of the opacities (4.2.72)-(4.2.75). To show that this approximation is valid in the hydrodynamic regime, we evaluate the contribution of each component of the 2-point function to the integral, specifying to the case of the electronic neutrino emissivity j_{e^-} (it is analogous for anti-neutrinos and/or positronic processes). The precise analysis is done in Appendix Q, and we reproduce here the main steps and results.

We consider the degenerate and hydrodynamic regime, where $r_H\mu_e = \epsilon$ is much smaller than 1, with all the leptonic energies of the same order and much larger than $r_H T$

$$r_H E_\nu \sim r_H\mu_\nu = r_H\mu_e = \epsilon \quad , \quad r_H T = \mathcal{O}(\epsilon^a) \quad , \quad \epsilon \ll 1, \quad a \gg 1\,. \tag{4.5.18}$$

Since the temperature is assumed to be negligible, the degenerate expression of the statistical distributions can be used (4.5.2) and (4.5.4). j_{e^-} (4.2.72) can then be written as an integral over the first argument of the charged current 2-point function ω

$$j_{e^-}(E_\nu) = -\frac{G_F^2}{8\pi^2}\int_0^\pi \mathrm{d}\theta \sin\theta \int_0^{\mu_\nu - E_\nu} \mathrm{d}\omega \frac{\omega+E_\nu}{E_\nu} L_e^{\lambda\sigma}\, \mathrm{Im}\, G^R_{c,\sigma\lambda}\big(\omega, k(\omega,\theta)\big)\,, \tag{4.5.19}$$

with

$$k(\omega,\theta) \equiv \sqrt{(\omega+E_\nu)^2 + E_\nu^2 - 2(\omega+E_\nu)E_\nu\cos\theta}\,.$$

From (4.4.28) and (4.4.30), the imaginary part of the hydrodynamic retarded correlator is given by

$$\mathrm{Im}\, G^R_{c,\sigma\lambda}(\omega,k) = -\sigma\omega\left(P^\perp_{\sigma\lambda}(\omega,k) + P^\parallel_{\sigma\lambda}(\omega,k)\frac{\omega^2-k^2}{\omega^2+D^2k^4}\right) + \mathcal{O}(\epsilon^2)\,, \tag{4.5.20}$$

bounding curves deviates significantly from straight lines. However, the size of the region is still controlled by the scales indicated in figure 4.10, up to factors of order 1.

where $P^{\perp}$ and $P^{\parallel}$ are the projectors defined in (4.4.5)-(4.4.6). The 2-point function reaches the maximum of the diffusion peak when ω is equal to $\omega^*(E_\nu, \theta)$, whose expression is given in (Q.8). Since ω^* is of order $\mathcal{O}(\epsilon^2)$, which is parametrically smaller than the upper bound of the integral in the hydrodynamic limit, the integral can be split into two parts: the first part including the diffusion peak and the other being such that $\omega \gg k^2$. These two parts are respectively labeled by the subscripts "diff" and "lin". The following hydrodynamic scalings can then be derived for the contribution of each component of the 2-point function to the emissivity

$$\begin{aligned} j^{(00)}_{e^-,\text{diff}} &= \mathcal{O}(\epsilon^4) \quad , \quad j^{(00)}_{e^-,\text{lin}} = \mathcal{O}(\epsilon^4 \log \epsilon)\,, \\ j^{(0i)}_{e^-,\text{diff}} &= \mathcal{O}(\epsilon^6) \quad , \quad j^{(0i)}_{e^-,\text{lin}} = \mathcal{O}(\epsilon^4)\,, \\ j^{\perp,(ij)}_{e^-,\text{diff}} &= \mathcal{O}(\epsilon^6) \quad , \quad j^{\perp,(ij)}_{e^-,\text{lin}} = \mathcal{O}(\epsilon^4)\,, \\ j^{\parallel,(ij)}_{e^-,\text{diff}} &= \mathcal{O}(\epsilon^8) \quad , \quad j^{\parallel,(ij)}_{e^-,\text{lin}} = \mathcal{O}(\epsilon^4)\,, \end{aligned} \tag{4.5.21}$$

where the powers in ϵ are determined by the form of the hydrodynamic 2-point function (4.5.20). As long as $\mu_\nu - E_\nu$ is much larger than $\mathcal{O}(\epsilon^2)$, the term $j^{(00)}_{e^-,\text{lin}}$ dominates all the other contributions to the neutrino emissivity. When E_ν is so close to the neutrino chemical potential that $\mu_\nu - E_\nu$ is smaller than $\mathcal{O}(\epsilon^2)$, the integral includes only the diffusive part, and the leading term becomes $j^{(00)}_{e^-,\text{diff}}$. Since in both cases, the time-time component dominates, this shows that the diffusive approximation is valid in the hydrodynamic limit[13].

To illustrate the above discussion, figure 4.11 compares the contribution to the neutrino emissivity from the various components of the hydrodynamic 2-point function, at $E_\nu = 0$ and $n_B = 1\,\text{fm}^{-3}$. Two cases are considered for the values of the leptonic chemical potentials. The right plot shows the result for the actual values of μ_e and μ_ν derived from thermodynamic (4.3.22) and $\beta-$equilibrium (4.2.38), whereas in the left plot we consider values fifty times smaller, which goes deeper into the hydrodynamic regime.

The left figure is completely consistent with the hydrodynamic scalings shown in (4.5.21). It confirms in particular that the time-time component of the 2-point function gives the largest contribution in the hydrodynamic limit. Also, it shows that the leading contribution to the time-time integral does not come from the diffusion peak itself, but rather from the region $D\vec{k}^2 \ll \omega < \mu_\nu - E_\nu$.

For the actual equilibrium values of μ_e and μ_ν (on the right), the contribution from the time-time component is found to be of the same order as the other contributions. This indicates that the diffusive approximation to the neutrino radiative coefficients is not accurate to describe the actual result, and is only of the right order of magnitude. The latter is not surprising, since in this case $r_H\mu_e$ and $r_H\mu_\nu$ are not much smaller than one.

[13] With the exception of vanishing E_ν; see the discussion in appendix Q.

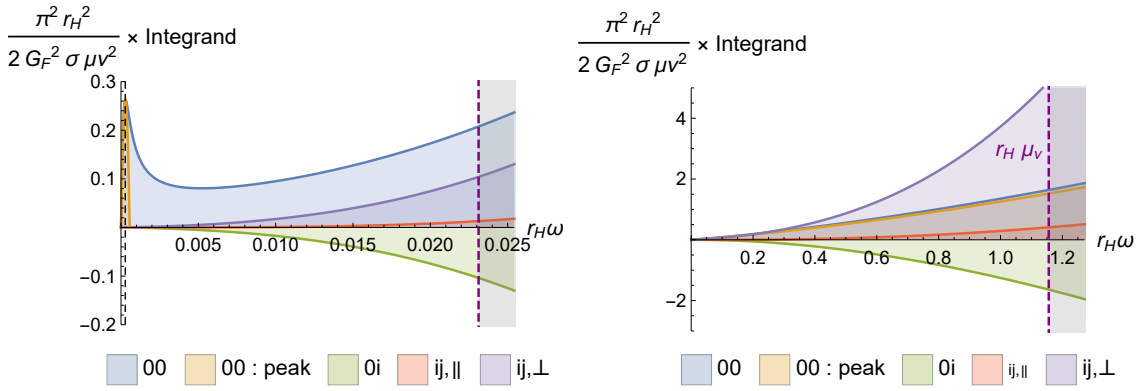

Figure 4.11: Comparison between the contributions of the various components of the charged current 2-point function to the integrand of the neutrino emissivity, in the hydrodynamic approximation. We fix $n_B = 10^{-1}\,\mathrm{fm}^{-3}$, $T = 10\,\mathrm{MeV}$ and $E_\nu = \mu_n/2$. The right plot is for the actual values of the leptonic chemical potentials μ_e and μ_ν derived from equilibrium, whereas the left plot is for values fifty times smaller. The various contributions include the time-time (blue), time-space (green) and space-space (red) components. The orange line shows the contribution from the diffusive peak to the time-time component, which corresponds to the lower bound (Q.9). In the right plot the orange and blue lines are almost confounded. The areas under the curves give the corresponding contributions to the emissivity, whereas the grayed area does not contribute to the integral due to the statistical factor.

Approximate expressions We now use the crudest diffusive (and degenerate) approximation to derive simple approximate expressions for the radiative coefficients. Details are again provided in Appendix Q. For generic values of the leptonic energies (much smaller than μ), the diffusive approximation is found to result in the following simplified expression for the neutrino opacity (defined in (4.2.82))

$$\kappa_{e^-}(E_\nu) = \frac{8G_F^2\sigma}{3\pi^2} E_\nu^4 \log\left(\frac{D|\mu_\nu - E_\nu|}{D^2 E_\nu^2}\right) + \mathcal{O}(\epsilon^4)\,, \tag{4.5.22}$$

where ϵ is the parameter of the hydrodynamic expansion (4.5.18). (4.5.22) is valid as long as $|\mu_\nu - E_\nu|$ is much larger than $\mathcal{O}(\epsilon^2)$.

The point $E_\nu = \mu_\nu$ is a peculiar point, since the opacity vanishes there in the degenerate limit. This translates in the presence of a dip at $E_\nu = \mu_\nu$ in the logarithm of κ_{e^-}, which is clearly visible in the numerical analysis we carry out in section 4.5.3. When taking into account the finite temperature, the finite value of the opacity at $E_\nu = \mu_\nu$ can be

calculated at leading order in T/μ from the corrections to the equilibrium distribution functions (4.5.2) and (4.5.4)

$$\kappa_{e^-}(\mu_\nu) = \frac{8G_F^2\sigma}{3}T^2 r_H^{-2}\left[4\log\left(\frac{2\mu_\nu}{m_e}\right) - 1\right](1 + \mathcal{O}(\epsilon) + \mathcal{O}(m_e/\mu_\nu)^2)\,. \tag{4.5.23}$$

This expression gives the depth of the dip in opacity in the hydrodynamic limit. In Appendix Q, the typical width of the dip is also estimated

$$\Delta E_\nu = \sqrt{\frac{3N_c}{w_0^2}}\frac{\mu_\nu^2}{\mu}\,. \tag{4.5.24}$$

As for the anti-neutrino opacity, the degenerate and diffusive approximation is given by

$$\bar{\kappa}_{e^-}(E_\nu) = \frac{8G_F^2\sigma}{3\pi^2}E_\nu^4\log\left(\frac{D(\mu_\nu + E_\nu)}{D^2E_\nu^2}\right) + \mathcal{O}(\epsilon^4)\,, \tag{4.5.25}$$

$$\bar{\kappa}_{e^+}(E_\nu) = \frac{8G_F^2\sigma}{3\pi^2}E_\nu^4\log\left(DE_\nu\right) + \mathcal{O}(\epsilon^4)\,. \tag{4.5.26}$$

Note that the leading log term in (4.5.23) and (4.5.26) actually vanishes as the neutrino energy goes to zero. In this limit, the appropriate expression is given by the term of order $\mathcal{O}(\epsilon^4)$, which results in the following approximation

$$\bar{\kappa}_{e^-}(0) = \kappa_{e^-}(0) \equiv \kappa_{e,0} = \frac{G_F^2\sigma}{\pi^2}\mu_\nu^4 + \mathcal{O}(\epsilon^5)\,. \tag{4.5.27}$$

This gives an estimate of the typical size of the opacity at a given baryon density.

To summarize, the analysis of Appendix Q shows that the approximate expressions given above (4.5.22) and (4.5.25)-(4.5.27) are valid in the hydrodynamic limit. This occurs when the leptonic energies are much smaller than the baryonic chemical potential. Figure 4.10 and equation (4.5.17) indicate that the conditions in the medium, where the neutrinos scatter, are such that the leptonic and baryonic energies are of the same order. Therefore, the approximate expressions shown above are expected to give a rough estimate of the exact opacities.

To obtain a more precise idea of the usefulness of those expressions in the present context, we would like to compare them with the exact opacities. In figure 4.12, the plots of the approximate expressions as a function of neutrino energy are shown together with the numerical solution for the opacities, which is discussed in the next subsection. The state variables that characterize the medium are fixed to $T = 10\,\mathrm{MeV}$ and $n_B = 0.31\,\mathrm{fm}^{-3}$. The approximation to the neutrino opacity is given by (4.5.22), and for anti-neutrinos in (4.5.25)-(4.5.26), to which we add the expression at zero-energy (4.5.27). It is observed that $\kappa_{e,0}$ as defined in (4.5.27) gives a good approximation of the opacities at zero neutrino energy. However, the energy dependence given by (4.5.22) and (4.5.25)-(4.5.26) is quite

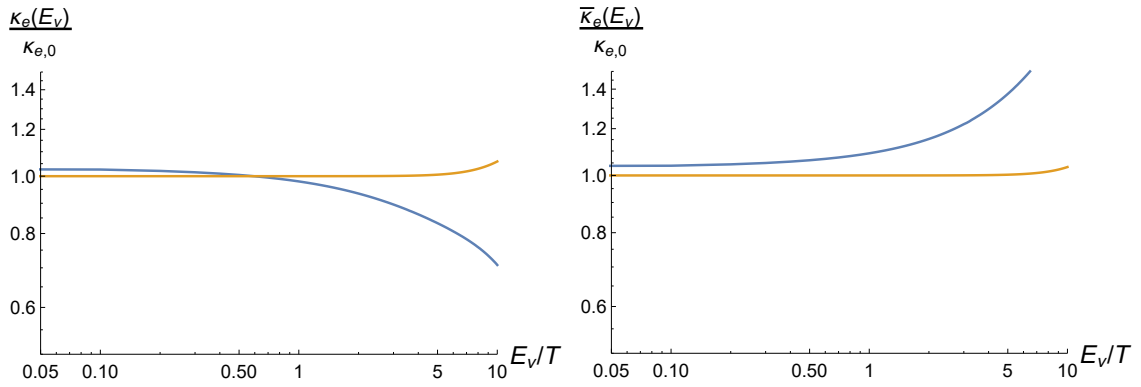

Figure 4.12: Comparison of the hydrodynamic-degenerate approximations (orange), with the exact numerical opacities (blue), for neutrinos (**Left**) and anti-neutrinos (**Right**). The approximations are given by (4.5.22) and (4.5.25)-(4.5.26), summed with the typical value at $E_\nu = 0$, $\kappa_{e,0}$ in (4.5.27). The medium is characterized by $T = 10\,\text{MeV}$ and $n_B = 0.31\,\text{fm}^{-3}$, and the opacities are normalized by $\kappa_{e,0}$.

far from the actual result. This is particularly striking in the case of the neutrino opacity, where even the monotonicity is not correctly reproduced.

Therefore, the conclusion from figure 4.12 is that, although the expression (4.5.27) gives a good estimate of the opacities at leading order in the hydrodynamic limit, the dependence on the neutrino energy derived from (4.5.22) and (4.5.25)-(4.5.26) is not accurate. It is likely that more accurate expressions could be obtained by including the terms of order $\mathcal{O}(\epsilon^4)$, beyond the leading log term. However, those result in complicated expressions that are not very useful for a qualitative understanding.

4.5.3 Numerical results

We present here the results of the numerical calculation of the neutrino transport coefficients (4.2.72)-(4.2.75). We first discuss the strongly-coupled component which is computed holographically. This is the imaginary part of the charged current polarization functions. The latter are calculated according to the procedure described in Section 4.4. In particular, we are interested in estimating the accuracy of the hydrodynamic approximation (4.4.44) and (4.4.53) to the 2-point function for the parameters of interest. Then, we analyze the radiative coefficients themselves, that are obtained by computing the integrals over the loop electron momentum (4.2.72)-(4.2.75), which include the charged current 2-point function. We estimate the accuracy of the approximations introduced in the previous subsection over a range of parameters relevant for neutron stars.

In the following, we fix the temperature to a value that is typically relevant to neutrino

transport calculations, for example in a cooling proto-neutron star

$$T = 10\,\mathrm{MeV}\,. \tag{4.5.28}$$

We shall investigate the numerical results for the remaining 2-dimensional parameter space, spanned by the baryon number density n_B and neutrino energy E_ν.

4.5.3.1 Charged current polarization functions

Figure 4.13 shows the numerical result for the imaginary part of the charged current polarization functions $\Pi^{\perp}(\omega, k)$ and $\Pi^{\parallel}(\omega, k)$, for $n_B = 1\,\mathrm{fm}^{-3}$. In terms of chemical potentials, this corresponds to $\mu/T \simeq 65$. $r_H\omega$ and $r_H k$ are varied between 0 and 2, which includes the region over which the integral is performed to compute the radiative coefficients[14] (see figure (4.15)).

For the smallest values of ω and k, the hydrodynamic approximations (4.4.44) and (4.4.53) are expected to be relevant. This is confirmed at the qualitative level by comparing figure 4.13 with the hydrodynamic result plotted in figure 4.14: whereas the longitudinal polarization function $\mathrm{Im}\,\Pi^{\parallel}$ shows a peak at a location set by the position of the diffusive pole $\omega = Dk^2$, the transverse one $\mathrm{Im}\,\Pi^{\perp}$ goes to zero near the origin, remaining relatively close to a linear behavior in ω up to $r_H\omega = 1$.

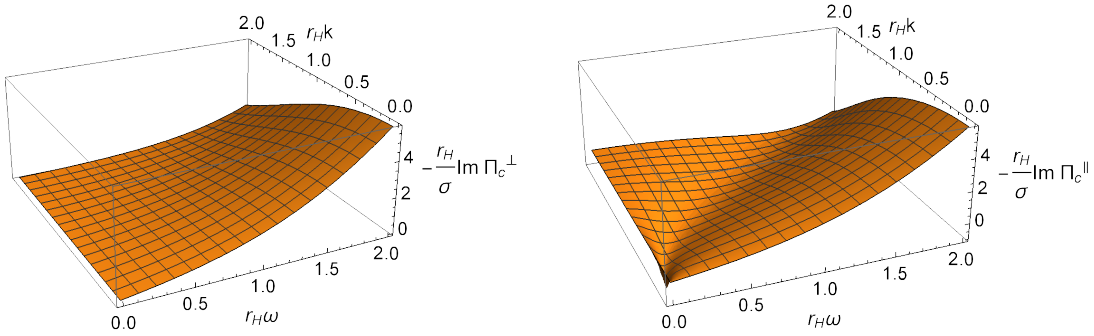

Figure 4.13: Imaginary part of the transverse (**Left**) and longitudinal (**Right**) charged current retarded polarization functions. The energy and momentum are expressed in units of r_H^{-1}, and the polarization functions are normalized by σ/r_H. The medium is characterized by $n_B = 1\,\mathrm{fm}^{-3}$ and $T = 10\,\mathrm{MeV}$.

[14] In principle, the integrals go up to infinite electron momentum, but the contribution from high energies is exponentially suppressed by the statistical factors. In practice, computing the integral over a finite region as the one shown in figure 4.15 is sufficient, and the contribution from outside of this region is completely negligible.

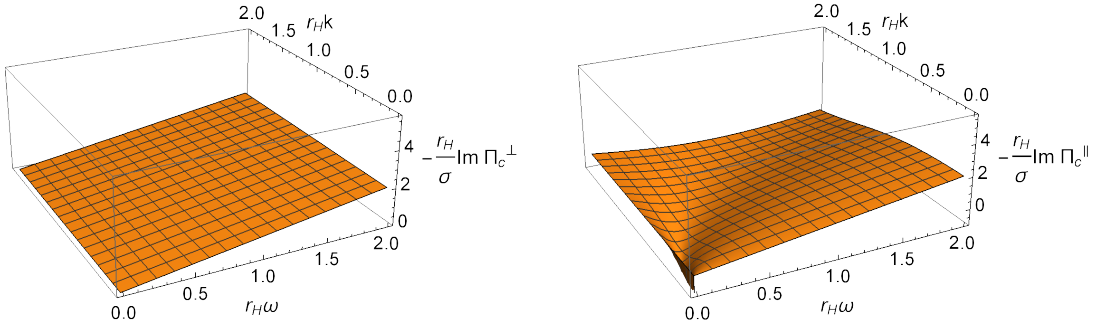

Figure 4.14: Same as figure 4.13 but for the hydrodynamic approximation to the polarization functions (4.4.44) and (4.4.53).

To extend the previous discussion to the quantitative level, we show in figure 4.15 the relative difference between figures 4.13 and 4.14, together with the region in the (ω, k) plane which gives a sizable contribution to the radiative coefficients. We consider a range of neutrino energies which is typical of transport in a neutron star $E_\nu = 0 - 100\,\mathrm{MeV}$ [274]. For this range of neutrino energies, the dominant coefficients are given by the neutrino emissivity j_{e^-} and the anti-neutrino absorption $1/\bar{\lambda}_{e^-}$. The region which contributes to the calculation of the radiative coefficients is indicated by the purple polygon in figure 4.15.

Figure 4.15 shows that, in the region relevant for the calculation of j_{e^-} and $1/\bar{\lambda}_{e^-}$, the accuracy of the hydrodynamic approximation is of about 0 to 50% for the transverse part, and 0 to 100% for the longitudinal part. Also, the largest deviation from the hydrodynamic result is consistently reached in the corners of the plots, that is for the largest values of ω and k. Note that the region where the hydrodynamic approximation is the best, is different for the transverse and longitudinal parts : whereas it is located near the line $\omega = k$ for the transverse part, it is close to the location of the diffusive peak $\omega = D\vec{k}^2$ for the longitudinal part. This observation is consistent with the respective leading order of the corrections in the hydrodynamic expansion, as shown in (4.4.28) and (4.4.30). It also indicates that the first corrections in ω and $\vec{k}^2$ have opposite signs.

All in all, the numerical results for the polarization functions presented in this subsection indicate that, at $n_B = 1\,\mathrm{fm}^{-3}$ and for the region in the (ω, k) plane which is relevant for neutrino transport, the hydrodynamic approximations (4.4.28) and (4.4.30) not only reproduce the qualitative features of the exact numerical result, but are also quite good quantitatively. This is especially true for the transverse part of the correlator. This suggests that, in the calculation of the radiative coefficients (4.2.72)-(4.2.75), replacing the retarded 2-point function by its leading order hydrodynamic approximation may give a rather good approximation to the coefficients. In the following, we investigate the validity of this statement for a whole range of baryon densities n_B and neutrino energies E_ν.

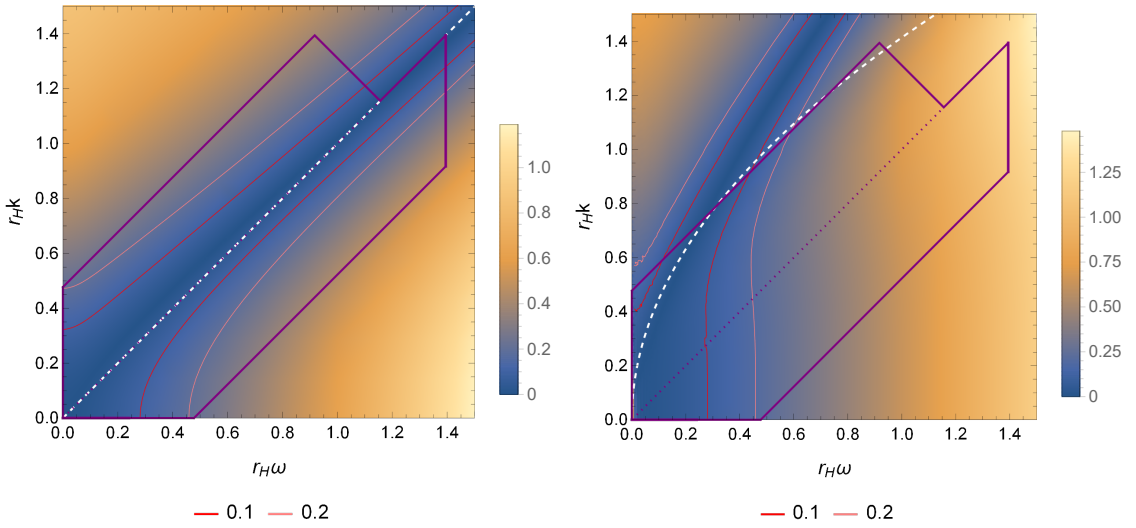

Figure 4.15: Relative difference of the imaginary part of the transverse (**Left**) and longitudinal (**Right**) charged current retarded polarization functions with the hydrodynamic approximation. The relative difference is defined as the absolute value of the difference divided by the hydrodynamic approximation. The parameters of the medium are the same as in figures 4.13 and 4.14. The red and pink contours correspond respectively to the 10% and 20% lines, and the purple polygon encloses the area that is relevant for the calculation of j_{e^-} and $1/\bar{\lambda}_{e^-}$. The way this region is determined is detailed in Section 4.5.2. The white dashed lines indicate the location where the relative difference typically goes to 0. For the transverse part (**Left**) it corresponds to the line of lightlike momenta $\omega = k$, and for the longitudinal part (**Right**) to the location of the diffusive peak $\omega = Dk^2$.

4.5.3.2 Radiative coefficients

We now turn to the analysis of the radiative coefficients themselves, that are the emissivities and absorptions listed in (4.2.72)-(4.2.75). More specifically, we shall be analyzing the opacities defined as in (4.2.82). We consider a range of baryon number densities, n_B, between 10^{-3} and $1\,\mathrm{fm}^{-3}$, and neutrinos energies between 0 and 100 MeV. These are typical values for neutrinos scattering in a cooling neutron star [274].

For the parameters of interest, the neutrino chemical potential is positive and large compared with the temperature, so that the emission of anti-neutrinos (4.5.15) is suppressed.

The two quantities that will be the object of our analysis are therefore

$$\bar{\kappa}_e(E_\nu) \equiv \bar{\kappa}_{e^-}(E_\nu) + \bar{\kappa}_{e^+}(E_\nu) = \frac{1}{\bar{\lambda}_{e^-}(E_\nu)} + \frac{1}{\bar{\lambda}_{e^+}(E_\nu)}\,, \tag{4.5.29}$$

$$\kappa_e(E_\nu) \equiv \kappa_{e^-}(E_\nu) = j_{e^-}(E_\nu) + \frac{1}{\lambda_{e^-}(E_\nu)}\,.$$

We first present in figure 4.16 plots of the opacities at the two extreme values of baryonic density that we considered,

$$n_B^{(1)} = 10^{-3}\,\mathrm{fm}^{-3} \quad \text{and} \quad n_B^{(2)} = 1\,\mathrm{fm}^{-3}\,. \tag{4.5.30}$$

which correspond to the values of the chemical potentials

$$\mu_1 \simeq 47\,\mathrm{MeV} \quad \text{and} \quad \mu_2 \simeq 650\,\mathrm{MeV}\,, \tag{4.5.31}$$

respectively. We also show in figure 4.17 the full density dependence of the opacity at zero neutrino energy. The qualitative behavior is essentially dictated by statistics, so it is the same that was observed in previous works, for example[15] in [274]. The anti-neutrino opacity increases with the baryon density and the neutrino energy. As for the neutrino opacity, it also increases with density, but has a different behavior as a function of the neutrino energy: it is more or less a constant until a threshold located near $E_\nu \sim \mu_\nu$, where it decreases in relative value to a number of order $\mathcal{O}(T/\mu)^2$. An estimate of the typical magnitude and parameter dependence of the opacities at $E_\nu \lesssim T$ is given by (4.5.27), which was derived within the diffusive approximation.

To estimate quantitatively the accuracy of the approximations presented in Section 4.5.2, the opacities were numerically computed and compared to the results from the approximations over the whole 2-dimensional parameter space of baryon number density $n_B = 10^{-3} - 1\,\mathrm{fm}^{-3}$ and neutrino energy $E_\nu = 0 - 100\,\mathrm{MeV}$. We discuss in turn the degenerate, hydrodynamic, diffusive and diffusive and degenerate approximations, analyzing each time both the neutrino and anti-neutrino opacities.

Figure 4.18 shows the relative difference between the exact opacities calculated numerically and the opacities calculated within the degenerate approximation. In the case of the neutrino opacity, the approximation is worst on the curve $E_\nu = \mu_\nu$, where the degenerate approximation goes to 0 whereas the exact result remains finite. Apart from that curve, the magnitude of the error is of about 5 to 30% over most of the parameter space, and it reduces when $|E_\mu - \mu_\nu|$ increases, that is both at larger baryon density and larger neutrino energy.

For anti-neutrinos, the degenerate approximation becomes very good at high density, and it reaches less than 5% of error at $n_B = n_B^{(2)}$. On the contrary, the approximation becomes unreliable for the lowest densities, reaching more than 50% at $n_B = n_B^{(1)}$. The error depends only marginally on the neutrino energy over the range investigated.

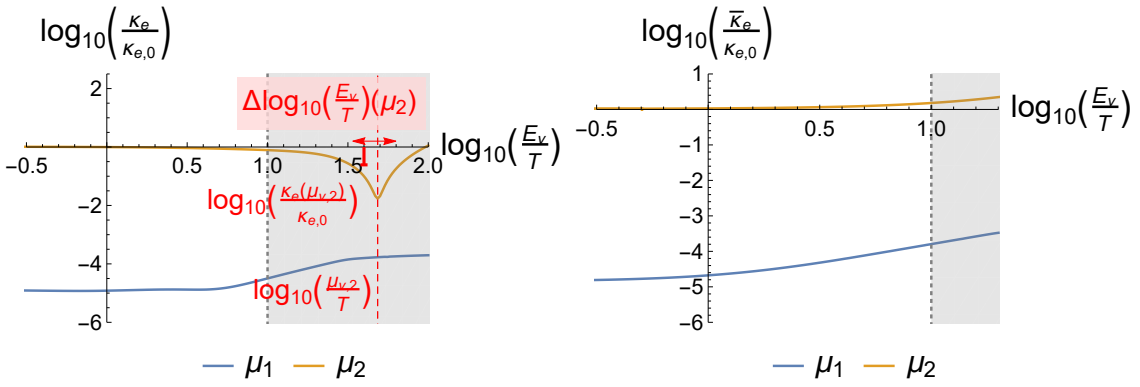

Figure 4.16: Neutrino (**Left**) and anti-neutrino (**Right**) opacities as a function of the neutrino energy E_ν. We show two values of the baryon density, $n_B^{(1)} = 10^{-3}\,\mathrm{fm}^{-3}$ and $n_B^{(2)} = 1\,\mathrm{fm}^{-3}$, associated to the corresponding chemical potentials μ_1 and μ_2. The opacities are normalized by the typical value at $E_\nu = 0$ (4.5.27), evaluated for the largest density $n_B^{(2)}$. In the plot for the neutrino opacity, the typical scales that control the location, depth (4.5.23) and width (4.5.24) of the observed dip are indicated, where we defined $\Delta \log_{10}(E_\nu/T)(\mu) \equiv \log_{10}(\mu_\nu + \Delta E_\nu(\mu)/2) - \log_{10}(\mu_\nu - \Delta E_\nu(\mu)/2)$. The region in gray corresponds to neutrino energies larger than 100 MeV, which is not expected to be relevant for transport in a neutron star. It is included in the plot in order to show the complete qualitative behavior of the neutrino opacities as a function of E_ν, including the threshold at $E_\nu = \mu_\nu$.

We now focus on the hydrodynamic approximation. We start by discussing separately the transverse and longitudinal components, for which the relative difference between the hydrodynamic and the exact opacity is respectively shown in figures 4.19 and 4.20.

The qualtative behavior for the transverse part of the opacity is similar for neutrinos and anti-neutrinos: the error becomes larger at higher neutrino energy and smaller at higher density. There is an exception to this trend in the case of anti-neutrinos, for which the approximation crosses the exact result on a curve at low density and high energy (which appears as a blue line in the bottom-right corner of right Figure 4.19). In both cases, the error is smaller than 30% for $n_B = n_B^{(2)}$ or $E_\nu < T$. However, the error grows large at low density and high energy, reaching more than 800% at $n_B = n_B^{(1)}$ and $E_\nu = 10T$ in the case of neutrinos, and about 70% for anti-neutrinos. That being said, we note that the error is smaller than 40% over most of the parameter space for anti-neutrinos, whereas the

[15]Note that the neutrino chemical potential was negative in [274], whereas it is positive here. This implies that the role of neutrinos and anti-neutrinos are exchanged with respect to [274].

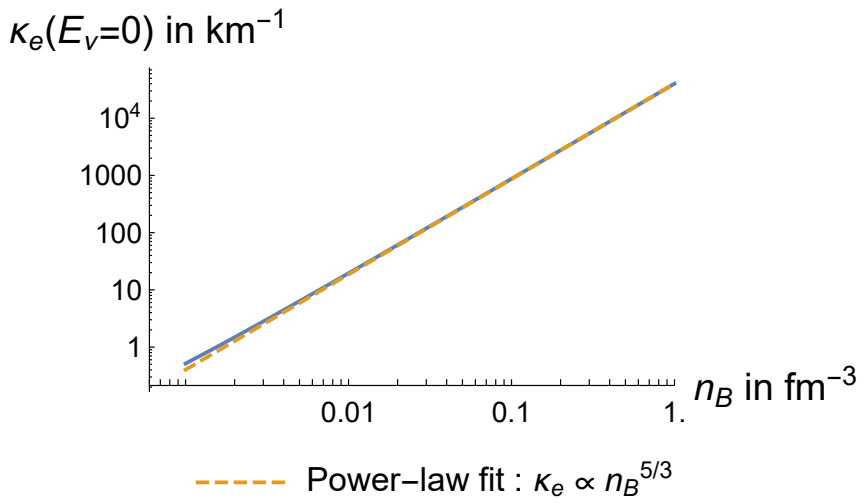

Figure 4.17: Neutrino opacity at zero neutrino energy, as a function of the baryon density n_B. At $E_\nu = 0$, the opacities are the same for neutrinos and anti-neutrinos. The dashed orange line shows the asymptotic power-law behavior at $n_B \gg T^3$, $\kappa_e \sim n_B^{5/3}$ (see equation (4.5.33) in the next subsection).

error on the neutrino opacity is already larger than 60% for a wide range of energies at $n_B < 0.1\,\mathrm{fm}^3$.

In short, the main information from figure 4.19 is that the hydrodynamic approximation to the transverse part of the opacities is reasonably good at high density and low E_ν, but becomes mostly unreliable at low density and high E_ν. The situation turns out to be better for the anti-neutrino opacity, which remains quite good over the whole parameter space that was investigated. This last point is most probably accidental, and we would expect no significant difference were we to take into account all possible values of energies and densities.

The error from the hydrodynamic approximation to the longitudinal part of the opacities is shown in figure 4.20. The qualitative behavior of the error on the neutrino opacity is essentially similar to the transverse case, apart from the presence of a curve where the error vanishes (in blue in the left of figure 4.20). Quantitatively, the error is smaller than the transverse case: at high density it is of about 20%, and although it grows large at low density and high energy, it remains below 80%. As for the error on the anti-neutrino opacity, it is very similar to the transverse case. It depends marginally on the parameters over the range that is investigated, and is typically comprised between 30% and 50%. All in all, the comparison between figures 4.20 and 4.19 indicate a similar qualitative behavior, but with the approximation to the longitudinal opacity typically more accurate than for

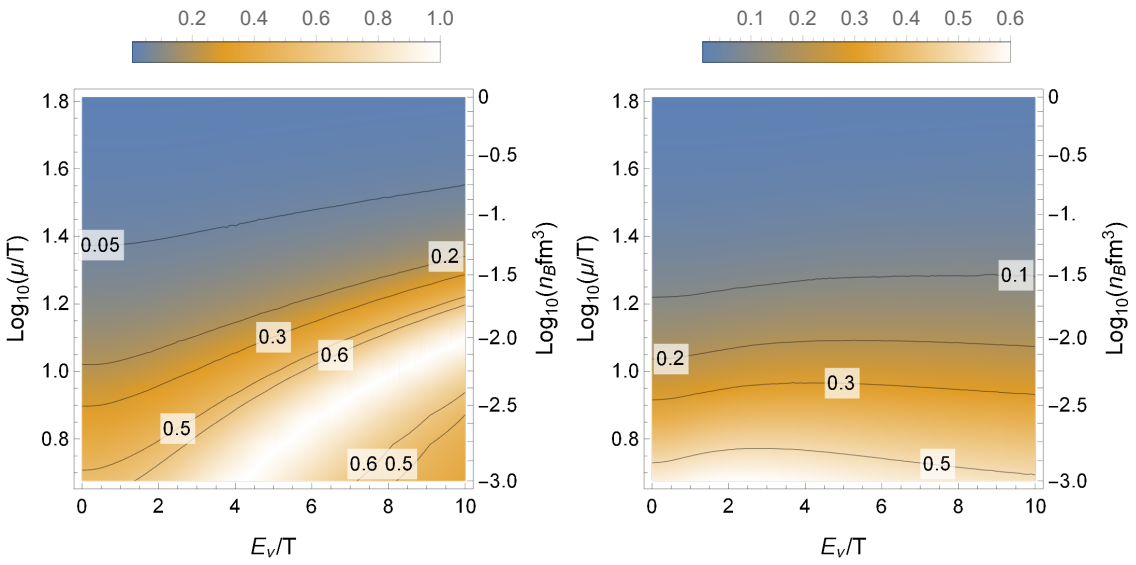

Figure 4.18: Relative difference between the degenerate approximation and the exact opacities, for neutrinos (**Left**) and anti-neutrinos (**Right**).

the transverse opacity.

Finally, figure 4.21 shows the error from the hydrodynamic approximation for the total opacity, which is the sum of the transverse and longitudinal parts. On the whole, figure 4.21 looks similar to the figure for the transverse part (figure 4.19). This indicates that the latter contributes more to the opacity than the longitudinal part over a large part of the parameter space. This is true for sure at small neutrino energy, where the longitudinal part becomes very small, of order $\mathcal{O}(m_e/\mu_\nu)^4$. The contribution from the longitudinal part implies that the error on the total opacity is lower than for the transverse part.

On the whole, figure 4.21 indicates that the hydrodynamic approximation to the opacities is reasonably accurate at high density and/or low neutrino energy, whereas it becomes unreliable in the opposite limit. More precisely, the following quantitative results are observed

- The error from the hydrodynamic approximation to the neutrino opacity is between 0 and 40% for densities $n_B > 10^{-1}\,\mathrm{fm}^{-3}$ or neutrino energies $E_\nu < 20\,\mathrm{MeV}$. The error exceeds 100% for densities typically smaller than $3 \times 10^{-3}\,\mathrm{fm}^{-3}$ and $E_\nu > 60\,\mathrm{MeV}$. Some additional information can be extracted from the comparison of figure 4.21 with the plot for the degenerate approximation (figure 4.18). In figure 4.18, the white line where the error is equal to 100% corresponds to the place where $E_\nu = \mu_\nu$. In the degenerate limit, this line separates the region where the neutrino opacity is

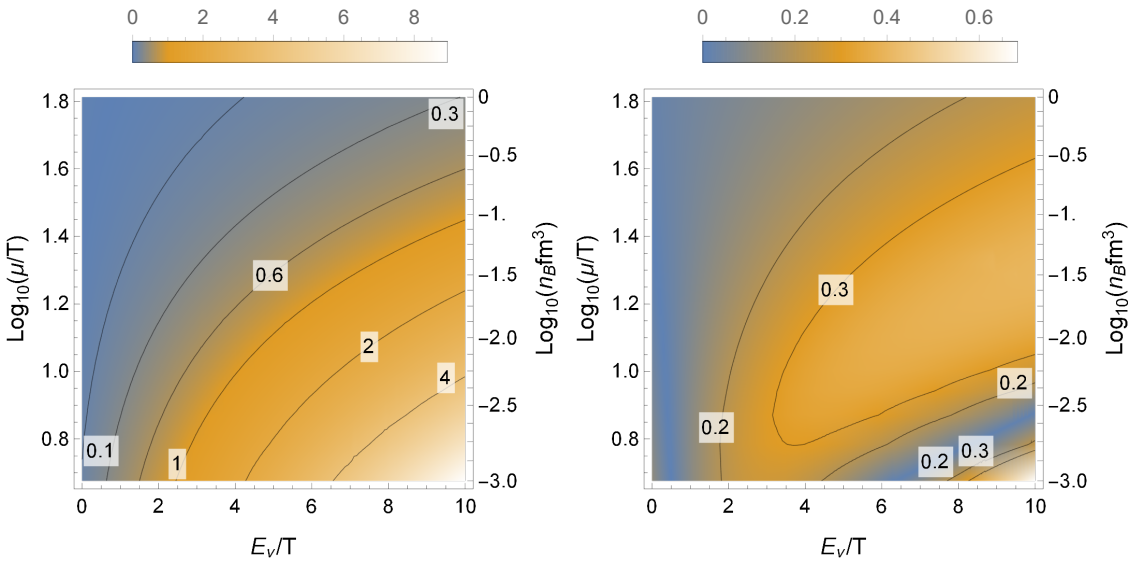

Figure 4.19: Relative difference between the hydrodynamic approximation and the exact transverse opacities, for neutrinos (**Left**) and anti-neutrinos (**Right**).

dominated by emissivity j_{e^-} from that where it is dominated by the absorption $1/\lambda_{e^-}$ (see Table 4.1). Since the location of the $E_\nu = \mu_\nu$ line is close to the contour at 90% accuracy in the right of figure 4.21, this means that the hydrodynamic approximation describes reasonably well the neutrino emissivity, whereas it is very rough as far as the absorption is concerned.

- The accuracy of the hydrodynamic approximation to the anti-neutrino opacity is between 10 and 40% over the range of parameters that was considered.

The last approximation that we investigate is the so-called diffusive approximation, in which only the contribution from the time-time component of the current-current correlators is included in the hydrodynamic approximation. The error for this approximation is shown in figure 4.22. On the whole, the error for neutrinos is observed to take values typically between 20 and 60%, whereas for anti-neutrinos the range is between 60 and 80%. For neutrinos, the difference is observed to vanish on one curve in the parameter space, which is located close to the curve $E_\nu = \mu_\nu$ (the white curve at 100% error in figure 4.18). Comparing with the previous analysis of the hydrodynamic approximation, we see that the accuracy of the diffusive approximation is worse for anti-neutrinos. In the case of neutrinos, the comparison depends on the parameters: although the diffusive approximation is found to be less accurate at low energy or high density, the error is actually much smaller at high energy and low density.

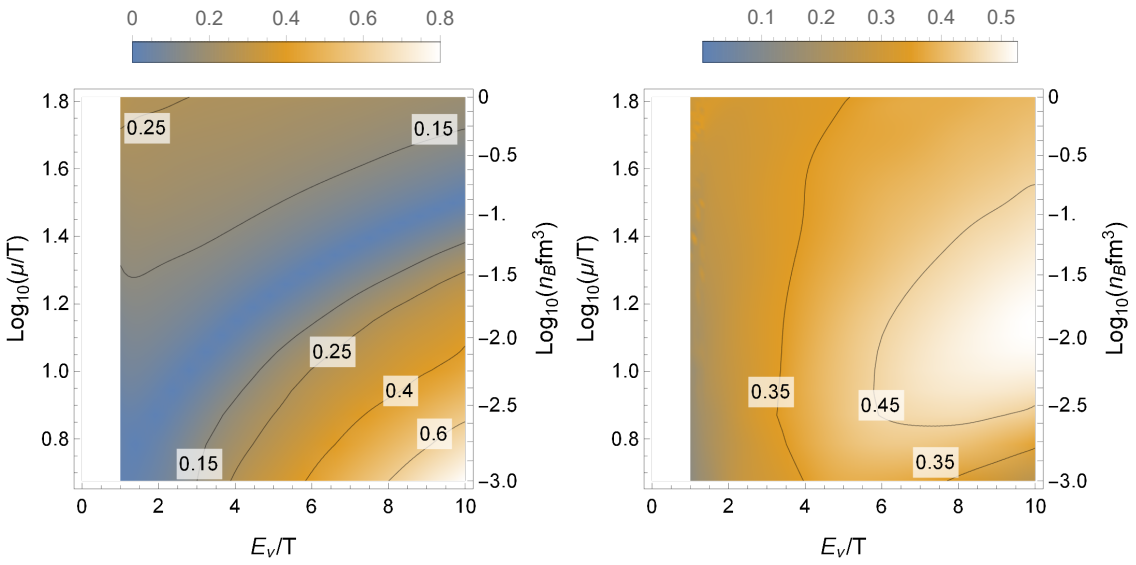

Figure 4.20: Relative difference between the hydrodynamic approximation and the exact longitudinal opacities, for neutrinos (**Left**) and anti-neutrinos (**Right**). We do not show the region of small E_ν since there are large numerical errors there. The reason is that the longitudinal opacity becomes very small in this region, of order $\mathcal{O}(m_e/\mu_\nu)^4$, with m_e the electron mass.

To conclude, the general outcome observed in figure 4.22 is that, as expected, the diffusive approximation is essentially less accurate than the hydrodynamic approximation. However, there is an exception in the case of the neutrino opacity, at low density and high energy. The latter is due to accidental cancellations, which are not expected to occur for general setups.

For completeness, we also analyze the accuracy of the crudest approximation to the opacities, which is obtained by combining the degenerate approximation with the diffusive approximation. This specific approximation is the one that is used to derive the approximate expressions (4.5.22) and (4.5.25)-(4.5.26). The error for this diffusive and degenerate approximation is shown in figure 4.23. As expected, the error is dominated by the degenerate approximation at low density, whereas the main cause of error comes from the diffusive approximation at high density.

In order to give another view on the above analysis, we compare in figures 4.24 and 4.25 the exact opacity computed numerically with the various approximations at the two extreme values considered for the baryon density. Figure 4.24 shows the result for neutrinos and figure 4.25 for anti-neutrinos. These figures illustrate the general results from the

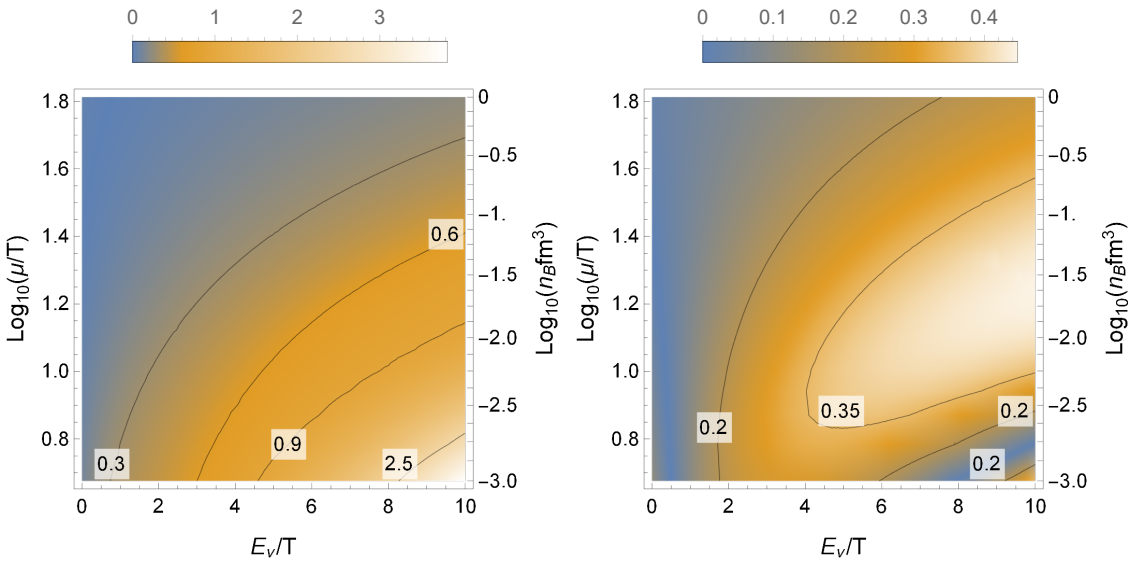

Figure 4.21: Relative difference between the hydrodynamic approximation and the exact total opacities, for neutrinos (**Left**) and anti-neutrinos (**Right**).

analysis of this section. The degenerate approximation is good at high density and becomes unreliable at low density. At high density $n_B = n_B^{(2)}$, the hydrodynamic approximation is within a few tens of percents of error from the exact result, whereas the diffusive one is off by about a factor of 2. At low density $n_B = n_B^{(1)}$, both approximations tend to lose accuracy. However, they appear in some cases to be quite close to the exact result over the range of neutrino energies considered here, which is due to accidental crossings with the exact result. This happens for the diffusive approximation in the case of neutrinos, and for the hydrodynamic approximation in the case of anti-neutrinos.

The main conclusion from the analysis of this subsection is that, for neutrino energies of a few times the temperature, the accuracy of the hydrodynamic approximation depends on the baryonic density. At $n_B \gtrsim 10^{-1}\,\mathrm{fm}^{-3}\big(T/(10\,\mathrm{MeV})\big)^3$, the holographic opacities are quite well approximated by using the leading order hydrodynamic expressions of the correlators (4.4.28) and (4.4.30), whereas higher order corrections become large at lower densities. In practice, this means that, for the highest densities realized in neutron stars, computing only the leading order flavor transport coefficients σ and D from the holographic model is a sufficient input to obtain a good estimate of the neutrino opacities. At lower densities, higher order transport coefficients are required to produce a reasonable approximation. Eventually, as μ/T becomes of order 1, $r_H E_\nu$ becomes significantly larger than 1 for $E_\nu \gtrsim T$. When this is the case, the hydrodynamic expansion cannot be used any-

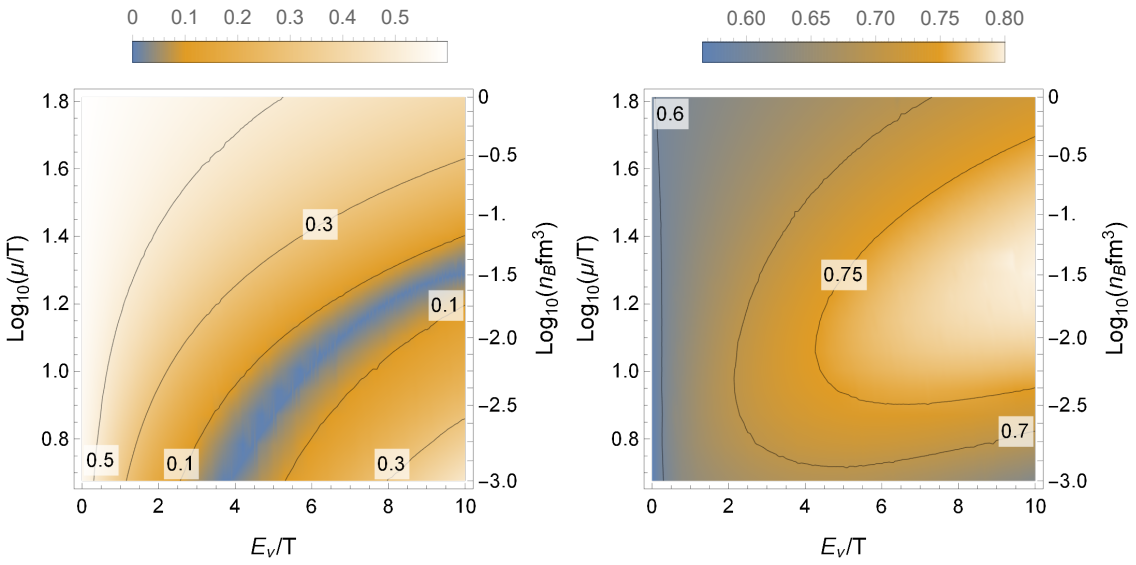

Figure 4.22: Relative difference between the diffusive approximation and the exact opacities, for neutrinos (**Left**) and anti-neutrinos (**Right**).

more, and the full holographic calculation of the chiral current 2-point function is needed to compute the opacities.

4.5.4 Comparison with other calculations

We conclude this section by comparing the results obtained for the neutrino opacities with other calculations from the literature. We start by evaluating the typical order of magnitude of the opacities and compare it with other references. The leading process of neutrino emission is known to be qualitatively different in quark matter compared with nuclear matter. Indeed, whereas the direct Urca process is kinematically suppressed in nuclear matter, it can be realized in quark matter [229, 230]. Since our calculations take place in deconfined matter, the second part of this subsection brings the focus on the comparison with previous results in quark matter.

In Appendix Q, approximate expressions for the opacities are derived within the diffusive and degenerate approximation (defined in Section 4.5.2). In particular, at zero neutrino energy the final result is given by (Q.24)

$$\kappa_{e,0}(n_B) = \frac{G_F^2 |M_{ud}|^2}{2304} \left(3\pi^4\right)^{\frac{1}{6}} N_c^{\frac{1}{2}} (M\ell)^7 w_0^{25/3} \big(\mu(n_B)\big)^5 + \mathcal{O}(\epsilon^4)\,, \tag{4.5.32}$$

where ϵ is the small parameter of the hydrodynamic expansion (4.5.18). We compare

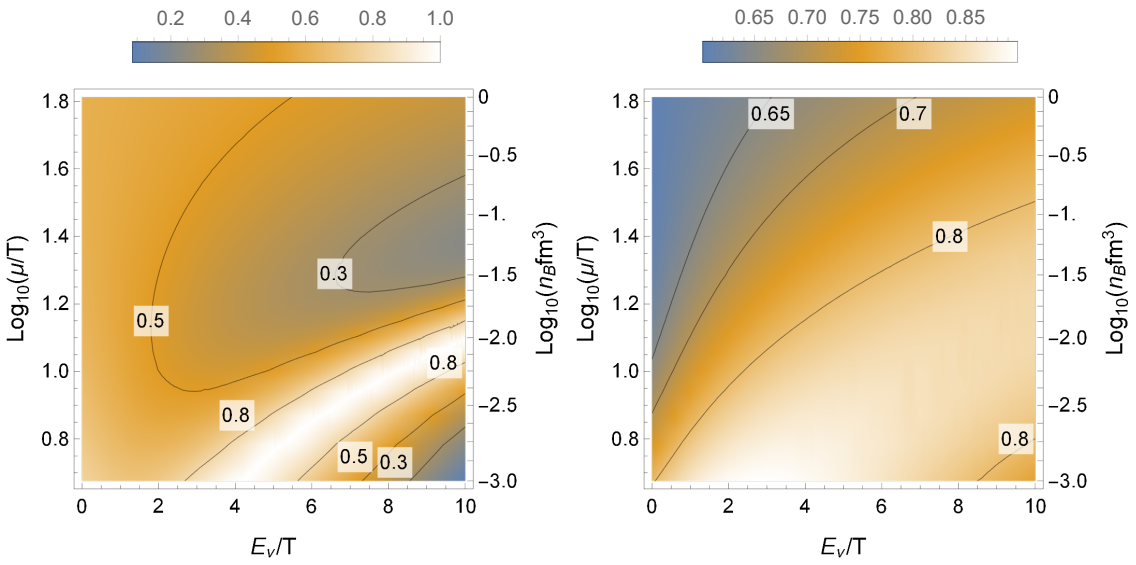

Figure 4.23: Relative difference between the diffusive and degenerate approximation and the exact opacities, for neutrinos (**Left**) and anti-neutrinos (**Right**).

(4.5.32) with the exact value of the opacity at $E_\nu = 0$ in figure 4.26, which shows that (4.5.32) reproduces the correct order of magnitude for the opacity at $n_B > 10^{-2}\,\mathrm{fm}^{-3}$. Substituting the numerical values of the parameters results in the following number

$$\kappa_{e^-}(0) \simeq 6.2 \times 10^2\,\mathrm{km}^{-1} \left(\frac{n_B}{0.1\,\mathrm{fm}^{-3}}\right)^{\frac{5}{3}} \left(\frac{(M\ell)^3}{(M\ell)^3_{\mathrm{free}}}\right)^{-\frac{1}{2}} \left(\frac{w_0^2(M\ell)^3}{(w_0^2(M\ell)^3)_{\mathrm{free}}}\right)^{\frac{5}{6}}, \qquad (4.5.33)$$

where we also used (4.3.21) to express μ as a function of the baryon density n_B.

It is interesting to compare (4.5.33) with the values of the opacities that are currently used in numerical simulations of neutrino transport. The most common rates that are used to describe neutrino transport in nuclear matter are based on mean-field calculations [223], often completed by the random phase approximation to include some degree of nucleon-nucleon correlations [224, 225]. The latest results using these methods in the non-relativistic regime are summarized in [274]. To compare with (4.5.33), we note that the opacities computed in [274] at $E_\nu = 0$ and $n_B = 0.11\,\mathrm{fm}^{-3}$ are between 1 and about $30\,\mathrm{km}^{-1}$. The value that we obtained (4.5.33) is therefore about one order of magnitude larger than the largest opacities from [274]. Also, in [274] multiplying the baryon density by 10 results in opacities which are about 100 times larger. This dependency is close to the behavior in $n_B^{5/3}$ from our conformal result (4.5.33).

We now consider the comparison with references that address the calculation of the

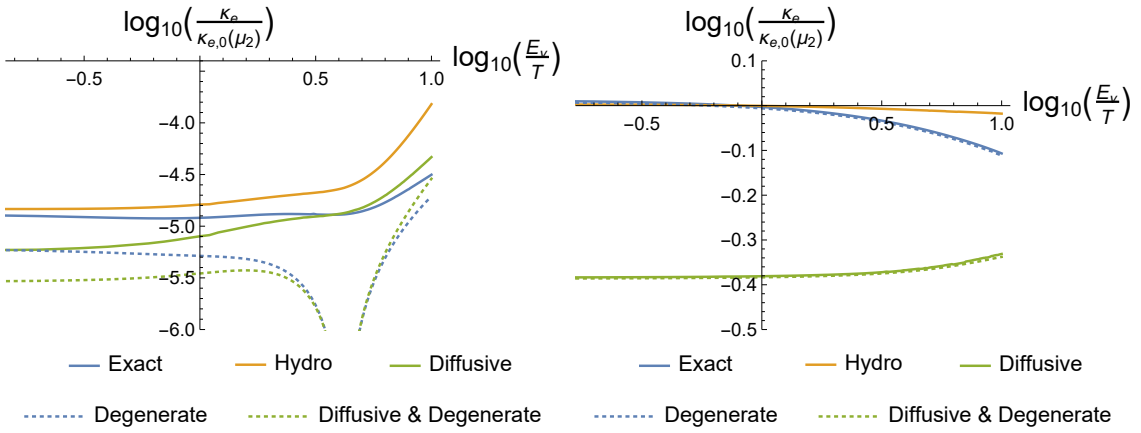

Figure 4.24: Neutrino opacity κ_{e^-} and its various approximations as a function of the neutrino energy E_ν, for $n_B = n_B^{(1)}$(**Left**) and $n_B = n_B^{(2)}$ (**Right**). The opacity is normalized by the approximate value at $E_\nu = 0$ (Q.24), evaluated at $n_B = n_B^{(2)}$.

neutrino radiative coefficients in quark matter [229, 230, 231, 232, 233]. The approach considered in those references is qualitatively very different from ours, since the calculations are done in perturbative QCD. The comparison with our results will therefore indicate how much our strongly-coupled calculation differs from the weakly-coupled result. More specifically, the results that are most readily compared with those presented in this work are derived in [231]. The neutrino opacity $\kappa_{e^-}(E_\nu)$ for degenerate neutrinos is given by equation (6.27) of [231]

$$\kappa_{e^-}^{\mathrm{pQCD}}(E_\nu) = \frac{4G_F^2}{\pi^3}|M_{ud}|^2 p_F(d)^2 p_F(\nu) \times \\ \times \left[1 + \frac{1}{2}\frac{p_F(\nu)}{p_F(d)} + \frac{1}{10}\left(\frac{p_F(\nu)}{p_F(d)}\right)^2\right]\left[(E_\nu - \mu_\nu)^2 + (\pi T)^2\right], \tag{4.5.34}$$

where the $p_F(f_i)$ refer to the Fermi momentum of the corresponding species. We considered the case $|p_F(d) - p_F(\nu)| \geq |p_F(u) - p_F(d)|$, since it is the right ordering in isospin symmetric matter. The weakly coupled quark matter is described by a Fermi liquid, for which the relation between the Fermi momentum and the chemical potential is given by

$$p_F(u) = \mu_u\,(1 + \mathcal{O}(\alpha_s)) \quad , \quad p_F(d) = \mu_d\,(1 + \mathcal{O}(\alpha_s))\ , \tag{4.5.35}$$

where $\alpha_s \equiv g^2/(4\pi)$, g being the strong interaction Yang-Mills coupling. At leading order

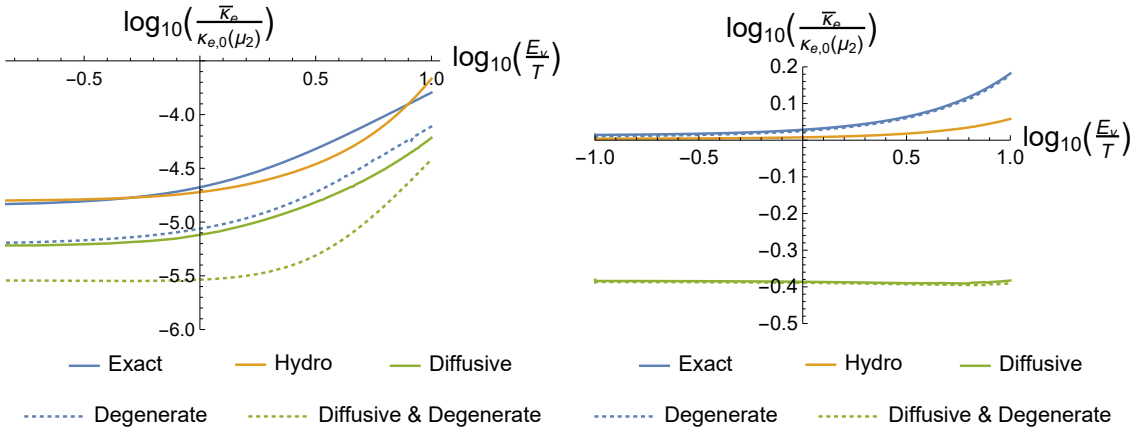

Figure 4.25: Anti-neutrino opacity $\bar{\kappa}_{e^-}$ and its various approximations as a function of the neutrino energy E_ν, for $n_B = n_B^{(1)}$(**Left**) and $n_B = n_B^{(2)}$ (**Right**). The opacity is normalized by the approximate value at $E_\nu = 0$ (Q.24), evaluated at $n_B = n_B^{(2)}$.

$\mathcal{O}(\alpha_s^0)$, (4.5.34) becomes

$$\kappa_{e^-}^{\text{pQCD}}(E_\nu) = \frac{8G_F^2}{\pi^3}|M_{ud}|^2\mu^2\mu_\nu\Big[(E_\nu-\mu_\nu)^2+(\pi T)^2\Big]\left[1+\frac{1}{2}\frac{\mu_\nu}{\mu}+\frac{1}{10}\left(\frac{\mu_\nu}{\mu}\right)^2\right]. \quad (4.5.36)$$

The comparison between the perturbative result (4.5.36) and the exact neutrino opacity computed from our holographic model is shown in figure 4.27. We consider fixed values of the temperature $T = 10\,\text{MeV}$ and baryon density $n_B = 0.11\,\text{fm}^{-3}$, whereas the neutrino energy E_ν is varied. Figure 4.27 shows that, although the qualitative behavior of the two opacities is the same, the perturbative opacity is about two orders of magnitude larger than the result from our calculation.

Note that the widths of the dip in opacity at $E_\nu = \mu_\nu$ scale differently in the energy scales for the two results. Whereas the estimate for the width in our calculation is given by (4.5.24), which is controlled by the neutrino and baryonic chemical potentials, it is clear from (4.5.36) that the width of the perturbative result is controlled by the temperature

$$\Delta E_\nu \simeq \sqrt{\frac{3N_c}{w_0^2}}\frac{\mu_\nu^2}{\mu} \quad , \quad \Delta E_\nu^{\text{pQCD}} = \pi T\,. \quad (4.5.37)$$

We conclude this comparative analysis by a numerical estimate of the two opacities, which should support the results shown in figure 4.27. The typical order of magnitude of κ_{e^-} will be estimated from its value at $E_\nu = 0$. For our holographic result the estimate is

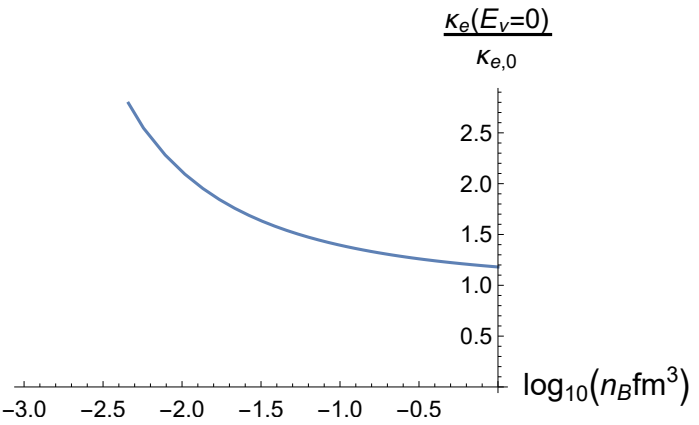

Figure 4.26: The ratio of the neutrino opacity at $E_\nu = 0$ over the approximate expression from the hydrodynamic and degenerate approximation (4.5.32). The ratio is shown as a function of the baryon density in fm^{-3}.

given by (4.5.33). For the perturbative result, the corresponding number can be inferred from equation (6.28) of [231], together with (7.27)

$$\kappa_{e^-}^{\mathrm{pQCD}}(0) \simeq 7.9 \times 10^4\,\mathrm{km}^{-1} \left(\frac{n_B}{0.1\,\mathrm{fm}^{-3}}\right)^{\frac{5}{3}} , \tag{4.5.38}$$

This shows that the perturbative opacity is about two orders of magnitude larger than our holographic calculation (4.5.33). The dependence on the baryon number density n_B is given by the same power 5/3, which is a consequence of the degenerate limit.

All in all, the analysis of this section indicates that the magnitudes of the rates computed from our strongly-coupled holographic model are larger than the results from approximate calculations in nuclear matter, but still much smaller than the perturbative result, by about two orders of magnitude . Since the holographic calculation was done in the deconfined phase, it is rather surprising that we obtain rates that are much closer in magnitude to the nuclear result. The quark matter that we considered is also such that the direct Urca process is not kinematically suppressed, so we might have expected the resulting opacities to be closer to the result from [231]. The lesson from this comparison is that the neutrino emissivity is highly suppressed when taking full account of the non-perturbative nature of the strong interaction.

4.6 Outlook

The results of the work presented in this chapter were summarized in section 4.1. There are two main points. First, we observed that the neutrino radiative coefficients in the kind

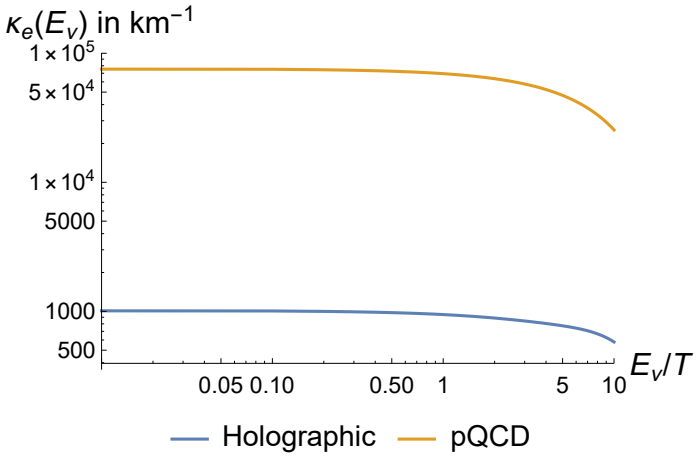

Figure 4.27: Neutrino opacity from our holographic result (blue) compared with the perturbative QCD result [231] (orange), at $n_B = 0.11\,\mathrm{fm}^{-3}$ and $T = 10\,\mathrm{MeV}$. The opacity is expressed in km^{-1}.

of dense quark matter that was considered, were quite well described by hydrodynamics for neutrino energies E_ν smaller than the baryonic chemical potential μ. Second, by comparing with previous results in the literature, we found that the numerical values of the opacities that we computed are larger than the estimates in nuclear matter [274] by about an order of magnitude, and two orders of magnitude smaller than the result in weakly-coupled quark matter [231]. These results suggest that the neutrino transport properties of the strongly-coupled matter show an interesting hydrodynamic behavior, which is very different from the weakly-coupled regime. However, despite the common points (especially the strong coupling), the simple setup considered in this work is by many aspects not very close to the target problem of neutrino transport in QCD matter. The results obtained in this work therefore need to be corroborated by further studies.

The analysis presented here can be extended and improved in several ways. Since we focused on the charged current correlators, an obvious extension is the holographic analysis of the neutral current correlators and their impact on neutrino transport, simply by using the setup described here. As we already mentioned above, this will be the topic of a future publication.

As for the setup, perhaps the most natural place to search for improvements is the holographic model. We shall now provide a summarized description of the physics of the toy model, in order to sketch possible improvements.

The model describes a strongly coupled large-N_c plasma, and N_f quarks with $N_f \sim N_c$ so that they have non-trivial backreaction on the glue dynamics. There is a $U(N_f) \times U(N_f)$

chiral symmetry that is unbroken (no pions here). The theory is conformal like $N = 4$ super-Yang-Mills, ie. at zero temperature and density, the mesons are vectorial and massless, and the spectrum continuous, as is the case in conformal theories. The spectral density is fixed by conformal invariance. This spectrum is quite similar in many respects (but not all) to what is expected in quark-gluon plasma phases. The axial $\mathrm{U}(1)_A$ is not anomalous here, but also does not enter in the dynamics.

This model is the simplest holographic model in which the calculation of chiral current 2-point functions at finite baryon density can be performed. There are several directions for its improvement

- As already mentioned, a next step is to add an isospin chemical potential together with the baryon chemical potential. It is well known that in real world QCD, two different extra phases are possible in such a case. The first, [286], is pion condensation, that can be established from the chiral Lagrangian, while the other, [287], is ρ-condensation that also breaks the rotational symmetry. In the model we use, there are no pions, but one in principle could have vector meson condensation. This possibility was already found to be realized in [281, 282], which discussed a similar holographic model but for a three-dimensional (ABJM) theory. A mapping of the phases and the determination of the (expected second order) phase transition of the four-dimensional theory is necessary before the calculations at finite baryon and isospin chemical potential is done.

- A Chern-Simons (CS) term can be added. In the absence of a tachyon, such a term is unique and is the same as in $N = 4$ super-Yang-Mills, [90]. It controls the P-odd structure of the correlators, it generates the chiral anomalies, and may have an interesting impact in the associated neutrino diffusion problem[16]. In the vacuum of the holographic theory, the CS term affects correlators of currents starting from the three point functions, while it is explicitly independent of the string coupling constant (dilaton). However, at finite baryon density, it affects also the two-point functions of currents.

- As flavor is added by adding flavour branes to the glue sector, [119], one could also upgrade the five-dimensional flavour action to the DBI action which include a class of long distance non-linearities of the flavour gauge fields, [90].

- The model used is relatively close to $\mathcal{N} = 4$ $\mathrm{SU}(N_c)$ SYM coupled to fundamental flavor fields ($N = 2$ hypermultiplets), [119], which is an interesting model to test our formalism. This is a top-down model with N_f D7 branes embedded non-trivially in the ten-dimensional background space-time, $AdS_5 \times S^5$. It is conformal to leading order, as the running of the gauge coupling due to the presence of the hypermultiplets

[16]The effects of the Chern-Simons term on transport in holographic theories has been discussed for example in [291, 292, 290].

is subleading in $1/N_c$ for $N_f \sim \mathcal{O}(1)$. Its associated holographic physics has been analysed in detail, [293, 275, 276]. Because the embedding of the flavor branes inside $AdS_5 \times S^5$ is non-trivial the flavour gauge fields are subjected to a different open string metric than in the previous items. In this case, the full DBI action is used as well as the CS term.

- A further improvement, but keeping to the top-down nature of the holographic theory, is to use the Sakai-Sugimoto model [121, 124], introduced in section 2.2. In this case the glue sector is confining and non-scale invariant while we have quarks and antiquarks with a chiral symmetry that is similar to QCD with chiral group $U(N_f)_L \times SU(N_f)_R$. This setup is close to QCD, with the only exception that the relevant field that is important for giving mass to the quarks, the open string tachyon is missing.[17]

- The bifundamental open string tachyon, which in the present setup is not included, is important in the holographic setup, as it is the order parameter for chiral symmetry breaking in QCD, [138], as well as a way of adding a mass to the quarks. A simple holographic model that includes the bifundamental open string tachyon, using Sen's string theory action, [295], was proposed and analyzed in [156, 157, 186]. The model does extremely well in describing chiral symmetry breaking and meson spectra. It is therefore a good laboratory for testing the calculations of the present paper.

- As mentioned in the introduction to this thesis, eventually the goal is to analyze neutrino tranpsort in V-QCD (reviewed in section 2.3), which is the best holographic model so far to address QCD dynamics in a variety of arenas.

- In all the setups mentioned above, including V-QCD, either quarks are all massless or all quarks have the same mass. In the case studied in this paper, the flavor sector is assumed to contain two massless flavors. In QCD, this would correspond to including only the two lightest flavors up and down, and neglecting their masses. At the densities relevant for neutron stars, it is expected that neglecting the up and down masses is a good approximation. On the other hand, it cannot be excluded that neutron star cores exhibit some degree of strangeness. In order to take into account strange quarks, the current model would need to be extended to include a third massive flavor. Working with an $SU(3)$ chiral group instead of $SU(2)$ is just a matter of algebra, but including quark masses actually requires the bulk theory to include the bifundamental tachyon field T^{ij}, with a non-trivial matrix structure. This involves the analogue of the non-abelian DBI action for the tachyon. An example of this was worked out in the appendix of reference [157]. The formalism needs to be

[17] Of course, as mentioned in section 2.2, it is part of that theory, but for the relevant configuration, the tachyon string is non-local, [132].

developed so that we can address masses of the strange quark substantially different from those of up or down quarks.

Apart from the simplicity of the holographic model, our approach included other approximations and simplifications of the general formalism which are typical in the literature on neutrino transport.

- The derivation of the Boltzmann equation for neutrinos used the semiclassical gradient approximation (see (4.2.27) below), which holds when the mean free paths of the neutrinos are much longer than their de Broglie wavelengths. A particular higher order correction includes the effects of the (maximal) breaking of parity by the neutrinos (which are left-handed), and results in the so-called chiral kinetic theory [288]. Those corrections were found to be particularly relevant to neutrino transport [289].

- We used the so-called quasi-particle approximation for neutrinos, so that their propagator has the same form as the free propagator but with generalized particle distribution functions (see (4.2.35)-(4.2.36) below).

- We assumed that the neutrinos are sufficiently close to equilibrium so that their chemical potential is well defined, and at β-equilibrium with the medium.

- We also assumed that the medium composed of electrons and quark matter was at thermal equilibrium. This is expected to be a good approximation as the astrophysical times should always be much longer than the thermalization time for the medium.

While it is expected that these approximations work well in many cases relevant for neutron stars and supernovae, it is also clear that they will not apply to all regimes, and eventually a description of neutrino transport which is valid for neutrinos fully out of equilibrium is desirable. This would require to solve the full Kadanoff-Baym equations instead of the Boltzmann equations, which is much more involved numerically.

In addition to going fully out of equilibrium, there are other extensions to our formalism related to the leptonic component, that are mentioned in section 4.2.3:

- We did not include muons (or muon neutrinos). While muons are relatively massive, their effect may be significant at the highest densities reached in neutron stars or core-collapse supernovae [277, 278].

- We did not include the purely elecroweak interactions between neutrinos and leptons. Since these interactions are weak, they may be analyzed separately, and their effect can be added on top of the results presented here.

We leave such extensions of our approach for future work.

General discussion

In this work, we made progress towards the description of dense baryonic matter using the holographic V-QCD model. On the one hand, we constructed the single baryon solution in V-QCD, and analyzed some of its properties. On the other hand, we made the first step towards an analysis of neutrino transport in V-QCD, by considering first a toy model of strongly-coupled quark matter.

Specific directions of improvement for each of these topics were mentioned in the previous chapters. In particular, obvious extensions include the calculation of the static properties of the V-QCD baryon, and the analysis of the neutrino rates from neutral current interactions in the toy model presented above.

From a wider perspective, the general program that follows from this work, is to obtain a description of dense baryonic matter from V-QCD. The exact gravitational dual of such a boundary state would be given by a finite density of instantons. Computing a solution of this sort is probably out of our reach, but we expect that it should be effectively well described in terms of a codimension-1 baryonic membrane. The idea will be to use the single baryon solution as an input to determine the dynamics of this membrane.

Once the solution for baryonic matter is obtained, it will be interesting to understand what are the improvements compared with the homogeneous approximations considered in [174]. In particular, it will make it possible to examine the robustness of the results obtained in the context of neutron stars [165].

Eventually, this project should converge with the analysis of neutrino transport, to investigate the transport of neutrinos in neutron star matter with V-QCD. As mentioned in section 1.4, the transport properties are of particular interest for investigating the phases of dense QCD matter, since they are expected to be more sensitive to the phase structure than bulk thermodynamic properties [82].

The final goal of this approach with the V-QCD framework is to provide a state-of-the-art holographic model for dense (large N) QCD. The advantages of V-QCD make it a good framework for this purpose. Its structure based on (non-critical) string theory ensures a good match with QCD properties, and is quite rigid, depending on a few scalar functions. The asymptotic behavior of these functions is constrained by qualitative properties of QCD, and the remaining freedom is contained in a few parameters. The model is in good qualitative agreement with QCD for generic values of the parameters. By adjusting the

parameters, QCD data can be fitted with a good accuracy, with a number of parameters much smaller than the amount of data.

In analogy with the phases where the comparison with QCD is possible, it is expected that the predictions of V-QCD in the bayonic phase should also be qualitatively reliable. Moreover, because the model applies to the whole part of the phase diagram where QCD is strongly coupled, it offers a unique opportunity to go further and fit jointly QCD data in different regimes. Then, predictions can be made for dense QCD, based on a consistent model solidly anchored in available data. As explained in section 3.2.2, it is typically not easy to produce a simultaneous fit of quark-gluon-plasma thermodynamics and meson spectra. Including baryonic properties will make the fit even more challenging. Eventually, the best approach for this procedure should probably involve the methods of machine learning, that would hopefully result in a V-QCD model that can reproduce well most available QCD data, with a minimal set of parameters.

Appendix

A Conventions and Symmetry Transformations for V-QCD

A.1 Conventions for the gauge fields

For the $SU(N_f)$ generators λ^a, $A = 1, \dots N_f^2 - 1$, we take

$$(\lambda^a)^\dagger = \lambda^a \quad , \quad \mathrm{Tr}(\lambda^a \lambda^b) = \frac{1}{2}\delta^{ab} \,. \tag{A.1}$$

On the other hand the normalization for the $U(1)$ generator is

$$\lambda^0 = \mathbb{I} \,, \tag{A.2}$$

where $\mathbb{I}$ is the $N_f \times N_f$ identity matrix. For the $SU(N_f)$ generators λ^a, $a = 1, \dots, N_f^2 - 1$, we have

$$[\lambda^a, \lambda^b] = i f^{ab}{}_c \, \lambda^c \quad , \quad \mathrm{Tr}(\lambda^a \{\lambda^b, \lambda^c\}) = d^{abc} \,, \tag{A.3}$$

where $f^{ab}{}_c$ and d^{abc} are, respectively, the structure constants and the normalized anomaly Casimir for $SU(N_f)$. Because of (A.1) $f^{ab}{}_c$ and d^{abc} are real numbers.

We define the gauge fields to be Hermitian

$$A_\mu = A_\mu^{U(1)} \mathbb{I} + A_\mu^a \lambda^a \,, \tag{A.4}$$

where $A^{U(1)}$ and A_μ^a are real. In differential form notation[18], the field strength and covariant derivative then read

$$F = dA - iA \wedge A \quad , \quad D \equiv d - iA\cdot \tag{A.5}$$

where $A\cdot$ indicates the representation-dependent action of the gauge algebra. In particular the Bianchi identity reads

$$DF = dF + iF \wedge A - iA \wedge F = 0 \,, \tag{A.6}$$

and the covariant derivative of the tachyon is given by

$$DT = dT + i\,T A_L - i A_R T \qquad\qquad DT^\dagger = dT^\dagger - i A_L T^\dagger + i\,T^\dagger A_R \,. \tag{A.7}$$

[18] We use the conventions of Appendix B of [90].

A.2 Normalization of the chiral currents

Currents are defined to be Hermitian. We decompose a $U(N_f)$ flavor current as

$$J_\mu = \frac{1}{2N_f} J_\mu^{U(1)} \mathbb{I} + J_\mu^a \lambda^a. \tag{A.8}$$

This decomposition corresponds to the following normalization for the currents

$$J_{L,R}^{a\,\mu} = \mathrm{Tr}_{\mathrm{flavor}} \left(i\bar{q}\gamma^\mu \frac{1 \pm \gamma_5}{2} \lambda^a q \right) , \tag{A.9}$$

$$J_{L,R}^{U(1)\,\mu} = \mathrm{Tr}_{\mathrm{flavor}} \left(i\bar{q}\gamma^\mu \frac{1 \pm \gamma_5}{2} q \right) . \tag{A.10}$$

Notice that the normalization of the currents and gauge field (A.4) has been chosen in such a way that the boundary coupling of the current to the gauge field reads

$$2 \int d^4x \, \mathrm{Tr}(J^\mu A_\mu) = \int d^4x \left(J^{U(1)\,\mu} A_\mu^{U(1)} + J^{a\,\mu} A_\mu^a \right) . \tag{A.11}$$

A.3 Gauge Transformations

Under gauge transformations with parameters $(V_L, V_R) \in SU(N_f)_L \times SU(N_f)_R$, the gauge fields and tachyon transform in the following way

$$\begin{gathered} A_L \to V_L A_L V_L^\dagger - i d V_L V_L^\dagger \quad , \quad A_R \to V_R A_R V_R^\dagger - i d V_R V_R^\dagger , \\ F_L \to V_L \, F_L \, V_L^\dagger \quad , \quad F_R \to V_R \, F_R \, V_R^\dagger , \\ T \to V_R T V_L^\dagger \quad , \quad T^\dagger \to V_L T^\dagger V_R^\dagger . \end{gathered} \tag{A.12}$$

An infinitesimal gauge transformation is defined as $V_\epsilon(x) = e^{\epsilon\Lambda(x)} \simeq 1 + \epsilon\,\Lambda(x)$ and the gauge transformation of a field as $A \to A + \epsilon \delta_\Lambda A$. From (A.12) we have then:

$$\begin{aligned} &\delta_\Lambda A = -i\, D\Lambda = -i\, d\Lambda + [\Lambda, A] , \\ &\delta_\Lambda F = [\Lambda, F] , \\ &\delta_{\Lambda_L} T = -T\Lambda_L , \\ &\delta_{\Lambda_R} T = \Lambda_R T . \end{aligned} \tag{A.13}$$

Notice that the generators of gauge transformations are antihermitian. When we decompose them in their $U(1)$ and $SU(N_f)$ parts, we will write

$$\Lambda = i\alpha \mathbb{I} + i\Lambda^a \lambda^a , \tag{A.14}$$

with α and Λ^a real parameters. In particular we have, from (A.4) and (A.14)

$$\delta A_\mu^{U(1)} = \partial_\mu \alpha \qquad \text{and} \qquad \delta A_\mu^a = (D_\mu \Lambda)^a . \tag{A.15}$$

A.4 Discrete symmetries

We describe here the transformation properties of the flavor fields under parity and charge conjugation. These were presented in [138].

Parity

The parity transformation is

$$P = P_1 \cdot P_2 \,. \tag{A.16}$$

where P_2 is the action of parity on space

$$P_2 : (x_1, x_2, x_3) \to (-x_1, -x_2, -x_3) \,. \tag{A.17}$$

and P_1 the action on the flavor fields.

$$P_1 : L \leftrightarrow R \quad , \quad T \leftrightarrow T^\dagger \,. \tag{A.18}$$

Charge conjugation

The action of charge conjugation on the flavor fields is

$$C : L \to -R^t \quad , \quad R \to -L^t \quad , \quad T \to T^t \quad , \quad T^\dagger \to \left(T^\dagger\right)^t \,. \tag{A.19}$$

A.5 The 2D theory for the ansatz fields

We present in this subsection conventions and definitions for the theory of the fields of the instanton ansatz (3.1.50)-(3.1.52) and (3.1.62) that live on the 2D space $(\xi, r) \equiv x^{\bar{\mu}}$. The first thing to note is that we choose the following convention for the 2D Levi-Civita tensor

$$\epsilon^{\xi r} = 1 \,. \tag{A.20}$$

Before imposing the parity symmetry, the fields of the gauge-field ansatz exist in two copies L and R that each have a residual gauge freedom (3.1.53) under which the fields have well-defined transformation properties :

- $\Phi^{(L/R)}$ is neutral.
- $\phi^{(L/R)} \equiv \phi_1^{(L/R)} + i\phi_2^{(L/R)}$ has charge 1.
- $A_{\bar{\mu}}^{(L/R)} \equiv \left(A_\xi^{(L/R)}, A_r^{(L/R)}\right)$ is the gauge field.

From these, we construct the L/R covariant derivatives of the complex scalars $\phi^{(L/R)}$ under the residual gauge freedom

$$D_{\bar{\mu}}\phi^{(L/R)} \equiv \left(\partial_{\bar{\mu}} - iA_{\bar{\mu}}^{(L/R)}\right)\phi^{(L/R)}\,, \tag{A.21}$$

which in component reads

$$D_{\bar{\mu}}\phi_1^{(L/R)} = \partial_{\bar{\mu}}\phi_1^{(L/R)} + A_{\bar{\mu}}^{(L/R)}\phi_2^{(L/R)} \quad , \quad D_{\bar{\mu}}\phi_2^{(L/R)} = \partial_{\bar{\mu}}\phi_2^{(L/R)} - A_{\bar{\mu}}^{(L/R)}\phi_1^{(L/R)}\,. \tag{A.22}$$

We define also the gauge-invariant field strength for $A_{\bar{\mu}}^{(L/R)}$

$$F_{\bar{\mu}\bar{\nu}}^{(L/R)} = \partial_{\bar{\mu}}A_{\bar{\nu}}^{(L/R)} - \partial_{\bar{\nu}}A_{\bar{\mu}}^{(L/R)}\,. \tag{A.23}$$

Once the parity symmetry (3.1.56)-(3.1.58) is imposed, the L/R fields collapse into a single set with the residual gauge freedom (3.1.60). Also, the ansatz for the tachyon takes the form of (3.1.64) and the tachyon phase θ can be absorbed into the gauge fields to build gauge invariant quantities (3.1.80)

$$\tilde{A}_{\bar{\mu}} \equiv A_{\bar{\mu}} + \partial_{\bar{\mu}}\theta \quad , \quad \tilde{\phi} \equiv \mathrm{e}^{i\theta}\phi\,. \tag{A.24}$$

B The P-odd instanton

We justify in this appendix the statement made in Section 3.1.4 that a baryon state in the boundary theory corresponds to an axial instanton for the bulk gauge fields, that is an instanton solution even under parity

$$P \;:\; \mathbf{x} \to -\mathbf{x} \quad , \quad L \leftrightarrow R\,, \tag{B.1}$$

and that a P-odd instanton cannot have a finite energy. This implies that not only a P-odd instanton cannot generate baryon number, but also does not correspond to any other finite energy state in the boundary theory.

Requiring the ansatz to be P-odd imposes the following relation between the left and right-handed ansatz fields, instead of (3.1.56)- (3.1.58)

$$A_1 \equiv A_1^L = A_1^R \quad , \quad A_2 \equiv A_2^L = A_2^R\,, \tag{B.2}$$

$$\phi_1 \equiv \phi_1^L = \phi_1^R \quad , \quad \phi_2 \equiv \phi_2^L = -\phi_2^R - 2\,, \tag{B.3}$$

$$\Phi \equiv \Phi^L = -\Phi^R\,. \tag{B.4}$$

Note that, because of the condition for ϕ_2 (B.3), the P-odd ansatz completely fixes the residual gauge (3.1.53). The P-odd tachyon ansatz is

$$T^{SU(2)} = i\tau(r,\xi)\exp\left(i\theta(r,\xi)\frac{x\cdot\sigma}{\xi}\right) \quad , \quad \tau,\theta \in \mathbb{R}\,. \tag{B.5}$$

We still consider the chiral limit where the quark masses are equal to 0. In this case, due to the factor i, the P-odd ansatz is not continuously connected to a vacuum state with tachyon UV asymptotics given by (2.3.20). It is rather connected to a $U(1)_A$ rotation of the vacuum, which is not degenerate with the vacuum due to the $U(1)_A$ anomaly. There is therefore no such thing as a static P-odd instanton solution taking root on the vacuum. This result can be interpreted as the bulk equivalent of the non-conservation of the $U(1)_A$ charge.

C The DBI contribution to the baryon equations of motion

The DBI equations of motion for the flavor sector are obtained from varying (3.1.18) with respect to the gauge fields $\mathbf{L}$ and $\mathbf{R}$ and the tachyon field τ.

abelian EoM The left-handed abelian equations of motion are obtained to be

$$\begin{aligned}
&\partial_N \Bigg[V_f(\lambda,\tau^2)\sqrt{-\det \tilde{g}^{(L)}}w \times \\
&\quad \times \left(\mathcal{L}^{(L)} \left((\tilde{g}^{(L)})^{-1} \right)^{[MN]} + \frac{1}{4}w^2 \mathrm{Tr}\left(F^{MS}_{(L)} F^{(L)N}_S - F^{NS}_{(L)} F^{(L)M}_S \right) - \right. \\
&\qquad \left. -\frac{1}{4}w^2 \mathrm{Tr}\left(F^{(L)[MN]} F^{(L)C}_C \right) - \frac{1}{2}\kappa\tau^2 S^{[MN]} \right) \Bigg] = \\
&= \frac{1}{4} V_f(\lambda,\tau^2) \left(\sqrt{-\det \tilde{g}^{(L)}} \left((\tilde{g}^{(L)})^{-1} \right)^{(MN)} + \sqrt{-\det \tilde{g}^{(R)}} \left((\tilde{g}^{(R)})^{-1} \right)^{(MN)} \right) \times \\
&\qquad \times \kappa\tau^2 \mathrm{Tr}\left[i D_N U^\dagger U + h.c. \right] + \hat{J}^{(L)}_{CS} \,, \qquad \text{(C.1)}
\end{aligned}$$

where the indices are raised according to (3.1.15). Note that, because $\tilde{g}$ is not symmetric, S^{MN} is a priori not symmetric either. We denoted by $\mathcal{L}^{(\mathcal{L}/\mathcal{R})}$ the left-handed/right-handed integrand of (3.1.18) divided by $V_f(\lambda,\tau^2)\sqrt{-\det \tilde{g}^{(L/R)}}$

$$\begin{aligned}
\mathcal{L}^{(L/R)} \equiv \frac{1}{2} &+ \frac{1}{4}\kappa\tau^2 \left((\tilde{g}^{(L/R)})^{-1} \right)^{(MN)} S_{MN} \qquad \text{(C.2)} \\
&- \frac{1}{8}w^2 \left((\tilde{g}^{(L/R)})^{-1} \right)^{MN} \left((\tilde{g}^{(L/R)})^{-1} \right)^{PQ} \mathrm{Tr}\, F^{(L/R)}_{NP} F^{(L/R)}_{QM} \\
&+ \frac{1}{16}w^2 \mathrm{Tr}\left(\left((\tilde{g}^{(L/R)})^{-1} \right)^{[MN]} F^{(L/R)}_{NM} \right)^2 ,
\end{aligned}$$

and the contribution from the TCS action to the abelian EoMs is denoted by $\hat{J}_{CS}$

$$-\frac{1}{M^3 N_c}\delta_{\hat{L}} S_{CS} = \delta\hat{L} \wedge \hat{J}^{(L)}_{CS} \,, \qquad \text{(C.3)}$$

and likewise for R. The right-handed equations of motion are the same[19] upon $L \leftrightarrow R$ and $U \leftrightarrow U^\dagger$.

Tachyon EoM Because it also appears in the effective metric (3.1.14), the equations of motion for the modulus of the tachyon field have a form similar to the abelian gauge field equations of motion

$$\begin{aligned}
&\partial_N \Bigg[V_f(\lambda,\tau^2)\sqrt{-\det \tilde{g}^{(L)}}\kappa\partial_M\tau \times \\
&\quad \times \Bigg(\mathcal{L}^{(L)} \left((\tilde{g}^{(L)})^{-1} \right)^{(MN)} + \frac{1}{4} w^2 \mathrm{Tr} \left(F^{MS}_{(L)} F^{(L)N}_S + F^{NS}_{(L)} F^{(L)M}_S \right) \\
&\qquad -\frac{1}{4} w^2 \mathrm{Tr} \left(F^{(L)(MN)} F^{(L)C}_C \right) - \frac{1}{2}\kappa\tau^2 S^{(MN)} \Bigg) + (L \leftrightarrow R) \Bigg] = \\
&= V_f(\lambda,\tau^2) \left[\sqrt{-\det \tilde{g}^{(L)}} \left(\frac{1}{2} \left((\tilde{g}^{(L)})^{-1} \right)^{(MN)} \kappa\tau S_{MN} + \frac{1}{V_f} \frac{\delta V_f}{\delta \tau} \mathcal{L}^{(L)} \right) + (L \leftrightarrow R) \right] + \\
&\quad + J^\tau_{CS} \,,
\end{aligned} \tag{C.4}$$

where the contribution of the TCS action to the tachyon EoM is denoted by J^τ_{CS}

$$-\frac{1}{M^3 N_c} \delta_\tau S_{CS} = \delta\tau J^\tau_{CS} \,. \tag{C.5}$$

The equations of motion for U are

$$\frac{1}{4} \left[D_{(M} \left(V_f(\lambda,\tau^2)\kappa\tau^2 \sqrt{-\det \tilde{g}^{(L)}} \left((\tilde{g}^{(L)})^{-1} \right)^{(MN)} D_{N)} U^\dagger \right) U - h.c. + (L \leftrightarrow R) \right] = J^U_{CS} \,, \tag{C.6}$$

where the contribution of the CS action to the U EoM is denoted by J^U_{CS}

$$-\frac{1}{M^3 N_c} \delta_U S_{CS} = \mathrm{Tr} \left(\delta U J^U_{CS} U^\dagger \right) \,. \tag{C.7}$$

Non-abelian EoM As the non-abelian part of the gauge fields does not appear in the effective metric $\tilde{g}$, the DBI contribution to the non-abelian equations of motion is much simpler than for the abelian part and the tachyon

$$\begin{aligned}
&\frac{1}{2} D_N \left[V_f(\lambda,\tau^2) \sqrt{-\det \tilde{g}^{(L)}} w^2 \left(\frac{1}{2} F^{(L)[NM]} - \frac{1}{4} \left((\tilde{g}^{(L)})^{-1} \right)^{[NM]} F^{(L)C}_C \right) \right] = \\
&= \frac{1}{8} V_f(\lambda,\tau^2) \left(\sqrt{-\det \tilde{g}^{(L)}} \left((\tilde{g}^{(L)})^{-1} \right)^{(MN)} + \sqrt{-\det \tilde{g}^{(R)}} \left((\tilde{g}^{(R)})^{-1} \right)^{(MN)} \right) \times
\end{aligned} \tag{C.8}$$

[19] Here it shouldn't be forgotten that it also changes the definition of the raising of indices.

$$\times \kappa\tau^2 \left(iD_N U^\dagger U - \frac{1}{N_f}\mathrm{Tr}(iD_N U^\dagger U) + h.c. \right) + J_{CS}^{(L)} \,,$$

and the right-handed equations are obtained by exchanging $(L \leftrightarrow R)$ and $U \leftrightarrow U^\dagger$. The contribution of the TCS action to the non-abelian EoMs is denoted by J_{CS}

$$-\frac{1}{M^3 N_c}\delta_L S_{CS} = \delta L^a \wedge J_{CS}^{(L)\,a} \,, \tag{C.9}$$

and likewise for R.

D Tachyon-dependent Chern-Simons terms

In this appendix, we discuss the TCS action for a tachyon proportional to a unitary matrix $(T = \tau U)$.

First, we construct the most general single-trace Ω_5 form out of the fields τ, U, L and R, which is invariant under global $SU(N_f)_L \times SU(N_f)_R$ transformations. Moreover, the exterior derivative $F_6 = d\Omega_5$ must be gauge invariant (i.e., invariant under local transformations also), and have the expected eigenvalues under parity and charge conjugation. That is, we require that our ansatz for Ω_5 is odd under the action of the P_1 operator and charge conjugation even, with definitions of Appendix A.

In order to write down our ansatz, we first construct all possible single trace 5-forms and 4-forms built out of the non-abelian 1-forms $\mathbf{L}/\mathbf{R}$ and $DU = dU - i\mathbf{R}U + iU\mathbf{L}$ as well as the 2-forms $F^{(L/R)}$ (recall that $DU^\dagger = -U^\dagger DUU^\dagger$ is not independent). They are then made covariant under global transformations by adding instances U or $U^\dagger$ in the traces. We then apply the projector $\mathbb{I} + P_1 - C - P_1 C$ on the forms, which projects to the P_1-odd C-even subspace. This leaves us with 45 independent P odd and C even 5-forms, which we denote by $F_5^{(i)}[U, \mathbf{L}, \mathbf{R}]$, and 11 independent 4-forms, which we denote by $F_4^{(i)}[U, \mathbf{L}, \mathbf{R}]$. The complete list of 4-forms is given by

$$\begin{aligned}
F_4^{(1)} &= \mathrm{Tr}(\mathbf{L} \wedge \mathbf{F}^{(L)} U^\dagger \wedge DU) + \mathrm{Tr}(\mathbf{L}U^\dagger \wedge DU \wedge \mathbf{F}^{(L)}) + \\
&\quad + \mathrm{Tr}(\mathbf{R} \wedge DUU^\dagger \wedge \mathbf{F}^{(R)}) + \mathrm{Tr}(\mathbf{R} \wedge \mathbf{F}^{(R)} \wedge DUU^\dagger) \\
F_4^{(2)} &= \mathrm{Tr}(\mathbf{L}U^\dagger \wedge DUU^\dagger \wedge \mathbf{F}^{(R)} U) + \mathrm{Tr}(\mathbf{L}U^\dagger \wedge \mathbf{F}^{(R)} \wedge DU) + \\
&\quad + \mathrm{Tr}(\mathbf{R}U \wedge \mathbf{F}^{(L)} U^\dagger \wedge DUU^\dagger) + \mathrm{Tr}(\mathbf{R} \wedge DU \wedge \mathbf{F}^{(L)} U^\dagger) \\
F_4^{(3)} &= -\mathrm{Tr}(\mathbf{L} \wedge \mathbf{L}U^\dagger \wedge DUU^\dagger \wedge \mathbf{R}U) + \mathrm{Tr}(\mathbf{L}U^\dagger \wedge DUU^\dagger \wedge \mathbf{R} \wedge \mathbf{R}U) + \\
&\quad + \mathrm{Tr}(\mathbf{L} \wedge \mathbf{L}U^\dagger \wedge \mathbf{R} \wedge DU) + \mathrm{Tr}(\mathbf{L}U^\dagger \wedge \mathbf{R} \wedge \mathbf{R} \wedge DU) \\
F_4^{(4)} &= \mathrm{Tr}(\mathbf{L} \wedge \mathbf{F}^{(L)} U^\dagger \wedge \mathbf{R}U) + \mathrm{Tr}(\mathbf{L}U^\dagger \wedge \mathbf{R}U \wedge \mathbf{F}^{(L)}) + \\
&\quad + \mathrm{Tr}(\mathbf{L}U^\dagger \wedge \mathbf{R} \wedge \mathbf{F}^{(R)} U) + \mathrm{Tr}(\mathbf{L}U^\dagger \wedge \mathbf{F}^{(R)} \wedge \mathbf{R}U) \\
F_4^{(5)} &= -\mathrm{Tr}(\mathbf{L} \wedge \mathbf{L} \wedge \mathbf{L}U^\dagger \wedge DU) - \mathrm{Tr}(\mathbf{R} \wedge \mathbf{R} \wedge \mathbf{R} \wedge DUU^\dagger)
\end{aligned}$$

$$
\begin{aligned}
F_4^{(6)} &= \mathrm{Tr}(\mathbf{L}\wedge\mathbf{L}\wedge\mathbf{L}U^\dagger\wedge\mathbf{R}U) + \mathrm{Tr}(\mathbf{L}U^\dagger\wedge\mathbf{R}\wedge\mathbf{R}\wedge\mathbf{R}U)\\
F_4^{(7)} &= \mathrm{Tr}(\mathbf{L}U^\dagger\wedge DUU^\dagger\wedge DUU^\dagger\wedge\mathbf{R}U) + \mathrm{Tr}(\mathbf{L}U^\dagger\wedge\mathbf{R}\wedge DUU^\dagger\wedge DU)\\
F_4^{(8)} &= \mathrm{Tr}(\mathbf{R}\wedge DUU^\dagger\wedge\mathbf{R}\wedge DUU^\dagger) - \mathrm{Tr}(\mathbf{L}U^\dagger\wedge DU\wedge\mathbf{L}U^\dagger\wedge DU)\\
F_4^{(9)} &= \mathrm{Tr}(\mathbf{L}U^\dagger\wedge\mathbf{R}\wedge DUU^\dagger\wedge\mathbf{R}U) - \mathrm{Tr}(\mathbf{L}U^\dagger\wedge\mathbf{R}U\wedge\mathbf{L}U^\dagger\wedge DU)\\
F_4^{(10)} &= -\mathrm{Tr}(\mathbf{L}U^\dagger\wedge DUU^\dagger\wedge DUU^\dagger\wedge DU) - \mathrm{Tr}(\mathbf{R}\wedge DUU^\dagger\wedge DUU^\dagger\wedge DUU^\dagger)\\
F_4^{(11)} &= \mathrm{Tr}(\mathbf{L}U^\dagger\wedge\mathbf{R}U\wedge\mathbf{L}U^\dagger\wedge\mathbf{R}U)
\end{aligned}
\tag{D.1}
$$

The complete list of 5-forms is the following:

$$
\begin{aligned}
F_5^{(1)} &= \mathrm{Tr}(DU\wedge\mathbf{F}^{(L)}\wedge\mathbf{F}^{(L)}U^\dagger) + \mathrm{Tr}(DUU^\dagger\wedge\mathbf{F}^{(R)}\wedge\mathbf{F}^{(R)})\\
F_5^{(2)} &= \mathrm{Tr}(DU\wedge\mathbf{F}^{(L)}U^\dagger\wedge DUU^\dagger\wedge DUU^\dagger) + \mathrm{Tr}(DUU^\dagger\wedge DUU^\dagger\wedge DUU^\dagger\wedge\mathbf{F}^{(R)})\\
F_5^{(3)} &= \mathrm{Tr}(DUU^\dagger\wedge\mathbf{F}^{(R)}U\wedge\mathbf{F}^{(L)}U^\dagger) + \mathrm{Tr}(DU\wedge\mathbf{F}^{(L)}U^\dagger\wedge\mathbf{F}^{(R)})\\
F_5^{(4)} &= \mathrm{Tr}(DUU^\dagger\wedge DUU^\dagger\wedge DUU^\dagger\wedge DUU^\dagger)\\
F_5^{(5)} &= \mathrm{Tr}(\mathbf{L}\wedge\mathbf{L}\wedge\mathbf{L}\wedge\mathbf{L}\wedge\mathbf{L}) - \mathrm{Tr}(\mathbf{R}\wedge\mathbf{R}\wedge\mathbf{R}\wedge\mathbf{R}\wedge\mathbf{R})\\
F_5^{(6)} &= \mathrm{Tr}(\mathbf{L}\wedge\mathbf{L}\wedge\mathbf{L}\wedge\mathbf{L}U^\dagger\wedge\mathbf{R}U) - \mathrm{Tr}(\mathbf{L}U^\dagger\wedge\mathbf{R}\wedge\mathbf{R}\wedge\mathbf{R}\wedge\mathbf{R}U)\\
F_5^{(7)} &= \mathrm{Tr}(\mathbf{L}\wedge\mathbf{L}\wedge\mathbf{L}\wedge\mathbf{L}U^\dagger\wedge DU) + \mathrm{Tr}(\mathbf{R}\wedge\mathbf{R}\wedge\mathbf{R}\wedge\mathbf{R}\wedge DUU^\dagger)\\
F_5^{(8)} &= \mathrm{Tr}(\mathbf{L}\wedge\mathbf{L}\wedge\mathbf{L}U^\dagger\wedge\mathbf{R}\wedge\mathbf{R}U) - \mathrm{Tr}(\mathbf{L}\wedge\mathbf{L}U^\dagger\wedge\mathbf{R}\wedge\mathbf{R}\wedge\mathbf{R}U)\\
F_5^{(9)} &= \mathrm{Tr}(\mathbf{L}\wedge\mathbf{L}\wedge\mathbf{L}U^\dagger\wedge DUU^\dagger\wedge\mathbf{R}U) + \mathrm{Tr}(\mathbf{L}U^\dagger\wedge DUU^\dagger\wedge\mathbf{R}\wedge\mathbf{R}\wedge\mathbf{R}U) +\\
&\quad + \mathrm{Tr}(\mathbf{L}\wedge\mathbf{L}\wedge\mathbf{L}U^\dagger\wedge\mathbf{R}\wedge DU) + \mathrm{Tr}(\mathbf{L}U^\dagger\wedge\mathbf{R}\wedge\mathbf{R}\wedge\mathbf{R}\wedge DU)\\
F_5^{(10)} &= \mathrm{Tr}(\mathbf{L}\wedge\mathbf{L}\wedge\mathbf{L}U^\dagger\wedge DUU^\dagger\wedge DU) - \mathrm{Tr}(\mathbf{R}\wedge\mathbf{R}\wedge\mathbf{R}\wedge DUU^\dagger\wedge DUU^\dagger)\\
F_5^{(11)} &= \mathrm{Tr}(\mathbf{L}\wedge\mathbf{L}U^\dagger\wedge\mathbf{R}U\wedge\mathbf{L}U^\dagger\wedge\mathbf{R}U) - \mathrm{Tr}(\mathbf{L}U^\dagger\wedge\mathbf{R}\wedge\mathbf{R}U\wedge\mathbf{L}U^\dagger\wedge\mathbf{R}U)\\
F_5^{(12)} &= \mathrm{Tr}(\mathbf{L}\wedge\mathbf{L}U^\dagger\wedge\mathbf{R}U\wedge\mathbf{L}U^\dagger\wedge DU) + \mathrm{Tr}(\mathbf{L}\wedge\mathbf{L}U^\dagger\wedge DU\wedge\mathbf{L}U^\dagger\wedge\mathbf{R}U) +\\
&\quad + \mathrm{Tr}(\mathbf{L}U^\dagger\wedge\mathbf{R}\wedge\mathbf{R}\wedge DUU^\dagger\wedge\mathbf{R}U) + \mathrm{Tr}(\mathbf{L}U^\dagger\wedge\mathbf{R}\wedge DUU^\dagger\wedge\mathbf{R}\wedge\mathbf{R}U)\\
F_5^{(13)} &= \mathrm{Tr}(\mathbf{L}\wedge\mathbf{L}U^\dagger\wedge DUU^\dagger\wedge\mathbf{R}\wedge\mathbf{R}U) + \mathrm{Tr}(\mathbf{L}\wedge\mathbf{L}U^\dagger\wedge\mathbf{R}\wedge\mathbf{R}\wedge DU)\\
F_5^{(14)} &= \mathrm{Tr}(\mathbf{L}\wedge\mathbf{L}U^\dagger\wedge\mathbf{R}\wedge DUU^\dagger\wedge\mathbf{R}U) + \mathrm{Tr}(\mathbf{L}U^\dagger\wedge\mathbf{R}\wedge\mathbf{R}U\wedge\mathbf{L}U^\dagger\wedge DU)\\
F_5^{(15)} &= \mathrm{Tr}(\mathbf{L}\wedge\mathbf{L}U^\dagger\wedge DUU^\dagger\wedge DUU^\dagger\wedge\mathbf{R}U) +\\
&\quad - \mathrm{Tr}(\mathbf{L}U^\dagger\wedge DUU^\dagger\wedge DUU^\dagger\wedge\mathbf{R}\wedge\mathbf{R}U) +\\
&\quad + \mathrm{Tr}(\mathbf{L}\wedge\mathbf{L}U^\dagger\wedge\mathbf{R}\wedge DUU^\dagger\wedge DU) - \mathrm{Tr}(\mathbf{L}U^\dagger\wedge\mathbf{R}\wedge\mathbf{R}\wedge DUU^\dagger\wedge DU)\\
F_5^{(16)} &= \mathrm{Tr}(\mathbf{L}\wedge\mathbf{L}U^\dagger\wedge DU\wedge\mathbf{L}U^\dagger\wedge DU) - \mathrm{Tr}(\mathbf{R}\wedge\mathbf{R}\wedge DUU^\dagger\wedge\mathbf{R}\wedge DUU^\dagger)\\
F_5^{(17)} &= \mathrm{Tr}(\mathbf{L}\wedge\mathbf{L}U^\dagger\wedge DUU^\dagger\wedge\mathbf{R}\wedge DU) - \mathrm{Tr}(\mathbf{L}U^\dagger\wedge DUU^\dagger\wedge\mathbf{R}\wedge\mathbf{R}\wedge DU)
\end{aligned}
\tag{D.2}
$$

$$
\begin{aligned}
F_5^{(18)} &= \mathrm{Tr}(\mathbf{L}\wedge\mathbf{L}U^\dagger\wedge DUU^\dagger\wedge DUU^\dagger\wedge DU)+\\
&\quad+\mathrm{Tr}(\mathbf{R}\wedge\mathbf{R}\wedge DUU^\dagger\wedge DUU^\dagger\wedge DUU^\dagger)\\
F_5^{(19)} &= \mathrm{Tr}(\mathbf{L}U^\dagger\wedge\mathbf{R}\wedge DU\wedge\mathbf{L}U^\dagger\wedge\mathbf{R}U)+\mathrm{Tr}(\mathbf{L}U^\dagger\wedge\mathbf{R}U\wedge\mathbf{L}U^\dagger\wedge DUU^\dagger\wedge\mathbf{R}U)\\
F_5^{(20)} &= \mathrm{Tr}(\mathbf{L}U^\dagger\wedge\mathbf{R}U\wedge\mathbf{L}U^\dagger\wedge DUU^\dagger\wedge DU)+\\
&\quad-\mathrm{Tr}(\mathbf{L}U^\dagger\wedge\mathbf{R}\wedge DUU^\dagger\wedge DUU^\dagger\wedge\mathbf{R}U)\\
F_5^{(21)} &= \mathrm{Tr}(\mathbf{L}U^\dagger\wedge DU\wedge\mathbf{L}U^\dagger\wedge DUU^\dagger\wedge\mathbf{R}U)+\\
&\quad-\mathrm{Tr}(\mathbf{L}U^\dagger\wedge DUU^\dagger\wedge\mathbf{R}\wedge DUU^\dagger\wedge\mathbf{R}U)+\\
&\quad+\mathrm{Tr}(\mathbf{L}U^\dagger\wedge\mathbf{R}\wedge DU\wedge\mathbf{L}U^\dagger\wedge DU)-\mathrm{Tr}(\mathbf{L}U^\dagger\wedge\mathbf{R}\wedge DUU^\dagger\wedge\mathbf{R}\wedge DU)\\
F_5^{(22)} &= \mathrm{Tr}(\mathbf{L}U^\dagger\wedge DUU^\dagger\wedge DUU^\dagger\wedge DUU^\dagger\wedge\mathbf{R}U)+\\
&\quad+\mathrm{Tr}(\mathbf{L}U^\dagger\wedge\mathbf{R}\wedge DUU^\dagger\wedge DUU^\dagger\wedge DU)\\
F_5^{(23)} &= \mathrm{Tr}(\mathbf{L}U^\dagger\wedge DU\wedge\mathbf{L}U^\dagger\wedge DUU^\dagger\wedge DU)+\\
&\quad+\mathrm{Tr}(\mathbf{R}\wedge DUU^\dagger\wedge\mathbf{R}\wedge DUU^\dagger\wedge DUU^\dagger)\\
F_5^{(24)} &= \mathrm{Tr}(\mathbf{L}U^\dagger\wedge DUU^\dagger\wedge\mathbf{R}\wedge DUU^\dagger\wedge DU)+\\
&\quad+\mathrm{Tr}(\mathbf{L}U^\dagger\wedge DUU^\dagger\wedge DUU^\dagger\wedge\mathbf{R}\wedge DU)\\
F_5^{(25)} &= \mathrm{Tr}(\mathbf{L}U^\dagger\wedge DUU^\dagger\wedge DUU^\dagger\wedge DUU^\dagger\wedge DU)+\\
&\quad-\mathrm{Tr}(\mathbf{R}\wedge DUU^\dagger\wedge DUU^\dagger\wedge DUU^\dagger\wedge DUU^\dagger)\\
F_5^{(26)} &= \mathrm{Tr}(\mathbf{L}\wedge\mathbf{L}\wedge\mathbf{L}\wedge\mathbf{F}^{(L)})-\mathrm{Tr}(\mathbf{R}\wedge\mathbf{R}\wedge\mathbf{R}\wedge\mathbf{F}^{(R)})\\
F_5^{(27)} &= \mathrm{Tr}(\mathbf{L}\wedge\mathbf{L}\wedge\mathbf{L}U^\dagger\wedge\mathbf{F}^{(R)}U)-\mathrm{Tr}(\mathbf{R}\wedge\mathbf{R}\wedge\mathbf{R}U\wedge\mathbf{F}^{(L)}U^\dagger)\\
F_5^{(28)} &= \mathrm{Tr}(\mathbf{L}\wedge\mathbf{L}\wedge\mathbf{F}^{(L)}U^\dagger\wedge\mathbf{R}U)+\mathrm{Tr}(\mathbf{L}\wedge\mathbf{L}U^\dagger\wedge\mathbf{R}U\wedge\mathbf{F}^{(L)})+\\
&\quad-\mathrm{Tr}(\mathbf{L}U^\dagger\wedge\mathbf{R}\wedge\mathbf{R}\wedge\mathbf{F}^{(R)}U)-\mathrm{Tr}(\mathbf{L}U^\dagger\wedge\mathbf{F}^{(R)}\wedge\mathbf{R}\wedge\mathbf{R}U)\\
F_5^{(29)} &= -\mathrm{Tr}(\mathbf{L}\wedge\mathbf{F}^{(L)}U^\dagger\wedge\mathbf{R}\wedge\mathbf{R}U)-\mathrm{Tr}(\mathbf{L}U^\dagger\wedge\mathbf{R}\wedge\mathbf{R}U\wedge\mathbf{F}^{(L)})+\\
&\quad+\mathrm{Tr}(\mathbf{L}\wedge\mathbf{L}U^\dagger\wedge\mathbf{R}\wedge\mathbf{F}^{(R)}U)+\mathrm{Tr}(\mathbf{L}\wedge\mathbf{L}U^\dagger\wedge\mathbf{F}^{(R)}\wedge\mathbf{R}U)\\
F_5^{(30)} &= \mathrm{Tr}(\mathbf{L}\wedge\mathbf{L}\wedge\mathbf{F}^{(L)}U^\dagger\wedge DU)+\mathrm{Tr}(\mathbf{L}\wedge\mathbf{L}U^\dagger\wedge DU\wedge\mathbf{F}^{(L)})+\\
&\quad+\mathrm{Tr}(\mathbf{R}\wedge\mathbf{R}\wedge DUU^\dagger\wedge\mathbf{F}^{(R)})+\mathrm{Tr}(\mathbf{R}\wedge\mathbf{R}\wedge\mathbf{F}^{(R)}\wedge DUU^\dagger)\\
F_5^{(31)} &= \mathrm{Tr}(\mathbf{L}\wedge\mathbf{L}U^\dagger\wedge DUU^\dagger\wedge\mathbf{F}^{(R)}U)+\mathrm{Tr}(\mathbf{L}\wedge\mathbf{L}U^\dagger\wedge\mathbf{F}^{(R)}\wedge DU)+\\
&\quad+\mathrm{Tr}(\mathbf{R}\wedge\mathbf{R}U\wedge\mathbf{F}^{(L)}U^\dagger\wedge DUU^\dagger)+\mathrm{Tr}(\mathbf{R}\wedge\mathbf{R}\wedge DU\wedge\mathbf{F}^{(L)}U^\dagger)\\
F_5^{(32)} &= \mathrm{Tr}(\mathbf{L}\wedge\mathbf{F}^{(L)}\wedge\mathbf{L}U^\dagger\wedge\mathbf{R}U)-\mathrm{Tr}(\mathbf{L}U^\dagger\wedge\mathbf{R}\wedge\mathbf{F}^{(R)}\wedge\mathbf{R}U)\\
F_5^{(33)} &= \mathrm{Tr}(\mathbf{L}U^\dagger\wedge\mathbf{R}U\wedge\mathbf{L}U^\dagger\wedge\mathbf{F}^{(R)}U)-\mathrm{Tr}(\mathbf{L}U^\dagger\wedge\mathbf{R}U\wedge\mathbf{F}^{(L)}U^\dagger\wedge\mathbf{R}U)\\
F_5^{(34)} &= \mathrm{Tr}(\mathbf{L}\wedge\mathbf{F}^{(L)}U^\dagger\wedge DUU^\dagger\wedge\mathbf{R}U)+\mathrm{Tr}(\mathbf{L}U^\dagger\wedge\mathbf{R}\wedge DU\wedge\mathbf{F}^{(L)})+
\end{aligned}
$$

$$
\begin{aligned}
&+ \mathrm{Tr}(\mathbf{L}U^\dagger \wedge DUU^\dagger \wedge \mathbf{F}^{(R)} \wedge \mathbf{R}U) + \mathrm{Tr}(\mathbf{L}U^\dagger \wedge \mathbf{R} \wedge \mathbf{F}^{(R)} \wedge DU)\\
F_5^{(35)} &= \mathrm{Tr}(\mathbf{L}U^\dagger \wedge \mathbf{R}U \wedge \mathbf{F}^{(L)}U^\dagger \wedge DU) + \mathrm{Tr}(\mathbf{L}U^\dagger \wedge DU \wedge \mathbf{F}^{(L)}U^\dagger \wedge \mathbf{R}U) +\\
&+ \mathrm{Tr}(\mathbf{L}U^\dagger \wedge \mathbf{R} \wedge DUU^\dagger \wedge \mathbf{F}^{(R)}U) + \mathrm{Tr}(\mathbf{L}U^\dagger \wedge \mathbf{F}^{(R)} \wedge DUU^\dagger \wedge \mathbf{R}U)\\
F_5^{(36)} &= \mathrm{Tr}(\mathbf{L} \wedge \mathbf{F}^{(L)} \wedge \mathbf{L}U^\dagger \wedge DU) + \mathrm{Tr}(\mathbf{R} \wedge DUU^\dagger \wedge \mathbf{R} \wedge \mathbf{F}^{(R)})\\
F_5^{(37)} &= \mathrm{Tr}(\mathbf{L}U^\dagger \wedge DU \wedge \mathbf{L}U^\dagger \wedge \mathbf{F}^{(R)}U) + \mathrm{Tr}(\mathbf{R} \wedge DUU^\dagger \wedge \mathbf{R}U \wedge \mathbf{F}^{(L)}U^\dagger)\\
F_5^{(38)} &= \mathrm{Tr}(\mathbf{L}U^\dagger \wedge DUU^\dagger \wedge \mathbf{R}U \wedge \mathbf{F}^{(L)}) + \mathrm{Tr}(\mathbf{L} \wedge \mathbf{F}^{(L)}U^\dagger \wedge \mathbf{R} \wedge DU) +\\
&+ \mathrm{Tr}(\mathbf{L}U^\dagger \wedge DUU^\dagger \wedge \mathbf{R} \wedge \mathbf{F}^{(R)}U) + \mathrm{Tr}(\mathbf{L}U^\dagger \wedge \mathbf{F}^{(R)} \wedge \mathbf{R} \wedge DU)\\
F_5^{(39)} &= \mathrm{Tr}(\mathbf{L} \wedge \mathbf{F}^{(L)}U^\dagger \wedge DUU^\dagger \wedge DU) + \mathrm{Tr}(\mathbf{L}U^\dagger \wedge DUU^\dagger \wedge DU \wedge \mathbf{F}^{(L)}) +\\
&- \mathrm{Tr}(\mathbf{R} \wedge DUU^\dagger \wedge DUU^\dagger \wedge \mathbf{F}^{(R)}) - \mathrm{Tr}(\mathbf{R} \wedge \mathbf{F}^{(R)} \wedge DUU^\dagger \wedge DUU^\dagger)\\
F_5^{(40)} &= \mathrm{Tr}(\mathbf{L}U^\dagger \wedge DUU^\dagger \wedge DUU^\dagger \wedge \mathbf{F}^{(R)}U) + \mathrm{Tr}(\mathbf{L}U^\dagger \wedge \mathbf{F}^{(R)} \wedge DUU^\dagger \wedge DU) +\\
&- \mathrm{Tr}(\mathbf{R}U \wedge \mathbf{F}^{(L)}U^\dagger \wedge DUU^\dagger \wedge DUU^\dagger) - \mathrm{Tr}(\mathbf{R} \wedge DUU^\dagger \wedge DU \wedge \mathbf{F}^{(L)}U^\dagger)\\
F_5^{(41)} &= \mathrm{Tr}(\mathbf{L}U^\dagger \wedge DU \wedge \mathbf{F}^{(L)}U^\dagger \wedge DU) - \mathrm{Tr}(\mathbf{R} \wedge DUU^\dagger \wedge \mathbf{F}^{(R)} \wedge DUU^\dagger)\\
F_5^{(42)} &= \mathrm{Tr}(\mathbf{L}U^\dagger \wedge DUU^\dagger \wedge \mathbf{F}^{(R)} \wedge DU) - \mathrm{Tr}(\mathbf{R} \wedge DU \wedge \mathbf{F}^{(L)}U^\dagger \wedge DUU^\dagger)\\
F_5^{(43)} &= \mathrm{Tr}(\mathbf{L} \wedge \mathbf{F}^{(L)} \wedge \mathbf{F}^{(L)}) - \mathrm{Tr}(\mathbf{R} \wedge \mathbf{F}^{(R)} \wedge \mathbf{F}^{(R)})\\
F_5^{(44)} &= \mathrm{Tr}(\mathbf{L} \wedge \mathbf{F}^{(L)}U^\dagger \wedge \mathbf{F}^{(R)}U) + \mathrm{Tr}(\mathbf{L}U^\dagger \wedge \mathbf{F}^{(R)}U \wedge \mathbf{F}^{(L)}) +\\
&- \mathrm{Tr}(\mathbf{R} \wedge \mathbf{F}^{(R)}U \wedge \mathbf{F}^{(L)}U^\dagger) - \mathrm{Tr}(\mathbf{R}U \wedge \mathbf{F}^{(L)}U^\dagger \wedge \mathbf{F}^{(R)})\\
F_5^{(45)} &= \mathrm{Tr}(\mathbf{L}U^\dagger \wedge \mathbf{F}^{(R)} \wedge \mathbf{F}^{(R)}U) - \mathrm{Tr}(\mathbf{R}U \wedge \mathbf{F}^{(L)} \wedge \mathbf{F}^{(L)}U^\dagger)
\end{aligned}
$$

The most general single-trace ansatz for Ω_5 which is covariant under the global transformations and has the desired P and C eigenvalues can therefore be written as

$$\Omega_5 = \sum_{i=1}^{45} \bar{f}_i(\tau) F_5^{(i)}[U, \mathbf{L}, \mathbf{R}] + d\tau \wedge \sum_{i=1}^{11} g_i(\tau) F_4^{(i)}[U, \mathbf{L}, \mathbf{R}] \tag{D.3}$$

where we added the most general dependence on the scalar τ. Notice that the Ansatz includes 56 arbitrary functions of τ.

Requiring that $d\Omega_5$ is gauge invariant, i.e., requiring that $\delta d\Omega_5 = 0$, sets 41 conditions for the functions $\bar{f}_i$, g_i, of which 29 are algebraic and 12 involve their first derivatives. This reduces the number of free functions down to 15. Notice that the latter 12 constraints are differential equations, the solutions of which contain 12 integration constants. We comment on these integration constants below.

As it turns out, the result for Ω_5 after imposing the above constraints is something one could have guessed from the start: it is given as a sum of two terms, where the first term (involving 4 of the 15 free functions) is explicitly gauge invariant and the second term is

a closed form (involving 11 of the 15 free functions). For such a solution, it is immediate that indeed $\delta d\Omega_5 = 0$. The solution may be written explicitly as

$$\Omega_5 = \Omega_5^0 + \Omega_5^c + \mathrm{d}G_4\,, \tag{D.4}$$

where

$$\begin{aligned}
\Omega_5^0 = {} & f_1(\tau)\big[\mathrm{Tr}(DU \wedge \mathbf{F}^{(L)} \wedge \mathbf{F}^{(L)}U^\dagger) + \mathrm{Tr}(DUU^\dagger \wedge \mathbf{F}^{(R)} \wedge \mathbf{F}^{(R)})\big] + \\
& + f_2(\tau)\big[\mathrm{Tr}(DU \wedge \mathbf{F}^{(L)}U^\dagger \wedge DUU^\dagger \wedge DUU^\dagger) + \\
& \quad + \mathrm{Tr}(DUU^\dagger \wedge \mathbf{F}^{(R)} \wedge DUU^\dagger \wedge DUU^\dagger)\big] + \\
& + f_3(\tau)\big[\mathrm{Tr}(DUU^\dagger \wedge \mathbf{F}^{(R)}U \wedge \mathbf{F}^{(L)}U^\dagger) + \mathrm{Tr}(DU \wedge \mathbf{F}^{(L)}U^\dagger \wedge \mathbf{F}^{(R)})\big] + \\
& + f_4(\tau)\mathrm{Tr}(DUU^\dagger \wedge DUU^\dagger \wedge DUU^\dagger \wedge DUU^\dagger \wedge DUU^\dagger)
\end{aligned} \tag{D.5}$$

is the gauge-invariant term and $\Omega_5^c + \mathrm{d}G_4$ is the closed term. The latter was, for convenience, divided into two parts, where

$$\Omega_5^c = g_0 \mathrm{Tr}((U^\dagger \mathrm{d}U)^5) \tag{D.6}$$

with g_0 a constant, and G_4 is a general P_1 odd and C even 4-form, i.e.,

$$G_4 = \sum_{i=1}^{11} h_i(\tau) F_4^{(i)}[U, \mathbf{L}, \mathbf{R}]\ . \tag{D.7}$$

(Note that $g_i(\tau) = h_i'(\tau)$.)

Several comments are in order. Notice that the gauge invariant term is indeed the most general P_1-odd C-even 5-form composed of the covariant forms DU, $\mathbf{F}^{(L)}$, and $\mathbf{F}^{(R)}$. Only this term contributes to the $F_6 = d\Omega_5$, which is given as

$$\begin{aligned}
F_6 = d\tau \wedge \Big\{ & f_1'(\tau)\big[\mathrm{Tr}(DU \wedge \mathbf{F}^{(L)} \wedge \mathbf{F}^{(L)}U^\dagger) + \mathrm{Tr}(DUU^\dagger \wedge \mathbf{F}^{(R)} \wedge \mathbf{F}^{(R)})\big] + \\
& + f_2'(\tau)\big[\mathrm{Tr}(DU \wedge \mathbf{F}^{(L)}U^\dagger \wedge DUU^\dagger \wedge DUU^\dagger) + \mathrm{Tr}(DUU^\dagger \wedge \mathbf{F}^{(R)} \wedge DUU^\dagger \wedge DUU^\dagger)\big] + \\
& + f_3'(\tau)\big[\mathrm{Tr}(DUU^\dagger \wedge \mathbf{F}^{(R)}U \wedge \mathbf{F}^{(L)}U^\dagger) + \mathrm{Tr}(DU \wedge \mathbf{F}^{(L)}U^\dagger \wedge \mathbf{F}^{(R)})\big] + \\
& + f_4'(\tau)\mathrm{Tr}(DUU^\dagger \wedge DUU^\dagger \wedge DUU^\dagger \wedge DUU^\dagger \wedge DUU^\dagger)\Big\} + \\
& + f_1(\tau)\big[\mathrm{Tr}(DU \wedge \mathbf{F}^{(L)} \wedge \mathbf{F}^{(L)}U^\dagger \wedge DUU^\dagger) + \mathrm{Tr}(DUU^\dagger \wedge DUU^\dagger \wedge \mathbf{F}^{(R)} \wedge \mathbf{F}^{(R)}) + \\
& - i\mathrm{Tr}(\mathbf{F}^{(L)} \wedge \mathbf{F}^{(L)}U^\dagger \wedge \mathbf{F}^{(R)}U) + i\mathrm{Tr}(\mathbf{F}^{(L)}U^\dagger \wedge \mathbf{F}^{(R)} \wedge \mathbf{F}^{(R)}U) + \\
& + i\mathrm{Tr}(\mathbf{F}^{(L)} \wedge \mathbf{F}^{(L)} \wedge \mathbf{F}^{(L)}) - i\mathrm{Tr}(\mathbf{F}^{(R)} \wedge \mathbf{F}^{(R)} \wedge \mathbf{F}^{(R)})\big] + \\
& + f_2(\tau)\big[- 2i\mathrm{Tr}(DU \wedge \mathbf{F}^{(L)}U^\dagger \wedge DUU^\dagger \wedge \mathbf{F}^{(R)}) + \\
& - 2i\mathrm{Tr}(DU \wedge \mathbf{F}^{(L)} \wedge \mathbf{F}^{(L)}U^\dagger \wedge DUU^\dagger) + \\
& + \mathrm{Tr}(DU \wedge \mathbf{F}^{(L)}U^\dagger \wedge DUU^\dagger \wedge DUU^\dagger \wedge DUU^\dagger) +
\end{aligned}$$

$$
\begin{aligned}
&-2i\mathrm{Tr}(DUU^\dagger \wedge DUU^\dagger \wedge \mathbf{F}^{(R)} \wedge \mathbf{F}^{(R)})+\\
&+\mathrm{Tr}(DUU^\dagger \wedge DUU^\dagger \wedge DUU^\dagger \wedge DUU^\dagger \wedge \mathbf{F}^{(R)})\big]+\\
&+2f_3(\tau)\big[\mathrm{Tr}(DU \wedge \mathbf{F}^{(L)}U^\dagger \wedge DUU^\dagger \wedge \mathbf{F}^{(R)})+\\
&+i\mathrm{Tr}(\mathbf{F}^{(L)} \wedge \mathbf{F}^{(L)}U^\dagger \wedge \mathbf{F}^{(R)}U) - i\mathrm{Tr}(\mathbf{F}^{(L)}U^\dagger \wedge \mathbf{F}^{(R)} \wedge \mathbf{F}^{(R)}U)\big]+\\
&-5if_4(\tau)\big[\mathrm{Tr}(DU \wedge \mathbf{F}^{(L)}U^\dagger \wedge DUU^\dagger \wedge DUU^\dagger \wedge DUU^\dagger)+\\
&+\mathrm{Tr}(DUU^\dagger \wedge DUU^\dagger \wedge DUU^\dagger \wedge DUU^\dagger \wedge \mathbf{F}^{(R)})\big]
\end{aligned}
\tag{D.8}
$$

In particular, the 6-form derived by using the flat space expression in [138] is obtained for

$$
\begin{aligned}
f_1(\tau) &= -\frac{1}{6}e^{-\tau^2}\,, \qquad f_2(\tau) = \frac{i}{12}(1+\tau^2)e^{-\tau^2}\,,\\
f_3(\tau) &= -\frac{1}{12}e^{-\tau^2}\,, \qquad f_4(\tau) = \frac{1}{120}(2+2\tau^2+\tau^4)e^{-\tau^2}\,.
\end{aligned}
\tag{D.9}
$$

Moreover, we require that the bulk action agrees in the chirally symmetric case, $\tau = 0$ and $U = \mathbb{I}$, with the standard expression

$$
\Omega_5^0 = -\frac{i}{6}\mathrm{Tr}\left(\mathbf{L}(\mathbf{F}^{(L)})^2 + \frac{i}{2}\mathbf{L}^3\mathbf{F}^{(L)} - \frac{1}{10}\mathbf{L}^5 - (L \leftrightarrow R)\right) \tag{D.10}
$$

up to boundary terms. This is the case if

$$
f_1(0) = -\frac{1}{6}\,, \quad f_2(0) = \frac{i}{12}\,, \quad f_3(0) = -\frac{1}{12}\,, \quad f_4(0) = \frac{1}{60}\,. \tag{D.11}
$$

Notice that the choice in (D.9) satisfies these conditions.

In (D.4) Ω_5^c is a closed 5-form which cannot be expressed globally as a total exterior derivative. This form is related to the fifth de Rham cohomology group $H_5(SU(N_f)_L \times SU(N_f)_R/SU(N_f)_V)$ which reduces to the class of $\mathrm{Tr}((\mathrm{d}UU^{-1})^5)$.

We then comment on the 12 integration constants mentioned above. We find that these correspond to shifts of various linear combinations of the functions $\bar{f}_i$ in (D.3). In more detail, the 12 conditions involving derivatives are of the form

$$
\frac{d}{d\tau}\left(\text{linear combinations of } \bar{f}_i\right) = \text{linear combinations of } g_i \tag{D.12}
$$

Instead of solving these conditions for $\bar{f}_i$ one can eliminate the g_i's (as we have in practice done above by using the functions h_i instead in (D.7), which are derivatives of the g_i's), in which case the question of the integration constants does not arise explicitly. However notice that there are only 11 functions g_i (and equivalently 11 h_i's) but there are 12 conditions so only 11 of the constants can be removed this way and one of them remains. It is tempting to identify 11 of the integration constants with the freedom of adding

$$
\sum_{i=1}^{11} C_i F_4^{(i)}[U, \mathbf{L}, \mathbf{R}] \tag{D.13}
$$

in the closed contribution to Ω_5. However explicit computation shows that this is not precisely correct: one also needs to include contributions from the gauge invariant terms (D.5). Nevertheless, the conclusion is that 11 of the constants can be absorbed in the functions $h_i(\tau)$ and $f_i(\tau)$ without loss of generality. The remaining integration constant however cannot be absorbed in this way: it is identified as the constant g_0 in (D.6) – again explicit computation shows that it is actually a combination of g_0 and a constant term in the function f_4 in (D.5). Despite these technical complications, the computation shows that the result in (D.4)–(D.7) is consistent.

The result for Ω_5 is then constrained by requiring that it produces the correct QCD flavor anomaly at the boundary. To do this we first compute the (linearized) gauge transformation of the pure gauge term:

$$\delta\Omega_5^c = 5g_0 d\left\{\mathrm{Tr}[\Lambda_L d((U^\dagger \mathrm{d}U)^3) + \Lambda_R d((\mathrm{d}UU^\dagger)^3)]\right\} \ . \tag{D.14}$$

Moreover, the gauge transformation of the dG_4 can be written as

$$d\delta G_4 = d[\mathrm{Tr}(\Lambda_L dG_{3L} + \Lambda_R dG_{3R})] \tag{D.15}$$

where the 3-forms can be found by computing the gauge transformation of G_4,

$$\delta G_4 = -\mathrm{Tr}[d\Lambda_L \wedge G_{3L} + d\Lambda_R \wedge G_{3R}] \ . \tag{D.16}$$

Matching with the QCD anomalies therefore requires that, at the boundary,

$$\begin{aligned} &\mathrm{Tr}[\Lambda_L dG_{3L} + \Lambda_R dG_{3R}] + 5g_0 \mathrm{Tr}[\Lambda_L d((U^\dagger \mathrm{d}U)^3) + \Lambda_R d((\mathrm{d}UU^\dagger)^3)] \\ = \ &-\frac{1}{6}\mathrm{Tr}\left[\Lambda_L\left((\mathrm{d}\mathbf{L})^2 - \frac{i}{2}\mathrm{d}(\mathbf{L}^3)\right) - (L \leftrightarrow R)\right] \ . \end{aligned} \tag{D.17}$$

This equation fixes the boundary values of all the functions h_i in G_4 and the value of the constant g_0:

$$\begin{aligned} &g_0 = -\frac{1}{60} \ , \quad h_1(0) = \frac{1}{12} \ , \quad h_2(0) = \frac{1}{24} \ , \quad h_3(0) = \frac{i}{24} \ , \quad h_4(0) = \frac{i}{24} \ , \\ &h_5(0) = -\frac{i}{12} \ , \quad h_6(0) = -\frac{1}{12} \ , \quad h_7(0) = \frac{1}{12} \ , \quad h_8(0) = \frac{1}{24} \ , \quad h_9(0) = \frac{i}{12} \ , \\ &h_{10}(0) = \frac{i}{12} \ , \quad h_{11}(0) = \frac{1}{24} \ . \end{aligned} \tag{D.18}$$

Notice that since dG_4 integrates to a boundary term, $\int \Omega_5$ is therefore determined up to the four functions f_i, assuming that there is no IR boundary contribution. As for the G_4, this can be ensured by choosing the h_i such that they vanish in the IR. The IR contribution from Ω_5^c, however cannot be eliminated by the remaining freedom in the choice of the 5-form. Therefore the vanishing of this contribution needs to be required as an additional constraint on the solutions. We shall discuss this point in more detail below.

After imposing the constraints, the explicit form for G_4 at the boundary reads

$$
\begin{aligned}
24\,G_4\big|_{\text{bdry}} = \; & 2\Big[\mathrm{Tr}(\mathbf{L}\wedge\mathbf{F}^{(L)}\,U^\dagger\wedge DU)+\mathrm{Tr}(\mathbf{L}\,U^\dagger\wedge DU\wedge\mathbf{F}^{(L)})+ \\
& +\mathrm{Tr}(\mathbf{R}\wedge DU\,U^\dagger\wedge\mathbf{F}^{(R)})+\mathrm{Tr}(\mathbf{R}\wedge\mathbf{F}^{(R)}\wedge DU\,U^\dagger)\Big]+ \\
& +\Big[\mathrm{Tr}(\mathbf{L}\,U^\dagger\wedge DU\,U^\dagger\wedge\mathbf{F}^{(R)}\,U)+\mathrm{Tr}(\mathbf{L}\,U^\dagger\wedge\mathbf{F}^{(R)}\wedge DU)+ \\
& +\mathrm{Tr}(\mathbf{R}\wedge DU\wedge\mathbf{F}^{(L)}\,U^\dagger)+\mathrm{Tr}(\mathbf{R}\,U\wedge\mathbf{F}^{(L)}\,U^\dagger\wedge DU\,U^\dagger)\Big]+ \\
& +i\Big[-\mathrm{Tr}(\mathbf{L}\wedge\mathbf{L}\,U^\dagger\wedge DU\,U^\dagger\wedge\mathbf{R}\,U)+\mathrm{Tr}(\mathbf{L}\wedge\mathbf{L}\,U^\dagger\wedge\mathbf{R}\wedge DU)+ \\
& +\mathrm{Tr}(\mathbf{L}\,U^\dagger\wedge\mathbf{R}\wedge\mathbf{R}\wedge DU)+\mathrm{Tr}(\mathbf{L}\,U^\dagger\wedge DU\,U^\dagger\wedge\mathbf{R}\wedge\mathbf{R}\,U)\Big]+ \\
& +i\Big[\mathrm{Tr}(\mathbf{L}\wedge\mathbf{F}^{(L)}\,U^\dagger\wedge\mathbf{R}\,U)+\mathrm{Tr}(\mathbf{L}\,U^\dagger\wedge\mathbf{R}\,U\wedge\mathbf{F}^{(L)})+ \\
& +\mathrm{Tr}(\mathbf{L}\,U^\dagger\wedge\mathbf{R}\wedge\mathbf{F}^{(R)}\,U)+\mathrm{Tr}(\mathbf{L}\,U^\dagger\wedge\mathbf{F}^{(R)}\wedge\mathbf{R}\,U)\Big]+ \\
& +2i\Big[\mathrm{Tr}(\mathbf{L}\wedge\mathbf{L}\wedge\mathbf{L}\,U^\dagger\wedge DU)+\mathrm{Tr}(\mathbf{R}\wedge\mathbf{R}\wedge\mathbf{R}\wedge DU\,U^\dagger)\Big]+ \\
& -2\Big[\mathrm{Tr}(\mathbf{L}\wedge\mathbf{L}\wedge\mathbf{L}\,U^\dagger\wedge\mathbf{R}\,U)+\mathrm{Tr}(\mathbf{L}\,U^\dagger\wedge\mathbf{R}\wedge\mathbf{R}\wedge\mathbf{R}\,U)\Big]+ \\
& +2\Big[\mathrm{Tr}(\mathbf{L}\,U^\dagger\wedge DU\,U^\dagger\wedge DU\,U^\dagger\wedge\mathbf{R}\,U)+\mathrm{Tr}(\mathbf{L}\,U^\dagger\wedge\mathbf{R}\wedge DU\,U^\dagger\wedge DU)\Big]+ \\
& +\Big[-\mathrm{Tr}(\mathbf{L}\,U^\dagger\wedge DU\wedge\mathbf{L}\,U^\dagger\wedge DU)+\mathrm{Tr}(\mathbf{R}\wedge DU\,U^\dagger\wedge\mathbf{R}\wedge DU\,U^\dagger)\Big]+ \\
& +2i\Big[-\mathrm{Tr}(\mathbf{L}\,U^\dagger\wedge\mathbf{R}\,U\wedge\mathbf{L}\,U^\dagger\wedge DU)+\mathrm{Tr}(\mathbf{L}\,U^\dagger\wedge\mathbf{R}\wedge DU\,U^\dagger\wedge\mathbf{R}\,U)\Big]+ \\
& -2i\Big[\mathrm{Tr}(\mathbf{L}\,U^\dagger\wedge DU\,U^\dagger\wedge DU\,U^\dagger\wedge DU)+\mathrm{Tr}(\mathbf{R}\wedge DU\,U^\dagger\wedge DU\,U^\dagger\wedge DU\,U^\dagger)\Big]+ \\
& +\mathrm{Tr}(\mathbf{L}\,U^\dagger\wedge\mathbf{R}\,U\wedge\mathbf{L}\,U^\dagger\wedge\mathbf{R}\,U)\;.
\end{aligned}
\tag{D.19}
$$

Our final result can then be compared to the chiral Lagrangian Wess-Zumino term written in [141] and given below in (D.62). We find that

$$
\int\Omega_5^c+\int G_4\big|_{\text{bdry}}=\frac{40i\,\pi^2}{N_c}S_{WZ}+\frac{1}{24}\int d[\mathrm{Tr}(\mathbf{L}U^\dagger\wedge d\mathbf{R}U)-\mathrm{Tr}(\mathbf{R}U\wedge d\mathbf{L}U^\dagger)] \tag{D.20}
$$

where S_{WZ} is the action from this reference, discussed below in Appendix D.3. That is, the expressions agree up to a derivative term, which is C-odd. Notice that adding such a derivative in G_4 would leave Ω_5 unchanged. Because none of the P_1-odd C-even forms $F_4^{(i)}$ is gauge invariant, there is no freedom of adding gauge invariant terms such as (D.61) below. Moreover, the normalization of the action also agrees (up to differences in sign conventions) with [141].

IR contribution from Ω_5^c

We investigate here the contribution to $\int \Omega_5^c$ – where Ω_5^c is the non-exact closed part of the TCS 5-form (D.6) – that comes from the singular IR point at $r \to \infty$, and determine the condition for it to vanish. This will put constraints on the extreme IR behavior ($r \to \infty$) of the gauge transformations that are allowed in the bulk.

Ω_5^c is a closed form, so in principle it can be written locally as the exterior derivative of some 4-form ω_4. However, as noted in [140], there is no way to find an explicit expression in terms of U for such an ω_4. On the other hand, what can be done is to write ω_4 order by order in the pion field Π defined as

$$U = \mathrm{e}^{\frac{2i}{f_\pi}\Pi}\,. \tag{D.21}$$

Up to order $\mathcal{O}(\Pi^7)$, we find that locally Ω_5^c is equal to

$$\begin{aligned}\Omega_5^c = g_0 \mathrm{Tr}\left\{ i\left(\frac{2}{f_\pi}\right)^5 \mathrm{d}\left(\Pi\,(\mathrm{d}\Pi)^4\right)\right\} + \\ + g_0 \mathrm{Tr}\left\{\frac{160i}{21 f_\pi^7}\mathrm{d}\left(3\Pi^2\mathrm{d}\Pi\wedge\Pi\mathrm{d}\Pi^3 + 3\Pi\mathrm{d}\Pi\wedge\Pi\mathrm{d}\Pi\wedge\Pi\mathrm{d}\Pi^2 - 2\Pi^3\mathrm{d}\Pi^4\right) + \mathcal{O}(\Pi^8)\right\},\end{aligned} \tag{D.22}$$

where all higher orders will also be written as the exterior derivative of a 4-form containing four exterior derivatives of Π. When integrating over the bulk, Ω_5^c expanded in powers of Π can therefore be written as a boundary integral, with contributions from the UV boundary and IR singularity

$$\begin{aligned}\int \Omega_5^c = i g_0 \left(\frac{2}{f_\pi}\right)^5 \left[\int \mathrm{Tr}\left\{\Pi\,(\mathrm{d}\Pi)^4\right\}\right]_{UV}^{IR} + \\ + i g_0 \frac{160}{21 f_\pi^7}\Bigg[\int \mathrm{Tr}\{3\Pi^2\mathrm{d}\Pi\wedge\Pi\mathrm{d}\Pi^3 + \\ + 3\Pi\mathrm{d}\Pi\wedge\Pi\mathrm{d}\Pi\wedge\Pi\mathrm{d}\Pi^2 - 2\Pi^3\mathrm{d}\Pi^4 + \mathcal{O}(\Pi^8)\}\Bigg]_{UV}^{IR}.\end{aligned} \tag{D.23}$$

So the condition for the IR contribution to vanish at all orders in Π, is for the derivative of Π (or equivalently U) in one of the boundary coordinates x^μ to be identically 0 in the IR. Note that it is always obeyed by the instanton ansatz (3.1.64) because of its invariance under time reversal. Also, we expect that it should be possible for physically relevant solutions to impose the more natural stronger condition

$$\partial_\mu U(x,r) \underset{r\to\infty}{\to} 0\,, \tag{D.24}$$

which is Lorentz invariant.

D.1 Baryon charge

We now check the coupling of the non-abelian fields to the abelian vectorial charge. To do this, we separate the vectorial abelian term by replacing $\mathbf{L}/\mathbf{R} \to \Phi + L/R$ (see (3.1.41)). Notice that here Φ is a generic abelian one-form, $\Phi = \Phi_M dx^M$, where the index M runs over all the five coordinates. Consequently, the field strengths are replaced using the rules $\mathbf{F}^{(L/R)} \to d\Phi + F^{(L/R)}$, while DU is unchanged. Therefore the bulk term becomes

$$\begin{aligned}\Omega_5^0 = \Omega_5^0\big|_{\Phi=0} &+ 2d\Phi \wedge (f_1(\tau) + f_3(\tau))\mathrm{Tr}[DU \wedge (F^{(L)}U^\dagger + U^\dagger F^{(R)})] + \\ &+ 2d\Phi \wedge f_2(\tau)\mathrm{Tr}[(DU\,U^\dagger)^3] + 2(f_1(\tau) + f_3(\tau))d\Phi \wedge d\Phi \wedge \mathrm{Tr}(DU\,U^\dagger)\,.\end{aligned} \tag{D.25}$$

Notice that gauge invariance of these terms guarantees that the dependence on Φ is through the derivative. Moreover only the functions $f_1 + f_3$ and f_2 appear in the coupling term. For this expression, the constraints (D.11) impose that

$$f_1(0) + f_3(0) = -\frac{1}{4}\,, \qquad f_2(0) = \frac{i}{12}\,. \tag{D.26}$$

For the Ω_5 of [138], we find that

$$f_1(\tau) + f_3(\tau) = -\frac{1}{4}e^{-\tau^2}\,, \qquad f_2(\tau) = \frac{i}{12}(1+\tau^2)e^{-\tau^2}\,. \tag{D.27}$$

As it turns out, it is convenient to rewrite the coupling as

$$\begin{aligned}\Omega_5^0 =&\Omega_5^0\big|_{\Phi=0} + 2(f_1(\tau)+f_3(\tau))d\Phi \wedge d\Phi \wedge \mathrm{Tr}(DU\,U^\dagger) + \\ &- 2\Phi \wedge d\{(f_1(\tau)+f_3(\tau))\mathrm{Tr}[DU \wedge (F^{(L)}U^\dagger + U^\dagger F^{(R)})] + f_2(\tau)\mathrm{Tr}[(DU\,U^\dagger)^3]\} + \\ &+ 2d\{\Phi \wedge (f_1(\tau)+f_3(\tau))\mathrm{Tr}[DU \wedge (F^{(L)}U^\dagger + U^\dagger F^{(R)})] + f_2(\tau)\mathrm{Tr}[(DU\,U^\dagger)^3]\}\,.\end{aligned} \tag{D.28}$$

There are also boundary terms involving Φ, which arise from G_4. They can be written as

$$\begin{aligned}G_4\big|_{\mathrm{bdry}} = G_4\big|_{\Phi=0} + \frac{1}{12}\Phi \wedge [&-4i\mathrm{Tr}(L \wedge F^{(L)}) + \mathrm{Tr}(L \wedge L \wedge L) + 4i\mathrm{Tr}(R \wedge F^{(R)}) + \\ &- \mathrm{Tr}(R \wedge R \wedge R) + 6\mathrm{Tr}(DU \wedge F^{(L)}U^\dagger) + 6\mathrm{Tr}(DUU^\dagger \wedge F^{(R)}) + \\ &- 2i\mathrm{Tr}(DUU^\dagger \wedge DUU^\dagger \wedge DUU^\dagger)] + \\ &+ \frac{1}{12}d[\Phi \wedge (2i\mathrm{Tr}(LU^\dagger \wedge RU) + 3\mathrm{Tr}(LU^\dagger \wedge DU) + 3\mathrm{Tr}(R \wedge DUU^\dagger))]\,.\end{aligned} \tag{D.29}$$

Here, the total derivative term does not contribute to Ω_5 and we drop it. Interestingly, the covariant terms in (D.29) cancel against the boundary term arising from (D.28) after using the conditions (D.26). Therefore the full baryon coupling takes a simple form:

$$\int \Omega_5 - \int \Omega_5\big|_{\Phi=0}$$

$$
\begin{aligned}
=&-2\int \Phi\wedge d\{(f_1(\tau)+f_3(\tau))\mathrm{Tr}[DU\wedge(F^{(L)}U^\dagger+U^\dagger F^{(R)})]+f_2(\tau)\mathrm{Tr}[(DU\,U^\dagger)^3]\}+\\
&+2\int (f_1(\tau)+f_3(\tau))d\Phi\wedge d\Phi\wedge\mathrm{Tr}(DU\,U^\dagger)+\\
&+\frac{1}{12}\int \Phi\wedge[-4i\mathrm{Tr}(L\wedge F^{(L)})+\mathrm{Tr}(L^3)+4i\mathrm{Tr}(R\wedge F^{(R)})-\mathrm{Tr}(R^3)]\big|_{\mathrm{bdry}}\ . \qquad \text{(D.30)}
\end{aligned}
$$

Notice that here the integral on the last row is four dimensional whereas the other integrals are five dimensional.

We then extract the expression for the baryon number current and charge. The full action contains the dilaton gravity, DBI, and TCS terms. Only the DBI and TCS terms depend on the gauge fields and are therefore relevant for the analysis of the baryon number current. As it turns out, the charge of the baryon will only arise from the TCS term. The full action may be written as

$$
S=S^{(5D)}+S^{(4D)}=\int dr d^4x\ \mathcal{L}^{(5D)}+\int d^4x\ \mathcal{L}^{(4D)}\big|_{r=0} \qquad \text{(D.31)}
$$

where $r=0$ is the UV boundary and the bulk has $r>0$. The 5D piece arises from the DBI and TCS terms whereas the boundary term arises from the CS sector only. The DBI action is given in section 3.1.2, but the expression will not be needed here. The division of the CS term into 5D and 4D pieces is not well defined per se, but for concreteness we may take the 5D term to be (D.25) so that the 4D term is (D.29).

The variation of the on-shell action is then (after partial integration of the 5D term and using the EOM as usual)

$$
\delta S_{\mathrm{on-shell}}=-\int d^4x\ \frac{\partial\mathcal{L}^{(5D)}}{\partial\,\partial_r\Phi_M}\ \delta\Phi_M\big|_{r=0}+\int d^4x\ \frac{\partial\mathcal{L}^{(4D)}}{\partial\Phi_M}\ \delta\Phi_M\big|_{r=0}+\cdots \qquad \text{(D.32)}
$$

where the dots stand for boundary terms from the variations of the other fields and we assumed that the boundary Lagrangian $\mathcal{L}^{(4D)}$ is independent of the derivatives of Φ.

Moreover, in order to obtain this expression, the term $\frac{\partial\mathcal{L}^{(5D)}}{\partial\,\partial_r\Phi_M}\ \delta\Phi_M$ must vanish in the IR. Otherwise the variation will receive an inconsistent IR contribution. Similarly we must assume that contributions from spatial infinity in the partial integration vanish. This will be justified in the next subsection.

We can read off the (five dimensional) baryon current as

$$
J_B^M=\frac{\partial\mathcal{L}^{(5D)}}{\partial\,\partial_r\Phi_M}\Big|_{r=0}-\frac{\partial\mathcal{L}^{(4D)}}{\partial\Phi_M}\Big|_{r=0}\ . \qquad \text{(D.33)}
$$

We did not comment on the gauge dependence yet. Without loss of generality, we may assume that $\mathcal{L}^{(5D)}$ is gauge invariant and depends on Φ only through its derivatives, while $\mathcal{L}^{(4D)}$ is not gauge invariant. Indeed this holds for the choices of the TCS terms specified

above, i.e., that the 5D CS term is (D.25) while the 4D term is (D.29) (omitting the irrelevant last line). Gauge invariance implies, in particular, that the variation of $S^{(5D)}$ vanishes for any infinitesimal vectorial $U(1)$ transformation depending on the space-time coordinates, i.e., for $\delta\Phi_\mu = \partial_\mu\epsilon$. Inserting this in the formula (D.32) and integrating partially we observe that by gauge invariance we must have

$$\frac{\partial}{\partial x^\mu}\left(\frac{\partial\mathcal{L}^{(5D)}}{\partial\,\partial_r\Phi_\mu}\right)_{r=0} = 0 \tag{D.34}$$

where μ is summed over the four Minkowski coordinates. (Recall that these terms would vanish by the EOMs for homogeneous configurations.) Notice also that

$$\frac{\partial\mathcal{L}^{(5D)}}{\partial\,\partial_r\Phi_r} = 0 \tag{D.35}$$

i.e. the $5D$ action is independent of $\partial_r\Phi_r$ since the derivatives of Φ only appear either through the field strength or in the TCS term. Notice that we did not fix the gauge so far, but to make contact with field theory we should choose the gauge where $\Phi_r = 0$.

We now discuss the term arising from the 4D action. Recall that we chose to use (D.25) for the 5D action so that the full Φ dependent 4D piece is given in (D.29). Because this is a boundary term at $r = 0$, there is no dependence on Φ_r such that

$$\frac{\partial\mathcal{L}^{(4D)}}{\partial\Phi_r} = 0\ . \tag{D.36}$$

The other terms may be written as

$$\begin{aligned}-\frac{\partial\mathcal{L}^{(4D)}}{\partial\Phi_\mu}\,\omega_4\Big|_{r=0} = -\frac{iN_c}{48\pi^2}\,dx^\mu\wedge[&-4i\mathrm{Tr}(L\wedge F^{(L)}) + \mathrm{Tr}(L\wedge L\wedge L) + \\ &+ 4i\mathrm{Tr}(R\wedge F^{(R)}) - \mathrm{Tr}(R\wedge R\wedge R) + 6\mathrm{Tr}(DU\wedge F^{(L)}U^\dagger) + \\ &+ 6\mathrm{Tr}(DUU^\dagger\wedge F^{(R)}) - 2i\mathrm{Tr}(DUU^\dagger\wedge DUU^\dagger\wedge DUU^\dagger)]\end{aligned} \tag{D.37}$$

where $\omega_4 = dx^0\wedge dx^1\wedge dx^2\wedge dx^3$ is the four dimensional volume form. The first four terms in the square brackets reflect the mixed anomaly. They vanish for vectorial external gauge fields, $L = R$. For zero external gauge fields the last term gives the expected topological baryon current,

$$-\frac{N_c}{24\pi^2}\epsilon^{\mu\nu\rho\sigma}\ \mathrm{Tr}\left(\partial_\nu UU^\dagger\wedge\partial_\rho UU^\dagger\wedge\partial_\sigma UU^\dagger\right)\ . \tag{D.38}$$

The divergence of the current (D.37) is given by

$$-\partial_\mu\frac{\partial\mathcal{L}^{(4D)}}{\partial\Phi_\mu}\,\omega_4\Big|_{r=0} = -\frac{iN_c}{48\pi^2}\,d[-4i\mathrm{Tr}(L\wedge F^{(L)}) + \mathrm{Tr}(L\wedge L\wedge L) + 4i\mathrm{Tr}(R\wedge F^{(R)}) +$$

$$- \mathrm{Tr}(R\wedge R\wedge R)+6\mathrm{Tr}(DU\wedge F^{(L)}U^\dagger)+6\mathrm{Tr}(DUU^\dagger\wedge F^{(R)})+$$
$$- 2i\mathrm{Tr}(DUU^\dagger\wedge DUU^\dagger\wedge DUU^\dagger)] \ . \tag{D.39}$$

Explicit computation of the exterior derivative gives

$$-\partial_\mu \frac{\partial\mathcal{L}^{(4D)}}{\partial\Phi_\mu}\,\omega_4\Big|_{r=0} = \frac{N_c}{48\pi^2}\big[2\mathrm{Tr}(F^{(L)}\wedge F^{(L)}) - 2\mathrm{Tr}(F^{(R)}\wedge F^{(R)})+$$
$$+ i\mathrm{Tr}(L\wedge L\wedge F^{(L)}) - i\mathrm{Tr}(R\wedge R\wedge F^{(R)})\big] \ . \tag{D.40}$$

This anomaly contribution vanishes for vectorial gauge fields, $L = R$. In conclusion, since we have shown earlier that the divergence of the first contribution in (D.33) vanishes, we have that

$$\partial_\mu J^\mu_B = 0 \ , \qquad J^r_B = 0 \tag{D.41}$$

in the absence of axial gauge fields at the boundary.

The contribution from the TCS action to the first term in (D.33) can also be computed explicitly (omitting the nonlinear term):[20]

$$\frac{\partial\mathcal{L}^{(5D)}_{\mathrm{CS}}}{\partial\,\partial_r\Phi_\mu}\Big|_{r=0}\omega_4 = \tag{D.42}$$
$$-\frac{iN_c}{2\pi^2}dx^\mu\wedge\{(f_1(0)+f_3(0))\mathrm{Tr}[DU\wedge(F^{(L)}U^\dagger+U^\dagger F^{(R)})]+f_2(0)\mathrm{Tr}[(DU\,U^\dagger)^3]\} \ .$$

After imposing the conditions (D.26), this contribution cancels the last three terms in (D.37). This cancellation is however superficial: We can also use the equations of motion to write

$$\frac{\partial\mathcal{L}^{(5D)}}{\partial\,\partial_r\Phi_\mu}\Big|_{r=0} = \partial_\nu\int dr\frac{\partial\mathcal{L}^{(5D)}}{\partial\,\partial_\nu\Phi_\mu} \ . \tag{D.43}$$

Then the baryon number is, taking the configuration to be independent of time,

$$N_B = \int d^3\mathbf{x}J^0_B = \int dr d^3\mathbf{x}\ \partial_k\frac{\partial\mathcal{L}^{(5D)}}{\partial\,\partial_k\Phi_0} - \int d^3\mathbf{x}\ \frac{\partial\mathcal{L}^{(4D)}}{\partial\Phi_0}\Big|_{r=0} \tag{D.44}$$

where the first term, arising from the 5D bulk action, integrates into a boundary term at spatial infinity, so that the UV boundary contribution only arises from the second term

[20]The minus sign arises due to consistency with the chosen coordinate system. Because we have chosen that $r = 0$ is the UV boundary value of the holographic coordinate, taking $\omega_5 = dr\wedge\omega_4$, $\int_M g\omega_5 = -\int d^5x\,g$, and $\int_{\partial M} f\omega_4 = \int d^4x\,f$ is consistent with $\int_M df = \int_{\partial M} f$ where ∂M is the UV boundary. Notice that if we changed $r\mapsto 1/r$, there would be no need to include a minus sign in any of the definitions.

in (D.44) and the purported cancellation is absent. Assuming that the contributions from spatial infinity vanish, the result may be written as the following 3D boundary integral:

$$\begin{aligned} N_B = -\frac{iN_c}{48\pi^2}\int [&-4i\mathrm{Tr}(L\wedge F^{(L)}) + \mathrm{Tr}(L\wedge L\wedge L) + 4i\mathrm{Tr}(R\wedge F^{(R)}) + \\ &- \mathrm{Tr}(R\wedge R\wedge R) + 6\mathrm{Tr}(DU\wedge F^{(L)}U^\dagger) + 6\mathrm{Tr}(DUU^\dagger\wedge F^{(R)}) + \\ &- 2i\mathrm{Tr}(DUU^\dagger\wedge DUU^\dagger\wedge DUU^\dagger)] \ . \end{aligned} \tag{D.45}$$

Notice that, in the end, the derivation of the baryon number did not require using the conditions (D.26). Even more remarkably, N_B does not depend in any manner on the non-closed part of the TCS action Ω_5^0 and the corresponding TCS potentials $f_i(\tau)$. Here, the generation of the baryon number and the contribution of the TCS terms to the equations of motion (responsible for the stabilization of the baryon size) are ensured by two distinct parts of the CS action (closed and non-closed). Although slightly counter-intuitive, it is not a contradiction though. The reason is that the result for the baryon number simply tells us what should be the boundary behavior of the tachyon field for N_B to be non-zero (it should have a Skyrmion winding from (D.38)).It does not guarantee that a solution with such boundary conditions exists though. In particular, it is expected that no finite size solution should exist when Ω_5^0 vanishes ($f_i(\tau) = 0$).

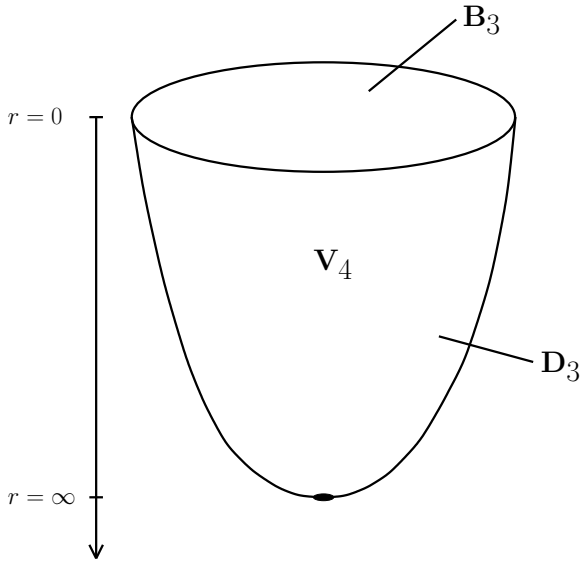

Figure 28: Volume of integration $\mathbf{V}_4$ for the baryon and its three-dimensional boundaries $\mathbf{B}_3 + \mathbf{D}_3$.

D.2 Boundary terms to the baryon charge

We finish by discussing the boundary terms at spatial infinity. That is, we consider the baryon number in a finite 3D volume. We take this volume to be the three ball $\mathbf{B}_3$, but the analysis is the same for any shape of the volume. By using the equations of motion as above, the charge may be written as

$$N_B = \int_{\mathbf{B}_3} d^3\mathbf{x} J_B^0 = \int dr \int_{\partial\mathbf{B}_3} dS\ n_k \frac{\partial\mathcal{L}^{(5D)}}{\partial\,\partial_k\Phi_0} - \int_{\mathbf{B}_3} d^3\mathbf{x}\ \frac{\partial\mathcal{L}^{(4D)}}{\partial\Phi_0} \tag{D.46}$$

where the unit vector n is normal to the surface element dS of $\partial\mathbf{B}_3$. We can also write down the TCS contributions explicitly:

$$\begin{aligned}
N_B = &\int dr \int_{\partial\mathbf{B}_3} dS\ n_k \frac{\partial\mathcal{L}^{(5D)}_{\rm DBI}}{\partial\,\partial_k\Phi_0} + \\
&+ \frac{iN_c}{2\pi^2}\int_{\mathbf{D}_3}\big[(f_1(\tau)+f_3(\tau))\mathrm{Tr}[DU\wedge(F^{(L)}U^\dagger + U^\dagger F^{(R)})] + \\
&\qquad + f_2(\tau)\mathrm{Tr}[(DU\,U^\dagger)^3]\big] + \\
&+ \frac{iN_c}{\pi^2}\int_{\mathbf{D}_3}(f_1(\tau)+f_3(\tau))d\Phi\wedge\mathrm{Tr}[DU\,U^\dagger] + \\
&- \frac{iN_c}{48\pi^2}\int_{\mathbf{B}_3}\big[-4i\mathrm{Tr}(L\wedge F^{(L)}) + \mathrm{Tr}(L\wedge L\wedge L) + 4i\mathrm{Tr}(R\wedge F^{(R)}) + \\
&\quad - \mathrm{Tr}(R\wedge R\wedge R) + 6\mathrm{Tr}(DU\wedge F^{(L)}U^\dagger) + 6\mathrm{Tr}(DUU^\dagger\wedge F^{(R)}) + \\
&\quad - 2i\mathrm{Tr}(DUU^\dagger\wedge DUU^\dagger\wedge DUU^\dagger)\big]
\end{aligned} \tag{D.47}$$

where $\mathbf{D}_3$ is the boundary at spatial infinity. The boundary of the whole four-dimensional (holographic and spatial dimensions) volume therefore breaks into two terms, $\partial\mathbf{V}_4 = \mathbf{B}_3 + \mathbf{D}_3$ where $\mathbf{B}_3$ lies at the holographic boundary $r = 0$ and $\mathbf{D}_3$ lies at spatial infinity, see figure 28. Notice that there is no boundary at $r = \infty$ as the geometry shrinks into a single point in the IR, where it ends in a singularity (represented by a blob in the figure). It is important to check that the boundary contributions of the first three lines vanish for soliton configurations at large volumes, i.e., when $\partial\mathbf{B}_3$ is far from the soliton.

If the conditions (D.26) hold, the most important contributions (i.e., those that are expected to contribute to the charge of the soliton solution in the limit of large volume) can be written as a four dimensional bulk integral:

$$\begin{aligned}
N_B = &\frac{iN_c}{2\pi^2}\int_{\mathbf{V}_4}\mathrm{d}\Big\{(f_1(\tau)+f_3(\tau))\mathrm{Tr}[DU\wedge(F^{(L)}U^\dagger + U^\dagger F^{(R)})] + \\
&\qquad + f_2(\tau)\mathrm{Tr}[(DU\,U^\dagger)^3]\Big\} + \\
&+ \int dr\int_{\partial\mathbf{B}_3} dS\ n_k\frac{\partial\mathcal{L}^{(5D)}_{\rm DBI}}{\partial\,\partial_k\Phi_0} + \frac{iN_c}{\pi^2}\int_{\mathbf{D}_3}(f_1(\tau)+f_3(\tau))d\Phi\wedge\mathrm{Tr}[DU\,U^\dagger] +
\end{aligned}$$

$$-\frac{iN_c}{48\pi^2}\int_{\mathbf{B}_3}\big[-4i\mathrm{Tr}(L\wedge F^{(L)})+\mathrm{Tr}(L\wedge L\wedge L)+4i\mathrm{Tr}(R\wedge F^{(R)})+$$
$$-\mathrm{Tr}(R\wedge R\wedge R)\big]_{r=0}\,. \tag{D.48}$$

That is, while the conditions (D.26) were not necessary to derive the main formula (D.45), they are necessary to write down the charge as a compact bulk integral for finite volumes.

We now show the vanishing of the contribution to (D.47) at spatial infinity for the baryon solution. This is most conveniently done by using the gauge fields redefined to absorb the tachyon phase as in (3.1.78). The 3-forms that are integrated on $\mathbf{D}_3$ can then be written as

$$\mathrm{Tr}\left[\tilde{A}\wedge\left(\tilde{F}^{(L)}+\tilde{F}^{(R)}\right)\right]\,, \tag{D.49}$$

$$\mathrm{Tr}\left[\tilde{A}^3\right]\,, \tag{D.50}$$

$$\mathrm{d}\Phi\wedge\mathrm{Tr}\left[\tilde{A}\right]=0\,, \tag{D.51}$$

where A is defined in (3.1.42). On the other hand, the DBI action[21] can be written in terms of the redefined gauge fields as

$$S_{\mathrm{DBI}}=-M^3N_c\int\mathrm{d}^5x\,V_f(\lambda,\tau^2)\sqrt{-\det\tilde{g}}\,\times \tag{D.52}$$
$$\times\left(\left[\frac{1}{2}+\frac{1}{4}\kappa\tau^2\left(\tilde{g}^{-1}\right)^{MN}\mathrm{Tr}\,\tilde{\mathbf{A}}_M\tilde{\mathbf{A}}_N-\right.\right.$$
$$\left.\left.-\frac{1}{8}w^2\left(\tilde{g}^{-1}\right)^{MN}\left(\tilde{g}^{-1}\right)^{PQ}\mathrm{Tr}\,\tilde{\mathbf{F}}^{(L)}_{NP}\tilde{\mathbf{F}}^{(L)}_{QM}+\mathcal{O}\left((\mathbf{F}^{(L)})^3\right)\right]+(L\leftrightarrow R)\right)\,,$$

from which it is clear that both $\tilde{A}$ and $\tilde{F}^{(L/R)}$ should vanish at spatial infinity for a finite energy cylindrically symmetric baryon solution. This implies that there is no contribution from spatial infinity to the baryon number (D.47).

D.2.1 Details on the relation to the bulk instanton number

We derive in this subsection the condition for the baryon number (3.1.96) to equal the bulk instanton number

$$N_{\mathrm{instanton}}=\frac{1}{8\pi^2}\int_{\mathrm{bulk}}\mathrm{Tr}\,\left(\mathbf{F}^{(L)}\wedge\mathbf{F}^{(L)}-\mathbf{F}^{(R)}\wedge\mathbf{F}^{(R)}\right)\,, \tag{D.53}$$

or in terms of the ansatz fields (3.1.70)

$$N_{\mathrm{instanton}}=\frac{1}{2\pi}\int\mathrm{d}r\mathrm{d}\xi\,\epsilon^{\bar{\mu}\bar{\nu}}\left(F_{\bar{\mu}\bar{\nu}}+\partial_{\bar{\mu}}\left(-i\phi^*D_{\bar{\nu}}\phi+h.c.\right)\right)\,. \tag{D.54}$$

[21] In the probe limit. The result extends straightforwardly to the inhomogeneous tachyon case.

We first notice that (3.1.96) can be rewritten in terms of the redefined gauged fields of (3.1.78) at the boundary as

$$N_B = \frac{1}{24\pi^2}\int \left[-i\mathrm{Tr}(\tilde{\mathbf{L}}^3 - \tilde{\mathbf{R}}^3 + 3\tilde{\mathbf{L}}\wedge\tilde{\mathbf{R}}^2 - 3\tilde{\mathbf{L}}^2\wedge\tilde{\mathbf{R}})\right]\Big|_{UV} . \tag{D.55}$$

Because the redefined gauge fields at the boundary take a pure gauge form, $\tilde{\mathbf{F}}^{(L/R)} = 0$, which implies that $\tilde{\mathbf{L}}^2 = -i\,\mathrm{d}\,\tilde{\mathbf{L}}$ and likewise for $\tilde{\mathbf{R}}$. (D.55) can then be rewritten as

$$\begin{aligned} N_B &= \frac{1}{24\pi^2}\int \left[-i\mathrm{Tr}(\tilde{\mathbf{L}}^3 - \tilde{\mathbf{R}}^3 - 3\,\mathrm{d}(\tilde{\mathbf{L}}\wedge\tilde{\mathbf{R}}))\right]\Big|_{UV} \\ &= \frac{1}{24\pi^2}\int \left[-i\mathrm{Tr}(\tilde{\mathbf{L}}^3 - \tilde{\mathbf{R}}^3)\right]\Big|_{UV} \\ &= -\frac{1}{8\pi^2}\int \left[\mathrm{Tr}\left(\tilde{\mathbf{F}}^{(L)}\wedge\tilde{\mathbf{L}} + \frac{1}{3}i\,\tilde{\mathbf{L}}^3 - \left(\tilde{\mathbf{F}}^{(R)}\wedge\tilde{\mathbf{R}} + \frac{1}{3}i\,\tilde{\mathbf{R}}^3\right)\right)\right]\Big|_{UV} . \end{aligned} \tag{D.56}$$

On the other hand $\mathrm{Tr}(\tilde{\mathbf{F}}^{(L)}\wedge\tilde{\mathbf{F}}^{(L)}) = \mathrm{d}\left[\mathrm{Tr}\left(\tilde{\mathbf{F}}^{(L)}\wedge\tilde{\mathbf{L}} + \frac{1}{3}i\,\tilde{\mathbf{L}}^3\right)\right] \equiv \mathrm{d}\,\omega_3(\tilde{\mathbf{L}})$, and likewise for R, where ω_3 is the Chern-Simons 3-form. So, using Stoke's theorem, we find that

$$N_B = N_{\text{instanton}} - \frac{1}{8\pi^2}\int \left[\omega_3(\tilde{\mathbf{L}}) - \omega_3(\tilde{\mathbf{R}})\right]\Big|_{IR} , \tag{D.57}$$

where the contribution from spatial boundaries was dropped because of the boundary conditions Table 3.1. Therefore, the condition for the baryon number to equal the instanton number is that

$$\int \left[\omega_3(\tilde{\mathbf{L}}) - \omega_3(\tilde{\mathbf{R}})\right]\Big|_{IR} = 0\,. \tag{D.58}$$

In terms of the baryon ansatz of equations (3.1.50)-(3.1.52) and (3.1.64) the condition reads

$$\int \mathrm{d}\xi\,\left(\,\tilde{A}_\xi(|\tilde{\phi}|^2 - 1) + \partial_\xi\tilde{\phi}_1 + \partial_\xi\tilde{\phi}_1\tilde{\phi}_2 - \partial_\xi\tilde{\phi}_2\tilde{\phi}_1\,\right)\Big|_{IR} = 0\,. \tag{D.59}$$

D.3 Gauged WZ term

The gauged WZ term was first written down fully by Witten in [140] (equation (24)) where he also derived the chiral anomalies (equation (25)). It was then noted that this expression has some typos and that it is defined up to a gauge invariant term by [141] and [142]. First note that the authors all have different conventions for the gauge fields:

$$A_{L/R}^{\text{Witten}} = -A_{L/R}^{\text{Kaymakcalan}} = -i(L/R)^{\text{Mañes}}\,. \tag{D.60}$$

Upon these conventions, the expressions derived in [141] (equation (4.18)) and [142] (equation (69)) are exactly the same and differ from Witten's expression by the following:

- As mentioned above, Witten's expression should be corrected, by adding iA_L^3 to $A_L\mathrm{d}A_L + \mathrm{d}A_L A_L$ in the second line, interchanging $R \leftrightarrow L$ in the second term of the third line and replacing the $\frac{1}{2}$ in front of $A_L^2 U A_R^2 U^{-1}$ by 1 in the last line.

- They add to Witten's $\tilde{\Gamma}$

$$\frac{i}{48\pi^2}\mathrm{Tr}\int(\mathrm{d}(A_L U\mathrm{d}A_R U^{-1}) - \mathbf{F}^{(L)}U\mathbf{F}^{(R)}U^{-1})\,, \tag{D.61}$$

  where the second term is such that the gauge-invariant form $\mathbf{F}^{(L)}U\mathbf{F}^{(R)}U^{-1}$ does not appear in the final expression and the first one yields a 3-dimensional boundary term that vanishes .

We write here their expression using the convention of [141]

$$\begin{aligned}
S_{\mathrm{WZ}}(U,A_L,A_R) = {} & C\int \mathrm{Tr}\Big[\beta^5\Big] + 5Ci\int \mathrm{Tr}\Big[A_L\alpha^3 + A_R\beta^3\Big] - \\
& - 5C\int \mathrm{Tr}\Big[(\mathrm{d}A_L A_L + A_L\mathrm{d}A_L)\alpha + (\mathrm{d}A_R A_R + A_R\mathrm{d}A_R)\beta\Big] + \\
& + 5C\int \mathrm{Tr}\Big[\mathrm{d}A_L\alpha U A_R U^{-1} + \mathrm{d}A_R\beta U^{-1}A_L U\Big] + \\
& + 5C\int \mathrm{Tr}\Big[A_R U^{-1}A_L U\beta^2 - A_L U A_R U^{-1}\alpha^2\Big] + \\
& + \frac{5C}{2}\int \mathrm{Tr}\Big[(A_L\alpha)^2 - (A_R\beta)^2\Big] + 5Ci\int \mathrm{Tr}\Big[A_L^3\alpha + A_R^3\beta\Big] + \\
& + 5Ci\int \mathrm{Tr}\Big[(\mathrm{d}A_R A_R + A_R\mathrm{d}A_R)U^{-1}A_L U - \\
& \qquad - (\mathrm{d}A_L A_L + A_L\mathrm{d}A_L)U A_R U^{-1}\Big] + \\
& + 5Ci\int \mathrm{Tr}\Big[A_L U A_R U^{-1}A_L\alpha + A_R U^{-1}A_L U A_R\beta\Big] + \\
& + 5C\int \mathrm{Tr}\Big[A_R^3 U^{-1}A_L U - A_L^3 U A_R U^{-1} + \frac{1}{2}(U A_R U^{-1}A_L)^2\Big]\,,
\end{aligned} \tag{D.62}$$

where $C = \frac{-iN_c}{240\pi^2}$, $\alpha = \mathrm{d}UU^{-1}$ and $\beta = U^{-1}\mathrm{d}U$. Note that all terms are P_1-odd. They are also C even, apart from the term in the third line which is the sum of a C-even non-closed 4-form and a C-odd exact 4-form.

Gauge transformations It can be checked that (D.62) reproduces the correct chiral anomalies

$$\delta S_{\rm WZ}(U, A_L, A_R) = -10C \int {\rm Tr}\left[\Lambda_L \left(({\rm d}A_L)^2 - \frac{i}{2}{\rm d}(A_L^3)\right) - (L \leftrightarrow R)\right] , \tag{D.63}$$

upon a general infinitesimal gauge transformation, where the various fields transform as

$$\delta U = \Lambda_L U - U\Lambda_R \,, \tag{D.64}$$

$$\delta A_{L/R} = -i{\rm d}\Lambda_{L/R} + [\Lambda_{L/R}, A_{L/R}] \,. \tag{D.65}$$

E The TCS contribution to the baryon equations of motion

The TCS action reads

$$S_{\rm CS} = \frac{iN_c}{4\pi^2}\int \Omega_5 \,, \tag{E.1}$$

where Ω_5 is the TCS 5-form, which is decomposed as in (3.1.26)

$$\Omega_5 = \Omega_5^0 + \Omega_5^c + dG_4 \,. \tag{E.2}$$

The expressions for each term are given in Appendix D. Upon a small variation of the fields, Ω_5^c and ${\rm d}G_4$ yield boundary terms which do not contribute to the equations of motion. The TCS contribution to the equations of motion is therefore given by varying the first term Ω_5^0 (D.5).

Gauge field EoM Upon a little variation of the gauge field $\mathbf{L} \to \mathbf{L} + \delta\mathbf{L}$, Ω_5^0 changes as

$$\begin{aligned}
\delta_{\mathbf{L}}\Omega_5^0 = {\rm Tr}\Big\{\delta\mathbf{L} \wedge \Big(& - if_1(\tau)\Big(\mathbf{F}^{(L)} \wedge \mathbf{F}^{(L)} + U^\dagger\mathbf{F}^{(R)} \wedge \mathbf{F}^{(R)}U - \mathbf{L} \wedge \mathbf{F}^{(L)} \wedge U^\dagger DU - \\
& - \mathbf{F}^{(L)} \wedge U^\dagger DU \wedge \mathbf{L} - \mathbf{L} \wedge U^\dagger DU \wedge \mathbf{F}^{(L)} - \\
& - U^\dagger DU \wedge \mathbf{F}^{(L)} \wedge \mathbf{L}\Big) - \\
& - {\rm d}\Big[f_1(\tau)(U^\dagger DU \wedge \mathbf{F}^{(L)} + \mathbf{F}^{(L)} \wedge U^\dagger DU)\Big] - \\
& - if_2(\tau)\Big(\mathbf{F}^{(L)} \wedge U^\dagger DU \wedge U^\dagger DU + U^\dagger DU \wedge U^\dagger DU \wedge \mathbf{F}^{(L)} + \\
& + U^\dagger DU \wedge \mathbf{F}^{(L)} \wedge U^\dagger DU - \\
& - \mathbf{L} \wedge U^\dagger DU \wedge U^\dagger DU \wedge U^\dagger DU -
\end{aligned}$$

$$
\begin{aligned}
&\quad - U^\dagger DU \wedge U^\dagger DU \wedge U^\dagger DU \wedge \mathbf{L} + \\
&\quad + \mathbf{F}^{(R)} \wedge DUU^\dagger \wedge DUU^\dagger + DUU^\dagger \wedge DUU^\dagger \wedge \mathbf{F}^{(R)} + \\
&\quad + DUU^\dagger \wedge \mathbf{F}^{(R)} \wedge DUU^\dagger \Big) - \\
&- \mathrm{d}\Big[f_2(\tau)\, U^\dagger DU \wedge U^\dagger DU \wedge U^\dagger DU \Big] - \\
&- i f_3(\tau) \Big(\mathbf{F}^{(L)} \wedge U^\dagger \mathbf{F}^{(R)} U + U^\dagger \mathbf{F}^{(R)} U \wedge \mathbf{F}^{(L)} - \mathbf{L} \wedge U^\dagger \mathbf{F}^{(R)} \wedge DU - \\
&\quad - U^\dagger \mathbf{F}^{(R)} \wedge DU \wedge \mathbf{L} - \mathbf{L} \wedge U^\dagger DU \wedge U^\dagger \mathbf{F}^{(R)} U - \\
&\quad - U^\dagger DU \wedge U^\dagger \mathbf{F}^{(R)} U \wedge \mathbf{L} \Big) - \\
&- \mathrm{d}\Big[f_3(\tau) (U^\dagger DU \wedge U^\dagger \mathbf{F}^{(R)} U + U^\dagger \mathbf{F}^{(R)} \wedge DU) \Big] - \\
&- 4 i f_4(\tau) U^\dagger DU \wedge U^\dagger DU \wedge U^\dagger DU \wedge U^\dagger DU \Big) \Big\} ,
\end{aligned}
\tag{E.3}
$$

and $\delta_{\mathbf{R}} \Omega_5^0$ is obtained by exchanging $L \leftrightarrow R$, $U \leftrightarrow U^\dagger$ and multiplying by -1. From the definition of the CS currents (C.3) and (C.9), (E.3) can be written as

$$
\delta_{\mathbf{L}} \Omega_5^0 = 4\pi^2 i M^3 \,\mathrm{Tr} \left\{ 2\delta L \wedge J_{CS}^{(L)} + \frac{1}{N_f} \delta \hat{L} \wedge \hat{J}_{CS}^{(L)} \, \mathbb{I}_{N_f} \right\} , \tag{E.4}
$$

where

$$
\begin{aligned}
\hat{J}_{CS}^{(L)} &= \frac{1}{4!} \epsilon_{MNPQR} \hat{J}_{CS}^{(L),M} \mathrm{d}x^N \wedge \mathrm{d}x^P \wedge \mathrm{d}x^Q \wedge \mathrm{d}x^R , \\
J_{CS}^{(L)\,a} &= \frac{1}{4!} \epsilon_{MNPQR} \hat{J}_{CS}^{(L)\,a,\,M} \mathrm{d}x^N \wedge \mathrm{d}x^P \wedge \mathrm{d}x^Q \wedge \mathrm{d}x^R ,
\end{aligned}
\tag{E.5}
$$

with the quantities $\hat{J}_{CS}^{(L),M}$ and $J_{CS}^{(L)\,a,\,M}$ appearing respectively in (C.1) and (C.8).

U EoM Upon a little variation of U, $U \to U + \delta U$, Ω_5^0 changes as

$$
\begin{aligned}
\delta_U \Omega_5^0 = \mathrm{Tr} \Big\{ \delta U \Big(&- f_1(\tau) \Big(i \mathbf{L} \wedge \mathbf{F}^{(L)} \wedge \mathbf{F}^{(L)} U^\dagger - i \mathbf{F}^{(L)} \wedge \mathbf{F}^{(L)} U^\dagger \wedge \mathbf{R} - \\
&\quad - U^\dagger DU \wedge \mathbf{F}^{(L)} \wedge \mathbf{F}^{(L)} U^\dagger + i \mathbf{L} \wedge U^\dagger \mathbf{F}^{(R)} \wedge \mathbf{F}^{(R)} - \\
&\quad - i U^\dagger \mathbf{F}^{(R)} \wedge \mathbf{F}^{(R)} \wedge \mathbf{R} - U^\dagger \mathbf{F}^{(R)} \wedge \mathbf{F}^{(R)} \wedge DUU^\dagger \Big) + \\
&+ \mathrm{d}\Big[f_1(\tau) (\mathbf{F}^{(L)} \wedge \mathbf{F}^{(L)} U^\dagger + U^\dagger \mathbf{F}^{(R)} \wedge \mathbf{F}^{(R)}) \Big] - \\
&- f_2(\tau) \Big(i \mathbf{L} \wedge \mathbf{F}^{(L)} \wedge U^\dagger DU \wedge U^\dagger DUU^\dagger - \\
&\quad - i \mathbf{F}^{(L)} \wedge U^\dagger DU \wedge U^\dagger DUU^\dagger \wedge \mathbf{R} -
\end{aligned}
$$

$$
\begin{aligned}
&- U^\dagger DU \wedge \mathbf{F}^{(L)} \wedge U^\dagger DU \wedge U^\dagger DUU^\dagger + \\
&+ i\mathbf{L} \wedge U^\dagger DU \wedge \mathbf{F}^{(L)} \wedge U^\dagger DUU^\dagger - \\
&- iU^\dagger DU \wedge \mathbf{F}^{(L)} \wedge U^\dagger DUU^\dagger \wedge \mathbf{R} - \\
&- U^\dagger DU \wedge U^\dagger DU \wedge \mathbf{F}^{(L)} \wedge U^\dagger DUU^\dagger + \\
&+ i\mathbf{L} \wedge U^\dagger DU \wedge U^\dagger DU \wedge \mathbf{F}^{(L)} U^\dagger - \\
&- iU^\dagger DU \wedge U^\dagger DU \wedge \mathbf{F}^{(L)} U^\dagger \wedge \mathbf{R} - \\
&- U^\dagger DU \wedge U^\dagger DU \wedge U^\dagger DU \wedge \mathbf{F}^{(L)} U^\dagger + \\
&+ i\mathbf{L} \wedge U^\dagger \mathbf{F}^{(R)} \wedge DUU^\dagger \wedge DUU^\dagger - \\
&- iU^\dagger \mathbf{F}^{(R)} \wedge DUU^\dagger \wedge DUU^\dagger \wedge \mathbf{R} - \\
&- U^\dagger DUU^\dagger \wedge \mathbf{F}^{(R)} \wedge DUU^\dagger \wedge DUU^\dagger + \\
&+ i\mathbf{L} \wedge U^\dagger DUU^\dagger \wedge \mathbf{F}^{(R)} \wedge DUU^\dagger - \\
&- iU^\dagger DUU^\dagger \wedge \mathbf{F}^{(R)} \wedge DUU^\dagger \wedge \mathbf{R} - \\
&- U^\dagger DUU^\dagger \wedge DUU^\dagger \wedge \mathbf{F}^{(R)} \wedge DUU^\dagger + \\
&+ i\mathbf{L} \wedge U^\dagger DUU^\dagger \wedge DUU^\dagger \wedge \mathbf{F}^{(R)} - \\
&- iU^\dagger DUU^\dagger \wedge DUU^\dagger \wedge \mathbf{F}^{(R)} \wedge \mathbf{R} - \\
&- U^\dagger DUU^\dagger \wedge DUU^\dagger \wedge DUU^\dagger \wedge \mathbf{F}^{(R)} \Big) + \\
&+ \mathrm{d}\Big[f_2(\tau) \Big(\mathbf{F}^{(L)} \wedge U^\dagger DU \wedge U^\dagger DUU^\dagger + U^\dagger DU \wedge \mathbf{F}^{(L)} \wedge U^\dagger DUU^\dagger + \\
&\qquad + U^\dagger DU \wedge U^\dagger DU \wedge \mathbf{F}^{(L)} U^\dagger + U^\dagger \mathbf{F}^{(R)} \wedge DUU^\dagger \wedge DUU^\dagger + \\
&\qquad + U^\dagger DUU^\dagger \wedge \mathbf{F}^{(R)} \wedge DUU^\dagger + \\
&\qquad + U^\dagger DUU^\dagger \wedge DUU^\dagger \wedge \mathbf{F}^{(R)} \Big) \Big] - \\
&- f_3(\tau) \Big(i\mathbf{L} \wedge \mathbf{F}^{(L)} \wedge U^\dagger \mathbf{F}^{(R)} - i\mathbf{F}^{(L)} \wedge U^\dagger \mathbf{F}^{(R)} \wedge \mathbf{R} - \\
&\qquad - U^\dagger \mathbf{F}^{(R)} DU \wedge \mathbf{F}^{(L)} U^\dagger + i\mathbf{L} \wedge U^\dagger \mathbf{F}^{(R)} \wedge U\mathbf{F}^{(L)} U^\dagger - \\
&\qquad - iU^\dagger \mathbf{F}^{(R)} \wedge U\mathbf{F}^{(L)} U^\dagger \wedge \mathbf{R} - U^\dagger \mathbf{F}^{(R)} \wedge U\mathbf{F}^{(L)} U^\dagger \wedge DUU^\dagger + \\
&\qquad + \mathbf{F}^{(L)} \wedge U^\dagger DUU^\dagger \wedge \mathbf{F}^{(R)} - U^\dagger DUU^\dagger \wedge \mathbf{F}^{(R)} \wedge U\mathbf{F}^{(L)} U^\dagger \Big) + \\
&+ \mathrm{d}\Big[f_3(\tau) \Big(\mathbf{F}^{(L)} \wedge U^\dagger \mathbf{F}^{(R)} + U^\dagger \mathbf{F}^{(R)} U \wedge \mathbf{F}^{(L)} U^\dagger \Big) \Big] - \\
&- 4 f_4(\tau) \Big(i\mathbf{L} \wedge U^\dagger DU \wedge U^\dagger DU \wedge U^\dagger DU \wedge U^\dagger DUU^\dagger - \\
&\qquad - iU^\dagger DU \wedge U^\dagger DU \wedge U^\dagger DU \wedge U^\dagger DUU^\dagger \wedge \mathbf{R} - \\
&\qquad - U^\dagger DU \wedge U^\dagger DU \wedge U^\dagger DU \wedge U^\dagger DU \wedge U^\dagger DUU^\dagger \Big) +
\end{aligned}
$$

$$+ 4\,\mathrm{d}\Big[f_4(\tau)\,U^\dagger DU \wedge U^\dagger DU \wedge U^\dagger DU \wedge U^\dagger DUU^\dagger\Big]\Big)\Big\}\,. \tag{E.6}$$

From (C.7), (E.6) can be written as

$$\delta_U \Omega_5^0 = 4\pi^2 i M^3\,\mathrm{Tr}\left(\delta U \mathbf{J}^U_{CS} U^\dagger\right)\,, \tag{E.7}$$

where

$$\mathbf{J}^U_{CS} \equiv J^U_{CS}\,\mathrm{d}t \wedge \mathrm{d}r \wedge \mathrm{d}x_1 \wedge \mathrm{d}x_2 \wedge \mathrm{d}x_3\,, \tag{E.8}$$

and where J^U_{CS} can be read off from (C.6).

F The baryon ansatz field equations

We present in this appendix the derivation of the differential equations obeyed by the fields of the baryon ansatz (3.1.70). We start with some general results which are useful to derive those equations and then specify to the two different regimes of approximation considered in this work, the probe instanton and the inhomogeneous tachyon.

We first write down the expression for the inverse of the effective metric $\tilde{g}$ (3.1.75), which is found to take a relatively simple form

$$-\det\tilde{g}\;\tilde{g}^{-1} = \left(\begin{array}{cc|c} \alpha_0 & -X_r & -\vec{X}^t \\ X_r & \alpha_r & \vec{Y}^t \\ \hline \vec{X} & \vec{Y} & g_S \end{array}\right)\,, \tag{F.1}$$

where we defined 2 scalars

$$\alpha_0 \equiv \mathrm{e}^{8A} + \mathrm{e}^{6A}\kappa\left((\partial_r\tau)^2 + (\partial_\xi\tau)^2\right)\,, \tag{F.2}$$

$$\alpha_r \equiv \mathrm{e}^{4A}\left(\mathrm{e}^{4A}f - w^2(\partial_\xi\Phi)^2 + \kappa(\partial_\xi\tau)^2\mathrm{e}^{2A}\right)\,, \tag{F.3}$$

the 4-vector X with components

$$X_r \equiv \mathrm{e}^{4A} w\left(\mathrm{e}^{2A}\partial_r\Phi + \kappa\partial_\xi\tau(\partial_r\Phi\partial_\xi\tau - \partial_\xi\Phi\partial_r\tau)\right)\,, \tag{F.4}$$

$$X_i \equiv \mathrm{e}^{4A}\frac{x_i}{\xi} w\left(\mathrm{e}^{2A}\partial_\xi\Phi - \kappa\partial_r\tau(\partial_r\Phi\partial_\xi\tau - \partial_\xi\Phi\partial_r\tau)\right)\,, \tag{F.5}$$

the 3-vector $\vec{Y}$ with components

$$Y_i \equiv -\mathrm{e}^{4A}\frac{x_i}{\xi}(-w^2\partial_r\Phi\partial_\xi\Phi + \mathrm{e}^{2A}\kappa\partial_r\tau\partial_\xi\tau))\,, \tag{F.6}$$

and the symmetric 3-matrix g_S with components

$$(g_S)_{ii} = \mathrm{e}^{8A} - \mathrm{e}^{4A} w^2 \left((\partial_r \Phi)^2 + (\partial_\xi \Phi)^2 \left(1 - \frac{x_i^2}{\xi^2} \right) \right) - \tag{F.7}$$
$$- \mathrm{e}^{2A} \kappa w^2 (\partial_\xi \tau \partial_r \Phi - \partial_r \tau \partial_\xi \Phi)^2 \left(1 - \frac{x_i^2}{\xi^2} \right) +$$
$$+ \mathrm{e}^{6A} \kappa \left((\partial_r \tau)^2 + (\partial_\xi \tau)^2 \left(1 - \frac{x_i^2}{\xi^2} \right) \right) ,$$

$$(g_S)_{ij} = -\mathrm{e}^{2A} \frac{x_i x_j}{\xi^2} (-\mathrm{e}^{2A} w^2 (\partial_\xi \Phi)^2 + \mathrm{e}^{4A} \kappa (\partial_\xi \Phi)^2 - \kappa w^2 (\partial_\xi \tau \partial_r \Phi - \partial_r \tau \partial_\xi \Phi)^2) . \tag{F.8}$$

Provided these results, the equations of motion (C.1),(C.6) and (C.8) are simplified in the following ways:

- The superscripts $^{(L)}$ and $^{(R)}$ can be removed from $\tilde{g}$.
- $F_C^{(L/R)C} = (\tilde{g}^{-1})^{[MN]} F_{NM}^{(L/R)} = 0$ because $F_{0M}^{(L/R)} = 0$.
- $$\mathrm{Tr}\, D_N U^\dagger U = 0 . \tag{F.9}$$
- In terms of the redefined gauge fields (3.1.78), the following replacements can be performed
$$i D_N U^\dagger U \to \sqrt{2} \tilde{\mathbf{A}}_N , \tag{F.10}$$

$$\frac{1}{4} \left[D_{(M} \left(V_f(\lambda, \tau^2) \kappa \tau^2 \sqrt{-\det \tilde{g}^{(L)}} \left((\tilde{g}^{(L)})^{-1} \right)^{(MN)} D_{N)} U^\dagger \right) U - h.c. + (L \leftrightarrow R) \right]$$
$$\to -i\sqrt{2} \partial_M \left(V_f(\lambda, \tau^2) \kappa \tau^2 \sqrt{-\det \tilde{g}} \left(\tilde{g}^{-1} \right)^{(MN)} \tilde{\mathbf{A}}_N \right) -$$
$$- V_f(\lambda, \tau^2) \kappa \tau^2 \sqrt{-\det \tilde{g}} \left(\tilde{g}^{-1} \right)^{(MN)} \left[\tilde{\mathbf{V}}_M, \tilde{\mathbf{A}}_N \right] , \tag{F.11}$$

  where $\mathbf{A}$ and $\mathbf{V}$ are defined in (3.1.42).

- Within the ansatz the matrices S_{MN} and $F_{MN}^{(L/R)}$ can be written
$$F_{MN}^{(L/R)} = \left(\begin{array}{c|c} 0 & 0 \\ \hline 0 & F_{(4)}^{(L/R)} \end{array} \right) , \tag{F.12}$$
$$S_{MN} = \left(\begin{array}{c|c} 0 & 0 \\ \hline 0 & S_{(4)} \end{array} \right) , \tag{F.13}$$

where $F^{(L/R)}_{(4)}$ is an antisymmetric 4-matrix

$$F^{(L/R)\,a}_{(4),ij} = \epsilon^{aij}\frac{\left(\phi_1^{(L/R)}\right)^2 - 2\left(1+\phi_2^{(L/R)}\right)}{\xi^2} + \tag{F.14}$$
$$+ (x_i\epsilon^{ajk} - x_j\epsilon^{aik})x_k\frac{\xi D_\xi\phi_2^{(L/R)} + \left(\phi_1^{(L/R)}\right)^2 - 2\left(1+\phi_2^{(L/R)}\right)}{\xi^4} +$$
$$+ (x_i\delta_{ja} - x_j\delta_{ia})\frac{D_\xi\phi_1^{(L/R)}}{\xi^2} + x_a\epsilon^{ijk}x_k\frac{\left(1+\phi_2^{(L/R)}\right)^2}{\xi^4}\,,$$

$$F^{(L/R)\,a}_{(4),ir} = -\epsilon^{aik}x_k\frac{D_r\phi_2^{(L/R)}}{\xi^2} - (\xi^2\delta_{ia} - x_ix_a)\frac{D_r\phi_1^{(L/R)}}{\xi^3} + x_ix_a\frac{F^{(L/R)}_{\xi r}}{\xi^2}\,, \tag{F.15}$$

where the covariant derivative $D\phi$ is defined in (A.21) and the field strength $F_{\bar\mu\bar\nu}$ in (A.23). We recall that the abelian part of the field strength is included in the effective metric $\tilde g$ and has the components

$$\hat F^{(L/R)}_{(4),r0} = \partial_r\Phi(r,\xi) \quad , \quad \hat F^{(L/R)}_{i0} = \frac{x_i}{\xi}\partial_\xi\Phi(r,\xi)\,. \tag{F.16}$$

$S_{(4)}$ is a symmetric 4-matrix

$$(S_{(4)})_{rr} = 2(\partial_r\theta + A_r)^2 = 2\tilde A_r^2\,, \tag{F.17}$$

$$(S_{(4)})_{ri} = 2(A_r + \partial_r\theta)(A_\xi + \partial_\xi\theta)\frac{x_i}{\xi} = 2\tilde A_r\tilde A_\xi\frac{x_i}{\xi}\,, \tag{F.18}$$

$$\begin{aligned}(S_{(4)})_{ij} &= 2\left(\frac{(\mathrm{e}^{i\theta}\phi + \mathrm{e}^{-i\theta}\phi^*)^2}{4\xi^2}\left(\delta_{ij} - \frac{x_ix_j}{\xi^2}\right) + (A_\xi + \partial_\xi\theta)^2\frac{x_ix_j}{\xi^2}\right)\\ &= 2\left(\frac{(\tilde\phi + \tilde\phi^*)^2}{4\xi^2}\left(\delta_{ij} - \frac{x_ix_j}{\xi^2}\right) + \tilde A_\xi^2\frac{x_ix_j}{\xi^2}\right)\,,\end{aligned} \tag{F.19}$$

where we recall that we defined the 2-vector $(A_\xi, A_r) = (A_1, A_2)$. Then, noting that $\tilde g^{-1}$ can be written

$$-\det\tilde g\ \tilde g^{-1} = \left(\begin{array}{c|c} \mathrm{e}^{8A} + \mathrm{e}^{6A}\kappa\left((\partial_r\tau)^2 + (\partial_\xi\tau)^2\right) & -X^t \\ \hline X & \mathcal{S}\end{array}\right)\,, \tag{F.20}$$

with $\mathcal{S}$ the symmetric 4-matrix

$$\mathcal{S} \equiv \left(\begin{array}{c|c} \mathrm{e}^{4A}\left(\mathrm{e}^{4A} - w^2(\partial_\xi\Phi)^2 + \kappa(\partial_\xi\tau)^2\mathrm{e}^{2A}\right) & \vec Y^t \\ \hline \vec Y & g_S\end{array}\right)\,, \tag{F.21}$$

the following expressions can be obtained for the matrices with raised indices

$$\left(F^{(L/R)}\right)^{MN} = (-\det\tilde{g})^{-2}\left(\begin{array}{c|c} 0 & X^t F^{(L/R)}_{(4)}\Sigma \\ \hline -\Sigma F^{(L/R)}_{(4)} X & \Sigma F^{(L/R)}_{(4)}\Sigma \end{array}\right), \tag{F.22}$$

$$S^{MN} = (-\det\tilde{g})^{-2}\left(\begin{array}{c|c} -X^t\mathcal{S}X & -X^t S_{(4)}\mathcal{S} \\ \hline \mathcal{S}S_{(4)}X & \mathcal{S}S_{(4)}\mathcal{S} \end{array}\right), \tag{F.23}$$

$$\left(F^{(L/R)}\right)^{MS}\left(F^{(L/R)}\right)_S{}^N = \tag{F.24}$$
$$= (-\det\tilde{g})^{-3}\left(\begin{array}{c|c} X^t F^{(L/R)}_{(4)}\mathcal{S}F^{(L/R)}_{(4)}X & -X^t F^{(L/R)}_{(4)}\mathcal{S}F^{(L/R)}_{(4)}\mathcal{S} \\ \hline \Sigma F^{(L/R)}_{(4)}\mathcal{S}F^{(L/R)}_{(4)}X & \mathcal{S}F^{(L/R)}_{(4)}\mathcal{S}F^{(L/R)}_{(4)}\mathcal{S} \end{array}\right),$$

$$\left(F^{(L/R)}\right)^{MN}\left(F^{(L/R)}\right)_{NM} = (-\det\tilde{g})^{-2}\mathrm{tr}\left(\mathcal{S}F^{(L/R)}_{(4)}\mathcal{S}F^{(L/R)}_{(4)}\right), \tag{F.25}$$

where the symmetric and antisymmetric parts are easily identified.

F.1 Probe instanton

We consider first the case of the probe regime. We recall the expressions of the non-abelian equations of motion in (C.6) and (C.8)

$$\frac{1}{2}\left[D_{(M}\left(V_f(\lambda,\tau^2)\kappa\tau^2\sqrt{-\det\tilde{g}}\left(\tilde{g}^{-1}\right)^{(MN)}D_{N)}U^\dagger\right)U - h.c.\right] = J^U_{CS}\,, \tag{F.26}$$

$$\frac{1}{2}D_N\left[V_f(\lambda,\tau^2)\sqrt{-\det\tilde{g}}\,w^2F^{(L)NM}\right] \tag{F.27}$$
$$= \frac{1}{2}V_f(\lambda,\tau^2)\sqrt{-\det\tilde{g}}\left(\tilde{g}^{-1}\right)^{MN}\kappa\tau^2\left(iD_NU^\dagger U - \frac{1}{N_f}\mathrm{Tr}(iD_NU^\dagger U) + h.c.\right) + 2J^{(L)}_{CS}\,.$$

With the quadratic expansion introduced in Section 3.1.5.1, the abelian gauge field equations (C.1) are modified to take the same shape as the non-abelian part

$$N_f\partial_N\left[V_f(\lambda,\tau^2)\sqrt{-\det\tilde{g}}\,w^2\hat{F}^{(L)NM}\right] \tag{F.28}$$
$$= V_f(\lambda,\tau^2)\sqrt{-\det\tilde{g}}\left(\tilde{g}^{-1}\right)^{MN}\kappa\tau^2\mathrm{Tr}\left(iD_NU^\dagger U + h.c.\right) + 2\hat{J}^{(L)}_{CS}\,,$$

where the result (F.9) was used to simplify the right-hand side.

SU(2) ansatz Substituting the ansatz (3.1.50)-(3.1.52), (3.1.56)-(3.1.58) and (3.1.64) into the equations of motion (F.26)-(F.28) yields the following system of equations for the fields of the ansatz (3.1.70)

$$\frac{x^a}{2\xi^3}\sigma^a\left[\partial_r\left(V_f(\lambda,\tau^2)\kappa\tau^2\frac{\mathrm{e}^{3A}}{\sqrt{1+\mathrm{e}^{-2A}\kappa(\partial_r\tau)^2}}\xi^2\tilde{A}_r\right)\right. \tag{F.29}$$
$$\left.+V_f(\lambda,\tau^2)\kappa\tau^2\mathrm{e}^{3A}\sqrt{1+\mathrm{e}^{-2A}\kappa(\partial_r\tau)^2}\,\left(\partial_\xi(\xi^2\tilde{A}_\xi)+2\tilde{\phi}_1\tilde{\phi}_2\right)\right]=\frac{i}{2}J^U_{CS}\,,$$

$$\partial_r\left[V_f(\lambda,\tau^2)w^2\mathrm{e}^A\frac{\partial_r\Phi}{\sqrt{1+\mathrm{e}^{-2A}\kappa(\partial_r\tau)^2}}\right] \tag{F.30}$$
$$+\,V_f(\lambda,\tau^2)w^2\mathrm{e}^A\sqrt{1+\mathrm{e}^{-2A}\kappa(\partial_r\tau)^2}\,\frac{\partial_\xi(\xi^2\partial_\xi\Phi)}{\xi^2}=-\hat{J}_{CS\,0}\,,$$

$$\frac{\mathrm{e}^A}{\sqrt{1+\mathrm{e}^{-2A}\kappa(\partial_r\tau)^2}}V_f(\lambda,\tau^2)w^2\frac{x^a}{\xi^3}\left[\partial_\xi(\xi^2F_{\xi r})-(i\phi^*D_r\phi-i\phi D_r\phi^*)\right] \tag{F.31}$$
$$=4V_f(\lambda,\tau^2)\frac{x^a}{\xi}\frac{\mathrm{e}^{3A}}{\sqrt{1+\mathrm{e}^{-2A}\kappa(\partial_r\tau)^2}}\kappa\tau^2\tilde{A}_r+4J^{(L)\,a}_{CS\,r}\,,$$

$$\frac{\epsilon^{iak}x_k}{2\xi^2}\left[V_f\mathrm{e}^A\sqrt{1+\mathrm{e}^{-2A}\kappa(\partial_r\tau)^2}w^2\left(iD_\xi D_\xi\tilde{\phi}-i\tilde{\phi}\frac{|\phi|^2-1}{\xi^2}+h.c.\right)\right. \tag{F.32}$$
$$\left.+\left(iD_r\left(\frac{V_f\mathrm{e}^Aw^2}{\sqrt{1+\mathrm{e}^{-2A}\kappa(\partial_r\tau)^2}}D_r\tilde{\phi}\right)+h.c.\right)\right]$$
$$+\,\frac{\xi^2\delta_{ia}-x_ix_a}{2\xi^3}\left[V_f\mathrm{e}^A\sqrt{1+\mathrm{e}^{-2A}\kappa(\partial_r\tau)^2}w^2\left(D_\xi D_\xi\tilde{\phi}-\tilde{\phi}\frac{|\phi|^2-1}{\xi^2}+h.c.\right)\right.$$
$$\left.+\left(D_r\left(\frac{V_f\mathrm{e}^Aw^2}{\sqrt{1+\mathrm{e}^{-2A}\kappa(\partial_r\tau)^2}}D_r\tilde{\phi}\right)+h.c.\right)\right]$$
$$-\,\frac{x_ix_a}{2\xi^4}\left[V_f\mathrm{e}^A\sqrt{1+\mathrm{e}^{-2A}\kappa(\partial_r\tau)^2}w^2\,(2i\phi^*D_\xi\phi+h.c.)+\right.$$
$$\left.+2\xi^2\partial_r\left(\frac{V_f\mathrm{e}^Aw^2}{\sqrt{1+\mathrm{e}^{-2A}\kappa(\partial_r\tau)^2}}F_{\xi r}\right)\right]$$
$$=4V_f\mathrm{e}^{3A}\sqrt{1+\mathrm{e}^{-2A}\kappa(\partial_r\tau)^2}\kappa\tau^2\left(\frac{\xi^2\delta_{ia}-x_ix_a}{2\xi^3}(\tilde{\phi}+\tilde{\phi}^*)-\frac{x_ix_a}{2\xi^4}(-2\xi^2\tilde{A}_\xi)\right)+4J^{(L)\,a}_{CS\,i}\,,$$

where we used the covariant quantities (A.21) and (A.23). The right-handed equations are obtained by performing

$$\phi \to -\phi^* \quad , \quad A_{\bar{\mu}} \to -A_{\bar{\mu}} \, . \tag{F.33}$$

It can be checked that (F.30), (F.31) and (F.32) yield the same form for the equations of motion as what was found in [173] and [175] when the tachyon and the CS contribution are set to 0. We derive the CS contribution in the next subsection.

F.1.1 TCS contribution

The general form of the contribution of the TCS term to the equations of motion is presented in Appendix E. For the $SU(2)$ ansatz (3.1.50)-(3.1.52) and (3.1.64), the CS currents $\hat{J}^{(L)}_{CS\,M}$, $J^{(L)\,a}_{CS\,M}$ and J^{U}_{CS} in the probe approximation are found to be

$$\begin{aligned}
\hat{J}^{(L)}_{CS\,0} = \hat{J}^{(R)}_{CS\,0} = \frac{-f_1(\tau)}{4\pi^2 M^3 \xi^2} \Bigg(& \left(1 + \frac{f_3(\tau)}{f_1(\tau)}\right) \epsilon^{\bar{\mu}\bar{\nu}} \left(F_{\bar{\mu}\bar{\nu}} + \partial_{\bar{\mu}}(-i\phi^* D_{\bar{\nu}}\phi + h.c.)\right) \\
& + \left(3i\frac{f_2(\tau)}{f_1(\tau)} - 1 - \frac{f_3(\tau)}{f_1(\tau)}\right) \epsilon^{\bar{\mu}\bar{\nu}} \left(\frac{1}{2} F_{\bar{\mu}\bar{\nu}} (\tilde{\phi} + \tilde{\phi}^*)^2 - A_{\bar{\mu}} \partial_{\bar{\nu}} (\tilde{\phi} + \tilde{\phi}^*)^2\right) \\
& + 2\tau' \left(\frac{f_1'(\tau) + f_3'(\tau)}{f_1(\tau)} (\tilde{A}_\xi (|\phi|^2 - 1) + \frac{i}{2} (\tilde{\phi} + \tilde{\phi}^*)(D_\xi \tilde{\phi} - D_\xi \tilde{\phi}^*))\right) \\
& - 3i\tau' \frac{f_2'(\tau)}{f_1(\tau)} \tilde{A}_\xi (\tilde{\phi} + \tilde{\phi}^*)^2 \Bigg) \, ,
\end{aligned} \tag{F.34}$$

$$\begin{aligned}
J^{(L)\,a}_{CS\,r} &= -J^{(R)\,a}_{CS\,r} \\
&= \frac{f_1(\tau)}{2\pi^2 M^3 \xi^3} x^a \, \partial_\xi \Phi \Bigg(\left(1 + \frac{f_3(\tau)}{f_1(\tau)}\right) (1 - |\phi|^2) + \\
&\qquad + \left(3i\frac{f_2(\tau)}{f_1(\tau)} - 1 - \frac{f_3(\tau)}{f_1(\tau)}\right) \frac{(\tilde{\phi} + \tilde{\phi}^*)^2}{2} \Bigg) \, ,
\end{aligned} \tag{F.35}$$

$$\begin{aligned}
J^{(L)\,a}_{CS\,i} = \frac{\xi^2 \delta_{ia} - x_i x_a}{2\xi^3} \frac{f_1(\tau) \epsilon^{\bar{\mu}\bar{\nu}}}{2\pi^2 M^3} \Bigg(& - i \left(1 + \frac{f_3(\tau)}{f_1(\tau)}\right) \partial_{\bar{\mu}} \Phi D_{\bar{\nu}} \tilde{\phi} + \\
& + 2 \left(3i\frac{f_2(\tau)}{f_1(\tau)} - 1 - \frac{f_3(\tau)}{f_1(\tau)}\right) \tilde{\phi} \partial_{\bar{\mu}} \Phi \tilde{A}_{\bar{\nu}} + h.c. \Bigg) + \\
- \frac{x_i x_a}{2\xi^4} \frac{f_1(\tau)}{2\pi^2 M^3} \Bigg(& - 2 \left(1 + \frac{f_3(\tau)}{f_1(\tau)}\right) \partial_r \Phi (|\phi|^2 - 1) + \\
& + \left(3i\frac{f_2(\tau)}{f_1(\tau)} - 1 - \frac{f_3(\tau)}{f_1(\tau)}\right) \partial_r \Phi (\tilde{\phi} + \tilde{\phi}^*)^2 \Bigg) +
\end{aligned}$$

$$+\frac{\epsilon^{iak}x_k}{2\xi^2}\frac{f_1(\tau)}{2\pi^2M^3}\Bigg(\left(1+\frac{f_3(\tau)}{f_1(\tau)}\right)\epsilon^{\bar\mu\bar\nu}(\partial_{\bar\mu}\Phi D_{\bar\nu}\tilde\phi+h.c.)+ \\ +\frac{f_1'(\tau)+f_3'(\tau)}{f_1(\tau)}\tau'(\tilde\phi+\tilde\phi^*)\partial_\xi\Phi\Bigg). \tag{F.36}$$

$$J^U_{CS}=\sigma^a\frac{x_a}{2\xi^3}\times\frac{-i}{\pi^2M^3}\Big((f_1(\tau)+f_3(\tau)-3if_2(\tau))\epsilon^{\bar\mu\bar\nu}(\tilde\phi+\tilde\phi^*)\partial_{\bar\mu}\Phi(D_{\bar\nu}\tilde\phi+D_{\bar\nu}\tilde\phi^*)+ \\ +(f_1'(\tau)+f_3'(\tau))\tau'\partial_\xi\Phi(|\phi|^2-1)-\frac{3i}{2}f_2'(\tau)\tau'\partial_\xi\Phi(\tilde\phi+\tilde\phi^*)^2\Big). \tag{F.37}$$

Note that only $f_1(\tau)+f_3(\tau)$ and $f_2(\tau)$ contribute to the equations of motion.

F.1.2 Full EoMs

Substituting (F.34)-(F.37) into (F.29),(F.30),(F.31) and (F.32) yields the full set of 6 real equations of motion for the 6 fields of the SU(2) ansatz (3.1.70) in the probe instanton limit (where the tachyon modulus τ is a background field)

$$\partial_r\left(\mathrm{e}^{2A}k\,\kappa\tau^2\xi^2\tilde A_r\right)+\mathrm{e}^{2A}h\,\kappa\tau^2\left(\partial_\xi(\xi^2\tilde A_\xi)+\frac{1}{2i}(\tilde\phi^2-(\tilde\phi^*)^2)\right) \\ =\frac{f_1(\tau)+f_3(\tau)-3if_2(\tau)}{2\pi^2M^3}\epsilon^{\bar\mu\bar\nu}(\tilde\phi+\tilde\phi^*)\partial_{\bar\mu}\Phi(D_{\bar\nu}\tilde\phi+D_{\bar\nu}\tilde\phi^*) \\ +\frac{1}{2\pi^2M^3}(f_1'(\tau)+f_3'(\tau))\tau'\partial_\xi\Phi(|\phi|^2-1)-\frac{3i}{4\pi^2M^3}f_2'(\tau)\tau'\partial_\xi\Phi(\tilde\phi+\tilde\phi^*)^2, \tag{F.38}$$

$$\partial_r\left[kw^2\,\xi^2\partial_r\Phi\right]+hw^2\,\partial_\xi(\xi^2\partial_\xi\Phi) \\ =\frac{f_1(\tau)}{4\pi^2M^3}\Bigg(\left(1+\frac{f_3(\tau)}{f_1(\tau)}\right)\epsilon^{\bar\mu\bar\nu}\left(F_{\bar\mu\bar\nu}+\partial_{\bar\mu}(-i\phi^*D_{\bar\nu}\phi+h.c.)\right)+ \\ +\left(3i\frac{f_2(\tau)}{f_1(\tau)}-1-\frac{f_3(\tau)}{f_1(\tau)}\right)\epsilon^{\bar\mu\bar\nu}\left(\frac{1}{2}F_{\bar\mu\bar\nu}(\tilde\phi+\tilde\phi^*)^2-\tilde A_{\bar\mu}\partial_{\bar\nu}(\tilde\phi+\tilde\phi^*)^2\right)+ \\ +2\tau'\frac{f_1'(\tau)+f_3'(\tau)}{f_1(\tau)}\left(\tilde A_\xi(|\phi|^2-1)+\frac{i}{2}(\tilde\phi+\tilde\phi^*)(D_\xi\tilde\phi-D_\xi\tilde\phi^*)\right)- \\ -3i\tau'\frac{f_2'(\tau)}{f_1(\tau)}\tilde A_\xi(\tilde\phi+\tilde\phi^*)^2\Bigg), \tag{F.39}$$

$$kw^2\left[\partial_\xi(\xi^2F_{\xi r})-(i\phi^*D_r\phi-i\phi D_r\phi^*)\right] \\ =4\mathrm{e}^{2A}k\,\kappa\tau^2\xi^2\tilde A_r$$

$$+\frac{2f_1(\tau)}{\pi^2M^3}\,\partial_\xi\Phi\left(\left(1+\frac{f_3(\tau)}{f_1(\tau)}\right)(1-|\phi|^2)+\frac{1}{2}\left(3i\frac{f_2(\tau)}{f_1(\tau)}-1-\frac{f_3(\tau)}{f_1(\tau)}\right)(\tilde\phi+\tilde\phi^*)^2\right), \tag{F.40}$$

$$\begin{aligned}
&hw^2\left(D_\xi D_\xi\tilde\phi-\tilde\phi\frac{|\phi|^2-1}{\xi^2}\right)+D_r\left(kw^2D_r\tilde\phi\right)+h.c.\\
&=4\mathrm{e}^{2A}h\,\kappa\tau^2\tilde\phi+\\
&\quad+\frac{2f_1(\tau)\epsilon^{\bar\mu\bar\nu}}{\pi^2M^3}\left(-i\left(1+\frac{f_3(\tau)}{f_1(\tau)}\right)\partial_{\bar\mu}\Phi D_{\bar\nu}\tilde\phi+\right.\\
&\qquad\left.+2\left(3i\frac{f_2(\tau)}{f_1(\tau)}-1-\frac{f_3(\tau)}{f_1(\tau)}\right)\tilde\phi\partial_{\bar\mu}\Phi\tilde A_{\bar\nu}\right)+h.c.\,,
\end{aligned} \tag{F.41}$$

$$\begin{aligned}
&hw^2\left(-i\phi^*D_\xi\tilde\phi+h.c.\right)+\xi^2\partial_r\left(kw^2F_{r\xi}\right)\\
&=4\mathrm{e}^{2A}h\kappa\tau^2\xi^2\tilde A_\xi\\
&\quad-\frac{2f_1(\tau)}{\pi^2M^3}\partial_r\Phi\left(\left(1+\frac{f_3(\tau)}{f_1(\tau)}\right)(1-|\phi|^2)+\frac{1}{2}\left(3i\frac{f_2(\tau)}{f_1(\tau)}-1-\frac{f_3(\tau)}{f_1(\tau)}\right)(\tilde\phi+\tilde\phi^*)^2\right),
\end{aligned} \tag{F.42}$$

$$\begin{aligned}
&hw^2\left(iD_\xi D_\xi\tilde\phi-i\tilde\phi\frac{|\phi|^2-1}{\xi^2}\right)+iD_r\left(kw^2D_r\tilde\phi\right)+h.c.\\
&=\frac{2f_1(\tau)}{\pi^2M^3}\left(\left(1+\frac{f_3(\tau)}{f_1(\tau)}\right)\epsilon^{\bar\mu\bar\nu}\partial_{\bar\mu}\Phi D_{\bar\nu}\tilde\phi+\frac{f_1'(\tau)+f_3'(\tau)}{f_1(\tau)}\tau'\tilde\phi\partial_\xi\Phi\right)+h.c.\quad.
\end{aligned} \tag{F.43}$$

where we defined

$$k(r)\equiv\frac{\mathrm{e}^A}{\sqrt{1+\mathrm{e}^{-2A}\kappa(\partial_r\tau)^2}}V_f(\lambda,\tau^2)\quad,\quad h(r)\equiv\mathrm{e}^A\sqrt{1+\mathrm{e}^{-2A}\kappa(\partial_r\tau)^2}V_f(\lambda,\tau^2)\,. \tag{F.44}$$

(F.38)-(F.43) are consistent with the equations of motion derived in [173] (equation (19)) and [175] (equations (2.16)-(2.19)) in the limit where the tachyon goes to 0[22].

F.1.3 Lorenz gauge

We write in this subsection the equations of motion (F.38)-(F.43) in the Lorenz gauge, which corresponds to the constraint

$$\partial_r A_r+\partial_\xi A_\xi=0\,. \tag{F.45}$$

[22]Except that γ should be divided by 2 in (2.19) of [175] and multiplied by -1 in (2.17) and (2.18). Also, to obtain the same coefficients for γ it is necessary to change the convention for the normalization of the abelian gauge field Φ: $\Phi\to\Phi/\sqrt{2N_f}$.

In this gauge, the equations of motion for the 2-dimensional gauge field $A_{\bar{\mu}}$ can be written in an elliptic form, which is the appropriate form to solve the equations numerically via the heat diffusion method. The full set of equations of motion in Lorenz gauge reads

$$\begin{aligned}
&\partial_r \left(\mathrm{e}^{2A} k\,\kappa\tau^2\xi^2\partial_r\theta\right) + \mathrm{e}^{2A} h\,\kappa\tau^2\partial_\xi(\xi^2\partial_\xi\theta) \\
&\quad + \partial_r \left(\mathrm{e}^{2A} k\,\kappa\tau^2\xi^2 A_r\right) + \mathrm{e}^{2A} h\,\kappa\tau^2 \left(\partial_\xi(\xi^2 A_\xi) + \frac{1}{2i}(\tilde{\phi}^2 - (\tilde{\phi}^*)^2)\right) \\
&= \frac{f_1(\tau) + f_3(\tau) - 3i f_2(\tau)}{2\pi^2 M^3}\epsilon^{\bar{\mu}\bar{\nu}}(\tilde{\phi} + \tilde{\phi}^*)\partial_{\bar{\mu}}\Phi\left(D_{\bar{\nu}}\tilde{\phi} + h.c.\right) \\
&\quad + \frac{1}{2\pi^2 M^3}(f_1'(\tau) + f_3'(\tau))\tau'\partial_\xi\Phi(|\tilde{\phi}|^2 - 1) - \frac{3i}{4\pi^2 M^3} f_2'(\tau)\tau'\partial_\xi\Phi(\tilde{\phi} + \tilde{\phi}^*)^2\,,
\end{aligned} \tag{F.46}$$

$$\begin{aligned}
&\partial_r\left[k w^2\,\xi^2\partial_r\Phi\right] + h w^2\,\partial_\xi(\xi^2\partial_\xi\Phi) \\
&= \frac{f_1(\tau)}{4\pi^2 M^3}\left(\left(1 + \frac{f_3(\tau)}{f_1(\tau)}\right)\epsilon^{\bar{\mu}\bar{\nu}}\left(F_{\bar{\mu}\bar{\nu}} + \partial_{\bar{\mu}}\left(-i\tilde{\phi}^* D_{\bar{\nu}}\tilde{\phi} + h.c.\right)\right)\right. \\
&\quad + \left(3i\frac{f_2(\tau)}{f_1(\tau)} - 1 - \frac{f_3(\tau)}{f_1(\tau)}\right)\epsilon^{\bar{\mu}\bar{\nu}}\left(\frac{1}{2}F_{\bar{\mu}\bar{\nu}}(\tilde{\phi} + \tilde{\phi}^*)^2 - \tilde{A}_{\bar{\mu}}\partial_{\bar{\nu}}(\tilde{\phi} + \tilde{\phi}^*)^2\right) \\
&\quad + 2\tau'\frac{f_1'(\tau) + f_3'(\tau)}{f_1(\tau)}\left(\tilde{A}_\xi(|\tilde{\phi}|^2 - 1) + \frac{i}{2}(\tilde{\phi} + \tilde{\phi}^*)\left(D_\xi\tilde{\phi} - h.c.\right)\right) \\
&\quad \left. - 3i\tau'\frac{f_2'(\tau)}{f_1(\tau)}\tilde{A}_\xi(\tilde{\phi} + \tilde{\phi}^*)^2\right)\,,
\end{aligned} \tag{F.47}$$

$$\begin{aligned}
&k w^2\left[\xi^2(\partial_\xi^2 A_r + \partial_r^2 A_r) + 2\xi F_{\xi r} - \left(i\tilde{\phi}^* D_r\tilde{\phi} + h.c.\right)\right] \\
&= 4\mathrm{e}^{2A} k\,\kappa\tau^2\xi^2\tilde{A}_r \\
&\quad + \frac{2f_1(\tau)}{\pi^2 M^3}\partial_\xi\Phi\left(\left(1 + \frac{f_3(\tau)}{f_1(\tau)}\right)(1 - |\tilde{\phi}|^2) + \frac{1}{2}\left(3i\frac{f_2(\tau)}{f_1(\tau)} - 1 - \frac{f_3(\tau)}{f_1(\tau)}\right)(\tilde{\phi} + \tilde{\phi}^*)^2\right),
\end{aligned} \tag{F.48}$$

$$\begin{aligned}
&h w^2\left(D_\xi D_\xi\tilde{\phi} - \tilde{\phi}\frac{|\tilde{\phi}|^2 - 1}{\xi^2}\right) + D_r\left(k w^2 D_r\tilde{\phi}\right) + h.c. \\
&= 4\mathrm{e}^{2A} h\,\kappa\tau^2\tilde{\phi} \\
&\quad + \frac{2f_1(\tau)\epsilon^{\bar{\mu}\bar{\nu}}}{\pi^2 M^3}\left(-i\left(1 + \frac{f_3(\tau)}{f_1(\tau)}\right)\partial_{\bar{\mu}}\Phi D_{\bar{\nu}}\tilde{\phi} + \right. \\
&\qquad \left. + 2\left(3i\frac{f_2(\tau)}{f_1(\tau)} - 1 - \frac{f_3(\tau)}{f_1(\tau)}\right)\tilde{\phi}\partial_{\bar{\mu}}\Phi\tilde{A}_{\bar{\nu}}\right) + h.c.\,,
\end{aligned} \tag{F.49}$$

$$h w^2\left(-i\tilde{\phi}^* D_\xi\tilde{\phi} + h.c.\right) + \xi^2 k w^2(\partial_\xi^2 A_\xi + \partial_r^2 A_\xi) + \xi^2(k w^2)' F_{r\xi}$$

$$= 4\mathrm{e}^{2A} h\kappa\tau^2\xi^2\tilde{A}_\xi$$
$$- \frac{2f_1(\tau)}{\pi^2 M^3}\partial_r\Phi\left(\left(1+\frac{f_3(\tau)}{f_1(\tau)}\right)(1-|\tilde{\phi}|^2)+\frac{1}{2}\left(3i\frac{f_2(\tau)}{f_1(\tau)}-1-\frac{f_3(\tau)}{f_1(\tau)}\right)(\tilde{\phi}+\tilde{\phi}^*)^2\right), \quad \text{(F.50)}$$

$$hw^2\left(iD_\xi D_\xi\tilde{\phi}-i\tilde{\phi}\frac{|\tilde{\phi}|^2-1}{\xi^2}\right)+iD_r\left(kw^2 D_r\tilde{\phi}\right)+h.c.$$
$$= \frac{2f_1(\tau)}{\pi^2 M^3}\left(\left(1+\frac{f_3(\tau)}{f_1(\tau)}\right)\epsilon^{\bar{\mu}\bar{\nu}}\partial_{\bar{\mu}}\Phi D_{\bar{\nu}}\tilde{\phi}+\frac{f_1'(\tau)+f_3'(\tau)}{f_1(\tau)}\tau'\tilde{\phi}\partial_\xi\Phi\right)+h.c. \ . \quad \text{(F.51)}$$

F.2 Inhomogeneous tachyon

This appendix presents the expressions for the equations of motion for the ansatz fields (3.1.70) in the case where the tachyon modulus τ is allowed to be dynamical.

The equations of motion involve the inverse effective metric which in this case takes the following form

$$\tilde{g}^{-1} = \begin{pmatrix} -\mathrm{e}^{-2A} & 0 & 0 & 0 & 0 \\ 0 & \Delta_{rr} & -\frac{x_1}{\xi}\Delta_{\xi r} & -\frac{x_2}{\xi}\Delta_{\xi r} & -\frac{x_3}{\xi}\Delta_{\xi r} \\ 0 & -\frac{x_1}{\xi}\Delta_{\xi r} & \mathrm{e}^{-2A}-\left(\frac{x_1}{\xi}\right)^2\Delta_{\xi\xi} & -\frac{x_1}{\xi}\frac{x_2}{\xi}\Delta_{\xi\xi} & -\frac{x_1}{\xi}\frac{x_3}{\xi}\Delta_{\xi\xi} \\ 0 & -\frac{x_2}{\xi}\Delta_{\xi r} & -\frac{x_1}{\xi}\frac{x_2}{\xi}\Delta_{\xi\xi} & \mathrm{e}^{-2A}-\left(\frac{x_2}{\xi}\right)^2\Delta_{\xi\xi} & -\frac{x_2}{\xi}\frac{x_3}{\xi}\Delta_{\xi\xi} \\ 0 & -\frac{x_3}{\xi}\Delta_{\xi r} & -\frac{x_1}{\xi}\frac{x_3}{\xi}\Delta_{\xi\xi} & -\frac{x_2}{\xi}\frac{x_3}{\xi}\Delta_{\xi\xi} & \mathrm{e}^{-2A}-\left(\frac{x_3}{\xi}\right)^2\Delta_{\xi\xi} \end{pmatrix}, \quad \text{(F.52)}$$

where we defined the symbol Δ as

$$\Delta_{\xi\xi} \equiv \frac{\mathrm{e}^{6A}\kappa\,(\partial_\xi\tau)^2}{-\det\tilde{g}} = \frac{\mathrm{e}^{-4A}\kappa\,(\partial_\xi\tau)^2}{1+\mathrm{e}^{-2A}\kappa\left((\partial_r\tau)^2+(\partial_\xi\tau)^2\right)}, \quad \text{(F.53)}$$

$$\Delta_{\xi r} \equiv \frac{\mathrm{e}^{6A}\kappa\,\partial_\xi\tau\partial_r\tau}{-\det\tilde{g}} = \frac{\mathrm{e}^{-4A}\kappa\,\partial_\xi\tau\partial_r\tau}{1+\mathrm{e}^{-2A}\kappa\left((\partial_r\tau)^2+(\partial_\xi\tau)^2\right)}, \quad \text{(F.54)}$$

$$\Delta_{rr} \equiv \frac{\mathrm{e}^{8A}(1+\mathrm{e}^{-2A}\kappa\,(\partial_\xi\tau)^2)}{-\det\tilde{g}} = \frac{\mathrm{e}^{-2A}\,(1+\mathrm{e}^{-2A}\kappa\,(\partial_\xi\tau)^2)}{1+\mathrm{e}^{-2A}\kappa\left((\partial_r\tau)^2+(\partial_\xi\tau)^2\right)}. \quad \text{(F.55)}$$

The equations themselves are then obtained by extremizing the energy (3.1.90) with respect to small deformations of the ansatz fields (3.1.70)

$$\partial_r\left(\kappa\tau^2\mathcal{X}\mathrm{e}^{4A}\Delta_{rr}\xi^2\tilde{A}_r\right)+\partial_\xi(\kappa\tau^2\mathcal{X}\mathrm{e}^{2A}(1-\mathrm{e}^{2A}\Delta_{\xi\xi})\xi^2\tilde{A}_\xi)$$
$$-\ \partial_r(\kappa\tau^2\mathcal{X}\mathrm{e}^{4A}\Delta_{\xi r}\xi^2\tilde{A}_\xi)-\ \partial_\xi(\kappa\tau^2\mathcal{X}\mathrm{e}^{4A}\Delta_{\xi r}\xi^2\tilde{A}_r)$$

$$
\begin{aligned}
&+\frac{1}{2i}\kappa\tau^2\mathcal{X}\mathrm{e}^{2A}(\tilde{\phi}^2-(\tilde{\phi}^*)^2)\\
&=\frac{\epsilon^{\bar{\mu}\bar{\nu}}}{2\pi^2M^3}\Big[(f_1(\tau)+f_3(\tau)-3if_2(\tau))(\tilde{\phi}+\tilde{\phi}^*)\partial_{\bar{\mu}}\Phi(D_{\bar{\nu}}\tilde{\phi}+D_{\bar{\nu}}\tilde{\phi}^*)\\
&\qquad+\partial_{\bar{\mu}}\Phi\partial_{\bar{\nu}}\tau\left((f_1'(\tau)+f_3'(\tau))(|\phi|^2-1)-\frac{3i}{2}f_2'(\tau)(\tilde{\phi}+\tilde{\phi}^*)^2\right)\Big]\,,
\end{aligned}
\tag{F.56}
$$

$$
\begin{aligned}
&\partial_r\left[w^2\mathcal{X}\mathrm{e}^{2A}\Delta_{rr}\xi^2\partial_r\Phi\right]+\partial_\xi\left[w^2\mathcal{X}(1-\mathrm{e}^{2A}\Delta_{\xi\xi})\xi^2\partial_\xi\Phi\right]\\
&\quad-\partial_r\left[w^2\mathcal{X}\mathrm{e}^{2A}\Delta_{\xi r}\xi^2\partial_\xi\Phi\right]-\partial_\xi\left[w^2\mathcal{X}\mathrm{e}^{2A}\Delta_{\xi r}\xi^2\partial_r\Phi\right]\\
&=\frac{f_1(\tau)}{4\pi^2M^3}\epsilon^{\bar{\mu}\bar{\nu}}\left(\left(1+\frac{f_3(\tau)}{f_1(\tau)}\right)(F_{\bar{\mu}\bar{\nu}}+\partial_{\bar{\mu}}(-i\phi^*D_{\bar{\nu}}\phi+h.c.))+\right.\\
&\qquad+\left(3i\frac{f_2(\tau)}{f_1(\tau)}-1-\frac{f_3(\tau)}{f_1(\tau)}\right)\left(\frac{1}{2}F_{\bar{\mu}\bar{\nu}}(\tilde{\phi}+\tilde{\phi}^*)^2-\tilde{A}_{\bar{\mu}}\partial_{\bar{\nu}}\left((\tilde{\phi}+\tilde{\phi}^*)^2\right)\right)+\\
&\qquad+2\partial_{\bar{\nu}}\tau\left(\frac{f_1'(\tau)+f_3'(\tau)}{f_1(\tau)}(\tilde{A}_{\bar{\mu}}(|\phi|^2-1)+\frac{i}{2}(\tilde{\phi}+\tilde{\phi}^*)(D_{\bar{\mu}}\tilde{\phi}-D_{\bar{\mu}}\tilde{\phi}^*))-\right.\\
&\qquad\left.\left.-3i\frac{f_2'(\tau)}{2f_1(\tau)}\tilde{A}_{\bar{\mu}}(\tilde{\phi}+\tilde{\phi}^*)^2\right)\right)\,,
\end{aligned}
\tag{F.57}
$$

$$
\begin{aligned}
&\partial_\xi\Big[w^2\mathcal{X}\mathrm{e}^{2A}\left[\Delta_{rr}(1-\mathrm{e}^{2A}\Delta_{\xi\xi})-\mathrm{e}^{2A}\Delta_{\xi r}^2\right]\xi^2F_{\xi r}\Big]-w^2\mathcal{X}\mathrm{e}^{2A}\Delta_{rr}(i\phi^*D_r\phi-i\phi D_r\phi^*)+\\
&\quad+w^2\mathcal{X}\mathrm{e}^{2A}\Delta_{\xi r}(i\phi^*D_\xi\phi-i\phi D_\xi\phi^*)\\
&=4\kappa\tau^2\mathcal{X}\mathrm{e}^{4A}\Delta_{rr}\xi^2\tilde{A}_r-4\kappa\tau^2\mathcal{X}\mathrm{e}^{4A}\Delta_{\xi r}\xi^2\tilde{A}_\xi+\\
&\quad+\frac{2f_1(\tau)}{\pi^2M^3}\partial_\xi\Phi\left(\left(1+\frac{f_3(\tau)}{f_1(\tau)}\right)(1-|\phi|^2)+\frac{1}{2}\left(3i\frac{f_2(\tau)}{f_1(\tau)}-1-\frac{f_3(\tau)}{f_1(\tau)}\right)(\tilde{\phi}+\tilde{\phi}^*)^2\right)\,,
\end{aligned}
\tag{F.58}
$$

$$
\begin{aligned}
&D_\xi\left[w^2\mathcal{X}(1-\mathrm{e}^{2A}\Delta_{\xi\xi})D_\xi\tilde{\phi}\right]+D_r\left[w^2\mathcal{X}\mathrm{e}^{2A}\Delta_{rr}D_r\tilde{\phi}\right]-\\
&\quad-D_\xi\left[w^2\mathcal{X}\mathrm{e}^{2A}\Delta_{\xi r}D_r\tilde{\phi}\right]-D_r\left[w^2\mathcal{X}\mathrm{e}^{2A}\Delta_{\xi r}D_\xi\tilde{\phi}\right]-w^2\mathcal{X}\,\tilde{\phi}\frac{|\phi|^2-1}{\xi^2}+h.c.\\
&=4\kappa\tau^2\mathcal{X}\mathrm{e}^{2A}\tilde{\phi}+\\
&\quad+\frac{2f_1(\tau)\epsilon^{\bar{\mu}\bar{\nu}}}{\pi^2M^3}\left(-i\left(1+\frac{f_3(\tau)}{f_1(\tau)}\right)\partial_{\bar{\mu}}\Phi D_{\bar{\nu}}\tilde{\phi}+\right.\\
&\qquad\left.+2\left(3i\frac{f_2(\tau)}{f_1(\tau)}-1-\frac{f_3(\tau)}{f_1(\tau)}\right)\tilde{\phi}\partial_{\bar{\mu}}\Phi\tilde{A}_{\bar{\nu}}\right)+h.c.\,,
\end{aligned}
\tag{F.59}
$$

$$
\partial_r\Big[w^2\mathcal{X}\mathrm{e}^{2A}\left[\Delta_{rr}(1-\mathrm{e}^{2A}\Delta_{\xi\xi})-\mathrm{e}^{2A}\Delta_{\xi r}^2\right]\xi^2F_{r\xi}\Big]-
$$

$$
\begin{aligned}
&- w^2\mathcal{X}(1-\mathrm{e}^{2A}\Delta_{\xi\xi})(i\phi^* D_\xi\phi - i\phi D_\xi\phi^*) + w^2\mathcal{X}\mathrm{e}^{2A}\Delta_{\xi r}(i\phi^* D_r\phi - i\phi D_r\phi^*)\\
&= 4\kappa\tau^2\mathcal{X}\mathrm{e}^{2A}(1-\mathrm{e}^{2A}\Delta_{\xi\xi})\xi^2\tilde{A}_\xi - 4\kappa\tau^2\mathcal{X}\mathrm{e}^{4A}\Delta_{\xi r}\xi^2\tilde{A}_r -\\
&\quad - \frac{2f_1(\tau)}{\pi^2M^3}\partial_r\Phi\left(\left(1+\frac{f_3(\tau)}{f_1(\tau)}\right)(1-|\phi|^2) + \frac{1}{2}\left(3i\frac{f_2(\tau)}{f_1(\tau)} - 1 - \frac{f_3(\tau)}{f_1(\tau)}\right)(\tilde{\phi}+\tilde{\phi}^*)^2\right), \quad \text{(F.60)}
\end{aligned}
$$

$$
\begin{aligned}
&iD_\xi\left[w^2\mathcal{X}(1-\mathrm{e}^{2A}\Delta_{\xi\xi})D_\xi\tilde{\phi}\right] + iD_r\left[w^2\mathcal{X}\mathrm{e}^{2A}\Delta_{rr}D_r\tilde{\phi}\right] -\\
&\quad - iD_\xi\left[w^2\mathcal{X}\mathrm{e}^{2A}\Delta_{\xi r}D_r\tilde{\phi}\right] - iD_r\left[w^2\mathcal{X}\mathrm{e}^{2A}\Delta_{\xi r}D_\xi\tilde{\phi}\right] - iw^2\mathcal{X}\,\tilde{\phi}\frac{|\phi|^2-1}{\xi^2} + h.c.\\
&= \frac{2f_1(\tau)}{\pi^2M^3}\epsilon^{\bar{\mu}\bar{\nu}}\left(\left(1+\frac{f_3(\tau)}{f_1(\tau)}\right)\partial_{\bar{\mu}}\Phi D_{\bar{\nu}}\tilde{\phi} + \frac{f_1'(\tau)+f_3'(\tau)}{f_1(\tau)}\partial_{\bar{\nu}}\tau\tilde{\phi}\partial_{\bar{\mu}}\Phi\right) + h.c. \quad , \qquad \text{(F.61)}
\end{aligned}
$$

$$
\begin{aligned}
&\partial_r\Big[\mathcal{Y}\Big(\partial_r\tau\mathcal{L}_{\mathrm{DBI}} +\\
&\quad + \mathrm{e}^{2A}\mathcal{X}\Big(\mathrm{e}^{2A}\xi^2\kappa(\lambda)\tau^2\left(\Delta_{rr,r}\tilde{A}_r^2 - \Delta_{\xi\xi,r}\tilde{A}_\xi^2 - 2\Delta_{\xi r,r}\tilde{A}_r\tilde{A}_\xi\right) +\\
&\quad\quad + w(\lambda)^2\left(\frac{1}{8}\Big(\Delta_{rr,r}\left(1-\mathrm{e}^{2A}\Delta_{\xi\xi}\right) - \mathrm{e}^{2A}\Delta_{rr}\Delta_{\xi\xi,r} - 2\mathrm{e}^{2A}\Delta_{\xi r,r}\Delta_{\xi r}\Big)\xi^2(F_{\bar{\mu}\bar{\nu}})^2 +\right.\\
&\quad\quad\quad + \frac{1}{2}\left(-\Delta_{\xi\xi,r}\left|\mathrm{D}_\xi\phi\right|^2 + \Delta_{rr,r}\left|\mathrm{D}_r\phi\right|^2\right) - \frac{1}{2}\Delta_{\xi r,r}(D_r\phi^* D_\xi\phi + h.c.) -\\
&\quad\quad\quad \left.-\xi^2\left(\Delta_{rr,r}(\partial_r\Phi)^2 - \Delta_{\xi\xi,r}(\partial_\xi\Phi)^2 - 2\Delta_{\xi r,r}\partial_\xi\Phi\partial_r\Phi\right)\right)\Big)\Big)\Big] +\\
&+ \partial_\xi\Big[\mathcal{Y}\Big(\partial_\xi\tau\mathcal{L}_{\mathrm{DBI}}\\
&\quad + \mathrm{e}^{2A}\mathcal{X}\Big(\mathrm{e}^{2A}\xi^2\kappa(\lambda)\tau^2\left(\Delta_{rr,\xi}\tilde{A}_r^2 - \Delta_{\xi\xi,\xi}\tilde{A}_\xi^2 - 2\Delta_{\xi r,\xi}\tilde{A}_r\tilde{A}_\xi\right) +\\
&\quad\quad + w(\lambda)^2\left(\frac{1}{8}\left(\Delta_{rr,\xi}\left(1-\mathrm{e}^{2A}\Delta_{\xi\xi}\right) - \mathrm{e}^{2A}\Delta_{rr}\Delta_{\xi\xi,\xi} - 2\mathrm{e}^{2A}\Delta_{\xi r,\xi}\Delta_{\xi r}\right)\xi^2(F_{\bar{\mu}\bar{\nu}})^2 +\right.\\
&\quad\quad\quad + \frac{1}{2}\left(-\Delta_{\xi\xi,\xi}\left|\mathrm{D}_\xi\phi\right|^2 + \Delta_{rr,\xi}\left|\mathrm{D}_r\phi\right|^2\right) - \frac{1}{2}\Delta_{\xi r,\xi}(D_r\phi^* D_\xi\phi + h.c.) -\\
&\quad\quad\quad \left.-\xi^2\left(\Delta_{rr,\xi}(\partial_r\Phi)^2 - \Delta_{\xi\xi,\xi}(\partial_\xi\Phi)^2 - 2\Delta_{\xi r,\xi}\partial_\xi\Phi\partial_r\Phi\right)\right)\Big)\Big)\Big] -\\
&- \frac{\delta}{\delta\tau}\left(\log V_f\right)\mathcal{L}_{\mathrm{DBI}}\\
&= 2\mathcal{X}\mathrm{e}^{2A}\xi^2\kappa\tau\left(\mathrm{e}^{2A}\Delta_{rr}\tilde{A}_r^2 + \left(1-\mathrm{e}^{2A}\Delta_{\xi\xi}\right)\tilde{A}_\xi^2 + \frac{(\phi+\phi^*)^2}{2\xi^2} - 2\mathrm{e}^{2A}\Delta_{\xi r}\tilde{A}_r\tilde{A}_\xi\right)\\
&\quad + \frac{1}{\pi^2M^3}\epsilon^{\bar{\mu}\bar{\nu}}\partial_{\bar{\mu}}\Phi\left[\left(f_1'(\tau)+f_3'(\tau)\right)\left(\tilde{A}_{\bar{\nu}} + \frac{1}{2}(-i\phi^* D_{\bar{\nu}}\phi + h.c.) + \frac{1}{4i}\partial_{\bar{\nu}}(\tilde{\phi}^2 - (\tilde{\phi}^*)^2)\right)\right.\\
&\quad\quad\quad \left. + \frac{1}{2}(3if_2'(\tau) - f_1'(\tau) - f_3'(\tau))(\tilde{\phi}+\tilde{\phi}^*)^2\tilde{A}_{\bar{\nu}}\right], \qquad \text{(F.62)}
\end{aligned}
$$

where we defined

$$\mathcal{X} \equiv \sqrt{1 + \mathrm{e}^{-2A}\kappa\left((\partial_r\tau)^2 + (\partial_\xi\tau)^2\right)}\, V_f(\lambda,\tau)\,\mathrm{e}^{A}\,, \tag{F.63}$$

$$\begin{aligned}
\mathcal{L}_{\mathrm{DBI}} \equiv\; & N_f\xi^2\mathcal{X}\mathrm{e}^{4A} + \\
& + \mathcal{X}\Bigg(\mathrm{e}^{2A}\xi^2\kappa(\lambda)\tau^2\times \\
& \quad\times\left(\mathrm{e}^{2A}\Delta_{rr}\tilde{A}_r^2 + \left(1-\mathrm{e}^{2A}\Delta_{\xi\xi}\right)\tilde{A}_\xi^2 + \frac{(\tilde{\phi}+\tilde{\phi}^*)^2}{2\xi^2} - 2\mathrm{e}^{2A}\Delta_{\xi r}\tilde{A}_r\tilde{A}_\xi\right) + \\
& + w(\lambda)^2\Bigg(\frac{1}{8}\mathrm{e}^{2A}\left[\Delta_{rr}\left(1-\mathrm{e}^{2A}\Delta_{\xi\xi}\right) - \mathrm{e}^{2A}\Delta_{\xi r}^2\right]\xi^2(F_{\bar{\mu}\bar{\nu}})^2 + \\
& \quad + \frac{1}{2}\left(\left(1-\mathrm{e}^{2A}\Delta_{\xi\xi}\right)|\mathrm{D}_\xi\phi|^2 + \mathrm{e}^{2A}\Delta_{rr}\,|\mathrm{D}_r\phi|^2\right) + \\
& \quad + \frac{\left(1-|\phi|^2\right)^2}{4\xi^2} - \frac{1}{2}\mathrm{e}^{2A}\Delta_{\xi r}(D_r\phi^* D_\xi\phi + h.c.) - \\
& \quad - \xi^2\Big(\mathrm{e}^{2A}\Delta_{rr}(\partial_r\Phi)^2 + \left(1-\mathrm{e}^{2A}\Delta_{\xi\xi}\right)(\partial_\xi\Phi)^2 - \\
& \qquad\qquad - 2\mathrm{e}^{2A}\Delta_{\xi r}\partial_\xi\Phi\partial_r\Phi\Big)\Bigg)\Bigg)\,,
\end{aligned} \tag{F.64}$$

$$\mathcal{Y} \equiv \frac{\mathrm{e}^{-2A}\kappa}{1+\mathrm{e}^{-2A}\kappa\left((\partial_r\tau)^2+(\partial_\xi\tau)^2\right)}\,, \tag{F.65}$$

and introduced the following condensed notation

$$\Delta_{xy,r} \equiv \frac{1}{\mathcal{Y}}\frac{\delta\Delta_{xy}}{\delta\,\partial_r\tau} \quad , \quad \Delta_{xy,\xi} \equiv \frac{1}{\mathcal{Y}}\frac{\delta\Delta_{xy}}{\delta\,\partial_\xi\tau} \quad , \quad x,y\in\{r,\xi\}\,. \tag{F.66}$$

These are equal to

$$\Delta_{rr,r} = -2\partial_r\tau\Delta_{rr} \quad , \quad \Delta_{rr,\xi} = 2\partial_\xi\tau\left[-\Delta_{rr}+\mathrm{e}^{-2A}\right]\,, \tag{F.67}$$

$$\Delta_{\xi\xi,r} = -2\partial_r\tau\Delta_{\xi\xi} \quad , \quad \Delta_{\xi\xi,\xi} = 2\partial_\xi\tau\left[-\Delta_{\xi\xi}+\mathrm{e}^{-2A}\right]\,, \tag{F.68}$$

$$\Delta_{\xi r,r} = -2\partial_r\tau\Delta_{\xi r} + \mathrm{e}^{-2A}\partial_\xi\tau \quad , \quad \Delta_{\xi r,\xi} = -2\partial_\xi\tau\Delta_{\xi r} + \mathrm{e}^{-2A}\partial_r\tau\,. \tag{F.69}$$

G Asymptotics of the probe instanton solution

We present in this appendix the analytical asymptotics near the boundaries of the 2-dimensional space (r,ξ) of the bulk instanton solution in the probe limit. The leading asymptotics will be necessary to determine the boundary conditions for the numerical method used to compute the instanton solution.

G.1 UV asymptotics

We start by analyzing the asymptotics of the solution near the AdS-like UV boundary, that is in the limit where $r \to 0$, which are obtained by solving the equations of motion (F.38)-(F.43) in this limit. This analysis involves the UV asymptotics of the background (2.3.14) and (2.3.18)-(2.3.20). According to the holographic dictionary, the UV asymptotics contain the external sources and vacuum expectation values (vev) for the operators dual to the instanton bulk fields.

At leading order in r, (F.39), (F.41), (F.42) and (F.43) respectively determine the power-law behavior of the two independent solutions for Φ, $\tilde{\phi}_1$, $\tilde{A}_\xi$ and $\tilde{\phi}_2$, which are the components of the gauge fields (3.1.50)-(3.1.52), redefined to absorb the tachyon phase as in (3.1.80). These power-laws correspond to the standard result for massless gauge fields on AdS

$$\varphi = \varphi^{(0)}(\xi)(1 + \cdots) + r^2 \varphi^{(2)}(\xi)(1 + \cdots)\,, \tag{G.1}$$

where φ represents all the above mentioned fields, the (0) index refers to the source for the dual operator, the (2) index to a term proportional to the vev for that operator and the dots terms that go to 0 at the boundary. Note that this behavior does not apply to $\tilde{A}_r$ as the equations of motion are first order for $\tilde{A}_r$ in the r direction.

For the baryon state under study, the chemical potential is set to 0 : $\Phi^{(0)} = 0$ and there is no source for the gauge field at the boundary, which for the redefined gauge fields (3.1.80) corresponds to

$$\tilde{A}_\xi^{(0)} = \partial_\xi \theta(0,\xi) \quad , \quad \tilde{\phi}_1^{(0)} = \sin\theta(0,\xi) \quad , \quad \tilde{\phi}_2^{(0)} = -\cos\theta(0,\xi)\,, \tag{G.2}$$

where θ is the phase in the tachyon ansatz (3.1.64). Near the boundary, the ansatz fields at leading order therefore behave as

$$\Phi = \Phi^{(2)}(\xi)\, r^2(1 + \cdots)\,, \tag{G.3}$$

$$\tilde{\phi}_1 = \sin\theta(0,\xi)(1 + \cdots) + \tilde{\phi}_1^{(2)}(\xi)\, r^2(1 + \cdots)\,, \tag{G.4}$$

$$\tilde{\phi}_2 = -\cos\theta(0,\xi)(1 + \cdots) + \tilde{\phi}_2^{(2)}(\xi)\, r^2(1 + \cdots)\,, \tag{G.5}$$

$$\tilde{A}_\xi = \partial_\xi\theta(0,\xi)(1 + \cdots) + \tilde{A}_\xi^{(2)}(\xi)\, r^2(1 + \cdots)\,. \tag{G.6}$$

Then, the constraint (F.38) imposes that $\tilde{A}_r$ vanishes at the boundary, and behaves at most linearly in r

$$\tilde{A}_r = \tilde{A}_r^{(1)}(\xi)\, r\,(1 + \cdots)\,, \tag{G.7}$$

where $\tilde{A}_r^{(1)}$ obeys

$$\partial_\xi(\xi^2 \partial_\xi \theta(0,\xi)) - \sin(2\theta(0,\xi)) + 4\xi^2 \tilde{A}_r^{(1)}(\xi) = 0\,. \tag{G.8}$$

From the behavior of the background (2.3.14) and (2.3.18)-(2.3.20), we deduce the order of the next terms in the UV expansion

$$\Phi = \Phi^{(2)}(\xi)\, r^2 \left(1 + \mathcal{O}\left(\frac{1}{r \log r\Lambda}\right)\right) , \tag{G.9}$$

$$\tilde{\phi}_1 = \sin\theta(0,\xi) + \tilde{\phi}_1^{(2)}(\xi)\, r^2 \left(1 + \mathcal{O}\left(\frac{1}{r \log r\Lambda}\right)\right) , \tag{G.10}$$

$$\tilde{\phi}_2 = -\cos\theta(0,\xi) + \tilde{\phi}_2^{(2)}(\xi)\, r^2 \left(1 + \mathcal{O}\left(\frac{1}{r \log r\Lambda}\right)\right) , \tag{G.11}$$

$$\tilde{A}_\xi = \partial_\xi\theta(0,\xi) + \tilde{A}_\xi^{(2)}(\xi)\, r^2 \left(1 + \mathcal{O}\left(\frac{1}{r \log r\Lambda}\right)\right) , \tag{G.12}$$

$$\tilde{A}_r = \tilde{A}_r^{(1)}(\xi)\, r \left(1 + \mathcal{O}\left(\frac{1}{r \log r\Lambda}\right)\right) . \tag{G.13}$$

Note the peculiar feature that the source mode does not receive r-dependent corrections when moving away from the boundary. This property is specific to the chiral limit $m_q = 0$.

G.2 Asymptotics at $\xi \to \infty$

We study here the EoMs (F.38)-(F.43) in the limit where $\xi \to \infty$, given the boundary conditions of the second column of Table 3.1, which impose that the instanton energy is finite. These asymptotics contain information about the tail of the meson cloud far from the baryon, which determines the long range meson-exchange interaction between baryons.

We assume that the fields can be expanded as Taylor series in $1/\xi$ and analyse the EoMs order by order in $1/\xi$. This yields the following behavior for the instanton fields in the limit $\xi \to \infty$

$$\Phi(r,\xi) = \frac{\hat{\Phi}_6(r)}{\xi^6} + \mathcal{O}(\xi^{-7}) , \tag{G.14}$$

$$\tilde{\phi}_1(r,\xi) = \frac{\hat{\phi}_{1,1}(r)}{\xi} + \frac{\hat{\phi}_{1,2}(r)}{\xi^2} + \frac{\hat{\phi}_{1,3}(r)}{\xi^3} + \frac{\hat{\phi}_{1,4}(r)}{\xi^4} + \frac{\hat{\phi}_{1,5}(r)}{\xi^5} + \mathcal{O}(\xi^{-6}) , \tag{G.15}$$

$$\tilde{\phi}_2(r,\xi) = 1 + \frac{\hat{\phi}_{2,1}}{\xi} + \frac{\hat{\phi}_{2,2}}{\xi^2} + \frac{\hat{\phi}_{2,3}}{\xi^3} + \frac{\hat{\phi}_{2,4}(r)}{\xi^4} + \frac{\hat{\phi}_{2,5}(r)}{\xi^5} + \mathcal{O}(\xi^{-6}) , \tag{G.16}$$

$$\tilde{A}_\xi(r,\xi) = \frac{\hat{A}_{\xi,2}(r)}{\xi^2} + \frac{\hat{A}_{\xi,3}(r)}{\xi^3} + \frac{\hat{A}_{\xi,4}(r)}{\xi^4} + \frac{\hat{A}_{\xi,5}(r)}{\xi^5} + \mathcal{O}(\xi^{-6}) , \tag{G.17}$$

$$\tilde{A}_r(r,\xi) = \frac{\hat{A}_{r,3}(r)}{\xi^3} + \frac{\hat{A}_{r,4}(r)}{\xi^4} + \frac{\hat{A}_{r,5}(r)}{\xi^5} + \frac{\hat{A}_{r,6}(r)}{\xi^6} + \mathcal{O}(\xi^{-7}) , \tag{G.18}$$

where $\hat{\phi}_{2,1}, \hat{\phi}_{2,2}$ and $\hat{\phi}_{2,3}$ are constants and $\hat{A}_{r,n}$ is a linear combination (with r-dependent coefficients) of $\hat{\phi}'_{1,n-2}, \hat{\phi}'_{1,n-4}, \cdots$, $\hat{A}'_{\xi,n-1}, \hat{A}'_{\xi,n-3}, \cdots$. The other coefficients obey second order differential equations:

$$F'' + \frac{(kw^2)'}{kw^2} F' = S_F \quad , \quad F = \hat{\phi}_{2,n}, \hat{\Phi}_n \,, \tag{G.19}$$

$$G'' + \frac{(kw^2)'}{kw^2} G' - 4\frac{\mathrm{e}^{2A} h\kappa\tau^2}{kw^2} G = S_G \quad , \quad G = \hat{\phi}_{1,n}, \hat{A}_{\xi,n} \,, \tag{G.20}$$

where k and h are defined in (F.44) and S_G and S_F are source terms that depend on lower order coefficients. In particular

$$S_{\hat{\phi}_{1,1}} = S_{\hat{\phi}_{1,2}} = S_{\hat{A}_{\xi,2}} = S_{\hat{A}_{\xi,3}} = 0 \,. \tag{G.21}$$

Note that, because of the UV boundary conditions of Table 3.2, the boundary values of the coefficients $\hat{\phi}_{1,n}, \hat{\phi}_{2,n}$ and $\hat{A}_{\xi,n}$ can all be written explicitly in terms of the asymptotics of $\theta(0,\xi)$ at $\xi \to \infty$. In particular, this implies that $\hat{\phi}_{2,1} = 0$.

Another interesting observation is that the source terms are such that the solution at $\xi \to \infty$ can be divided into two independent parity sets

$$\Phi \text{ even} \quad , \quad \phi_1 \text{ odd} \quad , \quad \phi_2 \text{ even up to r-independent terms} \quad , \quad A_\xi \text{ even} \quad , \quad A_r \text{ odd} \,, \tag{G.22}$$

or

$$\Phi \text{ odd} \quad , \quad \phi_1 \text{ even} \quad , \quad \phi_2 \text{ odd up to r-independent terms} \quad , \quad A_\xi \text{ odd} \quad , \quad A_r \text{ even} \,. \tag{G.23}$$

G.2.1 IR behavior of the large ξ coefficients

The homogeneous solutions of (G.19) are of the form

$$F(r) = c_1 + c_2 \int \frac{\mathrm{d}r}{k(r)w(r)^2} \,, \tag{G.24}$$

where $c_{1,2}$ are two independent constants. From (2.3.16) and (G.26), it is clear that the second term in (G.24) is singular in the IR. For regularity in the IR c_2 should therefore be set to 0 for every coefficients obeying (G.19). Note that in the UV, c_2 parametrizes the freedom for the vev term that goes like $\sim r^2$ as $r \to 0$. Comparing with the UV expansions (G.3)-(G.6), we see that this constraint imposes that $\Phi^{(2)}$ and $\tilde{\phi}_2^{(2)}$ are fixed in terms of $\theta(0,\xi), \tilde{\phi}_1^{(2)}$ and $\tilde{A}_\xi^{(2)}$.

Near the IR boundary, the homogeneous solutions of (G.20) are found to behave as

$$G(r) = c_1' \exp\left(a_{\mathrm{IR}} \tau_0^2 \left(\frac{r}{R}\right)^{2C_\tau} \left(1 + \mathcal{O}(r^{-2})\right)\right)$$

$$+ c_2' \exp\left(-\frac{2C_\tau}{3a_{\rm IR}(C_\tau-1)}\left(\frac{\kappa_{IR}}{w_{IR}}\right)^2 \tau_0^2 \left(\frac{r}{R}\right)^{2C_\tau-2}\left(1+\mathcal{O}(r^{-2})\right)\right). \tag{G.25}$$

The first solution diverges in the IR so for all coefficients obeying (G.20), c_1' should be set to 0. In terms of the UV expansion of (G.3)-(G.6), this should impose $\tilde{\phi}_1^{(2)}$ and $\tilde{A}_\xi^{(2)}$ in terms of $\theta(0,\xi)$.

G.3 IR asymptotics

We consider in this subsection the asymptotic behavior of the fields near the IR boundary, that is in the limit where $r \to \infty$. For each field, there exist generically two independent solutions in the IR as in (G.24) and (G.25), only one of which is regular. The asymptotics we present in the following are the unique regular asymptotics.

From the asymptotics of the background (2.3.16) and (2.3.22)-(2.3.24) we find the functions $k(r)$ and $h(r)$ defined in (F.44) to behave in the IR as

$$k(r) \sim \frac{W_{\rm IR} R}{\tau_0 C_\tau}\left(\sqrt{\frac{3}{2}}\kappa_{IR}\right)^{-1/2} \mathrm{e}^{2A_c+(5/3)\lambda_c}\left(\frac{r}{R}\right)^{3/2-C_\tau} \times \\ \times \exp\left(-\tau_0^2\left(\frac{r}{R}\right)^{2C_\tau}\left(1+\mathcal{O}(r^{-2})\right)+2\frac{r^2}{R^2}\right), \tag{G.26}$$

$$h(r) \sim \frac{W_{\rm IR}\tau_0 C_\tau}{R}\left(\sqrt{\frac{3}{2}}\kappa_{IR}\right)^{1/2} \mathrm{e}^{(1/3)\lambda_c}\left(\frac{r}{R}\right)^{C_\tau-1/2} \times \\ \times \exp\left(-\tau_0^2\left(\frac{r}{R}\right)^{2C_\tau}\left(1+\mathcal{O}(r^{-2})\right)+2\frac{r^2}{R^2}\right). \tag{G.27}$$

The IR behavior of the fields is obtained by solving the equations of motion (F.38)-(F.43) in the IR limit. In this limit the CS terms become negligible, which simplifies a lot the EoMs.

The IR behavior of Φ, $\tilde{\phi}_1$ and $\tilde{A}_\xi$ is found to be separable in ξ and r

$$\Phi(r) = \frac{1}{r}\alpha_\Phi(\xi)\left(1+\mathcal{O}\left(r^{-2C_\tau}\right)\right), \tag{G.28}$$

$$\tilde{\phi}_1(r) = \alpha_1(\xi)\exp\left(-\zeta\left(\frac{r}{R}\right)^{2C_\tau-2}\left(1+\mathcal{O}(r^{-2})\right)\right), \tag{G.29}$$

$$\tilde{A}_\xi(r) = \alpha_\xi(\xi)\exp\left(-\zeta\left(\frac{r}{R}\right)^{2C_\tau-2}\left(1+\mathcal{O}(r^{-2})\right)\right), \tag{G.30}$$

where we defined the constant

$$\zeta \equiv \frac{2}{3}\frac{C_\tau}{a_{\rm IR}(C_\tau-1)}\left(\frac{\kappa_{IR}}{w_{IR}}\right)^2 \tau_0^2\,. \tag{G.31}$$

and $\alpha_\Phi(\xi)$ obeys an independent linear ODE

$$\alpha''(\xi)+\frac{2}{\xi}\alpha'(\xi)-\frac{1}{\beta}\alpha(\xi)=0\,, \tag{G.32}$$

with

$$\beta \equiv \sqrt{\frac{3}{8}}\frac{\mathrm{e}^{-2A_c}\kappa_{IR}C_\tau R}{a_{\rm IR}}\,. \tag{G.33}$$

(G.32) is compatible with the condition that Φ goes to 0 at $\xi\to\infty$ and admits a unique solution up to overall normalization once the boundary condition that $\partial_\xi\Phi$ goes to 0 at $\xi\to 0$ is imposed.

From (G.29) and (G.30), the constraint (F.38) in the IR limit then fixes the leading behavior for $\tilde{A}_r$ to be

$$\tilde{A}_r(r)=\frac{\alpha_r(\xi)}{r}\exp\left(-\zeta\left(\frac{r}{R}\right)^{2C_\tau-2}\left(1+\mathcal{O}(r^{-2})\right)\right), \tag{G.34}$$

We finally discuss the $\tilde{\phi}_2$ field, whose IR behavior is more subtle as the r and ξ dependence cannot be factorized. Instead, the relevant ansatz is found to be of the form

$$\tilde{\phi}_2(r,\xi)=F\left(\frac{\xi}{\beta\log r}\right), \tag{G.35}$$

where β is defined in (G.33) and the function F obeys a second order non-linear ODE

$$F''(X)-F(X)\frac{F(X)^2-1}{X^2}+F'(X)=0 \quad , \quad X\equiv\frac{\xi}{\beta\log r}\,. \tag{G.36}$$

It can be checked numerically that (G.36) admits a unique solution compatible with the boundary conditions

$$F(0)=-1 \quad , \quad F(\infty)=1\,. \tag{G.37}$$

The plot of the corresponding solution is shown in figure 29

G.4 Asymptotics at $\xi=0$

We present here the asymptotics of the instanton solution near the center of the baryon at $\xi=0$. We assume that the fields are regular at $\xi=0$ and can be expanded as Taylor series. Then, solving the EoMs (F.38)-(F.43) order by order in ξ with the condition that

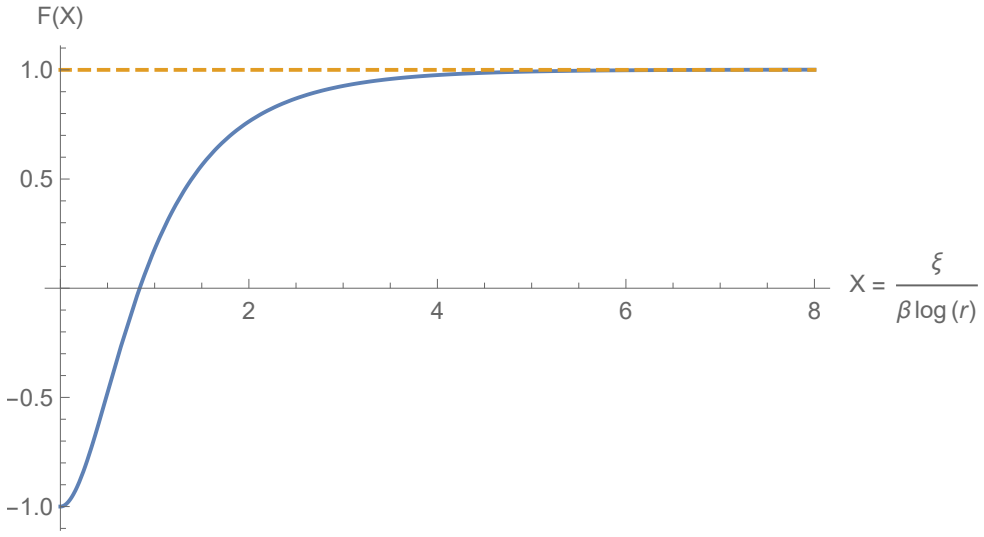

Figure 29: Numerical solution to (G.36) with the boundary conditions of (G.37).

the gauge fields (3.1.50)-(3.1.52) are well defined at $\xi = 0$, yields the following asymptotics up to order $\mathcal{O}(\xi^4)$

$$\Phi(r,\xi) = \bar{\Phi}_0(r) + \bar{\Phi}_2(r)\xi^2 + \bar{\Phi}_4(r)\xi^4 + \mathcal{O}(\xi^6)\,, \tag{G.38}$$

$$\tilde{\phi}_1(r,\xi) = \bar{\phi}_{1,0}(r)\xi + \bar{\phi}_{1,3}(r)\xi^3 + \mathcal{O}(\xi^5)\,, \tag{G.39}$$

$$\tilde{\phi}_2(r,\xi) = -1 + \bar{\phi}_{2,2}(r)\xi^2 + \bar{\phi}_{2,4}(r)\xi^4 + \mathcal{O}(\xi^6)\,, \tag{G.40}$$

$$\tilde{A}_\xi(r,\xi) = \bar{A}_{\xi,0}(r) + \bar{A}_{\xi,2}(r)\xi^2 + \bar{A}_{\xi,4}(r)\xi^4 + \mathcal{O}(\xi^6)\,, \tag{G.41}$$

$$\tilde{A}_r(r,\xi) = \bar{A}_{r,1}(r)\xi + \bar{A}_{r,3}(r)\xi^3 + \mathcal{O}(\xi^5)\,, \tag{G.42}$$

where $\Phi, \tilde{\phi}_2$ and $\tilde{A}_\xi$ are even and $\tilde{\phi}_1$ and $\tilde{A}_r$ are odd. All the coefficients of the expansions are expressed in terms of the 4 functions $\bar{\Phi}_0, \bar{\phi}_{1,0}, \bar{\phi}_{2,0}$ and $\bar{A}_{r,0}$. Note that, as in the $\xi \to \infty$ limit, the UV boundary conditions of Table 3.2 imply that the boundary values of the coefficients $\bar{\phi}_{1,n}, \bar{\phi}_{2,n}$ and $\bar{A}_{\xi,n}$ can all be written explicitly in terms of the asymptotics of $\theta(0,\xi)$ at $\xi \to 0$.

H Numerical method for the computation of the baryon solution

We detail in this appendix the numerical method that was used to solve the static soliton equations of motion. We summarize how the gradient descent method works, and specify

the type of grid that was used to obtain the solution. We also present some precision tests that support the validity of the numerical solution.

H.1 Method and grid choice

In the gradient descent method, the solution to the equations of motion is found by rephrasing the original minimisation of the energy M_0 problem, into a flow in a fictitious time, so that the limit of that flow is the solution of the original problem. Specifically, the limiting field configuration of the flow will minimize the soliton energy M_0. The limiting solution is found, by starting from a reasonable initial field configuration that satisfies the boundary conditions, and then evolving the fields. In practice, the fictitious time evolution equations are taken to be

$$\partial_\tau \Phi = \frac{\delta M_0}{\delta \Phi} \quad , \quad \partial_\tau \tilde{\phi}_{1,2} = -\frac{\delta M_0}{\delta \tilde{\phi}_{1,2}} \quad , \quad \partial_\tau A_{\bar{\mu}} = -\frac{\delta M_0}{\delta A_{\bar{\mu}}} \quad , \quad \partial_\tau \theta = -\frac{\delta M_0}{\delta \theta} \,, \tag{H.1}$$

and they are solved numerically. The fields above have been defined in section 3.1.4. Equations (H.1) must be also supplemented by the boundary conditions of table 3.2 for any value of the fictitious time.

Note that the gradients of the action with respect to the fields are nothing but the respective equations of motion. Also, the signs in front of the gradients, mean that M_0 is maximized with respect to Φ, and minimized with respect to all the other fields. This choice of sign ensures that the coefficient of the Laplacian is positive in the right hand sides of (H.1). In these conditions, the ellipticity of the equations of motion guarantees that the diffusive problem has a limiting solution which is the solution we are looking for.

The numerical algorithm is then constructed by discretizing the differential equations (H.1). That is, the bulk is covered by a grid, and the derivatives are approximated by finite differences between the values of the fields at the points of this grid. We denote by n the number of points in the holographic direction and by m the number in the radial direction. Note that the bulk has infinite extent, but the soliton solution is confined to a finite region. Therefore, it can be computed by considering finite cut-offs. In practice, the following cut-offs

$$r_{\max} \simeq 30 M_0^{-1} \quad , \quad \xi_{max} \simeq 100 M_0^{-1}$$

were found to be good enough to solve the problem reliably. Those numbers may seem large given that the baryon density is mainly confined to rM_0 and ξM_0 of order 1, as seen on Figure 3.5. However, the chiral gauge fields have non-trivial power-law asymptotics[23] away from the baryon center, which can only be captured by using sufficiently large cut-offs. The gradients associated with these long-range tails are small though, so that a few grid points are sufficient to describe them. Instead of a linear grid, we therefore considered

[23] This long-range behavior of the meson cloud is due to the fact that we consider the chiral limit, and will be suppressed exponentially when introducing finite quark masses.

a logarithmic grid, where most points are concentrated near the baryon center, and only a few points cover the region that separates the baryon from the cut-offs. The precise definition of the grid that we used is given by

$$r(k) = \exp\big(k\Delta r + \log\left(r_{min}+1\right)\big) - 1 \quad , \quad 0 \leq k \leq n\,, \tag{H.2}$$

$$\xi(j) = \exp\big(j\Delta\xi\big) - 1 \quad , \quad 0 \leq j \leq m\,, \tag{H.3}$$

where the spatial steps are

$$\Delta r = \frac{1}{n}\big(\log\left(r_{max}+1\right) - \log\left(r_{min}+1\right)\big) \quad , \quad \Delta\xi = \frac{1}{m}\log\left(\xi_{max}+1\right). \tag{H.4}$$

Note that we introduced a UV cut-off r_{min} since the boundary is a singular point of the equations and the boundary conditions there must be imposed on a shifted boundary, as usual. As long as $r_{min} \ll r(1)$ in (H.2), having r_{min} finite does not influence the baryon solution. In practice we found that the precision of the vacuum solution for the tachyon field is very good for $r > r_{min} \simeq 0.02 M_0^{-1}$. Also, the size of the grid that was chosen to produce the numerical results presented in the text is $(n, m) = (100, 100)$. Below, we show evidence that the baryon solution has already converged well for such a grid size.

A remark is that, instead of (H.1), one can consider the diffusive problem with general diffusion coefficients, which are generically field and position-dependent

$$\partial_\tau \Phi = D_\Phi(r,\xi)\frac{\delta M_0}{\delta\Phi} \quad , \quad \partial_\tau \tilde{\phi}_{1,2} = -D_\phi(r,\xi)\frac{\delta M_0}{\delta\tilde{\phi}_{1,2}} \quad , \quad \partial_\tau A_{\bar{\mu}} = -D_A(r,\xi)\frac{\delta M_0}{\delta A_{\bar{\mu}}}\,, \tag{H.5}$$

$$\partial_\tau \theta = -D_\theta(r,\xi)\frac{\delta M_0}{\delta\theta}\,.$$

Although a uniform diffusion coefficient amounts to a redefinition of the fictitious time τ, the dependence on the fields and position in the bulk actually modify the diffusive problem. A good choice for the purpose of solving (H.5) numerically is to set the diffusion coefficients such that the coefficients of the fields' Laplacians are equal to 1. This choice has the advantage that the stability properties of the discretized version of (H.5) are more tractable. If we ignore the first and zeroth order derivatives, requiring the absence of modes growing with τ implies the famous bound on the time step $\Delta\tau$ (see for example chapter 3.6 of [209])

$$\Delta\tau < \frac{\Delta\xi^2\Delta r^2}{2(\Delta\xi^2+\Delta r^2)}\,, \tag{H.6}$$

which is valid for uniform spatial grids, with steps Δx in the ξ direction, and Δr in the r direction. For the logarithmic grid that we used (H.2)-(H.3), (H.6) would still apply with the definitions of Δr and $\Delta\xi$ from (H.4), since they correspond to the smallest point separation on the grid. However, the full equations of motion include first and zeroth order

derivatives of the fields, so that the stability bound is more complicated than (H.6). For the grid that we used, we found that using as a bound

$$\Delta\tau < \frac{\Delta r^2}{4}\,, \tag{H.7}$$

resulted in stable algorithms. We do not claim any generality of this result though, and different bounds were actually observed for different grids.

H.2 Precision tests

We now present some tests of the numerical precision of the soliton solution computed via the gradient-descent method. We first investigate the convergence of the observables as a function of the grid size. Left figure 31 shows the evolution of the calculated soliton mass as a function of the grid size for $n = m$. It is observed that the soliton mass converges in the limit of large grid size, and the value that we derive at $n = m = 100$ is already within 0.2% of accuracy from the limiting value. Actually, even at $n = 50$, the error on the mass is already less than one percent.

As another test of the precision of the solution, we also investigated the convergence for the divergence of the 2-dimensional gauge field

$$L_A(r,\xi) \equiv |\partial_r A_r + \partial_\xi A_\xi|\,. \tag{H.8}$$

Due to the Lorenz gauge fixing (3.1.107), the baryon solution should be such that L_A vanishes everywhere in the bulk. To estimate what is the error on the Lorenz condition in the numerical solution, $L_A(r,\xi)$ is computed numerically and compared with the typical scale of the gradients of $A_{\bar{\mu}}$. One way of defining this typical scale, is via the combination of derivatives orthogonal to (H.8)

$$D_A(r,\xi) \equiv |\partial_r A_r - \partial_\xi A_\xi|\,. \tag{H.9}$$

The accuracy of the Lorenz gauge fixing will therefore be estimated by comparing the two quantities L_A and D_A, where the criterion for accuracy is that L_A should be much smaller than D_A. Because D_A vanishes in some places in the bulk, calculating the ratio of L_A over D_A does not give a globally well-defined indicator of the precision of the Lorenz gauge. Instead, we will use two global indicators, that are defined from the maxima and mean values of L_A and D_A

$$i_1 \equiv \frac{\bar{L}_A}{\bar{D}_A} \quad , \quad i_2 \equiv \frac{L_{A,max}}{\bar{D}_A}\,. \tag{H.10}$$

The first indicator i_1 estimates the average error on the Lorenz gauge fixing over the whole solution, whereas i_2 indicates what is the error at the location in the bulk where it is the worst. Here, it should be clarified what we mean by the mean values $\bar{L}_A$ and $\bar{D}_A$ in

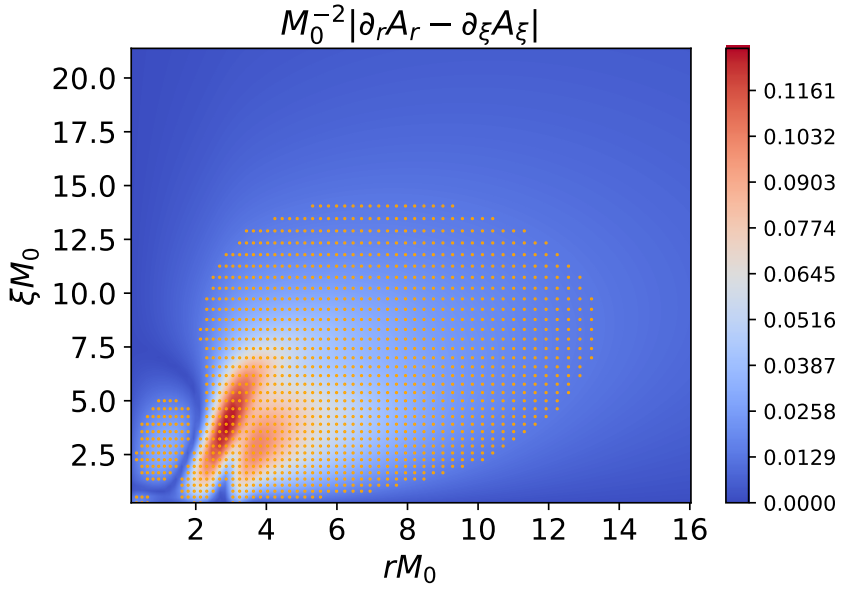

Figure 30: Density plot of the quantity D_A defined in (H.9), as an function of r and ξ. All dimensionful quantities are expressed in units of the soliton mass M_0, and the grid size is $(n, m) = (100, 100)$. The orange dots correspond to the grid points that belong to the region $\mathcal{A}_D$ (H.11), where D_A is significantly different from 0.

(H.10). The definition is similar to what was used to define the mean of the Lagrangian density (3.2.44). That is, the mean value is computed over a region of the bulk where the derivatives of $A_{\bar{\mu}}$ are significantly different from zero. Specifically, the corresponding region $\mathcal{A}_D$ is defined as

$$(r, \xi) \in \mathcal{A}_D \iff D_A(r, \xi) \geq 0.1 D_{A,max} \,. \tag{H.11}$$

In the numerical solution, $\mathcal{A}_D$ contains a finite number of grid cells, N_{cells}, and the definition of the mean values over $\mathcal{A}_D$ is analogous to (3.2.44)

$$\bar{L}_A = \frac{1}{N_{\text{cells}}} \sum_{i \in \mathcal{A}_D} L_A(i) \quad , \quad \bar{D}_A = \frac{1}{N_{\text{cells}}} \sum_{i \in \mathcal{A}_D} D_A(i) \,. \tag{H.12}$$

For concreteness, Figure 30 shows the density plot of D_A over the (r, ξ) plane for a grid of size $(n, m) = (100, 100)$, together with the grid points that belong to $\mathcal{A}_D$.

The plot of the two indicators i_1 and i_2 defined in (H.10) is shown in the right of Figure 31, as a function of the grid size. Although it is much slower than for the baryon

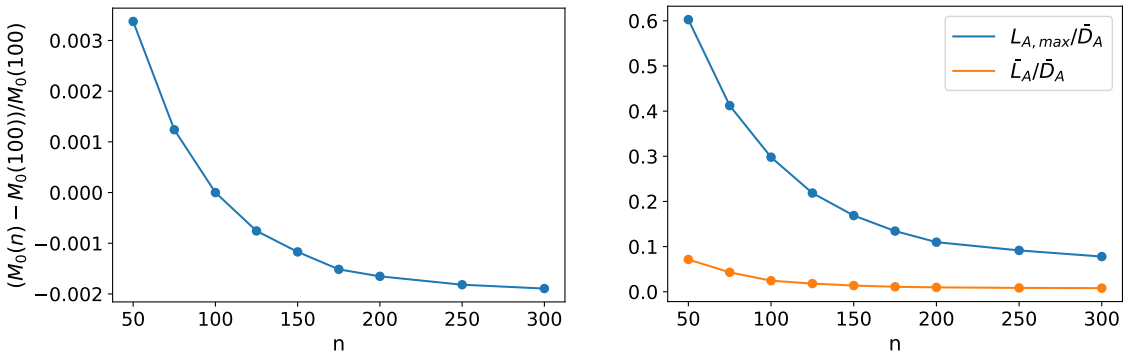

Figure 31: **Left** : Relative difference of the soliton mass M_0 with the value at $n_0 = 100$, as a function of the grid size n. **Right** : the two indicators for the accuracy of the Lorenz gauge fixing, i_1 (orange) and i_2 (blue) from (H.10), as a function of the grid size n.

mass, i_1 and i_2 are also found to converge, towards a value which is consistent with zero. The indicator i_2 is observed to be much larger than i_1, which means that the maximum of the gauge field divergence L_A is reached at the top of a narrow peak. In particular, for the grid that we used to produce the numerical results presented in the main text $(n, m) = (100, 100)$, i_1 and i_2 are found to take the following values

$$i_1(100) \simeq 2.5\% \quad , \quad i_2(100) \simeq 30\% \,. \tag{H.13}$$

This means that on average the Lorenz condition is well obeyed within 2% over most of the baryon solution, but there is a narrow region in the bulk where the error grows up to 30%. For the largest grid investigated that has $(n, m) = (300, 300)$, the average accuracy of the Lorenz gauge fixing is given by $i_1(300) \simeq 0.8\%$, and the maximum error by $i_2(300) \simeq 8\%$.

The fact that the value $i_2(100)$ is quite high, indicates that there is a small region in the bulk where the Lorenz condition is not very well obeyed for the solution on the grid that we used, with $(n, m) = (100, 100)$. Since $i_2(300) \simeq 8\%$ is much smaller, another way of checking the quality of the solution at $n = 100$ is to compare the numerical field configurations computed at $n = 100$ with those at $n = 300$. In particular, we will focus on the two bulk quantities that were analyzed in this work, that are the instanton number and Lagrangian densities (3.2.33) and (3.2.32). The relative differences of the two types of densities between the $n = 100$ and the $n = 300$ solutions are shown in Figure 32. The definition for the relative differences is the same as (3.2.44), where the mean of the bulk Lagrangian density is still computed over the region bounded by the green line in Figure 3.5. For the instanton number density, the average is computed over the region where $|\rho_{N_i}| M_0^{-4} \geq 2.8 \times 10^{-3}$. The two solutions are compared on the grid with $n = 100$. Figure

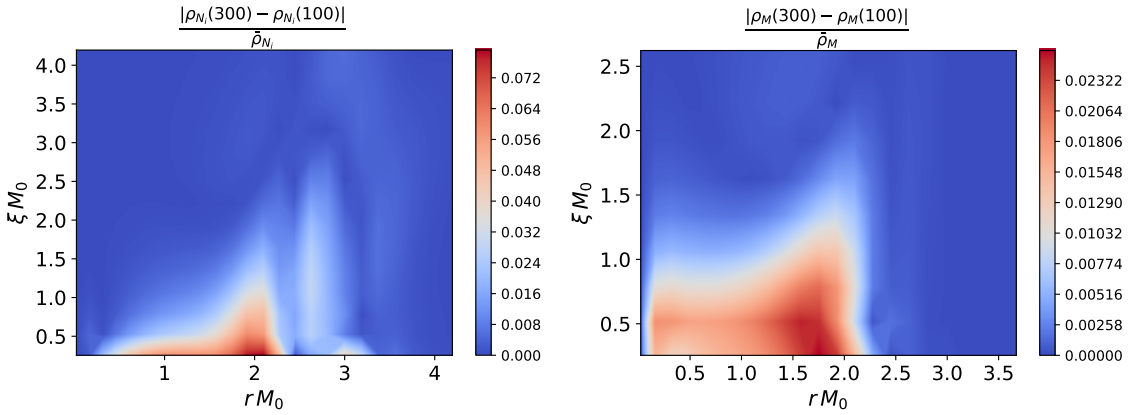

Figure 32: **Left** : Relative difference of the instanton number densities computed on the grids with $(n, m) = (100, 100)$ and $(n, m) = (300, 300)$. **Right** : Relative difference of the bulk Lagrangian densities computed on the grids with $(n, m) = (100, 100)$ and $(n, m) = (300, 300)$.

32 shows that the densities computed at $n = 100$ and $n = 300$ only differ by a few percent of the mean value, with a maximum of about 8% in the case of the instanton number density.

In addition to the grid size, we also studied the convergence of the soliton mass as a function of the cut-offs ξ_{max} and r_{max}. As far as the radial cut-off is concerned, we found that larger ξ_{max} modified the soliton mass by less than 0.01%. For the holographic coordinate, it was found that larger IR cut-offs r_{max} do not affect the soliton mass by more than about 0.2%.

The conclusion of this analysis of the numerical precision is that the grid that we used with $(n, m) = (100, 100)$ gives a very precise value for the soliton mass M_0, and a result within a few percent of accuracy for the densities. This means that the solution can be trusted at the qualitative level, and also at the quantitative level as far as M_0 is concerned, which is the observable that we were interested in in this work. When extracting other observables from the baryon solution, one should check in each case the properties of convergence, and adapt the grid size to the desired level of accuracy. In particular, the analysis of the densities in Figure 32 indicates that accuracies better than the percent level may require grid sizes larger than $(n, m) = (100, 100)$.

I Numerical baryon solutions for a different set of potentials

In this appendix we present, for comparison, the numerical baryon solution obtained for a different set of V-QCD potentials. We focus on the leading order probe baryon case, for static and rotating baryons. The potentials are those derived in [165], the set "7a" in Appendix A of this reference, and can also be found in Appendix B of [174]. The value of the pion decay constant f_π for these potentials is significantly smaller than the experimental value, so they are not expected to give a quantitatively good description of all baryonic properties. The potentials of [165] have the same UV and IR asymptotics fitted to QCD properties as the ones that were used in this work though (with parameters given in Table 3.2), so the qualitative behavior should be the same. The purpose of this appendix is to check the previous statement by reproducing the plots of the main text for the potentials of [165]. We also compute the baryon spectrum in this case and compare with Table 3.8.

I.1 Static soliton

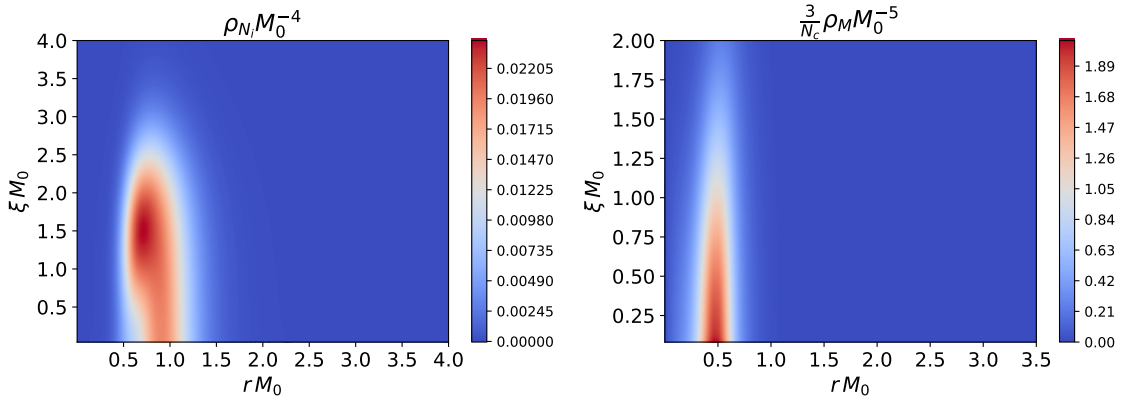

Figure 33: Instanton number (left) and bulk Lagrangian (right) density for the static soliton solution in the probe baryon regime. All quantities are expressed in units of the classical mass of the soliton (3.2.27). The center of the soliton is located at $\xi = 0$ where the density diverges as ξ^{-1}.

The instanton number and Lagrangian density in the (ξ, r)-plane are presented in Figure 33, where all dimensionful quantities are expressed in units of the classical soliton mass (3.2.27). By comparing with Figure 3.5, it is observed that the qualitative shape of the densities are similar. However, the densities are typically located significantly closer to the

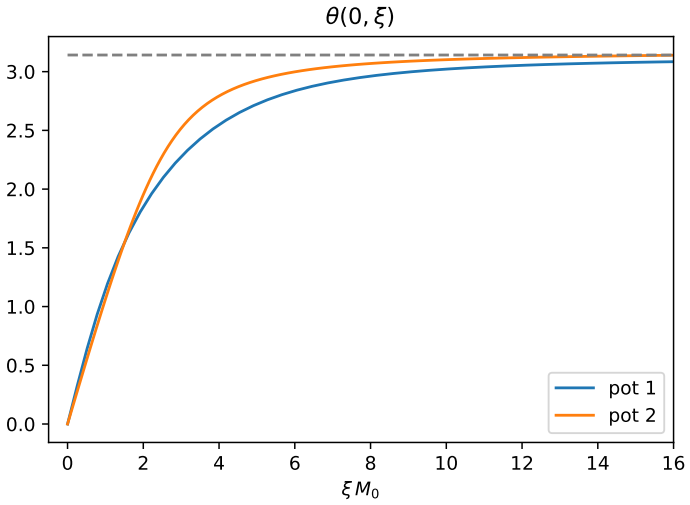

Figure 34: Radial profile of the non-abelian phase of the tachyon field (3.1.64) at the UV boundary. The blue line corresponds to the solution for the V-QCD potentials presented in Section 3.2.2, and the orange line for those of [165]. The dashed gray line indicates the asymptotic value π.

UV boundary for the potentials of [165], in units of the soliton mass. Also, the extent of the densities in the holographic direction is smaller, especially for the Lagrangian density. The numerical value for the classical soliton mass M_0 is obtained by integrating the Lagrangian density in Figure 33

$$M_0 \simeq \frac{N_c}{3} \times 265\,\text{MeV}\,. \tag{I.1}$$

This value is about 4 times smaller than for the potentials used in the main text (3.2.34). Our numerical analysis indicate that this small value for M_0 can be traced back to the smallness of the pion decay constant for the potentials of [165].

In Figure 34, we also plot the profile at the boundary ($r = 0$) for the non-abelian phase θ of the tachyon field (3.1.64), and compare with Figure 3.6. We see that the results are close up to the rescaling of the radial coordinate as a function of the soliton mass M_0. That being said, we notice that $\theta(\xi M_0)$ increases somewhat faster from the baryon center for the potentials of [165] compared with those of the main text.

I.2 Rotating soliton

The bulk Lagrangian density for the rotating fields in the (ξ, r)-plane is presented in Figure 35, where all dimensionful quantities are expressed in units of the classical soliton mass M_0

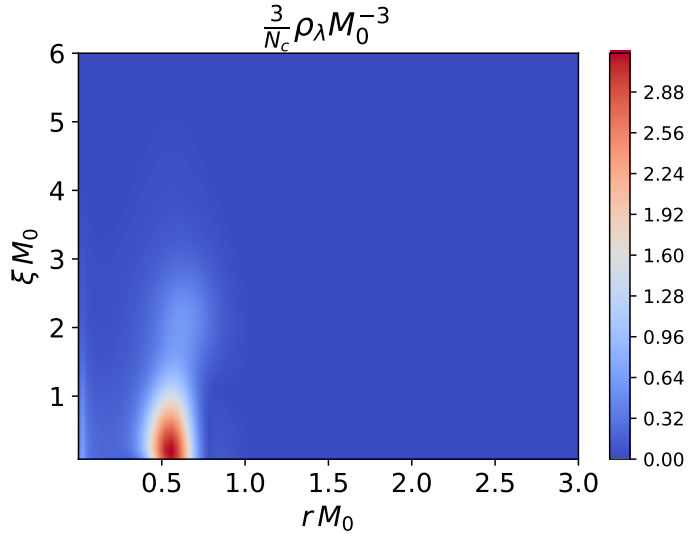

Figure 35: Lagrangian density for the rotating fields in the probe baryon approximation, for the potentials of [165]. All quantities are expressed in units of the classical mass of the static soliton M_0 (3.2.27). The center of the soliton is located at $\xi = 0$ where the density diverges as ξ^{-1}. The UV boundary is at $r = 0$.

Spin	Pot 2	Pot 1	Experimental mass
$s = \frac{1}{2}$	$M_N \simeq 340\,\text{MeV}$	$M_N \simeq 1170\,\text{MeV}$	$M_N = 940\,\text{MeV}$
$s = \frac{3}{2}$	$M_\Delta \simeq 640\,\text{MeV}$	$M_\Delta \simeq 1260\,\text{MeV}$	$M_\Delta = 1234\,\text{MeV}$

Table 2: Baryon spin-isospin spectrum in the V-QCD model with the potentials of [165] (Pot 2), compared with the potentials used in the main text (Pot 1) and experimental data.

(3.2.27). Comparing with Figure 3.9, we see that the Lagrangian densities for the two sets of potentials are qualitatively different. In particular, the maximum of the density is well separated from the boundary for the potentials of [165]. As stated in the main text, we believe that this behavior is more generic than that of Figure 3.9. Also, as was observed for the static solution, the density has a lesser extent in the holographic direction (in units of M_0) for the potentials of [165].

The numerical value for the classical moment of inertia density λ in (3.2.75) is obtained

by integrating the Lagrangian density in Figure 35

$$\frac{1}{\lambda} \simeq \frac{3}{N_c} \times 200\,\mathrm{MeV}\,. \tag{I.2}$$

From this result, the spin-isospin spectrum of the baryons can be computed and compared with the result for the potentials of the main text, shown in Table 3.8. This comparison is presented in Table 2, setting $N_c = 3$ in the large N result. Table 2 indicates that the baryon masses for the potentials of [165] are much smaller than experimental data, which is a consequence of the low mass of the soliton (I.1). Note however that the mass difference between the nucleon and the Δ is much closer to experimental data than for the potentials of section 3.2.2.

J Equations of motion for the rotating soliton

We present in this appendix the expressions for the equations of motion for the rotating soliton ansatz fields. These equations are obtained by extremizing the moment of inertia (3.2.75) with respect to variation of the fields. We start by giving the expression of the components of the field strength that are turned on by the slow rotation, as those are useful to compute the moment of inertia. We then write the equations of motion, first in the general tachyon back-reaction regime and then in the probe baryon regime.

J.1 Field strength

For the slowly rotating soliton ansatz of (3.2.57)-(3.2.60) and (3.2.64), the components of the field strength that are already non-zero in the static soliton solution are identical to the static solution at linear order in ω. Their expressions are given by equations (F.14)-(F.16). The effect of slow rotation at linear order is to source the components F_{0r}, F_{0i}, $\hat{F}_{ij}$ and $\hat{F}_{ir}$, where the superscript (L/R) is implicit. These components are expressed in terms of the fields of the ansatz as

$$\begin{aligned} F_{0r} = V(t) \Bigg(& -\left(\partial_r \chi_1 + A_r \chi_2\right) \epsilon^{abc} \omega^b \frac{x^c}{\xi} \\ & + \left(\partial_r \chi_2 - A_r \chi_1\right) \left(\omega^a - (\vec{\omega}.\vec{x}) \frac{x^a}{\xi^2} \right) - \partial_r v \, (\vec{\omega}.\vec{x}) \frac{x^a}{\xi^2} \Bigg) \frac{\sigma^a}{2} V(t)^\dagger \,, \end{aligned} \tag{J.1}$$

$$\begin{aligned} F_{0i} = V(t) \Bigg(& x^a \epsilon^{ibc} \omega^b \frac{x^c}{\xi^2} \left(-\chi_1 \frac{1+\phi_2}{\xi} \right) \\ & + \frac{x^a}{\xi} \left(\omega^i - \frac{x^i}{\xi^2} (\vec{\omega}.\vec{x}) \right) \left(\chi_2 \frac{\phi_2}{\xi} + \chi_1 \frac{\phi_1}{\xi} - \frac{v}{\xi} \right) \end{aligned}$$

$$
\begin{aligned}
&+\frac{\vec{\omega}.\vec{x}}{\xi}\left(\frac{x^i x^a}{\xi^2}-\delta^{ia}\right)\frac{\chi_2-v\phi_2}{\xi}\\
&+\epsilon^{aki}\frac{(\vec{\omega}.\vec{x})x^k}{\xi^2}(\chi_2+v)\frac{\phi_1}{\xi}+\epsilon^{aki}\omega^k\left(-\frac{\chi_1+\chi_2\phi_1}{\xi}\right)\\
&+x^i\epsilon^{abc}\omega^b\frac{x^c}{\xi^2}\left(\frac{\chi_1+\chi_2\phi_1}{\xi}-(\partial_\xi\chi_1+A_\xi\chi_2)\right)\\
&+\frac{x^i}{\xi}\left(\omega^a-\frac{x^a}{\xi^2}(\vec{\omega}.\vec{x})\right)(\partial_\xi\chi_2-A_\xi\chi_1)+\frac{(\vec{\omega}.\vec{x})x^i x^a}{\xi^3}(-\partial_\xi v)\Big)\frac{\sigma^a}{2}V(t)^\dagger\,, \qquad \text{(J.2)}
\end{aligned}
$$

$$
\hat{F}_{ir}=\frac{x^i(\vec{\omega}.\vec{x})}{\xi^2}\left(\partial_\xi B_r-\partial_r B_\xi\right)+\left(\omega^i-\frac{x^i(\vec{\omega}.\vec{x})}{\xi^2}\right)\frac{B_r-\partial_r\rho}{\xi}-\epsilon^{ibc}\omega^b\frac{x^c}{\xi}\partial_r Q\,, \qquad \text{(J.3)}
$$

$$
\hat{F}_{ij}=\frac{x^i\omega^j-\omega^i x^j}{\xi^2}\left(\partial_\xi\rho-B_\xi\right)+2\frac{Q}{\xi}\epsilon^{ijk}\omega^k+\left(\partial_\xi Q-\frac{Q}{\xi}\right)\omega^b\frac{x^c}{\xi}\left(\epsilon^{jbc}\frac{x^i}{\xi}-\epsilon^{ibc}\frac{x^j}{\xi}\right)\,. \qquad \text{(J.4)}
$$

J.2 Equations of motion in the tachyon back-reaction regime

The general equations of motion in the tachyon back-reaction regime are given by

$$
\begin{aligned}
&w^2\Big[\partial_\xi\big(\mathcal{X}(1-\mathrm{e}^{2A}\Delta_{\xi\xi})\xi^2\partial_\xi v\big)-2\mathcal{X}\big(v(1+|\phi|^2)-(\chi\phi^*+h.c.)\big)\Big]+\\
&+\partial_r\Big(\xi^2w^2\mathcal{X}\mathrm{e}^{2A}\Delta_{rr}\partial_r v\Big)-\partial_r\Big(\xi^2w^2\mathcal{X}\mathrm{e}^{2A}\Delta_{\xi r}\partial_\xi v\Big)-\partial_\xi\Big(\xi^2w^2\mathcal{X}\mathrm{e}^{2A}\Delta_{\xi r}\partial_r v\Big)=\\
&\frac{2\epsilon^{\bar{\mu}\bar{\nu}}}{\pi^2M^3}\Big(B_{\bar{\mu}\bar{\nu}}\left[\frac{1}{2}(f_1+f_3)\left(|\phi|^2-1\right)+(f_1-f_3-if_2)\tilde{\phi}_1^2\right]+\\
&\qquad+(f_1+f_3)\xi Q F_{\bar{\mu}\bar{\nu}}-2(f_3-if_2)\tilde{B}_{\bar{\mu}}(D_{\bar{\nu}}\tilde{\phi}+h.c.)\tilde{\phi}_1+\\
&\qquad+\partial_{\bar{\nu}}\tau\left[(f_1'+f_3')\left(\tilde{B}_{\bar{\mu}}(1-|\phi|^2)-2\xi Q\tilde{A}_{\bar{\mu}}\right)+2if_2'\tilde{B}_{\bar{\mu}}\tilde{\phi}_1^2\right]\Big)\,, \qquad \text{(J.5)}
\end{aligned}
$$

$$
\begin{aligned}
&w^2\Big[D_\xi\big(\mathcal{X}(1-\mathrm{e}^{2A}\Delta_{\xi\xi})\xi^2D_\xi\tilde{\chi}\big)+\mathcal{X}\big(2v\tilde{\phi}-\tilde{\chi}(1+|\phi|^2)\big)\Big]+D_r\big(\xi^2w^2\mathcal{X}\mathrm{e}^{2A}\Delta_{rr}D_r\tilde{\chi}\big)-\\
&-D_r\big(\xi^2w^2\mathcal{X}\mathrm{e}^{2A}\Delta_{\xi r}D_\xi\tilde{\chi}\big)-D_\xi\big(\xi^2w^2\mathcal{X}\mathrm{e}^{2A}\Delta_{\xi r}D_r\tilde{\chi}\big)+h.c.\\
&=4\xi^2\mathrm{e}^{2A}\mathcal{X}\kappa\tau^2\tilde{\chi}+\\
&+\frac{\epsilon^{\bar{\mu}\bar{\nu}}}{\pi^2M^3}\Big(6(f_1-f_3)D_{\bar{\mu}}\rho D_{\bar{\nu}}\tilde{\phi}-4i(f_3-if_2)\tilde{\rho}\,\tilde{A}_{\bar{\mu}}\partial_{\bar{\nu}}\tilde{\phi}+\\
&\qquad+\partial_{\bar{\mu}}(\xi Q)\Big(2i(f_1+f_3)D_{\bar{\nu}}\tilde{\phi}+4(f_1+f_3-3if_2)\tilde{A}_{\bar{\nu}}\tilde{\phi}\Big)+\\
&\qquad+2\partial_{\bar{\nu}}\tau\Big[(f_1'-f_3')D_{\bar{\mu}}\rho\,\tilde{\phi}-(f_1'-f_3')\tilde{\rho}D_{\bar{\mu}}\tilde{\phi}\Big]\Big)+h.c.\,, \qquad \text{(J.6)}
\end{aligned}
$$

$$
w^2\Big[-iD_\xi\big(\mathcal{X}(1-\mathrm{e}^{2A}\Delta_{\xi\xi})\xi^2D_\xi\tilde{\chi}\big)-i\mathcal{X}\big(2v\tilde{\phi}-\tilde{\chi}(1+|\phi|^2)\big)\Big]-
$$

$$
\begin{aligned}
&- iD_r\Big(\xi^2\mathcal{X}\mathrm{e}^{2A}\Delta_{rr}w^2D_r\tilde{\chi}\Big) + iD_r\Big(\xi^2\mathcal{X}\mathrm{e}^{2A}\Delta_{\xi r}w^2D_\xi\tilde{\chi}\Big)+\\
&+ iD_\xi\Big(\xi^2\mathcal{X}\mathrm{e}^{2A}\Delta_{\xi r}w^2D_r\tilde{\chi}\Big) + h.c.\\
&= \frac{\epsilon^{\bar{\mu}\bar{\nu}}}{\pi^2M^3}\Bigg(D_{\bar{\mu}}\rho\left(-2i(f_1+f_3)D_{\bar{\nu}}\tilde{\phi} - 4(f_1-f_3-if_2)\tilde{A}_{\bar{\nu}}\tilde{\phi}\right)+\\
&\qquad + 2\partial_{\bar{\mu}}(\xi Q)(f_1+f_3)D_{\bar{\nu}}\tilde{\phi} + 2(f_3-if_2)\tilde{\rho}\left(2\tilde{A}_{\bar{\mu}}\partial_{\bar{\nu}}\tilde{\phi} - F_{\bar{\mu}\bar{\nu}}\tilde{\phi}\right)+\\
&\qquad + 2\partial_{\bar{\nu}}\tau\Big[i(f_1'+f_3')\tilde{\rho}\,D_{\bar{\mu}}\tilde{\phi} - 2if_2'\tilde{\rho}\tilde{A}_{\bar{\mu}}\tilde{\phi} + (f_1'+f_3')\partial_{\bar{\mu}}(\xi Q)\tilde{\phi}\Big]\Bigg) + h.c.\,, \qquad \text{(J.7)}
\end{aligned}
$$

$$
\begin{aligned}
&w^2\Big[\partial_\xi\big(\mathcal{X}\left[\mathrm{e}^{2A}\Delta_{rr}(1-\mathrm{e}^{2A}\Delta_{\xi\xi}) - \mathrm{e}^{4A}\Delta_{\xi r}^2\right]\xi^2B_{\xi r}\big) + 2\mathcal{X}\mathrm{e}^{2A}\big(\Delta_{rr}D_r\rho - \Delta_{\xi r}D_\xi\rho\big)\Big] =\\
&\quad 4\mathrm{e}^{4A}\mathcal{X}\Delta_{rr}\kappa\tau^2\xi^2\tilde{B}_r - 4\mathrm{e}^{4A}\mathcal{X}\Delta_{\xi r}\kappa\tau^2\xi^2\tilde{B}_\xi -\\
&\quad - \frac{1}{2\pi^2M^3}\Bigg((f_1+f_3)(D_\xi\phi\,\chi^* + h.c.) - 2(2f_3-f_1)\left(D_\xi\tilde{\phi} + h.c.\right)\tilde{\chi}_1 -\\
&\qquad\qquad - 4(f_1-f_3-if_2)\tilde{A}_\xi\tilde{\phi}_1\tilde{\chi}_2 - 8(f_1+f_3)\xi Q\partial_\xi\Phi +\\
&\qquad\qquad + 2v(f_3-if_2)(D_\xi\tilde{\phi} + h.c.)\tilde{\phi}_1 -\\
&\qquad\qquad - 2\partial_\xi\left(v\left[\frac{1}{2}(f_1+f_3)\left(|\phi|^2-1\right) + (f_1-f_3-if_2)\tilde{\phi}_1^2\right]\right) -\\
&\qquad\qquad - \partial_\xi\tau\Big[(f_1'+f_3')v(1-|\phi|^2) + 2if_2'\,v\tilde{\phi}_1^2 - 2(f_1'-f_3')\tilde{\chi}_1\tilde{\phi}_1\Big]\Bigg)\,, \qquad \text{(J.8)}
\end{aligned}
$$

$$
\begin{aligned}
&\xi^2\partial_r\Big(w^2\mathcal{X}\left[\mathrm{e}^{2A}\Delta_{rr}(1-\mathrm{e}^{2A}\Delta_{\xi\xi}) - \mathrm{e}^{4A}\Delta_{\xi r}^2\right]B_{r\xi}\Big)+\\
&+ 2w^2\mathcal{X}\Big((1-\mathrm{e}^{2A}\Delta_{\xi\xi})D_\xi\rho - \mathrm{e}^{2A}\Delta_{\xi r}D_r\rho\Big) =\\
&\quad 4\mathrm{e}^{2A}\mathcal{X}(1-\mathrm{e}^{2A}\Delta_{\xi\xi})\kappa\tau^2\xi^2\tilde{B}_\xi - 4\mathrm{e}^{4A}\mathcal{X}\Delta_{\xi r}\kappa\tau^2\xi^2\tilde{B}_r +\\
&\quad + \frac{1}{2\pi^2M^3}\Bigg[(f_1+f_3)(D_r\phi\,\chi^* + h.c.) - 2(2f_3-f_1)(D_r\tilde{\phi} + h.c.)\tilde{\chi}_1 -\\
&\qquad\qquad - 4(f_1-f_3-if_2)\tilde{A}_r\tilde{\phi}_1\tilde{\chi}_2 - 8(f_1+f_3)\xi Q\partial_r\Phi +\\
&\qquad\qquad + 2v(f_3-if_2)(D_r\tilde{\phi} + h.c.)\tilde{\phi}_1 -\\
&\qquad\qquad - 2\partial_r\left(v\left[\frac{1}{2}(f_1+f_3)\left(|\phi|^2-1\right) + (f_1-f_3-if_2)\tilde{\phi}_1^2\right]\right) -\\
&\qquad\qquad - \partial_r\tau\Big[(f_1'+f_3')v(1-|\phi|^2) + 2if_2'\,v\tilde{\phi}_1^2 - 2(f_1'-f_3')\tilde{\chi}_1\tilde{\phi}_1\Big]\Bigg)\,, \qquad \text{(J.9)}
\end{aligned}
$$

$$
\partial_r\Big(w^2\mathcal{X}\mathrm{e}^{2A}\Delta_{rr}D_r\rho\Big) + \partial_\xi\Big(w^2\mathcal{X}(1-\mathrm{e}^{2A}\Delta_{\xi\xi})D_\xi\rho\Big) -
$$

$$
\begin{aligned}
&-\partial_r\Big(w^2\mathcal{X}\mathrm{e}^{2A}\Delta_{\xi r}D_\xi\rho\Big)-\partial_\xi\Big(w^2\mathcal{X}\mathrm{e}^{2A}\Delta_{\xi r}D_r\rho\Big)\\
&\quad=4\mathrm{e}^{2A}\mathcal{X}(1-\mathrm{e}^{2A}\Delta_{\xi\xi})\kappa\tau^2\tilde{\rho}+\\
&\qquad+\frac{\epsilon^{\bar{\mu}\bar{\nu}}}{4\pi^2M^3}\Big[\partial_{\bar{\mu}}\Big((f_1+f_3)(D_{\bar{\nu}}\phi\,\chi^*+h.c.)-2(2f_3-f_1)(D_{\bar{\nu}}\tilde{\phi}+h.c.)\tilde{\chi}_1-\\
&\qquad\qquad-4(f_1-f_3-if_2)\tilde{A}_{\bar{\nu}}\tilde{\phi}_1\tilde{\chi}_2-8(f_1+f_3)\xi Q\partial_{\bar{\nu}}\Phi\Big)-\\
&\qquad\qquad-2(f_3-if_2)\Big(-F_{\bar{\mu}\bar{\nu}}\,\tilde{\phi}_1\tilde{\chi}_2+\tilde{A}_{\bar{\mu}}(-i\partial_{\bar{\nu}}\tilde{\phi}\tilde{\chi}+h.c.)\Big)+\\
&\qquad\qquad+\partial_{\bar{\nu}}\tau\Big(f_1'(D_{\bar{\mu}}\phi\chi^*+h.c.)-f_3'(D_{\bar{\mu}}\tilde{\phi}\tilde{\chi}+h.c.)+2if_2'\tilde{A}_{\bar{\mu}}\tilde{\phi}_1\tilde{\chi}_2+\\
&\qquad\qquad\qquad+2(f_1'-f_3')\partial_{\bar{\mu}}(\tilde{\chi}_1\tilde{\phi}_1)-8(f_1'+f_3')\xi Q\partial_{\bar{\mu}}\Phi\Big)\Big],
\end{aligned}
\tag{J.10}
$$

$$
\begin{aligned}
&\xi^2\partial_r\Big(w^2\mathcal{X}\mathrm{e}^{2A}\Delta_{rr}\partial_rQ\Big)+w^2\partial_\xi\Big(\mathcal{X}(1-\mathrm{e}^{2A}\Delta_{\xi\xi})\xi^2\partial_\xi Q\Big)-\\
&-\partial_\xi\Big(w^2\mathcal{X}\mathrm{e}^{2A}\Delta_{\xi r}\xi^2\partial_rQ\Big)-\partial_r\Big(w^2\mathcal{X}\mathrm{e}^{2A}\Delta_{\xi r}\xi^2\partial_\xi Q\Big)=\\
&\quad\mathcal{X}w^2\Big[2-\mathrm{e}^{2A}\xi\big(\partial_\xi\Delta_{\xi\xi}+\mathrm{e}^{2A}\partial_r(\mathrm{e}^{-2A}\Delta_{\xi r})\big)\Big]Q-\\
&\quad-\frac{\xi\epsilon^{\bar{\mu}\bar{\nu}}}{4\pi^2M^3}\Big[-\partial_{\bar{\mu}}\Big((f_1+f_3)(i\chi^*D_{\bar{\nu}}\phi+h.c.)+4(f_1+f_3-3if_2)\tilde{A}_{\bar{\nu}}\tilde{\phi}_1\tilde{\chi}_1\Big)-\\
&\qquad\qquad-8(f_1+f_3)D_{\bar{\mu}}\rho\partial_{\bar{\nu}}\Phi+(f_1+f_3)v\,F_{\bar{\mu}\bar{\nu}}+\\
&\qquad\qquad+2\partial_{\bar{\nu}}\tau(f_1'+f_3')\left(4\tilde{\rho}\partial_{\bar{\mu}}\Phi-\partial_{\bar{\mu}}(\tilde{\phi}_1\tilde{\chi}_2)-v\,\tilde{A}_{\bar{\mu}}\right)\Big],
\end{aligned}
\tag{J.11}
$$

$$
\begin{aligned}
&\xi^2\partial_r\left[\mathrm{e}^{4A}\mathcal{X}\Delta_{rr}\kappa\tau^2\left(B_r+\frac{1}{2}\partial_r\zeta\right)\right]+\\
&+\mathrm{e}^{2A}\kappa\left[\partial_\xi\left[\mathcal{X}(1-\mathrm{e}^{2A}\Delta_{\xi\xi})\tau^2\xi^2\left(B_\xi+\frac{1}{2}\partial_\xi\zeta\right)\right]-2\mathcal{X}(1-\mathrm{e}^{2A}\Delta_{\xi\xi})\tau^2\left(\rho+\frac{1}{2}\zeta\right)\right]-\\
&-\partial_r\left[\mathrm{e}^{4A}\mathcal{X}\Delta_{\xi r}\kappa\tau^2\xi^2\left(B_\xi+\frac{1}{2}\partial_\xi\zeta\right)\right]-\partial_\xi\left[\mathrm{e}^{4A}\mathcal{X}\Delta_{\xi r}\kappa\tau^2\xi^2\left(B_r+\frac{1}{2}\partial_r\zeta\right)\right]\\
&=-\frac{\epsilon^{\bar{\mu}\bar{\nu}}}{4\pi^2M^3}\Big[\partial_{\bar{\mu}}\Big((f_3-if_2)v(D_{\bar{\nu}}\tilde{\phi}+h.c.)\tilde{\phi}_1\Big)+\\
&\qquad\qquad+(f_3-if_2)\left(-F_{\bar{\mu}\bar{\nu}}\,\tilde{\phi}_1\tilde{\chi}_2+\tilde{A}_{\bar{\mu}}(-i\partial_{\bar{\nu}}\tilde{\phi}\tilde{\chi}+h.c.)\right)+\\
&\qquad\qquad+\partial_{\bar{\nu}}\tau\Big(-\frac{1}{2}(f_1'+f_3')\partial_{\bar{\mu}}\left(v(1-|\phi|^2)\right)-if_2'\partial_{\bar{\mu}}(v\tilde{\phi}_1^2)-\\
&\qquad\qquad\qquad-\frac{1}{2}f_1'(D_{\bar{\mu}}\phi\chi^*+h.c.)+\frac{1}{2}f_3'(D_{\bar{\mu}}\tilde{\phi}\tilde{\chi}+h.c.)-if_2'\tilde{A}_{\bar{\mu}}\tilde{\phi}_1\tilde{\chi}_2+
\end{aligned}
$$

$$+ 4(f_1' + f_3')\xi Q \partial_{\bar\mu}\Phi\Big)\Big]\,, \tag{J.12}$$

where

$$\mathcal{X} = \sqrt{1 + \mathrm{e}^{-2A}\kappa\left((\partial_r\tau)^2 + (\partial_\xi\tau)^2\right)}\, V_f(\lambda,\tau)\,\mathrm{e}^{A}\,, \tag{J.13}$$

and the symbol $\Delta_{\bar\mu\bar\nu}$ is given by

$$\Delta_{\xi\xi} \equiv \frac{\mathrm{e}^{6A}\kappa\,(\partial_\xi\tau)^2}{-\det\tilde g} = \frac{\mathrm{e}^{-4A}\kappa\,(\partial_\xi\tau)^2}{1+\mathrm{e}^{-2A}\kappa\left((\partial_r\tau)^2+(\partial_\xi\tau)^2\right)}\,, \tag{J.14}$$

$$\Delta_{\xi r} \equiv \frac{\mathrm{e}^{6A}\kappa\,\partial_\xi\tau\partial_r\tau}{-\det\tilde g} = \frac{\mathrm{e}^{-4A}\kappa\,\partial_\xi\tau\partial_r\tau}{1+\mathrm{e}^{-2A}\kappa\left((\partial_r\tau)^2+(\partial_\xi\tau)^2\right)}\,, \tag{J.15}$$

$$\Delta_{rr} \equiv \frac{\mathrm{e}^{8A}(1+\mathrm{e}^{-2A}\kappa\,(\partial_\xi\tau)^2)}{-\det\tilde g} = \frac{\mathrm{e}^{-2A}\,(1+\mathrm{e}^{-2A}\kappa\,(\partial_\xi\tau)^2)}{1+\mathrm{e}^{-2A}\kappa\left((\partial_r\tau)^2+(\partial_\xi\tau)^2\right)}\,. \tag{J.16}$$

J.3 Equations of motion in the probe baryon approximation

In the probe baryon approximation, the modulus of the tachyon field τ is fixed to its vacuum value. In particular, it does not depend on the radius ξ, so that the equations of motion are somewhat simplified

$$\begin{aligned}
&hw^2\left[\partial_\xi(\xi^2\partial_\xi v) - 2\left(v(1+|\phi|^2) - (\chi\phi^* + h.c.)\right)\right] + \partial_r\left(\xi^2 k w^2 \partial_r v\right) = \\
&\frac{2}{\pi^2 M^3}\Bigg(2B_{\xi r}\left[\frac{1}{2}(f_1(\tau)+f_3(\tau))\left(|\phi|^2-1\right) + (f_1(\tau)-f_3(\tau)-if_2(\tau))\tilde\phi_1^2\right] + \\
&\qquad + 2(f_1(\tau)+f_3(\tau))\xi Q F_{\xi r} - 2(f_3(\tau)-if_2(\tau))\epsilon^{\bar\mu\bar\nu}\tilde B_{\bar\mu}(D_{\bar\nu}\tilde\phi + h.c.)\tilde\phi_1\Bigg) + \\
&+ \frac{2}{\pi^2 M^3}\partial_r\tau\left[(f_1'(\tau)+f_3'(\tau))\left(\tilde B_\xi(1-|\phi|^2) - 2\xi Q\tilde A_\xi\right) + 2if_2'(\tau)\tilde B_\xi\tilde\phi_1^2\right]\,,
\end{aligned} \tag{J.17}$$

$$\begin{aligned}
&hw^2\left[D_\xi(\xi^2 D_\xi\tilde\chi) + 2v\tilde\phi - \tilde\chi(1+|\phi|^2)\right] + D_r\left(\xi^2 k w^2 D_r\tilde\chi\right) + h.c. = \\
&\quad 4\xi^2\mathrm{e}^{2A}h\kappa\tau^2\tilde\chi + \\
&+ \frac{\epsilon^{\bar\mu\bar\nu}}{\pi^2 M^3}\Big[6(f_1-f_3)D_{\bar\mu}\rho D_{\bar\nu}\tilde\phi + \partial_{\bar\mu}(\xi Q)\left(2i(f_1+f_3)D_{\bar\nu}\tilde\phi + 4(f_1+f_3-3if_2)\tilde A_{\bar\nu}\tilde\phi\right) - \\
&\qquad -4i(f_3-if_2)\tilde\rho\,\tilde A_{\bar\mu}\partial_{\bar\nu}\tilde\phi\Big] + \\
&+ \frac{2}{\pi^2 M^3}\partial_r\tau\left[(f_1'-f_3')D_\xi\rho\,\tilde\phi - (f_1'-f_3')\tilde\rho D_\xi\tilde\phi\right] + h.c.\,,
\end{aligned} \tag{J.18}$$

$$hw^2\left[-iD_\xi(\xi^2 D_\xi\tilde\chi) - 2iv\tilde\phi + i\tilde\chi(1+|\phi|^2)\right] - iD_r\left(\xi^2 k w^2 D_r\tilde\chi\right) + h.c.$$

$$= \frac{\epsilon^{\bar{\mu}\bar{\nu}}}{\pi^2 M^3}\Big[D_{\bar{\mu}}\rho\left(-2i(f_1+f_3)D_{\bar{\nu}}\tilde{\phi} - 4(f_1-f_3-if_2)\tilde{A}_{\bar{\nu}}\tilde{\phi}\right) + \\ + 2\partial_{\bar{\mu}}(\xi Q)(f_1+f_3)D_{\bar{\nu}}\tilde{\phi} + 2(f_3-if_2)\tilde{\rho}\left(2\tilde{A}_{\bar{\mu}}\partial_{\bar{\nu}}\tilde{\phi} - F_{\bar{\mu}\bar{\nu}}\tilde{\phi}\right)\Big] + \\ + \frac{2}{\pi^2 M^3}\partial_r\tau\left[i(f_1'+f_3')\tilde{\rho}\, D_\xi\tilde{\phi} - 2if_2'\,\tilde{\rho}\tilde{A}_\xi\tilde{\phi} + (f_1'+f_3')\partial_\xi(\xi Q)\tilde{\phi}\right] + h.c.\,, \tag{J.19}$$

$$kw^2\left[\partial_\xi(\xi^2 B_{\xi r}) + 2D_r\rho\right] = 4\mathrm{e}^{2A}k\kappa\tau^2\xi^2\tilde{B}_r - \\ - \frac{1}{2\pi^2 M^3}\Bigg[(f_1+f_3)(D_\xi\phi\,\chi^* + h.c.) - 2(2f_3-f_1)\left(D_\xi\tilde{\phi} + h.c.\right)\tilde{\chi}_1 - \\ - 4(f_1-f_3-if_2)\tilde{A}_\xi\tilde{\phi}_1\tilde{\chi}_2 - 8(f_1+f_3)\xi Q\partial_\xi\Phi + \\ + 2v(f_3-if_2)(D_\xi\tilde{\phi} + h.c.)\tilde{\phi}_1 - \\ - 2\partial_\xi\left(v\left[\frac{1}{2}(f_1+f_3)\left(|\phi|^2-1\right) + (f_1-f_3-if_2)\tilde{\phi}_1^2\right]\right)\Bigg], \tag{J.20}$$

$$\xi^2\partial_r(kw^2 B_{r\xi}) + 2hw^2 D_\xi\rho = 4\mathrm{e}^{2A}h\kappa\tau^2\xi^2\tilde{B}_\xi + \\ + \frac{1}{2\pi^2 M^3}\Bigg[(f_1+f_3)(D_r\phi\,\chi^* + h.c.) - 2(2f_3-f_1)\left(D_r\tilde{\phi} + h.c.\right)\tilde{\chi}_1 - \\ - 4(f_1-f_3-if_2)\tilde{A}_r\tilde{\phi}_1\tilde{\chi}_2 - 8(f_1+f_3)\xi Q\partial_r\Phi + \\ + 2v(f_3-if_2)(D_r\tilde{\phi} + h.c.)\tilde{\phi}_1 - \\ - 2\partial_r\left(v\left[\frac{1}{2}(f_1+f_3)\left(|\phi|^2-1\right) + (f_1-f_3-if_2)\tilde{\phi}_1^2\right]\right) - \\ - \partial_r\tau\left[(f_1'+f_3')v(1-|\phi|^2) + 2if_2'\,v\tilde{\phi}_1^2 - 2(f_1'-f_3')\tilde{\chi}_1\tilde{\phi}_1\right]\Bigg], \tag{J.21}$$

$$\partial_r(kw^2 D_r\rho) + hw^2\partial_\xi D_\xi\rho = 4\mathrm{e}^{2A}h\kappa\tau^2\tilde{\rho} + \\ + \frac{1}{4\pi^2 M^3}\Bigg[\epsilon^{\bar{\mu}\bar{\nu}}\partial_{\bar{\mu}}\Big((f_1+f_3)(D_{\bar{\nu}}\phi\,\chi^* + h.c.) - 2(2f_3-f_1)\left(D_{\bar{\nu}}\tilde{\phi} + h.c.\right)\tilde{\chi}_1 - \\ - 4(f_1-f_3-if_2)\tilde{A}_{\bar{\nu}}\tilde{\phi}_1\tilde{\chi}_2 - 8(f_1+f_3)\xi Q\partial_{\bar{\nu}}\Phi\Big) - \\ - 2(f_3-if_2)\epsilon^{\bar{\mu}\bar{\nu}}\left(-F_{\bar{\mu}\bar{\nu}}\,\tilde{\phi}_1\tilde{\chi}_2 + \tilde{A}_{\bar{\mu}}(-i\partial_{\bar{\nu}}\tilde{\phi}\tilde{\chi} + h.c.)\right) + \\ + \partial_r\tau\Big(f_1'(\tau)(D_\xi\phi\chi^* + h.c.) - f_3'(\tau)(D_\xi\tilde{\phi}\tilde{\chi} + h.c.) + 2if_2'(\tau)\tilde{A}_\xi\tilde{\phi}_1\tilde{\chi}_2 + \\ + 2(f_1'-f_3')\partial_\xi(\tilde{\chi}_1\tilde{\phi}_1) - 8(f_1'+f_3')\xi Q\partial_\xi\Phi\Big)\Bigg], \tag{J.22}$$

$$\xi^2\partial_r(kw^2\partial_r Q) + hw^2\left[\partial_\xi(\xi^2\partial_\xi Q) - 2Q\right] = \tag{J.23}$$

$$
\begin{aligned}
&- \frac{\xi}{4\pi^2 M^3}\Big[- \epsilon^{\bar\mu\bar\nu}\partial_{\bar\mu}\Big((f_1+f_3)(i\chi^* D_{\bar\nu}\phi + h.c.) + 4(f_1+f_3-3if_2)\tilde A_{\bar\nu}\tilde\phi_1\tilde\chi_1\Big) - \\
&\qquad - 8(f_1+f_3)\epsilon^{\bar\mu\bar\nu} D_{\bar\mu}\rho\partial_{\bar\nu}\Phi + (f_1+f_3) v\,\epsilon^{\bar\mu\bar\nu}F_{\bar\mu\bar\nu} + \\
&\qquad + 2\partial_r\tau(f_1'+f_3')\Big(4\tilde\rho\partial_\xi\Phi - \partial_\xi(\tilde\phi_1\tilde\chi_2) - v\,\tilde A_\xi\Big)\Big]\,,
\end{aligned}
$$

$$
\begin{aligned}
&\xi^2\partial_r\left[\mathrm{e}^{2A} k w^2\kappa\tau^2\left(B_r + \frac{1}{2}\partial_r\zeta\right)\right] + \\
&+ \mathrm{e}^{2A} h w^2\kappa\tau^2\left[\partial_\xi\left[\xi^2\left(B_\xi + \frac{1}{2}\partial_\xi\zeta\right)\right] - 2\left(\rho + \frac{1}{2}\zeta\right)\right] \\
&= -\frac{1}{4\pi^2 M^3}\Big[\epsilon^{\bar\mu\bar\nu}\partial_{\bar\mu}\Big((f_3 - if_2) v (D_{\bar\nu}\tilde\phi + h.c.)\tilde\phi_1\Big) + \\
&\qquad + (f_3 - if_2)\epsilon^{\bar\mu\bar\nu}\Big(-F_{\bar\mu\bar\nu}\,\tilde\phi_1\tilde\chi_2 + \tilde A_{\bar\mu}(-i\partial_{\bar\nu}\tilde\phi\tilde\chi + h.c.)\Big) + \\
&\qquad + \partial_r\tau\Big(- \frac{1}{2}(f_1'+f_3')\partial_\xi\left(v(1-|\phi|^2)\right) - if_2'\partial_\xi(v\tilde\phi_1^2) - \\
&\qquad\qquad - \frac{1}{2}f_1'(\tau)(D_\xi\phi\chi^* + h.c.) + \frac{1}{2}f_3'(\tau)(D_\xi\tilde\phi\tilde\chi + h.c.) - \\
&\qquad\qquad - if_2'(\tau)\tilde A_\xi\tilde\phi_1\tilde\chi_2 + 4(f_1'+f_3')\xi Q\partial_\xi\Phi\Big)\Big]\,,
\end{aligned}
\tag{J.24}
$$

where

$$
k(r) = \frac{\mathrm{e}^A}{\sqrt{1+\mathrm{e}^{-2A}\kappa(\partial_r\tau)^2}} V_f(\lambda,\tau^2) \quad , \quad h(r) = \mathrm{e}^A\sqrt{1+\mathrm{e}^{-2A}\kappa(\partial_r\tau)^2}\,V_f(\lambda,\tau^2)\,. \tag{J.25}
$$

K Quantization of the rigid rotor

We proceed in this subsection to the quantization of the classical Lagrangian (3.2.74) along the lines of [177]. For this purpose, it is more convenient to reintroduce the SU(2) matrix $V(t)$ from the definition of $\vec\omega$ in (3.2.50). It gives

$$
L_{\rm rot} = -M_0 + 2\lambda\sum_{a=0}^{3}\dot u_a^2\,, \tag{K.1}
$$

where we parametrized the SU(2) matrix $V(t)$ as

$$
V(t) = u_0\mathbb{I}_2 + iu_i\sigma^i\,, \tag{K.2}
$$

where the u_a's parametrize the 3-sphere[24] S^3

$$\sum_a u_a^2 = 1\,. \tag{K.3}$$

S^3 can be alternatively described by 3 unconstrained coordinates [177] $q^\alpha \equiv (y, \theta_1, \theta_2)$ in the domains

$$y \in [-1, 1] \quad , \quad \theta_1, \theta_2 \in [0, 2\pi)\,, \tag{K.4}$$

which are related to the u_a's as

$$u_1 + iu_2 \equiv z_1 = \sqrt{\frac{1-y}{2}}\mathrm{e}^{i\theta_1} \quad , \quad u_0 + iu_3 \equiv z_2 = \sqrt{\frac{1+y}{2}}\mathrm{e}^{i\theta_2}\,. \tag{K.5}$$

In terms of these coordinates, the Lagrangian (K.1) is rewritten as

$$L_{\rm rot} = -M_0 + 2\lambda\, G_{\alpha\beta}\dot{q}^\alpha\dot{q}^\beta\,, \tag{K.6}$$

where G is the metric of S^3, which in the q^α coordinates reads

$$G_{\alpha\beta}\mathrm{d}q^\alpha\mathrm{d}q^\beta = \frac{1}{4}\frac{1}{1-y^2}\mathrm{d}y^2 + \frac{1-y}{2}\mathrm{d}\theta_1^2 + \frac{1+y}{2}\mathrm{d}\theta_2^2\,. \tag{K.7}$$

The momentum conjugate to q^α is then

$$p_\alpha \equiv \frac{\partial L}{\partial\dot{q}^\alpha} = 4\lambda G_{\alpha\beta}\dot{q}^\beta\,, \tag{K.8}$$

and the classical Hamiltonian

$$H_c = M_0 + \frac{1}{8\lambda}G^{\alpha\beta}p_\alpha p_\beta\,. \tag{K.9}$$

The quantum Hamiltonian operator is found by applying the quantization rules

$$H_q = M_0 - \frac{1}{8\lambda}\frac{1}{\sqrt{G}}\partial_\alpha\left(\sqrt{G}\,G^{\alpha\beta}\partial_\beta\right) = M_0 - \frac{1}{8\lambda}\nabla_\alpha\nabla^\alpha\,, \tag{K.10}$$

which is hermitian [177] with respect to the scalar product

$$\langle A|B\rangle \equiv \int \mathrm{d}q^3\sqrt{G}\, f_A(q)^* f_B(q)\,. \tag{K.11}$$

[24]The u_a's actually parametrize $S^3/\mathbb{Z}_2$ because the collective coordinates live in $SU(2)_V/\mathbb{Z}_2$. This means that u_a and $-u_a$ correspond to the same point . In the q^α coordinates, the identification is between (y, θ_1, θ_2) and $(y, \theta_1 + \pi, \theta_2 + \pi)$.

Spin and Isospin operators The classical Hamiltonian (K.9) is invariant under an $SO(4)$ rotation of the momentum p^α. Because $SO(4) \simeq SU(2) \times SU(2)$, this symmetry can be mapped to two SU(2) symmetries which are

- (Time-independent) isospin rotation of the fields, which acts on $V(t)$ as

$$V(t) \to WV(t) \quad , \quad W \in SU(2)\,. \tag{K.12}$$

- 3D (time-independent) spatial rotation, which acts on $V(t)$ as[25]

$$V(t) \to V(t)R \quad , \quad R \in SU(2)\,. \tag{K.13}$$

After quantization, there should be an isospin operator I^i that generates the symmetry of (K.12) and a spin operator S^i that generates the symmetry of (K.13)

$$[I^i, V] = \frac{\sigma^i}{2} V \quad , \quad [S^i, V] = V\frac{\sigma^i}{2}\,, \tag{K.14}$$

where the multiplication should be understood as the action on the wave function. The expression for the spin and isospin operators can be derived explicitly

$$\begin{cases} S^3 = -\frac{i}{2}(\partial_{\theta_1} + \partial_{\theta_2})\,, \\ S^+ = \frac{1}{\sqrt{2}} \mathrm{e}^{i(\theta_1+\theta_2)} \left(i\sqrt{1-y^2}\partial_y + \frac{1}{2}\sqrt{\frac{1+y}{1-y}}\partial_{\theta_1} - \frac{1}{2}\sqrt{\frac{1-y}{1+y}}\partial_{\theta_2} \right)\,, \\ S^- = \frac{1}{\sqrt{2}} \mathrm{e}^{-i(\theta_1+\theta_2)} \left(i\sqrt{1-y^2}\partial_y - \frac{1}{2}\sqrt{\frac{1+y}{1-y}}\partial_{\theta_1} + \frac{1}{2}\sqrt{\frac{1-y}{1+y}}\partial_{\theta_2} \right)\,, \end{cases} \tag{K.15}$$

$$\begin{cases} I^3 = -\frac{i}{2}(\partial_{\theta_1} - \partial_{\theta_2})\,, \\ I^+ = -\frac{1}{\sqrt{2}} \mathrm{e}^{i(\theta_1-\theta_2)} \left(i\sqrt{1-y^2}\partial_y + \frac{1}{2}\sqrt{\frac{1+y}{1-y}}\partial_{\theta_1} + \frac{1}{2}\sqrt{\frac{1-y}{1+y}}\partial_{\theta_2} \right)\,, \\ I^- = -\frac{1}{\sqrt{2}} \mathrm{e}^{-i(\theta_1-\theta_2)} \left(i\sqrt{1-y^2}\partial_y - \frac{1}{2}\sqrt{\frac{1+y}{1-y}}\partial_{\theta_1} - \frac{1}{2}\sqrt{\frac{1-y}{1+y}}\partial_{\theta_2} \right)\,, \end{cases} \tag{K.16}$$

where the raising and lowering are defined as usual

$$S^\pm = \frac{1}{\sqrt{2}}(S^1 \pm iS^2) \quad , \quad I^\pm = \frac{1}{\sqrt{2}}(I^1 \pm iI^2)\,. \tag{K.17}$$

S^i and I^i are checked to be hermitian with the scalar product of (K.11).

The Hamiltonian (K.10) then takes a simple form in terms of the spin and isospin operators

$$H_q = M_0 + \frac{1}{2\lambda}S^2 = M_0 + \frac{1}{2\lambda}I^2\,, \tag{K.18}$$

[25] Under a spatial rotation $x_i\sigma^i \to R^\dagger x_i \sigma^i R$, so the fields of (3.2.57)-(3.2.58) and (3.2.64) are invariant if $V(t)$ transforms as in (K.13) .

which makes it clear that the eigenstates of H_q have same spin and isospin and the eigenvalues are given by

$$E_s = M_0 + \frac{1}{2\lambda} s(s+1)\,, \tag{K.19}$$

where s refers to the spin. In particular the nucleon states correspond to $s = 1/2$ and their wavefunctions are easily found to be

$$\begin{aligned} |p\uparrow\rangle &= \tfrac{1}{\pi} z_1\,, \qquad & |n\uparrow\rangle &= \tfrac{i}{\pi} z_2\,, \\ |p\downarrow\rangle &= -\tfrac{i}{\pi}\bar{z}_2\,, \qquad & |n\downarrow\rangle &= -\tfrac{1}{\pi}\bar{z}_1\,, \end{aligned} \tag{K.20}$$

where z_1 and z_2 where defined in (K.5). The next level $s = 3/2$ corresponds to the isobar Δ states.

L Details of the formalism for neutrino transport

We review in this appendix a few results of QFT at finite temperature, that are useful for the formalism which describes neutrino transport.

L.1 Bosonic correlators at equilibrium

In this subsection, we review in more detail the derivation of the equilibrium properties obeyed by the chiral current real-time two-point functions. Specifically, we explain how the results (4.2.15) and (4.2.16) are obtained. Instead of the chiral-current 2-point function, we consider the case of a scalar operator

$$iG_B(x_1, x_2) \equiv \langle T_C J(x_1) J(x_2)\rangle\ , \tag{L.1}$$

where J is a scalar hermitian operator. The case of a vector such as the chiral current is completely analogous.

As mentioned in the text, the first result (4.2.15) is related to the invariance of the system at equilibrium under time-translation. At the level of the bosonic 2-point function (L.1), this invariance implies that

$$G_B(t_1, t_2) = G_B(\Delta t, 0) \equiv G_B(\Delta t) \quad , \quad \Delta t \equiv t_1 - t_2\,. \tag{L.2}$$

The expressions for the retarded and advanced propagators are the equivalent of (4.2.14)

$$iG_B^R(\Delta t) = \theta(\Delta t)\,\langle [J(\Delta t), J(0)]\rangle \quad , \quad iG^A(\Delta t) = -\theta(-\Delta t)\,\langle [J(0), J(-\Delta t)]\rangle\ . \tag{L.3}$$

Taking the complex conjugate of the retarded correlator gives

$$-\,i(G_B^R(\Delta t))^* = \theta(\Delta t)\,\langle [J(0), J(\Delta t)]\rangle = -iG_B^A(-\Delta t)\,, \tag{L.4}$$

so that

$$(G_B^R(\Delta t))^* = G_B^A(-\Delta t)\,. \tag{L.5}$$

In momentum space, (L.5) reads

$$(G_B^R(p^0))^* = G_B^A(p^0)\,. \tag{L.6}$$

When combined with the property (which does not require equilibrium)

$$G_B^A(p^0) = G_B^R(-p^0)\,, \tag{L.7}$$

(L.5) fixes the behavior of the retarded (and advanced) 2-point function under a change of sign of p^0

$$\mathrm{Im}\, G_B^R(-p^0) = -\mathrm{Im}\, G_B^R(p^0) \quad , \quad \mathrm{Re}\, G_B^R(-p^0) = \mathrm{Re}\, G_B^R(p^0)\,. \tag{L.8}$$

Likewise, time-translation invariance implies that the time-ordered and anti-time-ordered propagators are related by

$$(G_B^F(p^0))^* = -G_B^{\bar{F}}(p^0)\,. \tag{L.9}$$

We now focus on the result (4.2.16), which is a consequence of the KMS symmetry. Because the Hamiltonian $\hat{H}$ is the generator for time translation, the operator J can be shifted with an imaginary time according to

$$J(t) = \mathrm{e}^{-\beta\hat{H}} J(t - i\beta)\mathrm{e}^{\beta\hat{H}}\,. \tag{L.10}$$

If we substitute this equality in the $G_B^<$ propagator, we obtain

$$\begin{aligned}
iG_B^<(\Delta t) &= \langle J(0)J(\Delta t)\rangle \\
&= \mathrm{Tr}\left[\mathrm{e}^{-\beta(\hat{H}-\mu\hat{N})} J(0)\mathrm{e}^{-\beta\hat{H}} J(\Delta t - i\beta)\mathrm{e}^{\beta\hat{H}}\right] \\
&= \mathrm{Tr}\left[\mathrm{e}^{\beta\mu\hat{N}} J(0)\mathrm{e}^{-\beta\hat{H}} J(\Delta t - i\beta)\right] \\
&= \mathrm{Tr}\left[\mathrm{e}^{-\beta\mu\hat{N}} J(\Delta t - i\beta)\mathrm{e}^{\beta\mu\hat{N}} J(0)\mathrm{e}^{-\beta(\hat{H}-\mu\hat{N})}\right] \\
&= \mathrm{Tr}\left[\mathrm{e}^{\beta\mu} J(\Delta t - i\beta)J(0)\mathrm{e}^{-\beta(\hat{H}-\mu\hat{N})}\right] \\
&= \mathrm{e}^{\beta\mu}\mathrm{Tr}\left[\mathrm{e}^{-\beta(\hat{H}-\mu\hat{N})} J(\Delta t - i\beta)J(0)\right] \\
&= \mathrm{e}^{\beta\mu} iG_B^>(\Delta t - i\beta)\,,
\end{aligned} \tag{L.11}$$

where $\hat{N}$ is the boson number operator, and μ the associated chemical potential. We used the cyclicity of the trace to go from the second to the third line, and the fact that $[\hat{N}, J] = J$ to go from the third to the fourth line. In momentum space (L.11) becomes

$$G_B^<(p) = \mathrm{e}^{-\beta(p^0-\mu)} G_B^>(p)\,. \tag{L.12}$$

Note that the bosonic chemical potentials are equal to zero in the nuclear matter. This is why no chemical potential appears in (4.2.16).

L.2 Free fermion propagator

We review here the derivation of the equilibrium free fermion propagator $G^0(x_1, x_2)$ at finite temperature and density. The expression for the latter is

$$iG^0_{\alpha\beta}(x_1, x_2) \equiv \frac{\mathrm{Tr}\left[\rho_0 T_C\{\psi_\alpha(x_1)\bar{\psi}_\beta(x_2)\}\right]}{\mathrm{Tr}\left[\rho_0\right]}\,, \tag{L.13}$$

where $\rho_0 \equiv \exp\left(-\beta(\mathcal{H}_0 - \mu N_0)\right)$ is the equilibrium grand canonical density matrix. The equilibrium Hamiltonian and particle number operators can be expressed in terms of the fermion and anti-fermion creation and annihilation operators as

$$N_0 = \int \frac{\mathrm{d}^3p}{(2\pi)^3 2E_p}\left(\mathrm{a}^\dagger_\mathrm{p}\mathrm{a}_\mathrm{p} - \mathrm{b}^\dagger_\mathrm{p}\mathrm{b}_\mathrm{p}\right) \quad , \quad \mathcal{H}_0 = \int \frac{\mathrm{d}^3p}{(2\pi)^3 2E_p}\, E_p\left(\mathrm{a}^\dagger_\mathrm{p}\mathrm{a}_\mathrm{p} + \mathrm{b}^\dagger_\mathrm{p}\mathrm{b}_\mathrm{p}\right), \tag{L.14}$$

where $E_p = \sqrt{\vec{p}^2 + m^2}$ is the fermion on-shell energy. We dropped the zero-point energy, which yields the same factor in the numerator and denominator of expectation values such as (L.13). Starting from the canonical anti-commutation relations of the fermionic creation and annihilation operators

$$\{\mathrm{a}_\mathrm{p}, \mathrm{a}^\dagger_{\mathrm{p}'}\} = (2\pi)^3 2E_p\delta\big(\vec{p} - \vec{p'}\big) \quad , \quad \{\mathrm{b}_\mathrm{p}, \mathrm{b}^\dagger_{\mathrm{p}'}\} = (2\pi)^3 2E_p\delta\big(\vec{p} - \vec{p'}\big)\,, \tag{L.15}$$

we obtain that

$$\{\mathrm{e}^{-\beta(\mathcal{H}_0-\mu N_0)}, \mathrm{a}_\mathrm{p}\} = \mathrm{e}^{-\beta(\mathcal{H}_0-\mu N)}\left(1 + \mathrm{e}^{-\beta(E_p-\mu)}\right)\mathrm{a}_\mathrm{p}\,, \tag{L.16}$$

$$\{\mathrm{e}^{-\beta(\mathcal{H}_0-\mu N_0)}, \mathrm{b}_\mathrm{p}\} = \mathrm{e}^{-\beta(\mathcal{H}_0-\mu N)}\left(1 + \mathrm{e}^{-\beta(E_p+\mu)}\right)\mathrm{b}_\mathrm{p}\,. \tag{L.17}$$

These commutators can then be used to compute the expectation values

$$\frac{\mathrm{Tr}\left[\rho_0\, \mathrm{a}^\dagger_\mathrm{p}\mathrm{a}_{\mathrm{p}'}\right]}{\mathrm{Tr}\left[\rho_0\right]} = (2\pi)^3 2E_p n_f(E_p - \mu)\delta\big(\vec{p} - \vec{p'}\big)\,, \tag{L.18}$$

$$\frac{\mathrm{Tr}\left[\rho_0\, \mathrm{b}^\dagger_\mathrm{p}\mathrm{b}_{\mathrm{p}'}\right]}{\mathrm{Tr}\left[\rho_0\right]} = (2\pi)^3 2E_p n_f(E_p + \mu)\delta\big(\vec{p} - \vec{p'}\big)\,, \tag{L.19}$$

where n_f is the Fermi-Dirac distribution

$$n_f(E) \equiv \frac{1}{\mathrm{e}^{\beta E} + 1}\,. \tag{L.20}$$

In terms of the creation and annihilation operators, the fermionic spinor field in the interaction picture reads

$$\psi_\alpha(x) = \sum_{s=\pm}\int \frac{\mathrm{d}^3p}{(2\pi)^3 2\mathrm{E}_\mathrm{p}}\left[\mathrm{a}_{\mathrm{s,p}}u_{s,\alpha}(\vec{p})\mathrm{e}^{-i\mathrm{p}\cdot x} + \mathrm{b}^\dagger_{\mathrm{s,p}}v_{s,\alpha}(\vec{p})\mathrm{e}^{i\mathrm{p}\cdot x}\right]. \tag{L.21}$$

Substituting (L.21) into (L.13) and using (L.18)-(L.19) gives the final result[26] for the free fermionic propagator at finite temperature and density

$$iG^0_{\alpha\beta}(x_1,x_2) = \int \frac{\mathrm{d}^3p}{(2\pi)^3 2\mathrm{E_p}} \Big[(\not{p}_+ + m)\left(\theta_C(x_1^0-x_2^0) - n_f(E_p-\mu)\right)\mathrm{e}^{-ip\cdot(x_1-x_2)} \\ +(\not{p}_- + m)\left(\theta_C(x_2^0-x_1^0) - n_f(E_p+\mu)\right)\mathrm{e}^{ip\cdot(x_1-x_2)}\Big]\,, \quad \text{(L.22)}$$

where θ_C is the Heaviside function on the CTP and we defined

$$\not{p}_\pm = \pm E_p\gamma_0 - \vec{p}\cdot\vec{\gamma}\,. \quad \text{(L.23)}$$

In particular, the Wightman functions for the free quasi-particles are given in momentum space by

$$iG^{0,<}(k) = -(\not{k} + m + \mu\gamma_0)\frac{\pi}{E_p}\Big[n_f(E_p-\mu)\delta(E_p-k^0-\mu) - \\ -(1-n_f(E_p+\mu))\delta(E_p+k^0+\mu)\Big]\,, \quad \text{(L.24)}$$

$$iG^{0,>}(k) = (\not{k} + m + \mu\gamma_0)\frac{\pi}{E_p}\Big[(1-n_f(E_p-\mu))\delta(E_p-k^0-\mu) - \\ -n_f(E_p+\mu)\delta(E_p+k^0+\mu)\Big]\,. \quad \text{(L.25)}$$

To go from (L.22) to (L.24)-(L.25), we used the fact that the 0-component of the quasi-particle momentum is shifted with respect to that of the particle as

$$k^0 = p^0 - \mu\,. \quad \text{(L.26)}$$

L.3 A discussion of the "quasi-particle" approximation

In this sub-appendix, we discuss in more detail the underlying assumptions of what is referred to as the quasi-particle approximation (introduced in section 4.2.2.2). The starting point of this approximation is more of a *near-equilibrium* approximation. At equilibrium, the fermionic Wightman functions obey relations similar to (4.2.17)-(4.2.18)

$$G^<_{\alpha\beta}(p_\nu) = -n_f(p^0_\nu - \mu_\nu)\rho_{\alpha\beta}(p_\nu)\,, \quad \text{(L.27)}$$

$$G^>_{\alpha\beta}(p_\nu) = (1-n_f(p^0_\nu - \mu_\nu))\rho_{\alpha\beta}(p_\nu)\,, \quad \text{(L.28)}$$

[26] Recall the spinor sum rules which in this normalization read $\sum_{s=\pm} u_{s,\alpha}(\mathbf{p})\bar{u}_{s,\beta}(\mathbf{p}) = (\not{p}+m)_{\alpha\beta}$ and $\sum_{s=\pm} v_{s,\alpha}(\mathbf{p})\bar{v}_{s,\beta}(\mathbf{p}) = (\not{p}-m)_{\alpha\beta}$.

where $\rho_{\alpha\beta}$ is the equilibrium spectral density. The approximation then assumes that the neutrinos are sufficiently close to equilibrium for the Wightman functions to be parametrized as

$$G^{<}_{\alpha\beta}(X,p_\nu) = -F(X,p^0_\nu,\vec{p}^{\,2}_\nu)\rho_{\alpha\gamma}(X,p^0_\nu,\vec{p}_\nu)\frac{\delta_{\gamma\beta}-\gamma^5_{\gamma\beta}}{2}\,, \tag{L.29}$$

$$G^{>}_{\alpha\beta}(X,p_\nu) = (1-F(X,p^0_\nu,\vec{p}^{\,2}_\nu))\frac{\delta_{\alpha\gamma}-\gamma^5_{\alpha\gamma}}{2}\rho_{\gamma\beta}(X,p^0_\nu,\vec{p}_\nu)\,, \tag{L.30}$$

where F is the neutrino distribution function, and the spectral density ρ is further assumed to be close to its equilibrium value, up to corrections in the coupling. Note the presence of the projectors $(1-\gamma^5)/2$, that implement the fact that the Standard Model neutrinos are left-handed.

Upon assuming the ansatz (L.29)-(L.30), the quasi-particle approximation is then a consequence of the weakly-coupled nature of the neutrino interactions. That is, the equilibrium spectral density is equal to the free spectral density, up to corrections from the interactions

$$\rho(p^0_\nu,\vec{p}_\nu) = \frac{\pi}{E_\nu}\not{p}_\nu\big(\delta(p^0_\nu-E_\nu)-\delta(p^0_\nu+E_\nu)\big)+\mathcal{O}(G_F^2) \quad , \quad E_\nu\equiv|\vec{p}_\nu|\,. \tag{L.31}$$

Another consequence of the weak coupling is that, at leading order, the energy of the neutrino quasi-particles is shifted with respect to that of the neutrinos as in (L.26)

$$k^0_\nu = p^0_\nu-\mu_\nu+\mathcal{O}(G_F^2)\,, \tag{L.32}$$

so that the Wightman functions for the quasi-neutrinos are given by

$$G^{<}_{\nu,\alpha\beta}(X,k_\nu) = -F_\nu(X,k^0_\nu,\vec{k}^{\,2}_\nu)\rho_{\alpha\gamma}(X,k^0_\nu+\mu_\nu,\vec{k}_\nu)\frac{\delta_{\gamma\beta}-\gamma^5_{\gamma\beta}}{2}\,, \tag{L.33}$$

$$G^{>}_{\nu,\alpha\beta}(X,k_\nu) = (1-F_\nu(X,k^0_\nu,\vec{k}^{\,2}_\nu))\frac{\delta_{\alpha\gamma}-\gamma^5_{\alpha\gamma}}{2}\rho_{\gamma\beta}(X,k^0_\nu+\mu_\nu,\vec{k}_\nu)\,. \tag{L.34}$$

The quasi-neutrino distribution function F_ν is split into neutrino and anti-neutrino distributions as

$$F_\nu(X,k^0_\nu,\vec{k}^{\,2}_\nu) = f_\nu(X,k^0_\nu,\vec{k}^{\,2}_\nu)\theta(k^0_\nu+\mu_\nu)+\big(1-f_{\bar\nu}(X,k^0_\nu,\vec{k}^{\,2}_\nu)\big)\theta(-k^0_\nu-\mu_\nu)\,. \tag{L.35}$$

The ansatz (L.33) is then substituted in the Kadanoff-Baym (KB) equation (4.2.31), that we reproduce here for convenience

$$i\partial^X_\mu \mathrm{Tr}\left\{\gamma^\mu G^<(X,k)\right\} = -\mathrm{Tr}\left\{G^>(X,k)\Sigma^<(X,k)-\Sigma^>(X,k)G^<(X,k)\right\}\,. \tag{L.36}$$

There is a similar equation for the other Wightman function

$$i\partial^X_\mu \mathrm{Tr}\left\{\gamma^\mu G^>(X,k)\right\} = -\mathrm{Tr}\left\{G^>(X,k)\Sigma^<(X,k)-\Sigma^>(X,k)G^<(X,k)\right\}\,. \tag{L.37}$$

The difference of the two KB equations implies that a specific trace of the spectral function is preserved by the kinetic evolution[27]

$$i\partial_\mu^X \mathrm{Tr}\left\{\gamma^\mu \rho(X,k)\right\} = 0\,. \tag{L.38}$$

The equation for the distribution functions is then given by

$$\begin{aligned} i\partial_\mu^X F_\nu(X,k)\mathrm{Tr}\left\{\gamma^\mu\rho(X,k)\right\} = -\mathrm{Tr}\big\{&F_\nu(X,k)\rho(X,k)\Sigma^<(X,k)+\\ &+(1-F_\nu)\Sigma^>(X,k)\rho(X,k)\big\}\,. \end{aligned} \tag{L.39}$$

At leading order in the weak coupling, this reduces to the Boltzmann equations for the neutrino and anti-neutrino distribution functions, (4.2.56) and (4.2.57).

In the general case, the ansatz for the Wightman functions contains several fields, that are organized according to the expansion in the generators of the Clifford algebra, with the condition of SO(3) symmetry

$$\begin{aligned} G^>(X,k_\nu^0,\vec{k}_\nu^2) = &\,\mathcal{S}(X,k_\nu^0,\vec{k}_\nu^2) + i\gamma^5\mathcal{P}(X,k_\nu^0,\vec{k}_\nu^2)+\\ &+\gamma^0\mathcal{V}_{(0)}(X,k_\nu^0,\vec{k}_\nu^2) + k_i\gamma^i\mathcal{V}_{(1)}(X,k_\nu^0,\vec{k}_\nu^2)+\\ &+\gamma^5\gamma^0\mathcal{A}_{(0)}(X,k_\nu^0,\vec{k}_\nu^2) + k_i\gamma^5\gamma^i\mathcal{A}_{(1)}(X,k_\nu^0,\vec{k}_\nu^2)+\\ &+k_i[\gamma^0,\gamma^i]\mathcal{D}(X,k_\nu^0,\vec{k}_\nu^2)\,. \end{aligned} \tag{L.40}$$

Imposing that the Standard Model neutrinos are left-handed further reduces the form of the ansatz

$$G^>(X,k_\nu^0,\vec{k}_\nu^2) = \frac{1-\gamma^5}{2}\Big(\gamma^0\mathcal{V}_{(0)}(X,k_\nu^0,\vec{k}_\nu^2) + k_i\gamma^i\mathcal{V}_{(1)}(X,k_\nu^0,\vec{k}_\nu^2)\Big)\,. \tag{L.41}$$

This can be rewritten in terms of an effective neutrino chemical potential out of equilibrium μ_{eff}

$$G^>(X,k_\nu^0,\vec{k}_\nu^2) = \frac{1-\gamma^5}{2}\mathcal{F}(X,k_\nu^0,\vec{k}_\nu^2)\Big(\not{k}+\mu_{\text{eff}}(X,k_\nu^0,\vec{k}_\nu^2)\gamma^0\Big)\,, \tag{L.42}$$

where the field $\mathcal{F}$ contains information about the spectrum and the distribution of neutrinos. The quasi-particle approximation assumes that μ_{eff} is close to the chemical potential of β-equilibrium, and that $\mathcal{F}$ can be factorized as a distribution function, times the sum of Dirac delta functions that appear in the leading order equilibrium spectral density (L.31). Instead of a single Boltzmann equation for the neutrino distribution function, the general transport problem with the ansatz (L.42) will involve two coupled equations for the two scalar fields μ_{eff} and $\mathcal{F}$. The formalism and computational setup we have in chapter 4, allows then the evaluation of the two independent distributions far from equilibrium.

[27] In deriving (L.38) and (L.39), we use the fact that the trace of $\gamma^5\gamma^{\mu_1}\dots\gamma^{\mu_n}$ is zero for all $n \leq 3$.

M Weak vertices for neutrino interactions

The charged current neutrino self-energy at leading order in the electroweak couplings is computed from the diagram in figure 4.6. The expression for the weak vertices appearing in this diagram is given by the Glashow-Weinberg-Salam (GSW) theory. We are interested in energy scales much lower than the W boson mass, in which regime the weak vertices are well described by a low energy effective theory, where the W and Z boson exchanges are replaced by weak current contact interactions. For easy reference, the purpose of this appendix is to give a review of the form that the effective vertices take.

After electroweak symmetry breaking, the GSW Lagrangian contains terms that couple the electroweak vector bosons to the fermion electroweak currents

$$S_{eff} = \int \left[-\frac{g_W}{\sqrt{2}} W^{\pm}_{\mu} (J^{\mu}_{\pm} + \bar{J}^{\mu}_{\pm}) + \frac{g_W}{\cos\theta_W} Z_{\mu} (J^{\mu}_0 + \bar{J}^{\mu}_0) + e A_{\mu} (J^{\mu}_{\rm em} + \bar{J}^{\mu}_{\rm em}) \right] \tag{M.1}$$

with g_W the electroweak coupling constant, θ_W the Weinberg angle and $e = g_W \sin\theta_W$ the elementary charge. From left to right, the currents that appear are respectively the charged, neutral and electromagnetic currents. The currents without bar are the lepton currents and those with the bar are the QCD currents made out of quarks.

Integrating out (classically) the weak bosons we get the quadratic effective action

$$S_{eff'} = \int \left[\frac{g_W^2}{2} (J^{\mu}_{+} + \bar{J}^{\mu}_{+}) D^W_{\mu\nu} (J^{\nu}_{-} + \bar{J}^{\nu}_{-}) + h.c. + \frac{g_W^2}{\cos^2\theta_W} (J^{\mu}_0 + \bar{J}^{\mu}_0) D^Z_{\mu\nu} (J^{\nu}_0 + \bar{J}^{\nu}_0) + \right.$$
$$\left. + e A_{\mu} (J^{\mu}_{\rm em} + \bar{J}^{\mu}_{\rm em}) + \mathcal{O}(e G_F^2) \right] \tag{M.2}$$

where $D^{W,Z}$ are the tree-level gauge boson propagators in a given gauge. The higher order corrections come from the cubic and quartic interactions between the electroweak gauge bosons, as well as Higgs interactions. They start at order $\mathcal{O}(eG_F^2)$, with the leading contribution coming from the $WW\gamma$ vertex. In the limit where all momenta are much smaller than M_W, the W, Z propagators are replaced by Dirac deltas and we obtain

$$S_{eff'} = \int \left[2\sqrt{2} G_F \Big((J^{\mu}_{+} + \bar{J}^{\mu}_{+}) \eta_{\mu\nu} (J^{\nu}_{-} + \bar{J}^{\nu}_{-}) + h.c. + 2 (J^{\mu}_0 + \bar{J}^{\mu}_0) \eta_{\mu\nu} (J^{\nu}_0 + \bar{J}^{\nu}_0) \Big) + \right.$$
$$\left. + e A_{\mu} (J^{\mu}_{\rm em} + \bar{J}^{\mu}_{\rm em}) + \mathcal{O}(e G_F^2) \right] \tag{M.3}$$

This can be decomposed as

$$S_{eff'} = S_W + S_S + S_{J^2} + S_{\gamma} \tag{M.4}$$

with

$$S_W = 2\sqrt{2} G_F \int \left[J^{\mu}_{+} J_{-\mu} + h.c. + 2 J^{\mu}_0 J_{0\mu} \right] + \mathcal{O}(e G_F^2) \tag{M.5}$$

$$S_S = 4\sqrt{2}G_F \int \left[J_+^\mu \bar{J}_{-\mu} + h.c. + 2J_0^\mu \bar{J}_{0\mu}\right] + \mathcal{O}(eG_F^2) \tag{M.6}$$

$$S_{J^2} = 2\sqrt{2}G_F \int \left[\bar{J}_+^\mu \bar{J}_{-\mu} + h.c. + 2\bar{J}_0^\mu \bar{J}_{0\mu}\right] + \mathcal{O}(eG_F^2) \tag{M.7}$$

and

$$S_\gamma = \int \left[eA_\mu(J_{\rm em}^\mu + \bar{J}_{\rm em}^\mu)\right] + \mathcal{O}(eG_F^2) \tag{M.8}$$

S_W is the standard leptonic Fermi interaction and its neutral counterpart, whereas S_γ gives the electromagnetic interaction of the fermions. S_S is the interaction of leptons with the QCD weak current, and S_{J^2} is the weak interaction of the strong currents. It is small and is therefore not expected to play an important role in the strongly-coupled quark-gluon plasma. It can be included if necessary in the holographic calculation by changing the boundary conditions of the gauge fields, according to the standard double-trace dictionary, [106]. The higher order corrections that start at order $\mathcal{O}(eG_F^2)$ include tree level terms, as well as electroweak loop corrections. These terms include higher-point couplings between the weak currents, as well as couplings of the charged current to the photon.

We now want to compute the effective interaction for neutrinos in the strong plasma and for this we must compute

$$e^{-W_{eff}} = \langle e^{-S_S} \rangle \tag{M.9}$$

where the expectation value is obtained in the state (or ensemble) of strongly coupled matter. This can be expanded as

$$W_{eff} = 4\sqrt{2}G_F \int \Big[2J_+^\mu \langle \bar{J}_{-\mu}\rangle + h.c. + 4J_0^\mu \langle \bar{J}_{0\mu}\rangle + \\ + 4\sqrt{2}G_F \Big(J_+^\mu J_{-\nu} \langle \bar{J}_{-\mu} \bar{J}_+^\nu\rangle + h.c. + 2J_0^\mu J_{0\nu}\langle \bar{J}_{0\mu}\bar{J}_0^\nu\rangle\Big) + \mathcal{O}(eG_F^2)\Big] \tag{M.10}$$

The contact interactions with the one point functions contribute to the neutrino chemical potential μ_ν, so they can be absorbed in the definition of μ_ν. Then, the effective action for the neutrino interactions contains the term quadratic in the neutrino current plus higher order corrections

$$W_{eff} = 32G_F^2 \int \left[J_+^\mu J_{-\nu}\langle \bar{J}_{-\mu}\bar{J}_+^\nu\rangle + h.c. + 2J_0^\mu J_{0\nu}\langle \bar{J}_{0\mu}\bar{J}_0^\nu\rangle + \mathcal{O}(eG_F^2)\right]$$

N Background solution for the transport analysis

We review in this appendix the derivation of the Reissner-Nordström background solution (4.3.11)-(4.3.14).

The equations of motion from the action (4.3.1) are the Einstein-Yang-Mills equations

$$R_{MN} - \frac{1}{2}\left(R + \frac{12}{\ell^2}\right) g_{MN} = -\frac{w_0^2 \ell^2}{4N_c} \mathrm{Tr}\Big\{ \mathbf{F}^{(L)}{}_{MP} \mathbf{F}^{(L)P}{}_{N} + \frac{1}{4} \mathbf{F}^{(L)}_{PQ} \mathbf{F}^{(L)PQ} g_{MN} + \\ + (L \leftrightarrow R) \Big\}, \tag{N.1}$$

$$D_M^{(L/R)} \Big(\sqrt{-g} F^{(L/R)MN} \Big) = 0 \,, \tag{N.2}$$

with $D_M^{(L/R)}$ the Yang-Mills covariant derivatives

$$D_M^{(L)} \equiv \partial_M - i[L_M, \,.\,] \quad , \quad D_M^{(R)} \equiv \partial_M - i[R_M, \,.\,] \,. \tag{N.3}$$

The background solution is found by starting from the ansatz

$$\mathrm{ds}^2 = \mathrm{e}^{2A(r)} \left(-f(r) \mathrm{dt}^2 + f(r)^{-1} \mathrm{dr}^2 + \vec{\mathrm{dx}}^2 \right) , \tag{N.4}$$

$$\mathbf{R}_M = \mathbf{L}_M = \frac{1}{4} \delta^0_M \hat{V}_0(r) \mathbb{I}_2 \,. \tag{N.5}$$

This ansatz fixes the gauge for the gauge field, up to a shift by a constant. As we shall see below, the regular boundary conditions in the IR (N.10) remove this degeneracy.

Substituting the ansatz (N.4)-(N.5) into the equations of motion (N.1)-(N.2) results in the following system of equations for the ansatz fields

$$\partial_r^2 A - (\partial_r A)^2 = 0 \,, \tag{N.6}$$

$$\partial_r A \big(\partial_r f + 4 \partial_r A f(r) \big) - \frac{4}{\ell^2} \mathrm{e}^{2A(r)} + \frac{w_0^2 \ell^2}{48 N_c} \mathrm{e}^{-2A(r)} (\partial_r \hat{V}_0)^2 = 0 \,, \tag{N.7}$$

$$\partial_r \Big(\mathrm{e}^{A(r)} \partial_r \hat{V}_0 \Big) = 0 = 0 \,. \tag{N.8}$$

The two integration constants of (N.6) correspond to translations and rescalings of r. We fix the definition of the coordinate r by writing the solution as

$$A(r) = \log \left(\frac{\ell}{r} \right) , \tag{N.9}$$

which implies in particular that the boundary is located at $r = 0$. We look for a solution with a horizon at $r = r_H$, where the blackening function $f(r)$ vanishes. For the gauge field to be regular at the horizon, the time component should vanish

$$\hat{V}_0(r_H) = 0 \,. \tag{N.10}$$

This implies that the solution of (N.8) is given by

$$\hat{V}_0 = 2\mu \left(1 - \left(\frac{r}{r_H}\right)^2\right) , \tag{N.11}$$

with the boundary source μ corresponding to the quark number chemical potential. Finally, the solutions for the gauge fields and the scale factor $A(r)$ can be substituted in (N.7), which yields an equation for $f(r)$

$$\partial_r f - \frac{4}{r}(f(r) - 1) - \frac{w_0^2 \mu^2}{3N_c} \left(\frac{r}{r_H}\right)^4 r = 0 . \tag{N.12}$$

The solution takes the form

$$f(r) = 1 - \left(\frac{r}{r_H}\right)^4 \left(1 + \frac{w_0^2}{6N_c}\mu^2 r_H^2\right) + \frac{w_0^2}{6N_c}\mu^2 r_H^2 \left(\frac{r}{r_H}\right)^6 . \tag{N.13}$$

To avoid a conical singularity of the Euclidean solution at finite temperature, the derivative of $f(r)$ at the horizon should be related to the field theory temperature

$$f'(r_H) = -4\pi T . \tag{N.14}$$

This condition results in an equation for the horizon radius r_H

$$\frac{w_0^2}{6N_c}\mu^2 r_H^2 = 2(1 - \pi T r_H) , \tag{N.15}$$

whose solution determines the location of the black-hole horizon as a function of the chemical potential μ and the temperature

$$r_H(T, \mu) = \frac{2}{\pi T} \left(1 + \sqrt{1 + \frac{w_0^2}{3N_c}\frac{\mu^2}{\pi^2 T^2}}\right)^{-1} . \tag{N.16}$$

Note that (N.15) allows to rewrite $f(r)$ in the form presented in the text

$$f(r) = 1 - \left(\frac{r}{r_H}\right)^4 (1 + 2(1 - \pi T r_H)) + 2(1 - \pi T r_H) \left(\frac{r}{r_H}\right)^6 . \tag{N.17}$$

O Parameters of the bulk action for neutrino transport

The bulk action (4.3.1) possesses two parameters: the five-dimensional Planck mass $M\ell$, which controls the overall normalization of the action, and the flavor coupling w_0. We

detail in this appendix how the values of these parameters are fixed by matching to QCD data.

First, the 5-dimensional Planck mass $M\ell$ is fixed by imposing that the zero-chemical potential limit of the pressure be that of a free quark-gluon plasma

$$p = \frac{\pi^2 N_c^2}{45} T^4 \left(1 + \frac{7N_f}{4N_c}\right) . \tag{O.1}$$

Lattice results [40] indicate that, for temperatures equal to a few times the deconfining temperature, the pressure in the quark-gluon plasma is already close (within about 20%) to the ideal result (O.1). Setting $(M\ell)$ to match (O.1) will therefore ensure that the thermodynamics of the holographic model is close to that of QCD in the deconfined phase. The pressure of the holographic model is computed from the grand-canonical potential (4.3.18). At $\mu \ll T$, it is given by

$$p = (M\ell)^3 \left[N_c^2 (\pi T)^4 + \frac{1}{8} N_f N_c w_0^2 (\pi T)^2 \mu^2 + \mathcal{O}(\mu^4)\right] . \tag{O.2}$$

(O.2) matches (O.1) at $\mu = 0$ if $(M\ell)^3$ is equal to

$$(M\ell)^3_{\text{free}} = \frac{13}{6} \frac{1}{45\pi^2} , \tag{O.3}$$

where the number of flavors was set to $N_f = 2$, and that of colors to $N_c = 3$.

As far as the parameter w_0 is concerned, it can be fixed such that the baryon number susceptibility at zero density agrees with the ideal Fermi gas result. As for the pressure, it was observed to give a good approximation to the exact result for the quark-gluon plasma on the lattice [205]. The baryon number susceptibility is defined as the first non-trivial cumulant of the pressure at $\mu_B = \mu_3 = 0$

$$\chi_B = \left.\frac{\partial^2 p}{\partial^2 \mu_B}\right|_{\mu_B = 0} . \tag{O.4}$$

From (O.2) it is equal to

$$\chi_B = \frac{N_f}{2N_c} w_0^2 (M\ell)^3 (\pi T)^2 , \tag{O.5}$$

whereas the ideal Fermi gas result is

$$\chi_{B,free} = \frac{N_f}{3N_c} T^2 . \tag{O.6}$$

Matching the two results fixes the value of w_0 to be

$$\left(w_0^2 (M\ell)^3\right)_{\text{free}} = \frac{2}{3\pi^2} . \tag{O.7}$$

In the numerical calculations done in this chapter 4, we used the values of the parameters given by (O.3) and (O.7). For comparison, we discuss below another choice for the value of the parameter w_0.

UV limit of the two-point function Fixing w_0 as in (O.7) also implies that the holographic two-point function agrees with the perturbative QCD result in the UV limit [161, 164]. Here, we will prove explicitly this result. So we now consider the Euclidean version of the correlator (4.4.23) and (4.4.24) in the UV limit where $\omega^2 + \vec{k}^2$ goes to infinity. In this case the temperature and chemical potential become irrelevant and the computation can be equivalently performed in (Euclidean) AdS space-time. It follows that the Lorentz invariance of the theory is effectively restored and the Euclidean correlator can be written as

$$\left\langle J_\lambda^{(L)} J_\sigma^{(L)} \right\rangle^E (k) = P_{\lambda\sigma}(k) \Pi^E_{(L)}(k) \,, \tag{O.8}$$

where the 4-dimensional projector transverse to k was defined in (4.4.7). The function $\Pi(k)$ is computed following the standard holographic method, starting from the perturbation

$$\delta L_\mu(r;x) = \int \frac{\mathrm{d}k^4}{(2\pi)^4} \mathrm{e}^{ik.x} \mathcal{L}^{(0)}_{\mu,k} \psi(r) \,, \tag{O.9}$$

which obeys the equation of motion

$$\partial_r^2 \psi - \frac{1}{r} \partial_r \psi - k^2 \psi = 0 \,, \tag{O.10}$$

together with a boundary condition fixing the normalization of the perturbation

$$\psi(0) = 1 \,. \tag{O.11}$$

The solution of this differential problem can be expressed in terms of a modified Bessel function of the second type

$$\psi(r) = kr K_1(kr) \,, \tag{O.12}$$

and the Euclidean on-shell action is

$$S_{on-shell} = -\frac{1}{8\ell} (M\ell)^3 w_0^2 N_c \int_{r=\epsilon} \mathrm{d}^4 k \frac{\ell}{r} \mathcal{L}^{(0)}_\mu(-k) P^{\mu\nu}(k) \mathcal{L}^{(0)}_\nu(k) \partial_r \psi \psi \,. \tag{O.13}$$

Near the boundary, K_1 has the following behavior

$$K_1(kr) \underset{r\to 0}{\sim} \frac{1}{kr} + \frac{1}{2} kr \log(kr) + C_0 kr \,, \tag{O.14}$$

where C_0 is a constant that does not depend on k. This implies that the on-shell action has a logarithmic divergence which is removed by the appropriate counter-term. This leaves the renormalized on-shell action

$$S_{ren} = -\frac{1}{16} (M\ell)^3 w_0^2 N_c \int_{r=\epsilon} \mathrm{d}^4 k \mathcal{L}^{(0)}_\mu(-k) P^{\mu\nu}(k) \mathcal{L}^{(0)}_\nu(k) k^2 \log(k^2) + \mathcal{O}(k^2) \,, \tag{O.15}$$

and

$$\Pi^{E}_{(L)}(k) = -\frac{N_c}{8}(M\ell)^3 w_0^2 k^2 \log(k^2)\,. \tag{O.16}$$

Identifying with the perturbative QCD result

$$\Pi^{E}_{(L),\mathrm{QCD}}(k) = -\frac{N_c}{8}\frac{2}{3\pi^2}k^2\log(k^2)\,, \tag{O.17}$$

fixes the value of w_0 in terms of $M\ell$

$$w_0^2 = \frac{2}{3\pi^2(M\ell)^3}\,, \tag{O.18}$$

which agrees with the value derived from the susceptibility (O.7).

P Eddington-Finkelstein coordinates

The general solution to the equations of motion (4.4.16) and (4.4.18) behaves near the horizon as the superposition of an infalling and outgoing waves

$$\mathcal{L}^{\perp} = c_1(r_H - r)^{-i\gamma} + c_2(r_H - r)^{i\gamma} \quad , \quad E^{\parallel} = d_1(r_H - r)^{-i\gamma} + d_2(r_H - r)^{i\gamma} \quad , \quad \gamma \equiv \frac{\omega}{4\pi T}\,. \tag{P.1}$$

Imposing infalling boundary conditions amounts to setting $c_2 = d_2 = 0$, and the infalling solution can be rewritten as

$$\mathcal{L}^{\perp} = c\exp\left(-i\gamma\log\left(1-\frac{r}{r_H}\right)\right) \quad , \quad E^{\parallel} = d\exp\left(-i\gamma\log\left(1-\frac{r}{r_H}\right)\right), \tag{P.2}$$

which makes it apparent that the solution oscillates very fast near the horizon as soon as ω in non-zero. When solving the equations of motion numerically, such fast oscillating solutions require high numerical precision to obtain good accuracy for the behavior of the solution near the boundary. To avoid working with such solutions, it is more convenient to do the numerical calculations in the natural coordinates for infalling solutions, that are the infalling Eddington-Finkelstein coordinates. The change of coordinate is given by

$$\vec{x} \to \vec{x} \quad , \quad t \to u = t - r^*(r) \quad , \quad r \to r\,, \tag{P.3}$$

where the tortoise coordinate $r^*(r)$ is such that

$$\frac{\mathrm{d}r^*}{\mathrm{d}r} = \frac{1}{f(r)}\,. \tag{P.4}$$

Then, the Fourier transform of the gauge field perturbation transforms as

$$\mathcal{L}_{\mu,k}(r) \to \mathrm{e}^{i\omega r^*(r)}\mathcal{L}_{\mu',k}(r)\,, \tag{P.5}$$

which can be decomposed into

$$\mathcal{L}^{\perp}(r) \to \mathrm{e}^{i\omega r^*}\mathcal{F}^{\perp}(r) \quad , \quad E^{\parallel}(r) \to \mathrm{e}^{i\omega r^*}\mathcal{F}^{\parallel}(r)\,. \tag{P.6}$$

Notice that, since near the horizon the tortoise coordinate behaves as

$$r^*(r) \sim -\frac{1}{4\pi T}\log\left(1-\frac{r}{r_H}\right), \tag{P.7}$$

the fields $\mathcal{F}^{\perp}$ and $\mathcal{F}^{\parallel}$ do not oscillate near the horizon, and are instead analytic at $r = r_H$[28].

Applying the transformation (P.5) to the equations of motion (4.4.16) and (4.4.18) gives the differential equations obeyed by the gauge-fields in Eddington-Finkelstein coordinates, $\mathcal{F}^{\perp}$ and $\mathcal{F}^{\parallel}$

$$\partial_r^2\mathcal{F}^{\perp} + \left(\frac{f'(r)+i\omega}{f(r)} - \frac{1}{r}\right)\partial_r\mathcal{F}^{\perp} - \frac{k^2}{f(r)}\mathcal{F}^{\perp} = 0\,, \tag{P.8}$$

$$\partial_r^2\mathcal{F}^{\parallel} + \left(\frac{f'(r)+i\omega}{f(r)} - \frac{1}{r} + \frac{k^2 f'(r)}{\omega^2 - f(r)k^2}\right)\partial_r\mathcal{F}^{\parallel} - \frac{k^2}{f(r)}\mathcal{F}^{\parallel} = 0\,. \tag{P.9}$$

These equations can be solved numerically by shooting from the horizon, where two boundary conditions are imposed. The first condition fixes the normalization of the solution

$$\mathcal{F}^{\perp}(r_H) = \mathcal{F}^{\parallel}(r_H) = 1\,, \tag{P.10}$$

and the second one selects the infalling solution at the horizon. In Eddington-Finkelstein coordinates, this corresponds to requiring that the fields $\mathcal{F}^{\perp}$ and $\mathcal{F}^{\parallel}$ are regular at $r = r_H$. By analyzing the equations of motion (P.8)-(P.9) near the horizon, for the regular solution we find the following relation between the fields and their first derivative at the horizon

$$\partial_r\mathcal{F}^{\perp}(r_H) = \frac{k^2}{i\omega - 4\pi T}\mathcal{F}^{\perp}(r_H) \quad , \quad \partial_r\mathcal{F}^{\parallel}(r_H) = \frac{k^2}{i\omega - 4\pi T}\mathcal{F}^{\parallel}(r_H)\,. \tag{P.11}$$

Q Analysis of the diffusive approximation

This appendix presents an analysis of the diffusive approximation, where the time-time component of the two-point function is assumed to give the largest contribution to the opacities. We first investigate the validity of this approximation, and then use it to derive approximate expressions for the radiative coefficients as a function of the various parameters.

[28]The infalling Eddington-Finkelstein coordinates are well-defined beyond the horizon, and there exists a solution to the equations of motion which is perfectly regular at $r = r_H$ in these coordinates.

Q.1 Radiative coefficients in the hydrodynamic limit

This subsection presents the analysis of the radiative coefficients in the hydrodynamic regime $r_H\mu_e, r_H\mu_\nu, r_H E_\nu \ll 1$, which results in the scalings (4.5.21). The results justify the validity of the diffusive approximation in the degenerate and hydrodynamic limit.

A small parameter ϵ is introduced, and we consider the following scaling of the parameters

$$r_H E_\nu \sim r_H\mu_\nu = r_H\mu_e = \epsilon \quad , \quad r_H T = \mathcal{O}(\epsilon^a)\,, \tag{Q.1}$$

where we take $a \gg 1$. This ensures that the temperature is much smaller than all other energy scales in the problem, such that the degenerate expression of the statistical distributions can be used (4.5.2) and (4.5.4). We then consider the integrals over the loop electron momentum which define the radiative coefficients (4.2.72)-(4.2.75). We focus on the neutrino emissivity j_{e^-} for concreteness, but the others are analogous. The integral over k_e can be rewritten as an integral over the energy $q^0_{e\nu}$

$$j_{e^-}(E_\nu) = -\frac{G_F^2}{8\pi^2}\int_0^\pi \mathrm{d}\theta \sin\theta \int_0^{\mu_\nu - E_\nu} \mathrm{d}\omega \frac{\omega + E_\nu}{E_\nu} L_e^{\lambda\sigma}\, \mathrm{Im}\, G^R_{c,\sigma\lambda}\big(\omega, k(\omega,\theta)\big)\,, \tag{Q.2}$$

$$\omega \equiv q^0_{e\nu} = E_e - E_\nu\,,$$
$$k(\omega,\theta) \equiv \sqrt{(\omega+E_\nu)^2 + E_\nu^2 - 2(\omega+E_\nu)E_\nu\cos\theta}\,,$$

where we neglected the mass of the electrons[29], and the boundaries of the energy integral are fixed by the Fermi-Dirac and Bose-Einstein distributions. Substituting the hydrodynamic expression of the correlators gives

$$j_{e^-}(E_\nu) = \frac{G_F^2}{8\pi^2}\int_0^\pi \mathrm{d}\theta \sin\theta \int_0^{\mu_\nu - E_\nu} \mathrm{d}\omega \frac{\omega + E_\nu}{E_\nu} L_e^{\lambda\sigma} \times \tag{Q.3}$$
$$\times\, \sigma\omega \left(P^\perp_{\lambda\sigma}(\omega, k(\omega,\theta)) + P^\parallel_{\lambda\sigma}(\omega, k(\omega,\theta)) \frac{\omega^2 - k^2(\omega,\theta)}{\omega^2 + D^2 k^4(\omega,\theta)} \right)\,,$$

which is the sum of several components

$$j^\perp_{e^-}(E_\nu) = \frac{2G_F^2\sigma}{\pi^2}\int_0^\pi \mathrm{d}\theta \sin\theta(1-\cos\theta) \int_0^{\mu_\nu - E_\nu} \mathrm{d}\omega\, \omega(\omega+E_\nu)^2 \times \tag{Q.4}$$
$$\times \left(1 + \frac{(\omega+E_\nu)E_\nu}{k^2(\omega,\theta)}(1+\cos\theta)\right)\,,$$

$$j^{(00)}_{e^-}(E_\nu) = \frac{G_F^2\sigma}{\pi^2}\int_0^\pi \mathrm{d}\theta \sin\theta(1+\cos\theta) \int_0^{\mu_\nu - E_\nu} \mathrm{d}\omega\, \omega(\omega+E_\nu)^2 \times \tag{Q.5}$$

[29] The mass of the electron is equal to about 0.5 MeV, which is much smaller than the temperature $T = 10\,\mathrm{MeV}$.

$$\times \frac{k^2(\omega,\theta)}{\omega^2 + D^2k^4(\omega,\theta)}\,,$$

$$j_{e^-}^{(0i)}(E_\nu) = -\frac{2G_F^2\sigma}{\pi^2}\int_0^\pi \mathrm{d}\theta \sin\theta(1+\cos\theta)\int_0^{\mu_\nu - E_\nu} \mathrm{d}\omega\, \omega^2(\omega+E_\nu)^2 \times \tag{Q.6}$$
$$\times \frac{\omega}{\omega^2 + D^2k^4(\omega,\theta)}\,,$$

$$j_{e^-}^{\parallel,(ij)}(E_\nu) = \frac{G_F^2\sigma}{\pi^2}\int_0^\pi \mathrm{d}\theta \sin\theta(1+\cos\theta)\int_0^{\mu_\nu - E_\nu} \mathrm{d}\omega\, \omega^3(\omega+E_\nu)^2 \times \tag{Q.7}$$
$$\times \frac{\omega^2}{k^2(\omega,\theta)(\omega^2 + D^2k^4(\omega,\theta))}\,.$$

The diffusive approximation assumes that the component $j_{e^-}^{(00)}$ dominates over the other contributions. We now proceed to investigate the validity of this statement in the hydrodynamic limit. This will be done by determining the hydrodynamic scaling (the scaling in ϵ) for each component of the emissivity (Q.4)-(Q.7).

For a given angle θ, the integration over ω meets the diffusive peak $\omega = Dk^2$ when ω is equal to

$$\begin{aligned}\omega^*(E_\nu,\theta) &\equiv \frac{1+2DE_\nu\cos\theta - \sqrt{(1+2DE_\nu\cos\theta)^2 - 4D(E_\nu + DE_\nu^2)}}{2D} - E_\nu \\ &= 2DE_\nu^2(1-\cos\theta)(1+\mathcal{O}(\epsilon))\,. \end{aligned}\tag{Q.8}$$

From (Q.1), ω^* is of order $\mathcal{O}(\epsilon^2)$ whereas the upper bound of the integral $\mu_\nu - E_\nu$ is of order $\mathcal{O}(\epsilon)$. The integrals are therefore such that, over most of the integration region, ω is much larger than Dk^2. Specifically, the integrals can be split into two parts as

$$\int_0^{\mu_\nu - E_\nu} = \int_0^{A\omega^*} + \int_{A\omega^*}^{\mu_\nu - E_\nu}\,, \tag{Q.9}$$

where A is a number much larger than one which is independent of ϵ. The first part contains the contribution from the diffusion peak, whereas $\omega \gg Dk^2$ in the second part.

We now investigate the scaling of the first part of the integral in (Q.9) that we label with the subscript "diff". Since the transverse integrand (Q.4) does not depend on r_H, its hydrodynamic scaling is easily derived

$$j_{e^-,\mathrm{diff}}^{\perp} = \mathcal{O}(\epsilon^6)\,. \tag{Q.10}$$

The longitudinal integrands require a more careful study since r_H appears via the diffusion constant $D = \frac{1}{2}r_H$. The hydrodynamic scaling of the longitudinal emissivity coming from

the first part of the integral in (Q.9) can be found by determining appropriate upper and lower bounds. The lower bound is determined according to the following

$$\int_0^{A\omega^*} \mathrm{d}\omega F(\omega,\theta)\frac{k^2(\omega,\theta)\omega}{\omega^2+D^2k^4(\omega,\theta)} > \int_0^{2\omega^*} \mathrm{d}\omega F(\omega,\theta)\frac{k^2(\omega,\theta)\omega}{\omega^2+D^2k^4(\omega,\theta)} \tag{Q.11}$$
$$\approx \int_0^{2\omega^*} \mathrm{d}\omega F(\omega,\theta)\frac{\omega^*\omega}{D\left(\omega^2+(\omega^*)^2\right)} > \int_0^{2\omega^*} \mathrm{d}\omega F(\omega,\theta)\frac{1}{2D}\left(1-\left(\frac{\omega}{\omega^*}-1\right)^2\right),$$

where $F(\omega,\theta)>0$ and the sign $\approx$ means that the two expressions are equal up to a factor $1+\mathcal{O}(\epsilon)$. To write the first expression on the second line, we used the fact that $D\omega$ is of order $\mathcal{O}(\epsilon^2)$ over the integration interval, so that $k^2(\omega,\theta)=\omega^*/D(1+\mathcal{O}(\epsilon))$. The upper bound is obtained by replacing the fraction in (Q.11) by its maximum value reached at $\omega=\omega^*$

$$\int_0^{A\omega^*} \mathrm{d}\omega F(\omega,\theta)\frac{k^2(\omega,\theta)\omega}{\omega^2+D^2k^4(\omega,\theta)} < \int_0^{A\omega^*} \mathrm{d}\omega\frac{F(\omega,\theta)}{2D}\,. \tag{Q.12}$$

Then, for each component of the longitudinal emissivity (Q.5)-(Q.7), the bounds on the contribution from the region around the diffusion peak are obtained by replacing $F(\omega,\theta)$ in (Q.9) and (Q.12) by the appropriate expression, and performing the integral. This results in the following bounds

$$j^{(00)}_{e^-,\mathrm{diff}} = \alpha_{(00)}\frac{4G_F^2\sigma}{3\pi^2}E_\nu^4(1+\mathcal{O}(\epsilon)) = \mathcal{O}(\epsilon^4)\,, \tag{Q.13}$$

$$j^{(0i)}_{e^-,\mathrm{diff}} = -\alpha_{(0i)}\frac{32G_F^2\sigma}{3\pi^2}D^2E_\nu^6(1+\mathcal{O}(\epsilon)) = \mathcal{O}(\epsilon^6), \tag{Q.14}$$

$$j^{\parallel,(ij)}_{e^-,\mathrm{diff}} = \alpha_{(ij)}\frac{64G_F^2\sigma}{5\pi^2}D^4E_\nu^8(1+\mathcal{O}(\epsilon)) = \mathcal{O}(\epsilon^8), \tag{Q.15}$$

$$\alpha_{(00)}\in\left(\frac{4}{3},A\right) \quad,\quad \alpha_{(0i)}\in\left(\frac{4}{5},\frac{A^3}{6}\right) \quad,\quad \alpha_{(ij)}\in\left(\frac{32}{21},\frac{A^5}{10}\right).$$

We now discuss the contribution from the second part of the integral in (Q.9), where $\omega\gg Dk^2$. Since this contribution includes essentially the region where ω and k are of the same order $\omega\sim k=\mathcal{O}(\epsilon)$, we label it with the subscript "lin". The scaling of the transverse part is again easily derived

$$j^{\perp}_{e^-,\mathrm{lin}} = \mathcal{O}(\epsilon^4)\,. \tag{Q.16}$$

For the longitudinal part, the integrals are computed by neglecting D^2k^4 in the denominator of the correlator, which results in integrands that are independent of the diffusion constant D. As for the transverse part, the hydrodynamic scaling of the $(0i)$ (Q.6) and (ij) (Q.7) components are then easily derived to be

$$j^{(0i)}_{e^-,\mathrm{lin}} = \mathcal{O}(\epsilon^4)\,, \tag{Q.17}$$

$$j^{\parallel,(ij)}_{e^-,\text{lin}} = \mathcal{O}(\epsilon^4)\,. \tag{Q.18}$$

The (00) component is somewhat more subtle since the integrand contains a term that goes as ω^{-1}. This implies that the time-time component contains a term of order $\mathcal{O}(\epsilon^4 \log(\epsilon^2))$

$$j^{(00)}_{e^-,\text{lin}} = \frac{8G_F^2\sigma}{3\pi^2} E_\nu^4 \log\left(\frac{D(\mu_\nu - E_\nu)}{D^2 E_\nu^2}\right) + \mathcal{O}(\epsilon^4)\,. \tag{Q.19}$$

As long as $\mu_\nu - E_\nu$ is much larger than $\mathcal{O}(\epsilon^2)$, this term dominates all the other contributions to the neutrino emissivity. When E_ν is so close to the neutrino chemical potential that $\mu_\nu - E_\nu$ is smaller than $\mathcal{O}(\epsilon^2)$, the integral includes only the diffusive part in (Q.10) and (Q.13)-(Q.15). Since in both cases the time-time component dominates, the conclusion of this analysis is that the diffusive approximation is valid in the hydrodynamic limit.

Note that there is one exception to this argument which happens in the limit where E_ν goes to zero. In this limit, the only remaining scale is the neutrino chemical potential, such that all contributions (Q.4)-(Q.7) behave like μ_ν^4. This means that the diffusive approximation does not apply when $E_\nu \ll \mu_\nu$.

Q.2 Approximate expressions for the radiative coefficients

In this subsection, we take the hydrodynamic limit (Q.1) to derive approximate expressions for the neutrino radiative coefficients. We consider the degenerate limit of the distribution functions (4.5.2) and (4.5.4), and assume in a first time that $|\mu_\nu - E_\nu| \gg \mathcal{O}(\epsilon^2)$.

According to the analysis of the previous subsection, the radiative coefficients are dominated by the log term coming from the time-time component of the 2-point function. For the opacities we obtain

$$\kappa_{e^-}(E_\nu) = \frac{8G_F^2\sigma}{3\pi^2} E_\nu^4 \log\left(\frac{D|\mu_\nu - E_\nu|}{D^2 E_\nu^2}\right) + \mathcal{O}(\epsilon^4)\,, \tag{Q.20}$$

$$\bar{\kappa}_{e^-}(E_\nu) = \frac{8G_F^2\sigma}{3\pi^2} E_\nu^4 \log\left(\frac{D(\mu_\nu + E_\nu)}{D^2 E_\nu^2}\right) + \mathcal{O}(\epsilon^4)\,. \tag{Q.21}$$

(Q.20) is valid as long as $|\mu_\nu - E_\nu|$ is much larger than $\mathcal{O}(\epsilon^2)$. In particular, instead of diverging, the opacity goes to zero at $E_\nu = \mu_\nu$ in the degenerate limit.

From Table 4.1, the anti-neutrino opacity also receives a contribution from the positronic processes. The latter is obtained from (Q.21) by replacing $\mu_\nu + E_\nu$ by $\mu_\nu + E_\nu - \mu_e = E_\nu$

$$\bar{\kappa}_{e^+}(E_\nu) = \frac{8G_F^2\sigma}{3\pi^2} E_\nu^4 \log(DE_\nu) + \mathcal{O}(\epsilon^4)\,. \tag{Q.22}$$

Note that the leading order log term in (Q.20)-(Q.22) vanishes when E_ν goes to zero, such that the opacities become of order $\mathcal{O}(\epsilon^4)$ in this limit. The expressions of the opacities

at $E_\nu = 0$ are of particular interest, since they set the typical opacity scale at a given value of the baryonic density n_B. The latter can easily be computed from (Q.4)-(Q.7)

$$\kappa_{e,0} \equiv \kappa_{e^-}(0) = \bar{\kappa}_{e^-}(0) = \frac{G_F^2 \sigma}{\pi^2} \mu_\nu^4 + \mathcal{O}(\epsilon^5)\,. \tag{Q.23}$$

Substituting the expressions for the conductivity σ (4.4.45), and the neutrino chemical potential (4.3.26), we obtain the dependence of the zero-energy opacities on μ and the parameters of the bulk action ($M\ell$) and w_0

$$\kappa_{e,0}(n_B) = \frac{G_F^2 |M_{ud}|^2}{2304} \left(3\pi^4\right)^{\frac{1}{6}} N_c^{\frac{1}{2}} (M\ell)^7 w_0^{25/3} \big(\mu(n_B)\big)^5 + \mathcal{O}(\epsilon^4)\,, \tag{Q.24}$$

which is valid in the degenerate and hydrodynamic limit.

We are now interested in the regime where $|\mu_\nu - E_\nu|$ is smaller than $\mathcal{O}(\epsilon^2)$. When $|\mu_\nu - E_\nu|$ goes to zero, both the neutrino emissivity and absorption calculated with the degenerate limit of the distribution functions go to zero. This implies the existence of a dip in the log of the neutrino opacity at $E_\nu = \mu_\nu$, which is clearly visible on figure 4.16. Here we would like to understand what are the typical width and depth of this dip. As soon as $|\mu_\nu - E_\nu|$ becomes of order $\mathcal{O}(\epsilon^2)$, the integral over energies that appears in the neutrino emissivity (Q.3) contains only the first part in (Q.9), where ω and Dk^2 are of the same order. Then, for $T \ll \mu_\nu - E_\nu = \mathcal{O}(\epsilon^2)$, the neutrino opacity is bounded from above by

$$\kappa_{e^-}(E_\nu) < \frac{G_F^2 \sigma}{D\pi^2} \int_0^{|\mu_\nu - E_\nu|} \mathrm{d}\omega (\omega + E_\nu)^2 = \frac{G_F^2 \sigma}{D\pi^2} \mu_\nu^2 |\mu_\nu - E_\nu| \big(1 + \mathcal{O}(\epsilon)\big)\,. \tag{Q.25}$$

This becomes much smaller than the leading contribution from the diffusion peak (Q.13) when

$$\frac{1}{D} \mu_\nu^2 |\mu_\nu - E_\nu| \ll E_\nu^4 \iff |\mu_\nu - E_\nu| \ll D\mu_\nu^2. \tag{Q.26}$$

Replacing the diffusion constant D by its expression $D = r_H/2$, we find that the typical width of the dip in opacity at $E_\nu = \mu_\nu$ is given by

$$\Delta E_\nu = \sqrt{\frac{3N_c}{w_0^2}} \frac{\mu_\nu^2}{\mu}\,. \tag{Q.27}$$

The depth of the dip is controlled by the value of the opacity at $E_\nu = \mu_\nu$. At zero temperature, the opacity will be exactly zero at $E_\mu = \mu_\nu$, and the depth of the dip infinite. At finite temperature, the finite value of the opacity comes from the order $\mathcal{O}(T/\mu)^2$ corrections in (4.5.2) and (4.5.4). The latter are evaluated as derivatives in energy at the point $E_\nu = \mu_\nu$

$$\kappa_{e^-}(\mu_\nu) = \frac{2G_F^2 \sigma}{3} T^2 \int_0^\pi \mathrm{d}\theta \sin\theta (1 + \cos\theta) \partial_\omega \left[\omega(\omega + \mu_\nu)^2 \frac{k^2(\omega, \theta)}{\omega^2 + D^2 k^4(\omega, \theta)} \right] \Bigg|_{\omega = 0} (1 + \mathcal{O}(\epsilon)). \tag{Q.28}$$

The angular integral in (Q.28) is singular, which translates the appearance of a non-analytic behavior in the temperature $\sim T^2 \log T$. The latter can be traced back to the divergence of the retarded 2-point function at $\theta = 0$, which is due to the forward scattering of soft electrons at $\mu_e = \mu_\nu$. As expected, the divergence is regularized when taking into account that the electron mass m_e is finite

$$\kappa_{e^-}(\mu_\nu) = \frac{8G_F^2\sigma}{3} T^2 r_H^{-2} \left[4 \log\left(\frac{2\mu_\nu}{m_e}\right) - 1 \right] \left(1 + \mathcal{O}(\epsilon) + \mathcal{O}(m_e/\mu_\nu)^2\right) . \tag{Q.29}$$

Bibliography

[1] H. Fritzsch, M. Gell-Mann and H. Leutwyler, *"Advantages of the Color Octet Gluon Picture,"* Phys. Lett. B **47**, 365-368 (1973).

[2] D. J. Gross and F. Wilczek, *"Ultraviolet Behavior of Non-Abelian Gauge Theories,"* Phys. Rev. Lett. **30**, 1343-1346 (1973).

[3] H. D. Politzer, *"Reliable Perturbative Results for Strong Interactions?,"* Phys. Rev. Lett. **30**, 1346-1349 (1973).

[4] J. Ghiglieri, A. Kurkela, M. Strickland and A. Vuorinen, *"Perturbative Thermal QCD: Formalism and Applications,"* Phys. Rept. **880**, 1-73 (2020); [ArXiv:2002.10188][hep-ph].

[5] M. Järvinen, E. Kiritsis, F. Nitti and E. Préau, *"Tachyon-dependent Chern-Simons terms and the V-QCD baryon,"* JHEP **12** (2022), 160; [ArXiv:2209.05868][hep-th].

[6] M. Järvinen, E. Kiritsis, F. Nitti and E. Préau, *"The V-QCD baryon : numerical solution and baryon spectrum,"* [ArXiv:2212.06747][hep-th].

[7] M. Laine and Y. Schroder, *"Quark mass thresholds in QCD thermodynamics,"* Phys. Rev. D **73**, 085009 (2006); [ArXiv:hep-ph/0603048].

[8] E. Annala, T. Gorda, A. Kurkela and A. Vuorinen, *"Gravitational-wave constraints on the neutron-star-matter Equation of State,"* Phys. Rev. Lett. **120**, no.17, 172703 (2018); [ArXiv:1711.02644][astro-ph.HE].

[9] T. Gorda, A. Kurkela, R. Paatelainen, S. Säppi and A. Vuorinen, *"Cold quark matter at N3LO: Soft contributions,"* Phys. Rev. D **104**, no.7, 074015 (2021); [ArXiv:2103.07427][hep-ph].

[10] L. Fernandez and J. L. Kneur, *"All Order Resummed Leading and Next-to-Leading Soft Modes of Dense QCD Pressure,"* Phys. Rev. Lett. **129**, no.21, 212001 (2022); [ArXiv:2109.02410][hep-ph].

[11] M. G. Alford, *"Color superconducting quark matter,"* Ann. Rev. Nucl. Part. Sci. **51**, 131-160 (2001); [ArXiv:hep-ph/0102047].

[12] M. G. Alford, A. Schmitt, K. Rajagopal and T. Schäfer, *"Color superconductivity in dense quark matter,"* Rev. Mod. Phys. **80**, 1455-1515 (2008); [ArXiv:0709.4635][hep-ph].

[13] K. G. Wilson, *"Confinement of Quarks,"* Phys. Rev. D **10**, 2445-2459 (1974).

[14] S. R. Coleman and E. Witten, *"Chiral Symmetry Breakdown in Large N Chromodynamics,"* Phys. Rev. Lett. **45**, 100 (1980).

[15] A. Ukawa, *"QCD PHASE TRANSITIONS AT FINITE TEMPERATURES,"* Nucl. Phys. B Proc. Suppl. **17**, 118-136 (1990)

[16] F. Karsch, E. Laermann and C. Schmidt, *"The Chiral critical point in three-flavor QCD,"* Phys. Lett. B **520**, 41-49 (2001); [ArXiv:hep-lat/0107020].

[17] S. Weinberg, *"Phenomenological Lagrangians,"* Physica A **96**, no.1-2, 327-340 (1979).

[18] J. Gasser and H. Leutwyler, *"Chiral Perturbation Theory to One Loop,"* Annals Phys. **158**, 142 (1984).

[19] J. Gasser and H. Leutwyler, *"Chiral Perturbation Theory: Expansions in the Mass of the Strange Quark,"* Nucl. Phys. B **250**, 465-516 (1985).

[20] E. Follana *et al.* [HPQCD and UKQCD], *"High Precision determination of the pi, K, D and D(s) decay constants from lattice QCD,"* Phys. Rev. Lett. **100**, 062002 (2008); [ArXiv:0706.1726][hep-lat].

[21] J. Gasser, M. E. Sainio and A. Svarc, *"Nucleons with Chiral Loops,"* Nucl. Phys. B **307**, 779-853 (1988).

[22] A. Nogga, P. Navratil, B. R. Barrett and J. P. Vary, *"Spectra and binding energy predictions of chiral interactions for Li-7,"* Phys. Rev. C **73**, 064002 (2006); [ArXiv:nucl-th/0511082].

[23] P. Navratil, V. G. Gueorguiev, J. P. Vary, W. E. Ormand and A. Nogga, *"Structure of A=10-13 nuclei with two plus three-nucleon interactions from chiral effective field theory,"* Phys. Rev. Lett. **99**, 042501 (2007); [ArXiv:nucl-th/0701038].

[24] G. Hagen, T. Papenbrock, D. J. Dean and M. Hjorth-Jensen, *"Medium-mass nuclei from chiral nucleon-nucleon interactions,"* Phys. Rev. Lett. **101**, 092502 (2008); [ArXiv:0806.3478][nucl-th].

[25] T. Otsuka, T. Suzuki, J. D. Holt, A. Schwenk and Y. Akaishi, *"Three-body forces and the limit of oxygen isotopes,"* Phys. Rev. Lett. **105**, 032501 (2010); [ArXiv:0908.2607][nucl-th].

[26] I. Tews, J. Carlson, S. Gandolfi and S. Reddy, *"Constraining the speed of sound inside neutron stars with chiral effective field theory interactions and observations,"* Astrophys. J. **860**, no.2, 149 (2018); [ArXiv:1801.01923][nucl-th].

[27] M. E. Fisher, *"The theory of condensation and the critical point,"* Physics Physique Fizika **3**, no.5, 255-283 (1967).

[28] G. Sauer, H. Chandra and U. Mosel, *"Thermal properties of nuclei,"* Nucl. Phys. A **264**, 221-243 (1976).

[29] M. W. Curtin, H. Toki and D. K. Scott, *"Liquid-gas phase instabilities in nuclear systems,"* Phys. Lett. B **123**, 289-292 (1983).

[30] H. Jaqaman, A. Z. Mekjian and L. Zamick, *"NUCLEAR CONDENSATION,"* Phys. Rev. C **27**, 2782-2791 (1983).

[31] S. Fiorilla, N. Kaiser and W. Weise, *"Chiral thermodynamics of nuclear matter,"* Nucl. Phys. A **880**, 65-87 (2012); [ArXiv:1111.2791][nucl-th].

[32] J. E. Finn, S. Agarwal, A. Bujak, J. Chuang, L. J. Gutay, A. S. Hirsch, R. W. Minich, N. T. Porile, R. P. Scharenberg and B. C. Stringfellow, *et al. "Nuclear Fragment Mass Yields From High-energy Proton - Nucleus Interactions,"* Phys. Rev. Lett. **49**, 1321 (1982).

[33] A. D. Panagiotou, M. W. Curtin, H. Toki, D. K. Scott and P. J. Siemens, *"EXPERIMENTAL EVIDENCE FOR A LIQUID - GAS PHASE TRANSITION IN NUCLEAR SYSTEMS,"* Phys. Rev. Lett. **52**, 496-499 (1984).

[34] J. Pochodzalla, T. Mohlenkamp, T. Rubehn, A. Schuttauf, A. Worner, E. Zude, M. Begemann-Blaich, T. Blaich, H. Emling and A. Ferrero, *et al. "Probing the nuclear liquid - gas phase transition,"* Phys. Rev. Lett. **75**, 1040-1043 (1995).

[35] J. W. Holt and N. Kaiser, *"Equation of state of nuclear and neutron matter at third-order in perturbation theory from chiral effective field theory,"* Phys. Rev. C **95**, no.3, 034326 (2017); [ArXiv:1612.04309][nucl-th].

[36] F. Karsch, K. Redlich and A. Tawfik, *"Hadron resonance mass spectrum and lattice QCD thermodynamics,"* Eur. Phys. J. C **29**, 549-556 (2003); [ArXiv:hep-ph/0303108].

[37] F. Karsch, K. Redlich and A. Tawfik, *"Thermodynamics at nonzero baryon number density: A Comparison of lattice and hadron resonance gas model calculations,"* Phys. Lett. B **571**, 67-74 (2003); [ArXiv:hep-ph/0306208].

[38] P. Braun-Munzinger, K. Redlich and J. Stachel, *"Particle production in heavy ion collisions,"* [ArXiv:nucl-th/0304013].

[39] A. Bazavov *et al.* [HotQCD], *"Equation of state in (2+1)-flavor QCD,"* Phys. Rev. D **90**, 094503 (2014); [ArXiv:1407.6387][hep-lat].

[40] S. Borsanyi, Z. Fodor, C. Hoelbling, S. D. Katz, S. Krieg and K. K. Szabo, *"Full result for the QCD equation of state with 2+1 flavors,"* Phys. Lett. B **730**, 99-104 (2014); [ArXiv:1309.5258][hep-lat].

[41] S. Borsanyi, Z. Fodor, J. Guenther, K. H. Kampert, S. D. Katz, T. Kawanai, T. G. Kovacs, S. W. Mages, A. Pasztor and F. Pittler, *et al. "Calculation of the axion mass based on high-temperature lattice quantum chromodynamics,"* Nature **539**, no.7627, 69-71 (2016); [ArXiv:1606.07494][hep-lat].

[42] A. Nakamura, T. Saito and S. Sakai, *"Lattice calculation of gluon screening masses,"* Phys. Rev. D **69**, 014506 (2004); [ArXiv:hep-lat/0311024].

[43] M. Cheng, S. Datta, A. Francis, J. van der Heide, C. Jung, O. Kaczmarek, F. Karsch, E. Laermann, R. D. Mawhinney and C. Miao, *et al. "Meson screening masses from lattice QCD with two light and the strange quark,"* Eur. Phys. J. C **71**, 1564 (2011); [ArXiv:1010.1216][hep-lat].

[44] E. Laermann and O. Philipsen, *"The Status of lattice QCD at finite temperature,"* Ann. Rev. Nucl. Part. Sci. **53**, 163-198 (2003); [ArXiv:hep-ph/0303042].

[45] P. Petreczky, *"Lattice QCD at non-zero temperature,"* J. Phys. G **39**, 093002 (2012); [ArXiv:1203.5320][hep-lat].

[46] C. Ratti, *"Lattice QCD and heavy ion collisions: a review of recent progress,"* Rept. Prog. Phys. **81**, no.8, 084301 (2018); [ArXiv:1804.07810][hep-lat].

[47] Y. Aoki, G. Endrodi, Z. Fodor, S. D. Katz and K. K. Szabo, *"The Order of the quantum chromodynamics transition predicted by the standard model of particle physics,"* Nature **443**, 675-678 (2006); [ArXiv:hep-lat/0611014][hep-lat].

[48] Y. Aoki, S. Borsanyi, S. Durr, Z. Fodor, S. D. Katz, S. Krieg and K. K. Szabo, *"The QCD transition temperature: results with physical masses in the continuum limit II.,"* JHEP **06**, 088 (2009); [ArXiv:0903.4155][hep-lat].

[49] S. Borsanyi *et al.* [Wuppertal-Budapest], *"Is there still any T_c mystery in lattice QCD? Results with physical masses in the continuum limit III,"* JHEP **09**, 073 (2010); [ArXiv:1005.3508][hep-lat].

[50] T. Bhattacharya, M. I. Buchoff, N. H. Christ, H. T. Ding, R. Gupta, C. Jung, F. Karsch, Z. Lin, R. D. Mawhinney and G. McGlynn, *et al.* *"QCD Phase Transition with Chiral Quarks and Physical Quark Masses,"* Phys. Rev. Lett. **113**, no.8, 082001 (2014); [ArXiv:1402.5175][hep-lat].

[51] M. Troyer and U. J. Wiese, *"Computational complexity and fundamental limitations to fermionic quantum Monte Carlo simulations,"* Phys. Rev. Lett. **94**, 170201 (2005); [ArXiv:cond-mat/0408370].

[52] H. T. Ding, A. Francis, O. Kaczmarek, F. Karsch, E. Laermann and W. Soeldner, *"Thermal dilepton rate and electrical conductivity: An analysis of vector current correlation functions in quenched lattice QCD,"* Phys. Rev. D **83**, 034504 (2011); [ArXiv:1012.4963][hep-lat].

[53] Y. Burnier and M. Laine, *"Towards flavour diffusion coefficient and electrical conductivity without ultraviolet contamination,"* Eur. Phys. J. C **72**, 1902 (2012); [ArXiv:1201.1994][hep-lat].

[54] P. de Forcrand and O. Philipsen, *"The QCD phase diagram for small densities from imaginary chemical potential,"* Nucl. Phys. B **642**, 290-306 (2002); [ArXiv:hep-lat/0205016].

[55] Z. Fodor and S. D. Katz, *"A New method to study lattice QCD at finite temperature and chemical potential,"* Phys. Lett. B **534**, 87-92 (2002); [ArXiv:hep-lat/0104001].

[56] A. Alexandru, M. Faber, I. Horvath and K. F. Liu, *"Lattice QCD at finite density via a new canonical approach,"* Phys. Rev. D **72**, 114513 (2005); [ArXiv:hep-lat/0507020].

[57] Z. Fodor, S. D. Katz and C. Schmidt, *"The Density of states method at non-zero chemical potential,"* JHEP **03**, 121 (2007); [ArXiv:hep-lat/0701022].

[58] C. R. Allton, S. Ejiri, S. J. Hands, O. Kaczmarek, F. Karsch, E. Laermann, C. Schmidt and L. Scorzato, *"The QCD thermal phase transition in the presence of a small chemical potential,"* Phys. Rev. D **66**, 074507 (2002); [ArXiv:hep-lat/0204010].

[59] C. R. Allton, M. Doring, S. Ejiri, S. J. Hands, O. Kaczmarek, F. Karsch, E. Laermann and K. Redlich, *"Thermodynamics of two flavor QCD to sixth order in quark chemical potential,"* Phys. Rev. D **71**, 054508 (2005); [ArXiv:hep-lat/0501030].

[60] M. Oertel, M. Hempel, T. Klähn and S. Typel, *"Equations of state for supernovae and compact stars,"* Rev. Mod. Phys. **89**, no.1, 015007 (2017); [ArXiv:1610.03361][astro-ph.HE].

[61] G. Baym, T. Hatsuda, T. Kojo, P. D. Powell, Y. Song and T. Takatsuka, *"From hadrons to quarks in neutron stars: a review,"* Rept. Prog. Phys. **81**, no.5, 056902 (2018); [ArXiv:1707.04966][astro-ph.HE].

[62] H. T. Janka, *"Explosion Mechanisms of Core-Collapse Supernovae,"* Ann. Rev. Nucl. Part. Sci. **62**, 407-451 (2012); [ArXiv:1206.2503][astro-ph.SR].

[63] P. Haensel, A. Y. Potekhin and D. G. Yakovlev, *"Neutron stars 1: Equation of state and structure,"* Astrophys. Space Sci. Libr. **326**, pp.1-619 (2007) Springer, 2007.

[64] F. Özel and P. Freire, *"Masses, Radii, and the Equation of State of Neutron Stars,"* Ann. Rev. Astron. Astrophys. **54**, 401-440 (2016); [ArXiv:1603.02698][astro-ph.HE].

[65] J. M. Lattimer, *"The nuclear equation of state and neutron star masses,"* Ann. Rev. Nucl. Part. Sci. **62**, 485-515 (2012); [ArXiv:1305.3510][nucl-th].

[66] P. Demorest, T. Pennucci, S. Ransom, M. Roberts and J. Hessels, *"Shapiro Delay Measurement of A Two Solar Mass Neutron Star,"* Nature **467** (2010), 1081-1083; [ArXiv:1010.5788][astro-ph.HE].

[67] Z. Arzoumanian *et al.* [NANOGrav], *"The NANOGrav 11-year Data Set: High-precision timing of 45 Millisecond Pulsars,"* Astrophys. J. Suppl. **235**, no.2, 37 (2018); [ArXiv:1801.01837][astro-ph.HE].

[68] J. Antoniadis, P. C. C. Freire, N. Wex, T. M. Tauris, R. S. Lynch, M. H. van Kerkwijk, M. Kramer, C. Bassa, V. S. Dhillon and T. Driebe, *et al. "A Massive Pulsar in a Compact Relativistic Binary,"* Science **340** (2013), 6131; [ArXiv:1304.6875][astro-ph.HE].

[69] H. T. Cromartie *et al.* [NANOGrav], *"Relativistic Shapiro delay measurements of an extremely massive millisecond pulsar,"* Nature Astron. **4** (2019) no.1, 72-76; [ArXiv:1904.06759][astro-ph.HE].

[70] E. Fonseca, H. T. Cromartie, T. T. Pennucci, P. S. Ray, A. Y. Kirichenko, S. M. Ransom, P. B. Demorest, I. H. Stairs, Z. Arzoumanian and L. Guillemot, *et al. "Refined Mass and Geometric Measurements of the High-mass PSR J0740+6620,"* Astrophys. J. Lett. **915** (2021) no.1, L12; [ArXiv:2104.00880][astro-ph.HE].

[71] E.F. Brown, L. Bildsten, and R.E. Rutledge, *"Crustal Heating and Quiescent Emission from Transiently Accreting Neutron Stars,"* The Astrophysical Journal, vol. **504**, no. 2, pp. L95–L98, 1998; [ArXiv:astro-ph/9807179].

[72] J. van Paradijs, *"Possible observational constraints on the mass-radius relation of neutron stars."*, The Astrophysical Journal, vol. **234**, pp. 609–611, 1979.

[73] K. R. Pechenick, C. Ftaclas, and J. Cohen, *"Hot spots on neutron stars - The near-field gravitational lens"*, The Astrophysical Journal, vol. **274**, pp. 846–857, 1983.

[74] T. E. Riley, A. L. Watts, S. Bogdanov, P. S. Ray, R. M. Ludlam, S. Guillot, Z. Arzoumanian, C. L. Baker, A. V. Bilous and D. Chakrabarty, *et al.* *"A NICER View of PSR J0030+0451: Millisecond Pulsar Parameter Estimation,"* Astrophys. J. Lett. **887**, no.1, L21 (2019); [ArXiv:1912.05702][astro-ph.HE].

[75] T. E. Riley, A. L. Watts, P. S. Ray, S. Bogdanov, S. Guillot, S. M. Morsink, A. V. Bilous, Z. Arzoumanian, D. Choudhury and J. S. Deneva, *et al.* *"A NICER View of the Massive Pulsar PSR J0740+6620 Informed by Radio Timing and XMM-Newton Spectroscopy,"* Astrophys. J. Lett. **918**, no.2, L27 (2021); [ArXiv:2105.06980][astro-ph.HE].

[76] M. C. Miller, F. K. Lamb, A. J. Dittmann, S. Bogdanov, Z. Arzoumanian, K. C. Gendreau, S. Guillot, A. K. Harding, W. C. G. Ho and J. M. Lattimer, *et al.* *"PSR J0030+0451 Mass and Radius from NICER Data and Implications for the Properties of Neutron Star Matter,"* Astrophys. J. Lett. **887**, no.1, L24 (2019); [ArXiv:1912.05705][astro-ph.HE].

[77] M. C. Miller, F. K. Lamb, A. J. Dittmann, S. Bogdanov, Z. Arzoumanian, K. C. Gendreau, S. Guillot, W. C. G. Ho, J. M. Lattimer and M. Loewenstein, *et al.* *"The Radius of PSR J0740+6620 from NICER and XMM-Newton Data,"* Astrophys. J. Lett. **918**, no.2, L28 (2021) [ArXiv:2105.06979][astro-ph.HE].

[78] S. Bogdanov, S. Guillot, P. S. Ray, M. T. Wolff, D. Chakrabarty, W. C. G. Ho, M. Kerr, F. K. Lamb, A. Lommen and R. M. Ludlam, *et al.* *"Constraining the Neutron Star Mass–Radius Relation and Dense Matter Equation of State with NICER. I. The Millisecond Pulsar X-Ray Data Set,"* Astrophys. J. Lett. **887**, no.1, L25 (2019); [ArXiv:1912.05706][astro-ph.HE].

[79] B. P. Abbott *et al.* [LIGO Scientific and Virgo], *"GW170817: Observation of Gravitational Waves from a Binary Neutron Star Inspiral,"* Phys. Rev. Lett. **119**, no.16, 161101 (2017); [ArXiv:1710.05832][gr-qc].

[80] B. P. Abbott *et al.* [LIGO Scientific and Virgo], *"GW190425: Observation of a Compact Binary Coalescence with Total Mass* $\sim 3.4 M_{\odot}$*,"* Astrophys. J. Lett. **892**, no.1, L3 (2020); [ArXiv:2001.01761][astro-ph.HE].

[81] B. P. Abbott *et al.* [LIGO Scientific and Virgo], *"GW170817: Measurements of neutron star radii and equation of state,"* Phys. Rev. Lett. **121**, no.16, 161101 (2018); [ArXiv:1805.11581][gr-qc].

[82] D. Page and S. Reddy, *"Dense Matter in Compact Stars: Theoretical Developments and Observational Constraints,"* Ann. Rev. Nucl. Part. Sci. **56**, 327-374 (2006); [ArXiv:astro-ph/0608360].

[83] D. G. Yakovlev and C. J. Pethick, *"Neutron star cooling,"* Ann. Rev. Astron. Astrophys. **42**, 169-210 (2004); [ArXiv:astro-ph/0402143].

[84] D. Page, U. Geppert and F. Weber, *"The Cooling of compact stars,"* Nucl. Phys. A **777**, 497-530 (2006); [ArXiv:astro-ph/0508056].

[85] M. Prakash, J. M. Lattimer, J. A. Pons, A. W. Steiner and S. Reddy, *"Evolution of a neutron star from its birth to old age,"* Lect. Notes Phys. **578**, 364-423 (2001); [ArXiv:astro-ph/0012136].

[86] D. Page, J. M. Lattimer, M. Prakash and A. W. Steiner, *"Minimal cooling of neutron stars: A New paradigm,"* Astrophys. J. Suppl. **155**, 623-650 (2004); [ArXiv:astro-ph/0403657].

[87] O. Aharony, S. S. Gubser, J. M. Maldacena, H. Ooguri and Y. Oz, *"Large N field theories, string theory and gravity,"* Phys. Rept. **323**, 183-386 (2000); [ArXiv:hep-th/9905111].

[88] M. Natsuume, *"AdS/CFT Duality User Guide,"* Lect. Notes Phys. **903**, pp.1-294 (2015); [ArXiv:1409.3575][hep-th].

[89] M. Ammon and J. Erdmenger, *"Gauge/gravity duality: Foundations and applications,"* Cambridge University Press, 2015.

[90] E. Kiritsis, *"String theory in a nutshell,"* Princeton University Press, 2019.

[91] J. M. Maldacena, *"The Large N limit of superconformal field theories and supergravity,"* Adv. Theor. Math. Phys. **2**, 231-252 (1998); [ArXiv:hep-th/9711200].

[92] S. S. Gubser, I. R. Klebanov and A. M. Polyakov, *"Gauge theory correlators from noncritical string theory,"* Phys. Lett. B **428**, 105-114 (1998); [ArXiv:hep-th/9802109].

[93] E. Witten, *"Anti-de Sitter space and holography,"* Adv. Theor. Math. Phys. **2**, 253-291 (1998); [ArXiv:hep-th/9802150].

[94] S. El-Showk and K. Papadodimas, *"Emergent Spacetime and Holographic CFTs,"* JHEP **10**, 106 (2012); [ArXiv:1101.4163][hep-th].

[95] E. Perlmutter, *"Bounding the Space of Holographic CFTs with Chaos,"* JHEP **10**, 069 (2016); [ArXiv:1602.08272][hep-th].

[96] N. Afkhami-Jeddi, S. Kundu and A. Tajdini, *"A Conformal Collider for Holographic CFTs,"* JHEP **10**, 156 (2018); [ArXiv:1805.07393][hep-th].

[97] E. T. Akhmedov, *"A Remark on the AdS / CFT correspondence and the renormalization group flow,"* Phys. Lett. B **442**, 152-158 (1998); [ArXiv:hep-th/9806217].

[98] D. Z. Freedman, S. S. Gubser, K. Pilch and N. P. Warner, *"Renormalization group flows from holography supersymmetry and a c theorem,"* Adv. Theor. Math. Phys. **3**, 363-417 (1999); [ArXiv:hep-th/9904017].

[99] K. Skenderis and P. K. Townsend, *"Gravitational stability and renormalization group flow,"* Phys. Lett. B **468**, 46-51 (1999); [ArXiv:hep-th/9909070].

[100] J. de Boer, E. P. Verlinde and H. L. Verlinde, *"On the holographic renormalization group,"* JHEP **08**, 003 (2000); [ArXiv:hep-th/9912012].

[101] R. C. Myers and A. Sinha, *"Seeing a c-theorem with holography,"* Phys. Rev. D **82**, 046006 (2010); [ArXiv:1006.1263][hep-th].

[102] T. Faulkner, H. Liu and M. Rangamani, *"Integrating out geometry: Holographic Wilsonian RG and the membrane paradigm,"* JHEP **08**, 051 (2011); [ArXiv:1010.4036][hep-th].

[103] I. Heemskerk and J. Polchinski, *"Holographic and Wilsonian Renormalization Groups,"* JHEP **06**, 031 (2011); [ArXiv:1010.1264][hep-th].

[104] E. Kiritsis, W. Li and F. Nitti, *"Holographic RG flow and the Quantum Effective Action,"* Fortsch. Phys. **62**, 389-454 (2014); [ArXiv:1401.0888][hep-th].

[105] K. Skenderis and B. C. van Rees, *"Real-time gauge/gravity duality,"* Phys. Rev. Lett. **101**, 081601 (2008); [ArXiv:0805.0150][hep-th].

[106] E. Witten, *"Multitrace operators, boundary conditions, and AdS / CFT correspondence,"* [ArXiv:hep-th/0112258].

[107] E. Witten, *"Anti-de Sitter space, thermal phase transition, and confinement in gauge theories,"* Adv. Theor. Math. Phys. **2**, 505-532 (1998); [ArXiv:hep-th/9803131].

[108] G. W. Gibbons and S. W. Hawking, *"Action Integrals and Partition Functions in Quantum Gravity,"* Phys. Rev. D **15**, 2752-2756 (1977).

[109] J. M. Maldacena, *"Wilson loops in large N field theories,"* Phys. Rev. Lett. **80**, 4859-4862 (1998); [ArXiv:hep-th/9803002].

[110] S. J. Rey and J. T. Yee, *"Macroscopic strings as heavy quarks in large N gauge theory and anti-de Sitter supergravity,"* Eur. Phys. J. C **22**, 379-394 (2001); [ArXiv:hep-th/9803001].

[111] A. Karch, E. Katz, D. T. Son and M. A. Stephanov, *"Linear confinement and AdS/QCD,"* Phys. Rev. D **74**, 015005 (2006); [ArXiv:hep-ph/0602229].

[112] K. Kajantie, T. Tahkokallio and J. T. Yee, *"Thermodynamics of AdS/QCD,"* JHEP **01**, 019 (2007); [ArXiv:hep-ph/0609254].

[113] U. Gursoy, E. Kiritsis, L. Mazzanti and F. Nitti, *"Holography and Thermodynamics of 5D Dilaton-gravity,"* JHEP **05**, 033 (2009); [ArXiv:0812.0792][hep-th].

[114] G. T. Horowitz and R. C. Myers, *"The AdS / CFT correspondence and a new positive energy conjecture for general relativity,"* Phys. Rev. D **59**, 026005 (1998); [ArXiv:hep-th/9808079].

[115] N. Itzhaki, J. M. Maldacena, J. Sonnenschein and S. Yankielowicz, *"Supergravity and the large N limit of theories with sixteen supercharges,"* Phys. Rev. D **58**, 046004 (1998); [ArXiv:hep-th/980204].

[116] C. Csaki, H. Ooguri, Y. Oz and J. Terning, *"Glueball mass spectrum from supergravity,"* JHEP **01**, 017 (1999); [ArXiv:hep-th/9806021].

[117] R. C. Brower, S. D. Mathur and C. I. Tan, *"Glueball spectrum for QCD from AdS supergravity duality,"* Nucl. Phys. B **587**, 249-276 (2000); [ArXiv:hep-th/0003115].

[118] H. Ooguri, H. Robins and J. Tannenhauser, *"Glueballs and their Kaluza-Klein cousins,"* Phys. Lett. B **437**, 77-81 (1998); [ArXiv:hep-th/9806171].

[119] A. Karch and E. Katz, *"Adding flavor to AdS / CFT,"* JHEP **06**, 043 (2002); [ArXiv:hep-th/0205236].

[120] T. Sakai and J. Sonnenschein, *"Probing flavored mesons of confining gauge theories by supergravity,"* JHEP **09**, 047 (2003); [ArXiv:hep-th/0305049].

[121] T. Sakai and S. Sugimoto, *"Low energy hadron physics in holographic QCD,"* Prog. Theor. Phys. **113**, 843-882 (2005); [ArXiv:hep-th/0412141].

[122] E. Witten, *"Current Algebra Theorems for the U(1) Goldstone Boson,"* Nucl. Phys. B **156**, 269-283 (1979).

[123] G. Veneziano, *"U(1) Without Instantons,"* Nucl. Phys. B **159**, 213-224 (1979).

[124] T. Sakai and S. Sugimoto, *"More on a holographic dual of QCD,"* Prog. Theor. Phys. **114**, 1083-1118 (2005); [ArXiv:hep-th/0507073].

[125] D. J. Gross and H. Ooguri, *"Aspects of large N gauge theory dynamics as seen by string theory,"* Phys. Rev. D **58**, 106002 (1998); [ArXiv:hep-th/9805129].

[126] E. Witten, *"Baryons and branes in anti-de Sitter space,"* JHEP **07**, 006 (1998); [ArXiv:hep-th/9805112].

[127] E. Witten, *"Baryons in the 1/N Expansion,"* Nucl. Phys. B **160**, 57-115 (1979).

[128] H. Hata, T. Sakai, S. Sugimoto and S. Yamato, *"Baryons from instantons in holographic QCD,"* Prog. Theor. Phys. **117**, 1157 (2007); [ArXiv:hep-th/0701280].

[129] K. Hashimoto, T. Sakai and S. Sugimoto, *"Holographic Baryons: Static Properties and Form Factors from Gauge/String Duality,"* Prog. Theor. Phys. **120**, 1093-1137 (2008); [ArXiv:0806.3122][hep-th].

[130] O. Bergman, S. Seki and J. Sonnenschein, *"Quark mass and condensate in HQCD,"* JHEP **12**, 037 (2007); [ArXiv:0708.2839][hep-th].

[131] A. Dhar and P. Nag, *"Sakai-Sugimoto model, Tachyon Condensation and Chiral symmetry Breaking,"* JHEP **01** (2008), 055; [ArXiv:0708.3233] [hep-th];
"Tachyon condensation and quark mass in modified Sakai-Sugimoto model," Phys. Rev. D **78** (2008), 066021; [ArXiv:0804.4807] [hep-th].

[132] O. Aharony and D. Kutasov, *"Holographic Duals of Long Open Strings,"* Phys. Rev. D **78**, 026005 (2008); [ArXiv:0803.3547][hep-th].

[133] K. Hashimoto, T. Hirayama and D. K. Hong, *"Quark Mass Dependence of Hadron Spectrum in Holographic QCD,"* Phys. Rev. D **81**, 045016 (2010); [ArXiv:0906.0402][hep-th].

[134] E. Kiritsis, *"Dissecting the string theory dual of QCD,"* Fortsch. Phys. **57**, 396-417 (2009); [ArXiv:0901.1772][hep-th].

[135] Y. Kinar, E. Schreiber and J. Sonnenschein, *"Q anti-Q potential from strings in curved space-time: Classical results,"* Nucl. Phys. B **566** (2000), 103-125; [ArXiv:hep-th/9811192].

[136] J. Babington, J. Erdmenger, N. J. Evans, Z. Guralnik and I. Kirsch, *"Chiral symmetry breaking and pions in nonsupersymmetric gauge / gravity duals,"* Phys. Rev. D **69** (2004), 066007; [ArXiv:hep-th/0306018];
M. Kruczenski, D. Mateos, R. C. Myers and D. J. Winters, *"Towards a holographic dual of large N(c) QCD,"* JHEP **05** (2004), 041; [ArXiv:hep-th/0311270].

[137] F. Bigazzi, R. Casero, A. L. Cotrone, E. Kiritsis and A. Paredes, *"Non-critical holography and four-dimensional CFT's with fundamentals,"* JHEP **10**, 012 (2005) [ArXiv:hep-th/0505140].

[138] R. Casero, E. Kiritsis and A. Paredes, *"Chiral symmetry breaking as open string tachyon condensation,"* Nucl.Phys.B **787** (2007), 98-134; [ArXiv:hep-th/0702155].

[139] T. H. R. Skyrme, *"A Unified Field Theory of Mesons and Baryons,"* Nucl. Phys. **31** (1962), 556-569.

[140] E. Witten, *"Global Aspects of Current Algebra,"* Nucl. Phys. B **223**, 422-432 (1983)

[141] O. Kaymakcalan, S. Rajeev and J. Schechter, *"Non-Abelian Anomaly and Vector Meson Decays,"* Phys. Rev. D **30**, 594 (1984)

[142] J. L. Manes, *"Differential Geometric Construction of the Gauged Wess-Zumino Action,"* Nucl. Phys. B **250**, 369-384 (1985)

[143] J. Erlich, E. Katz, D. T. Son and M. A. Stephanov, *"QCD and a holographic model of hadrons,"* Phys. Rev. Lett. **95** (2005) 261602 [ArXiv:hep-ph/0501128];
L. Da Rold and A. Pomarol, *"Chiral symmetry breaking from five dimensional spaces,"* Nucl. Phys. B **721** (2005) 79 [ArXiv:hep-ph/0501218].

[144] J. Polchinski and M. J. Strassler, *"The String dual of a confining four-dimensional gauge theory,"* [ArXiv:hep-th/0003136].

[145] U. Gursoy and E. Kiritsis, *"Exploring improved holographic theories for QCD: Part I,"* JHEP **0802** (2008) 032 [ArXiv:0707.1324][hep-th];
U. Gursoy, E. Kiritsis, F. Nitti, *"Exploring improved holographic theories for QCD: Part II,"* JHEP **0802**, 019 (2008) [ArXiv:0707.1349][hep-th].

[146] U. Gursoy, E. Kiritsis, L. Mazzanti, G. Michalogiorgakis and F. Nitti, *"Improved Holographic QCD,"* Lect. Notes Phys. **828** (2011) 79 [ArXiv:1006.5461][hep-th].

[147] U. Gursoy, E. Kiritsis, L. Mazzanti, F. Nitti, *"Deconfinement and Gluon Plasma Dynamics in Improved Holographic QCD,"* Phys. Rev. Lett. **101** (2008) 181601 [ArXiv:0804.0899][hep-th];
U. Gursoy, E. Kiritsis, L. Mazzanti, F. Nitti, *"Holography and Thermodynamics of 5D Dilaton-gravity,"* JHEP **0905**, 033 (2009) [ArXiv:0812.0792][hep-th];
"Improved Holographic Yang-Mills at Finite Temperature: Comparison with Data," Nucl. Phys. **B820** (2009) 148-177 [ArXiv:0903.2859][hep-th].

[148] M. Panero, *"Thermodynamics of the QCD plasma and the large-N limit,"* Phys. Rev. Lett. **103** (2009) 232001 [ArXiv:0907.3719][hep-lat].

[149] S. S. Gubser and A. Nellore, *"Mimicking the QCD equation of state with a dual black hole,"* [ArXiv:0804.0434] [hep-th];
O. DeWolfe, S. S. Gubser and C. Rosen, *"A holographic critical point,"* Phys. Rev. D **83** (2011) 086005 [ArXiv:1012.1864][hep-th].

[150] M. Järvinen and E. Kiritsis, *"Holographic Models for QCD in the Veneziano Limit,"* JHEP **03** (2012), 002; [ArXiv:1112.1261] [hep-ph].

[151] M. Järvinen, *"Holographic modeling of nuclear matter and neutron stars,"* Eur. Phys. J. C **82**, no.4, 282 (2022) [ArXiv:2110.08281] [hep-ph].

[152] G. Veneziano, *"Large N Expansion in Dual Models,"* Phys. Lett. B **52** (1974), 220-222.

[153] S. Kuperstein and J. Sonnenschein, *"A New Holographic Model of Chiral Symmetry Breaking,"* JHEP **09** (2008), 012; [ArXiv:0807.2897] [hep-th].

[154] R. McNees, R. C. Myers and A. Sinha, *"On quark masses in holographic QCD,"* JHEP **11** (2008), 056; [ArXiv:0807.5127] [hep-th].

[155] N. Jokela, M. Järvinen and S. Nowling, *"Winding effects on brane/anti-brane pairs,"* JHEP **07**, 085 (2009) [ArXiv:0901.0281] [hep-th].

[156] I. Iatrakis, E. Kiritsis and A. Paredes, *"An AdS/QCD model from Sen's tachyon action,"* Phys. Rev. D **81** (2010), 115004; [ArXiv:1003.2377] [hep-ph].

[157] I. Iatrakis, E. Kiritsis and A. Paredes, *"An AdS/QCD model from tachyon condensation: II,"* JHEP **11** (2010), 123; [ArXiv:1010.1364] [hep-ph].

[158] M. Goykhman and A. Parnachev, *"S-parameter, Technimesons, and Phase Transitions in Holographic Tachyon DBI Models,"* Phys. Rev. D **87** (2013) no.2, 026007; [ArXiv:1211.0482] [hep-th].

[159] A. Sen, *"Tachyon dynamics in open string theory,"* Int. J. Mod. Phys. A **20** (2005), 5513-5656; [ArXiv:hep-th/0410103].

[160] M. Järvinen, *"Massive holographic QCD in the Veneziano limit,"* JHEP **07** (2015), 033; [ArXiv:1501.07272] [hep-ph].

[161] D. Arean, I. Iatrakis, M. Järvinen and E. Kiritsis, *"V-QCD: Spectra, the dilaton and the S-parameter,"* Phys. Lett. B **720** (2013), 219-223; [ArXiv:1211.6125] [hep-ph];
"The discontinuities of conformal transitions and mass spectra of V-QCD," JHEP **11**, 068 (2013) [ArXiv:1309.2286][hep-ph];
D. Arean, I. Iatrakis and M. Järvinen, *"The spectrum of (h)QCD in the Veneziano limit,"* PoS **Corfu2012**, 129 (2013) doi:10.22323/1.177.0129 [ArXiv:1305.6294][hep-ph].

[162] A. Amorim, M. S. Costa and M. Järvinen, *"Regge theory in a holographic dual of QCD in the Veneziano limit,"* JHEP **07**, 065 (2021); [ArXiv:2102.11296][hep-ph].

[163] T. Alho, M. Järvinen, K. Kajantie, E. Kiritsis and K. Tuominen, *"On finite-temperature holographic QCD in the Veneziano limit,"* JHEP **01** (2013), 093; [ArXiv:1210.4516] [hep-ph];
"Quantum and stringy corrections to the equation of state of holographic QCD matter and the nature of the chiral transition," Phys. Rev. D **91** (2015) no.5, 055017; [ArXiv:1501.06379] [hep-ph].

[164] T. Alho, M. Järvinen, K. Kajantie, E. Kiritsis, C. Rosen and K. Tuominen, *"A holographic model for QCD in the Veneziano limit at finite temperature and density,"* JHEP **04** (2014), 124; [erratum: JHEP **02** (2015), 033] [ArXiv:1312.5199] [hep-ph].

[165] N. Jokela, M. Järvinen and J. Remes, *"Holographic QCD in the Veneziano limit and neutron stars,"* JHEP **03**, 041 (2019); [ArXiv:1809.07770][hep-ph].

[166] D. Arean, I. Iatrakis, M. Järvinen and E. Kiritsis, *"CP-odd sector and θ dynamics in holographic QCD,"* Phys. Rev. D **96** (2017) no.2, 026001; [ArXiv:1609.08922] [hep-ph].

[167] J. Bijnens, L. Girlanda and P. Talavera, *"The Anomalous chiral Lagrangian of order p^6,"* Eur. Phys. J. C **23** (2002), 539-544; [ArXiv:hep-ph/0110400];
T. Ebertshauser, H. W. Fearing and S. Scherer, *"The Anomalous chiral perturbation theory meson Lagrangian to order p^6 revisited,"* Phys. Rev. D **65** (2002), 054033; [ArXiv:hep-ph/0110261].

[168] K. Kampf and J. Novotny, *"Resonance saturation in the odd-intrinsic parity sector of low-energy QCD,"* Phys. Rev. D **84** (2011), 014036; [ArXiv:1104.3137] [hep-ph].

[169] J. Bijnens, N. Hermansson-Truedsson and S. Wang, *"The order p^8 mesonic chiral Lagrangian,"* JHEP **01** (2019), 102; [ArXiv:1810.06834][hep-ph];
J. Bijnens, K. Kampf and S. Lanz, *"Leading logarithms in the anomalous sector of two-flavour QCD,"* Nucl. Phys. B **860** (2012), 245-266; [ArXiv:1201.2608][hep-ph].

[170] P. H. C. Lau and S. Sugimoto, *"Chern-Simons five-form and holographic baryons,"* Phys. Rev. D **95** (2017) no.12, 126007; [ArXiv:1612.09503] [hep-th]

[171] D. K. Hong, M. Rho, H. U. Yee and P. Yi, *"Chiral Dynamics of Baryons from String Theory,"* Phys. Rev. D **76** (2007), 061901; [ArXiv:hep-th/0701276].

[172] A. Pomarol and A. Wulzer, *"Stable skyrmions from extra dimensions,"* JHEP **03** (2008), 051; [ArXiv:0712.3276] [hep-th].

[173] A. Pomarol and A. Wulzer, *"Baryon Physics in Holographic QCD,"* Nucl. Phys. B **809** (2009), 347-361; [ArXiv:0807.0316] [hep-ph].

[174] T. Ishii, M. Järvinen and G. Nijs, *"Cool baryon and quark matter in holographic QCD",* JHEP **07** (2019), 003; [ArXiv:1903.06169] [hep-ph].

[175] A. Cherman and T. Ishii, *"Long-distance properties of baryons in the Sakai-Sugimoto model,"* Phys. Rev. D **86**, 045011 (2012) [ArXiv:1109.4665][hep-th].

[176] G. S. Adkins, C. R. Nappi and E. Witten, *"Static Properties of Nucleons in the Skyrme Model,"* Nucl. Phys. B **228** (1983), 552

[177] G. Panico and A. Wulzer, *"Nucleon Form Factors from 5D Skyrmions,"* Nucl. Phys. A **825** (2009), 91-114 [ArXiv:0811.2211][hep-ph].

[178] A. Gorsky, S. B. Gudnason and A. Krikun, *"Baryon and chiral symmetry breaking in holographic QCD,"* Phys. Rev. D **91** (2015) no.12, 126008 [ArXiv:1503.04820][hep-th].

[179] N. S. Manton, *"Scaling Identities for Solitons beyond Derrick's Theorem,"* J. Math. Phys. **50** (2009), 032901 [ArXiv:0809.2891][hep-th].

[180] S. K. Domokos, C. Hoyos and J. Sonnenschein, *"Deformation Constraints on Solitons and D-branes,"* JHEP **10** (2013), 003 [ArXiv:1306.0789][hep-th].

[181] C. Charmousis, B. Gouteraux, B. S. Kim, E. Kiritsis and R. Meyer, *"Effective Holographic Theories for low-temperature condensed matter systems,"* JHEP **11** (2010), 151 [ArXiv:1005.4690][hep-th].

[182] C. Kennedy and A. Wilkins, *"Ramond-Ramond couplings on Brane - anti-Brane systems,"* Phys. Lett. B **464**, 206-212 (1999) [ArXiv:hep-th/9905195].

[183] P. Kraus and F. Larsen, *"Boundary string field theory of the D anti-D system,"* Phys. Rev. D **63**, 106004 (2001) [ArXiv:hep-th/0012198].

[184] T. Takayanagi, S. Terashima and T. Uesugi, *"Brane - anti-brane action from boundary string field theory,"* JHEP **03**, 019 (2001) [ArXiv:hep-th/0012210].

[185] D. T. Son and N. Yamamoto, *"Holography and Anomaly Matching for Resonances,"* [ArXiv:1010.0718] [hep-ph].

[186] I. Iatrakis and E. Kiritsis, *"Vector-axial vector correlators in weak electric field and the holographic dynamics of the chiral condensate,"* JHEP **02** (2012), 064; [ArXiv:1109.1282][hep-ph].

[187] S. Nakamura, H. Ooguri and C. S. Park, *"Gravity Dual of Spatially Modulated Phase,"* Phys. Rev. D **81** (2010), 044018; [ArXiv:0911.0679] [hep-th].

[188] A. Donos and J. P. Gauntlett, *"Holographic striped phases,"* JHEP **08** (2011), 140; [ArXiv:1106.2004] [hep-th].

[189] O. Bergman, N. Jokela, G. Lifschytz and M. Lippert, *"Striped instability of a holographic Fermi-like liquid,"* JHEP **10**, 034 (2011) [ArXiv:1106.3883] [hep-th].

[190] N. Jokela, M. Järvinen and M. Lippert, *"Fluctuations and instabilities of a holographic metal,"* JHEP **02**, 007 (2013) [ArXiv:1211.1381] [hep-th].

[191] H. Kanno and S. Sugimoto, *"Anomaly and superconnection,"* PTEP **2022** (2022) no.1, 013B02; [ArXiv:2106.01591] [hep-th].

[192] J. Sonnenschein, *"Holography Inspired Stringy Hadrons,"* Prog. Part. Nucl. Phys. **92** (2017), 1-49; [ArXiv:1602.00704] [hep-th].

[193] K. Y. Kim, S. J. Sin and I. Zahed, "Dense hadronic matter in holographic QCD," J. Korean Phys. Soc. **63**, 1515-1529 (2013) [ArXiv:hep-th/0608046];
K. Y. Kim, S. J. Sin and I. Zahed, "The Chiral Model of Sakai-Sugimoto at Finite Baryon Density," JHEP **01**, 002 (2008) [ArXiv:0708.1469][hep-th].

[194] H. Hata and M. Murata, *"Baryons and the Chern-Simons term in holographic QCD with three flavors,"* Prog. Theor. Phys. **119** (2008), 461-490 doi:10.1143/PTP.119.461 [ArXiv:0710.2579][hep-th].

[195] S. Bolognesi and P. Sutcliffe, "The Sakai-Sugimoto soliton," JHEP **01**, 078 (2014) [ArXiv:1309.1396][hep-th].

[196] A. Gorsky and A. Krikun, "Baryon as dyonic instanton," Phys. Rev. D **86**, 126005 (2012) [ArXiv:1206.4515][hep-th];
A. Gorsky, P. N. Kopnin and A. Krikun, "Baryon as dyonic instanton-II. Baryon mass versus chiral condensate," Phys. Rev. D **89**, no.2, 026012 (2014) [ArXiv:1309.3362][hep-th].

[197] A. Ballon-Bayona, H. Boschi-Filho, L. A. H. Mamani, A. S. Miranda and V. T. Zanchin, *"Effective holographic models for QCD: glueball spectrum and trace anomaly,"* Phys. Rev. D **97**, no.4, 046001 (2018) [ArXiv:1708.08968][hep-th].

[198] A. Ballon-Bayona, L. A. H. Mamani, A. S. Miranda and V. T. Zanchin, *"Effective holographic models for QCD: Thermodynamics and viscosity coefficients,"* Phys. Rev. D **104**, no.4, 046013 (2021) [ArXiv:2103.14188][hep-th].

[199] G. Veneziano, *"Some Aspects of a Unified Approach to Gauge, Dual and Gribov Theories,"* Nucl. Phys. B **117**, 519-545 (1976).

[200] S. S. Gubser, *"Curvature singularities: The Good, the bad, and the naked,"* Adv. Theor. Math. Phys. **4**, 679-745 (2000) [ArXiv:hep-th/0002160].

[201] M. Shifman and A. Vainshtein, *"Highly Excited Mesons, Linear Regge Trajectories and the Pattern of the Chiral Symmetry Realization,"* Phys. Rev. D **77** (2008), 034002 [ArXiv:0710.0863] [hep-ph].

[202] B. Lucini, M. Teper and U. Wenger, *"Glueballs and k-strings in SU(N) gauge theories: Calculations with improved operators,"* JHEP **06**, 012 (2004) [ArXiv:hep-lat/0404008].

[203] B. Lucini, M. Teper and U. Wenger, *"Properties of the deconfining phase transition in SU(N) gauge theories,"* JHEP **02**, 033 (2005) [ArXiv:hep-lat/0502003].

[204] A. Athenodorou and M. Teper, *"SU(N) gauge theories in 3+1 dimensions: glueball spectrum, string tensions and topology,"* JHEP **12**, 082 (2021) [ArXiv:2106.00364][hep-lat].

[205] S. Borsanyi, Z. Fodor, S. D. Katz, S. Krieg, C. Ratti and K. Szabo, *"Fluctuations of conserved charges at finite temperature from lattice QCD,"* JHEP **01**, 138 (2012) [ArXiv:1112.4416][hep-lat].

[206] R. L. Workman *et al.* [Particle Data Group], *"Review of Particle Physics,"* PTEP **2022**, 083C01 (2022).

[207] U. Gursoy, "Continuous Hawking-Page transitions in Einstein-scalar gravity," JHEP **01**, 086 (2011) [ArXiv:1007.0500] [hep-th].

[208] T. Demircik, C. Ecker and M. Järvinen, *"Dense and Hot QCD at Strong Coupling,"* Phys. Rev. X **12**, no.4, 041012 (2022) [ArXiv:2112.12157][hep-ph].

[209] Anderson, D., Tannehill, J.C., Pletcher, R.H., Munipalli, R., & Shankar, V. (2020). *"Computational Fluid Mechanics and Heat Transfer"*; (4th ed.). CRC Press.

[210] H. T. Janka, F. Hanke, L. Huedepohl, A. Marek, B. Mueller and M. Obergaulinger, *"Core-Collapse Supernovae: Reflections and Directions,"* PTEP **2012**, 01A309 (2012) [ArXiv:1211.1378][astro-ph.SR].

[211] A. Burrows and D. Vartanyan, *"Core-Collapse Supernova Explosion Theory,"* Nature **589**, no.7840, 29-39 (2021); [ArXiv:2009.14157][astro-ph.SR].

[212] A. Y. Potekhin, J. A. Pons and D. Page, *"Neutron stars - cooling and transport,"* Space Sci. Rev. **191**, no.1-4, 239-291 (2015); [ArXiv:1507.06186][astro-ph.HE].

[213] B. P. Abbott *et al.* [LIGO Scientific, Virgo, Fermi GBM, INTEGRAL, IceCube, AstroSat Cadmium Zinc Telluride Imager Team, IPN, Insight-Hxmt, ANTARES, Swift, AGILE Team, 1M2H Team, Dark Energy Camera GW-EM, DES, DLT40, GRAWITA, Fermi-LAT, ATCA, ASKAP, Las Cumbres Observatory Group, OzGrav, DWF (Deeper Wider Faster Program), AST3, CAASTRO, VINROUGE, MASTER, J-GEM, GROWTH, JAGWAR, CaltechNRAO, TTU-NRAO, NuSTAR, Pan-STARRS, MAXI Team, TZAC Consortium, KU, Nordic Optical Telescope, ePESSTO, GROND, Texas Tech University, SALT Group, TOROS, BOOTES, MWA, CALET, IKI-GW Follow-up, H.E.S.S., LOFAR, LWA, HAWC, Pierre Auger, ALMA, Euro VLBI Team, Pi of Sky, Chandra Team at McGill University, DFN, ATLAS Telescopes, High Time Resolution Universe Survey, RIMAS, RATIR and SKA South Africa/MeerKAT], *"Multi-messenger Observations of a Binary Neutron Star Merger,"* Astrophys. J. Lett. **848**, no.2, L12 (2017) [ArXiv:1710.05833][astro-ph.HE].

[214] Y. Sekiguchi, K. Kiuchi, K. Kyutoku and M. Shibata, *"Gravitational waves and neutrino emission from the merger of binary neutron stars,"* Phys. Rev. Lett. **107**, 051102 (2011) [ArXiv:1105.2125][gr-qc].

[215] F. Foucart, E. O'Connor, L. Roberts, L. E. Kidder, H. P. Pfeiffer and M. A. Scheel, *"Impact of an improved neutrino energy estimate on outflows in neutron star merger simulations,"* Phys. Rev. D **94**, no.12, 123016 (2016) [ArXiv:1607.07450][astro-ph.HE].

[216] F. Foucart, *"Neutrino transport in general relativistic neutron star merger simulations,"* [ArXiv:2209.02538][astro-ph.HE].

[217] R. Gill, A. Nathanail and L. Rezzolla, *"When Did the Remnant of GW170817 Collapse to a Black Hole?,"* Astrophys. J. **876**, no.2, 139 (2019); [ArXiv:1901.04138][astro-ph.HE].

[218] M. Cusinato, F. M. Guercilena, A. Perego, D. Logoteta, D. Radice, S. Bernuzzi and S. Ansoldi, *"Neutrino emission from binary neutron star mergers: characterizing light curves and mean energies,"* Eur. Phys. J. A **58**, 99 (2022) [ArXiv:2111.13005][astro-ph.HE].

[219] D. G. Yakovlev, A. D. Kaminker, O. Y. Gnedin and P. Haensel, *"Neutrino emission from neutron stars,"* Phys. Rept. **354**, 1 (2001) [ArXiv:astro-ph/0012122].

[220] N. Chamel and P. Haensel, *"Physics of Neutron Star Crusts,"* Living Rev. Rel. **11**, 10 (2008) [ArXiv:0812.3955][astro-ph].

[221] A. Schmitt and P. Shternin, *"Reaction rates and transport in neutron stars,"* Astrophys. Space Sci. Libr. **457**, 455-574 (2018) [ArXiv:1711.06520][astro-ph.HE].

[222] A. Sedrakian, *"The Physics of dense hadronic matter and compact stars,"* Prog. Part. Nucl. Phys. **58**, 168-246 (2007); [ArXiv:nucl-th/0601086].

[223] S. Reddy, M. Prakash and J. M. Lattimer, *"Neutrino interactions in hot and dense matter,"* Phys. Rev. D **58**, 013009 (1998); [ArXiv:astro-ph/9710115].

[224] A. Burrows and R. F. Sawyer, *"The Effects of correlations on neutrino opacities in nuclear matter,"* Phys. Rev. C **58**, 554-571 (1998); [ArXiv:astro-ph/9801082].

[225] S. Reddy, M. Prakash, J. M. Lattimer and J. A. Pons, *"Effects of strong and electromagnetic correlations on neutrino interactions in dense matter,"* Phys. Rev. C **59**, 2888-2918 (1999); [ArXiv:astro-ph/9811294].

[226] J. Margueron, I. Vidana and I. Bombaci, *"Microscopic calculation of neutrino mean free path inside hot neutron matter,"* Phys. Rev. C **68**, 055806 (2003) [ArXiv:nucl-th/0307073].

[227] J. Margueron, J. Navarro and N. Van Giai, *"Effects of spin-orbit interaction on nuclear response and neutrino mean free path,"* Phys. Rev. C **74**, 015805 (2006) [ArXiv:nucl-th/0604019].

[228] S. W. Bruenn, *"Stellar core collapse: Numerical model and infall epoch,"* Astrophys. J. Suppl. **58**, 771-841 (1985)

[229] N. Iwamoto, *"QUARK BETA DECAY AND THE COOLING OF NEUTRON STARS,"* Phys. Rev. Lett. **44**, 1637-1640 (1980)

[230] A. Burrows, *"BETA DECAY IN QUARK STARS,"* Phys. Rev. Lett. **44**, 1640-1643 (1980)

[231] N. Iwamoto, *"Neutrino emissivities and mean free paths of degenerate quark matter,"* Annals Phys. **141**, 1-49 (1982)

[232] Z. G. Dai, Q. H. Peng and T. Lu, *"The conversion from two - flavor to three - flavor quark matter in a supernova core,"* Astrophys. J. **440**, 815 (1995)

[233] T. Schäfer and K. Schwenzer, *"Neutrino emission from ungapped quark matter,"* Phys. Rev. D **70**, 114037 (2004); [ArXiv:astro-ph/0410395].

[234] J. N. Bahcall and R. A. Wolf, *"Neutron Stars,"* Phys. Rev. Lett. **14**, 343-346 (1965)

[235] J. N. Bahcall and R. A. Wolf, *"Neutron Stars. 2. Neutrino-Cooling and Observability,"* Phys. Rev. **140**, B1452-B1466 (1965)

[236] O. Maxwell, G. E. Brown, D. K. Campbell, R. F. Dashen and J. T. Manassah, *"Beta decay of pion condensates as a cooling mechanism for neutron stars,"* Astrophys. J. **216**, 77-85 (1977)

[237] G. E. Brown, K. Kubodera, D. Page and P. Pizzochero, *"Strangeness Condensation and Cooling of Neutron Stars,"* Phys. Rev. D **37**, 2042-2046 (1988)

[238] V. Thorsson, M. Prakash and J. M. Lattimer, *"Composition, structure and evolution of neutron stars with kaon condensates,"* Nucl. Phys. A **572**, 693-731 (1994) [erratum: Nucl. Phys. A **574**, 851 (1994)] [ArXiv:nucl-th/9305006].

[239] E. Flowers, M. Ruderman and P. Sutherland, *"Neutrino pair emission from finite-temperature neutron superfluid and the cooling of young neutron stars,"* Astrophys. J. **205**, 541 (1976)

[240] A. W. Steiner and S. Reddy, *"Superfluid Response and the Neutrino Emissivity of Neutron Matter,"* Phys. Rev. C **79**, 015802 (2009) [ArXiv:0804.0593][nucl-th].

[241] S. Reddy, M. Sadzikowski and M. Tachibana, *"Neutrino rates in color flavor locked quark matter,"* Nucl. Phys. A **714**, 337-351 (2003) [ArXiv:nucl-th/0203011].

[242] P. Jaikumar, M. Prakash and T. Schäfer, *"Neutrino emission from Goldstone modes in dense quark matter,"* Phys. Rev. D **66**, 063003 (2002) [ArXiv:astro-ph/0203088].

[243] P. Jaikumar, C. D. Roberts and A. Sedrakian, *"Direct Urca neutrino rate in colour superconducting quark matter,"* Phys. Rev. C **73**, 042801 (2006) [ArXiv:nucl-th/0509093].

[244] I. Tews, J. Margueron and S. Reddy, *"Critical examination of constraints on the equation of state of dense matter obtained from GW170817,"* Phys. Rev. C **98**, no.4, 045804 (2018); [ArXiv:1804.02783][nucl-th].

[245] A. Kurkela, P. Romatschke and A. Vuorinen, *"Cold Quark Matter,"* Phys. Rev. D **81**, 105021 (2010); [ArXiv:0912.1856][hep-ph].

[246] E. Annala, T. Gorda, E. Katerini, A. Kurkela, J. Nättilä, V. Paschalidis and A. Vuorinen, *"Multimessenger Constraints for Ultradense Matter,"* Phys. Rev. X **12**, no.1, 011058 (2022); [ArXiv:2105.05132][astro-ph.HE].

[247] S. Altiparmak, C. Ecker and L. Rezzolla, *"On the Sound Speed in Neutron Stars,"* Astrophys. J. Lett. **939**, no.2, L34 (2022); [ArXiv:2203.14974][astro-ph.HE].

[248] M. P. Heller, R. A. Janik and P. Witaszczyk, *"The characteristics of thermalization of boost-invariant plasma from holography,"* Phys. Rev. Lett. **108**, 201602 (2012); [ArXiv:1103.3452][hep-th].

[249] M. P. Heller, R. A. Janik and P. Witaszczyk, *"Hydrodynamic Gradient Expansion in Gauge Theory Plasmas,"* Phys. Rev. Lett. **110**, no.21, 211602 (2013); [ArXiv:1302.0697][hep-th].

[250] G. Policastro, D. T. Son and A. O. Starinets, *"The Shear viscosity of strongly coupled N=4 supersymmetric Yang-Mills plasma,"* Phys. Rev. Lett. **87**, 081601 (2001) [ArXiv:hep-th/0104066].

[251] P. Kovtun, D. T. Son and A. O. Starinets, *"Viscosity in strongly interacting quantum field theories from black hole physics,"* Phys. Rev. Lett. **94**, 111601 (2005); [ArXiv:hep-th/0405231].

[252] S. S. Gubser, A. Nellore, S. S. Pufu and F. D. Rocha, *"Thermodynamics and bulk viscosity of approximate black hole duals to finite temperature quantum chromodynamics,"* Phys. Rev. Lett. **101**, 131601 (2008); [ArXiv:0804.1950][hep-th].

[253] S. S. Gubser, S. S. Pufu and F. D. Rocha, *"Bulk viscosity of strongly coupled plasmas with holographic duals,"* JHEP **08**, 085 (2008); [ArXiv:0806.0407][hep-th].

[254] U. Gursoy, E. Kiritsis, G. Michalogiorgakis and F. Nitti, *"Thermal Transport and Drag Force in Improved Holographic QCD,"* JHEP **12**, 056 (2009); [ArXiv:0906.1890][hep-ph].

[255] U. Gursoy, E. Kiritsis, L. Mazzanti and F. Nitti, *"Langevin diffusion of heavy quarks in non-conformal holographic backgrounds,"* JHEP **12**, 088 (2010); [ArXiv:1006.3261][hep-th].

[256] C. Eling and Y. Oz, *"A Novel Formula for Bulk Viscosity from the Null Horizon Focusing Equation,"* JHEP **06**, 007 (2011); [ArXiv:1103.1657][hep-th].

[257] I. Iatrakis and I. Zahed, *"Spectral Functions in V-QCD with Matter: Masses, Susceptibilities, Diffusion and Conductivity,"* JHEP **04**, 080 (2015); [ArXiv:1410.8540][hep-th].

[258] C. Hoyos, N. Jokela and A. Vuorinen, *"Holographic approach to compact stars and their binary mergers,"* Prog. Part. Nucl. Phys. **126**, 103972 (2022); [ArXiv:2112.08422][hep-th].

[259] K. Ghoroku, K. Kashiwa, Y. Nakano, M. Tachibana and F. Toyoda, *"Stiff equation of state for a holographic nuclear matter as instanton gas,"* Phys. Rev. D **104**, no.12, 126002 (2021); [ArXiv:2107.14450][hep-th].

[260] N. Kovensky, A. Poole and A. Schmitt, *"Building a realistic neutron star from holography,"* Phys. Rev. D **105**, no.3, 034022 (2022); [ArXiv:2111.03374][hep-ph].

[261] L. Bartolini, S. B. Gudnason, J. Leutgeb and A. Rebhan, *"Neutron stars and phase diagram in a hard-wall AdS/QCD model,"* Phys. Rev. D **105**, no.12, 126014 (2022); [ArXiv:2202.12845][hep-th].

[262] C. Hoyos, D. Rodríguez Fernández, N. Jokela and A. Vuorinen, *"Holographic quark matter and neutron stars,"* Phys. Rev. Lett. **117**, no.3, 032501 (2016); [ArXiv:1603.02943][hep-ph].

[263] K. Bitaghsir Fadafan, J. Cruz Rojas and N. Evans, *"Deconfined, Massive Quark Phase at High Density and Compact Stars: A Holographic Study,"* Phys. Rev. D **101**, no.12, 126005 (2020); [ArXiv:1911.12705][hep-ph].

[264] L. A. H. Mamani, C. V. Flores and V. T. Zanchin, *"Phase diagram and compact stars in a holographic QCD model,"* Phys. Rev. D **102**, no.6, 066006 (2020); [ArXiv:2006.09401][hep-th].

[265] K. Ghoroku, K. Kashiwa, Y. Nakano, M. Tachibana and F. Toyoda, *"Color superconductivity in a holographic model,"* Phys. Rev. D **99**, no.10, 106011 (2019); [ArXiv:1902.01093][hep-th].

[266] N. Kovensky and A. Schmitt, *"Holographic quarkyonic matter,"* JHEP **09**, 112 (2020); [ArXiv:2006.13739][hep-th].

[267] S. Pinkanjanarod and P. Burikham, *"Massive neutron stars with holographic multi-quark cores,"* Eur. Phys. J. C **81**, no.8, 705 (2021); [ArXiv:2007.10615][nucl-th].

[268] K. Bitaghsir Fadafan, J. Cruz Rojas and N. Evans, *"Holographic quark matter with colour superconductivity and a stiff equation of state for compact stars,"* Phys. Rev. D **103**, no.2, 026012 (2021); [ArXiv:2009.14079][hep-ph].

[269] N. Kovensky, A. Poole and A. Schmitt, *"Phases of cold holographic QCD: baryons, pions and rho mesons,"* [ArXiv:2302.10675][hep-ph].

[270] C. Hoyos, N. Jokela, M. Jarvinen, J. G. Subils, J. Tarrio and A. Vuorinen, *"Transport in strongly coupled quark matter,"* Phys. Rev. Lett. **125**, 241601 (2020); [ArXiv:2005.14205][hep-th].

[271] C. Hoyos, N. Jokela, M. Järvinen, J. G. Subils, J. Tarrio and A. Vuorinen, *"Holographic approach to transport in dense QCD matter,"* Phys. Rev. D **105**, no.6, 066014 (2022); [ArXiv:2109.12122][hep-th].

[272] H. W. Lin, J. Maldacena, L. Rozenberg and J. Shan, *"Holography for people with no time,"* [ArXiv:2207.00407] [hep-th]. H. W. Lin, J. Maldacena, L. Rozenberg and J. Shan, *"Looking at supersymmetric black holes for a very long time,"* [ArXiv:2207.00408] [hep-th].

[273] D. Facoetti, G. Biroli, J. Kurchan and D. R. Reichman, *"Classical Glasses, Black Holes, and Strange Quantum Liquids,"* Phys. Rev. B **100** (2019) no.20, 205108; [ArXiv:1906.09228][hep-th].

[274] M. Oertel, A. Pascal, M. Mancini and J. Novak, *"Improved neutrino-nucleon interactions in dense and hot matter for numerical simulations,"* Phys. Rev. C **102** (2020) no.3, 035802; [ArXiv:2003.02152][astro-ph.HE].

[275] J. Erdmenger, N. Evans, I. Kirsch and E. Threlfall, *"Mesons in Gauge/Gravity Duals - A Review,"* Eur. Phys. J. A **35** (2008), 81-133 [ArXiv:0711.4467/[hep-th]].

[276] C. Nunez, A. Paredes and A. V. Ramallo, *"Unquenched Flavor in the Gauge/Gravity Correspondence,"* Adv. High Energy Phys. **2010** (2010), 196714; [ArXiv:1002.1088][hep-th].

[277] R. Bollig, H. T. Janka, A. Lohs, G. Martinez-Pinedo, C. J. Horowitz and T. Melson, *"Muon Creation in Supernova Matter Facilitates Neutrino-driven Explosions,"* Phys. Rev. Lett. **119**, no.24, 242702 (2017); [ArXiv:1706.04630][astro-ph.HE].

[278] E. Loffredo, A. Perego, D. Logoteta and M. Branchesi, *"Muons in the aftermath of neutron star mergers and their impact on trapped neutrinos,"* Astron. Astrophys. **672**, A124 (2023); [ArXiv:2209.04458][astro-ph.HE].

[279] A. Chamblin, R. Emparan, C. V. Johnson and R. C. Myers, *"Charged AdS black holes and catastrophic holography,"* Phys. Rev. D **60** (1999), 064018; [ArXiv:hep-th/9902170].

[280] A. Chamblin, R. Emparan, C. V. Johnson and R. C. Myers, *"Holography, thermodynamics and fluctuations of charged AdS black holes,"* Phys. Rev. D **60** (1999), 104026; [ArXiv:hep-th/9904197].

[281] S. S. Gubser, *"Colorful horizons with charge in anti-de Sitter space,"* Phys. Rev. Lett. **101**, 191601 (2008); [ArXiv:0803.3483][hep-th].

[282] S. S. Gubser and S. S. Pufu, *"The Gravity dual of a p-wave superconductor,"* JHEP **11**, 033 (2008); [ArXiv:0805.2960][hep-th].

[283] A. Y. Potekhin, A. F. Fantina, N. Chamel, J. M. Pearson and S. Goriely, *"Analytical representations of unified equations of state for neutron-star matter,"* Astron. Astrophys. **560**, A48 (2013); [ArXiv:1310.0049][astro-ph.SR].

[284] S. Goriely, N. Chamel and J. M. Pearson, *"Further explorations of Skyrme-Hartree-Fock-Bogoliubov mass formulas. XII: Stiffness and stability of neutron-star matter,"* Phys. Rev. C **82**, 035804 (2010); [ArXiv:1009.3840][nucl-th].

[285] W.R. Yueh and J.R. Buchler, *"Neutrino transport in supernova models: S/N method,"* Astrophysical Journal, Part 1, vol. **217**, Oct. 15, 1977, p. 565-577.

[286] D. T. Son and M. A. Stephanov, *"QCD at finite isospin density: From pion to quark - anti-quark condensation,"* Phys. Atom. Nucl. **64** (2001), 834-842; [ArXiv:hep-ph/0011365].

[287] O. Aharony, K. Peeters, J. Sonnenschein and M. Zamaklar, *"Rho meson condensation at finite isospin chemical potential in a holographic model for QCD,"* JHEP **02** (2008), 071; [ArXiv:0709.3948][hep-th].

[288] Y. Hidaka, S. Pu and D. L. Yang, *"Relativistic Chiral Kinetic Theory from Quantum Field Theories,"* Phys. Rev. D **95** (2017) no.9, 091901; [ArXiv:1612.04630] [hep-th];

[289] N. Yamamoto and D. L. Yang, *"Chiral kinetic theory with self-energy corrections and neutrino spin Hall effect,"* [ArXiv:2308.08257][hep-ph].

[290] K. Landsteiner, E. Megias, L. Melgar and F. Pena-Benitez, *"Holographic Gravitational Anomaly and Chiral Vortical Effect,"* JHEP **09**, 121 (2011); [ArXiv:1107.0368/[hep-th]].

[291] J. Erdmenger, M. Haack, M. Kaminski and A. Yarom, *"Fluid dynamics of R-charged black holes,"* JHEP **01**, 055 (2009); [ArXiv:0809.2488/[hep-th]].

[292] D. T. Son and P. Surowka, *"Hydrodynamics with Triangle Anomalies,"* Phys. Rev. Lett. **103**, 191601 (2009); [ArXiv:0906.5044][hep-th].

[293] M. Kruczenski, D. Mateos, R. C. Myers and D. J. Winters, *"Meson spectroscopy in AdS / CFT with flavor,"* JHEP **07**, 049 (2003); [ArXiv:hep-th/0304032].

[294] D. Mateos, R. C. Myers and R. M. Thomson, *"Thermodynamics of the brane,"* JHEP **05**, 067 (2007); [ArXiv:hep-th/0701132].

[295] A. Sen, *"Dirac-Born-Infeld action on the tachyon kink and vortex,"* Phys. Rev. D **68**, 066008 (2003); [ArXiv:hep-th/0303057].

[296] L. Kadanoff and G. Baym, (1962), *"Quantum Statistical Mechanics,"* W.A. Benjamin Inc. , New York.

[297] D. T. Son and A. O. Starinets, *"Minkowski space correlators in AdS / CFT correspondence: Recipe and applications,"* JHEP **09**, 042 (2002); [ArXiv:hep-th/0205051].

[298] P. Kovtun, *"Lectures on hydrodynamic fluctuations in relativistic theories,"* J. Phys. A **45**, 473001 (2012); [ArXiv:1205.5040][hep-th].

[299] R. A. Davison and A. Parnachev, *"Hydrodynamics of cold holographic matter,"* JHEP **06**, 100 (2013); [ArXiv:1303.6334][hep-th].

[300] D. Arean, R. A. Davison, B. Goutéraux and K. Suzuki, *"Hydrodynamic Diffusion and Its Breakdown near AdS2 Quantum Critical Points,"* Phys. Rev. X **11** (2021) no.3, 031024. [ArXiv:2011.12301][hep-th].

[301] U. Gürsoy, M. Järvinen, G. Policastro and N. Zinnato, *"Analytic long-lived modes in charged critical plasma,"* JHEP **06**, 018 (2022) [ArXiv:2112.04296][hep-th].

[302] N. Iqbal and H. Liu, *"Universality of the hydrodynamic limit in AdS/CFT and the membrane paradigm,"* Phys. Rev. D **79**, 025023 (2009); [ArXiv:0809.3808][hep-th].